Constraining Orogenic Volcanism in the Western Alps Using Volcaniclastic Deposits from Foreland Basins

Chenhang Lyu (吕晨航)

School of Earth and Environmental Sciences

Cardiff University

Submitted in partial fulfilment of the requirements for the degree of *Doctor of Philosophy*

March 2023

Abstract

This study aims at reconstructing the source-to-sink system of Tertiary volcaniclastic deposits preserved in Alpine foreland basin. The mafic-intermediate syn-orogenic Alpine magmatism is recorded in volcaniclastic deposits in the north Alpine foreland basin (NAFB) in Switzerland and SE France, and in Periadriatic intrusions in N Italy ca. 30 - 40 Ma. The volcaniclastic deposits mainly include volcaniclastic flysch turbidites (regionally named Taveyannaz sandstone and its equivalents varying along the arc), igneous pebbles in conglomerates, block-and-ash flow deposits, primary fallout deposits and lavas. This study focused on (i) the Taveyannaz sandstones in Glarus, Taveyannaz, Aravis and Champsaur, (ii) igneous pebbles in Champsaur and Clumanc, (iii) block-and-ash flow deposits (i.e., andesite breccia) and tuffs in St. Antonin and La Vanade, and (iv) andesitic lavas in Biella. The methods use field observations, quantitative petrographic analysis (grain counting), whole-rock geochemistry (ICP-OES+ICP-MS), clinopyroxene and amphibole geochemistry (SEM-EDS+LA-ICP-MS). This was combined with a new discrimination method for clinopyroxenes and amphiboles based on Principle Component Analysis (PCA) to characterise the compositional variability of volcaniclastic components in foreland basins, to ultimately determine their possible sources in the Alpine orogen.

New integrated results reveal two types of volcano-sedimentary environments and igneous affinities, which correspond to the Alpine and Provence volcanic provinces. The volcaniclastic deposits of the Alpine volcanic province (Glarus, W Switzerland, Aravis, and Clumanc) are very likely secondary deposits, whereas the volcaniclastic deposits of Provence volcanic province (Champsaur, Saint Antonin, and La Vanade) are proximal, with common primary deposits.

PCA results on clinopyroxenes show high compositional variability of the mafic volcanic components preserved in the samples from Glarus, La Tièche, Taveyannaz and Aravis, with distinct compositions and sources for each single locality. Therefore, the provenance of the volcanic components seems more complex than that proposed in new sediment provenance models based on U-Pb and isotope composition of detrital zircons, which have linked the volcaniclastic deposits only to Adamello and Biella sources. In addition, the quenched amoeboid andesitic clasts were identified in previous and new data from Glarus and Flaine. This is a very significant observation that clearly indicates very limited transport of materials from local submarine effusive

volcanism, thus suggesting previously undocumented proximal volcanic activity in the foreland basins.

Whole-rock and mineral geochemistry results allow to refine the extension of the Provence magmatism from southern France all the way up to the Champsaur region, where pyroclastic deposits with Provence-like geochemical affinities were identified for the first time. In Clumanc (Barrême foreland basin), volcaniclastic materials with Biella-like affinity are found, which suggests derivation from another proximal volcanic centre of the Alpine volcanic front on the other side of the Alps. This apparently undocumented (fully eroded?) source is the southernmost expression of the erosion of the Alpine volcanic province. Further south, in the Provence volcanic system, the terrestrial proximal pyroclastic deposits in St. Antonin and La Vanade have clear geochemical similarity with Provence magmatism.

This work outlines the value of clinopyroxene geochemistry in provenance studies, where volumetrically significant mafic volcaniclastics are preserved in the geological record, most particularly in convergent tectonic settings that are associated with arc and/or orogenic volcanism. This contrasts with the use of detrital zircons, that are predominantly formed in slowly crystallised felsic magmas and have more limited value in sedimentary systems dominated by the erosion of mafic igneous rocks (e.g., andesitic volcanoes). A similar observation was made in the Nankai forearc, Japan, where the PCA of trace elements in detrital pyroxenes reveals complex sedimentary patterns unrecognised with other traditional approaches. Thus, the new provenance method developed in this study can offer an innovative insight into the provenance of mafic-intermediate volcaniclastics globally.

Acknowledgements

When I start to think of who I should mention in this part, memories flooded into my mind and I realised this amazing journey has finally come to an end. From conceiving the idea of pursuing a PhD degree abroad seven years ago until now, I would not be where I am today without the immense help and full support of a number of amazing people throughout the journey, in particular in the middle of a global pandemic.

First and foremost, I would like to thank my supervisor David Buchs. Without his offer at the very beginning, there were no chance for me to even start this journey and study in the UK. During the four-year time working with David, his pure passion for geology has really impressed me and inspired me immensely. I indeed learned a lot from him, from fieldwork experience to lab skills, from Alpine tectonics to Tertiary Taveyannaz, from how to drive a car in the mountain area to how to properly use knife and folk, from clinopyroxene to amphibole, etc. David has given me unlimited support and encouragement, which have been essential in making me a better and professional geologist. His numerous remarks and suggestions on every single piece of work I had ever completed and our academic discussions through email or face-to-face were always constructive, enlightening and thought-provoking, leading me closer to the 'truth' hidden inside the rocks step by step. I am so lucky working with David for the last four years, not only because of his professionalism as an excellent academic, but also his integrity, sincerity and inclusiveness as a person. There is an old Chinese saying: He who teaches me for one day is my teacher for life.

I would like to thank Jean-Luc Epard for his logistic support and professional guidance on Alpine geology during our fieldwork in the Alps, as well as his warm help on making part of my thin sections in Switzerland. I also owe a lot of thanks to Anthony Oldroyd for his great patience on making a large amount of thin sections for my project. His humour and optimism were contagious and made me feel pleasant during our small talks in the basement. Many thanks are also given to Duncan Muir for his assistance and training on the SEM. I benefited a lot from our discussions on SEM-related questions. In addition, I am grateful for the help I got from Iain McDonald and Marc-Alban Millet for ICP-MS analyses, which was essential for my project. I would like to thank Michael Nairn for introducing LAtools to me on processing laser ablation data.

I would also like to acknowledge financial support from China Scholarship Council (No. 200806400012) for providing the PhD studentship, and in-kind support from Cardiff

University with tuition fee waiver and analytical facilities. Acknowledgement is also extended to The Geological Society of London, which funded me the second fieldwork trip in the Alps. I would like to thank Tom Blenkinsop and Tim Jones for their support on the application of the research grant.

My Cardiff life would not have been the same or as colourful without those incredible people I met in Open House, where people from all over the world get together, chilling, chatting, playing games and holding events, etc. All made Cardiff like a second home for me. I must thank Levon for his great patience and kindness organising everything and inviting us to eat dinner at his home every week. More importantly, I met Mieko there, got to know her further and fell in love with her. Now, she is my wife.

I would like to thank the Chinese cohort Wang Jian, Lei Zhibin, Jing Song in the department. We had great times getting together, in particular during Chinese festivals, which made us more united as a group. Special mentions go to Wang Jian. We are both working with David and from the same old university in China. Our discussions on my project and his advice were always beneficial.

Last but not least, I would like to thank the unwavering and unconditional support from family. Parents are always my biggest and staunchest supporter, and the source of my strength. It goes without saying but I would not be where I am today without you.

Finally, to Mieko. You are the one who has always been there for all the highs and lows throughout this journey. You cheered for me during the highs. You encouraged me during the lows. Days between highs and lows are called life. Thank you for your company in my life!

Table of contents

List of figures

List of tables

Chapter 1: Introduction

1.1 Background and significance

The Alpine Orogeny is accompanied by a pulse of andesitic volcanism ca. 40 - 30 Ma, which is recorded in turbiditic deposits of northwestern alpine foreland basins in SE France, Switzerland (e.g., Rahn et al., 1995; Ruffini et al., 1997; Boyet et al., 2001; Lu et al. 2018), and intrusions (dykes and plutons) along the Periadriatic Line in N Italy (e.g., von Blanckenburg and Davies, 1995) (Figure 1.1). Volcanism of the Periadriatic Line is believed by many researchers to result from injection and melting of the asthenospheric mantle below the continental lithosphere, following slab breakoff during collision between the Adriatic/Apulian and European Plates (Davies and von Blanckenburg, 1995; von Blanckenburg and Davies, 1995; Boyet et al., 2001), though alternative models have been proposed to explain this magmatism, including (1) lithospheric delamination (Bird, 1979), (2) lithospheric extension-related melting (McKenzie and Bickle, 1988) and (3) thermal boundary layer detachment (Houseman et al., 1981). Perhaps problematically, the interpretation of Periadriatic Line source requires that the volcaniclastic material in the northern alpine foreland basins (NAFB) transited rapidly across more than 100 km of a developing nappe system, which was most likely associated with tall east-west striking mountain ranges (Vuagnat, 1952; Lateltin, 1988). Moreover, recent tomographic images favour an unbroken European slab beneath the Western and Central Alps, however without definitive geophysical evidence supporting the occurrence or exact timing of a possible slab break-off (e.g., Zhao et al., 2016; Hua et al., 2017; Salimbeni et al., 2018; Kästle et al. 2020). Similarly, oceanic slab detachment after continental collision is still not unequivocally demonstrated, either in the Eocene (von Blanckenburg and Davies, 1995), in the Early Oligocene (Schmid et al., 1996; Bistacchi et al., 2001; Dal Piaz et al., 2003; Schlunegger and Kissling, 2015; Schlunegger and Castelltort, 2016), or in recent few million years (Kästle et al. 2020). Several PhD theses in Switzerland and France and some peer-reviewed regional studies (e.g., Sawatzki, 1975; Waibel, 1990; Ruffini et al., 1997; Boyet et al., 2001; Lu et al., 2018) have suggested that another volcanic front, more proximal to the NAFB, could have existed in the

Late Eocene-Oligocene but was removed since then by erosion or burial below nappe stacks. The location of this speculative volcanic system in the northern Alps could have greatly facilitated the transport of abundant andesitic volcaniclastics into NAFB. Therefore, volcaniclastic material preserved in the foreland basins offers a unique and valuable opportunity to test its existence.

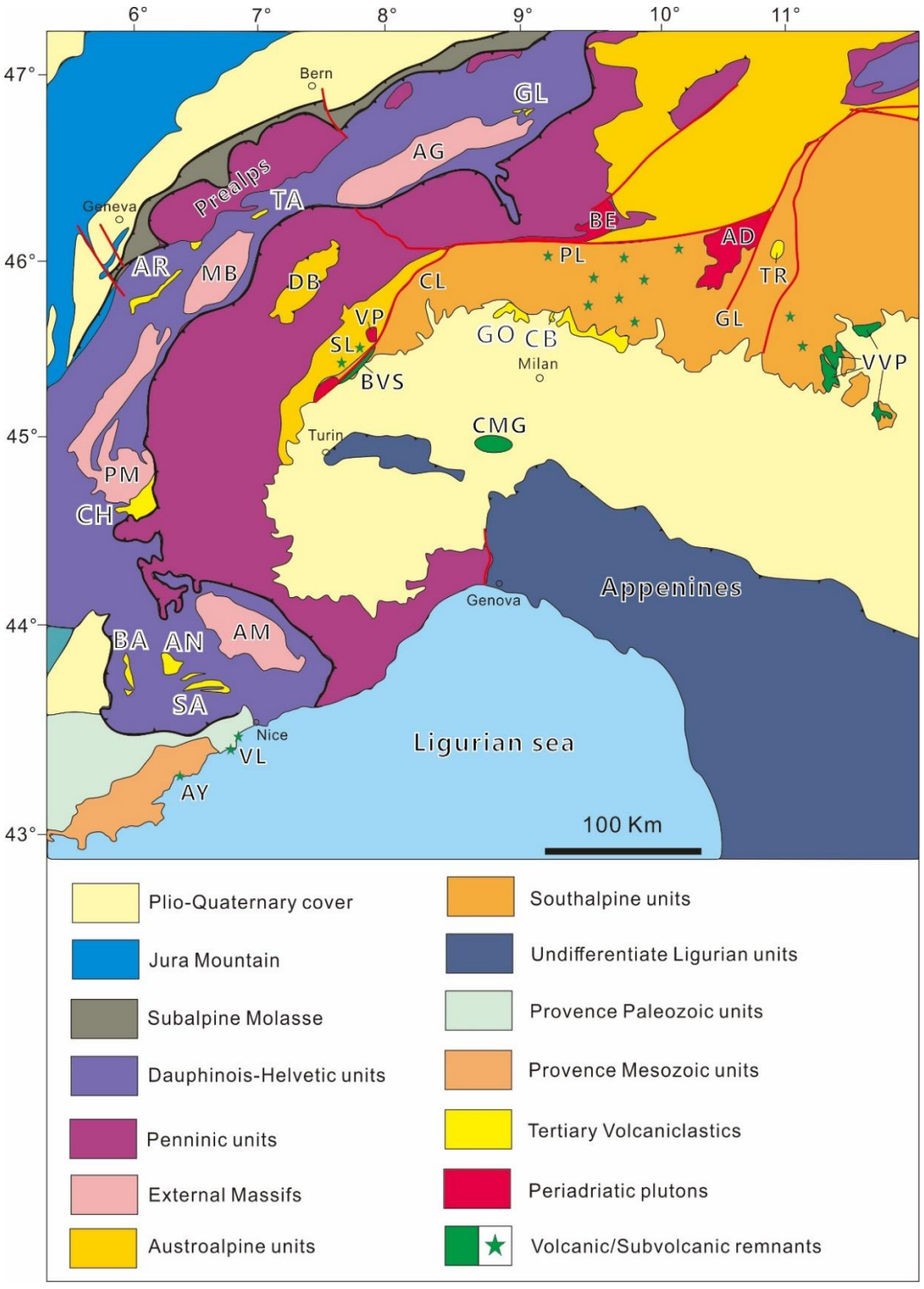

Figure 1.1 Geological map of the Alps with representative localities of Alpine syn-orogenic magmatism (modified from Pfiffner, 2014; Lu et al., 2020; Di Capua and Groppelli, 2021). Volcaniclastics: GL = Glarus, TA = Taveyannaz, AR = Aravis, CH = Champsaur, BA = Barrême, AN = Annot, SA = Saint Antonin, GO = Gonfolite, CB = Cibrone, TR = Trento; External Massifs: AG = Ara-Gotthard, MB = Mont-Blanc, PM = Pelvoux, AM = Argentera; Plutons: VP = Valle del Cervo Pluton, BE = Bergell, AD = Adamello; Volcanic remnants: BVS = Biella Volcanic Suites, CMG = Cerano-Mortara-Garlasco Volcanic sequences, VVP = Venetian Volcanic Province, AY = Agay, VL = Villeneuve-Loubet; Tectonic lines: PL = Periadriatic Line, GL = Giudicarie Line, CL = Canavese Line; Margna Sesia fragment: DB = Dent Blanche, SL = Sesia Lanzo Zone.

Formation of a cryptic volcanic system in the northern Alps would have important implications for the origin of alpine magmatism as it would be difficult to account for by melting of asthenospheric mantle close to a breaking slab (Waibel, 1990; Ruffini et al., 1997) and could instead be related to distinct upper asthenospheric or intra-lithospheric melting processes (e.g., Boyet et al., 2001, and references therein). Should the volcaniclastic materials have been derived from a Periadriatic Line source area as commonly assumed, its geochemical study would nonetheless greatly extend our understanding of syn-collisional alpine magmatism by providing an insight into otherwise inaccessible (eroded) parts of the southern alpine volcanic system.

Several hundred meters thick sequences of volcaniclastic turbidites (Figure 1.2) are preserved within NAFB, which contain abundant andesitic fragments and fresh magmatic clinopyroxenes, with less common amphiboles (Vuagnat, 1952; Sinclair, 1997; Ruffini et al., 1997; Boyet et al., 2001). All these components clearly support subaerial to submarine reworking of andesitic volcanic source(s), with variable mixing with other detrital components from the orogen (Lateltin, 1988; Lu et al., 2018). The whole-rock composition of rare andesitic pebbles from localities in France seems consistent with a provenance from a volcanic source close to the Periadriatic Line (Boyet et al., 2001). In addition, the age and geochemical composition of detrital zircons studied in several volcaniclastic sequences in Switzerland and France are also consistent with reworking from a volcanic source close to the Periadriatic Line (Lu et al., 2018). However, by focusing on (i) rare andesite pebbles that only occur locally in France and (ii) zircon geochronology and geochemistry that are intrinsically limited to characterise the magmatic evolution of andesitic volcanic systems, previous provenance studies have not provided a full

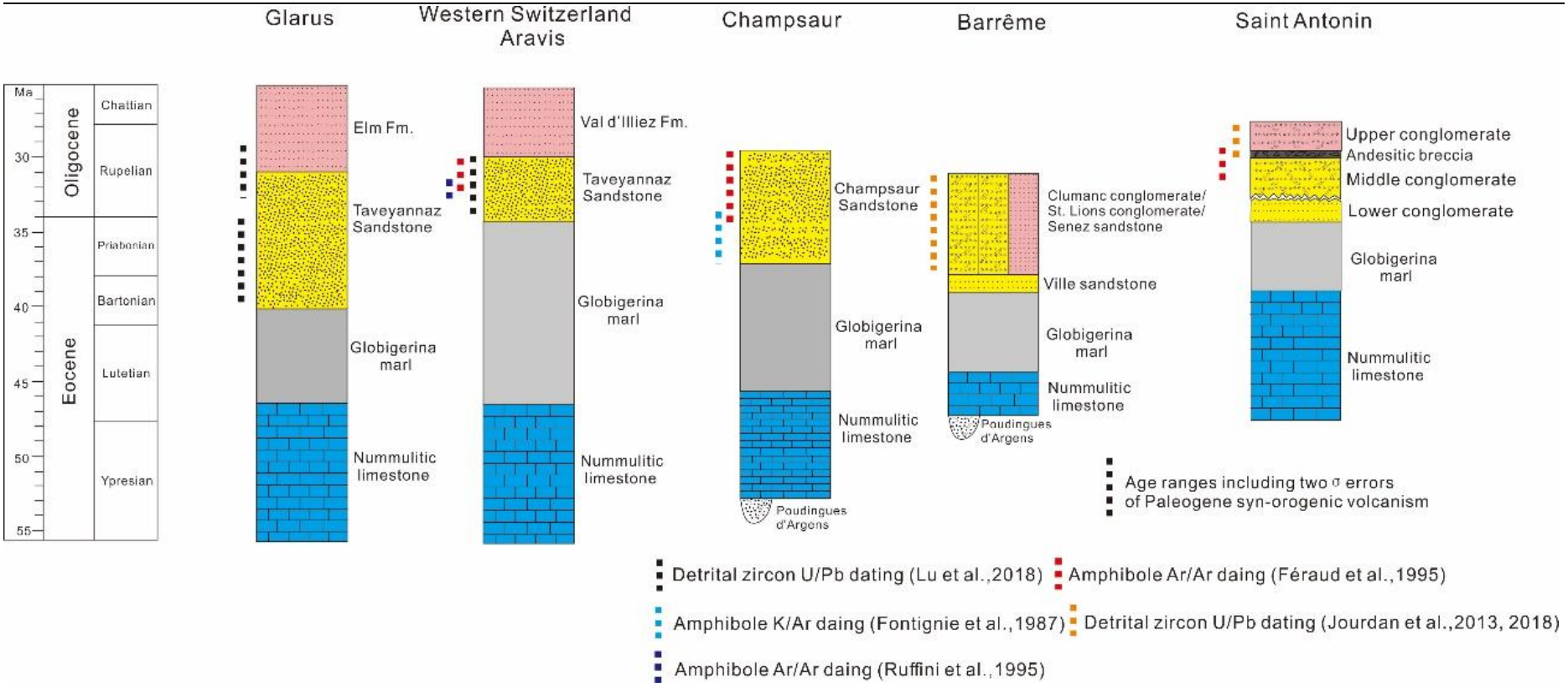

Figure 1.2 Composite stratigraphy of the Paleogene sections studied in the Alpine foreland basin. Taveyannaz sandstone and its equivalents denote volcaniclastic deposits in NAFB (compiled from Siegenthaler, 1974; Fontignie et al., 1987; Féraud et al., 1995; Lateltin, 1988; Callec, 2001; Jourdan et al., 2013; Jourdan et al., 2018; Lu et al., 2018).

characterisation of andesitic volcanism at a regional scale. Therefore, it is most expected that the complexity of the volcaniclastic record remains underestimated. As described below, this study managed to address this fundamental problem and test the provenance(s) of the volcaniclastic material through the study of the geochemistry of detrital clinopyroxenes and amphiboles, which was conducted systematically at a regional scale along the NAFB and compared with their possible source(s) along the Periadriatic Line.

1.2 Research objectives

The overall aim of this study is to characterise regional differences of volcanic sources along the NAFB from E Switzerland to SE France and to reconstruct the source-to-sink system of Tertiary volcaniclastic deposits in the NAFB.

This includes four main objectives:

(1) Acquire a large dataset of petrographic, whole-rock (i.e., lithics and igneous pebbles) and single-grain geochemical composition (i.e., clinopyroxenes and amphiboles) of volcanic components in volcaniclastic deposits to characterise the compositional heterogeneity in as many as possible available localities in the whole NAFB, extending from E Switzerland to coastal area of SE France along the Alpine arc.

(2) Similar data should be collected from Alpine intrusions that could correspond to the roots of eroded volcanoes preserved as volcaniclastic deposits in foreland basins. Sampling regions include available contemporary Tertiary plutons and dykes along the Periadriatic Line in N Italy, such as Biella, Adamello, Bergell plutons and associated dyke swarms in southern Alps.

(3) Compare (1) and (2) above to determine the possible sources (single source or several sources) of the volcanic material in different regions along the Alpine arc.

(4) Reconstruct the provenance of volcaniclastic sediments by comparing the geochemical composition of volcaniclastic deposits and dyke swarms. This provides significant constraints on tectono-sedimentary processes associated with the formation of foreland basins and possibly coeval erosion of volcanic centres.

Short COVID-19 impact statement:

Due to the outbreak of COVID, our third field campaign to N Italy for collecting Periadriatic intrusions and dykes had to be canceled. The data of large Alpine intrusions (e.g., Bergell and Adamello batholiths) was compiled from previous literature for comparison. It is however anticipated that the dominantly felsic composition of these intrusions will not match that of volcanic clasts that have mafic-intermediate affinities.

1.3 Thesis content

Following this general introduction, Chapter 2 will present the regional geological background the Alps, reviewing and summarising key geological concepts and processes related to this study. These includes Oligocene Alpine magmatism, the formation and tectono-sedimentary evolution of north Alpine foreland basins, and previous studies on Oligocene volcaniclastic deposits. Chapters 3 to 8 are the results chapters, subdivided into field observations (Chapter 3), petrographic observations (Chapter 4), whole-rock geochemistry (Chapter 5), clinopyroxene geochemistry (Chapter 6), amphibole geochemistry (Chapter 7) and new discrimination methods (Chapter 8). Chapter 8 introduces a new discrimination method for detrital pyroxenes and amphiboles based on Principle Component Analysis (PCA) using trace elements measured by LA-ICP-MS. This method is an important outcome of this study, that aims to resolve the relative inefficiency of existing discrimination techniques based on analyses presented in Chapters 6 and 7. Chapter 8 also includes an application of the new method using a previously published pyroxene dataset from Pliocene volcaniclastic turbidites in the Kumano forearc basin in Japan, thus offering a valuable point of comparison with the Alpine foreland system. The PCA approach is additionally evaluated through a comparison of its output with that of another method of data reduction (orthogonal polynomials) using both the Alpine and Japanese datasets. Chapter 9 integrates and discusses new field, petrographic, and geochemical (including PCA) results (Chapters 3 to 8) with previous studies to constrain the sediment routing system in the Alps. Conclusions are presented in Chapter 10.

Chapter 2: Geological background

2.1 The Alps

The Alps was formed during the closure of the Tethys Ocean that led to continental collision between the African and the European Plates in the Late Cretaceous-Paleogene (Trümpy et al., 1980; Gerrard, 1990; De Graciansky et al., 2010). Two oceanic sub-basins (Liguria-Piemont Ocean and Valais trough) formed from the Early Jurassic (ca. 190 Ma) until Late Cretaceous (ca. 100 Ma), which were separated by the (thinned) continental crust-of the Briançonnais domain or microcontinent (Trümpy et al., 1980). The southern European and northern African (Adriatic) continental margins, and probably the northern Valais trough, also consisted of thinned continental crust which was extended by continental rifting during the opening of the Tethys Ocean in the Jurassic. Upon subduction initiation at ca. 85 - 100 Ma (Rosenbaum and Lister, 2005; Handy et al., 2010; Zanchetta et al., 2012), enormous stress was exerted on the Alpine Tethys basin and on both northern and southern continental margins which were pushed against the stable European Plate to the NW by the moving Adriatic Plate, breaking and sliding one over the other to form large thrust faults/nappes (Gerrard, 1990). The Africa-Europe regional convergence was oriented north-south (Dewey et al., 1989; Rosenbaum et al., 2002) but the Adriatic microplate may have moved independently during the Tertiary (Handy et al., 2010).

The orogenic suture of the Alps, which marks the main contact between the European and African Plates is called the Periadriatic Line and runs through the orogen arc from east to west (Figure 2.1). The term “Insubric Line” is sometimes used to address the whole Periadriatic Line, but it is more commonly used for the western part of the Line.

North of the Periadriatic Line, three main palaeogeographical domains are defined and separated based on the palaeogeographical origins of the thrust sheets/nappes: the Helvetic (Brianconnais), the Penninic (including Brianconnais) and the Austroalpine domains. The Helvetic nappes are composed of materials from the European continental margin; the Penninic nappes contain ophiolitic materials from the Tethys ocean (serpentinised mantle, igneous crust and sedimentary rocks), oceanic sediments and thinned

continental crust (Briançonnais); the Austroalpine nappes are made up of materials from the Adriatic continental margin. South of the Periadriatic Line (on the Adriatic Plate) folded and thrusted units of the Southalpine nappes are found (Schmid et al., 2004; Pfiffner, 2014). In general, at the scale of the Alps, the Penninic units lie on top of the Helvetic units and the Austroalpine units on top of the Penninic units. All these units include autochthonous to allochtonous nappe complexes that were locally transported up tens to hundreds of kilometers from their substratum in the form of relatively thin sheets of rock (De Graciansky et al., 2010; Pfiffner, 2014). Within the eastern Alps, the Periadriatic Line marks the border between the Austroalpine domain and the Southalpine domain. In the western Alps it forms the division between the Southalpine domain and the Penninic domain.

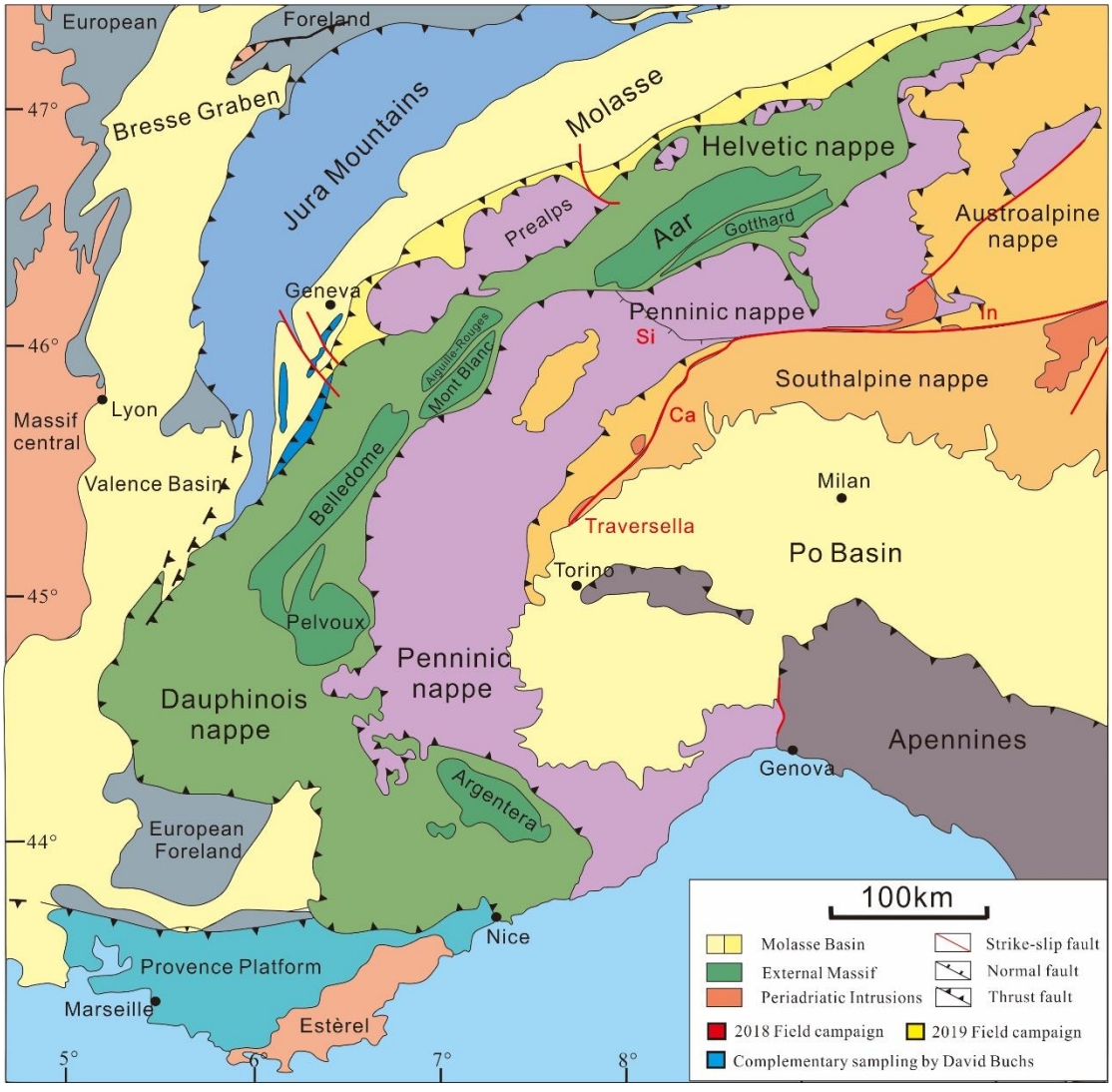

Figure 2.1 Simplified tectonic map of the Alps (modified after Pfiffner, 2014).

2.2 Alpine magmatism

2.2.1 Amagmatic stage (~100 Ma - ~45 Ma)

There is no magmatic record in the Alps during the subduction initiation and the closure of the Alpine Tethys between 100 Ma and 45 Ma (Callegari and Brack 2002; D'Adda et al. 2011; Zanchetta et al. 2012), leading to a ca. 50 Ma gap in magmatism after continental convergence initiated. This is supported by McCarthy et. al (2018) after compiling a large detrital zircon dating dataset (n = 9268 zircons) in sediments deposited between the initiation of convergence and Quaternary-age deposition in riverbeds.

The lack of magmatism in the Alps during subduction has previously been attributed to low-angle or flat-slab subduction (Bergomi et al., 2015), slow and oblique subduction (Zanchetta et al., 2012), or efficient scraping-off of hydrated subducted slab (McCarthy et al., 2018; Müntener et al., 2021).

Low-angle subduction is however difficult to reconcile with a range of observations. For example, recorded low-angle slab was transient and may have either delayed magmatism for a short period of time (~10 Ma) or led to the shift of arc magmatism away from the trench (Ramos and Folguera, 2009). Moreover, the occurrence of Alpine high-pressure metamorphic rocks reaching up to 2.7 GPa (ca. 90 km deep) seems inconsistent with the low-angle subduction hypothesis. Therefore, low-angle subduction could not explain the reason of the long duration of 50 m.yr. arc gap and high-pressure metamorphism. Meanwhile, a slow (1 - 2 cm/yr) subduction promotes the heating of subducted slab by the convective asthenospheric mantle, thus leading to shallower volatile/water release and flux melting of mantle wedge (< 2 GPa), although slow convergence and oblique subduction could subdue decompression melting due to less degree of mantle wedge convection/corner flow. However, compared to other slow and oblique subduction zones, as exemplified by the western Aleutians (e.g., Yogodzinski et al., 2015), slow and oblique subduction should not be the reason to inhibit the production of large scale of arc magmas (e.g., van Keken et al., 2011).

A more recent hypothesis to explain the lack of magmatism is related to the efficient scraping-off of the upper, hydrated lithosphere, largely preventing the volatiles down to the convective upper mantle depth to induce flux

melting (Müntener et al., 2021). Efficient mechanical decoupling of the serpentinites of the upper portion of the lithospheric mantle from the underlying “dry” mantle during incipient subduction could have caused the shallow accretion of hydrated serpentinites, thereby inhibiting the transfer of them to the base of mantle wedge at depth (McCarthy et al., 2018; McCarthy et al., 2020). The occurrence of voluminous seafloor serpentinites and high-grade metamorphic rocks exposed in the internal Alps suggests that deep subduction and sinking of hydrous rocks could have been inefficient (Agard and Handy, 2021; Tajčmanová et al., 2021). However, this hypothesis is still far from a final comprehensive solution. The volume of serpentinite preserved in the Alps has not been estimated and it is difficult to know if this could fully account for the closure of the ocean.

McCarthy et al., (2018) proposed a viewpoint that the complex architecture of the rifted Tethys Ocean basins predominantly floored by exhumed subcontinental mantle, similar to transitional areas between typical continental and oceanic crustal domains (ocean-continent transition; OCT) in present-day magma-poor rifted margins, rather than mature oceanic crust, plays an essential role in the mechanism of controlling the arc magmatism (e.g., Manatschal and Müntener, 2009; Picazo et al., 2016). This “dry” Alpine subduction is consistent with the concept of Ampferer-type subduction (Ampferer and Hammer, 1911), related to the amagmatic closure of magma-poor areas formed of thinned continental crust, magma-poor oceanic crust, and exhumed mantle, as opposed to more common Wadadi-Benioff-type subduction, which implies the subduction of mature oceanic lithosphere, the efficient subduction and sinking of hydrous rocks, and the production of voluminous arc magmatism (McCarthy et al., 2018).

Another alternative explanation is proposed that 200 - 300 km of oceanic subduction of Alpine slab, which likely had never reached beyond the 660 km discontinuity, may have been too short to trigger sufficient counter-flow and mantle upwelling, and to sufficiently hydrate the mantle wedge at sub-arc depths, therefore hindering the formation of a magmatic arc (Agard, 2021).

In summary, the magmatic gap during the first ~50 m.yr. of Alpine subduction could have been caused by limited supply of volatiles to the mantle either due to efficient scraping-off and accretion of the upper hydrated lithosphere, flat

slab subduction, “dry” lithospheric subduction, and/or limited supra-subduction mantle flow dynamics, ultimately leading to an unusual subduction setting which prevented initiation of sustainable (hydrous) arc magmatism.

2.2.2 Alpine syn-orogenic magmatism (~43 Ma - ~25 Ma)

Alpine syn-orogenic magmatism took place from the Middle Eocene to Late Oligocene (~ 43 - ~25 Ma), a climax of activity reached around ~ 34 - 28 Ma (von Blanckenburg and Davies, 1995; Rosenberg, 2004). As discussed above, despite subduction processes appear to have characterised Alpine geodynamics since ~ 100 - 85 Ma (Berger and Bousquet, 2008; Stampfli and Hochard, 2009; Handy et al., 2010), no convincing evidence of subduction-related magmatism was reported until the presence of Adamello batholith in the Middle Eocene (~42 Ma) (Schaltegger et al. 2009; Schoene et al. 2012; Broderick et al., 2015). In contrast, the Periadriatic magmatism of Late Eocene-Oligocene age is more widespread in the Alps. The volumetric ratio of Alpine volcanic-to-plutonic rocks is remarkably low, and difficult to estimate, with most evaluation around 1:5 to 1:30 (de Silva and Grosnold, 2007).

The Middle Eocene - Late Oligocene syn-orogenic magmatism in the Alps, resulted from the southeast-ward subduction of the Alpine Tethys ocean beneath the Adriatic continental plate, and subsequent continental collision, is represented in the successive order from External Alps to Internal Alps of occurrence by (Figure 2.2): (1) abundant volcanic detritus preserved in the volcaniclastic deposits of the external North Alpine Foreland Basins (NAFB) (Vuagnat, 1952; Siegenthaler 1974; Lateltin, 1988; Wabel, 1990; Sinclair, 1997; Rahn et al., 1995; Ruffini et al., 1997; Evans and Elliott, 1999; Boyet, 2001; Di Capua et al., 2016; Lu et al., 2018) and retro-side Adriatic foreland basins (Sciunnach and Borsato, 1994; Gavazzi et al., 2003; Di Giulio et al., 2005; Martin and Macera, 2014; Lu et al., 2018; Lu et al., 2019); (2) plutonic bodies intruded along the internal Periadriatic Line, including three large plutons, the Adamello pluton (Schaltegger et al., 2009; Tiepolo et al., 2014; Broderick et al., 2015; Hürlimann et al., 2016), the Bergell pluton (von Blankenburg et al., 1992; Gianola et al., 2014; Tiepolo et al., 2014; Samperton et al., 2015) and the Biella pluton (Bigioggero et al., 1994; Peccerillo and Martinotti, 2006; Berger et al., 2012) and more widely-spread dykes (Beccaluva et al., 1983; Venturelli et al.,

1984; Conticelli et al., 2009; D'Adda et al., 2011; Bergomi et al., 2015); (3) rarely exposed volcanoes and volcanogenic sequences in northern Italy, including the Biella Volcanic Suite (Callegari et al., 2004; Kapferer et al., 2012), the Veneto Volcanic Province (Beccaluva et al., 2007; Bianchini et al. 2008; Bellieni et al., 2010) and the Cerano-Mortara-Garlasco volcanic sequences (Ruffini et al., 1995; Fantoni et al., 1999; Mattioli et al., 2002).

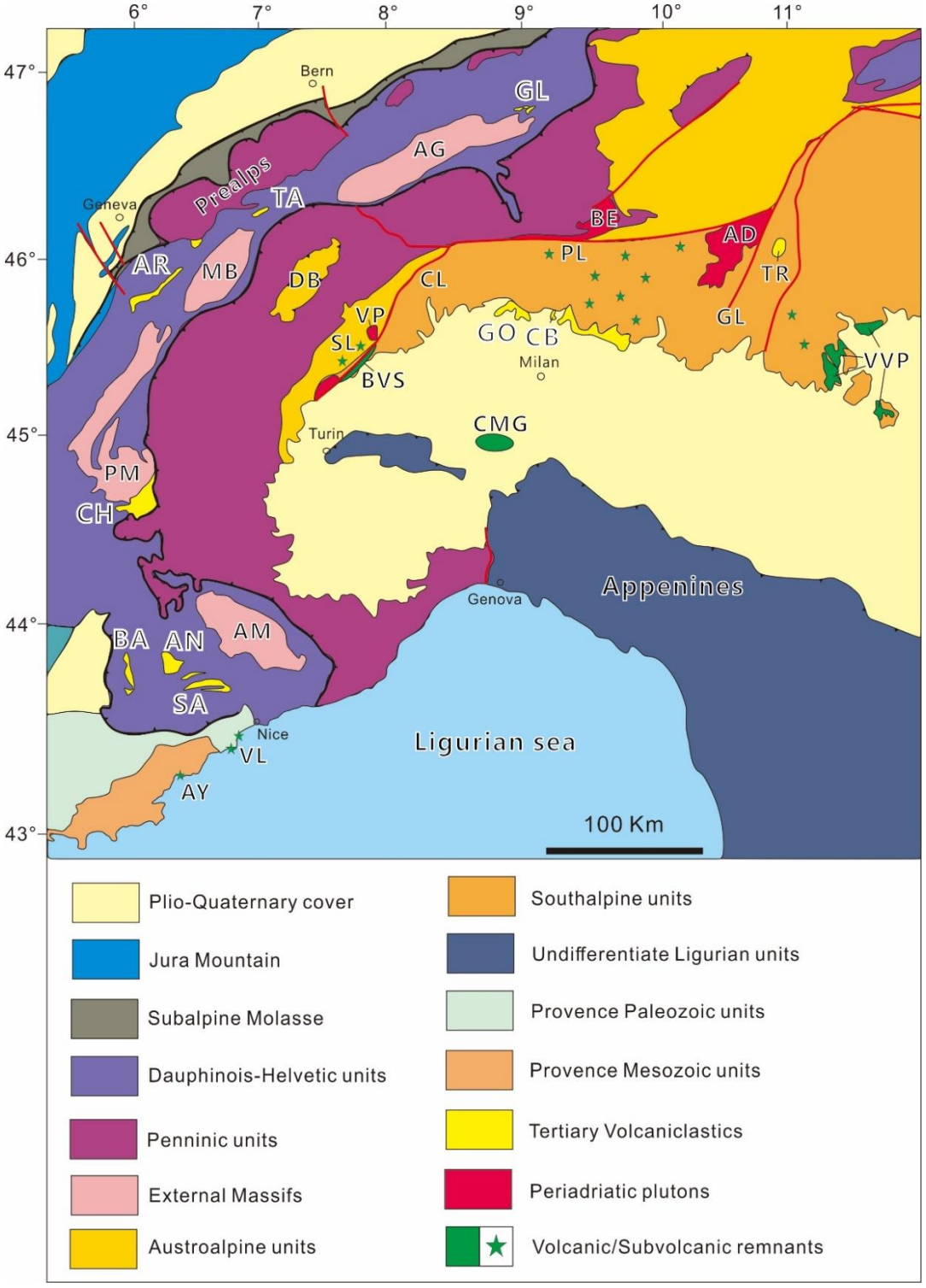

Figure 2.2 Geological map of the Alps with representative localities of Alpine syn-orogenic magmatism (modified from Pfiffner, 2014; Lu et al., 2020; Di Capua and Groppelli, 2021). Volcaniclastics: GL = Glarus, TA = Taveyannaz, AR = Aravis, CH = Champsaur, BA = Barrême, AN = Annot, SA = Saint Antonin, GO = Gonfolite, CB = Cibrone, TR = Trento; External Massifs: AG = Ara-Gotthard, MB = Mont-Blanc, PM = Pelvoux, AM = Argentera; Plutons: VP = Valle del Cervo Pluton, BE = Bergell, AD = Adamello; Volcanic remnants: BVS = Biella Volcanic Suites, CMG = Cerano-Mortara-Garlasco Volcanic sequences, VVP = Venetian Volcanic Province, AY = Agay, VL = Villeneuve-Loubet; Tectonic lines: PL = Periadriatic Line, GL = Giudicarie Line, CL = Canavese Line; Margna Sesia fragment: DB = Dent Blanche, SL = Sesia Lanzo Zone.

The three largest plutons are Adamello, Bergell and Biella plutons, of which emplacement is spatially and temporally associated with the formation of the Periadriatic Fault System. Magmas were channeled from the base of the thickened continental crust into the narrow orogenic belt along the Periadriatic Fault System (Rosenberg, 2004). Most of the plutonic bodies are tonalitic and granodioritic in composition, with minor granitic and dioritic intrusions with calc-alkaline to shoshonitic/ultrapotassic affinities, associated with a general increase in potassium from the eastern to western Alps (Rosenberg, 2004; Alagna et al., 2010; Müntener et al., 2021). Except for the southern Adamello pluton that has an earlier age of ~42 Ma, most of the Periadriatic plutons have a peak emplacement age between 34 - 28 Ma (Bigioggero et al., 1994; Schaltegger et al. 2009; Schoene et al., 2012; Gianola et al., 2014). A large range of petrogenetic constraints from major and trace elements to radiogenic isotopes and mineral compositions indicate that the magmatism resulted from partial melting of a variously metasomatised upper mantle followed by subsequent fractional crystallisation and crustal assimilation (e.g., Venturelli et al., 1984).

In contrast, dykes, more widespread in all Alpine domains, range in composition from basalts and basaltic andesites to andesites and dacites, showing calc-alkaline to shoshonitic affinity. The emplacement ages of these dykes are in a wider time span of 42-30 Ma (D'Adda et al., 2011; Bergomi et al., 2015). Unlike larger plutonic bodies, the petrographic and geochemical characteristics of Periadriatic dykes vary along the orogenic belt. The ultrapotassic (lamproites) dykes, which are commonly exposed in the Western Alps, are absent in the central and eastern Alps (Dal Piaz et al. 1979; Beccaluva et al., 1983; Venturelli et al. 1984; Peccerillo and Martinotti 2006; Conticelli et

al. 2009). Moreover, it appears that dykes are younging from SE to NW, in an opposite direction with respect to the Alpine subduction polarity (Bergomi et al., 2015). The spatial correlation between the ultrapotassic rocks and the location of subduction of continental crust as noted by Venturelli et al. (1984) suggests that the ultrapotassic magmas may have formed under conditions of thickened lithosphere when compared to the associated calcalkaline magmas. This indicates that the sub-Alpine mantle structure and composition were probably changing dramatically and rapidly over time.

The magmatic products generated in the Alps resemble with those of subduction-related magmatic arcs and are chemically and texturally indistinguishable with those of typical Wadadi-Benioff subduction-related arc settings. The similarities include negative Nb-Ta and Zr-Hf anomalies, enrichments in large ion lithophile elements (LILE) and hydrous arc-tholeiitic to calcalkaline affinity of typical arc signatures (Alagna et al., 2011; Hürlimann et al., 2016; McCarthy et al., 2018; Müntener et al., 2021). However, unlike typical arc magmatism, syn-orogenic Alpine magmatism is characterised by (1) the scarcity of magmatic rocks, in particular volcanic rocks, and the abundance of exposed high-pressure metamorphic rocks (Goffe and Bousquet, 2004), in contrast to circum-Pacific subduction zones, where magmatic rock is predominant, with subordinate occurrence of exhumed metamorphic rocks; (2) the narrow distribution of Alpine magmatism, which is confined to a narrow belt along the Periadriatic Line, in contrast to arc settings where magmatism could be found as far as several-hundred kilometers from the trench; (3) the unusual deep source (~2.7 GPa) in contrast to the shallower depth (1-2 GPa) of mantle-wedge melting in typical subduction zones (Ulmer and Trommsdorff, 1995).

2.3 Mechanism of Alpine magmatism: slab breakoff vs unbroken slab

The origin and mechanism of relatively short-lived syn-orogenic Alpine magmatism, following a long period of amagmatic subduction, has been a long-standing issue in the history of Alpine research. Different models have been proposed to explain this magmatism, including (1) delamination (Bird, 1979), (2) lithospheric extension-related melting (McKenzie and Bickle, 1988), (3) thermal boundary layer detachment (Houseman et al., 1981) and (4) the

extensively adopted, but recently challenged, slab breakoff model (Davies and von Blanckenburg, 1995; von Blanckenburg and Davies, 1995). However, recent tomographic images imply an unbroken European slab beneath the Western and Central Alps (e.g., Zhao et al., 2016; Hua et al., 2017; Salimbeni et al., 2018), which contrast with the hypothesis of oceanic slab detachment after continental collision, either in the Eocene (von Blanckenburg and Davies, 1995) or in the Early Oligocene (Schmid et al., 1996; Bistacchi et al., 2001; Dal Piaz et al., 2003; Schlunegger and Kissling, 2015; Schlunegger and Castelltort, 2016).

2.3.1 Slab breakoff

In order to explain the geodynamic mechanism and the initiation of Alpine magmatism, von Blanckenburg and Davies (1995) proposed their well-known slab breakoff hypothesis by modelling (Figure 2.3 and 2.4). They provided a

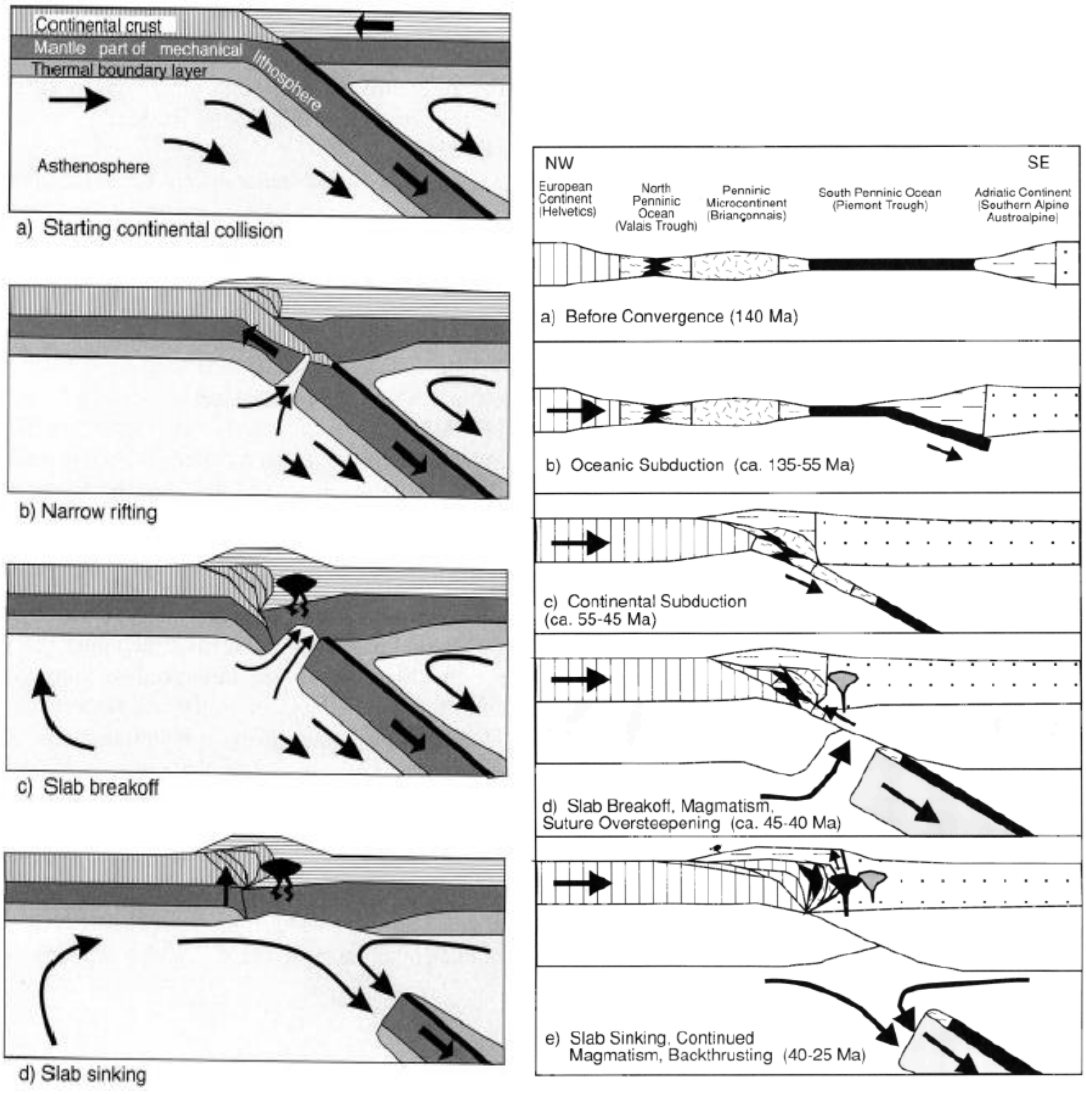

Figure 2.3. (left) Schematic breakoff process (from Davies and von Blanckenburg, 1995).

Figure 2.4. (right) Tentative cartoon illustrating the tectonic evolution of the Alps, including the postulated breakoff of the subducted slab (from von Blanckenburg and Davies, 1995).

groundbreaking idea that when the subducted portion of the European plate broke off, this led to the upwelling of the asthenospheric mantle into the gap which was left by breakoff. The associated heating of the Adriatic plate's lithospheric mantle then resulted in differential melting around the gap, thus inducing the magmatism (Davies and von Blanckenburg, 1995; von Blanckenburg and Davies, 1995).

Compared with the above-mentioned other models (i.e., delamination, thermal boundary layer detachment and lithospheric extension), slab breakoff model could better explain the combined appearance of the following characteristic features in the process of Alpine orogeny: (1) bimodal magmatism comprising basaltic partial mantle melts and granitic crustal melts, most likely formed by lower crustal melting with a mantle origin; (2) rapidly uplifted and later exhumed high-pressure metamorphic rocks of mantle depth; (3) regional metamorphism; (4) extensional structures (von Blanckenburg and Davies, 1995).

In addition, the slab breakoff was first proved by teleseismic P-wave tomography model of Lippitsch et al. (2003), which suggests a discontinuity of high velocity anomaly beneath the Western Alps in the Alpine upper mantle, also supported by a group of researchers holding similar interpretations (e.g., Piromallo and Morelli, 2003; Spakman and Wortel, 2004; Kissling and Schlunegger, 2018; Beller et al., 2018; Kästle et al., 2020).

However, some of these models showed high-velocity anomalies in areas where no slab was expected based on geologic evidence (e.g., the Provençal margin of SE France), and different models were not always consistent. For example, teleseismic P-wave tomography model proposed by Piromallo and Morelli (2003) suggests a continuous slab beneath the Western Alps and potential slab breakoff beneath the Central Alps whereas tomography model proposed by Lippitsch et al. (2003) suggests a shallow slab breakoff beneath the Western Alps and a more continuous slab beneath the Central Alps.

2.3.2 Unbroken/continuous slab

The complex slab structure beneath the Alpine region is only partly resolved by available geophysical data, leaving many geological and geodynamical issues widely open (Zhao et al., 2016). The interpretations in terms of lateral and vertical slab continuities, length of the subducted slabs, and their relationship with geodynamic processes strongly depend on the resolution of the seismic tomography. With the recent developments in the fields of seismic data acquisition and tomography model computation, especially the CIFALPS experiment, further geophysical constraints based on different tomographic methods are acquired to provide an updated image of the deep structure of the Alps at the scale of the lithosphere and the upper mantle (Zhao et al, 2016; Lyu et al., 2017; Malusà et al., 2017; Beller et al., 2018; Salimbeni et al., 2018; Solarino et al., 2018; Sun et al., 2019).

Zhao et al. (2016)'s tomography model based on a finite-frequency kernel method was the first to explicitly propose a continuous slab under the Western Alps, although similar evidence is also provided by teleseismic tomography models from other working groups (e.g., Piromallo and Morelli, 2003; Koulakov et al., 2009; Giacomuzzi et al., 2011; Hua et al., 2017; Paffrath et al., 2020). Their results document the lateral continuity of the European slab from the Western Alps to the central Alps, and the downdip slab continuity beneath the central Alps, ruling out the hypothesis of slab breakoff to explain syn-orogenic Alpine magmatism.

Comparison of upper mantle Vp perturbations between the tomography models of Lippitsch et al. (2003) and Zhao et al. (2016b) has been made in the synthesis work of Malusà et al. (2020) (Figure 2.5). Two evidences have been proposed as to explain why slab breakoff is not correct: (1) no low-velocity anomaly, which represents the associated passive asthenospheric upwelling crosscuts the high-velocity anomaly, which represents the broken slab given that the shape of a low-velocity body, if present, would be well recovered as a low-velocity anomaly by the inversion; (2) the small low-velocity anomaly at ~120 km depth detected by Lippitsch et al. (2003) under the Dora-Maira is not connected with the main low-velocity anomaly beneath the European foreland. In fact, the two regions are separated by a region with Vp (%) > 0. Based on these considerations, the Lippitsch et al. (2003)'s model may provide

no clear support to the hypothesis of a slab detachment, which would also imply a much stronger and continuous negative anomaly beneath the Dora-Maira.

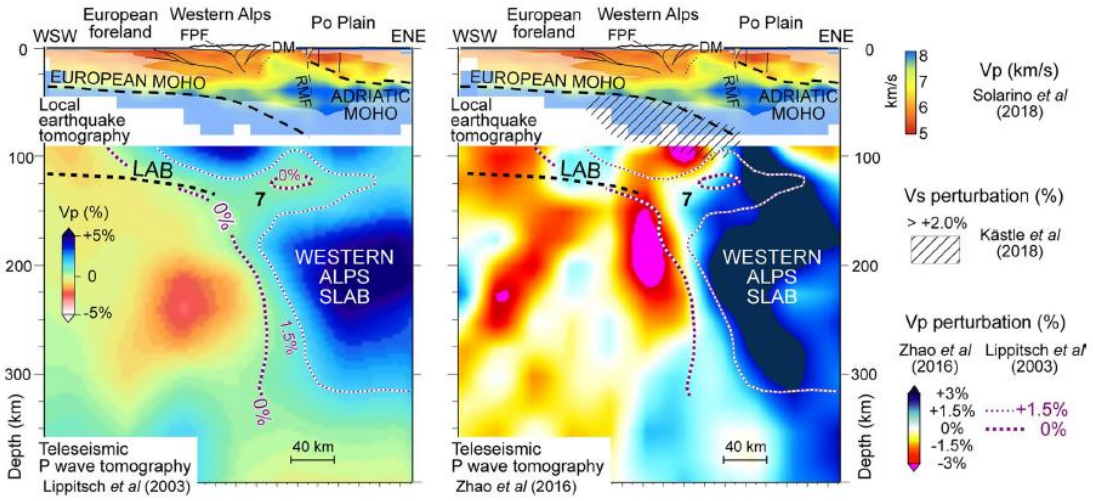

Figure 2.5 Comparison of upper mantle Vp perturbations beneath the CIFALPS transect according to the teleseismic P-wave tomography models of Lippitsch et al. (2003) (left) and Zhao et al. (2016) (right) (from Malusà et al. 2020).

According to Lyu et al. (2017)'s model based on array analysis of seismic surface waves, very low Vs values (7 in Figure 2.6a) are found at the base of the European lithosphere at depth ~120 km beneath the Alpine subduction wedge, corresponding to the low-velocity area imaged by teleseismic P-wave tomography discussed above (Lippitsch et al., 2003; Zhao et al., 2016b), and a low-Vs anomaly has been also detected by Beller et al. (2018). Beller et al. (2018) have suggested that the low-Vs anomaly detected in their S-wave velocity model may be supportive of a slab detachment beneath the Western Alps, an interpretation recently reintroduced by Dal Zilio et al. (2020) and Kästle et al. (2020).

However, given the sharp Vs increase at depth >70 km along the subduction channel (Figure 2.6b), interpreted by Zhao et al. (2020) as due to transformation of serpentinite into peridotite after destabilization of antigorite, the low Vs anomaly detected by Beller et al. (2018) at 75–95 km depth (8 in Figure 2.6b) may also indicate a metasomatized mantle peridotite due to infiltration of slab fluids. Malusà et al. (2020) concluded that the results provided by Beller et al. (2018) are not supportive of European slab detachment. Instead, they are consistent with the results provided by other

tomography approaches that have been applied during the CIFALPS experiment (e.g., Lyu et al., 2017; Zhao et al., 2020).

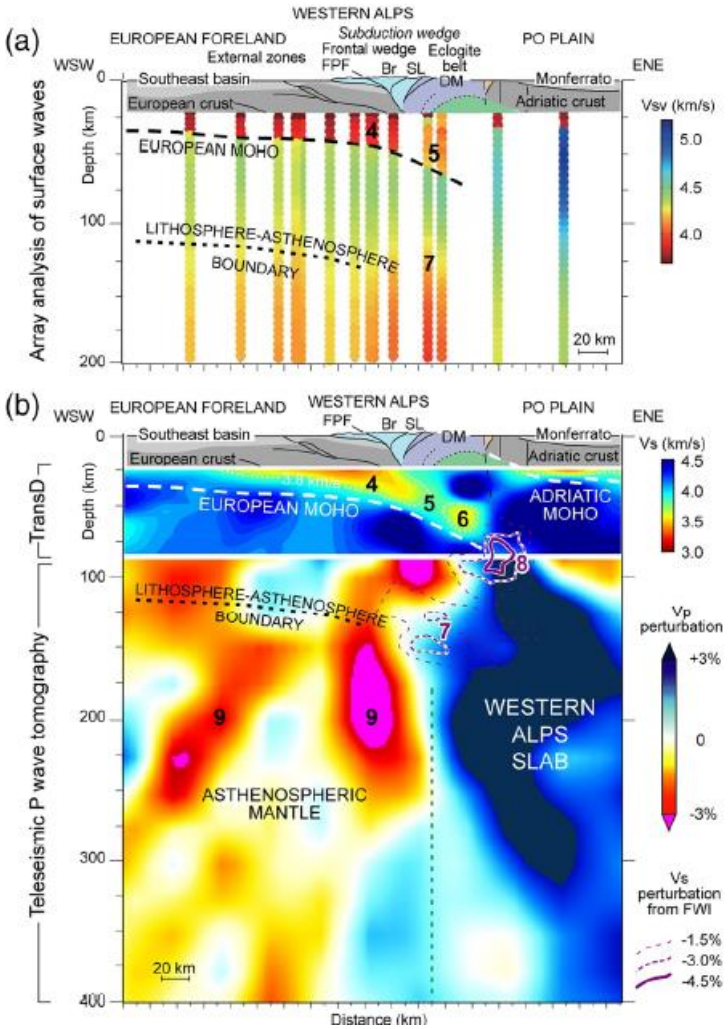

Figure 2.6 Upper mantle velocity structure along the CIFALPS transect. (a) Absolute Vs based on array analysis of seismic surface waves (after Lyu et al., 2017); (b) Composite cross-section showing, in the upper panel (20–90 km depth), the absolute Vs values based on Bayesian TransD inversion of surface-wave dispersion data (Zhao et al., 2020) and, in the lower panel (90–400 km depth), the Vp perturbations (in %) based on teleseismic P-wave tomography (Zhao et al., 2016b) (from Malusà et al. 2020).

Recent work by Kästle et al. (2020) based on surface-wave tomography suggests a continuous slab of at least 100 km length without slab breakoff in the central Alps whereas no clear continuous high-velocity anomaly was inferred in the western Alps. They conclude that the European slab underneath the western Alps is not as thick and continuous as under the central Alps and may have broken off. They also proposed three scenarios in the context of a possible slab break-off in western Alps: a recent (few Ma), an

old (onset of continental collision) and no slab break-off. After full discussion and analysis, the scenario of a recent breakoff was concluded as the most likely one though the uncertainty remains high and the no break-off scenario cannot be excluded (Kästle et al. 2020).

2.3.3 Relationship between slab geometry and magmatism

Alpine magmatism has long been explained by the slab breakoff model since Davies and von Blanckenburg (1995) first described the magmatic effects of oceanic lithosphere detachment during continental collision, but this interpretation is challenged by geophysical data suggesting the existence of a continuous slab (e.g., Koulakov et al., 2009; Giacomuzzi et al., 2011; Zhao et al., 2016; Hua et al., 2017; Salimbeni et al., 2018). If there is no slab breakoff, what are the other alternative options to explain the Alpine magmatism, associated (U)HP exhumation and surface uplift (von Blanckenburg and Davies, 1995).

Zhao et al. (2016) proposed that Alpine Periadriatic magmatism may simply record the progressive subduction of oceanic and transitional lithosphere beneath the Adriatic Plate and, in SE France, magmatism is more likely related to flow and upwelling of hot mantle material beneath the European plate in relation to subduction of the nearby Apenninic slab (Jourdan et al., 2013), which started retreating during the Neogene leading to the opening of the Ligurian-Provençal basin in the back-arc region (Jolivet and Faccenna, 2000). The exhumation of (U) HP rocks in the Western Alps is possibly explained by divergence between the upper plate and the accretionary wedge (Malusà et al., 2011; Malusà et al., 2015). The Neogene topographic uplift of the external massifs may be a far-field effect of the progressive rollback of the Apenninic slab (Jolivet et al., 2009). None of the above mechanisms implies slab break off.

The lack of slab breakoff has also been supported by geochemical datasets. Bergomi et al. (2015) have suggested slab steepening to explain a trend of northward decreasing ages in the Periadriatic mafic dykes of the central Southern Alps. This younging trend was also found in the zircon U–Pb ages of western Periadriatic intrusions by the work of Ji et al., (2019). They further proposed that slab steepening enhanced the corner flow, and this process was more effective near the torn edge of the European slab, and triggered

Periadriatic magmatism in the absence of slab breakoff (Figure 2.7). Recent tomography model of Zhao et al., (2016) confirm the presence of a steeper slab beneath the Central Alps (dip angle ~70–80°) compared to the Western Alps (dip angle ~60°).

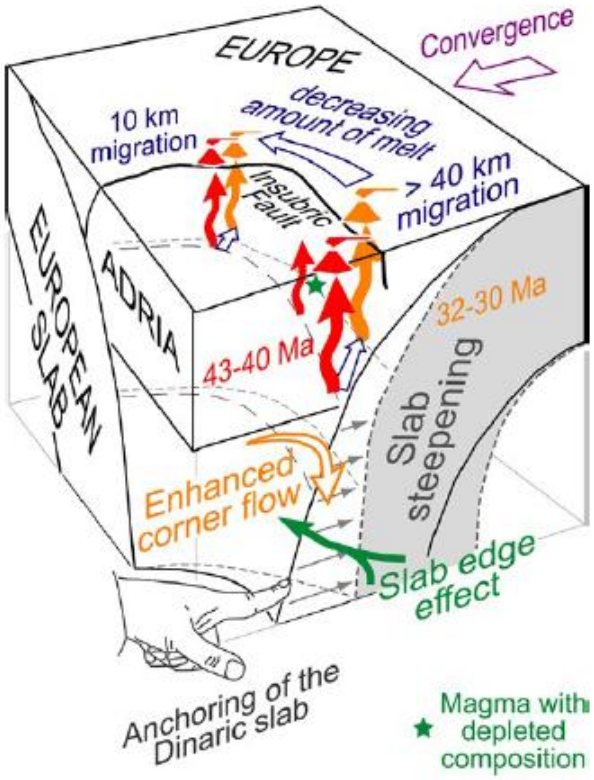

Figure 2.7 3-D model showing the proposed relationships between slab steepening and Periadriatic magmatism in the absence of slab breakoff (from Ji et al., 2019).

2.4 Stratigraphy

The Tertiary stratigraphy of the Alpine Foreland Basin consists of two stages: a Paleocene to middle-Oligocene deep marine underfilled (Flysch) stage followed by a middle-Oligocene to late-Miocene shallow marine and continental overfilled (Molasse) stage (Homewood et al., 1986; Allen et al., 1991). The lower stratigraphic boundary to the entire foreland basin is marked by a major unconformity, which separates the Mesozoic passive margin succession from the overlying Tertiary foreland basin infill. Locally, the foreland basin infill starts from a set of conglomerate and marlstone deposits named “Poudingues d'Argens”, derived from the adjacent crystalline basement, interpreted to be the fills to subaerially incised paleo-valleys (e.g., Gupta, 1997).

Underfilled stage stratigraphy has a common signature across the Alpine foreland basin that can be described in terms of three lithostratigraphic units, termed “the underfilled trinity” by (Sinclair, 1997), which are commonly diachronous and superimposed on top of one another during craton-ward migration of the facies belts. The underfilled trinity can be summarised as follows (Allen et al., 1991) (Figure 2.11):

(1) Nummulitic Limestone (Einsiedeln Fm.), a lower shallow marine unit underlain by a basal unconformity and that comprises a variable thickness (20-50 m in central Switzerland; up to 130 m in Haute-Savoie; 5-50 m in southern French Alps) of limestones rich in nummulites;

(2) Globigerina/Blue Marl (Stad Fm.), a middle semi-pelagic to pelagic unit overlying Nummulitic limestone, composed of up to 400 m (in Annot basin) of calcareous mudstones rich in Globigerina;

(3) Flysch turbidite (Taveyannaz Fm. s.l.), an upper deep marine unit, overlying Globigerina marl, comprised of 50-2000 m of thick successions of alternating turbiditic sandstone and mudstone that have been classically termed “Flysch”, which is characteristically highly immature and rich in lithic and volcanic detritus derived from erosion of the thrust wedge (Schwab, 1986).

This series of consecutive succession reflects the initial northwest-ward transgression over the underlying Mesozoic passive margin succession. During this transgression, the Nummulitic limestones were first deposited and then covered by Globigerina marls, reflecting continued deepening of water depth (Herb, 1988). The upper part of the middle unit (Globigerina marls) commonly represents the deepest part of the basin (Sinclair, 1997). Micropaleontological studies of the Globigerina marls from around the Alps (Pairis, 1988; Herb, 1988) have identified high planktonic-to-benthonic foraminiferal ratios in the marls, and have been used to interpret depositional water depths at 500–1000 m.

The names given to the flysch turbidites vary around the Alpine arc, but the commonly used ones include the Taveyannaz Sandstone (usually representing the sandstone extending from Glarus to Haute-Savoie), the Champsaur Sandstone (denoting the sandstone in Champsaur basin), and the Annot Sandstone (denoting the sandstone in Annot basin and structurally associated

surrounding Tertiary basins in the southern French Alps). In addition, in the westernmost Barrême basin, the stratigraphically equivalent formation is represented by the Oligocene Ville Sandstone, the Clumanc Conglomerate and Saint Lions Conglomerate (Evans and Mange-Rajetzky, 1991). In the southernmost Saint Antonin basin, the coeval clastic formation has been subdivided into three units called the lower, middle, and upper member of the Saint Antonin conglomerate by Stanley (1980), or simply Formations 1, 2 and 3 by Bodelle (1971) and Callec (2001).

The Taveyannaz Sandstones (s.l.) commonly give way to younger and more external clastic formations, characterised by continued turbidite deposition containing less or no volcanic detritus, represented by the Elm and Matt Formations in Glarus region (Siegenthaler, 1974), by the Val d'Illiez and Matt-Gruontal Sandstones in western Switzerland and Haute-Savoie regions (Vuagnat, 1952; Martini, 1968; Lateltin, 1988), by the Saint Didier Sandstone in Champsaur region (Waibel, 1993), by Third clastic formation or Formation 3 in Saint Antonin basin (Stanley, 1980; Callec, 2001) and by the Senez Sandstone in Barrême basin (Evans and Mange-Rajetzky, 1991). All above-mentioned overlying formations terminate the underfilled stage of the NAFB.

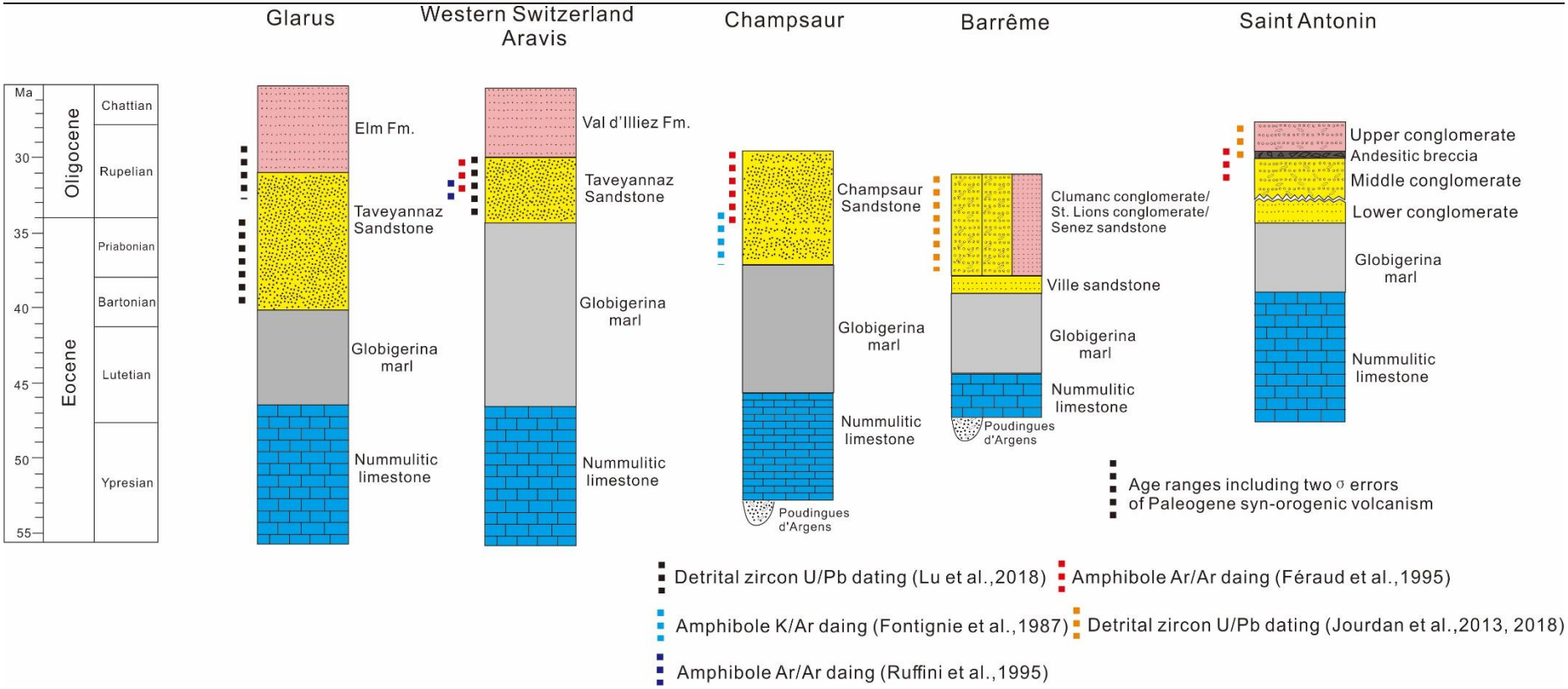

Figure 2.8 Composite stratigraphy of the Paleogene sections studied in the Alpine foreland basin (compiled from Siegenthaler, 1974; Fontignie et al., 1987; Féraud et al., 1995; Ruffini et al., 1995; Lateltin, 1988; Callec, 2001; Apps et al., 2004; Jourdan et al., 2013; Jourdan et al., 2018; Lu et al., 2018).

2.5 Alpine foreland basin

Alpine foreland basins, formed on both sides adjacent and parallel to the Alpine belt, have developed in response to the enormous mass created by crust thickening that resulted from continental collision between European and Adriatic Plates during the Alpine orogeny (Dickinson, 1974; Allen and Homewood, 2009). Foreland basin development is controlled by a variety of factors, including flexural rigidity of the subducted plate, sedimentary load, orogenic load, forward migration of the orogenic front and orogenic uplift (Allen et al., 1991; Ford and Lickorish, 2004). As mountains were growing and underwent erosion, foreland basin receives sediment that is eroded off the adjacent mountain belt, filling with thick sedimentary successions that thin away from the mountain belt (De Celles and Giles, 1996).

When sedimentation occurs in a basin located at the front of an active thrust sheet, it is called "foredeep basin"; when the deformation propagates under the basin, within the substratum (e.g., in a preferential detachment surface), and the latter is itself transported, it is called "thrust-sheet (top) basin" or "piggy-back basin" or “wedge-top basin” (Ori and Friend, 1984; Ricci-Lucchi, 1986).

In Switzerland, the remnants of the underfilled foreland basin are now located in the Helvetic nappes and are characterised by stacked thrust sheets overlying a deformed, but not detached, cover to the external basement massifs (Trümpy, 1980; Pfiffner, 1986). Most extensive exposures of the underfilled deposits in Switzerland are found within this deformed cover (Allen et al., 1991). Further southwest to the border of France and Switzerland, the underfilled deposits are preserved within the detached Helvetic nappes in Switzerland and in footwall synclines in Haute-Savoie in France (Lateltin, 1988). Further south, extensive outcrops of underfilled deposits are exposed in thrust sheets within the relatively undeformed cover of the Pelvoux Massif at Champsaur region (Waibel, 1990). Further south, the least-deformed and best-preserved remnants of the underfilled foreland basin are found in the Maritime-Provençal (southern French) Alps (Elliott et al., 1985; Joseph and Lomas, 2004). The underfilled deposits are preserved in synclines perched on top of the thin-skinned fold and thrust structures (Evans and Elliott, 1999).

2.5.1 Northern Alpine (Peripheral) foreland basin (NAFB)

The NAFB is a narrow (15-20 km width), discontinuous and structurally confined foreland basin in a wedge-top position over 200 km long from the Haute Savoie region in France to the southwest to the Glarus area in the eastern Switzerland to the northeast (Allen and Homewod, 2009; Lateltin, 1988). According to Sinclair (1992), the sediments was deposited in two sub-basins (i.e., Inner and Outer basins) separated by a topographic high trending ENE-WSW in Glarus. The southern Inner basin is considered as a "piggy-back" basin while the depositional style and structural pattern of the northern Outer basin are analogous to those in an accretion-wedge sedimentary environment. Paleo-geographically, the narrow wedge-top basins were bounded to the southeast by the growing Alpine orogen, and to the northwest by the European craton (Sinclair, 1992).

The most exposed outcrop of the NAFBs is mainly in the parautochthon to the external massifs and within the Helvetic nappes which extends from Subalpine Chain (Haute-Savoie), and the type locality "Alpe de Taveyanne" to the Glarus area in the northeast. South of Haute-Savoie region, the foreland basin is less obvious due to subsequent Oligocene–Miocene uplift and deformation associated with the Bresse and Rhône graben systems (Ford et al., 1999).

The basin, or very likely a series of sub-basins sharing a common stratigraphic evolution, is characterised by an initial underfilled flysch stage during which a suite of deep marine turbiditic flysch sediments was deposited in the NAFBs over the underlying Helvetic Einsiedeln and Stad formations during Eocene to early Oligocene (Allen et al. 1991; Sinclair 1992). They are also known as Nummulitic limestones and Globigerina marls, respectively. Combined with the flysch unit, these three stratigraphic units, also termed "the underfilled trinity", have been interpreted to reflect sedimentation of an underfilled peripheral foreland basin (Figure 2.8). The lower unit (Nummulitic limestone), dominated by carbonate platform deposits, reflects shallow marine sedimentation on the European craton-ward margin of the basin. This unit accumulates on top of the underlying passive margin succession. The middle unit (Globigerina marls), dominated by mudstone rich in planktonic organisms, reflects sedimentation offshore from the craton-ward margin of the basin and the upper part of the middle unit commonly represents the deepest part of

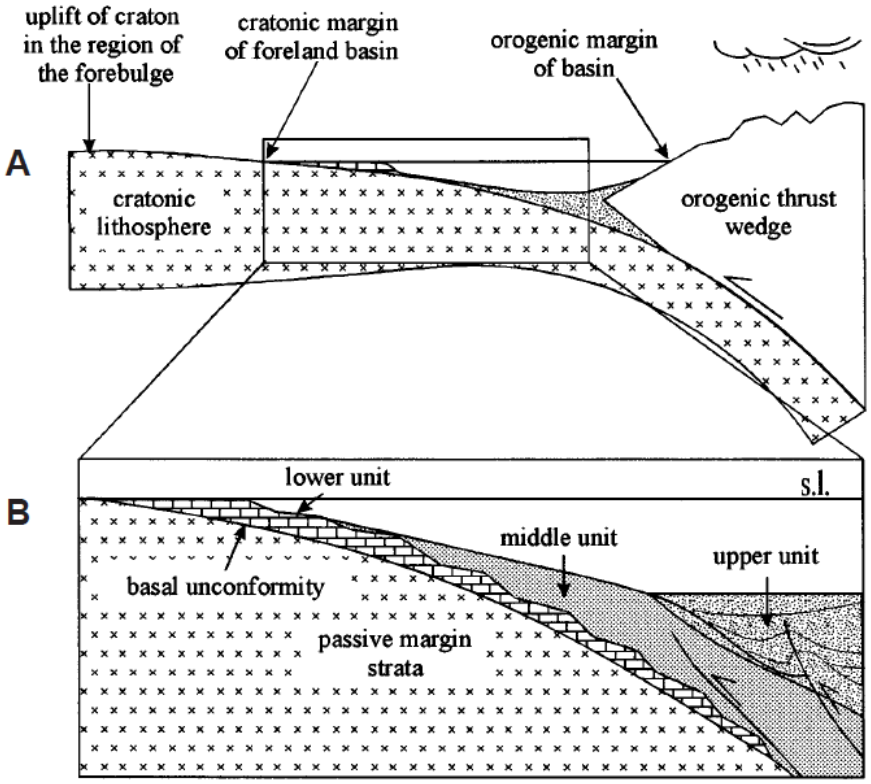

Figure 2.9 Basinal setting of the under-filled trinity in a peripheral foreland basin setting (from Sinclair, 1997).

the basin. The upper unit (flysch), dominated by thick successions of alternating turbiditic sandstone and mudstone derived from the thrust wedge, reflects deep marine sedimentation accumulated at the toe and on top of the thrust wedge in a way similar to the sedimentation processes in accretionary wedge settings.

2.5.2 Southern Alpine (Adriatic) foredeep

The southeastward Alpine subduction was replaced by westward Apenninic subduction along the front of the Alpine retro-belt to the south (Doglioni et al., 1998). A foredeep, formed on Adriatic continental crust, was proofed by a succession of calcareous deposits termed Tabiago/Scaglia Formation of Paleocene-middle Eocene in the western Lombardy region of southern Alps (Kleboth, 1982; Poletti et al., 2004), which is the oldest foredeep deposits generated at the onset of strong subsidence associated with westward subduction (Giulio et al., 2001).

The reason of using term “foredeep” rather than “foreland basin” here is to denote the largely-underfilled turbidite basins with high subsidence rates formed in front of low-relief belts associated with westward subduction, in

contrast to shallow foredeeps with low subsidence rates formed in front of high-relief orogens related to eastward subduction (Doglioni, 1994; Garzanti et al., 2007). Therefore, the fundamental difference between the shallow and slowly subsiding NAFB, developed along the Alpine pro-side, and the rapidly subsiding Adriatic foredeep, formed along the Alpine retro-side after the onset of Apenninic subduction should be emphasised (Doglioni, 1994).

The Adriatic foredeep received a very small volume of clastic sediments supplied by the Alpine belt during the Eocene and early Oligocene (Elter et al., 1999; Di Giulio et al., 2001). Sedimentation was mainly represented by carbonate strata Tabiago/Scaglia Formation and overlying Gallare Marls, locally interrupted by limited siliciclastic detritus (e.g., Montorfano member and Paderno nummulitic breccias within Scaglia Formation) and clastic calcareous deposits (e.g., Ternate Formation of late Eocene within Gallare Marls) probably fed by proximal thrust-sheet-top carbonate platforms which are now completely eroded (Di Giulio et al., 2001; Sciunnach, 2014; Coletti et al., 2016).

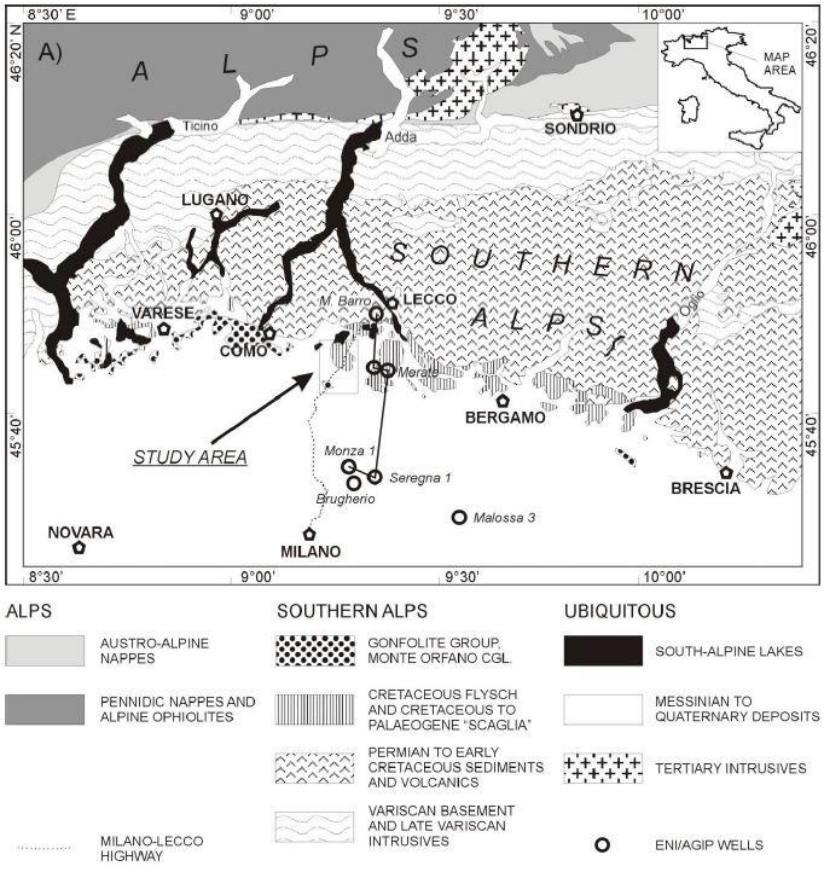

Figure 2.10 Tectonic sketch map of the Western Southern Alps (from Sciunnach, 2014).

The occurrence of volcaniclastic input into Adriatic foredeep is temporally and spatially limited, and represented by the Cibrone Formation in Brianza area which is the only exposed unit within the Gallare Marl. The Cibrone Formation, accumulated on top of the Tabiago Formation, is a marly sequence in which frequent fine sandstone turbidite layers are intercalated (Sciunnach, 2014). Some of these turbidite successions are defined as plagioclase-arenite (PA) by Gavazzi et al. (2003) and Di Giulio et al. (2005), because they are mainly constituted of fresh and euhedral single minerals of plagioclase, with subordinate volcanic rock fragments and single minerals of amphibole, biotite and opaques (Di Giulio et al., 2005). Paleocurrent measurements on volcanogenic sands indicate that detritus was sourced from ESE and NE (Bini et al., 2015). Based on biostratigraphic data, the Cibrone Formation has been dated to the middle Lutetian–upper Bartonian (44-39 Ma, Premoli Silva et al., 2009), whereas fission track measurements on apatites conducted by Malusà et al. (2011) indicate that the detritus has a Rupelian age (ca. 30 Ma). The latter authors also interpret these layers as distal dispersals of a hypothetic volcanic center once located above the Bergell pluton.

2.5.3 Alpine Maritime - Provençal foreland basin (southern French Alps)

The Maritime-Provençal Alpine foreland basins in southeastern France are located in the French departments of Alpes Maritimes, Alpes de Haute Provence and Hautes Alpes, represented by a series of Paleogene foreland basins (Figure 2.9), famously known as, for example, Champsaur basin, Barrême basin, Annot basin, Saint Antonin basin. From a structural point these basins are the southern part of the external Alpine foreland basin system, which is bounded by the Pelvoux massif to the north, the Maures-Esterel massifs to the south, the Argentera massif to the east and the Massif Central to the west (Callec, 2001). Castellane Arc is the joint of the N-S oriented basins and E-W oriented basins.

The structural complexity of the Maritime-Provençal foreland basin system results from the interference of multi-phase orogenic events, acting on a heterogenous Paleozoic and Mesozoic basement (Joseph, 2004). According to Apps (1987), the paleo-topography of the southern French foreland basin was controlled by the interaction of three different orogenic events: (1) the N-S

oriented Pyrenean-Provençal compression during the late Cretaceous-Paleocene, which established a structural fabric that influenced later, syn-depositional thrust geometries (Rosenbaum et al., 2002; Lacombe and Jolivet, 2005); (2) the NE-SW oriented Alpine convergence between the Adriatic and

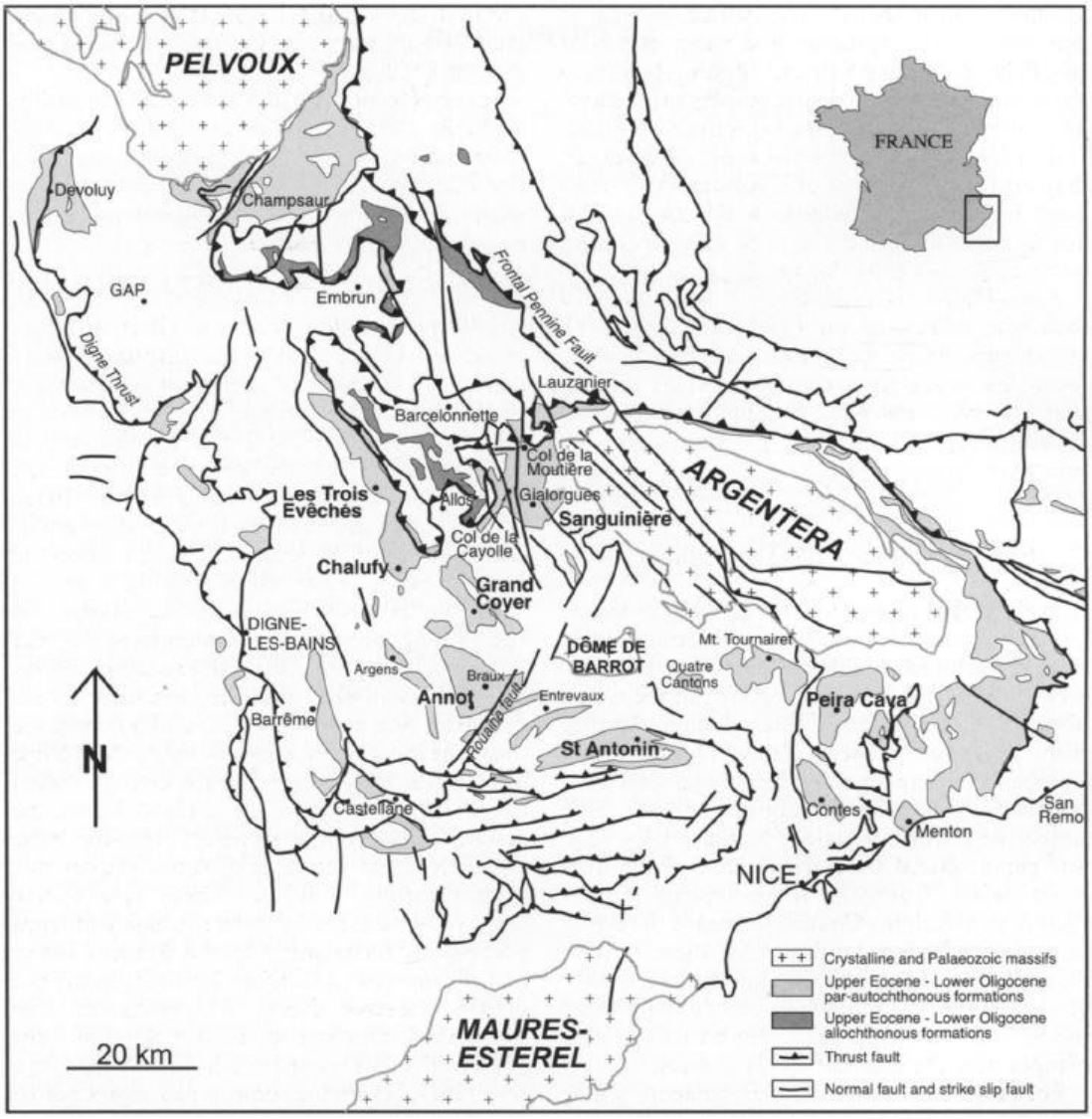

Figure 2.11 Structural map of SE France and location of outcrops of Annot sandstone and related systems (from Joseph and Lomas, 2014).

European plates during Middle Eocene to Early Oligocene, which created the flexural foreland basin system by the loading effects of the Alpine orogeny (e.g., Lacombe and Jolivet, 2005; Dumont et al., 2012); and (3) to the south, the subduction of the Tethyan oceanic crust below the southeast margin of the newly assembled Europe-Iberia plate during late Cretaceous to Eocene (Apps et al., 2004). This East Iberian orogeny induced the uplift of the Corsica-Sardinia massif and the rejuvenation of the Maures-Esterel massif, which

provided clastic sediments northward to the southern French Alpine foreland basins during the late Eocene. During early Oligocene, the rollback of the subduction slab or retreat of the subduction hinge towards SE induced the beginning of the rifting of the Liguria-Provençal basin, and the counter-clockwise rotation of the Corsica-Sardinia massif away from the Maures-Esterel massif, therefore leading to the cease of sediment supply from the Corsica-Sardinia massif (Sèranne, 1999; Malusà et al., 2016).

The Maritime-Provencal foreland basin is mainly characterised by a classic turbidite sandstone system named “Annot Sandstone” which was deposited in a broadly N-S directed connecting foreland basin system (Figure 2.10) including a series of originally linked sub-basins, extending from the Maures–Esterel massif together with Corsica-Sardinia massif to the south, presumably over and beyond what is now the Pelvoux basement massif to the north (Joseph and Lomas, 2004; Apps et al., 2004). Therefore, the Champsaur Sandstone in the Champsaur basin, located at the southeastern margin of the Pelvoux massif, represents a continuation of the time equivalent Annot sandstone system to the north (Vinnels et al., 2010; Butler et al., 2020).

The westernmost Barrême basin experienced E-W shortening, principally on its eastern flank during 28-30 Ma, when the first sediments arrived from the internal Alps (e.g., Evans and Mange-Rajetzky, 1991; Schwartz et al., 2012; Jourdan et al., 2013). A significant change from a southern source to a northeastern source in sediment provenance has been recorded in the Barrême basin. This change in provenance in the Barrême basin and the E-W shortening have been explained with a change in convergence directions from N-S to E-W in the western Alps between the Adriatic and European plates during the mid-Oligocene (Dumont et al., 2012), thus leading to the uplift of the internal Alpine domain. The presence of materials of Alpine affinity in the Barrême basin results from the dismantling of the internal reliefs (Bodelle, 1971; Evans and Elliott, 1999). This interval characterises a pivotal period of strong paleo-geographical change with the transition from a "Southern provenance" to an "Alpine provenance", highlighting the establishment of thrust belt of the Penninic domain (Evans and Mange-Rajetzky, 1991; Evans and Elliott, 1999; Callec, 2001).

The syn-sedimentary deformation in the Saint Antonin basin from the late Eocene to the early Oligocene was N-S directed and mainly affected the southern flank of the basin and the Saint Antonin basin was sourced always only from the south (Joseph and Lomas, 2014; Jourdan et al., 2018). Therefore, the Barrême and Saint Antonin basins show similar deformation styles but with different orientation of tectonic structures while in the same southern Alpine pro-side foreland basin system (e.g., Ford et al., 1999; Ford and Lickorish, 2004).

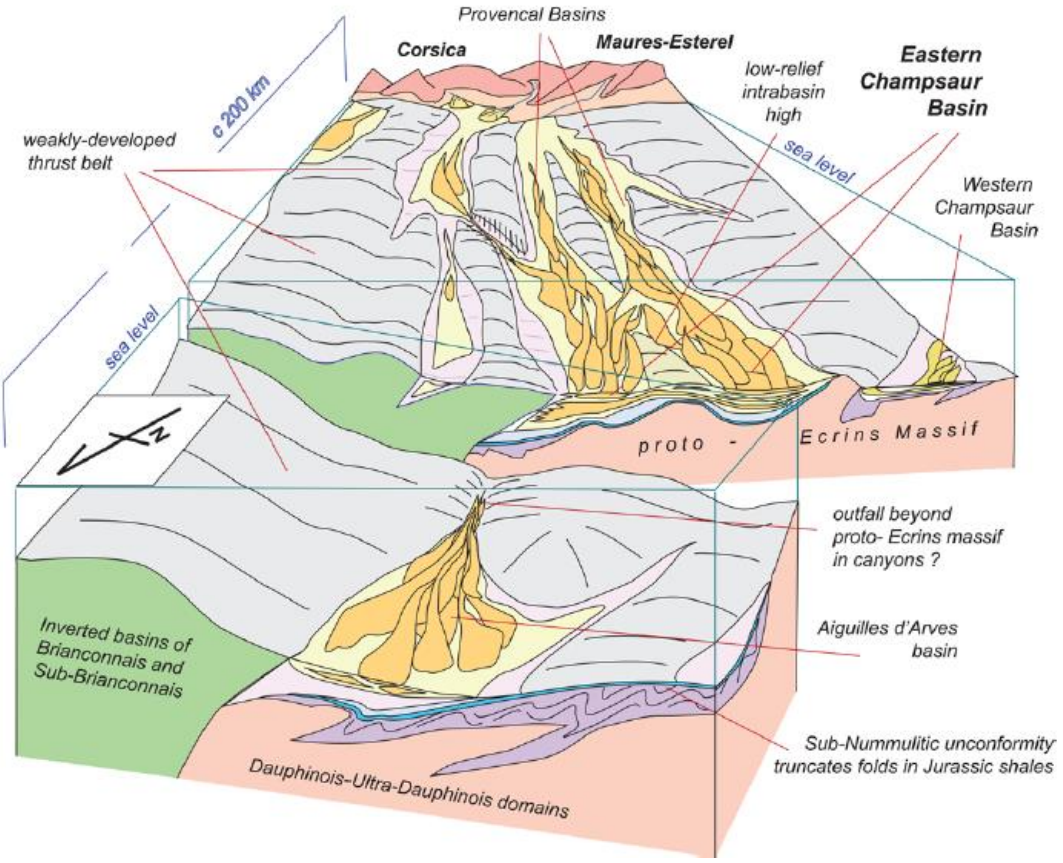

Figure 2.12 A schematic representation of the extent of the Annot turbidite system, connecting its well-studied proximal areas in Provence to the almost unstudied, more distal regions that include the Aiguilles d'Arves basin, via the Eastern Champsaur Basin (from Butler et al., 2020).

In summary, the main Alpine orogen was responsible for the majority of the flexural subsidence in the southern French foreland basin, but it did not provide clastic materials into the basin for most of its life. In contrast, the subduction-related East Iberian orogen, which was at the southern side of the foreland basin, hadn't contributed much during basin formation, but it was

responsible for uplift of the Corsica-Sardinia massif, creating the sediment source area for the Annot Sandstone (s.l.) (Apps et al., 2004).

2.6 Lithology and petrography of Taveyannaz sandstone

Despite a long tradition of geological research in volcaniclastic deposits in NAFB, there are still significant gaps associated with the volcanic sources of these deposits that remain very poorly investigated and understood. In particular, relatively little is known about the nature and origins of cryptic volcanic activity that took place during the orogeny. In fact, few geologists are aware that alpine volcanoes existed regionally, because the top of these edifices have been entirely eroded during the uplift of the Alps and therefore do not appear on geological maps. Therefore, to study the rarely-accessible erosional remnants preserved in NAFB represented by the classic “Taveyannaz sandstone” is a good way to investigate the nature and origins of these ancient volcanoes.

The lithologic and petrographic study of the Taveyannaz sandstone has been conducted by previous researchers. An impressive list of associated publications, of unequal value, is now available to study, and more importantly, to compare with. De Quervain (1928) conducted the first petrographic study of these rocks, including data on variations in lithology along the Alpine arc, and mineralogical descriptions. Vuagnat (1952) refined these observations, making a detailed qualitative description and quantitative microscopic examination of the petrography, and a first profound classification of Taveyannaz sandstone and volcanic rock fragments, based on the variation of texture and composition of the volcanic rock fragments. The regional study of Martini (1968) in the Platé Massif distinguishes better than Vuagnat (1952) from what is primary mineral to what is secondary mineral. He proposed that the only classification with an indisputable stratigraphic value must be based solely on the quantity of volcanic material, i.e., without taking into account the nature of the plagioclase or the degree of alteration of the ferromagnesian elements. The regional study of Sawatzki (1975) in the Thônes syncline proved the existence of intermediate sandstones among Northhelvetic Flysch sandstones, i.e., Ultrahelvetic flysch (GUH), Taveyannaz sandstone (GT) and Val d'llliez sandstone (GVI) based on quantitative study

and proposed the gradual variation trend of the percentage of volcanic components from southeast to northwest of the syncline.

2.6.1 Lithology and petrography

The Taveyannaz Sandstone consists of a volcaniclastic-rich flysch unit of several hundred meters thick formed of intercalated layers of green-grey turbiditic sandstones and dark-grey hemipelagic shales (Ruffini et al., 1997; Lu et al., 2018). The maximum bed thickness of sandstone is around 5 metres, and usually coarse sandstones could be 2 metres thick. On microscope scale, Taveyannaz Sandstones contain a variable proportion of volcanogenic and non-volcanic materials (e.g., Vuagnat, 1952; Lu et al., 2018). Volcanic material consists of a variety of volcanic lithoclasts, ranging from basaltic andesite to rhyolite, mainly andesite, and isolated mineral fragments such as amphibole, clinopyroxene, biotite and zoned volcanogenic plagioclase. Non-volcanic material is essentially composed of (1) fragments of granitoid plutonic rocks and, to a lesser extent, sedimentary, metamorphic rocks and basin intraclasts (e.g., reworked nummulitic limestone), (2) isolated minerals derived from the disintegration of the rocks mentioned above (e.g., Vuagnat, 1952; Martini, 1968). Mudclasts are also incorporated in these turbidites mostly at the base of erosive sequences, especially in Aravis and Taveyannaz localities (Lateltin and Müller, 1987; Lu et al., 2018). The sandstones are generally arkosic to lithoarenitic, poorly sorted with angular to sub-angular (rarely rounded) grains, which are typical features of turbiditic sediments. Grain size varies from fine to coarse, sporadically also containing larger-sized pebbles (e.g., Vuagnat, 1952; Sawatski, 1975; Lu et al., 2018). It should be noted that grain morphology (roundness) is an important indicator of subaerial transport, in particular that of andesite lithics and pebbles, ranging from angular to well-rounded in different samples (Sawatski, 1975).

Taveyannaz Sandstones are characterised by their richness in volcanic elements with more than 50 % on average according to the quantitative studies by Vuagnat, 1952 (41 - 88 %), Martini, 1968 (56 - 81 %), Sawatzki, 1975 (50 – 74 %), Ruffini et al., 1997 (65 – 92 %), Lateltin, 1988 (nearly 80 %). The enrichment of volcanic components is also a crucial criterion for dividing Taveyannaz sandstone into two subgroups: (1) typical Taveyannaz sandstone

(GTT) rich in andesitic components; (2) Taveyannaz sandstone poor (GTP or GTI) in andesitic components (Martini, 1968; Sawatzki, 1975).

The non-volcanogenic material usually plays a subordinate role in typical Taveyannaz sandstone. It is only in the varieties that are close to the overlying sandstones of the Val d'Illiez that non-volcanic material begins to become important (Vuagnat, 1952; Lateltin and Müller, 1987). However, it still provided quartz in notable quantities sometimes, feldspars including alkaline feldspar and plagioclase, scattered white mica and calcite (Lu et al., 2018). Cement and matrix are mainly composed of clay minerals and secondary products (e.g., chlorite, rarely laumontite), subordinate very fine-grained felsitic materials and locally calcite in the calcitised zones (Martini, 1968).

The content of quartz grains varies from $<$ 10 % up to even 50% in some fine-grained samples, implying the various degree of incidence of basement erosion in the source area (Lu et al., 2018) or the effect caused by grain size. In the Val d'Illiez sandstone a further increase of quartz ($>$ 60 %, Lateltin, 1988) and white micas is obvious. A similar increase of quartz grains and white micas in the Elm and Matt Formations was also reported from the Glarus area (Siegenthaler, 1974).

Feldspar, including both volcanic and non-volcanic origins, is the most abundant grain type. De Quervain (1928) used Fédoroff's method to determine 18 plagioclases selected from Swiss Taveyannaz sandstone samples, 13 of which are between 85% and 40% anorthite. Later, Vuagnat (1952) conducted more than 60 analyses using the Fédoroff microscope on sections with sufficient crystallographic directions so that there can be no ambiguity. These results all suggest an albite nature (Vuagnat, 1952). Martini (1968) concluded that there are two main types of plagioclases: (1) albite, derived from secondary albitisation; (2) often zoned primary calcic plagioclase. The latter are contained mainly in sandstones strongly cemented by calcite. He illustrated that the calcitised sandstones making up the margins of the strata allow the preservation of plagioclases in their primary state (Martini, 1968).

The non-volcanic lithics are distributed as follows: (a) granitoid plutonic rocks, which is the most abundant, represented by granite; (b) sedimentary rocks, represented mainly by local Mesozoic limestone and Eocene nummulitic limestone and globigerina marls, as well as rare sandstone and shale; (c)

metamorphic rocks, represented by gneiss and quartzite (Vuagnat, 1952; Martini, 1968; Sawatzki, 1975).

2.6.2 Influence of grain size on volcanic concentration

There are two reasons for variation of modal composition with grain size: 1) the breakage of fragments into constituent grains, and 2) actual mineralogic variation with grain size (Zuffa, 1980; Ingersoll et al., 1984). The Gazzi-Dickinson method successfully eliminates the first source of compositional grain-size dependency. However, grain size still has a huge influence on volcanic concentration in Taveyannaz sandstone (Martini, 1968), though Gazzi-Dickinson method has been applied (Gazzi, 1966; Dickinson, 1970; Ingersoll et al., 1984; Zuffa, 1985). De Quervain (1928) and Martini (1968) had observed that the quantity of volcanic components varies along with the grain size classes. When Martini (1968) compared his data with those of Vuagnat (1952), the proportions of volcanic components determined by Vuagnat (1952) are systematically higher than his. This difference may be due to the fact that Vuagnat studied very coarse rocks compared to his without taking into account of grain size effect. The variation diagram created by Martini (1968) presents positive correlation between the concentration of volcanic components and the value of the median particle size (Figure 2.12). The explanation for this phenomenon is as follows: volcanic components (e.g., volcanogenic plagioclase, ferromagnesian minerals, and volcanic glasses) are less resistant to weathering during transport than the other terrigenous constituents (e.g., quartz) which will be then more comparatively concentrated in the fine grades.

Sawatzki (1975) concluded the percentage of volcanic components is a function of two factors: stratigraphic variation and grain size. Limited number of collected samples which are suitable for quantitative analysis of each locality and complex regional tectonic movements hampered the thorough study on stratigraphic variation of each foreland region along the arc. Thus, it is assumed that the medium to coarse sandstone samples in this study are of the same group - typical Taveyannaz sandstone rich in volcanic components.

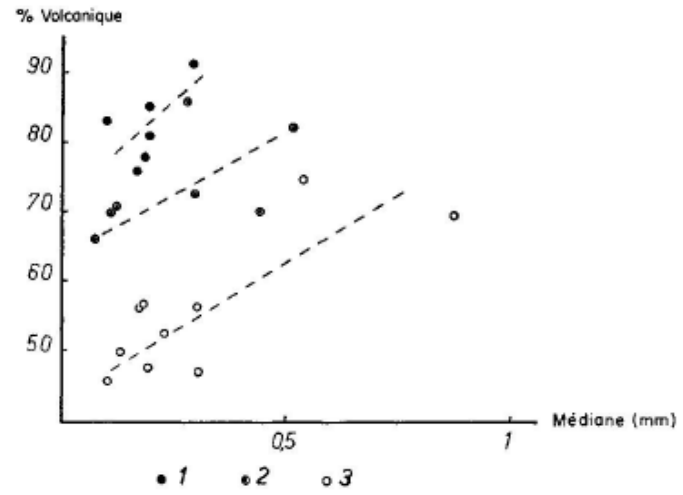

Figure 2.13 Variation of the content of volcanic material as a function of particle size: 1 = Typical Taveyannaz sandstone of the upper Gers Series, 2 = Typical Taveyannaz sandstone of the Barres de l'Arbaron and Tete Pelouse, 3 = Taveyannaz sandstone poor in volcanic material (from Martini, 1968).

2.6.3 Previous petrographic classifications of Taveyannaz sandstone

The petrographic classifications of Taveyannaz sandstone have been proposed by a group previous researcher (Table 2.1). De Quervain (1928) was the first to subdivide Taveyannaz turbiditic sandstones according to their petrographic facies. Vuagnat (1952) classified sandstones in detail in terms of the textures of andesitic facies rocks and the mineralogical composition of volcanic rocks. It distinguishes four subtypes: (1) GT Ⅰ: True andesite or basalt; (2) GT Ⅱa: Spilites (albite replacing plagioclase) with augite and/or hornblende, containing debris of albite, augite and/or hornblende; GT Ⅱb: Andesites or altered basalts with remains of augite and/or hornblende, containing abundant calcium alteration minerals, augite debris and/or hornblende; (3) GT Ⅲ: Andesites or altered basalts without fresh augite and/or hornblende, containing abundant calcium alteration minerals, absence of augite debris or hornblende (chlorite); (4) GTⅣ: Albito-chloritic spilites, containing albite debris and cemented chlorite. Later, Martini (1968) distinguishes better than Vuagnat (1952) from what is primary mineral to what is secondary mineral. He proposed that the only classification with an indisputable stratigraphic value must be based solely on the quantity of volcanic material, i.e., without taking into consideration the nature of the plagioclase or the degree of alteration of the ferromagnesian elements. Thus, Martini (1968) outlined two broad categories: (1) Typical G.T.: sandstone rich in volcanic components; (2) Poor

G.T.: sandstone poor in volcanic components. Sawatzki (1975) introduced new terms (i.e., GUH: ultrahelvetic sandstone; GI: intermediate sandstones; GTI: intermediate Taveyanne sandstone; GTT: typical Taveyanne sandstone; GTP: poor Taveyanne sandstone; GVI: sandstone of the Val d'Illiez) without changing much on subdividing criteria. Lateltin (1988) adopted the nomenclature and classification established by Vuagnat (1952), while this classification has been proved outdated. The summary table below makes it possible to understand the terminology equivalences between the different authors:

Table 2.1 Subdivision of Taveyannaz sandstone by previous authors

Vuagnat (1952)	G.T. Ⅰ	G.T. Ⅱ (Ⅱa, Ⅱb)	G.T. Ⅲ	G.T. Ⅳ
Martini (1968)	Typical G.T.			Poor G.T.
Siegenthaler (1974)	Vorstegsandstein			Muttenbergensandstein Ruchisandstein
Sawatzki (1975)	GTI, GTT			GTP
Lateltin (1988)	G.T. Ⅰ	G.T. Ⅱ	G.T. Ⅲ	G.T. Ⅳ

2.6.4 Compilation of previous petrographic data

A compilation of previous petrographic quantitative analytical results (modal analysis) of Taveyannaz sandstone is given in Table 2.2. The first three datasets compiled below (Vuagnat, 1952; Martini, 1968; Sawatski, 1975) mainly focus on volcanic and non-volcanic grain types. In contrast, Lateltin (1988) focused on modal analysis on detrital framework components (e.g., quartz, feldspar and lithics QFL, Q_mPK) to apply to tectonic discrimination diagrams (Dickinson and Suczek, 1979; Dickinson et al., 1983; Dickinson, 1985), without detailing the nature of volcanic components. Unfortunately, part of these studies only showed mean compositional values without providing the modal composition of individual samples (Martini, 1968; Lateltin, 1988), which limits the possibility to compare these results among themselves and with new datasets. Ruffini et al. (1997) focused on parameters BL-IL-AL (BL: basic lava clast; IL: intermediate lava clast; AL: acid lava clast) in order to stress out the information about different types of lava, but the components selected

for the modal analysis partly differ from those used in previous studies. In order to compare these data with each other and with our own results, the compilation used here focused on three main type of components: (1) volcanic material (V), in the form of volcanic rock fragments or volcanogenic isolated minerals (plagioclase, clinopyroxene, amphibole, biotite); (2) sedimentary material (S), including sedimentary rock fragments (sandstone, limestone, shale), chert, radiolarite and white mica debris; (3) crystalline material, including metamorphic (gneiss, quartzite) and plutonic (granite) rock fragments, and isolated minerals (e.g., quartz, alkaline feldspar, non-volcanic plagioclase). The symbols (V, S, C) represent the sum of recalculated volcanic, sedimentary and crystalline materials, without taking into consideration of cement and matrix, V+S+C=100. The results of these integrations are shown on the V-C-S ternary diagram (Figure 2.13).

Table 2.2 Summary of published modal analysis data of Taveyannaz sandstone

Vuagnat (1952)	Sp(andesitic except Fm)	Fm (cpx/ amph)	Qtz	Fsp(non-volcanic)	Sed. rock	Carbonate	Cement	**V**	**S**	**C**
GT Ⅱ	86	4	2	2	0	2	5	94	2	5
GT Ⅱ	50	6	13	5	0	1	26	72	6	22
GT Ⅱ	29	8	3	1	0	1	58	81	8	11
GT Ⅱ	64	9	3	2	0	3	18	83	8	10
GT Ⅱ	81	2	5	3	0	0	8	89	2	9
GT Ⅱ	87	2	7	2	0	1	1	90	2	8
GT Ⅱ	73	4	6	2	0	4	11	86	6	8
GT Ⅱ	88	1	7	2	0	1	0	89	1	9
GT Ⅱ	70	7	9	7	0	2	4	81	2	17
GT Ⅲ	33	0	10	6	0	1	50	70	1	29
GT Ⅳ	48	0	12	10	2	5	23	55	14	30
GT Ⅳ	53	0	11	5	2	3	26	62	14	24
GT Ⅳ	74	0	6	2	0	3	15	85	5	10
GT Ⅳ	58	0	13	9	0	0	20	68	0	32

GT Ⅳ	69	0	13	6	5	3	4	71	8	20
GT Ⅳ	71	0	9	4	2	2	10	76	8	16
GT Ⅳ	85	0	7	2	0	2	3	87	2	10
GT Ⅳ	52	0	16	6	4	2	19	59	13	28
GT Ⅳ	48	0	12	8	2	0	31	67	8	26
GT Ⅳ	41	0	6	2	2	8	41	55	23	22
GT Ⅳ	40	0	8	2	2	8	40	53	23	23

Martini (1968) (Mean)	**V**	**S**	**C**
TS poor in volcanic components	55.7	2.4	41.9
Typical TS rich in volcanic components (Série de Gers)	81.0	1.5	17.5
Typical TS rich in volcanic components (Barres de l'Arbaron)	73.2	2.3	24.5

Sawatzki (1975)	V(andesitic including Fm)	Qtz	Acid lithics	Plu. lithics	Meta. lithics	Sed. lithics	Carb.	Cement	**V**	**S**	**C**
GTI(mean)	50	28	1.9	15	0.2	1.4	2	3	51.8	1.5	46.7
GTT(mean)	74	13	0.3	6	0	1.9	0	5	77.7	2.0	20.3
GTP(mean)	53	25	0.7	12	0.1	2.8	3	3	56.7	3.0	40.3

Lateltin (1988)	**Q**	**F**	**L**	Qm	F	Lt	Qm	P	K
GT Ⅱ-Ⅲ(mean)	30	42	28	22	65	13	30	65	5
GT Ⅳ(mean)	44	32	24	35	49	16	26	65	9

Ruffini (1997)	**Q**	**F**	**L**	Lm	Lv	Ls	**BL** (basic)	**IL** (inter-mediate)	**AL** (acid)
Flaine (Platé)	27	48	25	20	74	6	1	85	14
Araches (Platé)	23	63	14	5	95	1	4	84	12
Oulette (Aravis)	20	49	31	5	90	5	11	85	4
La Clusaz (Aravis)	17	50	33	2	96	2	1	94	5

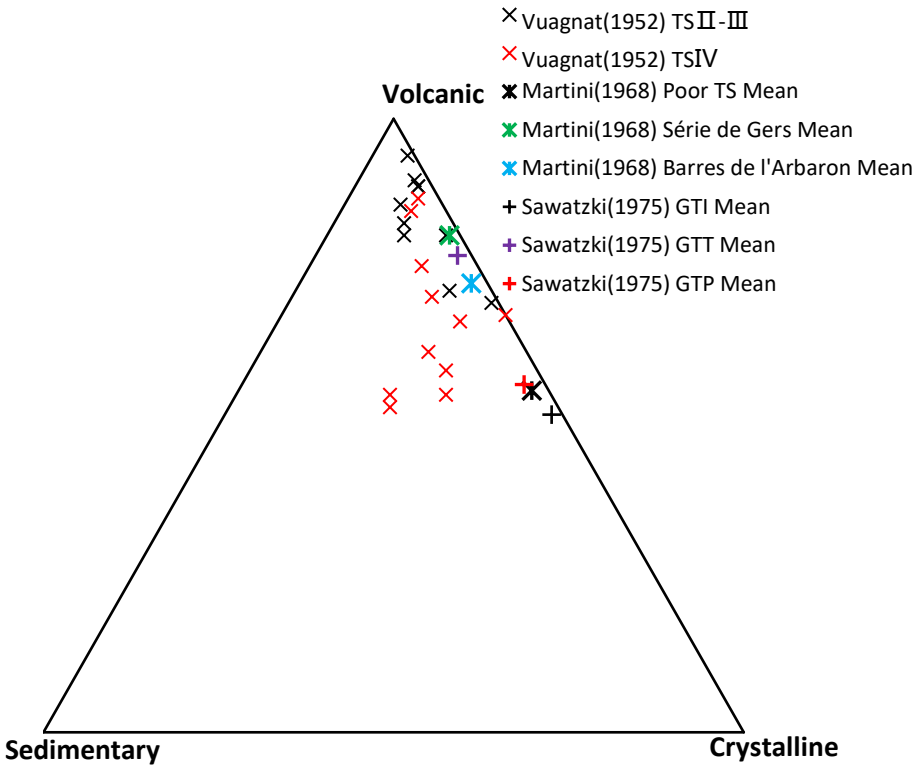

Figure 2.14 Ternary diagram of volcanic, sedimentary and crystalline material compiled from previous data

2.6.5 Established textural and mineralogical classification schemes of volcanic rock fragments

The volcanic rock fragments in Taveyannaz sandstone have a predominant porphyritic texture determined by large phenocrysts of plagioclase and by subordinate clinopyroxene and/or amphibole phenocrysts encompassed in a fine-grained or glassy groundmass (Vuagnat, 1952; Martini, 1968). These Taveyannaz volcanic lithics composed of dominant andesite clasts over 85% by volume with minor basic and acid volcanic clasts (Ruffini et al., 1997) are characterised by a high feldspar to ferromagnesian minerals ratio either included in a microcrystalline groundmass or appearing as phenocrysts (Vuagnat, 1952). In practice it seems that it is more complex, especially with the textural and compositional variability.

(1) Textural classification

Vuagnat (1952) is the first researcher who systematically studied the classification of volcanic rock fragments within Taveyannaz sandstone based on their textural variation and mineralogical variation. In his study, andesitic clasts are subdivided into vitrophyric, felsitic and microlitic categories based

on the differences in the texture of the microcrystalline groundmass. The small plagioclase crystals are the predominant element of the texture, and they are the ones that determine its texture (Vuagnat, 1946). In addition, the microlitic texture is further divided into fine/coarse hyalopilitic, fluidal hyalopilitic, pilotaxitic, and trachytic (Vuagnat, 1952).

Dickinson (1970) summarised similar classification of volcanic rock fragments with that of Vuagnat, added with one more type, which is lathwork texture, including intersertal and intergranular texture. The most common textures based on the previous classifications are summarised in Table 2.3. Dickinson (1970) also pointed out that volcanic fragments characterised by lathwork textures are generally basaltic, whereas those exhibiting microlitic or felsitic textures are mainly of intermediate to felsic composition. The application and significance of textural variation of volcanic rock fragments in determining volcanic provenance has been justified by previous workers. Specifically, microlitic and lathwork volcanic lithic proportions have been used to distinguish intermediate from basaltic sources by plotting on ternary diagrams (Lundberg, 1991; Marsaglia, 1991; Marsaglia, 1992; Marsaglia, 1993).

Table 2.3 Various types of textures of groundmass of andesite rock fragments (after Vuagnat, 1952; Dickinson, 1970)

<table>
<tr><td colspan="6">Vitrophyric</td></tr>
<tr><td rowspan="2">Felsitic</td><td rowspan="2">Microlitic</td><td>Hyalopilitic</td><td>Pilotaxitic</td><td rowspan="2">Lathwork</td><td>Intersertal</td></tr>
<tr><td>Fluidal hyalopilitic</td><td>Trachytic</td><td>Intergranular</td></tr>
<tr><td colspan="6">Felsic ⟶ Mafic</td></tr>
</table>

The upper part of this table corresponds to vitrophyric texture where the groundmass is almost entirely made of glassy material, having been commonly devitrified and/or altered to clay minerals and chlorite; while the lower part corresponds to the three major types of texture (i.e., felsitic, microlitic, lathwork) in the order of felsic to mafic composition from left to right (Dickinson, 1970).

Felsitic texture is characterised by anhedral, microcrystalline mosaic crystals composed mainly of quartz and feldspar, and often exists in felsic volcanic rocks (Vuagnat, 1952; Dickinson, 1970).

Microlitic texture contains small subhedral to euhedral elongate microlites in a range of patterns, which could be further divided by the orientation of microlites. The upper row of microlitic texture zone includes hyalopilitic and pilotaxitic textures with random to sub-parallel orientation and the lower row represents fluidal or trachytic textures where microlites tend to arrange in parallel to each other. Microlitic texture often exists in intermediate volcanic rocks (Vuagnat, 1952; Dickinson, 1970).

Lathwork texture contains euhedral plagioclase laths in intergranular and intersertal patterns where spaces between larger crystals are occupied by glass or small crystals. Lathwork texture often exists in basaltic rocks (Vuagnat, 1952; Dickinson, 1970).

(2) Mineralogical classification

Secondary minerals (i.e., albite, calcite, sericite and chlorite) play a leading role in many samples replacing plagioclase, clinopyroxene, amphibole and groundmass; other various secondary minerals include zeolite, epidote, prehnite, pumpellyite and opaque minerals. Clinopyroxenes and amphiboles do not only be altered to chlorite, but also altered to quartz, calcite, epidote, opaque minerals, and very fine-grained aggregates (Vuagnat, 1952; Martini, 1968; Sawatzki, 1975). All these secondary alterations make the classification work more complex with a higher degree of uncertainty.

Vuagnat (1952) firstly subdivided the andesitic clasts using the mineralogical composition characteristics of the rocks. It distinguishes four types of andesitic clasts including Type A, B, C and D (D'), unfortunately determining the primary composition of the sandstones and characterising their sources was biased by including secondary minerals (e.g., metamorphic albite and chlorite) in the primary components. Later, Martini (1968) had a further understanding of secondary products of alteration, benefitted from the development of the discipline, and proposed that the only classification with an indisputable petrographic value must be solely based on the primary volcanogenic material, i.e., without considering the nature of the plagioclase

or the degree of alteration of the ferromagnesian elements. Therefore, all four types of andesite clasts established by Vuagnat (1952) are perhaps derived from the same original type, but later transformed into different subgroups due to tectonic or metamorphic variations in different places. Martini (1968) pointed out that all andesite clasts vary between clinopyroxene andesite and amphibole andesite. The variation of the clinopyroxene to amphibole ratio could be characteristic of original andesite clast.

2.7 Provenance of volcanic components

The provenance of volcanic components within the Taveyannaz Sandstone (s.l.) is one of the most attractive and complex problems of the Alpine geological history. Many studies have been dedicated to this problem for decades, but the hypotheses on the magmatic sources, the original position of the volcanic edifices and especially the mysterious geodynamic mechanism controlling the generation and distribution of andesitic volcanism remained highly uncertain (De Quervain, 1928; Vuagnat, 1952). After reviewing and synthesising tens of associated published literatures in terms of andesite origin (Table 2.4), two groups of distinct hypotheses with each single group containing further two scenarios respectively are summarised based on the original position of the volcanic edifice (i.e., internal or external Alps) and the way of transport (i.e., tectonic transport of andesitic rocks by long-distance overthrusting or sedimentary transport). In addition, a special model, proposed by Di Capua and Groppelli (2016) reckoning that volcaniclastic deposits are actually disaggregated PDCs discharged from internal Alps crossing tens to hundreds of kilometers directly to the basin, was also included.

2.7.1 Local volcanic source

(1) Primary volcaniclastic deposits of local volcanic source

Some authors of early studies (e.g., Beuf, 1961; Giraud and Didier, 1981; Giraud, 1983; Doudoux et al., 1987; Lapierre et al., 1995; Féraud et al., 1995) consider the Taveyannaz andesites as primary volcanic deposits, related directly to volcanic eruptions in or near the depositional basin, such as pyroclastic fallout and flow deposits, lava flows and andesitic dykes. This explanation is supported by evidence, including the immaturity of sandstone components, large amounts of volcanic detritus (> 90 %) and freshness of the

amphiboles and clinopyroxenes isolated or present in the volcanic fragments which suggest instantaneous production and remobilisation of volcanic detritus rather than erosion and transport by fluvial processes (Giraud, 1983; Lapierre et al., 1995).

(2) Secondary volcaniclastic deposits of local volcanic source

Some authors (Sawatzki, 1975; Evans and Mange-Rajetzky, 1991; Jourdan et al., 2013; Pfiffner, 2014; Glarus B in Lu et al., 2018) represented by Boyet et al. (2001) proposed that volcanic detritus is derived from the erosion of volcanoes located near or in the foreland basin, but they are epiclastic rather than pyroclastic and deposited with other reworked rocks. This argument is supported by the evidence that the volcanic components are well preserved and the volcanism and sediment deposition took place over a very short period of time (Boyet et al., 2001). In addition, the volcanic fragments are not rounded, which excludes a long river transport. This argument is confirmed both by the high percentage of these elements (80 %) in the flysch and by the homogeneity of the flysch over the 400 km of their extension along the Alpine arc. As a result, the source of the volcanic fragments must have been close to the SE margin of the foreland basin (Sawatzki, 1975).

2.7.2 Distal Alpine source along the Periadriatic Line

(1) Volcanic detritus transported from internal zone to external zone by fluvial process

Generally, plutons and dykes along the Periadriatic Line, in the Adamello, Bergell and Biella magmatic systems are regarded as the volcanic sources of Taveyannaz Sandstone by various authors (Vuagnat, 1952; Lateltin, 1988; Rahn et al., 1995; Sinclair, 1997; Lu et al., 2018; Lu et al., 2019). Vuagnat (1952) summarised that the Taveyannaz sandstones have no tuff and there is no indication that the andesitic eruptions were contemporaneous with the deposit, because no glass shards were observed; these sandstones are normal detrital rocks. Volcanic detritus is derived from a long transport of more internal origin in the Alps, which represents a reworked and typical epiclastic products (Lateltin, 1988). According to a recent study by Lu et al. (2018) (Figure 2.14), the summary of geochronological results suggests that the volcanic materials in the Taveyannaz Fm. come from surficial extrusions and

dykes along the Peri-Adriatic Line between 41 and 29 Ma. The presence of numerous Neo-Proterozoic and Paleozoic detrital zircon infers a mixture of the volcanic products with Alpine basement material, hence, common long-distance fluvial transport to the basin margins (Lu et al., 2018; Lu et al., 2019). Lateltin (1988) also summarised that the almost total absence of vitreous fragments in the Taveyannaz Sandstone suggests that these are epiclastic products. The diversity of andesitic textures encountered in the Taveyannaz Sandstone (Vuagnat 1952), the alteration of volcanic fragments (Vuagnat 1952, Martini, 1968), the sedimentology of these deposits (Vuagnat, 1952; Martini, 1968; Sawatski, 1975; Lateltin, 1988), as well as the considerable proportion of non-volcanic material (Lu et al., 2018) all argue for a reworking of volcanic products from distal volcanic sources to the foreland basin.

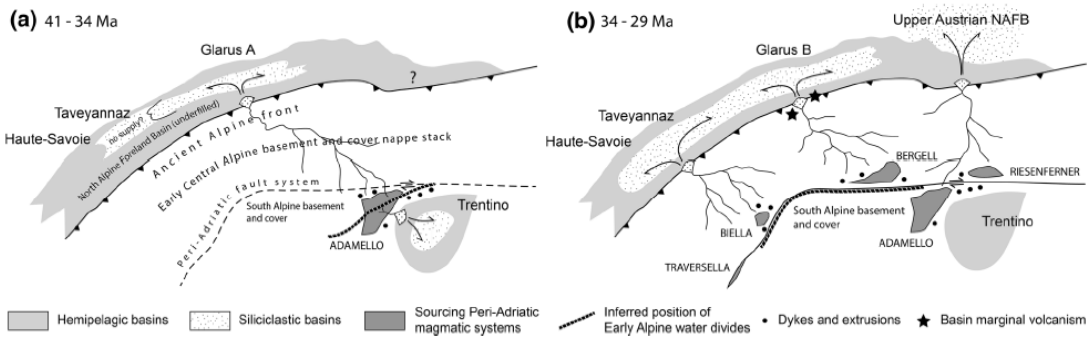

Figure 2.15 Paleogeographic reconstruction of the Late Eocene-Early Oligocene Alpine source-to-sink systems (from Lu et al., 2018).

(2) Volcanic rocks transported by tectonic long-distance overthrusting and/or gravity sliding

Since the discussion of andesitic origin in Taveyannaz Sandstone, a long-standing issue is how to explain the abundance and well-preservation of volcanic detritus within Taveyannaz Sandstone after the long-distance riverine transport from the internal Alps to the external foreland basin if a Periadriatic Line source is assumed. Alternatively, as mentioned above, if andesitic volcanism initially occurred in proximity to the foreland basin, it could resolve the issue. However, in the light of subduction model, subduction-related andesitic volcanism should be positioned on the upper Adriatic Plate somewhere near the Penninic/Austroalpine boundary rather than on the underlying European Plate (Waibel, 1990). Therefore, a genius idea had been proposed by Waibel (1990) and Waibel (1993).

He proposed that a likely position of the original andesitic volcanoes was in the immediate vicinity of subduction zone on top of the Austroalpine nappes, more specifically, perhaps above the intrusive bodies situated along the Periadriatic Line. Then the volcanic edifices were detached from their foundation during continental collision, incorporated into one or several nappes, and transported by long-distance overthrusting and/or gravity sliding. It may reasonably be assumed that the andesitic rocks were taken to somewhere between the SE margin of foreland basin and the front of the approaching Penninic nappes (Waibel, 1990; Waibel, 1993). This proposal was supported by Ruffini et al. (1997) as well. According to Ruffini et al. (1995) and Ruffini et al. (1997) (Figure 2.15), the volcanism of the Taveyannaz sandstone and the Periadriatic magmatism should have had a common magmatic source. The very short time span between the volcanism and the deposition of the volcanic clasts suggests that only a rapid tectonic transport of the volcanic sources at the front of the active "fold and thrust" Alpine belt can account for the assumed distance between the original position of the volcanic edifices in the more internal Alps and the present-day position of the Taveyannaz sandstones in the Helvetic nappes. Subsequent complete erosion of the volcanic edifices supplied the volcanic clasts that were deposited in a migrating basin of the accretionary wedge.

This model perfectly fits the two following conditions: (1) a local andesitic source providing abundant fresh andesitic detritus to the basin; (2) an original Periadriatic Line source which is consistent with the calc-alkaline nature of the andesitic volcanism, typical for subduction-related arc volcanic systems.

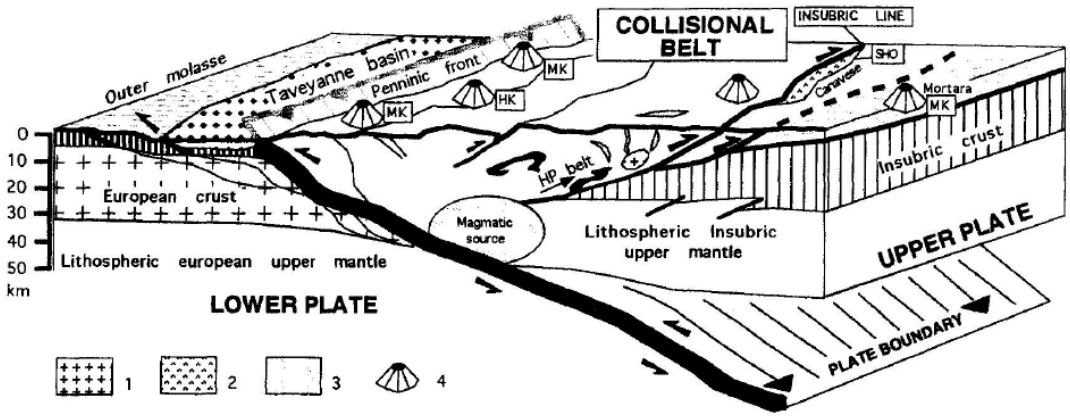

Figure 2.16 Simplified sketch representing the position of the volcanic bodies whose dismantlement gave origin to the Taveyannaz volcanic clasts in the

Oligocene Alpine orogenic belt. 1 Periadriatic plutons; 2 Canavese volcanic flows; 3 Periadriatic dykes; 4 volcanic bodies (from Ruffini et al., 1997)

2.7.3 Disaggregated PDCs discharged from internal Alps directly to the basin

Besides the above-mentioned four main hypotheses, a bold hypothesis was proposed by Di Capua and Groppelli (2016) (Figure 2.16). They interpreted the internal part of the Alpine chain as a suitable source of the volcanic detritus in the sense that volcaniclastic detritus was produced by violent explosions due to water/flow mixing, which disaggregated pyroclastic density currents (PDCs) entering the basin. In other words, the explosive volcanic eruption of the Periadriatic volcanic centers provided the mass supply of volcanic detritus crossing tens to hundreds of kilometers all the way to the basin. In addition, they also proposed the volcaniclastic deposits are not typical pyroclastic deposits because shoreline and submarine explosions while pyroclasts entering the water disaggregate the PDC. This process made the pyroclastic flow move downslope as cold, water-supported turbidite currents rather than hot, volatile-supported PDCs (Trofimovs et al., 2008; Carey and Schneider, 2011).

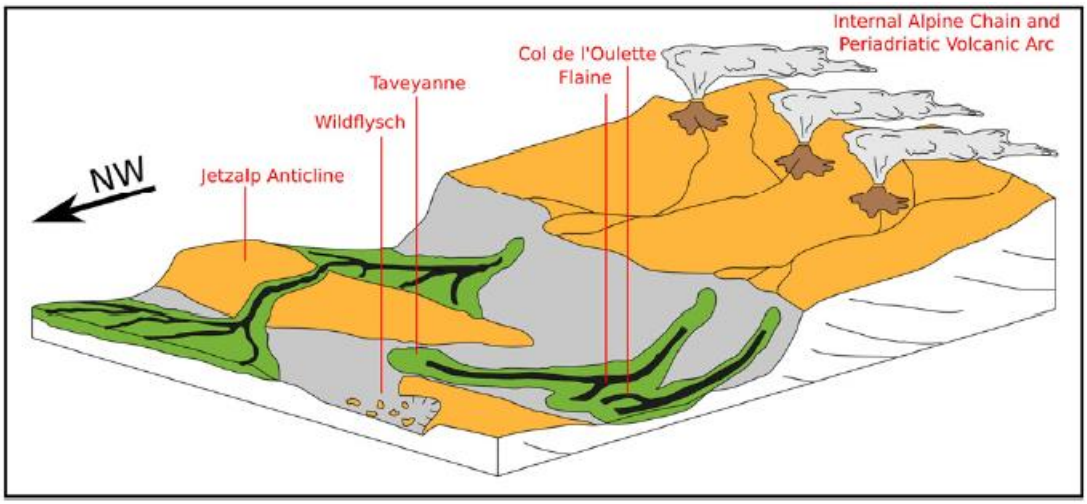

Figure 2.17 Paleogeographic reconstruction of the Oligocene Alpine source-to-sink system, fed by PDC events and reworked of volcaniclastic material, coming from the internal part of the Alps (from Di Capua and Groppelli, 2016).

Table 2.4 Summary of various hypothesis on the provenance and associated reasons of andesitic detritus within Taveyannaz sandstone

Hypothesis	Author	Study area	Provenance	Reasons
1. Primary volcaniclastic deposits of local volcanic source	Beuf et al., 1961	Thone, Champsaur, Clumanc	proximity of the emission centers	freshness and distribution of andesitic detritus
	Giraud, 1983	Western Alps		
	Doudoux et al., 1987	Haute-Savoie	a most probably in situ phreato-magmatic volcanism	spatial and temporal classification of andesitic volcano-sedimentary deposits
	Lapierre et al., 1995	Taveyanne, Champsaur	intrabasinal phreatomagmatic explosions of an intra-continent extensive context comparable to that of the Tertiary calc-alkaline volcanism of Colorado	freshness of the amphiboles and clinopyroxenes isolated or present in the volcanic fragments
		St. Antonin	local source linked to the subduction of an oceanic plate leaning towards the N-W under the Corsica-Sardinia-Provence block	pyroclastic deposits, the contemporary intrusions of Esterellite, and the slightly younger volcanic points of the Ligurian province (Biot, Vence, Antibes, Villeneuve-Loubet)
	Feraud et al. (1995)	Esterellite of Drammont, St Antonin, Taveyanne and Champsaur	a brief and unique event affecting the external and internal Alpine domains between the Mediterranean and the North of the study area	clearly identified contemporaneity of the whole of this volcanism

(Continued)

Hypothesis	Author	Study area	Provenance	Reasons
2. Secondary volcaniclastic deposits of local volcanic source	Sawatzki 1975	Thones	close to the SE shore of the flysch basin	1 volcanic fragments not rounded, exclude a long river transport 2 high percentage of these elements (80%) 3 homogeneity of the GT over the 400 km of their extension
	Evans and Mange-Rajetzky, 1991	Barrême	a currently unexposed centre existed in close proximity to the basin	Not mentioned
	Boyet et al., 2001	Champsaur - Western Switzerland	derived from the erosion of volcanoes located near or in the foreland basin, but not pyroclastic, still epiclastic, deposited with other reworked rocks.	1 volcanic components are well preserved 2 a short period of time between volcanism and deposition
	Jourdan et al., 2013	Barrême	first from southern Maures-Esterel massif and Corsica-Sardinia block, 30–29 Ma changed to north-eastern Alpine source	deposition of so-called ‘exotic’ pebbles such as gabbro, basalt, radiolarite, quartzite, and gneiss derived from the internal western Alps
		Andesitic detritus	very local andesitic source on the European plate	Not mentioned
	Pfiffner 2014	Haute-Savoie - Eastern Switzerland	a volcanic belt in the hinterland of the flysch basin	volcanic debris was deposited shortly after the eruptions and transported over short distances only.
	Lu et al., 2018, 2019	Glarus B	local volcanic activity likely along the southern margin of the NAFB in Glarus	out-sized fragile phreato-volcanic pebbles

(Continued)

Hypothesis	Author	Study area	Provenance	Reasons
3. Volcanic detritus transported from internal zone to external zone by fluvial process	Vuagnat, 1952	Haute-Savoie - Eastern Switzerland	transporting from inner zone to outer zone	No tuff, no shards, no remnants of lavas, epiclastic sediments, associated ophiolite debris from inner zone
	Lateltin, 1988	Haute-Savoie	1 a long transport of more internal origin in the Alps 2 a reworking of pyroclastic products with the surrounding land, exclude the source in the northern Subalpine Chains, 3 not only one volcano but rather several eruption centers, separated from each other by a hundred kilometers	1 typical epiclastic products, no glass shards, no dyke 2 diversity of andesitic textures, the alteration of volcanic fragments, non-negligible proportion of non-volcanic material 3 presence of sedimentary gravity flow structures such as water escape figures ("dish and pillars") and fluidization phenomena
	Rahn et al., 1995	Glarus	an extended volcanic island arc system along the Alpine front related to an underlying subduction zone	The presence of Taveyannaz and equivalent sandstones along the long Alpine arc can hardly be explained by a large central source volcano
	Sinclair, 1997	Western Alps	Behind the evolving thrust wedge, an active island-arc system may feed volcanic detritus into the trench	Not mentioned
	Lu et al., 2018, 2019	Haute-Savoie - Eastern Switzerland	surficial extrusions and dykes along the Periadriatic Line	TF bears variable and high amounts of siliciclastic grains probably derived from continental basement, presence of numerous Neo-Proterozoic and Palaeozoic Detrital Zircon indicates common long-distance fluvial transport

Hypothesis	Author	Study area	Provenance	Reasons
4. Periadriatic volcanic rocks transported by tectonic long-distance overthrusting	Waibel, 1990	Champsaur	1 andesitic volcanoes originally situated somewhere near the Penninic/Austroalpine boundary 2 they must have been thrust over the Penninic units before sliding down to their frontal position in the foreland	1 calc-alkaline nature 2 their widespread curvilinear occurrence adjacent and parallel to a plate boundary 3 their appearance during a convergent episode, there is ample justification for relating their origin to a subduction zone and associated magmatic arc.
	Waibel, 1993	Champsaur	1 a likely position of the original volcanoes is on top of the Austroalpine nappes, more specifically, above the granitic intrusive bodies situated along the Periadriatic Line 2 a local andesitic source, andesitic masses were exposed somewhere in the immediate hinterland and along the length of the internal coast.	1 mostly epiclastic with little dilution, most lava flows with little evidence of explosive eruption, but negligible dilution 2 associated ophiolite debris and high-P/low-T mafic cobbles from internal zone and blue amphibole with subduction overprint 3 compatible with the polarity of thrusting, calc-alkaline nature, widespread curvilinear occurrence adjacent and parallel to a sutured plate boundary, appearance during a convergent episode
	Ruffini et al., 1997	Haute-Savoie	1 dismantlement of extra-basinal volcanic bodies 2 a same magmatic source with Periadriatic Line magmatism 3 a rapid tectonic transport of the volcanic sources at the front of the active "fold and thrust" Alpine belt	1 absence of volcanic signature in the field and the sedimentological characteristics 2 very short time span between deposition and volcanism

2.8 Geochemistry of andesitic materials in Taveyannaz Sandstone (s.l.)

In the early studies, whole rock analyses of the Taveyannaz sandstones with more than 90% by volume of volcanic clasts were conducted, indicating a basaltic to basalt-andesitic composition, derivation from an orogenic, medium to high K calc-alkaline volcanism (Rahn et al., 1995; Ruffini et al., 1997). Compositional changes due to detrital input during sedimentation and alterations during Alpine metamorphism are characterised by a 10 wt. % enrichment of SiO_2, a slight depletion of Al_2O_3, FeO, and a slight enrichment of Na_2O, K_2O, and TiO_2 (Rahn et al., 1995). According to Ruffini et al. (1997), in the K_2O vs SiO_2 diagram (Peccerillo and Taylor, 1976), most points are scattered throughout the medium to high-K andesite field with only a few points in the basaltic andesite field (Ruffini et al., 1997). The low TiO_2 content of the sandstones suggests an orogenic rock series (Ewart and Le Maitre, 1980). Basaltic andesites with $SiO_2 < 56$ % plot in the field of calc-alkaline basalts in the Pearce and Cann's (1973) diagrams, meanwhile the MORB-normalized spider-diagram closely resembles that of the high-K orogenic andesite of Wilson (1989). Minor and trace element concentrations also suggest a calc-alkaline magmatism (Rahn et al., 1995), which is typical for island arc volcanic systems above the subduction zone (Condie, 1989).

However, the usefulness of geochemical interpretation of whole rock analyses is limited by the presence of detrital, non-volcanogenic material and by the metamorphic overprint (Rahn et al., 1995a; Rahn et al., 1995b). Therefore, major, trace element and isotopic analysis on pure andesitic clasts and associated mineral separates (e.g., amphibole, clinopyroxene and zircon) were conducted (Rahn et al., 1995; Ruffini et al., 1997; Boyet et al., 2001; Lu et al., 2018).

According to Boyet et al. (2001), trace element compositions of andesitic clasts and mineral separates are consistent with the calc-alkaline affinity of the volcanic components of Taveyannaz sandstone and Champsaur sandstone. All the samples are enriched in light rare earth elements (LREE) relative to heavy rare earth elements (HREE) ($2 < (La/Yb) < 15$) (Sun and McDonough, 1989). The primitive mantle-normalised composition (Sun and McDonough,

1989) of the andesitic clasts shows negative anomalies in Nb, Ta, Ti and enrichment in U and Pb (Boyet et al., 2001).

Isotopic data show that andesitic detritus in Champsaur sandstone have positive εNd while those from the Taveyannaz sandstone have negative εNd (Boyet et al., 2001). The decrease of εNd (+ 3.4 to - 2.6) correlates with an increase of ($^{86}Sr/^{87}Sr$) (0.70570 to 0.70571), $(La/Yb)_N$ and Th. These data suggest that this andesitic suite was derived from a mixture of mantle and continental crust sources. This conclusion is also confirmed by the range of ƐNd from + 4 to -9 and $^{87}Sr/^{86}Sr$ from 0.704 to 0.712, which is a typical mixing array between mantle and crustal isotopic values (von Blanckenburg and Davies, 1995). Contribution of the continental crustal component is lower in the Champsaur sandstone and higher in those of the Taveyannaz sandstone. Pb isotopic ratios confirm the continental crustal contribution in the source of andesitic volcanism, and the $\delta^{18}O$ measured on three clinopyroxene separates fall within the range of mantle values (Boyet et al., 2001).

According to Rahn et al. (1995), compositions of clinopyroxenes from the Glarus and Loèche (Coombs et al., 1976) are compared and are identical within the analytical diagram. Thus, clinopyroxenes display a close relationship between different Taveyannaz sandstone occurrences separated by around 120 km. Clinopyroxenes from the Glarus region are plotted in the diagrams of Nisbet and Pearce (1977) and Le Bas (1962), showing good correlation with the chemical pattern of Volcanic Arc Basalt (VAB). In the SiO_2-Al_2O_3 diagram, most analyses plot above the sub-alkaline/alkaline boundary (Le Bas, 1962), which points to an evolved basalt composition, as it is typical for fractionation within volcanic arcs. The low Ti values are typical for the absence of a thick continental crust, because clinopyroxenes from within-plate basalts are generally Ti-rich (Pearce, 1976; Leterrier et al., 1982). A slight increase in Ca relative to Fe and Mg is observed in clinopyroxenes from the more acid lava clasts, which is typical for clinopyroxenes of high-K calc-alkaline series (Gill, 1981; Ruffini et al., 1997).

The amphibole composition ranges from ferroan pargasite to ferroan pargasitic hornblende according to Leake's nomenclature (2004). The biotite in the acid andesites is a typical Ti-biotite (with Ti > 0.25 per formula unit)

(Rahn et al., 1995). According to Gill (1981), the presence of biotite in andesitic lavas is essentially recorded in rocks belonging to the high-K series.

According to Lu et al. (2018), the REE patterns of detrital zircon in Taveyannaz sandstone are characterised by a positive Ce anomaly (Ce_N/Ce^*=26.2 – 353.6, $Ce^*=(La_N*Pr_N)^{1/2}$), characteristic for oxidizing environment, as a result of the preferential incorporation of Ce^{4+} instead of Ce^{3+} in zircons (Schaltegger et al. 2009). Furthermore, all zircon grains from the Taveyannaz sandstone have chondrite-normalized REE patterns enriched in HREE. A slight difference in the values of εEu ($Eu_N/Eu^*=Eu^*2/(Sm+Gd)$, ~0.1 - 0.9) suggests the diversity of the magma source during the crystallisation of zircons (Lu et al., 2018). In addition, initial $^{176}Hf/^{177}Hf$ ratios (εHf(t)) reveal a clear clustering of the detrital zircon regarding ages and Hf isotopic signatures (Lu et al., 2018). Late mid-Eocene to late-Eocene zircons from the Glarus A Taveyannaz sandstone yield negative values of εHf (- 1.6 to - 5.6). Early Oligocene Glarus B Taveyannaz sandstone zircons reveal positive values of εHf (+ 4.1 to + 7.8). Rupelian Taveyannaz sandstone zircons in the Haute-Savoie area disclose negative values of εHf (- 1.2 to - 5.7).

In summary, based on the whole rock geochemistry of Taveyannaz sandstone, and major, trace elements and isotopic composition of andesitic clasts and mineral separates, it could be concluded that the Taveyannaz volcanism is related to an orogenic, medium to high K calc-alkaline, subduction-related volcanic arc system derived from a mixture of mantle and continental crust sources (Rahn et al., 1995; Ruffini et al., 1997; Boyet et al., 2001; Lu et al., 2018). The calc-alkaline serial affinity and late Eocene-early Oligocene ages of the Taveyannaz andesites fits well the geochemical characters and the time interval of the development of the magmatic activity in the internal sector of the Western Alps (Dal Piaz et al. 1979; Beccaluva et al., 1983; Venturelli et al., 1984; Callegari et al., 2004), indicating the cogenetic relationship between Taveyannaz volcanism (e.g., Rahn et al., 1995; Ruffini et al., 1997; Boyet et al., 2001; Lu et al., 2018) and Periadriatic Line magmatism (e.g., von Blanckenburg and Davies, 1995).

Chapter 3: Approach and Methods

3.1 Introduction

This chapter first explains the sampling and analytical strategy of this study, then presents the detailed information of visited localities/outcrops and collected samples. In order to achieve the aim of recognising and characterising regional differences of volcanic components preserved in NAFB along the whole Alpine arc, a comprehensive sampling strategy is needed to have a better understanding of any regional variations throughout the foreland basins. According to the literature review work which was finished in Section 2.2.2, a series of accessible outcropped localities of volcaniclastic deposits along the external NAFB were compiled (see Figure 2.2, in yellow). Therefore, the sampling strategy of this study is to visit all of these localities and collect as many as possible fresh volcaniclastic samples containing abundant volcanic detritus. The analytical strategy includes (1) quantitative petrographic analysis (grain-counting) in Chapter 4, (2) whole-rock geochemistry (ICP-OES+ICP-MS) in Chapter 5 and (3) clinopyroxene and amphibole geochemistry (SEM-EDS+LA-ICP-MS) in Chapter 6 and 7. All these analytical methods are used to classify and differentiate the volcanic components, ultimately achieving the overall goal of characterising different volcanic sources along the Alpine arc.

3.2 Fieldwork overview

3.2.1 Fieldwork campaign

Two field campaigns were carried out in 2018 and 2019. A first field campaign of 5 days was conducted in the western Swiss Alps in November 2018, during which 25 samples of volcaniclastic turbidites were collected at 5 localities. A second field campaign of approximately 3 weeks was carried out in southeast France and northwest Italy in September 2019 with 71 samples collected at 12 localities. These samples complemented sampling by my PhD advisor David Buchs in other north Alpine foreland basins, including 14 rock samples retrieved in Glarus, east Switzerland, in May 2019 and 14 samples retrieved from the Clumanc and St Antonin areas in southeast France, in July 2019.

Figure 3.1 Geological map of the Alps with field campaign localities (modified from Pfiffner, 2014).

A third personal field campaign was planned in 2020 in northern Italy to collect andesite dykes close to the Periadriatic Line, which had to be cancelled due to the start of the COVID pandemic. However, existing sampling allowed me to investigate the most typical outcrops of Taveyannaz-type sandstones in the North Alpine Foreland Basin (NAFB) along the western/northern side of Alpine orogenic arc (Figure 3.1). Details on the field observations and collected samples from a series of localities are discussed in the sections below. The location and rock type of all collected samples are presented in Table 3.1, with more detail information presented in Appendix E1.

Table 3.1 The location and rock type of all collected samples in this study.

Sample	Lat. (°)	Lon. (°)	Locality	Rock type
CL18-001	46.30167	7.12602	Taveyannaz	volcaniclastic sandstone/arkose

CL18-002	46.30145	7.12624	Taveyannaz	siltstone
CL18-003	46.30133	7.12614	Taveyannaz	volcaniclastic sandstone/arkose
CL18-004	46.30131	7.12608	Taveyannaz	volcaniclastic sandstone/arkose
CL18-005	46.29426	7.12150	Chaux Ronde	volcaniclastic sandstone/arkose
CL18-006	46.29429	7.12140	Chaux Ronde	volcaniclastic sandstone/arkose
CL18-007	46.32591	7.17768	Creux de Champ	volcaniclastic sandstone/arkose
CL18-008	46.32690	7.17752	Creux de Champ	volcaniclastic sandstone/arkose
CL18-009	46.32697	7.17755	Creux de Champ	volcaniclastic sandstone/arkose
CL18-010	46.32695	7.17769	Creux de Champ	volcaniclastic sandstone/arkose
CL18-011	46.32794	7.18134	Creux de Champ	volcaniclastic sandstone/arkose
CL18-012	46.32819	7.18159	Creux de Champ	mudstone
CL18-013	46.32927	7.16193	La Laya	volcaniclastic sandstone/arkose
CL18-014	46.32717	7.15963	La Laya	volcaniclastic sandstone/arkose
CL18-015	46.32703	7.16011	La Laya	volcaniclastic sandstone/arkose
CL18-016	46.34800	7.53535	La Tièche	epiclastic sandstone/quartz arenite
CL18-017	46.35468	7.53347	La Tièche	volcaniclastic sandstone/arkose
CL18-018	46.35468	7.53406	La Tièche	volcaniclastic sandstone/arkose
CL18-019	46.35466	7.53395	La Tièche	volcaniclastic sandstone/arkose
CL18-020	46.35294	7.53373	La Tièche	volcaniclastic sandstone/arkose
CL18-021	46.35263	7.53375	La Tièche	Micaceous sandstone/arkose
CL18-022	46.35244	7.53415	La Tièche	Micaceous siltstone
CL18-023	46.35500	7.53303	La Tièche	Calcareous siltstone
CL18-024	46.35592	7.54290	La Tièche	volcaniclastic sandstone/arkose
CL18-025	46.35592	7.54290	La Tièche	siltstone
DB19-032	47.14034	9.10299	Weesen	sandstone/arkose
DB19-033	47.13856	9.10274	Weesen	sandstone/arkose
DB19-034	46.99649	9.09161	Schwanden	micaceous sandstone/arkose
DB19-035	46.97620	9.05780	Haslen	sandstone/arkose

DB19-036	46.97620	9.05780	Haslen	sandstone/arkose
DB19-037	46.94667	9.03325	Betschwanden	sandstone/arkose
DB19-038	46.94667	9.03325	Betschwanden	sandstone/lithic arkose
DB19-039	46.94667	9.03325	Betschwanden	sandstone/lithic arkose
DB19-040	46.96787	9.02994	Luchsingen	sandstone/arkose
DB19-041	46.91134	8.98384	Linthal	sandstone/arkose
DB19-042	46.92562	9.01413	Linthal	siltstone
DB19-043	46.92562	9.01413	Linthal	sandstone/arkose
DB19-044	46.92562	9.01413	Linthal	sandstone/arkose
DB19-045	46.96778	9.17120	Matt	micaceous sandstone/lithic arkose
DB19-046	44.03402	6.37511	Clumanc	sandstone/arkose
DB19-047	44.03381	6.37521	Clumanc	sandstone/lithic arkose
DB19-048	44.03315	6.37563	Clumanc	sandstone/arkose
DB19-049	44.03309	6.37594	Clumanc	sandstone/arkose
DB19-050	44.03295	6.36967	Clumanc	sandstone/arkose
DB19-051	44.03150	6.37095	Clumanc	sandstone/lithic arkose
DB19-052	44.03276	6.37785	Clumanc	conglomerate/lithic arkose
DB19-053	44.03276	6.37785	Clumanc	sandstone/arkose
DB19-054	44.02767	6.38240	Clumanc	sandstone/arkose
DB19-055	44.02767	6.38240	Clumanc	collection of andesite cobbles
DB19-056	43.90633	6.86204	St Antonin	andesite clast
DB19-057	43.90633	6.86204	St Antonin	andesite clast
DB19-058	43.90646	6.86278	St Antonin	andesite clast
DB19-059	43.90646	6.86278	St Antonin	tuffaceous matrix
CL19-001	46.00998	6.67770	Flaine	greenish sandstone/arkose
CL19-002	46.00998	6.67770	Flaine	sandstone/arkose
CL19-003	46.01293	6.68553	Flaine	sandstone/arkose
CL19-004	45.96443	6.53646	Col de l'Oulettaz	greenish sandstone/arkose
CL19-005	45.96392	6.53442	Col de l'Oulettaz	polymictic sandstone/lithic arkose
CL19-006	45.96367	6.53387	Col de l'Oulettaz	greenish sandstone/arkose
CL19-007	45.96373	6.52998	Col de l'Oulettaz	polymictic conglomerate/lithic arkose
CL19-008	45.96373	6.52998	Col de l'Oulettaz	sandstone/lithic arkose
CL19-009	45.89251	6.43889	La Clusaz	sandstone/arkose

CL19-010	45.89251	6.43889	La Clusaz	sandstone/arkose
CL19-011	45.89419	6.44066	La Clusaz	sandstone/lithic arkose
CL19-012	45.88011	6.34932	Thônes	sandstone/arkose
CL19-013	45.87994	6.34945	Thônes	sandstone/arkose
CL19-014	45.87993	6.34973	Thônes	sandstone/lithic arkose
CL19-015	45.88000	6.35009	Thônes	sandstone/lithic arkose
CL19-016	45.88000	6.35038	Thônes	sandstone/lithic arkose
CL19-017	45.88000	6.35000	Thônes	sandstone/arkose
CL19-018	44.72287	6.29537	Champsaur	polymictic sandstone/litharenite
CL19-019	44.72287	6.29537	Champsaur	microgranite pebble
CL19-020	44.72287	6.29537	Champsaur	rhyolite pebble
CL19-021	44.72287	6.29537	Champsaur	rhyolite pebble
CL19-022	44.72287	6.29537	Champsaur	sandstone/siltstone
CL19-023	44.72287	6.29537	Champsaur	microgranite pebble
CL19-024	44.72302	6.29537	Champsaur	basaltic andesite pebble
CL19-025	44.72302	6.29537	Champsaur	rhyolite pebble
CL19-026	44.72302	6.29537	Champsaur	basaltic andesite pebble
CL19-027	44.72302	6.29537	Champsaur	basaltic andesite pebble
CL19-028	44.72302	6.29537	Champsaur	basaltic andesite pebble
CL19-029	44.71796	6.27680	Champsaur	sandstone/litharenite
CL19-030	44.72384	6.28918	Champsaur	diorite pebble
CL19-031	44.72384	6.28918	Champsaur	dacite pebble
CL19-032	44.72384	6.28918	Champsaur	andesite pebble
CL19-033	44.72384	6.28918	Champsaur	andesite pebble
CL19-034	44.72384	6.28918	Champsaur	microdiorite pebble
CL19-035	44.72384	6.28918	Champsaur	sandstone/arkose
CL19-036	44.72384	6.28918	Champsaur	sandstone/arkose
CL19-037	44.72384	6.28918	Champsaur	andesite pebble
CL19-038A	44.72319	6.28906	Champsaur	monomictic andesite breccia
CL19-038B	44.72319	6.28906	Champsaur	monomictic andesite breccia
CL19-039	44.72365	6.29585	Champsaur	sandstone/arkose
CL19-040	44.72371	6.29584	Champsaur	monomictic andesite breccia
CL19-041	44.72371	6.29592	Champsaur	sandstone/arkose
CL19-042	44.03388	6.37527	Clumanc	collection of andesite pebbles
CL19-043	43.89663	6.84938	St Antonin	andesite breccia

CL19-044	43.89663	6.84938	St Antonin	andesite breccia
CL19-045	43.41820	6.84627	Agay	esterellite
CL19-046	43.41575	6.84499	Agay	mafic enclave in esterellite
CL19-047	43.41575	6.84499	Agay	mafic enclave in esterellite
CL19-048	43.66439	7.08693	La Vanade	andesite breccia
CL19-049	43.66439	7.08693	La Vanade	tuffaceous matrix
CL19-050	43.66573	7.08582	La Vanade	andesite breccia
CL19-051	43.66573	7.08582	La Vanade	andesite breccia
CL19-052	43.66606	7.08625	La Vanade	white tuff
CL19-053	45.58933	8.05533	Biella	microdiorite dyke
CL19-054	45.58933	8.05533	Biella	microdiorite dyke
CL19-055	45.59830	8.05379	Biella	gabbro
CL19-056	45.59886	8.05351	Biella	microdiorite dyke
CL19-057	45.62967	8.03771	Biella	margin of gabbro intrusion
CL19-058	45.66083	8.05768	Biella	andesite lava flow
CL19-059	45.66207	8.05834	Biella	andesite lava flow
CL19-060	45.66320	8.05963	Biella	andeiste lava flow
CL19-061	45.66398	8.05602	Biella	andesite lava flow
CL19-062	45.66420	8.05818	Biella	andesite breccia
CL19-066	46.23862	10.58064	Passo del Tonale	biotite-rich tonalite
CL19-067	46.24255	10.57895	Passo del Tonale	biotite-rich tonalite
CL19-068	46.24708	10.57597	Passo del Tonale	amph-rich tonalite
CL19-069	46.20758	9.63001	Bergell	amph-rich tonalite
CL19-070	46.21366	9.65056	Bergell	amph-biotite tonalite
CL19-071	46.23695	9.60538	Bergell	amph-biotite tonalite
CL19-072	46.24045	9.60990	Bergell	amph-biotite tonalite
CL19-073	46.31366	9.75868	Bergell	biotite-rich tonalite
CL19-074	46.17734	9.44039	Bergell	amph-biotite tonalite

3.2.2 Sedimentation of two distinct volcano-sedimentary environments

Field observations give constrains on the nature of sediment transport and the extent of reworking of the volcanogenic components in the North Alpine Foreland Basins in a range of at least 500 km from Glarus (eastern Switzerland) to Saint Antonin (southeast France). Overall, two distinct volcano-sedimentary environments have been distinguished:

(1) In Glarus, Taveyannaz and Aravis regions where detrital components are mostly extensively-reworked material with a variable and high proportion of basement reworking; andesite clasts are well-rounded to rounded, of various types of textures and composition; rare evidence exists for poorly reworked angular andesite pebbles and even primary volcaniclastic deposits.

(2) Further south, in Champsaur, Saint Antonin and La Vanade regions where the abundance of poorly reworked angular andesite clasts and pyroclastic deposits is obviously increasing; volcanic components are more homogeneous in terms of texture and composition; grain size is generally coarser with higher abundance of conglomerate and breccia.

The Aravis and Champsaur regions are kind of in a transition zone accommodating the both distinct types of volcano-sedimentary deposits. Evidence is as follows:

a) In Flaine (northern Aravis), irregular-shaped amoeboid andesite pebbles with quenched/glassy margin (Figure 3.15) were observed within the turbidite sequences. However, these fragile angular pebbles are not commonly observed in the turbidites in which most detrital components have been reworked.

b) Further south, in Col de l'Oulettaz (central Aravis), granule conglomerate succession was found, composing of mostly well-rounded clasts of andesite and some black glassy/cryptocrystalline clasts, and less abundant angular to sub-angular andesite clasts. Different grains might have different angularity/roundness.

c) Further south, once entering Champsaur region, as mentioned above, the volcano-sedimentary environment has changed dramatically: granule and pebble-sized andesite clasts are generally in greater abundances with more uniform composition and texture; and even start seeing primary volcaniclastic breccia composed of angular, homogeneous andesite clasts and matrix of the same material, interpreted as block-and-ash flow deposits induced by the collapse of proximal volcanic dome. However, a few meters away, a succession of debris flow composed of well-rounded metamorphic and plutonic rock fragments was observed.

3.3 Fieldwork localities

Detailed field observations of sedimentary structures of turbidity currents, morphology of sediment grains, thickness of beds, intercalating relationship of fine-grained layers and coarse layers, composition of deposits as well as sample collections on each individual locality are described in the following sections.

3.3.1 Eastern Switzerland (Glarus) localities

The Glarus Alps of Eastern Switzerland are a classic area of Alpine tectonics, with the geology dominated by a spectacular northward-dipping thrust plane between Panix Pass of Linthal and Walensee Lake (Pfiffner et al., 1990). Along the thrust the Helvetic nappes were thrusted more than 100 km to the north over the external Aar massif and Infrahelvetic complex. Tectonic units below the Glarus overthrust comprise the North Helvetic Flysch (NHF), the Infrahelvetic complex and the Aar massif basement; while tectonic units above the Glarus overthrust consist of older Helvetic Permo-Triassic rocks of the Verrucano group and younger Mesozoic Helvetic nappes (Trümpy , 1980; Trümpy , 1991). The NHF in Glarus is stratigraphically equivalent to the Helvetic Flysch deposits where Taveyannaz sandstone occurs in western Switzerland. The Taveyannaz sandstone is overlain by continued flysch deposits represented by the Elm and Matt Formations in Glarus, and by the equivalent Val d'Illiez sandstone in western Switzerland and southeast France, respectively (Sinclair, 1992; Lu et al., 2019). The NHF takes on a striking extension of U-shape exposure mainly distributed along the Linth valley to the west and the Sernft valley to the east. The presence of laumontite in the northern Glarus Alps and pumpellyite in the southern Glarus Alps indicate an increase of metamorphic grade ranging from zeolite facies to prehnite-pumpellyite and pumpellyite-actinolite facies from north to south (Rahn et al., 1994; Rahn et al., 1995). The localities visited in Glarus area include Haslen, Betschwanden, Luchsingen and Linthal located at the western part (Linth valley) of the region, and Schwanden, Matt located at the eastern part (Sernft valley) of the region. A geological map showing the sample locations in Glarus area is shown in Figure 3.2.

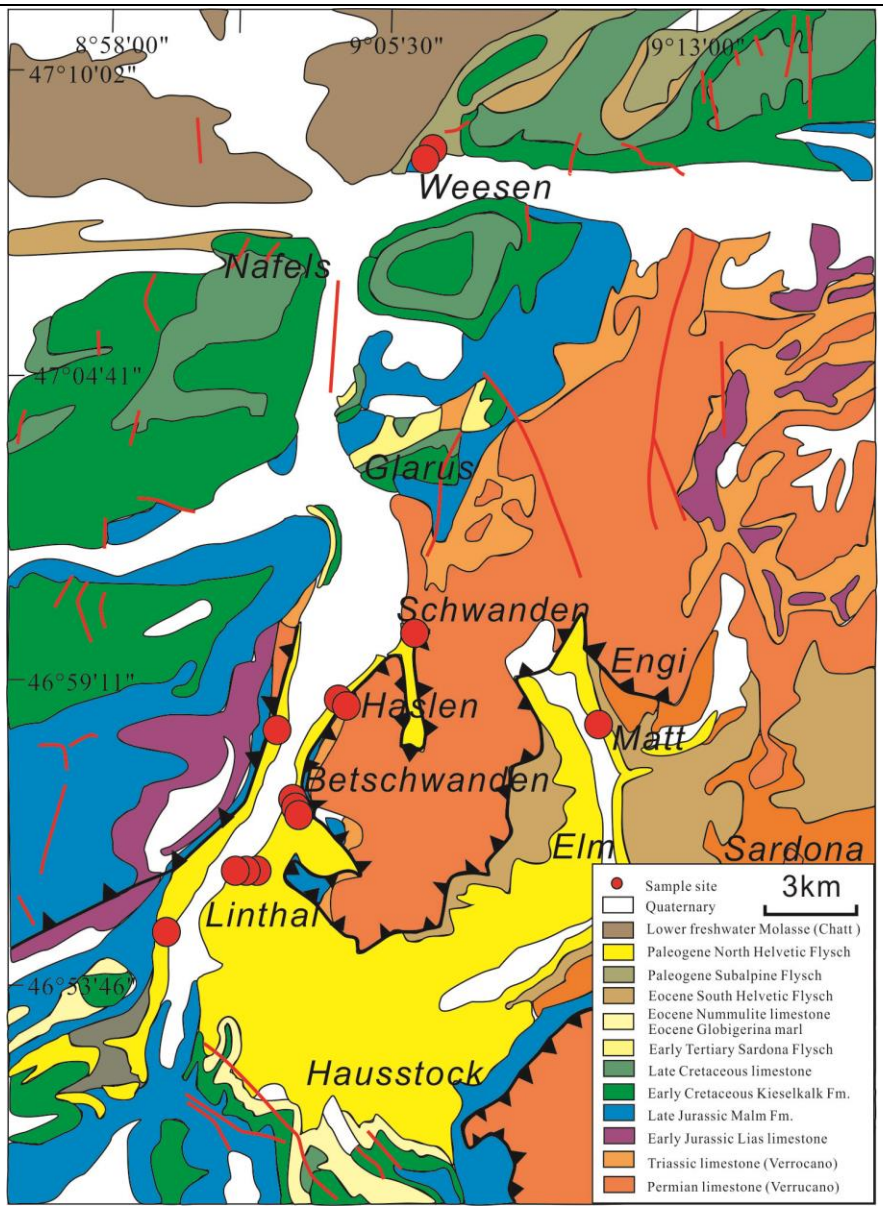

Figure 3.2 Geological map of Glarus area in Eastern Switzerland with location of collected samples (After Geology 500 on Swisstopo; Rahn et al., 1994).

(1) Schwanden Locality

Schwanden is located in the north of the Glarus thrust. A series of exposures are present in the stream next to road below the Lochsile thrust. A set of 10 cm thick medium micaceous sandstone (DB19-034) poor in pyroxene lying on the stream bottom was overlain by layers of thinly bedded mudstone-siltstone. Sandstone beds are distributed less than 20% of this suite of flysch.

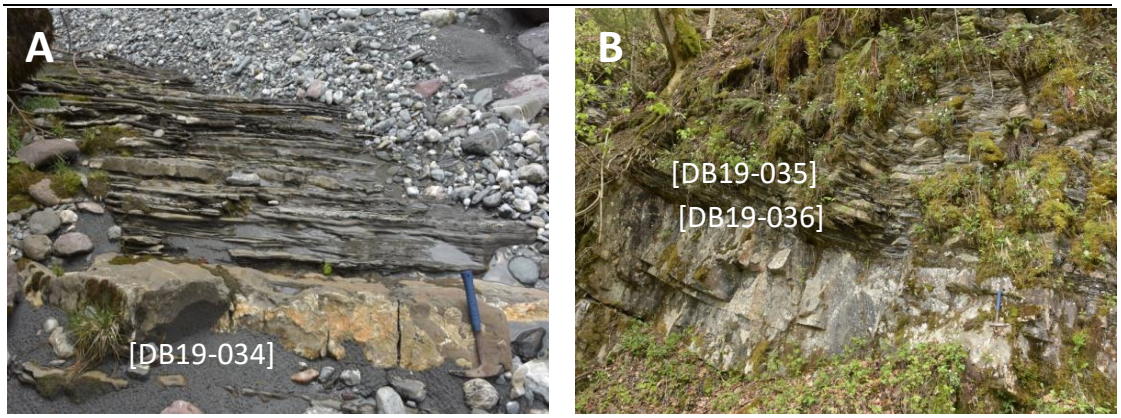

Figure 3.3 Outcrops of turbidites at Schwanden(A) and Haslen(B) locality. (A) A set of 10 cm thick medium micaceous sandstone poor in pyroxene lying on the stream bottom was overlain by multiple layers of thinly bedded mudstone-siltstone (DB19-034). (B) This locality is characteristic of fine-grained turbidites containing thin layered mudstone-siltstone with rare occasional thick yellow-dotted coarse sandstone (normal grading, erosive base). Plagioclase alteration makes them look yellow and not very fresh (DB19-035, DB19-036).

(2) Haslen Locality

Haslen locality is located around 3.5 km to the southwest of Schwanden locality. Next to a small dam in valley, this locality is characteristic of fine-grained turbidites containing thin layered mudstone-siltstone with rare occasional thick layered yellow-dotted coarse sandstone with normal grading and erosive base. Plagioclase alteration makes them look yellow and not very fresh. Two samples were collected, at the base of a set of coarse sandstone bed of 180 cm thick (DB18-035) containing pyroxene and mica, and at the middle of another set of underlying bed of 120 cm thick (DB19-036), respectively. The bedding of this turbidites sequence is 156°/22° with normal polarity, crosscut by low angle faults.

(3) Betschwanden Locality

Further towards south of around 3 km along the Linth valley, Betschwanden locality is located next to the grand Betschwanden waterfall. Dominated by thick coarse beds with minor mudstone-siltstone intervals, this suite of turbidite sequence contains massive coarser sandstones with abundant ferromagnesian minerals and mica observed under hand lens. Syn-depositional soft-sediment deformation structures are observed. Two samples were collected, at the middle of 1 m thick coarse sandstone bed (DB18-037), and at the base of 60 cm thick coarse sandstone bed (DB19-038) respectively.

In stream, a sample of very coarse sandstone with small andesite lithics and rounded pyroxenes (DB19-039) was collected.

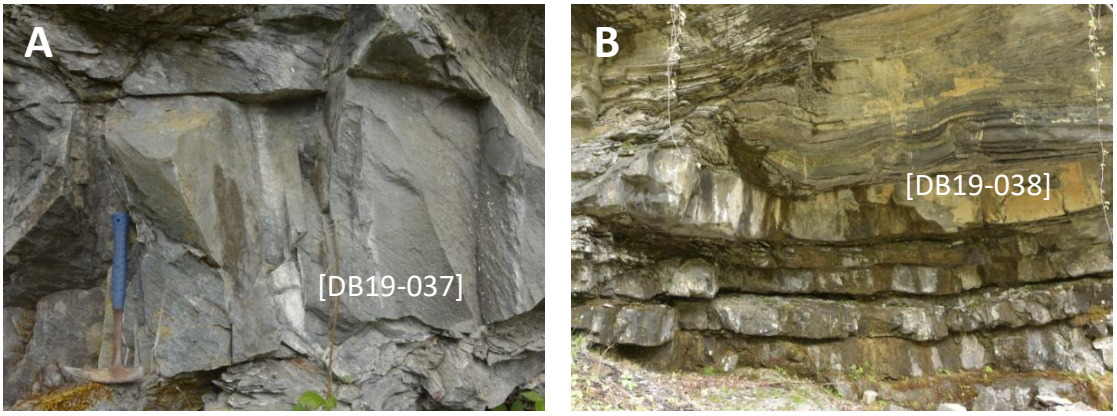

Figure 3.4 Outcrops of turbidites at Betschwanden locality. Dominated by thick beds with minor mudstone-siltstone intervals, this suite of turbidite sequence contains coarser sandstones with abundant ferromagnesian minerals and mica under hand lens. (A) At the middle of 1 m thick bed (DB18-037). (B) Soft-sediment deformation structures at the base of 60 cm thick bed.

(4) Luchsingen Locality

Located at the other side (NW) of the Linth valley, below the Murtschen nappe, Luchsingen locality is close to the thrust boundary. Coarse massive sandstone bed of 120 cm thick (DB19-040) is outcropped on top of thin layered mudstone-siltstone intervals at the side of track. The retrieved sample is not very fresh, and the rock surface is covered by green/brown lichen.

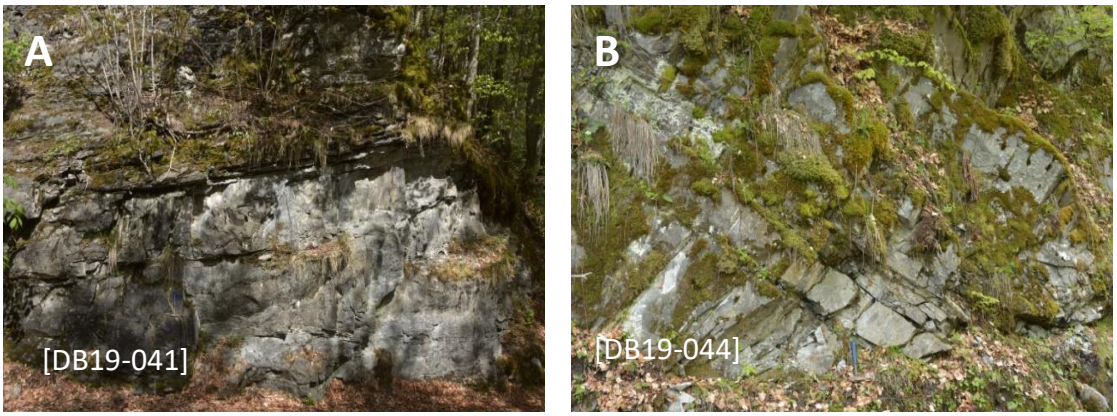

Figure 3.5 Outcrops of turbidites at Linthal locality. (A) Coarse sandstone bed of 1 m thick (DB19-041). (B) Coarse sandstone of the base of 2 m thick bed (DB19-044).

(5) Linthal Locality

Linthal localities are 5 km south to the previous locality. A high cliff featured by flysch sequences is dominated by highly schistose dark gray turbidites with

rare thick bed of coarse sandstone containing mudclasts. Coarse sandstone beds are commonly structurally boundinaged along with large scale ramps truncating part of these large thick beds; around ten-meter amplitude folds are also observed in tunnel. All these tectonic characteristics demonstrate the complex multiphase deformation of Alpine tectonics which gives rise to the dismembered formation. A sample (DB19-041) was collected at the base of 1 m thick coarse sandstone bed. The second site visited in Linthal is along the road with a series of roadcut outcrops. The overall occurrence of beds is very steep. This suite of massive turbidites with break of slope is dominated by multiple layers of thick coarse sandstone beds. Three coarse sandstone samples (DB19-042,043,044) at bases of three separate coarse sandstone beds of 50 cm, 2 m and 2 m thick respectively were collected.

(6) Matt Locality

Matt locality is located at Matt Quarry, north to the Matt village. The quarry provides a good outcrop of overturned thick layered coarse turbidites comprising abundant clasts in the size of granules to pebbles, including rounded quartz crystals, and locally very abundant flattened mudclasts (up to 8 cm) present at base, indicating the transport mechanism of high-density turbidity current. No or rare ferromagnesian minerals are contained in the sandstone under the observation through hand lens. Some blocks in gully are probably wildflysch from further up. A coarse sandstone sample (DB19-045) was collected at the base of 1.5 m thick bed.

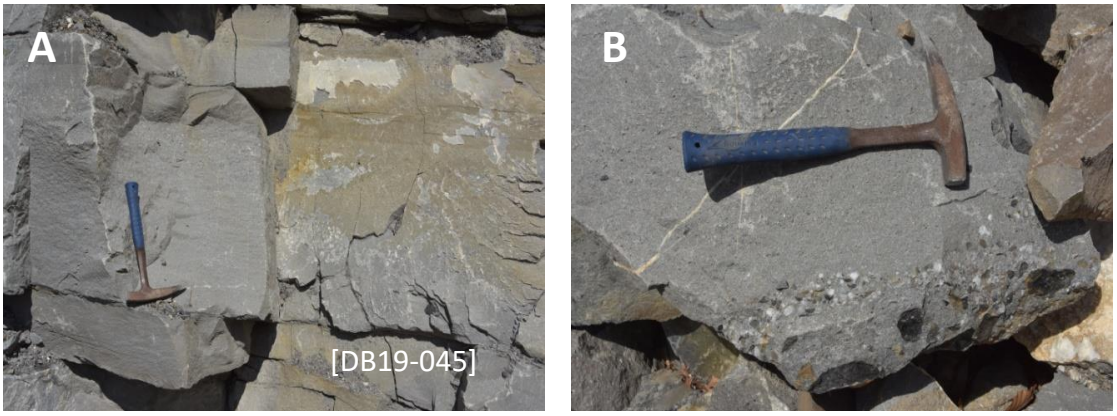

Figure 3.6 Outcrops of turbidites at Matt locality. (A) Overturned thick coarse turbidites comprising rounded quartz crystals and cherts, with no or rare ferromagnesian minerals (DB19-045). (B) Very abundant clasts at base indicating high-density turbidity current.

Overall, Glarus area is characteristic of volcaniclastic turbidites with reworked material and typical sedimentary signatures, interpreted as secondary volcaniclastic deposits transported by low/high-density turbidity currents. Only one exception of the presence of irregular-shaped amoeboid andesitic pebbles in Lu's paper (Figure 4a of Lu et al., 2018) indicates very limited reworking because these soft fragile pebbles could break down easily during transport. However, pebbles of this kind are rarely distributed and poorly investigated in the Glarus region; they perhaps only exist in a very limited area, and could not find this type of andesite pebbles during our field campaign in the region.

3.3.2 Western Switzerland localities

Cenozoic volcaniclastic localities are part of the north Alpine flysch and occur generally less than 30 km south from the north Alpine Thrust Front. In western Switzerland, these localities include Alpe de Taveyannaz, where the "Taveyannaz Sandstones" were defined. Other localities visited in this region include Chaux Ronde, Creux de Champ, La Laya and La Tièche, as detailed below. The geological background of the area is well established and documented by the Swiss topographic service (Swisstopo), with a detailed geological base map available from Swisstopo website (Geological Atlas GA25). This map was used in combination with peer-reviewed scientific papers and unpublished PhD theses to identify suitable locations of volcaniclastic turbiditic flysch and associated strata.

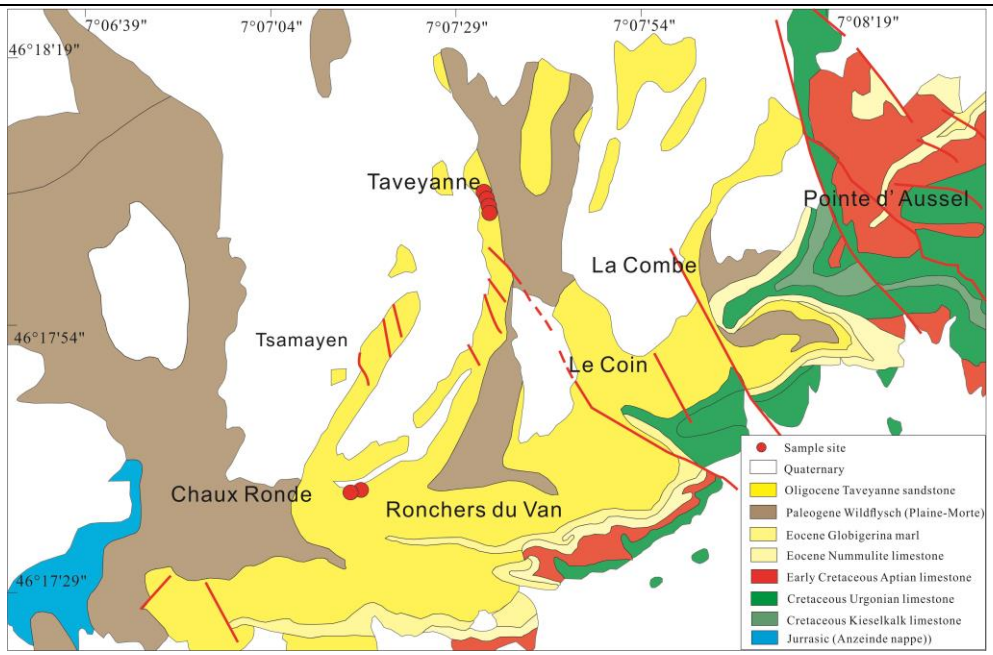

Figure 3.7 Geological map of Taveyannaz and Chaux Ronde locality in Western Switzerland with location of collected samples (After Geological Atlas GA25 on Swisstopo).

(1) Taveyannaz locality

The Taveyannaz locality is located near Diablerets and Taveyanne in the north of the Diablerets nappe. The turbiditic flysch of this region belongs to the Diablerets nappe, and is accumulated within the frontal digitations of this tectonic unit overlapped with ultra-helvetic nappe (Escher et al., 1993; Girault et al., 2020). The multiple folds, in complete disharmony with the basement, which can be seen on the southern flank of the Rochers du Van, suggest that the tectonics of the flysch is complex (Vuagnat, 1952). The flysch has experienced very low-grade metamorphism, characterised by the presence of laumontite, which is the typical mineral type of zeolite metamorphic facies (Kisch et al., 1979; Schmidt et al., 1997). This area is categorised as the laumontite zone of the four metamorphic zones of Taveyannaz metagraywacke by Bussy and Epard (1984). A wide natural cliff well exposed halfway up the peak is located very close to the southeast of “Refuge de Taveyanne” providing a good opportunity to investigate Taveyannaz Sandstone in this area. All four samples collected in this locality are from the well-exposed cliff. A series of faults and folds can be seen on the front of the cliff, suggesting the tectonics of the flysch is complex caused by late orogenic movement. Facing towards the steep exposure, it could be seen the high

mountain peak of Diablerets in the background with snowy cap. A geological map showing the sample locations in Taveyannaz and Chaux Ronde localities is shown in (Figure 3.7).

A large suite of layered greenish/gray sandstone intercalated with dark-gray/gray shale beds are exposed in total of several tens of meters in the cross section. A set of 115 cm thick bed with normal grading containing coarse sandstone is shown in Figure 3.8, interbedded with multiple layers of finer grained sandstone and siltstone intervals with cross-laminations. The variation of grain size and beddings gives indication of the alterations of current velocity changing from high in coarse grained sediment to low in fine grained sediment, and the flow regime changing from strong to waning with time passing by. The sediment thickness of over 1 m indicates the sediment load is quite large and the sedimentation process lasted a certain period of time. A most typical macroscopic nature of Taveyannaz sandstone of this locality is the presence of scattered laumontite in the form of small spotted fabric with a diameter of 3 to 10 mm, making the rock look more porous and lighter in colour. That is the reason the name “speckled Taveyannaz sandstone” derived from (Vuagnat, 1952; Sawatski, 1975). Around 2.1 m below CL18-001, multiple layers of approximate 10 cm thickness alternating sequences of fine sandstone to siltstone with mm level laminations are present above massive light gray coarse sandstone beds (CL18-002).

At the base of massive coarse sandstone bed (CL18-003, figure 3.8), elongate rip-up mudclasts up to 5 cm long are present with the occurrence of coarse-grained dark colour minerals and lithics as well, illustrating the erosive nature of the turbidites.

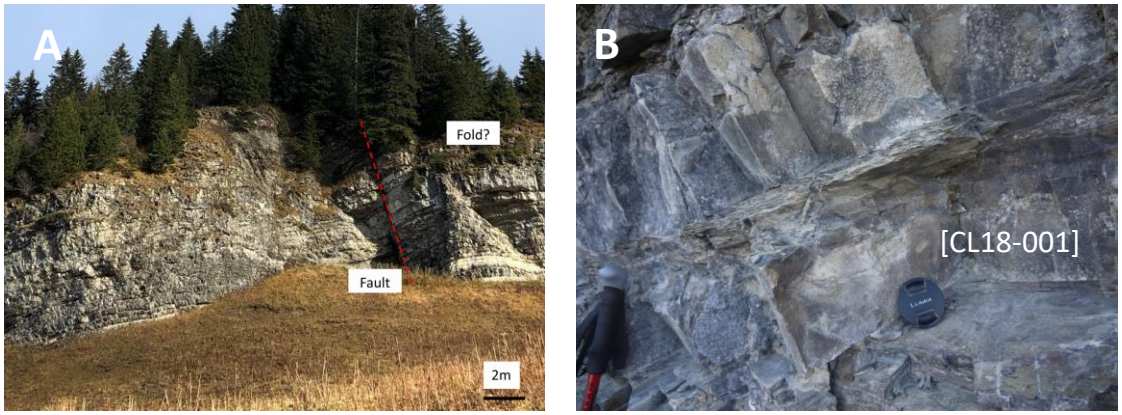

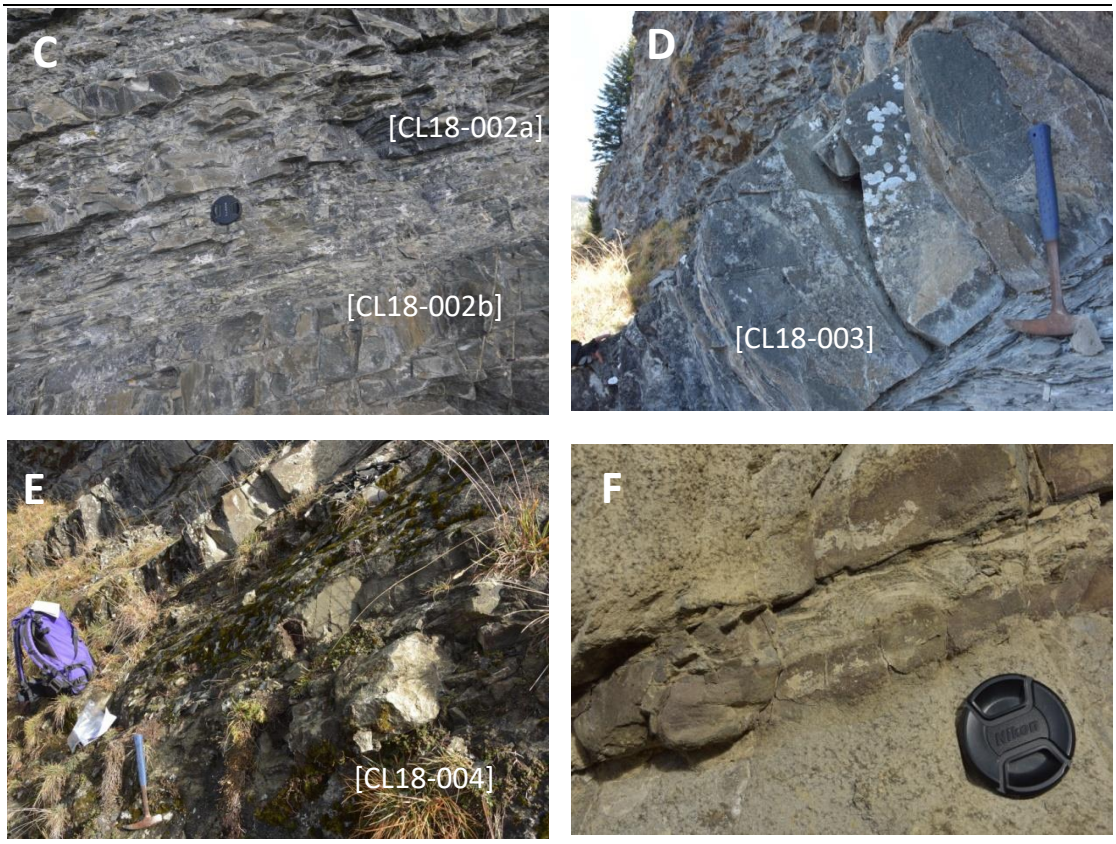

Figure 3.8 Outcrops of turbidites at Taveyannaz type locality. (A) Layered greenish/gray sandstone intercalated with dark-gray/gray shale layers of variable thickness in the turbiditic unit. (B) A set of 115 cm thick sequence, normal grading bed with coarse sandstone at base (CL18-001). (C) 10 cm intervals of fine sandstone with mm level laminations are present between massive coarse sandstone beds (CL18-002). (D) At the base of massive bed, elongate rip-up mudclasts up to 5 cm long are present with the occurrence of coarse-grained dark colour minerals and lithics as well (CL18-003). (E) Typical Taveyannaz sandstone, green and white spotted massive bed with abundant secondary laumontite replacing feldspars (CL18-004). (F) Spotted greenish sandstone with laumontite alteration/metamorphism, in between darker fine- to silty sandstone containing ripple laminations.

Around 2.3 m downward along the cliff, the most typical spotted “Taveyannaz Sandstone” was identified. The white spotted massive coarse sandstone bed with abundant secondary laumontite (CL18-004, Figure 3.8) is a type of typical sandstone in Taveyannaz Formation. Compared with upper gray coarse sandstone beds at base, this suite of sandstone is softer and easier to hammer down, probably due to the stronger weathering and alteration. Moreover, climbing ripple laminations were observed in fine-to-silty grained intervals between coarse grained beds, indicating that deposition occurred under lower flow regime conditions where there is enough energy for the flow to carry fine

sand by saltation. As grains settle out, current ripples develop, with climbing ripples developing if sedimentation rates are high enough (Bouma, 1962).

(2) Chaux Ronde Locality

Driving through the Ski Station and then walking to the crest to Chaux Ronde, along the path on the ridge where the continuation of normal limb of a large fold could be seen to the south. This locality is close to the previous one, therefore in the same tectonic unit (Diablerets nappe). Sandstones of this locality are more typical of "Taveyannaz sandstone" with heavy laumontisation covered by greenish lichen on the surface. A layer of coarse massive sandstone (CL18-005) of 50 cm thick is exposed on the side of the path without knowing the total thickness of this set due to the coverage by plants. Around 6 m below along the path, sample CL18-006 was collected within a coarse sandstone bed covered by lichen as well.

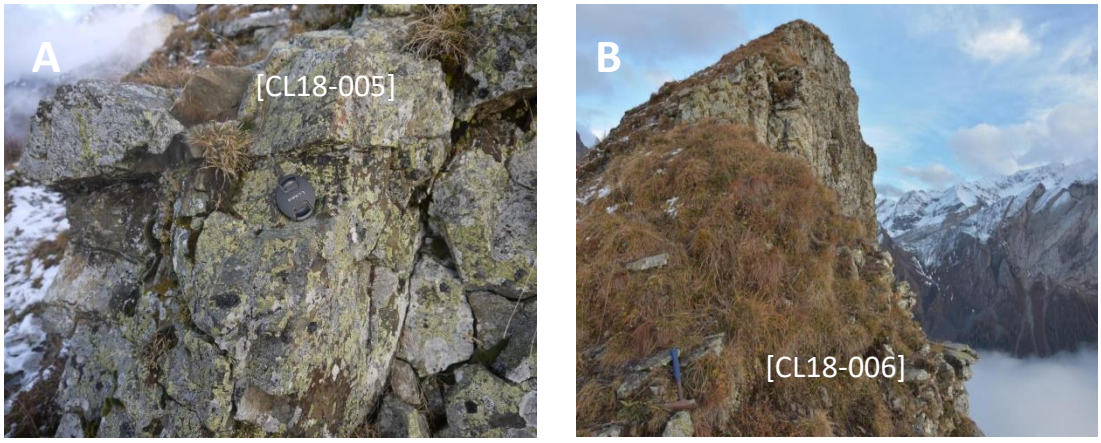

Figure 3.9 Outcrops of turbidites at Chaux Ronde locality. (A) A layer of coarse massive sandstone of 50 cm thick is exposed on the side of the path (CL18-005). (B) A set of greenish coarse sandstone bed covered by lichen (CL18-006).

(3) Creux de Champ

The Creux de Champ locality, south of Château d'Oex, is located around 5 km to the east of Taveyanne, however it took around one hour to take a detour driving there. The flysch of this region belongs to Diablerets nappe as well (Escher et al., 1993; Girault et al., 2020). A magnificent steep exposure with over 1000 m height and over 2000 m width of Diablerets nappe exhibits the complex Alpine thrust-nappe system with a series of combination of folds and faults deformed by strong push during the formation of Alpine orogen. Thus, it is pretty difficult to figure out the stratigraphic sequences of this huge cross section standing from far away, let alone to find out the exact location of

Taveyannaz sandstone. A geological map showing the sample locations in Creux de Champ and La Laya localities is shown in Figure 3.10.

Walking along the Pierredar trail, below the ruin of Prapio a suite of overturned turbidites above a thrust with flysch exists at the side of the trail. This set of gray, even blue-ish spotted sandstone (CL18-007) seems containing less mafic minerals without many black spots under hand lens. The opposite feature to the spotted sandstones of Taveyannaz locality is that these spotted sandstones are very hard. This difference means the hardness of the rock has nothing to do with dotted spots. The upper part of the suite may contain marine fossil debris or calcite cement when reacted with HCl, while the base does not react. Around 60 cm thick of coarse sandstone bed at the base seems richer in pyroxenes than the upper part.

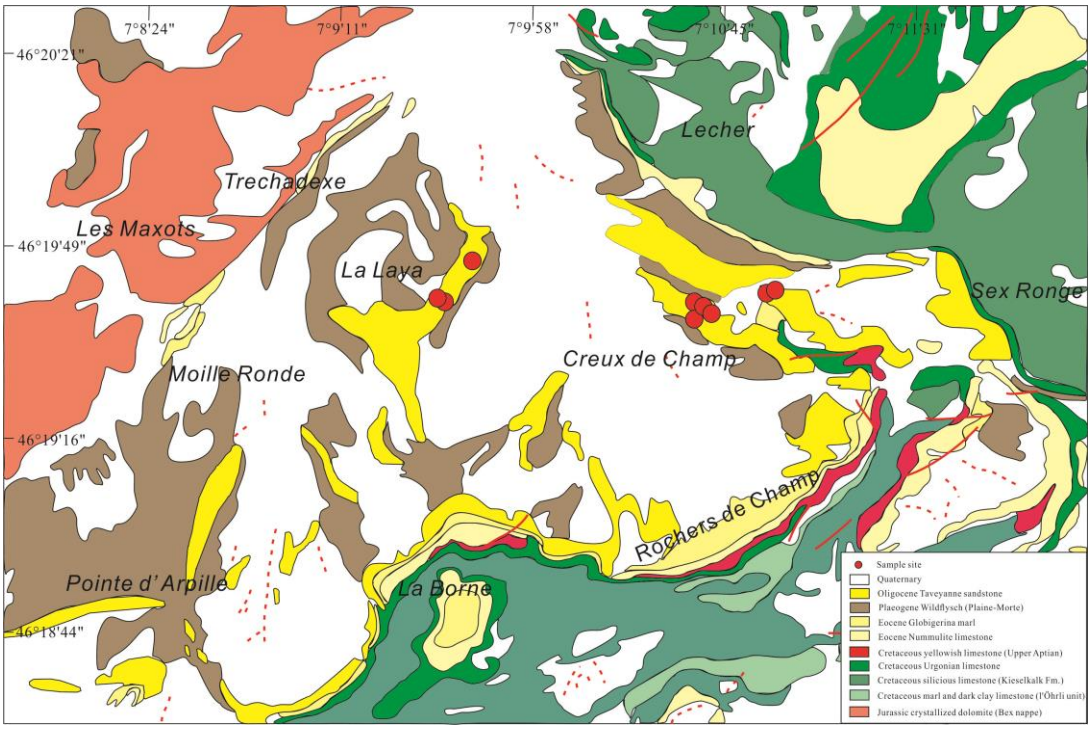

Figure 3.10 Geological map of Creux de Champ and La Laya locality in Western Switzerland with location of collected samples (After Geological Atlas GA25 on Swisstopo).

Walking towards north around 100 m, a small stream flowing to the west was present. There are a series of small outcrops at each step of the gully. Most exposures exhibit normally graded turbidite sequences. Intervals with thin massive to cross-laminated beds less than 30 cm are interbedded with thin

layered mudstone. Abundant mudclasts are incorporated in the rare laumontite spotted beds with rare pyroxene/amphibole contained. A sample of gray, very hard sandstone (CL18-008) was collected in a layer of 25 cm thick bed.

Around 3 m above CL18-008, a set of frequent interbedding turbidite sequences exists with the thickness of sandstone beds becoming thinner upwards. The thicker layered coarse-grained beds of 90 cm thick (CL18-009) display parallel laminations and are rich in large mudclasts at the base, possibly indicating the traction deposition of S1 layer of Lowe sequence by high-density turbidity current (Lowe, 1982). Further walking upwards 6 m, a set of 1 m thick turbidites (CL18-010) was divided by a small fault where the left side is the upper plate through observing the continuity of mud-rich intervals and coarse massive beds. No mudclasts exist in the coarse-grained bed in this outcrop.

Further going upwards 300 m along the gully, a small mountain trail exists connecting two gullies which mix together into the stream climbed upstream all the way along. Fortunately and surprisingly the hinge of a major reversed antiform was found out which could be seen below Diablerets. The lower part of the turning point is the normal limb. The inner part of the hinge is Globigerina marls (CL18-012) with cleavages perpendicular to beds and with nannofossils incorporated, while the outer part is Taveyannaz sandstone. Around 20 m above the hinge, a strip of exposure is present at the side of trail. This set of coarse sandstone (CL18-011) with more than 50 cm thick is typical Taveyannaz sandstone characteristic of massive spotted beds. This site is still part of the normal limb from our preliminary judgement.

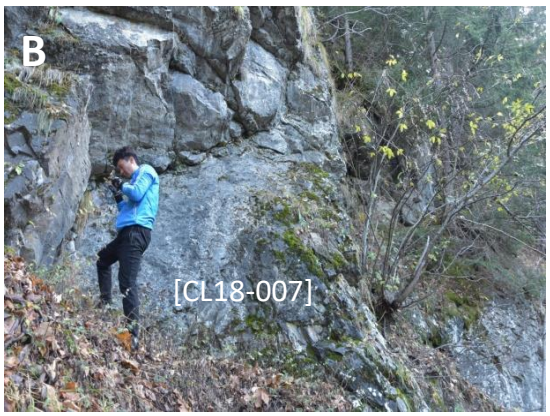

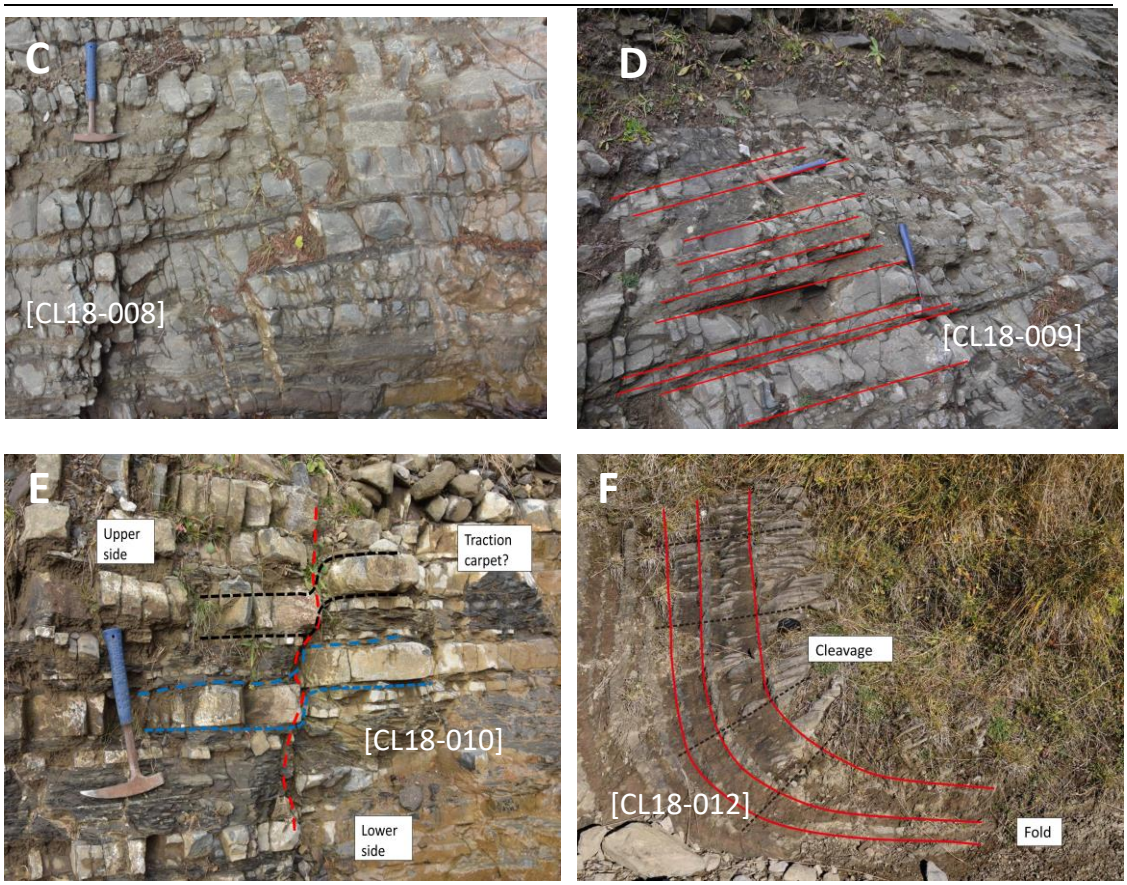

Figure 3.11 Outcrops of turbidites at Creux de Champ locality. (A) A magnificent steep exposure with over 1000 m height and over 2000 m width of Diablerets nappe exhibits the complex Alpine thrust-nappe system with a series of combination of folds and faults. (B) Grey-blue spotted sandstone inside overturned turbidite sequence (CL18-007). (C) Graded turbidite sequences, thin massive to cross-laminated beds are interbedded with mudstone. Abundant mudclasts are incorporated (CL18-008). (D) A set of frequent interbedding turbidite sequences with the thickness of sandstone beds becoming thinner upwards (CL18-009). (E) A set of 1 m thick turbidites divided by a small fault where the left side is the upper plate (CL18-010). (F) Hinge of a major reversed antiform (CL18-012).

(4) La Laya Locality

In the middle of the forest is the locality visited close to La Laya. There are spotted sandstone blocks sub in-situ along the forest road. This suite of coarse sandstones (CL18-013) seems containing more pyroxenes than sample CL18-007 to 011. Further up along the ridge, around 150 m above CL18-013, a set of spotted massive sandstone with more than 1.5 thick (CL18-014) was noticed alongside the mountain trail. These sandstones are partly rusted due to weathering. From this site, complex and grand folds could be seen below the cliff from other side of the valley. Around 30 m below CL18-014, a set of

unspotted coarse sandstone of 1.5 thick (CL18-015) interbed with thin layers of mudstone at the bend of the trail.

Figure 3.12 Outcrops of turbidites at La Laya locality. (A) A set of spotted sandstone with more than 1.5 thick alongside the mountain trail (CL18-014).

(5) La Tièche Locality

La Tièche is located at the southern side of Diablerets-Wildhorn mountain chain, in the southeast end of Wildhorn nappe, 30 km east to previous four localities we've visited. The flysch in this region belongs to the Jagerchrüz nappe, which extends over a small area in between the Wildhorn nappe to the west and the Doldenhorn nappe to the east (Pfiffner, 2014; Girault et al., 2020). This region has experienced low-grade metamorphism, characterised by prehnite-pumpellyite facies assemblages according to the distribution map of a regular mineral zonation of metamorphosed Taveyannaz sandstone proposed by Bussy and Epard (1984). A geological map showing the sample locations in La Tièche locality is shown in Figure 3.13.

Close to a crucifix, there are a series of outcrops of sandy intervals within nummulitic limestone. These well–sorted medium sandstones are likely quartz arenite (CL18-016), locally calcareous with angular grains, no apparent sedimentary structures. Further north of 800 m across a forest, next to a small dam, an outcrop at the side of the trail shows typical greenish spotted massive sandstone beds (CL18-017) in upper sequence. Going down 40 m to the east along the trail, a set of very thick layered coarse sandstone (CL18-018) contains large mudclasts (30 cm x 10 cm) at the base, suggesting that the sedimentary process was driven by high density turbidity currents. The direction of paleocurrent is from east to west according to the current occurrence of turbidite beds. A bit above CL18-018 after less than 5 cm

mudstone interval, laminated sandstone beds contain aggregates of large mudclasts. These sandstones are medium-sized, unspotted (CL18-019). Few flute casts were observed at the wall of the cliff with bedding N358°/48° indicating that the paleocurrent is generally in E-W direction if not considering the late overturn or tilting during tectonics. The east half of the flute cast is wider and more convex compared to west half, demonstrating the paleocurrents were coming from East, hitting the proximal side of soft underlying sediments more heavily while unloading.

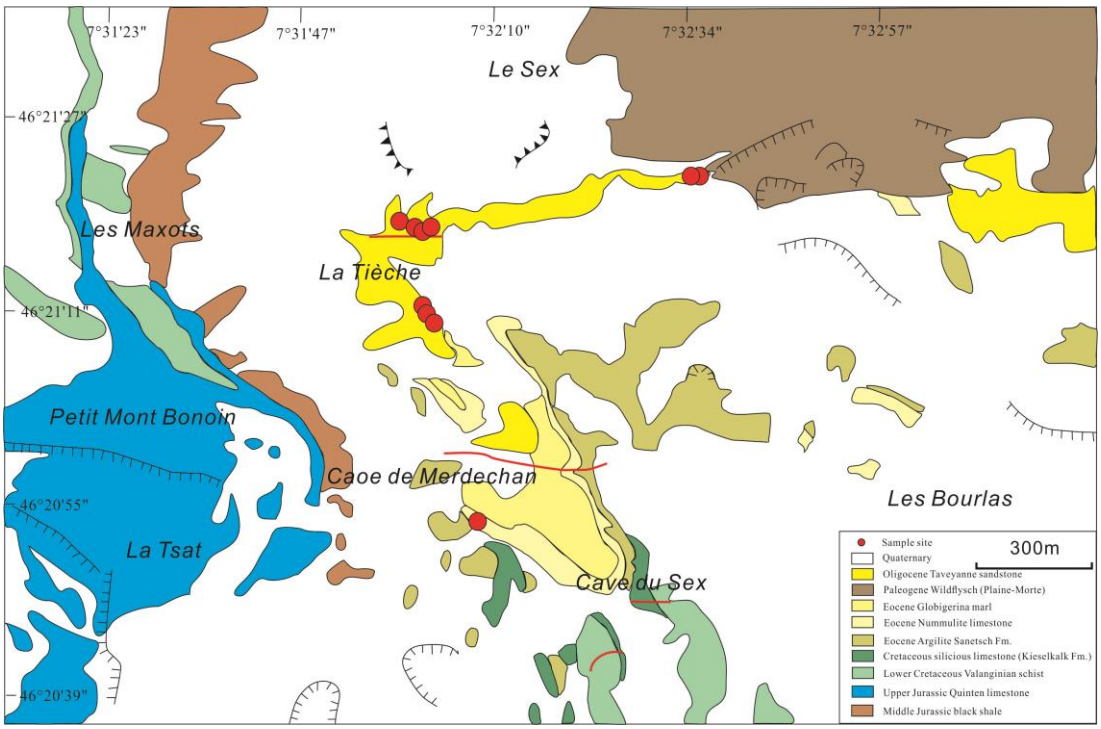

Figure 3.13 Geological map of La Tièche locality in Western Switzerland with location of collected samples (After Geological Atlas GA25 on Swisstopo).

Walking towards south back to the small path, passed before along the small stream at one side, the other side is a cliff which provides a good outcrop to observe. A suite of massive spotted medium sandstone (CL18-020) beds of 3 m thick within finer-grained intervals (no mudstone) and rich in pyroxenes/amphiboles exists over the underlying undifferentiated flysch which is the transition between the underlying marls and overlying Taveyannaz sandstone, manifesting this set of sediments is the base of Taveyannaz sandstone. Further south along the cliff, a suite of underlying cm-level flysch comprises of schistose mudstone-siltstone interbedded with lens of fine micaceous sandstone. They have an abrupt contact with the overlying Taveyannaz sandstone. Sample CL18-021 was collected from a layer of

micaceous fine sandstone of 50 cm thick without knowing the abundance of mafic minerals. Around 2 m above, still below the Taveyannaz Formation, sample CL18-022 was collected from a suite of micaceous fine sandstone of 30 cm thick with normal grading. It is unclear whether this suite of transitional flysch contains pyroxene/amphibole under the observation of hand lens. At the top of Tièche canyon close to a small pond, a set of calcareous thinly bedded sandstone and mudstone of 3-10 cm thick above CL18-017 interbeds between layered and spotted coarse sandstone (CL18-023). Around 10 repeated mudstone and sandstone of 1.2m thick in total are preserved in the interval overlying a block of massive high density turbidites.

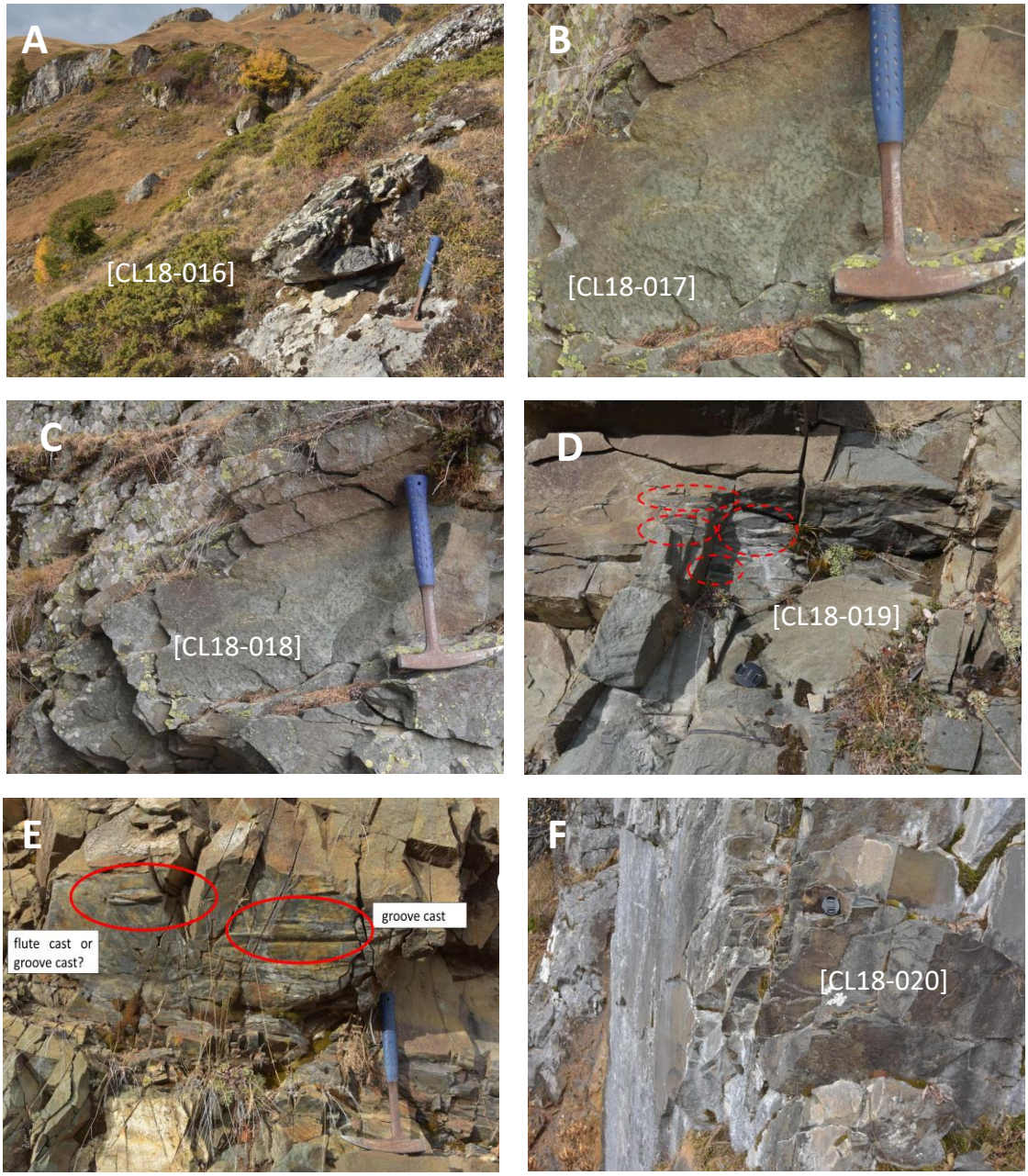

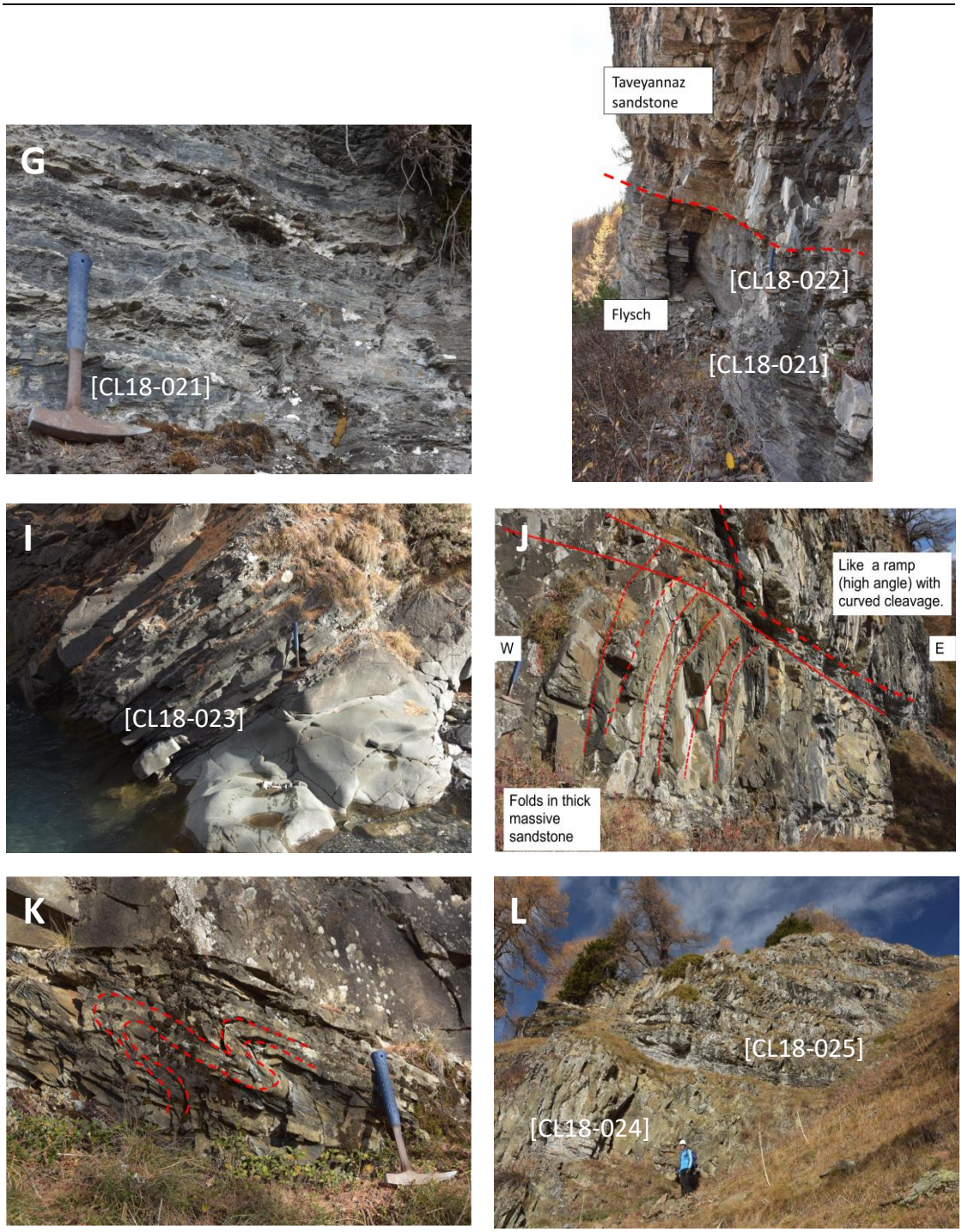

Figure 3.14 Outcrops of turbidites at La Tièche locality. (A) A series of outcrops of sandy intervals within nummulitic limestone (CL18-016). (B) Typical greenish spotted massive sandstone beds in upper part of the sequence (CL18-017). (C) Very thick layered coarse sandstone (CL18-018). (D) Laminated medium-sized, unspotted sandstone beds containing aggregates of large mudclasts (CL18-019). (E) Flute casts observed with bedding N358°/48° indicating that the paleocurrent is generally in E-W direction. (F) Massive spotted sandstone beds of 3 m thick within massive interval (no mudstone) and rich in pyroxenes/ amphiboles (CL18-020). (G) Turbidites comprise schistose mudstone-siltstone interbedded with lens of fine micaceous sandstone (CL18-021). (H) Micaceous

medium sandstone of 30 cm thick with normal grading (CL18-022). (I) Calcareous thinly bedded sandstone and mudstone of 3-10 cm thick above CL18-017 interbeds between layered and spotted coarse sandstone (CL18-023). (J) Meters-scale thrust fault with high angle like a ramp with curved cleavages. (K) Heavily folded sandstone sequence, maybe close to hinge. (L) A large outcrop of tens of meters high comprising sets of unspotted thick sandstone beds with increased abundance of fine sandstone and mudstone intervals upwards (CL18-024, CL18-025).

Further 600 m to east, a meter-scale thrust fault was found with high angle like a ramp with curved cleavages. Below the fault surface are a series of parallel folds in thick layered massive sandstone beds intercalated with small intervals of fine sandstone-mudstone in a nearly vertical position. Furthering towards east, an outcrop of tens of meters high exists comprising sets of unspotted coarse sandstone beds at base with increased abundance of fine sandstone and mudstone intervals upwards. One bed has clear erosive base and inverse grading, characteristic of traction carpet deposition of S2 layer of Lowe sequence (Lowe, 1982). Unspotted sandstones of this site containing less volcaniclasts are probably upper Taveyannaz Formation or the transition sequence to the overlying Val d'Illiez Formation. A bulk of unspotted coarse sandstone (CL18-024) was collected in a 3 m thick bed characteristic of abundant pyroxene and locally cm-sized white-ish lithics. Further going up along the slope, a bulk of gray fine-medium sandstone (CL18-025) with black minerals contained was collected in calcareous clayey intervals of 15 cm thick. This sample looks similar to CL18-023. Further up on ridge, more abundant mudstones and brownish sandstones similar to CL18-025 present, probably giving rise to the decrease of volcaniclasts. However, clear increase of deformation (folds, boundinage) towards top could be observed, suggesting stronger tectonics upwards.

In summary, localities of western Switzerland are represented by volcaniclastic deposits with typical sedimentary structures and epiclastic reworking signatures. Volcanic components are generally in finer grain size compared to those in the southern part of NAFB; no andesite granules or pebbles are observed; no tuffs or glass shards are observed.

3.3.3 Northern SE France (Aravis) localities

The Taveyannaz sandstones incorporated in the Helvetic flysch deposits exist in the less deformed northern Subalpine Chains (Bornes, Aravis and Platé

massif) in southeast France compared to those in the Diablerets and Morcles nappes of western Switzerland (Martini, 1968; Lateltin, 1988). A series of associated parautochthonous outcrops is generally arranged in a NE-SW direction in a range of 30 km along the outer border of Platé Massif and Aravis Chain in the Haute-Savoie region, including Flaine, Col de l'Oulettaz, La Clusaz and Thônes from northeast to southwest. The last three sites are located in the Thônes syncline, which is occupied mainly by Helvetic flysch deposits overlain by ultrahelvetic units and Penninic Klippes of Annes and Sulens (Sawatzki, 1975). From the geological point of view, the syncline of Thônes connects the Aravis Chain to the southeast, with the autochthonous outer subalpine chains to the northwest, represented by the Bauges and Bornes massifs (Sawatzki, 1975). The current SWS-NEN direction of the southern part of the Thônes syncline is oblique to the old structures, i.e., ancient paleogeographical direction is WSW-ENE, inferred from the mode of transportation and the percentage of volcanic elements (Sawatzki, 1975). The Taveyannaz sandstone in this region was affected by very low-grade metamorphism, with the presence of mineral assemblages typical of the zeolite facies and prehnite-pumpellyite facies. The intensity of metamorphism generally decreases slightly from northeast to southwest along the subalpine chain. The presence of laumontite is more common in the southeast part of the region than that of prehnite and pumpellyite which are present only where formation is affected by an additional pressure exerted by Helvetic nappes (Martini and Vuagnat, 1965; Martini, 1968; Sawatzki, 1975; Ruffini et al., 1997).

(1) Flaine Locality

Flaine locality is in the Grands Vans massifs, which is at the north of the well-know Platé massif, and the two massifs make up the most northern part of French subalpine chain between the Arve valley and the Giffre valley (Martini, 1968). The Grands Vans massif, a triangle between the Combe de Gers, the Combe de Vernant and the chalets de Flaine, experienced folding and thrusting towards WNW direction of several tens of metres shortening (Butler, 1992). In general, it seems that the flysch is less deformed at the base than at the top in the region, probably due to the thrust of overlying Morcles nappe (Martini, 1968). Very low-grade metamorphism also exists commonly in the

region, characteristic of laumontite appearance of zeolite facies and pumpellyite-prehnite facies (Martini, 1968). A suite of turbidites containing greenish spotted thick beds interbedding with thin layered mudstones was observed at a roadcut exposure covered by safety net at north of Flaine. An angular amoeboid andesite pebble (CL19-001) with quenching margin was rarely found at the base of bed, probably derived from proximal submarine volcanism with very limited reworking. This new finding is significant to the possibility of a proximal volcanic source of Taveyannaz volcanic detritus in northern SE France. The speckled coarse sandstone (CL19-002) consists of rounded white spots with a few millimeters in diameter surrounded by a greenish bottom. Andesite clasts could be observed inside coarse sandstone bed, as well as mudclasts at the base of the bed with multiple layers of concentric rims produced by weathering or metamorphism, indicating the transport mechanism of high density current. On top of the thick coarse sandstone bed, a set of layered fine sandstone show normal grading and rare high angle cross-beddings, indicating the deposition on steep slopes of sand dunes on the seafloor with relative high flow velocity. The second site visited is located 700 m northeast to the first outcrop at the mountain trail along the ridge of a steep slope. A set of 7 m thick bed of coarse sandstone (CL19-003) incorporated with large size of lithics and mineral fragments interbeds with finer-grained intervals. From this location, it can be seen that Taveyannaz Formation clearly drapes over Mesozoic limestone in the north and south side of the region.

Figure 3.15 Photographs of outcrops in Flaine locality. (A) Turbidite sequence including greenish spotted thick beds interbedding with thin layered mudstones. (B) Large angular quenched andesite clast inside spotted coarse sandstone (CL19-001). (C) Large mudclast at base of the sequence with concentric weathering/metamorphic rims. (D) Coarse sandstone within thick bed incorporated with large lithics/mineral fragments (CL19-003).

(2) Col de l'Oulettaz Locality

The Col de l'Oulettaz locality, 12 km to the southwest of Flaine along the Aravis Chain, is in the northern part of Thônes syncline along the ridge towards Col des Annes. The autochthonous flysch sequences outcropped locally in a narrow band of the eastern edge of the syncline between the body of Aravis massif to the southeast and the Annes Klippe to the northwest (Sawatzki, 1975). The trilogy deposits are folded and overturned locally at base in contact with Mesozoic basement (Sawatzki, 1975; Boyet, 2001). Along the Col des Annes pass uphill, in the halfway towards localities, a huge exposure covering the whole side of the mountain could be observed from far away on the patchy unforested mountain slope. A layer of red terrestrial sediments of molasse turbidites are deposited overlying a set of gray/light gray interbedding flysch sediments, which is a perfect illustration of the stratigraphic sequence of Tertiary turbidites in foreland basin. Greenish, crumbly and heavily altered vertical bed inserted in the middle of flysch sequences, no reaction tested by acid; it could be a dyke or quartz vein. A nice view on Taveyannaz sandstone channel towards northeast truncates the sheared globigerina marls and turbidite sequences, representing the abrupt volcaniclastic supply to the basin. A block of greenish medium sandstone (CL19-004) with some cracks was outcropped above the quartz vein in sheared zone. Further along the trail, thick layered turbidites with polymictic, grain-supported andesite breccia (CL19-005) was found, representing the presence

of explosive eruption close to the basin. Though an inverse grading was not well observed, this suite of deposits still looks similar to high density turbidity current given the clasts seem floating on the underlying finer-grained base. Under hand lens, various types of subrounded to subangular clasts, among them glassy/vitreous lithics, plagioclase-phyric andesite lithics could be observed in clusters. The high concentration of andesite clasts and some, despite subordinate, angular to sub-angular clasts demonstrate a proximal volcanic source near the basin. Greenish medium sandstone (CL19-006) from 1 m thick bed within marly intervals was collected at the side of the trail. Further along the trail towards west, new occurrence of andesite breccia (CL19-007) in slightly altered coarse turbidity bed with large angular crystals and andesite clasts incorporated was found. Breccia is polymictic, grain-supported, and rich in chert and andesitic lithics, similar to CL19-005. Flute clasts in slope indicate paleocurrent towards southwest. Turbidites comprise polymictic lithic coarse sandstone (CL19-008) within beds of 20 cm thick, and thinly bedded finer-grained intervals.

Figure 3.16 Photographs of outcrops in Col de l'Oulettaz locality. (A) Red terrestrial sediments of molasse turbidites deposited overlying gray flysch sediments, which is a perfect illustration of the stratigraphic sequence of Tertiary turbidites in foreland basin. (B) Greenish medium sandstone with some cracks (CL19-004). (C) Polymictic, grain-supported andesite breccia (CL19-005). (D) Greenish sandstone within thick bed (CL19-006).

(3) Clusaz Locality

Clusaz locality is at the central part of the elongate Thônes syncline next to the anticline of Mont Durand, parallel to the general direction of the syncline of Thônes, which divides the syncline longitudinally into two secondary synclines (Sawatzki, 1975). The series of typical Taveyannaz sandstones of the Col de l'Oulettaz at northeast and that of the Crêt du Loup (S of Clusaz) at southwest show a petrographic and lithological correspondence and lateral correlation (Sawatzki, 1975). Thus, the autochthonous flysch deposits in this locality are kind of in a similar tectonic situation to that of previous Col de l'Oulettaz locality. Medium-coarse massive sandstone (CL19-009) interbeds with frequent marl intervals. At the base, thick coarse sandstone beds (CL19-011) of 20 cm thick exist, intercalating with thinly bedded intervals. Thick sandstone beds become thinner upwards, opposite trend to the increase of thinly bedded intervals. This represents less energy and slower current flow of turbidity current with time passing by within this phase of turbiditic sedimentation.

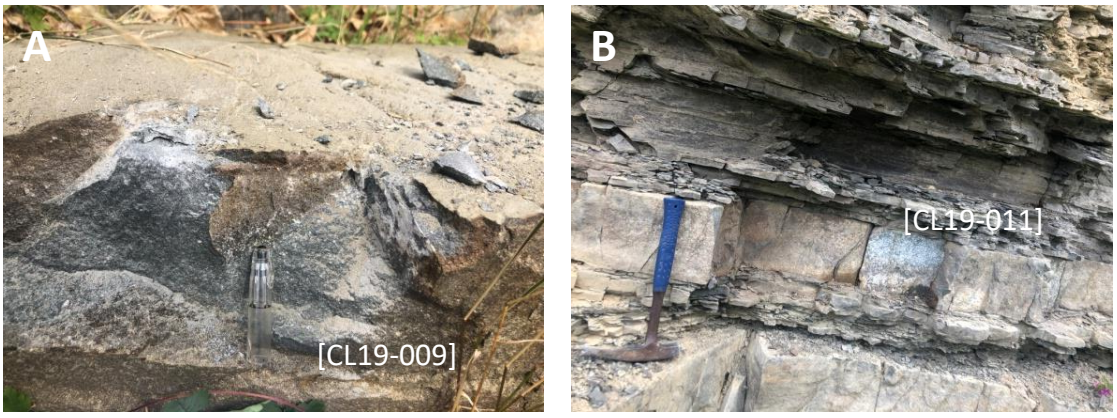

Figure 3.17 Photographs of outcrops in Clusaz locality. (A) Medium-coarse sandstone containing abundant ferromagnesian minerals (CL19-009). (B) Thick coarse sandstone beds of 20 cm thick intercalating with thinly bedded intervals (CL19-011).

(4) Thônes Locality

Thônes locality is at the central-southern part of the Thônes syncline. To the south is a small anticline as an extension of anticline of Mont Durand. Sulens klippe is also located to the south across Fier valley. Samples (CL19-012) to (CL19-015) were collected from a long roadcut outcrop of very thick 6 m coarse turbidites with abundant clasts extending around 100 m in the forest. Andesite clasts are sub-angular to sub-rounded up to 3 cm in diameter. All collected samples are coarse-sand to conglomerate sized Taveyannaz sandstone with spotted appearance and abundant volcanic materials. Sample (CL19-012) and (CL19-013) are both at the lower part of this suite of turbidites rich in andesite clasts and pyroxene fragments. Sample (CL19-014) and (CL19-015) are in the upper layer of thick sandstone bed, similar to previous samples, a bit weathered and not well-cemented. A block of conglomerate (CL19-016) containing amounts of commonly rounded andesite clasts up to pebble size lied on the side of road, probably from overlying beds, indicating that the clasts have been reworked to a certain degree before deposition. Abundant large andesite clasts concentrate at the base of bed (grain-supported), and less abundant few tens of cm above the base (matrix-supported).

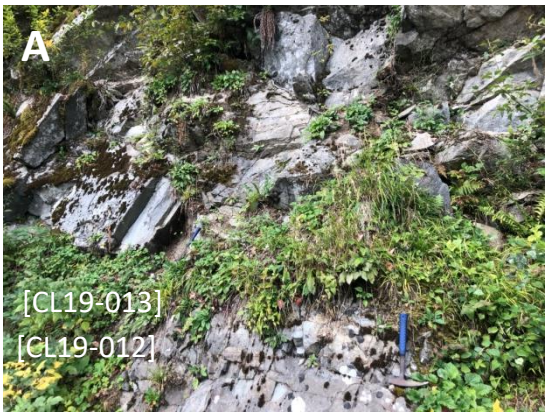

Figure 3.18 Photographs of outcrops in Thônes locality. (A) Spotted coarse sandstone rich in andesite clasts and pyroxene fragments (CL19-012, CL19-013). (B) Spotted coarse sandstone in the upper layer of thick sandstone bed, a bit weathered and not well-cemented (CL19-014, CL19-015). (C) A block of conglomerate comprising predominantly pebble-sized andesite clasts (CL19-016). (D) Medium sandstone rich in pyroxene minerals within thin black layers (CL19-017).

In summary, volcaniclastic deposits observed in Flaine and Aravis regions show a clear increasing abundance of volcanic material of coarser size, represented by the occurrence of abundant andesitic clasts and ferro-magnesian minerals. Andesitic breccias and conglomerates comprised of angular to sub-angular andesite clasts start to exist within turbidite sequences, indicating that these clasts have been poorly reworked, derived from proximal volcanic source. The volcano-sedimentary environment starts to change from mostly reworked sedimentary one to more proximal, volcanic one.

3.3.4 Central SE France (Champsaur) localities

Only one locality, Méollion of Champsaur area, was deeply sampled and studied in Champsaur region. This locality is situated at the central part of French Subalpine Chains. The Champsaur sandstone, equivalent to Taveyannaz sandstone in Switzerland and Aravis, is named after Champsaur valley formed by the Upper Drac (Vuagnat, 1952; Waibel, 1990). The Champsaur sandstone is structurally a part of parautochtonous units composed of Tertiary trilogy sequences and Mesozoic sedimentary basement. These units were detached, deformed, and transported in a westerly direction away from the orogenic belt (Gidon and Pairis, 1976; Gidon, 1979) during

subsequent thrusting in the late Oligocene-Miocene alpine compressional regime (Siddans, 1979; Beach, 1981). Very-low grade metamorphism occurs in Champsaur sandstone as well, represented by two mineral assemblages irregularly distributed across the region: the green facies and the zeolite facies. The characteristic assemblage may deviate to a higher metamorphic grade in hydrothermal veins and adjacent reaction zones within the host rock (Waibel, 1990). Compared to those assemblages characterising Taveyannaz sandstone in Aravis, they show similar, if not higher, grade of metamorphism, which contradicts the proposed pattern that metamorphic grade increases progressively from west to east along the alpine arc in western Switzerland and Aravis (Martini, 1968; Sawatzki, 1975; Waibel, 1990).

(1) Méollion Locality

On the dried stream floor, a large boulder with syn-depositional structures lies on the riverside, composed of white limestone interbedded with grey mudstone where thin laminations and slump structures could be clearly observed. It's very likely that a large slumped block dropped into the debris flow. Overlying the stream floor is a suite of debris flow deposits, comprising variable large clasts up to tens of cm, mainly calcareous clasts and volcanic clasts. At the base, ten-cm scale elongate mudclasts in alignment are also contained in debris flow. The large size of variable clasts including andesitic clasts clearly indicates that the source of sediments was not far, and was highly mixed; the origin of volcanic input was proximal. For some limestone clasts with amounts of vesicles on the surface, it could be explained by the irresistible weathering nature of calcareous rocks. Conglomerate comprised of well-rounded andesite clasts and large quartz gneiss clasts up to 4 cm and calcareous matrix (CL19-018) was collected. Rounded quartz crystals observed inside gneiss clasts could be explained that when felsic magma mixed with mafic magma, quartz had been resolved. Further climbing uphill, a series of intermediate to felsic subvolcanic-volcanic cobbles are found incorporated in the turbidite sequences. Five small cobbles (CL19-019 to 023) were collected as to compare with volcanic andesite clasts inside sandstones. A group of grain-supported conglomerates made of large andesitic pebbles and granitoid pebbles were emplaced onto the gully bottom. Four similar andesite and one rhyolite pebbles (CL19-024 to 028) were collected.

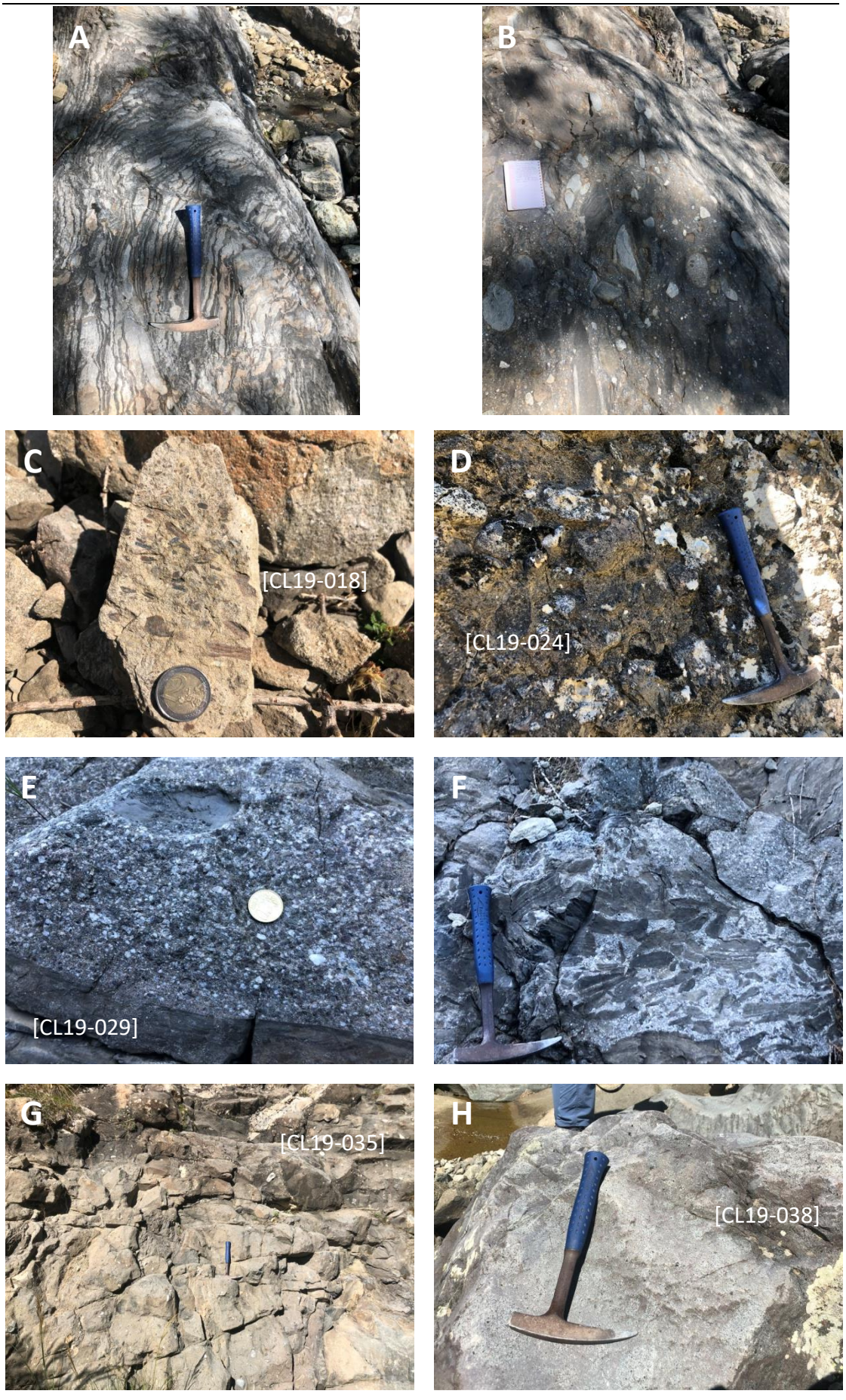
A
B
C
[CL19-018]
D
[CL19-024]
E
[CL19-029]
F
G
[CL19-035]
H
[CL19-038]

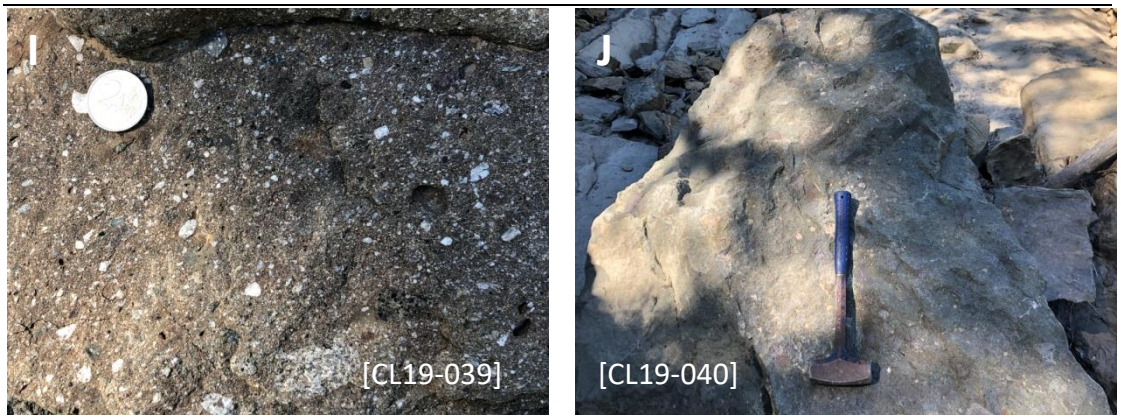

Figure 3.19 Photographs of outcrops in Champsaur locality. (A) A large boulder with syn-depositional structures composed of white limestone interbedded with grey mudstone. (B) Debris flow deposits containing ten-cm scale elongate mudclasts in alignment at the base and variable clasts including andesitic clasts. (C) Conglomerate incorporated with large andesitic clasts and quartz gneiss clasts (CL19-018). (D) Conglomerates made of large andesitic pebbles and granitoid pebbles (CL19-024). (E) Bottom of debris flow deposits, polymictic conglomerate containing abundant large andesite clasts (CL19-029). (F) Elongate mudclasts in cluster. (G) A suite of debris flow deposits of more than 2 m thick contains abundant elongate mudclasts at base (CL19-035). (H) Monomictic andesite breccia lying on the stream bottom, probably due to the collapse of proximal lava dome (CL19-038). (I) Coarse sandstone containing large andesite clasts and ferromagnesian minerals (CL19-039). (J) A block of andesite breccia similar to CL19-038 with angular/ subangular randomly oriented andesitic clasts (CL19-040).

A layer of coarse grain-supported spotted sandstone underlies a thinner layer of fine sandstone with cross-beddings; the sand/shale ratio is high for the whole section; the base of the sandy sequence is very coarse, even to granule-pebble size, incorporated with flattened large mudclasts up to 10 cm. All these features suit the explanation proposed by Lowe (1982) about debris flow and the basal traction carpet layer. A block of polymictic conglomerate (CL19-029) containing large andesite clasts was collected from the bottom of traction carpet deposits.

Further going along the stream, next to a small waterfall, a block of gabbro pebble (CL19-030) was found. Five small andesitic pebbles/cobbles found nearby (CL19-031 to 034, 037) were collected as to compare with volcanic andesite clasts inside sandstones. Further going up, a suite of debris flow deposits of 2 m thick contains abundant elongate mudclasts at base. Two samples of medium sandstone (CL19-035 to 036) were collected from the matrix of debris flow deposits.

Large blocks of monomictic andesite breccia-conglomerate (CL19-038, CL19-040) composed of mostly angular, subordinate rounded cobble-sized andesite clasts up to 15 cm, and compositionally similar matrix were found nearby, representing primary volcaniclastic deposits with no dilution, perhaps transported by block-and-ash flow of very proximal volcanism. Spotted pebbly sandstone (CL19-039) containing abundant amphibole-phyric andesite clasts and ferromagnesian minerals were found nearby with crumble texture due to weathering or metamorphic alterations. In-situ greenish spotted coarse sandstone (CL19-041) influenced by bioturbation underlying conglomerate was collected.

In summary, volcaniclastic deposits in Champsaur region are characterised by even coarser grain size compared to Aravis, and by the first presence of primary volcaniclastic material with no dilution, illustrating the further proximity to volcanic source. Meanwhile, variable well-rounded to rounded clasts within turbidite sequences or conglomerates demonstrate that these clasts have been transported and reworked to a certain degree by fluvial system. Thus, a binary transport system seems seasonable to interpret the coexistence of two distinct volcaniclastic sediments.

3.3.5 Southern SE France localities

This region is the southern part of French Alps and the striking direction of mountain range is shifting from NE-SW to NW-SE. Two foreland basin localities visited are Clumanc of Barrême basin and Saint Antonin basin. The Barrême basin, located on the Digne thrust sheet about 60 km to the west of the Penninic frontal thrust, 15 km to the east of the terminal Alpine thrust front, is an asymmetrical elongate syncline with a steeply dipping to overturned eastern limb and a more gently dipping western limb, interpreted as the most westerly part of a series of thrust-sheet-top basins created by a progressive propagation of the thrust front into the foreland (Evans & Elliott 1999; Evans et al. 2004). Andesitic detritus of Alpine affinities is mainly incorporated in the Clumanc and Saint Lions conglomerate units, stratigraphically equivalent to Taveyannaz sandstone and Champsaur sandstone in Swiss and northern French Alps (Bodelle, 1971; Evans and Mange-Rajetzky, 1991). The Saint Antonin basin, located in French Maritime Alps, is a structurally complex syncline with three minor sub-basins, formed

between two anticlines (Jourdan et al., 2018). The basin's axis is east-west with about 4.5 km wide and 20 km long, mainly caused by Eocene-early Oligocene Pyreneo-Provençal convergence of north-south directed deformation (Lacombe and Jolivet, 2005). Andesite breccia dated to late Oligocene was recorded in the middle and upper Clastic Formation, stratigraphically equivalent to conglomerate units in Barrême basin with slightly younger age (Bodelle, 1971; Stanley, 1980; Callec, 2001).

(1) Clumanc (Barrême) Locality

Clumanc locality is situated at the most northern part of Barrême basin, 5 km north of Saint Lions. Along the road D219, a series of roadcut outcrops is present, showing great exposures of Clumanc conglomerate sequences with grain-supported sandy matrix interbedded with turbidites. The whole sediment beds generally dip towards east-southeast. The coarse sandstones at base are weathered to some extent and rich in dark grains, probably pyroxenes, whereas conglomerate composition is dominated by Mesozoic micritic limestone clasts with subordinate igneous clasts and minor serpentinite clasts. Two sandstone samples (DB19-046 to 047) of weathered turbidites between 1 m thick middle conglomerate unit beds were collected. During our second field campaign in Clumanc, a collection of andesite-dacite granule-pebble-sized clasts (CL19-042) within conglomerate sequences were collected along the exposure with acid test to avoid limestone clasts. Further south along the road, a block of turbidites was outcropped, featured by rare fine sandstone beds (DB19-048) with planar-laminated beddings in which microdiorite lithics are also observed. Around 2 m below, erosive based sandy channel (DB19-049) incorporated with large mudclasts overlies marly intervals. Towards west crossing the small stream into the forest, blue marls transitioning to turbidites upwards, then lower conglomerate unit was observed. Smaller than 30 cm thick laminated sandstone interval, poor in dark clasts within marls underlies lower conglomerate unit. From distance wide sandstone channels below conglomerate with lateral variability also could be seen. 250 m towards northwest across the forest, calcareous sandstone (DB19-050) with load structures and hummocky cross-beddings, probably from Ville Formation which is interpreted as the first clastic formation preceding conglomerate units in the blue marl Barrême basin, but it seems no

volcanic material incorporated. Two pieces of medium-coarse sandstone (DB19-051) with plants within turbiditic channel deposits below lower conglomerate unit were collected. Upper part of middle conglomerate unit with variable types of clasts, including distinctive serpentinite clasts, rare sandstone clasts, and small granule of variolitic clasts. Fine microdiorite clasts with quartz and pyroxene-feldspar-phyric andesite clasts are also observed inside conglomerate. Sticking out serpentinite clasts are well preserved due to resistibility to weathering. Matrix of this set of conglomerates is similar to other conglomerate sequences in the area. Two pieces of polymictic conglomerate (DB19-052) were collected with a piece of sandy interval (DB19-053) containing andesite clasts. Around 50 m north at the crossroad between D219 and D19, A better outcrop of exposed conglomerate was found, showing lateral continuation of conglomerate sequences. Clast imbrications and unidirection of foreset sandy lens represent progradation of delta into the basin, paleocurrents suggesting current flow from east to west. Another outcrop of upper conglomerate unit with more abundant andesite-dacite clasts occurs, containing lithophaga marks and radiolarite. A piece of fine-medium sandstone (DB19-054) containing andesite clasts from sandy matrix was collected with collection of andesite-dacite granules to pebbles (DB19-055).

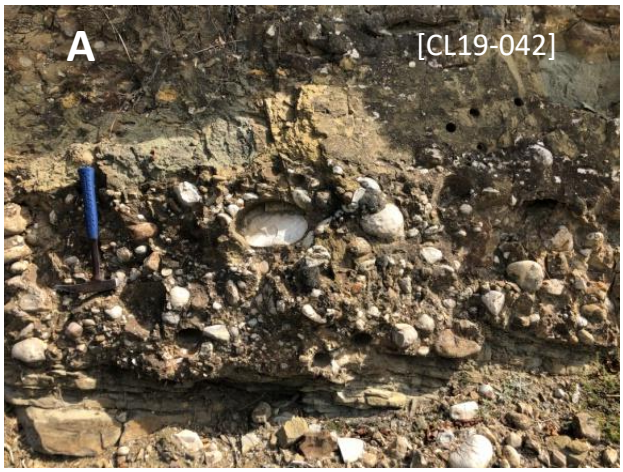

Figure 3.20 Photographs of outcrops in Clumanc locality. (A) Collection of andesite-dacite cobbles inside conglomerate units (CL19-042).

(2) Saint Antonin Locality

The localities visited are all situated at the western part of the Saint Antonin basin. A suite of yellow-grey massive very coarse sandstone rich in quartz was

found within the lower Clastic Formation of three Clastic Formations in Saint Antonin basin. Massive, poorly layered andesite breccia exposed over sandstone grades to overlying middle Clastic Formation composed of unconsolidated conglomerate with lateral variability. Breccia is generally cemented, mainly matrix-supported to rarely clast-supported. Matrix is softer and crystal-rich without fine ash or pumice, representing that the compositions between andesite clasts and matrix are different. Clast composition is generally polymictic, but monomictic locally. All these features support a suite of clastic sedimentary deposits which have been more or less reworked; however, the presence of andesite breccia also indicates a proximal volcanic source bordering the basin margin at the same time. Some amphibole-rich layers have amphibole cumulates. Two pieces of amphibole-rich andesite breccia (DB19-056 to 057) were sampled. 60 m towards northeast another andesite breccia exposure was present. Most andesite clasts are subangular to sub-rounded, some even very well rounded, especially at transition to conglomerate. A piece of glassy porphyritic andesite (DB19-058) rich in amphibole was collected. Another sample is a piece of rock from tuffaceous matrix (DB19-059) rich in clay and crystals. To the southeast, another andesite breccia outcrop was found in forest which is the continued exposure similar to the sites visited before, still very large blocks in tuffaceous crystal-rich matrix. Field observations show that andesite clasts in breccias are dominantly amphibole-rich andesite in this locality; they are proximal volcaniclastics of which elements resemble some of the andesite clasts in Barrême Basin.

Saint Antonin was revisited by David and me together during our second field campaign near Collongues. Deposits are characterised by poorly sorted sub-angular to angular andesite pebbles to cobbles within tuffaceous matrix, grain-supported to matrix-supported; no pumices incorporated; these features look like the debris flow deposits, or to be specific, the block-and-ash flow deposits, produced by the collapse of lava dome, representing proximal volcanic sources to the basin. The andesite breccia succession was cross-cut by wavy thin layered dykes of light grey siliciclastic material. The dykes branch out and are truncated by overlying matrix-supported breccia. Two blocks of

andesite breccia (CL19-043 to 044) rich in amphibole crystals (few pyroxenes) were sampled in this site.

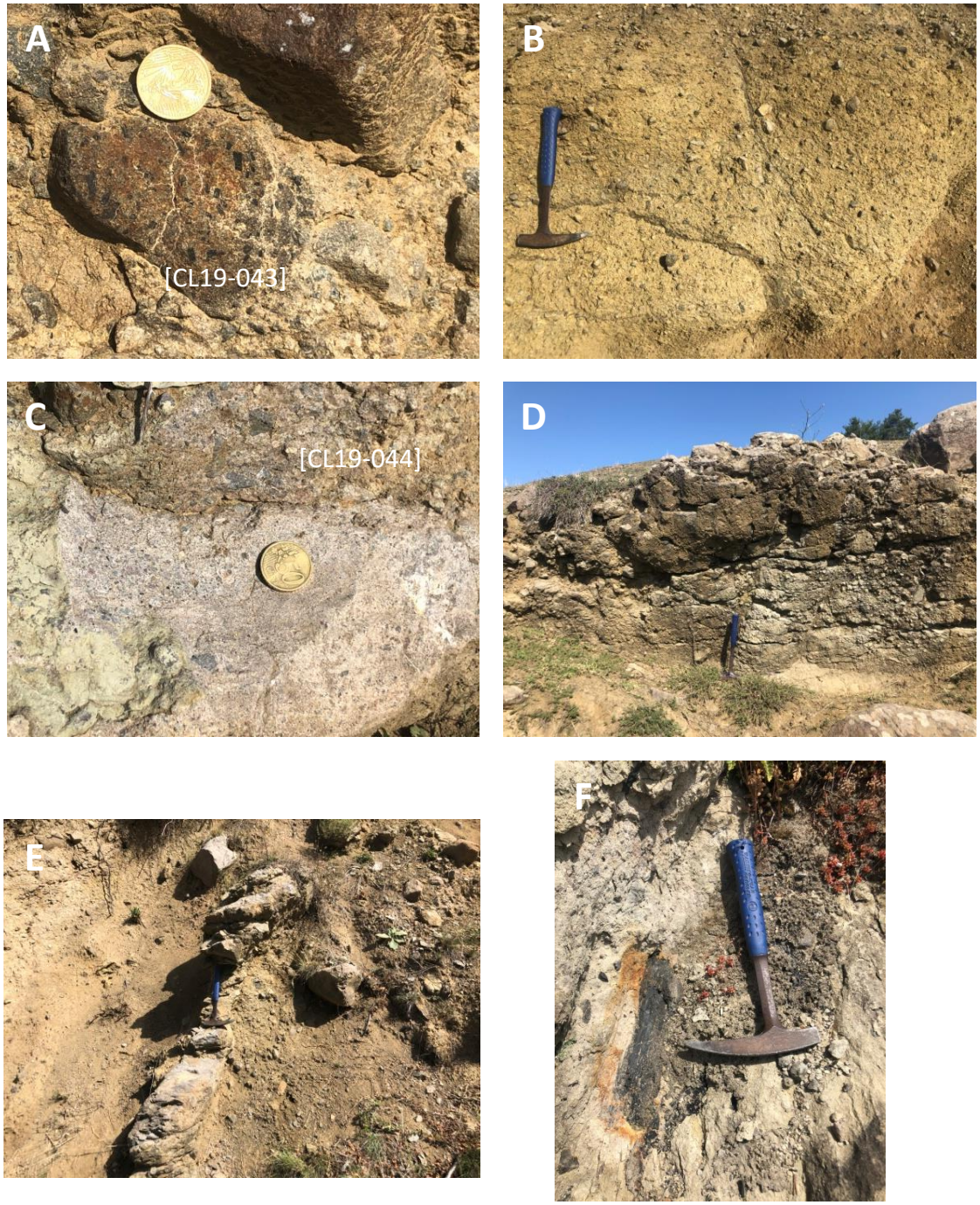

Figure 3.21 Photographs of outcrops in Saint Antonin locality. (A) Andesite cobble rich in amphibole phenocrysts (CL19-043). (B) Debris flow deposits containing diverse angular-subangular poorly-sorted clasts within tuffaceous matrix, no pumice present. (C) Andesite breccia with angular/subangular randomly oriented andesitic clasts (CL19-044). (D) Debris flow deposits, grain-supported, abundant large andesitic clasts. (E) Vertical andesitic dyke of variable thickness (20-40 cm) with red chilled margin. (F) Black carbonized wood of 30 cm long.

Towards south along road Chem.de Fontagne, a vertical dyke with variable thickness (20-45 cm) composed of heterogeneous andesitic clasts and supporting matrix was found at side of the road. Red chilled margin containing fine-grained sediments could be clearly observed. Matrix is rich in crystals. The presence of dykes represents volcanic activities nearby. Several metres away, black carbonized wood fragments up to 30 cm are concentrated at the base of well-cemented breccia with lenses of andesite clasts, interpreted as the high temperature of juvenile hot magma burning the wood during volcanic eruptions. All the phenomena provide solid proofs of the existence of primary volcaniclastic sediments whether the transport mechanism is pyroclastic flow or block-and-ash flow.

Overall, the volcaniclastic deposits in the Clumanc and western Saint Antonin localities are interpreted to be further close to the volcanic source compared to those in Swiss and northern-central French Alps. In particular, the extensive exposure of primary andesite breccia in Saint Antonin represents the vicinity of andesitic volcanoes to the basin.

3.3.6 Southmost SE France localities

The subduction of an oceanic plate of either Alpine Tethys (Handy et al., 2010; Oudet et al., 2010) or Mesogean origin (Carminati et al., 2010) beneath the southern European margin, could have resulted in the late Eocene to early Oligocene magmatic activity of Ligurian domain, SE France, which was mainly characterised by the emplacement of calc-alkaline igneous rocks with a geochemical signature resembling that of subduction-related igneous rocks (Beccaluva et al., 1994). The oldest dated products (~33–31 Ma) are represented by Le Dramont adakitic microdiorites forming a thick laccolith complex (locally called "estérellites"), together with andesitic and dacitic clasts within the Saint-Antonin pyroclastic deposits (Féraud et al., 1995). It is followed by the emplacement of basaltic to andesitic pyroclastic deposits cropping out around Villeneuve-Loubet area, and in the southwestern Corsica margin as well as in Sardinia (Réhault et al., 2012). Le Dramont and La Vanade (Villeneuve-Loubet) localities are chosen along the Ligurian margin for the investigation of magmatic evolution at the transition area between Alps and Apennines, compared to the contemporaneous Alpine Tertiary magmatism.

(1) Le Dramont Locality

The quartz-bearing microdiorites crops out near Cap Le Dramont in Agay-Estérel massif, locally called “estérellite”. The first site visited is an old quarry at the side of a small lake. Fluidal estérellite intrusion (CL19-045) with sub-horizontal foliation was sampled close to the layered and chilled margin at the top of the intrusion. Mafic igneous enclaves include dolerite texture. Walking south towards seashore, amounts of estérellite cobbles were laying on the beach. Mafic dioritic enclaves of estérellite (CL19-046 to 047) were sampled.

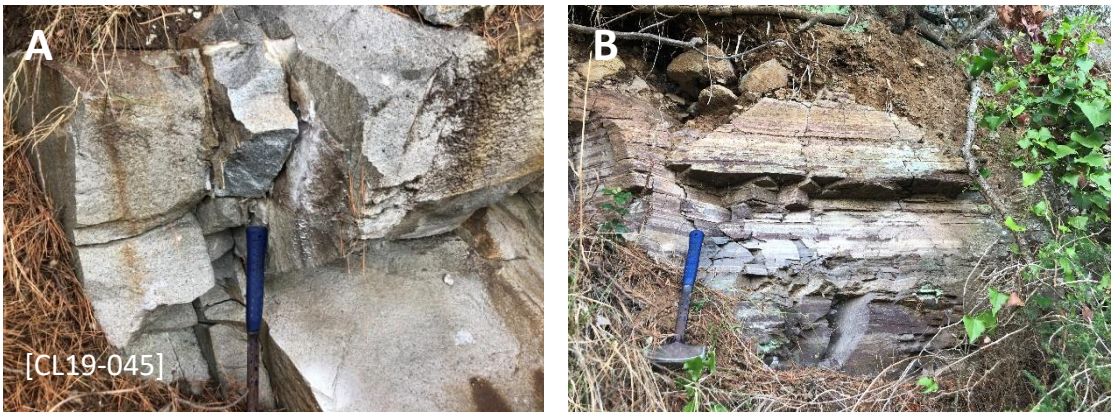

Figure 3.22 Photographs of outcrops in Dramont locality. (A) Estérellite outcrop at the side of a small lake (CL19-045). (B)Thin layers intercalated above estérellite intrusion.

(2) La Vanade Locality

La Vanade locality is located around 10 km north of Antibes at a disposed quarry with sparse vegetation. Stratigraphic sequences could be observed in this site. The first layer on top is brown andesitic breccia, overlying grey andesitic breccia-conglomerate which is on top of a set of coarse light grey tuff of 15 m thick; the bottom layer is a suite of grey breccia-conglomerate with abundant andesitic clasts. A block of amphibole andesite clast (CL19-048) was collected with a piece of tuffaceous matrix sample (CL19-049) both from bottom layer. Further north of 170 m, two more amphibole andesite clasts (CL19-050 to 051) were collected. 50 m further north along the small trail, a piece of medium grey crystal tuff (CL19-052) below the bottom layer was collected.

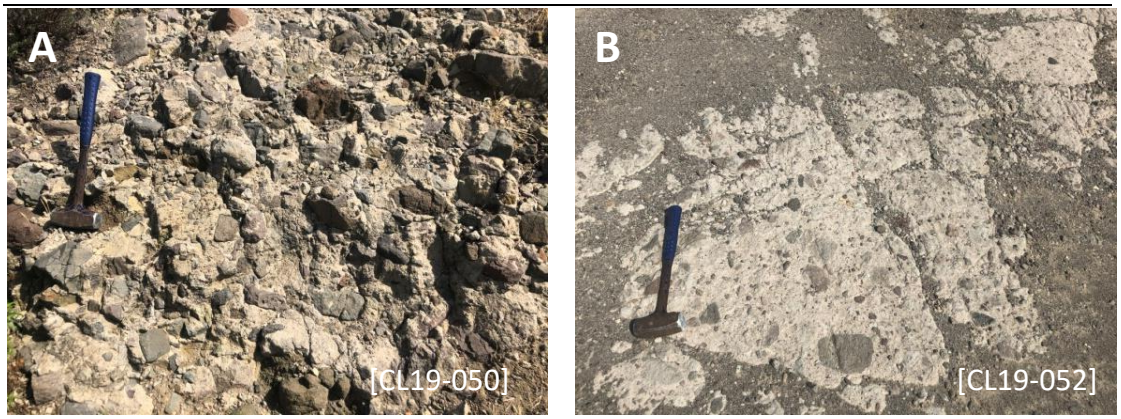

Figure 3.23 Photographs of outcrops in La Vanade locality. (A) Grey breccia-conglomerate with abundant andesitic clasts (CL19-050). (B) Light grey crystal tuff containing andesitic clasts and abundant ferromagnesian mineral fragments in tuffaceous matrix (CL19-052).

3.3.7 Northern Italy localities

Northern Italy localities are all located at the southern/eastern side of the Alpine chains, i.e., internal Alps. The Tertiary subduction-related magmatic activity in the internal Alps is represented by a series of granitoid plutons emplaced along the Periadriatic Line, and mainly located in Traversella, Biella, Bergell, Adamello Plutons. These plutonic suites are potential sources for volcanic materials in the North Helvetic foreland basins.

(1) Biella Locality

All Biella localities are located at north of Biella commune centre. In the river bottom next to a bridge, a phase of moderately curvilinear feldspar-phyric dykes (30-150 cm thick) with ferro-magnesian micro-phenocrysts was found injected into exhumated gneiss metamorphosed from granite after long-time and deep burial. Two andesitic dyke samples (CL19-053 to 054) were collected. Further north under another river, spectacular mingling textures of black mafic rocks with white felsic rocks was observed. At some points, mafic blocks/clasts behave like floating in the felsic groundmass. This could be explained by fractional crystallization that mafic minerals usually solidify earlier than felsic minerals in magma. A block of fine andesitic intrusive sample (CL19-055), syn-magmatic with granodiorite injections was collected to figure out whether they have similar composition compared to andesitic dykes. Further north beyond the third bridge, another phase of andesitic dyke (CL19-056) of 70 cm thick with large amphibole and white mica crystal was found on the river bottom, cutting through felsic rocks with chilled margins.

Further north to the Miagliano pluton area, a block of granulite with abundant cubic shape red garnet crystals was found in the river. Another diorite/microdiorite dyke sample at intrusive margin (CL19-057) was collected with chlorite alteration and severe deformation.

Figure 3.24 Photographs of outcrops in Biella locality. (A) Andesitic dyke

intrusion injected into gneiss (CL19-053). (B) Dark gray andesitic dyke (CL19-054). (C) Mingling tuxtuers with layering (CL19-055). (D) Andesitic dyke, cross-cutting felsic rocks with chilled margins (CL19-056). (E) Thick feldspar-pyroxene-phyric andesitic lava flow deposits outcropped at trail side (CL19-061). (F) Polymictic breccia with diverse clasts and dominant andesite sticking out on the slope (CL19-062).

Volcaniclastic lens outcropped at the mountainous area of Boccetto Sessera, north of Miagliano pluton. Roadcut exposures show a suite of thick feldspar-pyroxene-phyric andesitic lava flow deposits (CL19-058). Further up, another andesitic lava flow outcrop (CL19-059) was present at roadside. Further up for 300 m, one more piece of quartz-bearing dacite sample (CL19-060) was collected to see if there is any regional diversity. Climbing up along the hiking trail towards northwest, series of massive andesitic lava flow deposits (CL19-061) were outcropped, similar to what has been observed before. Polymictic poorly sorted andesite breccias (CL19-062) with diverse andesite clasts sticks out on the slope. Clasts include amygdaloidal andesite and andesite with abundant rounded pyroxene and amphibole phenocrysts in glassy matrix.

(2) Admello Locality

Admelleo locality visited is in Passo del Tonale, the type locality of tonalities, located in the Northern Admello region in the Italian and Austrian Alps. Driving from Edolo towards East along the mountain road SS42 until Passo del Tonale, there is a small path on the southern side of the road connecting to the mountain top. Walking uphill along the trail, a large tonalite outcrop with more than 100 m width was present showing homogeneous composition. Gold mica debris and mafic accumulate clasts could be observed on the rock surface easily as well as distinct quartz and feldspar crystals. Dark minerals are probably biotite. Where observed, grain size ranges up to ~3 cm. Around 150 m upwards, an another similar tonalite exposure exists with large biotite crystals on the surface. Climbing further up nearby a cable cabin stop, many tonalite pebbles are distributed around a small lake located at the mountain top. In total, three tonalite samples (CL19-066 to 068) were collected at the mountain foot, halfway and mountain top respectively.

Figure 3.25 Photographs of outcrops in Admelleo locality. (A) A large tonalite outcrop with more than 100 m width showing homogeneous composition (CL19-066). (B) Tonalite with large mica crystals on the surface (CL19-067).

(3) Bergell Locality

All Bergell localities are located at the southern side of Road SS38. Driving along the SP9 mountain road, the first site visited is in Cataeggio. A waterfall outcrop exhibits Bergell tonalite (CL19-068) with mafic enclaves in directional alignment. Another tonalite sample (CL19-069) with more ferromagnesian minerals was collected nearby the waterfall. Driving from Cataeggio towards east on the road to Preda Rossa, a small tonalite exposure outcropped at roadside. A tonalite sample (CL19-070) was collected in this site. The forest road was blocked with no entry to Preda Rossa, so went back and headed to next locality around Bagni di Masino. Passing by a beautiful forest village into the deep forest, a dried small stream exhibits outcrops of granodiorite (CL19-071) with large lath-shape feldspar crystals. Around 50 m below along the road, another granodiorite (CL19-072) roadcut exposure was present.

Figure 3.26 Photographs of outcrops in Bergell locality. (A) Tonalite with mafic enclaves in directional alignment (CL19-068). (B) Tonalite sample with more ferromagnesian minerals nearby the waterfall (CL19-069). (C) Granodiorite with large lath-shape feldspar crystals (CL19-071). (D) Granodiorite outcrop at a roadcut exposure (CL19-072). (E) Granodiorite exposures outcropped along the trail (CL19-073). (F) Abundant tonalite blocks distributed at the foot of a cliff (CL19-074).

Chiareggio is another locality visited in Bergell. Walking around 2 km towards west from Chiareggio along the river, then turn into the mountain trail. A series of granodiorite (CL19-073) exposures outcropped along the trail. The next locality is in an abandoned quarry in Nuova Olonio at the side of Road SS36. A huge cliff in the quarry exhibits large scale exposure of tonalite. Abundant tonalite blocks (CL19-074) are distributed at the foot of cliff.

Chapter 4: Petrography

4.1 introduction

In this chapter, this study is devoted to conducting a qualitative and quantitative petrographic study on volcaniclastic deposits (i.e., sandstones and igneous clasts) using our selected thin sections from various localities along the Alpine arc, in order to recognise the petrographic variability of sandstones and igneous clasts from different regions and characterise the primary and secondary volcaniclastic deposits for comparison with previous published results. The extent of abundance, roundness, textural and compositional variability of volcanic components will provide key information on transportation patterns and heterogeneity of volcanic sources.

In order to eliminate the influence of grain size and superficial alteration and metamorphism, samples were systematically analysed from similar sand grades and those least affected by secondary alterations. Classification ternary diagrams of andesitic clasts within sandstones are established in order to quantify each single thin section based on its texture and mineralogical composition according to the nomenclature and classification schemes established by Vuagnat (1952), Martini (1968), Dickinson (1970) and Marsaglia (1993). In addition, petrographic study on primary volcaniclastic rocks (volcanic breccia and tuff) and igneous pebbles has also been conducted in order to characterise primary and proximal volcaniclastics for petrographic comparison with the turbiditic sandstones. According to these petrographic results, samples showing fresh and high abundance of mafic minerals have been used to for geochemical analysis (i.e., whole-geochemistry and mineral geochemistry) and could also be used to differentiate the different types of volcanic sources and distinct sediment provenances in the study area.

4.2 Volcaniclastic sandstone petrography

4.2.1 Modal analysis of volcaniclastic sandstone

Fifty-five volcaniclastic sandstones were selected for modal analysis, carried out by using a point counter following the Gazzi-Dickinson method (Gazzi, 1966; Dickinson, 1970; Ingersoll et al., 1984), thus minimising dependence on grain size. The grain size effect on volcanic concentrations should be taken

care as discussed in Chapter 2.6. Coarse to medium-grained sandstones were analysed where available for consistency with published datasets, supplemented by counts of fine-grained sandstones as necessary. Each analysis is based on a total of 300 points per thin section. The results of modal analysis of volcaniclastic sandstone are attached at the end of this chapter (Table 4.4 - 4.7). The modal components of sandstones have been counted according to the following categories shown below:

(1) Primary parameters:

Qtz: quartz in isolated grains and in plutonic rocks, assuming all of them of non-volcanic origin;

Fsp(N): feldspars of non-volcanic origin, in the form of isolated grains or in plutonic lithics;

Fsp(V): feldspars of volcanic origin, in the form of isolated grains or in volcanic lithics;

Cpx: clinopyroxenes, in the form of isolated grains or in volcanic lithics;

Amph: amphiboles, in the form of isolated grains or in volcanic lithics;

Bt: biotites, in the form of isolated grains or in volcanic lithics;

Mica: white micas debris;

Lv: volcanic lithics;

Lp: plutonic lithics, including granite, microgranite, etc;

Ls: sedimentary lithics, including limestones, sandstone, shale, chert, radiolarite, etc;

Lm: metamorphic lithics, including quartzite, micaschist and gneiss, etc;

Opa: opaque minerals, including magnetite, ilmenite, hematite, etc.

Mtx/Cm: interstitial material, including detrital matrix mainly clay minerals, and cements mainly secondary chlorite or calcite;

(2) Secondary parameters:

Q'= Qtz = total quartz

F'= total isolated feldspar grains

L'= total unstable lithics

%Q=Q'/(Q'+F'+L')*100

%F= F'/(Q'+F'+L')*100

%L= L'/(Q'+F'+L')*100

V'=Fsp(V)+Cpx+Amph+Bt+Lv= volcanic material

C'=Qtz+Fsp(N)+Lp+Lm= crystalline material

S'=Mica+Ls= sedimentary material

%V=V'/(V'+C'+S')*100

%C=C'/(V'+C'+S')*100

%S=S'/(V'+C'+S')*100

Lvv= volcanic lithics with vitrophyric texture

Lvf= volcniac lithics with felsitic texture

Lvmi= volcanic lithics with microlitic texture

Lvl= volcanic lithics with lathwork texture

%Lvv= Lvv/(Lvv+Lvf+Lvmi)*100

%Lvf= Lvf/(Lvv+Lvf+Lvmi)*100

%Lvmi= Lvmi/(Lvv+Lvf+Lvmi)*100

%Lvf= Lvf/(Lvf+Lvmi+Lvl)*100

%Lvmi= Lvmi/(Lvf+Lvmi+Lvl)*100

%Lvl= Lvl/(Lvf+Lvmi+Lvl)*100

Lcpx= clinopyroxene andesite lithics

Lamph= amphibole andesite lithics

Lhal= heavily altered andesite lithics

%Lcpx= Lcpx/(Lcpx+Lamph+Lhal)*100

%Lamph= Lamph/(Lcpx+Lamph+Lhal)*100

%Lhal= Lhal/(Lcpx+Lamph+Lhal)*100

However, one issue that should be mentioned is microscopic observation will not be able to clearly distinguish the isolated quartz and plagioclase grains of volcanogenic origin from those of non-volcanic crystalline origin in many situations. Moreover, the volcaniclastic sandstones are a suite of deep-sea turbidite deposits which are characteristic of sub-angular to angular grains; this feature also fits the nature of broken/irregular crystals from syn-eruptive fragmentation, and/or from the tearing-off of the lava flow of pyroclastic origin. Therefore, in a turbiditic volcaniclastic metamorphosed sandstone, the aim of qualifying, and even quantifying the proportions of isolated quartz and feldspar grains from crystalline basement to those of volcanogenic origin is not easy to achieve.

Lateltin (1988) utilised cathode-luminescence technique acquiring the different luminescence colours of quartz crystals in thin sections: blue colour characterises quartz of magmatic origin, while volcanic quartz is represented by purple, and metamorphic quartz takes on brownish colour. Unfortunately, no detailed results were published in his paper. Nevertheless, it still can be assumed that the vast majority of isolated quartz grains in Taveyannaz sandstones (s.l.) are non-volcanic because quartz is almost in the form of groundmass rather than phenocrysts in andesite, therefore the breakdown of andesites during transportation would not end up in the presence of quartz grains incorporated in sandstone. Therefore, it can be assumed that all isolated quartz grains in Taveyannaz sandstone are of crystalline origin.

In terms of feldspar, both the disintegration of older plutonic rocks and neo-volcanic rocks can provide a large amount of isolated feldspars, especially plagioclases. In order to differentiate the origin of plagioclases, crystal zoning could be a good indicator because zoned plagioclase represents the chemical disequilibrium of magma during rapid cooling after eruption (Howie et al., 1992). However, vast majority of plagioclases underwent low-grade

metamorphism (Bussy and Epard, 1984; Rahn et al., 1994; Schmidt et al., 1997) and are more or less altered and replaced by secondary minerals, such as albite, laumontite, sericite, etc., obliterating the typical characteristics of volcanogenic plagioclase. Thus, the counts of zoned plagioclase will be much less than what it should be. As for alkali feldspars, it is safe to say most of them are of non-volcanic origin due to the scarcity of alkali feldspar phenocrysts in andesite.

4.2.2 Major detrital constituents (volcanic, crystalline, sedimentary)

All relevant detrital constituents are grouped into three major categories: (1) volcanic; (2) crystalline; (3) sedimentary. The counting results of this study are shown in Table 2 and plotted with previous data for comparison in Figure 4.1.

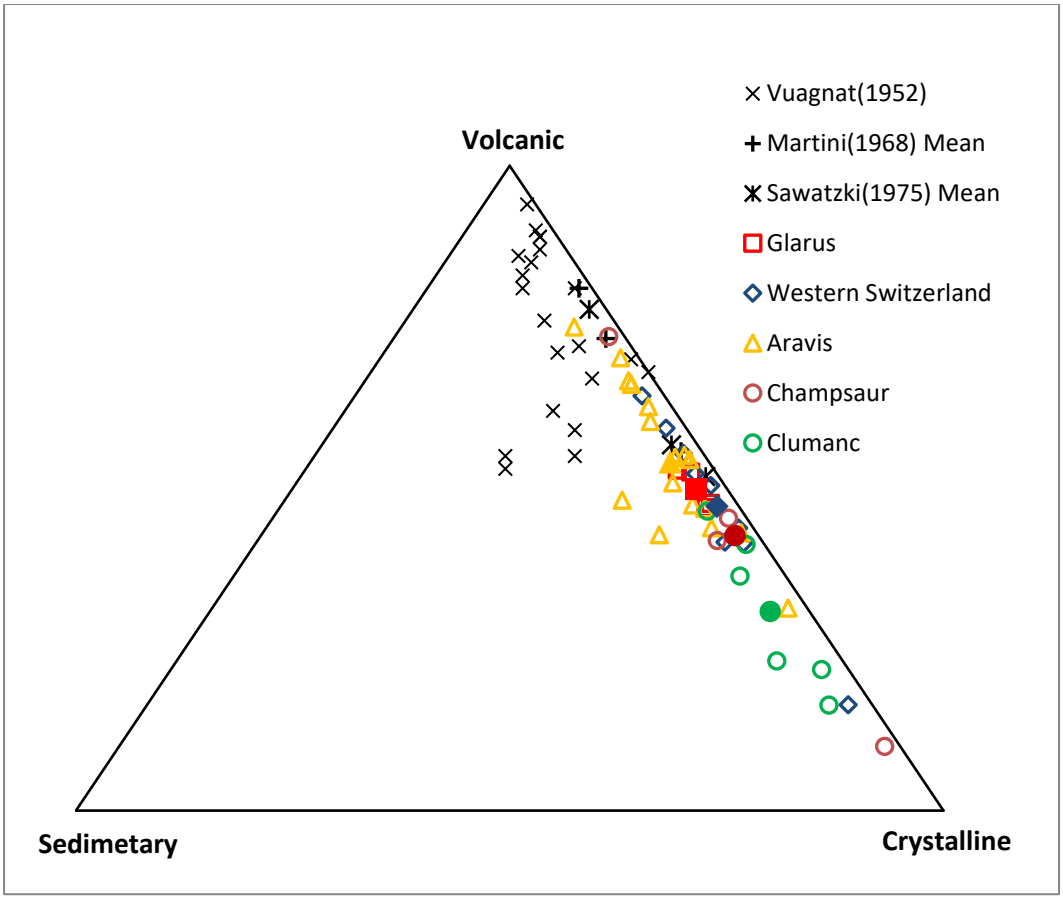

Figure 4.1 Ternary diagram of volcanic, sedimentary and crystalline (V-S-C) constituents of volcaniclastic sandstone from studied regions (solid symbols denote mean value)

The most obvious feature is that our results generally show lower volcanic, higher crystalline and similar sedimentary components compared with previous data conducted by Vuagnat (1952), Martini (1968) and Sawatzki

(1975). This disparity could be explained by the following reasons: (1) previous researchers studied coarser samples on average than ours; (2) different ways/criteria on categorising plagioclase into volcanogenic origin or crystalline origin as mentioned above in Section 4.1.1, if it is assumed that all (vast majority) of isolated plagioclase grains are volcanogenic, the results of our data will be considerably higher than what's shown in the diagram in terms of volcanic components; (3) slightly different way of operating and counting, all related to personal petrographic knowledge and experience.

Our data from different regions show that sandstones in Aravis are the richest in volcanic detritus among all regions, largely overlapping with typical Taveyannaz sandstone (GTT) zone of previous data. Western Switzerland and Glarus contain less volcanic, but more crystalline material. Champsaur only has four samples, showing a wide range of variation due to the large grain size and limited number of samples. Clumanc sandstone has the lowest volcanic concentration perhaps due to the distal position (westernmost) of Barrême basin in the Alpine thrust-and-fold belt.

4.2.3 QFL diagram and provenance type

Detrital framework modes of sandstone from different kinds of basins are a function of provenance types governed by plate tectonics (Dickinson and Suczek, 1979). Ternary diagrams showing framework proportions of quartz, feldspar and lithics successfully distinguish the key provenance types of sand with compositional fields established by Dickinson and associated authors (Dickinson et al., 1983; Dickinson, 1985). For this study, the modal compositions was recalculated into three major categories: Q, F, L. The results are shown in Table 4.4 – 4.7 and in the QFL ternary diagram of Figure 4.2 with provisional subdivisions according to inferred provenance type (Dickinson et al., 1983) and with Lateltin (1988)'s and Ruffini et al. (1997)'s results for comparison.

The QFL diagram shows that detrital modes of volcaniclastic sandstone of different localities typically spread across the lower parts of QFL diagram and are generally plotted in the region assigned to magmatic arc, reflecting dominant detritus from volcanic arcs in the early syn-collisional stage. However, contributions from high-pressure metamorphic rocks derived from axial belt in Penninic domain should not be neglected, as well as paleo-margin

basement provenance representing remnants of the continental margins and clastic wedge provenance representing sands recycled from fluvial to turbiditic foreland basin, foredeep, or clastic sequences of remnant ocean basin (Garzanti et al., 2007; Lu et al., 2018). Therefore, detrital modes of Taveyannaz sandstone (s.l.) are probably controlled by the mixing between basement granitoids either from neo-metamorphic/plutonic nappes of axial belt or from paleo-metamorphic continental basement of paleo-margin, and neo-volcanic rocks derived from magmatic arcs (Garzanti et al., 2007).

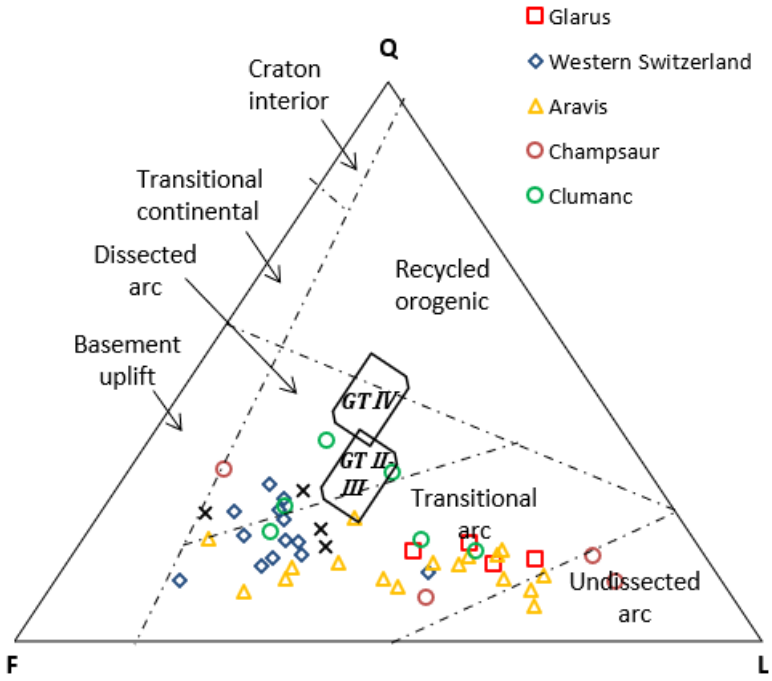

Figure 4.2 QFL ternary diagram of volcaniclastic sandstone showing compositional fields indicative of sand derivation of various provenance types (after Dickinson et al., 1983; Dickinson, 1985); two rectangles represent mean composition and standard deviations of the GT Ⅱ-Ⅲ and GTⅣ sandstone populations presented by Lateltin (1988); four crosses represent mean values in Haute-Savoie region compiled from Ruffini et al. (1997).

In the diagram, it's clear that sandstones in Aravis and Glarus regions, of which most are in the transitional arc field, few landing in the undissected arc field, are generally more lithic than those in Western Switzerland and Clumanc, of which most are plotting around the boundary between dissected arc and transitional arc fields. This trend indicates a less mixing of basement materials and more mixing of volcanic materials for the detritus in the Aravis and Glarus regions than those from Western Switzerland and Clumanc regions. Although

the sandstones in Champsaur are limited by the number of analysed samples, three out of four samples plotting around the undissected arc field still could prove the high concentration of volcanic detritus derived from essentially undissected arc.

The composition results of Lateltin (1988) show higher quartz content (> 30 %) compared with ours, basically landing in the dissected arc filed, indicating a more plutonic basement source (Dickinson et al., 1983). It's not clear why this difference has been caused and why the quartz content is higher in Lateltin's study. If refered to the quantitative data presented by Vuagnat (1952) and Sawatzki (1975), recalculated quartz content (Q/(Q+F+L) x 100) is generally less than 30%. As for typical Taveyannaz sandstone, the content is mostly less than 15 %.

4.2.4 Petrographic classification of volcanic clast within sandstone and related ternary diagrams

(1) Textural classification of volcanic clasts

In Chapter 2.6, previous textural classifications of volcanic clasts have been reviewed and discussed, as well as the importance of textural variation of volcanic clasts on provenance study. Based on the intermediate nature and the scarcity of lathwork texture of volcanic clasts in this study, vitrophyric, felsitic and microlitic textures were choosen as the three end-members of the ternary diagram (Lvv-Lvf-Lvmi) instead of vitrophyric, microlitic and lathwork as Marsaglia (1993) did on the study of volcanic sands from basaltic environment, with Lvf-Lvmi-Lvl diagram plotted as complement. The counting results are compiled in Table 4.4 – 4.7 and plotted in ternary diagrams (Figure 4.3 and Figure 4.4).

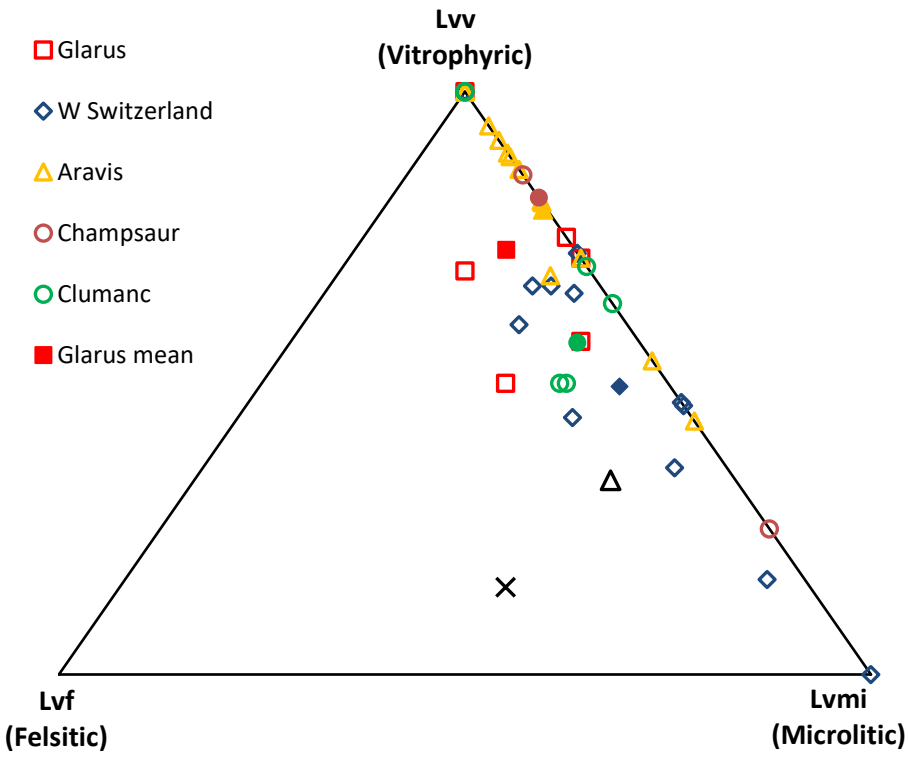

Figure 4.3 Ternary diagram of vitrophyric (Lvv), felsitic (Lvf) and microlitic (Lvmi) textures of volcanic clasts in Taveyannaz sandstone (black cross and triangle denote quantitative data in Vuagnat (1952) collected from two Taveyannaz sandstone samples of western Switzerland)

The Lvv-Lvf-Lvmi diagram (Figure 4.3) shows that the volcanic clasts from different localities are mostly distributed along the Lvv-Lvmi side of the triangle, prone to cluster towards the vitrophyric apex, demonstrating a very low proportion of felsitic texture, a relatively high proportion of vitrophyric texture and an intermediate proportion of microlitic texture. The generally high proportion of vitrophyric texture indicates quick cooling of volcanic lavas after eruption. Aravis and Champsaur sandstones which almost entirely landed on the right side of the triangle contain close to zero felsitic texture, indicating the scarce felsic volcanic input. The mean values of clasts from western Switzerland and Clumanc are plotted close to each other, characterised by higher proportion of felsitic texture, indicating a higher incorporation of dacitic or rhyolitic clasts compared with those of Aravis and Champsaur. The mean value of Glarus sandstone has similar proportion of felsitic texture but less proportion of microlitic texture compared with those from western Switzerland and Clumanc.

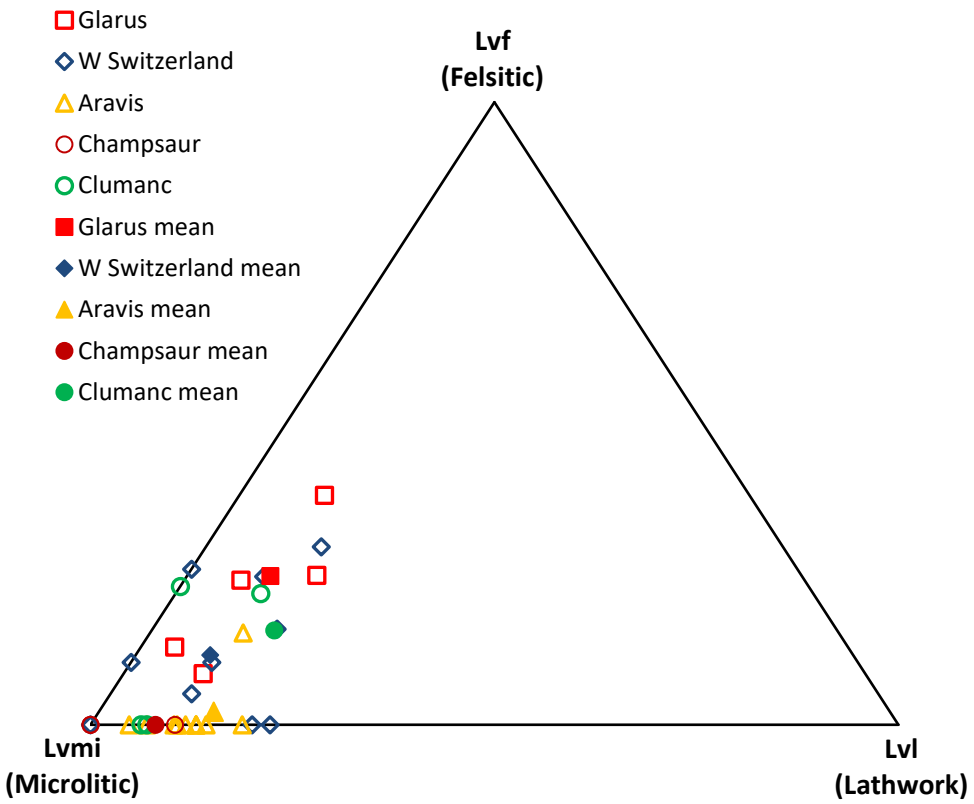

Figure 4.4 Ternary diagram of felsitic (Lvf), microlitic (Lvmi) and lathwork (Lvl) textures of volcanic clasts of Taveyannaz sandstone

The Lvf-Lvmi-Lvl ternary diagram (Figure 4.4) shows that the volcanic clasts from different localities cluster towards the Lvmi apex, clearly proving that microlitic texture is dominant, corresponding to the intermediate nature of Taveyannaz volcanism, with subordinate felsitic and lathwork textures, corresponding to the rare occurrence of basic and acidic volcanic clasts (Dickinson, 1970). The mean values of Aravis and Champsaur both fall nearly on the microlitic-lathwork boundary with rare felsitic clasts, representing the rare occurrence of dacitic or rhyolitic clasts. The clasts from Glarus, western Switzerland and Clumanc are generally more scattered with the mean values plotted above the base line with higher proportions of felsitic texture.

(2) Mineralogical classification of volcanic clasts

The main goal of classifying volcanic clasts in this research is to distinguish the differences of various original types of andesites and their related magmatic affinities. Thus, it is proposed that a mineralogical classification scheme of the andesitic clasts using petrographic method should be based on the types and the abundances of phenocrysts (i.e., plagioclase, clinopyroxene and

amphibole). For those sandstones undergoing various degrees of alteration, try to infer its original mineral type from the optical characteristics of the remaining unaltered residues or completely altered pseudomorphs; for those undergoing severe alteration and losing entire original optical information, they are classified into a separate group. Based on these rules, three general mineralogical subtypes are distinguished as follows:

(1) Clinopyroxene andesite, the most common type of andesite with clinopyroxene phenocrysts as the predominant ferromagnesian phenocrysts, subordinate amphibole/ biotite;

(2) Amphibole andesite, with amphibole phenocrysts as the dominant ferromagnesian phenocrysts and subordinate clinopyroxene, containing comparatively larger plagioclase phenocrysts than clinopyroxene andesite;

(3) Heavily altered andesite clasts or andesite clasts in which ferromagnesian phenocrysts were not recognisable optically; plagioclases are the only recognisable type of phenocrysts. These andesites could derive from any of the above-mentioned two general types originally.

However, ferromagnesian minerals of Taveyannaz sandstone are prone to be weathered and altered into chlorite, calcite, epidote and/or other silicates (e.g., Martini, 1968; Bussy and Epard, 1984; Rahn et al., 1995). In most cases of this study, microscopic observation shows that the alteration products are a kind of yellowish clayey phyllosilicate minerals under plane polarised light (PPL) view, appearing low-grade (gray, brown, yellow) interference colour under cross polarised light (XPL) view. These secondary products are most likely chlorite group minerals. The yellowish colour could be explained by the incorporation and precipitation of iron-rich pore fluid at a late stage turning the original colourless or pale green chlorite into yellow (Martini and Vuagnat, 1965; Martini, 1968; Rahn et al., 1995). The ultimate alteration products of clinopyroxenes and amphiboles both could be layered phyllosilicates, such as chlorite and vermiculite, making the differentiation between clinopyroxene and amphibole become difficult. Three practical methods were applied to help distinguish altered amphibole and clinopyroxenes under microscope:

(1) Some chloritised amphiboles are characteristic of rimming opaque minerals, such as magnetite and ilmenite, which could be regarded as one criterion for distinguishing them from clinopyroxene.

(2) The crystal shape of the pseudomorphs could be another method, since the diamond-shaped outline denotes the existence of the amphibole crystal prior to alteration whereas clinopyroxenes pseudomorphs are typical of rectangle or lath shape. However, this crystal shape difference is not always working because some crystals are dissolved and altered into anhedral to subhedral shapes, and the angle of view of these minerals in thin section can obscure their characteristic features.

(3) The third method stems from the different arrangement of cleavages and cracks of pseudo-morphic clinopyroxenes and amphiboles. The experiences gained from observing hundreds of totally altered clinopyroxenes and amphiboles allow to argue that amphibole pseudomorphs usually present distinct wide and regular cleavages on crystal surface, while clinopyroxene pseudomorphs often show irregular cracks.

However, as mentioned before, these methods can only provide a best estimate of clinopyroxene/amphibole ratio in the cases where alteration of the original andesite fragments is pervasive.

A quantitative analysis of mineralogical composition of andesite was conducted based on the classification scheme proposed above. The results are compiled in Table 4.4 – 4.7 and presented in the following ternary diagram (Figure 4.5).

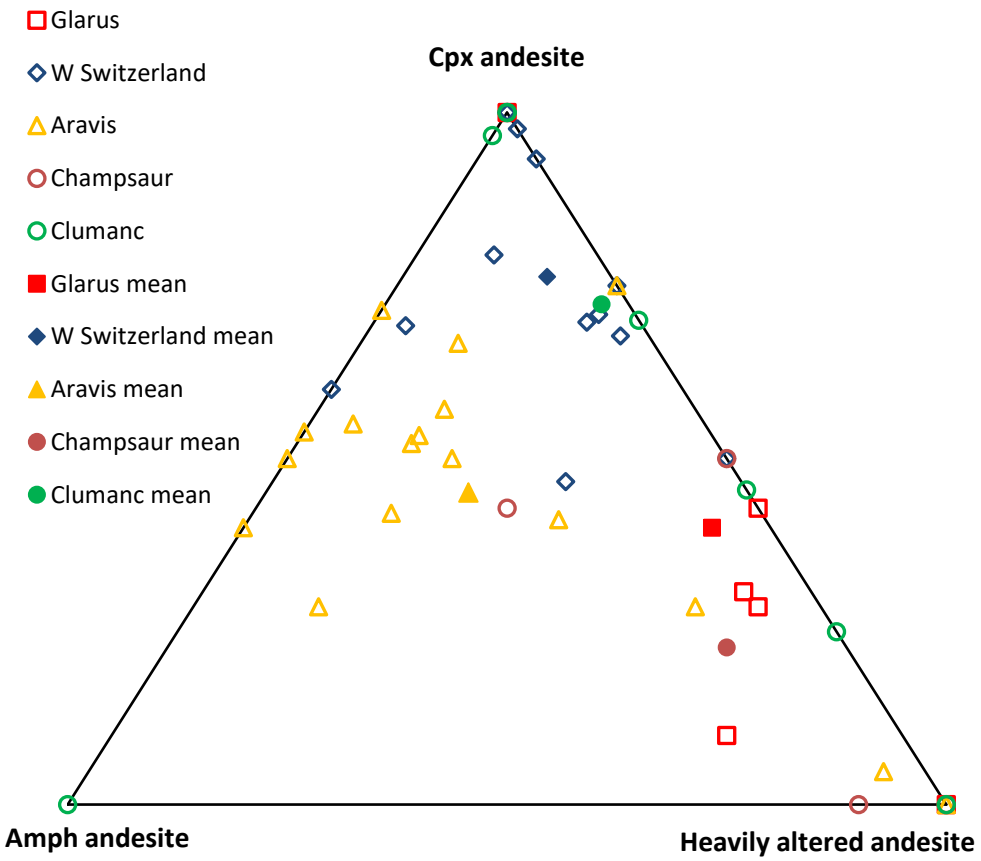

Figure 4.5 Ternary diagram on mineralogical classification of clinopyroxene, amphibole and heavily altered andesite of Taveyannaz sandstone

The ternary diagram (Figure 4.5) shows that most points fall in the upper and right side of the triangle, representing that most samples are enriched in clinopyroxene andesite clasts or heavily altered andesite clasts. Amphibole andesite clasts are depleted in general except for the Aravis sandstone where proportion of amphibole and clinopyroxene andesite clasts is almost equal with relatively low proportion of heavily altered andesite clasts. Glarus and Champsaur sandstones are characterised by their high content of heavily altered andesite clasts, caused by the general severe local calcitisation and low-grade metamorphism. Western Switzerland sandstones contain mostly clinopyroxene andesite clasts with low proportion of amphibole and heavily altered andesite clasts. Clumanc sandstones have rare amphibole andesite clasts with a wide range of variation between the clinopyroxene apex and the heavily altered apex. The mean values of Clumanc and western Switzerland sandstones are plotted close to each other, both indicating dominant clinopyroxene andesite clasts.

4.3 Igneous petrography

4.3.1 Primary/proximal volcaniclastic deposits

Eleven samples of sub-angular to angular andesitic clasts within volcanic breccias, two samples of tuffaceous matrix of andesitic breccias and one sample of crystal tuff from Flaine, Champsaur, Saint Antonin and La Vanade localities have been observed and analysed under microscope in thin sections with results shown in Table 4.1 and 4.2. The percentage of ferromagnesian elements and the ratio of amphibole phenocrysts over clinopyroxene phenocrysts have been counted as well with results shown in Table 4.1 and 4.2.

(1) Sub-angular to angular andesitic clasts in volcanic breccia

Under microscope, these andesitic clasts are commonly porphyritic determined by predominant large phenocrysts of feldspar, and by subordinate clinopyroxene and amphibole phenocrysts encompassed in vitrophyric or microlitic groundmass. Most of the clasts are clinopyroxene andesite with vitrophyric texture for groundmass, except two amphibole andesite clasts in St. Antonin. The percentage of ferro-magnesian phenocrysts varies between 8.5 - 21.7 %. The original plagioclase phenocrysts have been albitised and altered to various degrees. In the majority of cases, albitisation and chloritisation begin in the more basic core of plagioclases. Feldspar twinnings, in particular simple twinnings, and plagioclase zonings are commonly observed. Ferromagnesian minerals such as clinopyroxenes and amphiboles are variously altered to secondary minerals, including chlorite, calcite, epidote, opaque minerals, and very fine-grained aggregates (Vuagnat, 1952; Martini, 1968; Sawatzki, 1975).

In the Flaine area, a peculiar kind of large angular andesitic clast (CL19-001) of amoeboid shape with quenched margin interbedded in the coarse sandy matrix was observed in the field and was also documented by Lu et al. (2018). Similar volcanic pebbles were recorded by Siegenthaler (1974) in the Glarus area as well. The original porphyritic texture is well preserved in the andesite clast. The common alterations of plagioclase replaced by calcite/albite, and of clinopyroxene/amphibole replaced by chlorite document strong post-magmatic alteration most likely in an aqueous environment and it is suggested

that the fragile andesite pebbles were very poorly reworked with very limited transport produced by nearby sub-marine volcanism.

Table 4.1 Characteristics of andesitic clasts within volcanic breccias from Flaine, St. Antonin and La Vanade localities

Locality	Sample	Rock type	Texture of groundmass	Percentage of ferro-magnesian phenocrysts	Amph/Cpx ratio
Flaine	CL19-001	Clinopyroxene andesite	Vitrophyric	12.7 %	0.5
Champsaur	CL19-038	Clinopyroxene andesite	Vitrophyric	17.5 %	0.4
	CL19-040	Clinopyroxene andesite	Microlitic	6.8 %	0.0
St. Antonin	CL19-043	Amphibole andesite	Vitrophyric	21.7 %	9.5
	CL19-044	Amphibole andesite	Vitrophyric to Microlitic	18.5 %	3.5
	DB19-056	Clinopyroxene andesite	Microlitic	14.0 %	0.6
	DB19-057	Clinopyroxene andesite	Microlitic	14.7 %	0.3
	DB19-058	Clinopyroxene andesite	Microlitic	13.5 %	0.4
La Vanade	CL19-048	Clinopyroxene andesite	Vitrophyric	13.0 %	0.1
	CL19-050	Clinopyroxene andesite	Vitrophyric	8.5 %	0.0
	CL19-051	Clinopyroxene andesite	Vitrophyric	10.0 %	0.3

(2) Tuffaceous matrix and crystal tuff

Under microscope, these tuffaceous matrix and tuffs consist of crystal fragments, irregular hollows left by pumices during the making of thin sections and occasional lithic clasts in a glassy matrix, which had been recrystallised to fine siliceous material, probably an assemblage of quartz and

feldspar. These characters clearly indicate the existence of primary volcaniclastic deposits, resulting from syn-eruption fragmentation of the magma. Crystal fragments mainly include juvenile angular clasts of plagioclase, quartz, clinopyroxene, amphibole and rare cuspate glass shards. The percentage of ferro-magnesian crystals varies between 5.3 - 9.0 % and the ratio of amphibole crystals over clinopyroxene crystals varies between 0.1 - 0.3. Over-sized irregular andesitic clasts are observed in the tuffaceous matrix as well. The fragmentary nature of the assemblage is clear from the broken crystals and irregular/angular andesite lithics.

Table 4.2 Characteristics of tuffaceous matrix in volcanic breccia and crystal tuff from St. Antonin and La Vanade localities

Locality	Sample	Rock type	Percentage of ferro-magnesian crystals	Amph/Cpx ratio
St. Antonin	DB19-059	Tuffaceous matrix	5.3	0.3
La Vanade	CL19-049	Tuffaceous matrix	9.0	0.1
	CL19-052	Crystal tuff	7.0	0.1

4.3.2 Secondary volcaniclastic deposits (igneous pebbles in conglomerate)

Eleven igneous rounded/well-rounded pebbles to cobbles preserved in conglomeratic beds from Champsaur and Clumanc localities have been observed and analysed under microscope in thin sections with results shown in Table 4.3. The percentage of ferromagnesian elements and the ratio of amphibole phenocrysts over clinopyroxene phenocrysts have been counted as well with results shown in Table 4.3.

Under microscope, these igneous pebbles/cobbles are commonly porphyritic determined by predominant large phenocrysts of feldspar, and by subordinate clinopyroxene and amphibole phenocrysts encompassed in vitrophyric or microlitic groundmass. The igneous pebbles from Champsaur are all amphibole basalt/basaltic andesite with microlitic texture for groundmass. The andesitic pebbles from Clumanc are heavily altered, causing ferro-

magnesian phenocrysts unrecognisable, characterised by vitrophyric texture of groundmass. The percentage of ferro-magnesian phenocrysts varies between 17.0 – 27.3 % for those in Champsaur, which is higher than those from Clumanc of around 10 %. The ratios of amphibole phenocryst over clinopyroxene phenocryst are slightly over 1 for samples from Champsaur CL19-024, CL19-026 and CL19-027, and even up to 10 for sample CL19-028. In comparison, the andesite clasts within volcanic breccias in Champsaur (CL19-038, CL19-040) contain much less amount of amphibole phenocrysts, with amphibole/clinopyroxene ratio much smaller than 1.

Table 4.3 Characteristics of igneous pebbles/cobbles within conglomerate from Champsaur and Clumanc localities

Locality	Sample	Rock type	Texture of groundmass	Percentage of ferro-magnesian phenocrysts	Amph/Cpx ratio
Champsaur	CL19-024	Amphibole basalt	Microlitic	27.3	1.2
	CL19-026	Amphibole basalt	Microlitic	21.5	1.3
	CL19-027	Amphibole basaltic andesite	Microlitic	17.0	1.8
	CL19-028	Amphibole basaltic andesite	Microlitic	25.7	9.8
Clumanc	CL19-042(ABC)	Andesite	Vitrophyric	10.3	N.A.
	DB19-055(ABCD)	Andesite	Vitrophyric	9.5	N.A.

N.A. Ferro-magnesian phenocrysts heavily altered and replaced by chlorite and/or calcite, not recognisable their original mineral type under microscope

4.4 Synthesis of petrographic results

Glarus: The volcaniclastic sandstone in this region is characterised by heavy alteration of feldspar, ferromagnesian minerals and interstitial material, which are commonly replaced by calcite; nearly all plagioclases and volcanic lithics are moderately to greatly altered, giving rise to some uncertainty in the acquisition and interpretation of point-counting work. The average value of

volcanic content is around 50 %, slightly higher than those from western Switzerland (47.2 %), but lower than those from Aravis (54.1 %). In the QFL diagram, all sandstones fall in the Transitional Arc field, in between those from Aravis landing on the Undissected Arc field and those from western Switzerland clustering towards the Dissected Arc field. Andesite classification diagrams show a slightly higher proportion of felsitic texture (10.6 %) of andesite clasts in Glarus than other regions, as well as the highest proportion of heavily altered clasts (49 %).

Western Switzerland: The most distinctive nature of Taveyannaz sandstones in this region is the low proportion (47.2 %) and finer grain size (< 0.1 mm) of volcanic lithics and ferromagnesian minerals compared with other regions. These sandstones appear more like typical epiclastic turbidites mixed with a less proportion of volcanic lithics rather than like typical volcaniclastic rocks mixed with a high proportion (> 60 %) of volcanic detritus. The QPL diagram clearly indicated the mixture of sands derived from crystalline basement with Q content of 16.8 %. Andesite classification diagrams indicate the highest proportion of microlitic texture (42.6 %) of andesite clasts among all regions, as well as the highest proportion of clinopyroxene andesite clasts (75.2 %).

Aravis: The volcaniclastic sandstones in this region are characteristic of (1) the higher content of volcanic components (54.1 %) compared to the previous two regions in Switzerland, volcanic components encountered in every sample collected in this region; (2) the common presence of amphibole phenocrysts and amphibole andesite clasts which are rarely observed among other regions and (3) the presence of polymictic conglomerate containing abundant rounded andesite clasts which are mostly vitrophyric amphibole andesite. Andesite classification diagrams indicate the rare occurrence of felsitic texture (0.5 %) of andesite clasts and common occurrence of amphibole andesite clasts (31.9 %).

The large angular andesitic clast (CL19-001) of amoeboid shape with quenched margin in Flaine has 12.7 % of ferro-magnesian phenocrysts and the Amph/Cpx ratio is 0.5, consistent with the average ratio of amphibole andesite clasts over clinopyroxene andesite clasts of volcaniclastic sandstones (= 31.9/45.1 = 0.7) in this region.

Champsaur: Only six sandstone samples were collected in the region where most collected samples are igneous pebbles and andesitic clasts within volcanic breccia. The Champsaur sandstones are characteristic of polymictic sandstone with a variety of lithics, mainly containing large andesite and quartz gneiss. Therefore, the mean value of major constituents shows the highest proportion of crystalline material (54.6 %) among all regions. On the QFL diagram and andesite classification diagrams the variable composition gives rise to scattered spots spreading across those ternary diagrams.

The most significant feature in Champsaur is the contrasting characteristics between angular clinopyroxene andesitic clasts in breccias with very low Amph/Cpx ratio (= 0.2 in average) and rounded amphibole andesitic pebbles with more amphibole phenocrysts than clinopyroxene (ratio = 3.5 in average). This discrepancy clearly indicates the distinct sources of these igneous clasts. Most of the clasts have a microlitic texture except for sample CL19-038 of vitrophyric texture, consistent with the dominant microlitic texture (Lvmi = 92 %) of andesite clasts in volcaniclastic sandstones.

Clumanc: The most distinct nature of volcaniclastic sandstones in this region is that all samples contain andesitic lithics, but no fresh/recognisable ferromagnesian minerals were observed within these lithics; they are all heavily altered and replaced by chlorite and/or calcite. The proportion of volcanic detritus (30.9 %) is the lowest among all regions. On the QFL diagram, the average quartz content of sandstones in this region is the highest (24 %), clearly indicating a basement source from internal Alps. Andesite classification diagrams suggest the presence of felsitic texture (4.3 %) of andesite clasts and the high proportion of clinopyroxene andesite clasts (72.9 %).

The andesitic pebbles/cobbles in Clumanc are also largely influenced by secondary alterations with ferro-magnesian phenocrysts completely replaced by chlorite and/or calcite. Therefore, the mineralogical classification of these pebbles could not be defined (either clinopyroxene andesite or amphibole andesite). They all have a vitrophyric texture, consistent with the dominant vitrophyric texture of andesite clasts in volcaniclastic sandstones.

Saint Antonin: Primary/proximal volcaniclastic deposits are typical of this region. Two andesitic clasts in volcanic breccia (CL19-043, 044) are amphibole andesite with vitrophyric texture. The percentage of ferro-magnesian

phenocrysts is 20.1 % in average and the amphibole/clinopyroxene ratio is 6.5 in average. The other three andesitic clasts (DB19-056, 057, 058) are clinopyroxene andesite (Amph/Cpx ratio = 0.4 in average) with microlitic texture. The proportion of ferro-magnesian phenocrysts (14.1 % in average) is lower than the previous two clasts (20.1 %).

La Vanade: Primary/proximal volcaniclastic deposits are typical of this region. Three andesitic clasts in volcanic breccia are clinopyroxene andesite with vitrophyric texture. The percentage of ferro-magnesian phenocrysts is 10.5 % in average and the amphibole/clinopyroxene ratio is 0.1 in average. One typical crystal tuff with 7.0 % of ferro-magnesian crystals clearly indicates the occurrence of proximal volcanic activity.

4.5 Summary

A detailed quantitative petrographic study has been conducted on volcaniclastic sandstones, as well as a semi-quantitative study on igneous clasts. Various types of triangle diagrams have been used in order to classify these rocks based on the grain-counting data.

The V-S-C diagram (Figure 4.1) shows that the sandstones originated mainly from volcanic source rocks and crystalline basement rocks with minor contributions from sedimentary sources. Clumanc sandstones have the highest proportion of basement source. The wide range of spreading and highly overlapping of the samples limit the possibility to discriminate among different localities.

The Q-F-L diagram (Figure 4.2) shows that detrital modes of volcaniclastic sandstone typically spread across the lower parts of QFL diagram and are generally plotted in the field assigned to magmatic arc, reflecting the dominant contributions from volcanic arcs. In the diagram, it’s clear that sandstones in Aravis and Glarus regions mostly in the transitional arc field are separated from those in Western Switzerland and Clumanc plotted around the boundary between dissected arc and transitional arc fields.

The Lvv-Lvf-Lvmi diagram (Figure 4.3) shows that the volcanic clasts generally have a very low proportion of felsitic texture, a relatively high proportion of vitrophyric texture and an intermediate proportion of microlitic texture. The Lvf-Lvmi-Lvl diagram (Figure 4.4) shows that the volcanic clasts have a

dominant microlitic texture, corresponding to the intermediate nature of Taveyannaz volcanism. No clear zonation could be recognised on both diagrams due to the clustering nature of these samples on the diagrams.

The mineralogical diagram (Figure 4.5) shows that most samples are enriched in clinopyroxene andesite clasts or heavily altered andesite clasts. Glarus and Champsaur sandstones, characterised by their high content of heavily altered andesite clasts caused by the general severe local calcitisation and low-grade metamorphism, are distinguished from those from Western Switzerland and Clumanc which have dominant clinopyroxene andesite clasts. Aravis sticks out by its high proportion of amphibole andesite clasts.

The semi-quantitative petrographic study on primary igneous clasts shows that most of the igneous clasts are clinopyroxene andesite with vitrophyric texture. The percentage of ferro-magnesian phenocrysts varies between 5 - 22 %. The igneous pebbles from Champsaur are all amphibole basalt/basaltic andesite with microlitic texture and those from Clumanc are heavily altered, causing ferro-magnesian phenocrysts unrecognisable, characterised by vitrophyric texture. The percentage of ferro-magnesian phenocrysts varies between 10 - 30 %. No clear zonation could be recognised for the igneous components from different localities due to the limited number of analysed samples.

Overall, petrographic study provides a large amount of quantitative information (e.g., constituent composition, secondary alteration, texture, minerology, etc.) on the volcaniclastic sandstones and its related igneous materials compared with previous research. It is the first time a more comprehensive and holistic petrographic study has been conducted on both secondary deposits in the north and primary deposits in the south, along with a large amount of quantitative grain-counting analyses, which are more than any published literatures combined together in terms of volcaniclastic deposits in NAFB. However, the attempts of trying to discriminate samples from different localities have not succeeded due to (1) common secondary alteration, (2) mixing of other reworked igneous materials, and (3) limited number of analysed samples.

Table 4.4 Modal composition of Taveyannaz sandstone of western Switzerland.

W. Switzerland	Sample	Qtz	Fsp (N)	Fsp (V)	Cpx	Amph	Biotite	Mica	Vol. lithics	Plu. lithics	Sed. lithics	Meta. lithics	Opaque	Matrix/ Cement	Total
Coarse	CL18-005	48	96	74	15	5	2	3	10	0	3	0	2	42	300
	CL18-006	49	98	83	12	2	0	5	17	1	7	0	1	25	300
	CL18-007	29	58	159	2	0	0	3	12	1	4	1	6	25	300
	CL18-011	35	70	114	16	0	0	1	14	2	5	3	2	38	300
	CL18-013	36	72	100	11	0	0	2	16	0	4	2	4	53	300
	CL18-014	42	84	70	17	1	0	1	15	0	3	2	3	62	300
	CL18-015	69	128	27	0	0	0	5	14	2	2	3	3	47	300
	CL18-018	32	64	87	31	9	0	1	26	1	5	2	3	39	300
	CL18-020	39	78	86	25	0	0	1	15	1	3	2	3	47	300
Medium	CL18-001	52	104	33	16	7	0	3	3	0	5	2	1	74	300
	CL18-004	58	116	44	7	0	0	8	15	2	3	1	2	44	300
	CL18-009	59	118	21	20	0	0	2	10	1	3	0	3	63	300
	CL18-024	49	98	42	16	0	0	2	11	1	4	2	2	73	300
Fine	CL18-003	68	136	10	0	0	0	5	2	0	7	0	1	71	300
	CL18-008	65	130	18	10	0	0	2	5	2	3	0	5	60	300
	CL18-010	69	136	10	1	0	0	2	6	0	4	1	2	69	300
	CL18-017	74	128	7	0	0	0	2	4	0	1	1	1	82	300
	CL18-019	64	128	10	3	0	0	1	2	0	2	0	2	88	300
	CL18-021	82	131	3	0	0	0	3	1	0	1	0	1	78	300

(continued)

W. Switzerland	Sample	V'	S'	C'	Q	F	L	Lvv	Lvf	Lvmi	Lvf	Lvmi	Lvl	Lcpx	Lamph	Lhal
Coarse	CL18-005	41.4	2.3	56.3	19.1	59.8	21.1	60.0	13.3	26.7	28.6	57.1	14.3	46.7	20.0	33.3
	CL18-006	41.6	4.4	54.0	18.2	54.6	27.1	44.1	14.7	41.2	23.8	66.7	9.5	79.4	11.8	8.8
	CL18-007	64.3	2.6	33.1	10.9	72.6	16.5	66.7	8.3	25.0	25.0	75.0	0.0	70.8	4.2	25.0
	CL18-011	55.4	2.3	42.3	13.5	60.2	26.3	0.0	0.0	100.0	0.0	100.0	0.0	100.0	0.0	0.0
	CL18-013	52.3	2.5	45.3	14.9	58.1	27.0	65.4	3.8	30.8	10.0	80.0	10.0	69.2	26.9	3.8
	CL18-014	43.8	1.7	54.5	17.9	53.0	29.1	100.0	0.0	0.0	n/a	n/a	n/a	50.0	0.0	50.0
	CL18-015	16.4	2.8	80.8	28.2	51.8	20.0	66.7	6.1	27.3	15.4	69.2	15.4	69.7	6.1	24.2
	CL18-018	59.3	2.3	38.4	12.5	38.5	49.0	16.3	4.7	79.1	5.0	85.0	10.0	97.7	0.0	2.3
	CL18-020	50.4	1.6	48.0	15.7	53.8	30.5	46.7	0.0	53.3	0.0	80.0	20.0	93.3	0.0	6.7
Medium	CL18-001	26.2	3.6	70.2	23.4	59.0	17.6	100.0	0.0	0.0	n/a	n/a	n/a	60.0	40.0	0.0
	CL18-004	26.0	4.3	69.7	23.6	52.8	23.6	35.5	6.5	58.1	10.0	90.0	0.0	67.7	3.2	29.0
	CL18-009	21.8	2.1	76.1	25.4	51.3	23.3	72.3	0.0	27.7	0.0	100.0	0.0	75.0	0.0	25.0
	CL18-024	30.7	2.7	66.7	22.0	52.9	25.1	46.2	0.0	53.8	0.0	77.8	22.2	100.0	0.0	0.0
Fine	CL18-003	5.3	5.3	89.5												
	CL18-008	14.0	2.1	83.8												
	CL18-010	7.4	2.6	90.0												
	CL18-017	5.1	1.4	93.5												
	CL18-019	7.1	1.4	91.4												
	CL18-021	1.8	1.8	96.4												
Mean								49.5	6.2	44.3	11.2	79.6	9.2	76.3	7.3	16.4

Table 4.5 Modal composition of Taveyannaz sandstone of Glarus

Glarus	Sample	Qtz	Fsp (N)	Fsp (V)	Cpx	Amph	Biotite	Mica	Vol. lithics	Plu. lithics	Sed. lithics	Meta. lithics	Opaque	Matrix/ Cement	Total
Coarse	DB19-038	32	64	83	0	0	0	2	40	2	8	2	5	62	300
	DB19-039	35	70	77	4	0	0	2	46	0	5	3	3	55	300
	DB19-041	41	67	73	2	0	0	2	35	3	7	4	2	64	300
	DB19-044	37	74	60	25	2	0	2	23	1	5	2	3	66	300
Medium	DB19-035	92	83	19	2	0	0	2	7	2	11	5	2	75	300
	DB19-043	70	103	23	0	0	0	2	10	2	3	1	12	74	300
Fine	DB19-034	83	95	0	7	0	0	16	0	4	3	2	2	88	300
	DB19-045	127	73	0	5	0	0	15	0	7	19	6	10	38	300

Glarus	Sample	V’	S’	C’	Q	F	L	Lvv	Lvf	Lvmi	Lvf	Lvmi	Lvl	Lcpx	Lamph	Lhal
Coarse	DB19-038	52.8	4.3	42.9	13.9	29.0	57.1	50.0	20.0	30.0	24.0	60.0	16.0	10.0	20.0	70.0
	DB19-039	52.5	2.9	44.6	14.6	22.9	62.5	69.2	15.4	15.4	36.8	52.6	10.5	30.8	7.7	61.5
	DB19-041	47.0	3.8	49.1	17.7	30.2	52.2	100.0	0.0	0.0	100.0	0.0	0.0	28.6	7.1	64.3
	DB19-044	47.6	3.0	49.4	16.2	38.4	45.4	57.1	7.1	35.7	23.3	69.8	7.0	100.0	0.0	0.0
Medium	DB19-035	12.6	5.8	81.6	41.6	39.8	18.6	71.4	0.0	28.6	12.5	83.3	4.2	42.9	0.0	57.1
	DB19-043	15.4	2.3	82.2	33.0	50.0	17.0	75.0	0.0	25.0	8.2	82.0	9.8	0.0	0.0	100.0
Fine	DB19-034	3.3	9.0	87.6												
	DB19-045	2.0	13.5	84.5												
Mean								72.9	8.5	18.6	23.9	65.8	10.3	40.0	6.7	53.3

Table 4.6 Modal composition of Taveyannaz sandstone in Aravis, Northern SE France

Haute-Savoie	Sample	Qtz	Fsp (N)	Fsp (V)	Cpx	Amph	Biotite	Mica	Vol. lithics	Plu. lithics	Sed. lithics	Meta. lithics	Opaque	Matrix/ Cement	Total
Coarse	CL19-003	23	46	105	22	7	0	2	24	2	5	1	8	55	300
	CL19-004	35	70	71	26	13	0	1	25	0	4	3	5	47	300
	CL19-005	16	32	113	23	18	0	4	38	1	9	2	3	41	300
	CL19-007	34	68	46	17	13	0	3	27	2	6	4	6	74	300
	CL19-008	37	74	62	0	0	0	3	38	3	8	3	3	69	300
	CL19-012	25	50	102	15	5	0	2	12	0	6	5	9	69	300
	CL19-013	25	50	79	34	11	0	2	15	0	4	2	12	66	300
	CL19-014	24	48	66	7	5	0	2	26	0	26	12	7	77	300
	CL19-015	35	70	56	22	4	0	2	27	0	10	4	7	63	300
	CL19-016	22	44	79	36	15	0	2	30	4	5	5	6	52	300
	CL19-017	26	52	71	23	9	0	2	6	3	5	2	8	93	300
Medium	CL19-002	36	72	80	35	13	0	2	13	1	4	0	2	42	300
	CL19-006	41	82	83	2	0	0	2	11	0	2	0	5	72	300
	CL19-009	49	98	22	28	8	0	2	12	0	3	1	12	65	300
	CL19-010	33	66	59	30	12	0	2	22	0	12	6	11	47	300
	CL19-011	27	54	65	0	0	0	1	33	11	25	13	6	65	300

(continued)

Haute-Savoie	Sample	V'	S'	C'	Q	F	L	Lvv	Lvf	Lvmi	Lvf	Lvmi	Lvl	Lcpx	Lamph	Lhal
Coarse	CL19-003	66.7	3.0	30.4	9.8	43.8	46.4	81.3	0.0	18.8	0.0	88.2	11.8	50.0	31.3	18.8
	CL19-004	54.4	2.0	43.5	14.2	36.8	49.0	89.5	0.0	10.5	0.0	89.7	10.3	55.0	40.0	5.0
	CL19-005	75.0	5.1	19.9	6.3	27.4	66.3	91.7	0.0	8.3	0.0	87.0	13.0	50.0	50.0	0.0
	CL19-007	46.8	4.1	49.1	15.7	27.6	56.7	71.4	0.0	28.6	0.0	93.0	7.0	71.4	28.6	0.0
	CL19-008	43.9	4.8	51.3	16.4	26.7	56.9	94.1	0.0	5.9	0.0	95.2	4.8	41.2	23.5	35.3
	CL19-012	60.4	3.6	36.0	11.4	58.2	30.5	100.0	0.0	0.0	n/a	n/a	n/a	28.6	57.1	14.3
	CL19-013	62.6	2.7	34.7	11.4	45.0	43.6	53.8	0.0	46.2	0.0	85.7	14.3	53.8	46.2	0.0
	CL19-014	48.1	13.0	38.9	11.2	29.0	59.8	100.0	0.0	0.0	n/a	n/a	n/a	40.0	60.0	0.0
	CL19-015	47.4	5.2	47.4	15.4	31.6	53.1	100.0	0.0	0.0	n/a	n/a	n/a	57.1	28.6	14.3
	CL19-016	66.1	2.9	31.0	9.2	26.3	64.6	86.7	0.0	13.3	0.0	87.0	13.0	53.3	33.3	13.3
	CL19-017	54.8	3.5	41.7	13.2	56.3	30.5	100.0	0.0	0.0	n/a	n/a	n/a	0.0	0.0	100.0
Medium	CL19-002	55.1	2.3	42.6	14.2	49.6	36.2	43.5	0.0	56.5	0.0	81.3	18.8	52.2	34.8	13.0
	CL19-006	43.0	1.8	55.2	18.6	64.7	16.7	100.0	0.0	0.0	n/a	n/a	n/a	28.6	14.3	57.1
	CL19-009	31.4	2.2	66.4	22.2	43.4	34.4	100.0	0.0	0.0	n/a	n/a	n/a	75.0	0.0	25.0
	CL19-010	50.8	5.8	43.4	13.8	33.8	52.5	68.4	5.3	26.3	14.7	73.7	11.5	42.1	42.1	15.8
	CL19-011	42.8	11.4	45.9	11.8	23.2	64.9	81.0	0.0	19.0	0.0	87.0	13.0	4.8	4.8	90.5
Mean								79.8	0.5	19.7	2.1	83.7	14.2	45.1	31.9	23.0

Table 4.7 Modal composition of volcaniclastic sandstone in Champsaur and Clumanc

Champsaur	Sample	Qtz	Fsp (N)	Fsp (V)	Cpx	Amph	Biotite	Mica	Vol. lithics	Plu. lithics	Sed. lithics	Meta. lithics	Opaque	Matrix/ Cement	Total
Coarse	CL19-018	36	68	57	4	1	0	2	45	5	3	15	2	62	300
	CL19-029	27	71	59	0	0	0	1	47	21	12	15	1	46	300
	CL19-039	17	34	109	18	7	0	2	27	1	2	2	6	75	300
	CL19-041	67	123	3	5	13	0	2	1	0	2	5	2	77	300
Clumanc															
Coarse	DB19-047	42	84	65	0	0	0	2	32	2	3	5	2	63	300
	DB19-053	36	72	66	4	0	0	1	35	2	8	2	11	63	300
Medium	DB19-046	54	108	35	0	0	0	1	14	0	6	6	2	74	300
	DB19-048	40	80	62	0	0	0	5	14	0	6	2	16	75	300
	DB19-049	78	88	24	0	0	0	2	12	3	9	4	9	71	300
	DB19-051	67	78	34	0	0	0	2	18	5	15	5	4	72	300
Fine	DB19-052	89	98	9	0	0	0	2	4	0	3	0	7	88	300
	DB19-054	83	90	8	2	3	0	3	3	1	13	7	2	85	300

(continued)

Champsaur	Sample	V'	S'	C'	Q	F	L	Lvv	Lvf	Lvmi	Lvf	Lvmi	Lvl	Lcpx	Lamph	Lhal
Coarse	CL19-018	45.3	2.1	52.5	15.4	15.0	69.7	25.0	0.0	75.0	0.0	89.6	10.4	50.0	0.0	50.0
	CL19-029	41.9	5.1	53.0	10.7	14.3	75.0	100.0	0.0	0.0	n/a	n/a	n/a	0.0	10.0	90.0
	CL19-039	73.5	1.8	24.7	7.8	41.0	51.2	85.7	0.0	14.3	0.0	100.0	0.0	42.9	28.6	28.6
	CL19-041	10.0	1.8	88.2	30.6	56.6	12.8	100.0	0.0	0.0	n/a	n/a	n/a	0.0	0.0	100.0
Mean								81.8	0.0	18.2	0.0	92.0	8.0	22.7	13.6	63.6
Clumanc																
Coarse	DB19-047	41.3	2.1	56.6	18.0	36.5	45.5	70.0	0.0	30.0	0.0	93.8	6.3	70.0	0.0	30.0
	DB19-053	46.5	4.0	49.6	16.0	30.2	53.8	50.0	13.3	36.7	21.1	57.9	21.1	96.7	3.3	0.0
Medium	DB19-046	21.9	3.1	75.0	24.2	51.6	24.2	50.0	12.5	37.5	22.2	66.7	11.1	25.0	0.0	75.0
	DB19-048	36.4	5.3	58.4	19.6	55.9	24.5	100.0	0.0	0.0	n/a	n/a	n/a	100.0	0.0	0.0
	DB19-049	16.4	5.0	78.6	35.8	40.4	23.9	100.0	0.0	0.0	n/a	n/a	n/a	100.0	0.0	0.0
	DB19-051	23.2	7.6	69.2	30.2	34.2	35.6	63.6	0.0	36.4	0.0	93.0	7.0	45.5	0.0	54.5
Fine	DB19-052	6.3	2.4	91.2												
	DB19-054	7.5	7.5	85.0												
Mean								56.9	7.7	35.4	15.2	69.7	15.2	72.3	3.1	24.6

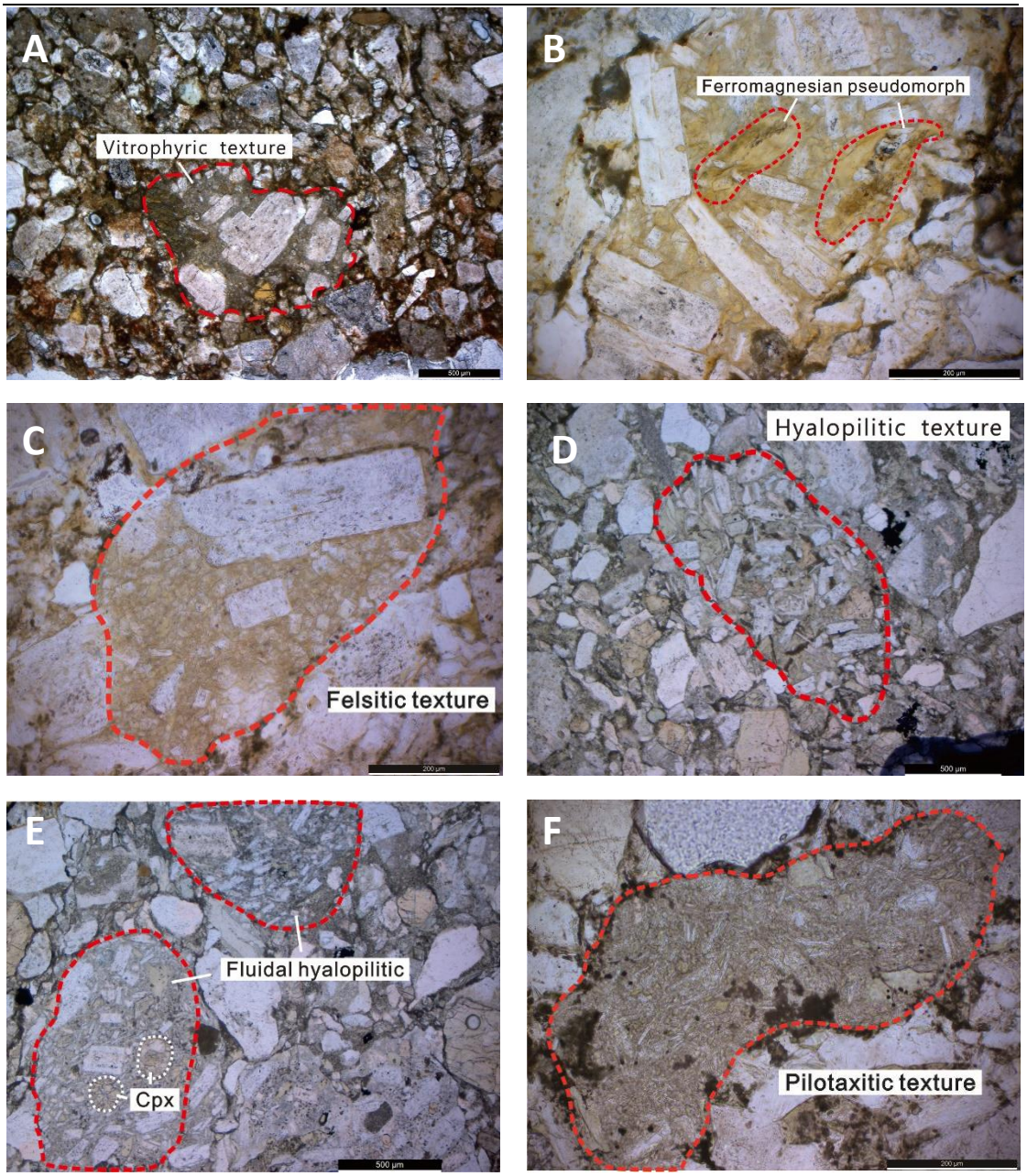

Figure 4.6 Microscopic images of Taveyannaz sandstone in western Switzerland. (A) Typical sandstone with low volcanic material incorporated red dashed curve circled is an andesitic clast with typical vitrophyric texture (CL18-005, PPL). (B) Ferro-magnesian minerals completely replaced by brownish iron-rich clay mineral, only preserving the original outlines, this andesitic clast categorised as heavily altered andesite (CL18-004, PPL). (C) Andesitic clast with typical felsitic texture (CL18-004, PPL). (D) Typical hyalopilitic texture of andesite clast containing lath-shape plagioclases in random orientation (CL18-018, PPL). (E) Typical fluidal hyalopilitic texture of andesitic clasts containing fresh clinopyroxene phenocrysts, microlites tend to orient in parallel (CL18-018, PPL). (F) Typical pilotaxitic texture of andesitic clast (CL18-015, PPL). (Abbreviation: Cpx-clinopyroxene)

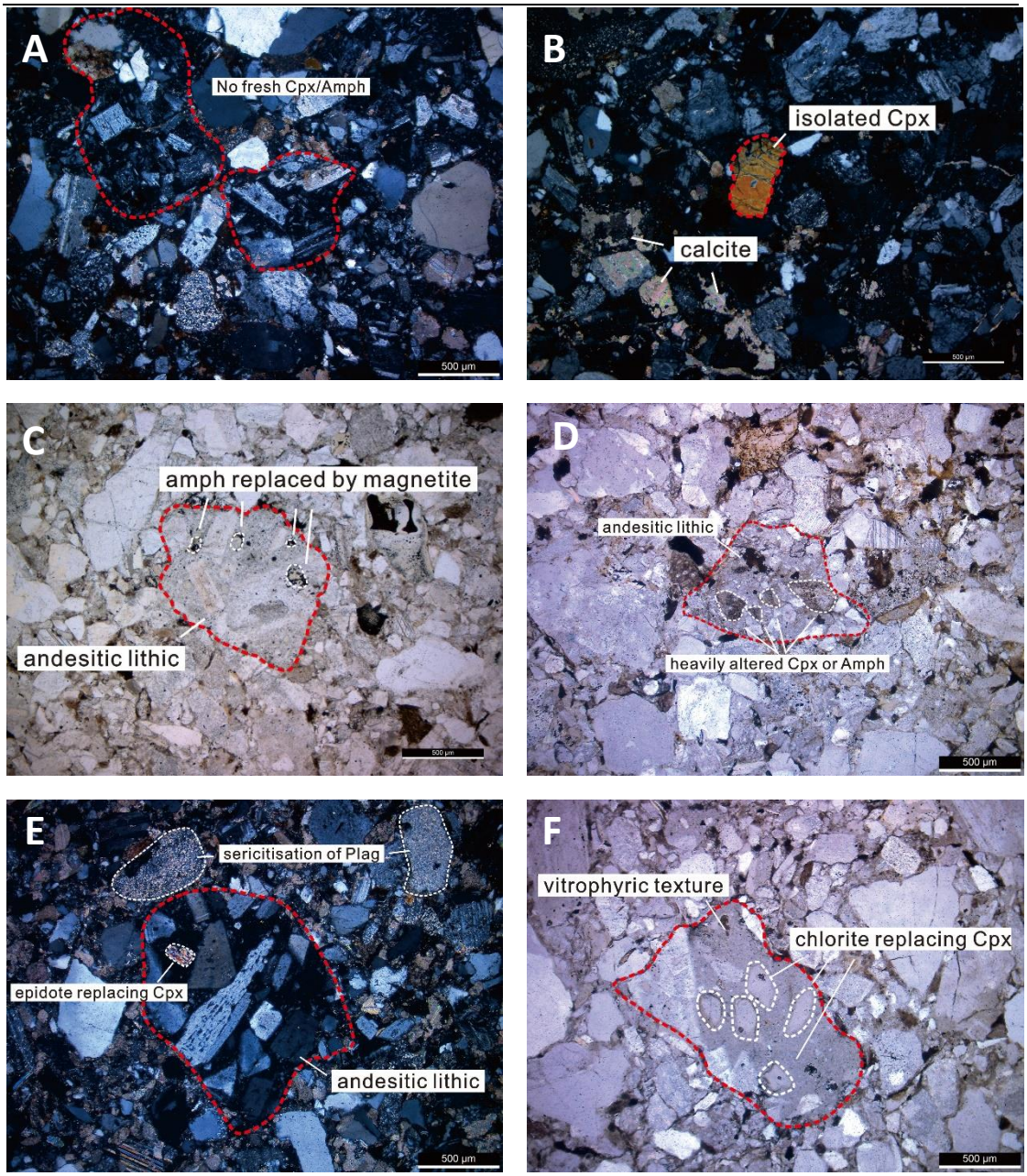

Figure 4.7 Microscopic images of Taveyannaz sandstone in Glarus. (A) Typical sandstone in Glarus with no fresh ferromagnesian minerals, circled by red dashed curves are andesitic clasts without observing any traces of original minerals (DB19-032, XPL). (B) Very rare fresh isolated clinopyroxene, surrounded by strong calcite replacement of feldspar and small lithics (DB19-032, XPL). (C) Andesitic lithic contains secondary opaque minerals substituting amphiboles, no fresh recognizable ferromagnesian minerals inside lithic (DB19-035, PPL). (D) Andesitic lithic contains heavily altered ferromagnesian minerals, unable to identify the original mineral type (DB19-038, PPL). (E) Andesitic lithic contains secondary epidote replacing clinopyroxene, sandstone heavily altered by calcite, strong sericitisation of plagioclase (DB19-039, XPL). (F) Typical vitrophyric texture of andesitic lithic in Glarus, secondary chlorite replacing clinopyroxene (DB19-039, PPL). (Abbreviation: Cpx-clinopyroxene, Amph-amphibole, Plag-plagioclase).

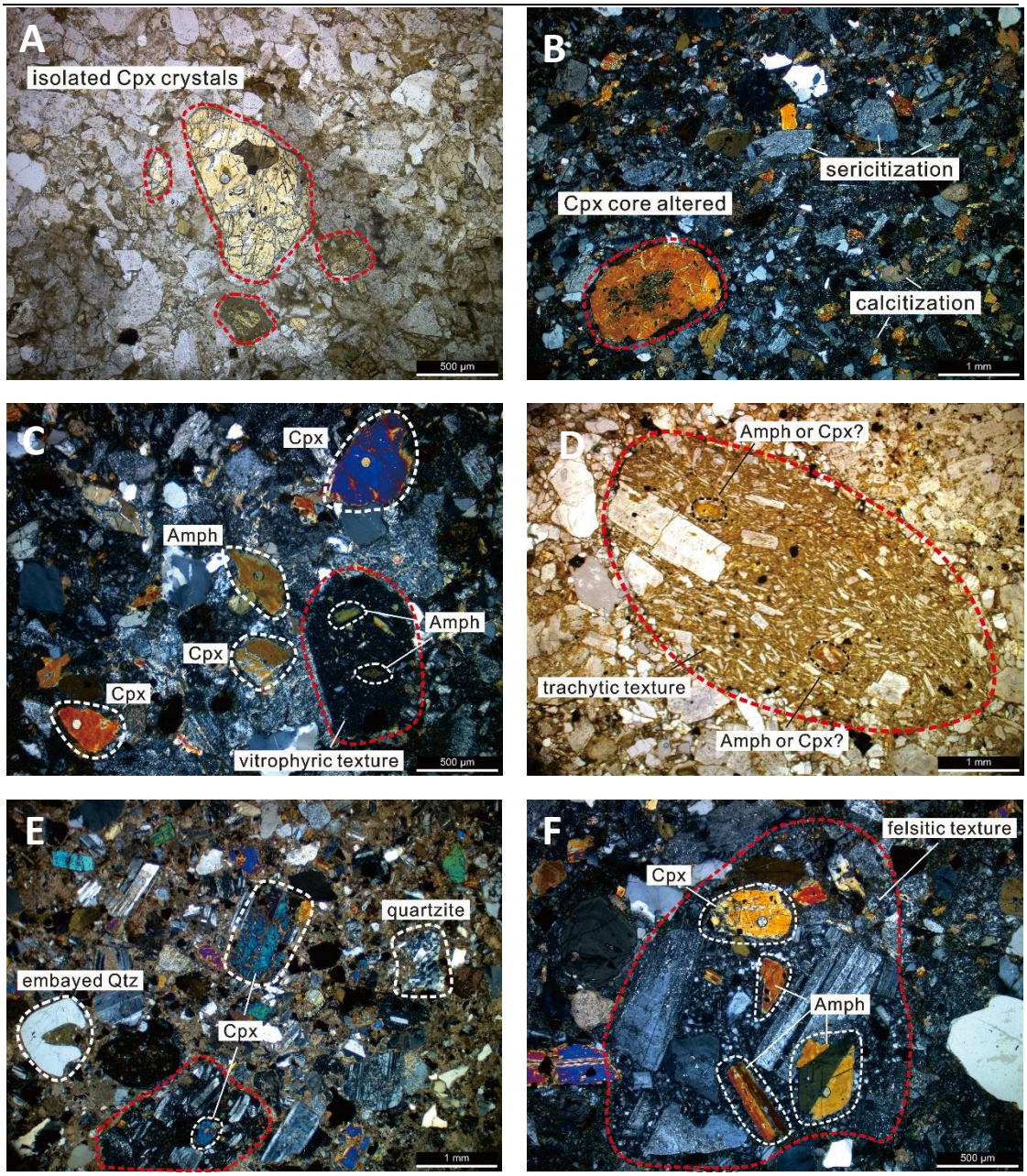

Figure 4.8 Microscopic images of Taveyannaz sandstones in Haute-Savoie. (A) Isolated clinopyroxene crystals with various degree of alteration, most crystals are broken, filled with cracks (CL19-002, PPL). (B) Core of a large isolated clinopyroxene crystal altered, full of small scattered clinopyroxene and amphibole crystals, sericitization and calcitisation pretty common (CL19-003, XPL). (C) Amphibole andesite with vitrophyric texture, isolated large ferromagnesian crystals, holes left after laser ablation on clinopyroxenes at top right and bottom left (CL19-004, XPL). (D) Large andesitic lithic with typical trachytic texture contains heavily altered ferromagnesian minerals, unable to identify the original mineral type (CL19-007, PPL). (E) Sandstone heavily cemented by calcite, full of isolated ferromagnesian minerals, embayed quartz indicating volcanic origin, quartzite lithic existing (CL19-009, XPL). (F) Typical felsitic texture of amphibole andesitic lithic (CL19-010, XPL). (Abbreviation: Cpx-clinopyroxene, Amph-amphibole, Plag-plagioclase, Qtz-quartz)

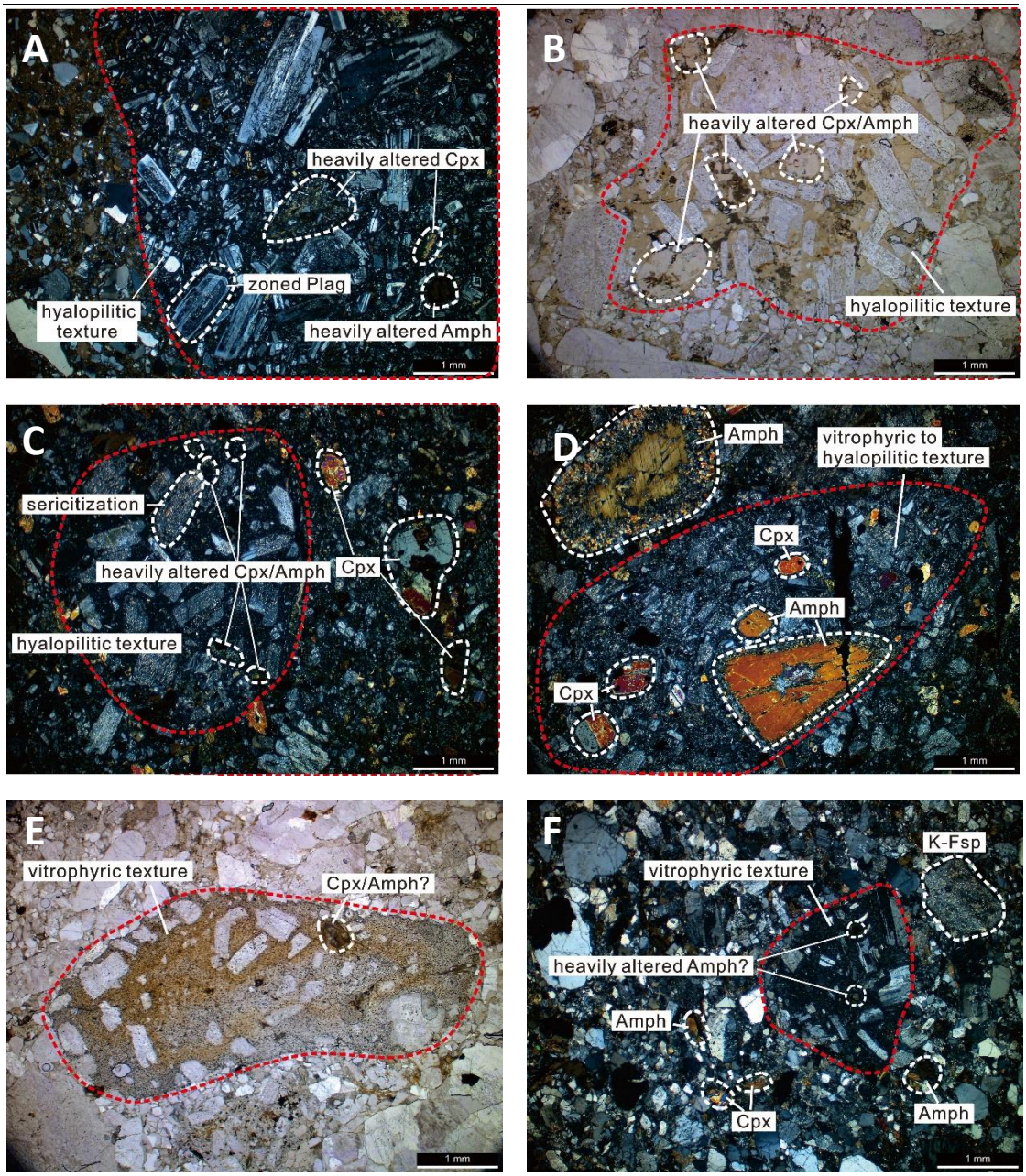

Figure 4.9 Microscopic images of Champsaur sandstones, Méollion in central SE France. (A) Large andesitic lithic with typical hyalopilitic texture, containing heavily altered clinopyroxenes and amphiboles, zoned plagioclase also present (CL19-018, XPL). (B) Andesitic lithic with hyalopilitic texture, containing heavily altered clinopyroxenes and amphiboles, unable to recognize original grain type (CL19-029, PPL). (C) Andesitic lithic with hyalopilitic texture, containing heavily altered clinopyroxenes and amphiboles, common sericitization for plagioclase, isolated clinopyroxene crystals preserved better than those inside andesitic lithic (CL19-039, XPL). (D) Large andesitic lithic with vitrophyric to hyalopilitic texture contains partially altered ferromagnesian minerals, especially a large amphibole crystal with its core totally replaced by silicic material, top left is another isolated amphibole crystal with its periphery altered to silicic materials and small aggregates of ferromagnesian minerals (CL19-039, XPL). (E) Large andesitic lithic with vitrophyric texture, of which most ferromagnesian minerals totally

disappear, only one piece of remain left with vague appearance (CL19-029, PPL). (F) Andesitic lithic with vitrophyric texture containing heavily altered amphibole, isolated recognizable ferromagnesian minerals and heavy sericitization of potassium feldspar (CL19-041, XPL). (Abbreviation: Cpx-clinopyroxene, Amph-amphibole, Plag-plagioclase, Qtz-quartz, K-Fsp-potassium feldspar)

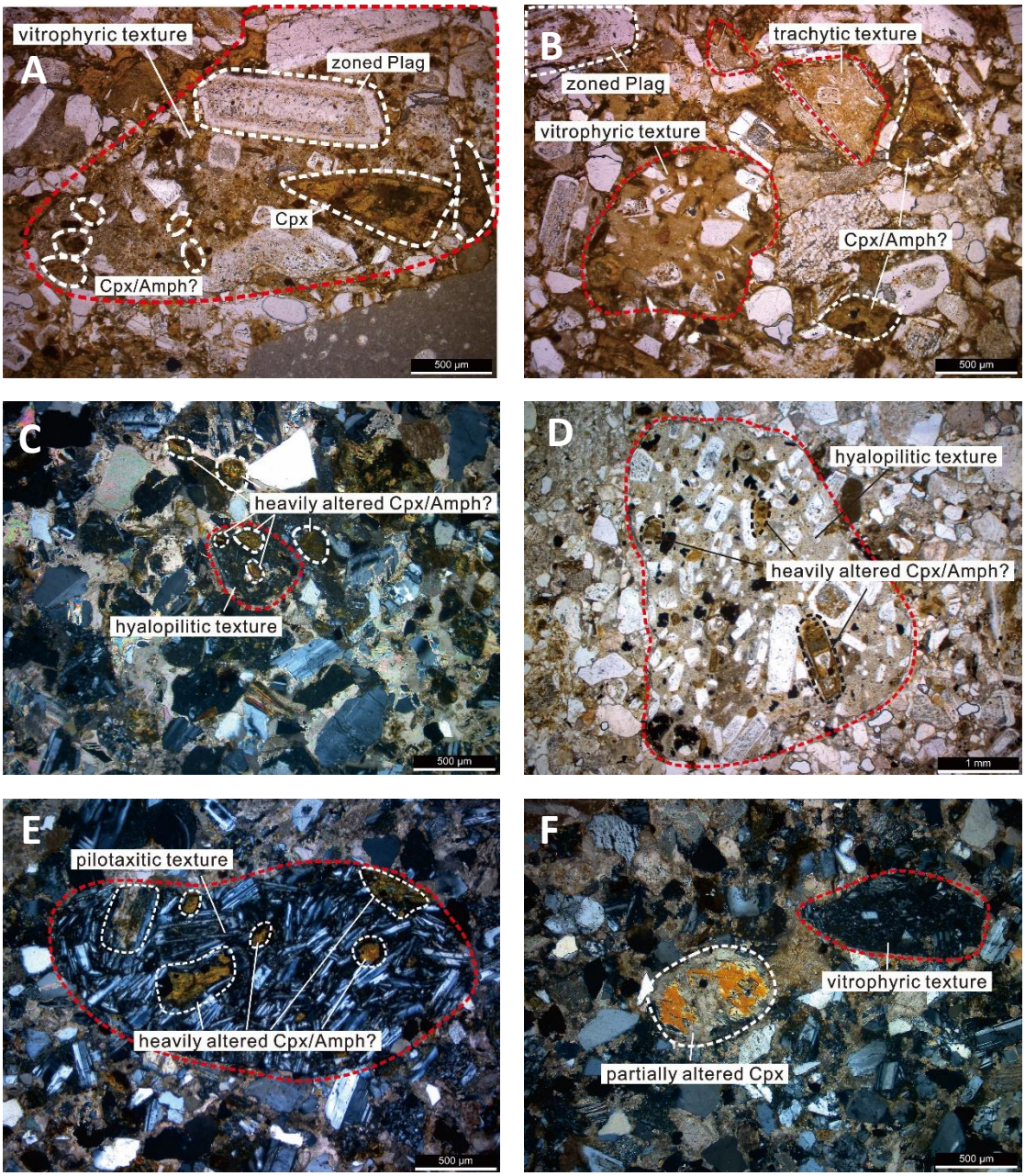

Figure 4.10 Microscopic images of Taveyannaz sandstones in Clumanc, Barrême. (A) Large andesitic lithic with vitrophyric texture, containing heavily altered clinopyroxenes and amphiboles, zoned plagioclase also present (DB19-047, PPL). (B) Andesitic lithics with vitrophyric texture and trachytic texture, containing heavily altered clinopyroxenes and amphiboles, unable to recognize original grain type (DB19-047, PPL). (C) Andesitic lithic with hyalopilitic texture, containing heavily altered clinopyroxenes and amphiboles, heavy calcitisation replacing plagioclase, matrix of sandstone (DB19-051, XPL). (D) Large andesitic lithic with

hyalopilitic texture containing abundant heavily altered yellowish iron-rich pseudomorphs of ferromagnesian minerals and opaque minerals produced by alteration of amphiboles or biotite (DB19-053, PPL). (E) Large andesitic lithic with uncommon pilotaxitic texture, of which ferromagnesian minerals totally disappear, replaced by secondary clay minerals, plagioclase replaced by calcite at top left of the lithic (DB19-053, XPL). (F) Andesitic lithic with vitrophyric texture containing heavily altered ferromagnesian minerals, isolated partially altered clinopyroxene which is rarely present in this region; most are heavily altered (DB19-053, XPL).

Chapter 5: Whole Rock Geochemistry of Andesitic Clasts

5.1 Introduction

This chapter presents the whole rock major and trace element results of the andesitic clasts incorporated in the conglomerate/breccia beds and tuffs from Flaine, Champsaur, Clumanc, Saint Antonin and La Vanade regions, and of the dykes and lava flow deposits from Agay and Biella regions. The purpose of conducting whole-rock geochemistry is to characterise the regional differences and differentiate volcanic detritus of various regions along the Alpine arc, ultimately trying to build the link between source and sink. The andesitic clasts in sandstones are mixed with other reworked igneous material, limiting the potential for geochemical study of the Taveyannaz volcanism. Therefore, to better characterise the source of the andesitic magma, only on pure andesitic clasts were investigated. Major elements wt. % concentrations have been recalculated to 100% on a volatile-free basis. Analytical procedures and related analytical uncertainties are described and discussed in Appendix A.1. All major and trace element data are provided in Appendix E2.

Before conducting any geochemical interpretation, the first step is to evaluate the effects of secondary alteration and element mobility on the whole rock geochemical results. This can be done by plotting each element potentially subject to alteration against an element known to be immobile during alteration (e.g., Zr), along with a consideration of loss on ignition (LOI) values and petrographic observations. Then the TAS diagram, Zr/Ti vs Nb/Y diagram and Th-Co discrimination diagram will be used to classify samples according to their rock type. The major and trace elements are also plotted against a fractionation index (i.e., SiO_2), along with primitive mantle-normalised multielement diagram, chondrite-normalised REE pattern and key trace element ratios to interpret the magmatic evolution and petrogenetic affinity of distinct volcanic sources.

5.2 Secondary alteration and element mobility

In Chapter 4, petrographic study shows that the sampled igneous rocks of this study have undergone variable degrees of alteration, with most samples

showing at least some signs of alteration. The loss on ignition (LOI) values of the samples mostly range between 0.5 and 5.0 wt.% with an average of 2.8 wt.% (n = 38) but can be up to ~ 10 wt.% in one sample with extensive calcareous alteration. Alteration processes can derive from early hydrothermal alteration, weathering, diagenesis, and metamorphism, all of which can ultimately modify the whole rock composition. Thus, it is essential to evaluate the effects of secondary alteration and element mobility on major and trace elements before using the data to differentiate magmatic affinities.

Many elements, in particular Large-Ion Lithophile Elements (LILEs) such as K, Ba, Rb, Pb and Sr, may become mobile during sub-solidus alteration in the presence of fluids (Pearce, 1996). Problematically for the study of altered igneous rocks, these elements are also incorporated in subduction-related fluids and are commonly used to trace slab components in fresh, unaltered samples. In contrast, the most immobile elements generally do not go into solution during alteration and can be used reliably in fresh and altered igneous rocks. These elements include the majority of Rare Earth Element (REE) and High Field Strength Elements (HFSE) (Arculus, 1987; Hastie et al., 2007). However, while Pearce (1996) suggested that these elements remain immobile until reaching amphibolite-granulite facies conditions, other studies suggest that secondary remobilisation of these elements can occur at lower pressures and temperatures, in particular when exposed to carbonate-, hydrogen sulphide- or halide-bearing fluids (e.g., Giere, 1993).

The assessment of element mobility is commonly conducted by plotting each studied element against element Zr, which is regarded as one of the most immobile and incompatible elements during secondary alteration and magma differentiation (Cann, 1970; Pearce, 1996). For rocks derived from the uniform or cogenetic mantle sources, the immobile elements are assumed to show a clear linear correlation between each element and element Zr, whereas those elements which have been mobilised are prone to have a more scattered pattern. Scattered patterns could also be observed for the immobile elements against Zr due to the heterogeneous mantle source region and variable amounts of crustal contamination rather than secondary alteration (Pearce, 1996).

Table 5.1 R^2 values for correlation of elements against Zr for samples from Champsaur, Clumanc, St. Antonin, La Vanade and Biella regions. Red indicates good correlation with R^2 value of > 0.7 and blue indicates moderate correlation with R^2 value of between 0.4 - 0.7.

Element	Champsaur (n=8)	Clumanc (n=7)	St. Antonin (n=6)	La Vanade (n=5)	Biella (n=8)
SiO_2	0.43	0.05	0.13	0.70	0.69
TiO_2	0.13	0.28	0.37	0.83	0.56
Al_2O_3	0.32	0.08	0.52	0.18	0.10
Fe_2O_3	0.04	0.11	0.02	0.86	0.00
MnO	0.00	0.20	0.01	0.91	0.03
MgO	0.02	0.06	0.06	0.93	0.72
CaO	0.17	0.04	0.42	0.64	0.08
Na_2O	0.00	0.23	0.00	0.68	0.35
K_2O	0.00	0.42	0.20	0.31	0.14
P_2O_5	0.10	0.06	0.37	0.24	0.49
Sc	0.11	0.00	0.53	0.83	0.19
V	0.00	0.11	0.06	0.62	0.15
Cr	0.13	0.12	0.79	0.30	0.46
Co	0.00	0.33	0.19	0.02	0.52
Ni	0.06	0.29	0.22	0.02	0.54
Zn	0.47	0.35	0.02	0.20	0.12
Ga	0.00	0.16	0.21	0.26	0.83
Rb	0.01	0.11	0.00	0.22	0.03
Sr	0.15	0.02	0.67	0.13	0.65
Y	0.34	0.82	0.72	0.00	0.88
Nb	0.81	0.54	0.96	0.54	0.92
Cs	0.17	0.00	0.01	0.27	0.46
Ba	0.30	0.10	0.47	0.10	0.11
La	0.13	0.86	0.76	0.89	0.82
Ce	0.16	0.87	0.85	0.87	0.87
Pr	0.14	0.87	0.88	0.83	0.89
Nd	0.09	0.85	0.92	0.62	0.91
Sm	0.06	0.82	0.95	0.09	0.87
Eu	0.01	0.46	0.88	0.19	0.86
Gd	0.06	0.81	0.96	0.06	0.90
Tb	0.19	0.85	0.96	0.02	0.91
Dy	0.42	0.84	0.96	0.00	0.91
Ho	0.51	0.88	0.96	0.00	0.90
Er	0.67	0.86	0.98	0.01	0.90
Tm	0.73	0.85	0.96	0.04	0.87
Yb	0.80	0.83	0.87	0.00	0.86
Lu	0.74	0.84	0.84	0.03	0.89
Hf	0.96	0.98	0.87	0.84	0.93

Ta	0.54	0.43	0.60	0.60	0.70
Pb	0.00	0.00	0.03	0.11	0.01
Th	0.07	0.49	0.00	0.21	0.32
U	0.06	0.50	0.06	0.49	0.02

Because more accurate correlation trends can develop in larger datasets (and not be a reflection of the degree of alteration), caution is required when using a correlation approach with a small dataset. However, considering the relatively limited number of data available in this study, any regions with more than 5 samples were used for correlation against Zr to assess element mobility. Therefore, Flaine (n=1) and Agay (n=2) regions were excluded from element mobility examination. Instead, the petrography was used to correlate the observed mineral assemblage with similar samples to assess the degree of alteration. In order to quantify the correlation between each element and element Zr, binary diagrams of Zr against elements were established for the other five regions (Champsaur, Clumanc, St. Antonin, La Vanade, Biella), and the R^2 correlation values were compiled in Table 5.1. As the magmatic/genetic relationship between these igneous suites of different regions is not clear, the Zr correlations for Champsaur, Clumanc, St. Antonin, La Vanade, and Biella were calculated individually. In this study, R^2 values > 0.7 are interpreted as reflecting a good correlation, those between 0.4 - 0.7 representing a moderate correlation, and those < 0.4 indicating a poor correlation.

5.2.1 Results

Petrographic observations indicate various amounts of secondary alteration on these igneous rocks of all regions, mainly including calcite and chlorite alteration. In addition, LOI values range from 0.3 - 10.9 wt. %, with an average of 2.8 wt. % (n = 38), indicating that some of these rocks have been affected by alteration. All regions have relatively wide range of Zr values from 100 - 250 ppm, except for those from La Vanade, ranging between 86 - 134 ppm. As a result, these samples tend to be clustered on the binary diagrams and may not give reliable R^2 values.

The samples in Champsaur region have LOI values ranging from 0.7 to 10.9 wt. % and show common calcite and chlorite alteration replacing volcanogenic matrix, feldspar and ferro-magnesian minerals in thin section. They show good correlations of Zr with Nb, Tm, Yb, Lu and Hf, moderate correlations with SiO_2, Zn, Dy, Ho, Er and Ta, and poor correlations with the remaining major and

trace elements (Table 5.1, Figure 5.1). Theoretically, the REEs should behave uniformly and show similar amounts of remobilisation during secondary alterations. Therefore, the correlation between Zr and REEs should be consistent with similar R^2 values. However, the R^2 values of Zr against LREEs are surprisingly lower than expected with most of them < 0.2, whereas the R^2 values of Zr against HREEs are as expected with values generally > 0.5. This anomaly could be explained by the presence of more than one magmatic suite. In other words, the igneous samples in Champsaur region are not genetically linked and derive from different magmatic sources. As for typical mobile elements (e.g., Rb, Sr, Ba, Cs), most of them have low correlations with Zr (< 0.15) except for Ba (0.3) with an abnormal value, which also could be due to the mixing of igneous samples from different magmatic sources.

The samples in Clumanc region have LOI values ranging from 3.1 to 6.1 wt. % and show common calcite and heavy chlorite alteration replacing volcanogenic matrix and ferro-magnesian minerals in thin section. It shows good correlations of Zr with Y, La, Ce, Pr, Nd, Sm, Gd, Tb, Dy, Ho, Er, Tm, Yb, Lu and Hf, moderate correlations with K_2O, Nb, Eu, Ta, Th and U, and poor correlations with the remaining major and trace elements (Table 5.1, Figure 5.1). The correlation results of this region are of typical characterisation with most immobile elements (e.g., REEs, Y, Hf) having good correlations with

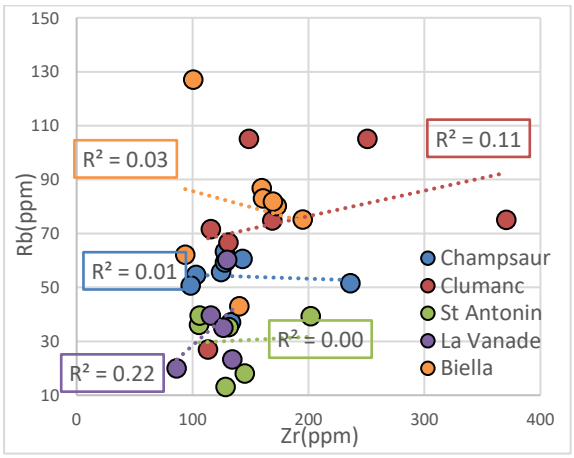

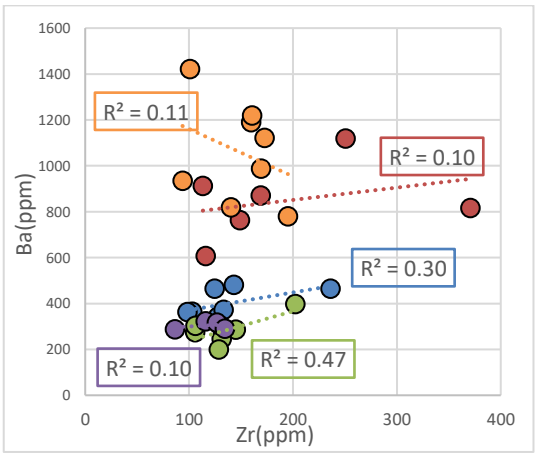

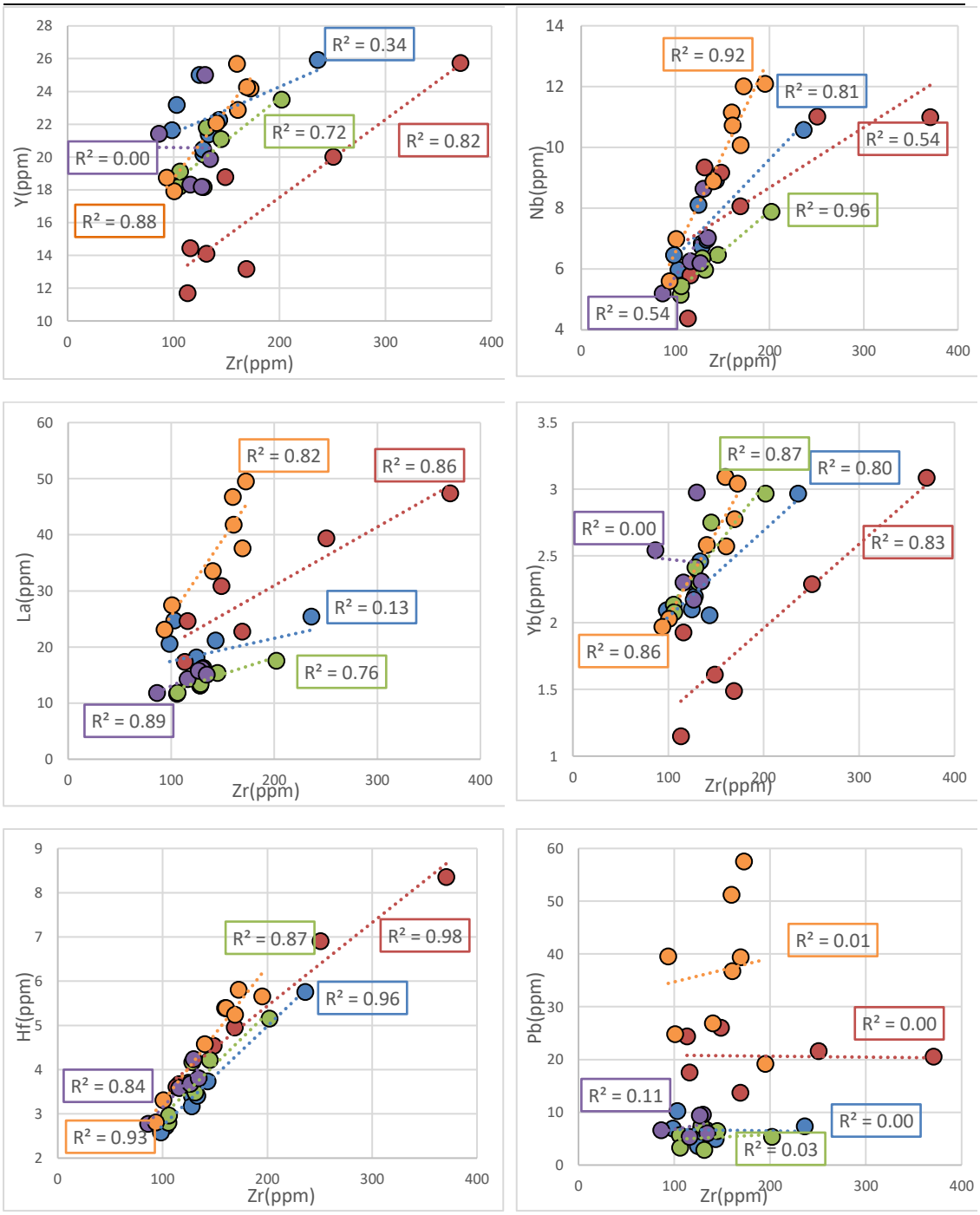

Figure 5.1 Binary diagrams of representative elements against element Zr of igneous samples from Champsaur, Clumanc, St. Antonin, La Vanade and Biella regions.

Zr (> 0.8), and with most mobile elements (e.g., Rb, Sr, Cs, Ba) having poor correlations with Zr (< 0.1). The relative lower correlation of Eu (0.46) is consistent with the variable Eu anomalies related to feldspar fractionation.

The samples in St. Antonin region have LOI values ranging from 0.5 to 2.1 wt. % and show common chlorite alteration replacing volcanogenic matrix and

ferro-magnesian minerals in thin section. It shows good correlations of Zr with Cr, Y, Nb, La, Ce, Pr, Nd, Sm, Eu, Gd, Tb, Dy, Ho, Er, Tm, Yb, Lu and Hf, moderate correlations with Al_2O_3, CaO, Sc, Sr, Ba and Ta, and poor correlations with remaining major and trace elements (Table 5.1, Figure 5.1). In general, the correlation results in the region are similar to those in Clumanc of typical characterisation. The point worth of noticing is the abnormal higher values of Ba and Sr correlation with Zr. This could be explained by the limited number of samples, causing the results less reliable.

The samples in La Vanade region have LOI values ranging from 0.3 to 2.6 wt. % and show general lower degree of alteration based on petrographic study compared with other regions. It shows good correlations of Zr with SiO_2, TiO_2, Fe_2O_3, MnO, MgO, Sc, La, Ce, Pr and Hf, moderate correlations with CaO, Na_2O, V, Nd, Ta and U, and poor correlations with remaining major and trace elements (Table 5.1, Figure 5.1). The correlation results of this region are just opposite to the typical one, with many mobile major elements of high values (> 0.7) and many immobile elements of low values (< 0.1). The good correlations between major elements and Zr correspond to less alteration and fresher petrographic appearance of samples in this region. These anomalous poor correlation values of immobile elements with Zr are likely related to the narrow range of analysed Zr and limited number of samples in this region, which possibly controls clustering effects.

The samples in Biella region have LOI values ranging from 0.3 to 5.1 wt. % and show common calcite and heavy chlorite alteration replacing volcanogenic matrix, feldspar and ferro-magnesian minerals in thin section. It shows good correlations of Zr with MgO, Ga, Y, Nb, La, Ce, Pr, Nd, Sm, Eu, Gd, Tb, Dy, Ho, Er, Tm, Yb, Lu, Hf and Ta, moderate correlations with SiO_2, P_2O_5, Cr, Co, Ni, Sr, and Cs, and poor correlations with remaining major and trace elements (Table 5.1, Figure 5.1). The correlation results of this region are of typical characterisation with most immobile elements (e.g., REEs, Y, Nb, Hf, Ta) having good correlations with Zr (> 0.8), and with most mobile elements (e.g., Rb, Ba) more scattered of poor correlations with Zr (< 0.1).

5.2.2 Summary of alteration patterns

In summary, the variable correlations between elements and Zr within these five regions reflect the various degree of alteration and element mobility,

consistent with petrographic results discussed in Chapter 4. Generally, trace elements traditionally considered to be immobile (e.g., REEs, HFSE) show significantly better correlations than those trace elements which are known to be mobile (e.g., Ba, Rb, and Sr) and major elements (e.g., Na, K, Ca) (Hofmann and White, 1983; Hastie et al., 2007). While correlations between immobile elements and Zr can be poor as illustrated in Champsaur and La Vanade regions, several factors, including narrow Zr ranges, slight differences in petrogenetic processes and heterogeneous magmatic sources, can lead to this rather than sub-solidus element remobilisation. Overall, the REEs and HFSE of samples in this study have not been significantly mobilised during secondary alteration and can provide reliable dataset for further geochemical study. On the contrary, mobile trace elements (e.g., LILE, Pb, U) and most major elements (e.g., Na, K, Ca) should be avoided or corrected prior to cautious utilisation due to their significant remobilisation during alteration processes.

5.3 Rock type classification

Major and trace elements were used to classify the igneous clasts in terms of their rock types. Both the total alkali silica (TAS) diagram (Le Maitre et al., 2005) and Zr/Ti vs Nb/Y diagram (Winchester and Floyd, 1977) were used for each of the regions. However, as discussed above, due to the potential remobilisation of the TAS elements within these rocks, in particular Na_2O and K_2O, samples which have LOI values > 3 wt. % are plotted separately from those of < 3 wt. % of each group. One would expect that those of higher LOI values are supposed to contain higher concentrations of Na_2O and K_2O due to Na^+ and K^+ replacing other cations during alteration. Therefore, the Zr/Ti vs Nb/Y diagram which utilises immobile elements is likely to give more accurate results for classifying the rocks than the TAS diagram, as originally discussed by Winchester and Floyd (1977). The comparison of results between these two classification schemes can provide an insight of the influence of alteration on the original concentrations of silica and alkalis as well as the reliability of the TAS classification scheme. The Co-Th diagram (Hastie et al., 2007) was also used to act as an immobile element equivalent for the Peccerillo and Taylor (1976) K_2O-SiO_2 diagram that was used to classify volcanic arc lavas given the samples in this study are very likely of volcanic arc origin.

On the TAS diagram (Figure 5.2 A), samples of LOI < 3 wt. % generally plot within the basaltic andesite and andesite fields, with only a few falling in the basalt, basaltic trachyandesite, trachyandesite, dacite and rhyolite fields. Samples with LOI > 3 wt. % mostly plot within the alkaline series, including trachybasalt, basaltic trachyandesite and trachyandesite.

On the Zr/Ti vs Nb/Y diagram (Figure 5.2 B), most samples plot in a cluster in the andesite field, with few exceptions falling in the dacite, basaltic andesite fields. Only two samples from Agay region plot within the alkali field.

In order to evaluate the effectiveness of Zr/Ti ratio as a differentiation index and check how much Zr/Ti ratio has been affected by Fe-Ti oxide accumulation or zircon source composition and fractionation during magma evolution, the Zr/Ti vs SiO_2 diagram was plotted as well. The linear regression line shows a moderate correlation between Zr/Ti and SiO_2 with R^2 value of 0.35 (Figure 5.3).

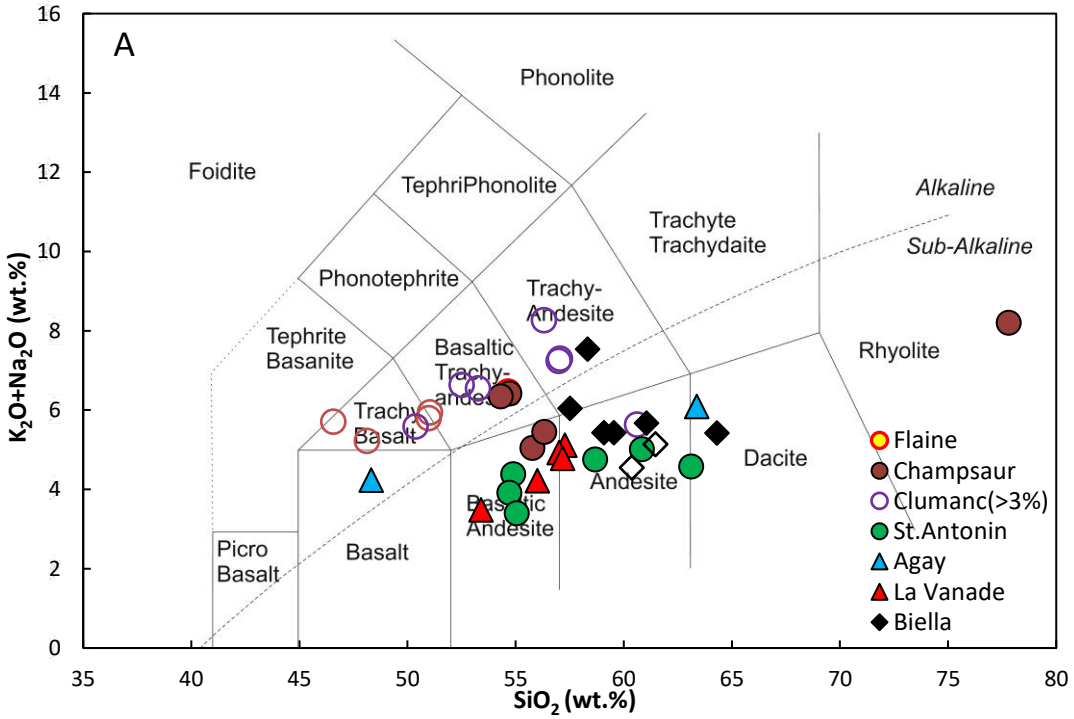

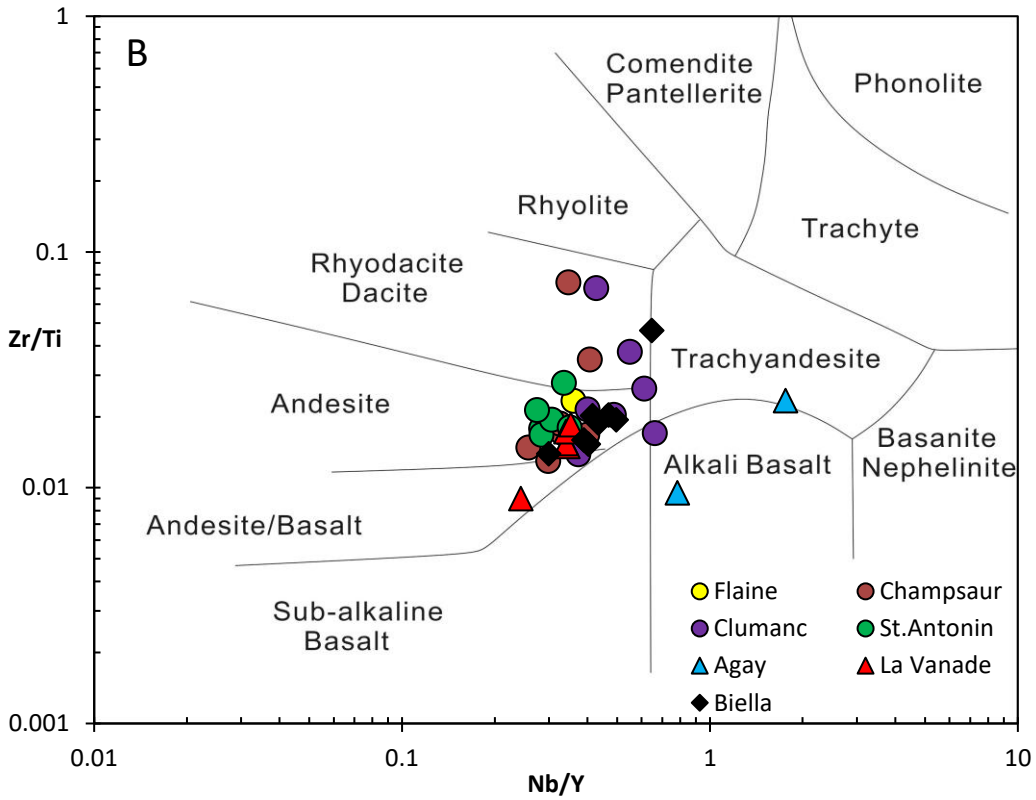

Figure 5.2 A) Total alkali silica classification diagram (Le Maitre et al., 2005). Hollows represent samples of LOI values > 3 wt. %. Solids represent samples of LOI values < 3 wt. %; B) Zr/Ti vs Nb/Y classification diagram (Winchester and Floyd, 1977) for the igneous samples in all regions.

On the Co-Th diagram (Figure 5.4), most samples plot in the basaltic andesite and andesite fields with few falling in the dacite/rhyolite field. Those from Clumanc and Biella regions generally contain higher amount of Th, plotting in the high-K calc-alkaline field, whereas those from Champsaur, St. Antonin and La Vanade mostly contain less Th, falling in the calc-alkaline field.

In the Champsaur region, samples with high LOI values (> 3 %) generally have lower SiO_2 content and higher Na_2O+K_2O content, thus plotting within the trachybasalt field on the TAS diagram. However, when these samples are plotted on the Zr/Ti vs Nb/Y diagram, they all fall in the andesite field. The contrasting results clearly illustrated the significant impact of alteration on TAS elements. In this study, the alteration processes increased the content of Na_2O and K_2O due to possibly increased concentration in the newly-formed clays, and reduced the content of SiO_2 due to decomposition of silicates and leaching. One sample (CL19-020) plotted in the rhyolite field on the TAS diagram falls in the rhyodacite field on the Zr/Ti vs Nb/Yb diagram, consistent

with expected disparity between these two differentiation indices (i.e., SiO_2 and Zr/Ti) (Figure 5.3).

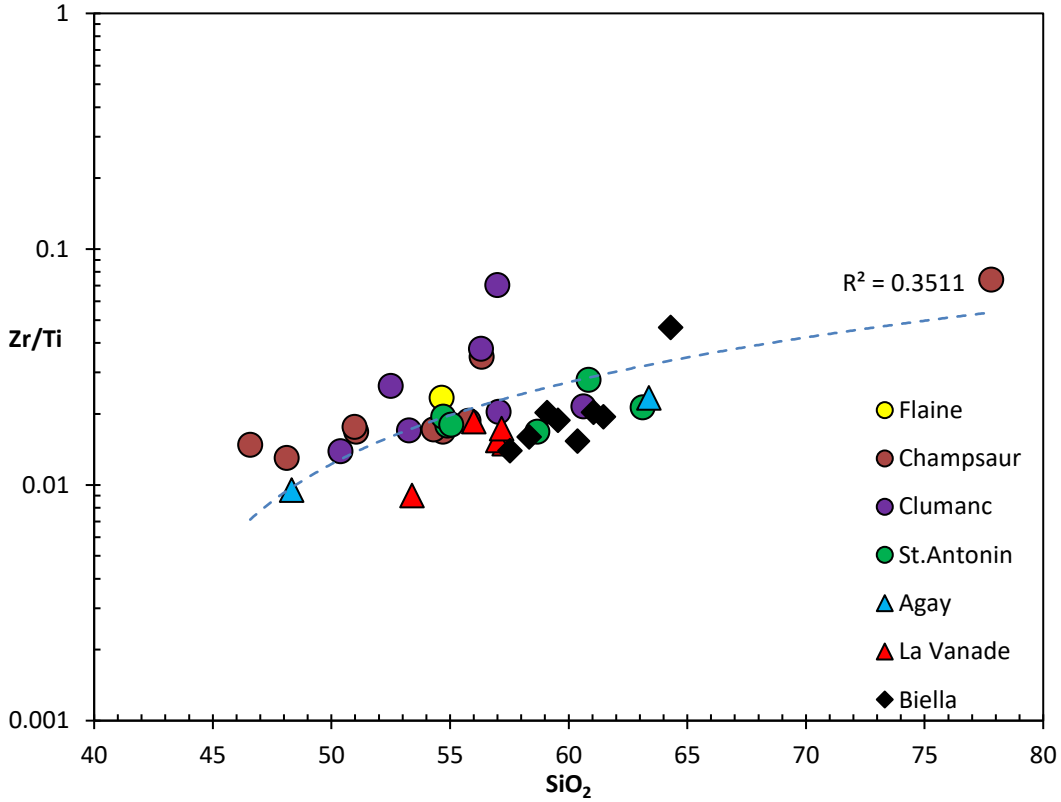

Figure 5.3 Zr/Ti vs SiO_2 diagram and related linear regression line with R^2 value.

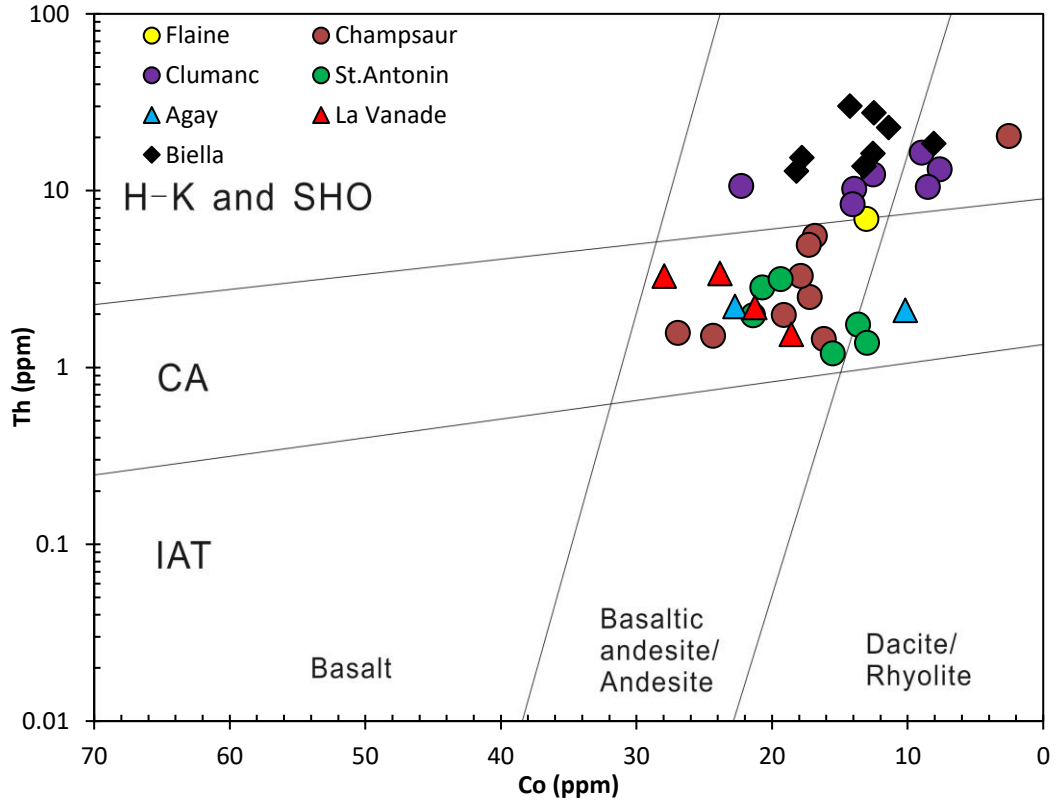

Figure 5.4 Th-Co discrimination diagram (Hastie et al., 2007) for the igneous samples from all regions. IAT = Island arc tholeiite, CA = Calc-alkaline, H-K = High-K calc alkaline, SHO = shoshonitic.

In the Clumanc region, all samples have > 3 wt. % LOI value and plot in the alkaline field (i.e., trachybasalt, basaltic trachyandesite and trachyandesite) on the TAS diagram except one sample (DB19-055A) in the andesite field, whereas on the Zr/Ti vs Nb/Yb diagram, all samples fall in the subalkaline field (i.e., andesite, dacite, rhyodacite), with one exception falling close to the alkaline and subalkaline boundary. Among all regions, samples in Clumanc are generally more alkaline and plot closer to the boundary in both the TAS and Zr/Ti vs Nb/Yb diagrams.

In the St. Antonin region, all samples have LOI values less than 3 wt. % and all plot in the subalkaline field (i.e., basaltic andesite and andesite) on the TAS diagram. On the Zr/Ti vs Nb/Yb diagram, all samples show a consistent pattern with TAS diagram due to the low LOI value, all falling in the subalkaline field, in particular andesite field. The only difference is that the samples on the Zr/Ti vs Nb/Yb diagram appear to shift slightly towards the more evolved direction (i.e., rhyolite). This could be explained by the discrepancy between the two differentiation indices. One possible reason could be the decrease of SiO_2 content during alteration; another could be the fractionation of Zr during magma evolution.

In the La Vanade region, all samples have LOI values < 3 wt. %, and thus are supposed to give consistent results based on the two diagrams as discussed above. On the TAS diagram, two samples plot in the basaltic andesite field, three plotting on the basaltic andesite and andesite boundary. On the Zr/Ti vs Nb/Yb diagram, four samples plot in the andesite field, with one in the basaltic andesite field. Therefore, similar patterns have been plotted on both diagrams as expected, further demonstrating that for fresh samples with low LOI values, both classification diagrams can give consistent results.

In the Biella region, all samples plot in the subalkaline field (i.e., andesite and dacite) except one falling in the trachyandesite field on the TAS diagram. It should be noted that two samples of LOI values > 3 wt. % do not fall in the alkaline field, on the contrary, they have the lowest total alkali content among this group of samples. On the Zr/Ti vs Nb/Yb diagram, all samples plot in the

andesite field, consistent with the results of TAS diagram, with only one sample falling on the boundary between dacite and trachyandesite.

5.4 Major elements

In this section, multiple major elements vs SiO_2 diagrams are presented individually for samples from each region (Figure 5.5), plotted with datasets from previously published studies (data after Ruffini et al., 1997; Jourdan et al., 2012; Bergomi et al., 2015; Lustrino et al., 2017). As previously discussed, these igneous clasts are variously altered, so relatively mobile major elements (e.g., K_2O, Na_2O) are supposed to be more scattered and may not be as valuable as immobile elements (e.g., TiO_2, Al_2O_3, MgO). Therefore, much of the discussion is focussed on TiO_2, Al_2O_3, CaO, MgO and Fe_2O_3*, which are more likely to reflect the geochemical and petrogenetic characteristics of samples in each region.

A regional negative correlation trend is shown by all samples presented on TiO_2, Al_2O_3, CaO, MgO and Fe_2O_3* vs SiO_2 diagrams, with the more consistent trends shown by Al_2O_3 and CaO. On the K_2O/Na_2O vs SiO_2 diagrams, samples are more scattered without a clear trend due to the remobilisation of mobile elements during alteration processes.

In the Champsaur region, samples have a range of SiO_2 content from 46.6 to 56.3 wt. %, except one rhyolite sample with high SiO_2 content of 77.8 wt. %. TiO_2, Al_2O_3, Fe_2O_3*, MgO and CaO contents range between 0.09 - 0.84 wt. %, 12.09 - 21.58 wt. %, 1.19 - 8.75 wt. %, 0.27 - 4.45 wt. % and 0.33 - 19.19 wt. %, respectively. Generally, samples in this region are less evolved with lower SiO_2 content, plotting on the top left of the diagrams. With increasing SiO_2, TiO_2, Al_2O_3, MgO and CaO contents are decreasing accordingly. However, Fe_2O_3* vs SiO_2 diagram does not show any clear trend, probably due to the limited amount of Fe-oxide fractionation which have not led to the rapid loss of iron in the magma.

In the Clumanc region, SiO_2 content of these samples ranges from 50.4 to 60.6 wt. %, slightly more evolved than Champsaur samples. TiO_2, Al_2O_3, Fe_2O_3*, MgO and CaO contents range between 0.54 - 0.80 wt. %, 17.68 - 21.52 wt. %, 3.45 - 13.51 wt. %, 0.81 - 3.92 wt. % and 5.03 - 10.21 wt. %, respectively. With increasing SiO_2, samples in this region show strongly decreasing Fe_2O_3 and

MgO values, indicating the fast fractionation of ferromagnesian minerals. CaO content is not changing along with the variation of SiO_2, showing random distribution of samples on the CaO vs SiO_2 diagram.

In the St. Antonin region, SiO_2 content of these samples ranges from 54.7 to 63.1 wt. %, slightly more evolved than the previous two regions. TiO_2, Al_2O_3, Fe_2O_3*, MgO and CaO contents range between 0.61 - 0.77 wt. %, 16.99 - 19.98 wt. %, 5.58 - 8.70 wt. %, 1.56 - 4.45 wt. % and 7.20 - 8.79 wt. %, respectively. With increasing SiO_2, samples in this region show strongly decreasing MgO values likely indicating fast fractionation of ferro-magnesian minerals. On other diagrams, samples tend to plot in cluster, in particular on the CaO diagram.

In the La Vanade region, samples have relative narrow range of SiO_2 content from 53.4 to 57.3 wt. %. TiO_2, Al_2O_3, Fe_2O_3*, MgO and CaO contents range between 0.72 - 0.99 wt. %, 18.36 - 20.73 wt. %, 7.26 - 10.38 wt. %, 2.59 - 3.54 wt. % and 7.43 - 9.03 wt. %, respectively. Generally, all samples are plotted in a cluster without showing clear trends.

In the Biella region, samples have relative higher SiO_2 content than other regions, ranging from 57.5 to 64.3 wt. %. TiO_2, Al_2O_3, Fe_2O_3*, MgO and CaO contents range between 0.43 - 0.93 wt. %, 17.37 - 18.84 wt. %, 5.03 - 8.35 wt. %, 1.19 - 4.37 wt. % and 3.97 - 6.43 wt. %, respectively. A general negative correlation is presented on TiO_2, Al_2O_3, CaO, MgO and Fe_2O_3* vs SiO_2 diagrams, with in particular MgO decreasing rapidly with increasing SiO_2. On the K_2O/Na_2O vs SiO_2 diagrams, samples are more scattered.

On the Fe_2O_3*/MgO vs SiO_2 diagram (Figure 5.5, from Arculus, 2003), most samples plot in the tholeiitic field with a relatively high FeO*/MgO ratio, except for those sample of Biella, of which most have calcalkaline affinity.

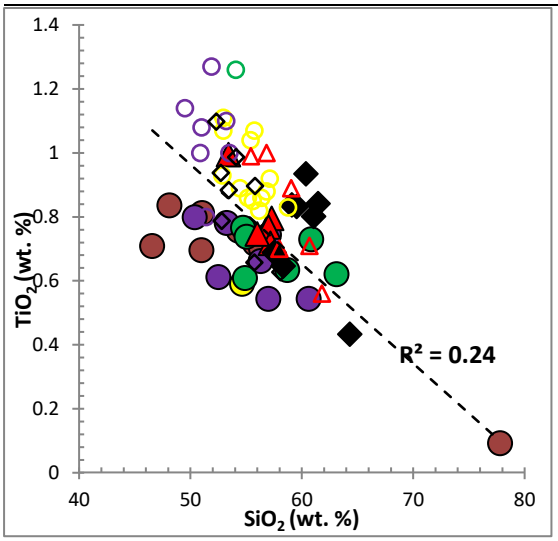
TiO2 (wt. %)
SiO2 (wt. %)
R² = 0.24

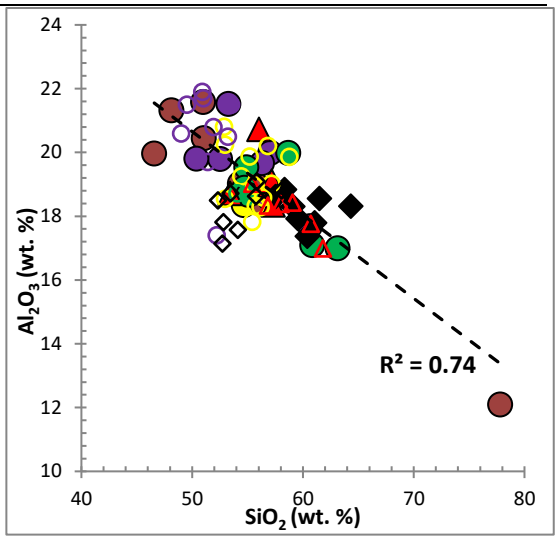
Al2O3 (wt. %)
SiO2 (wt. %)
R² = 0.74

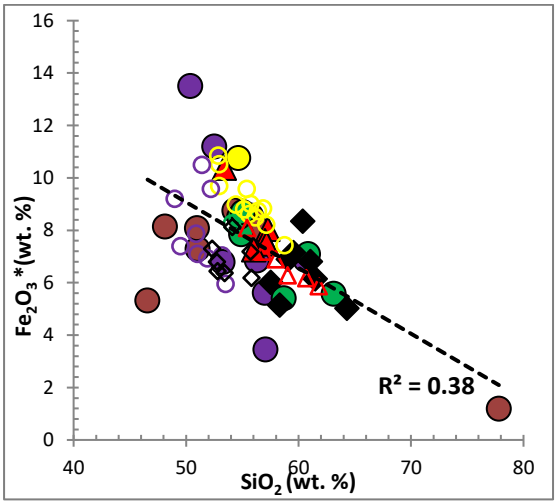
Fe2O3 *(wt. %)
SiO2 (wt. %)
R² = 0.38

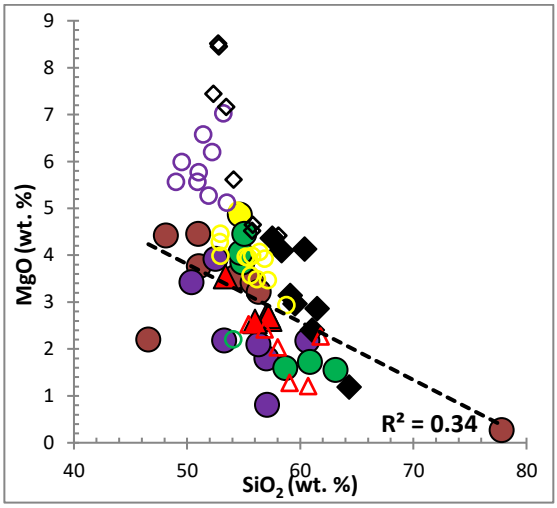
MgO (wt. %)
SiO2 (wt. %)
R² = 0.34

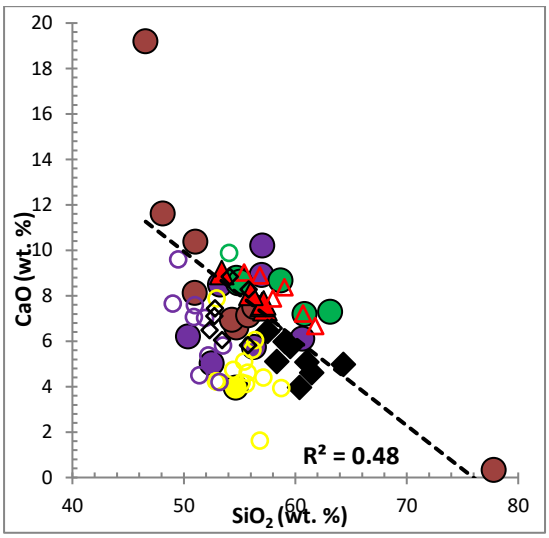
CaO (wt. %)
SiO2 (wt. %)
R² = 0.48

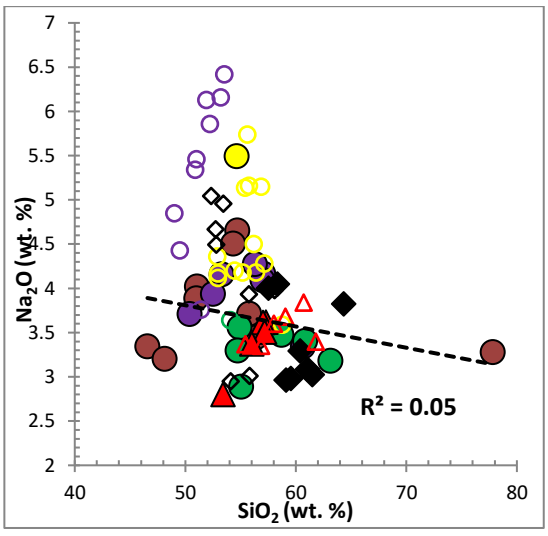
Na2O (wt. %)
SiO2 (wt. %)
R² = 0.05

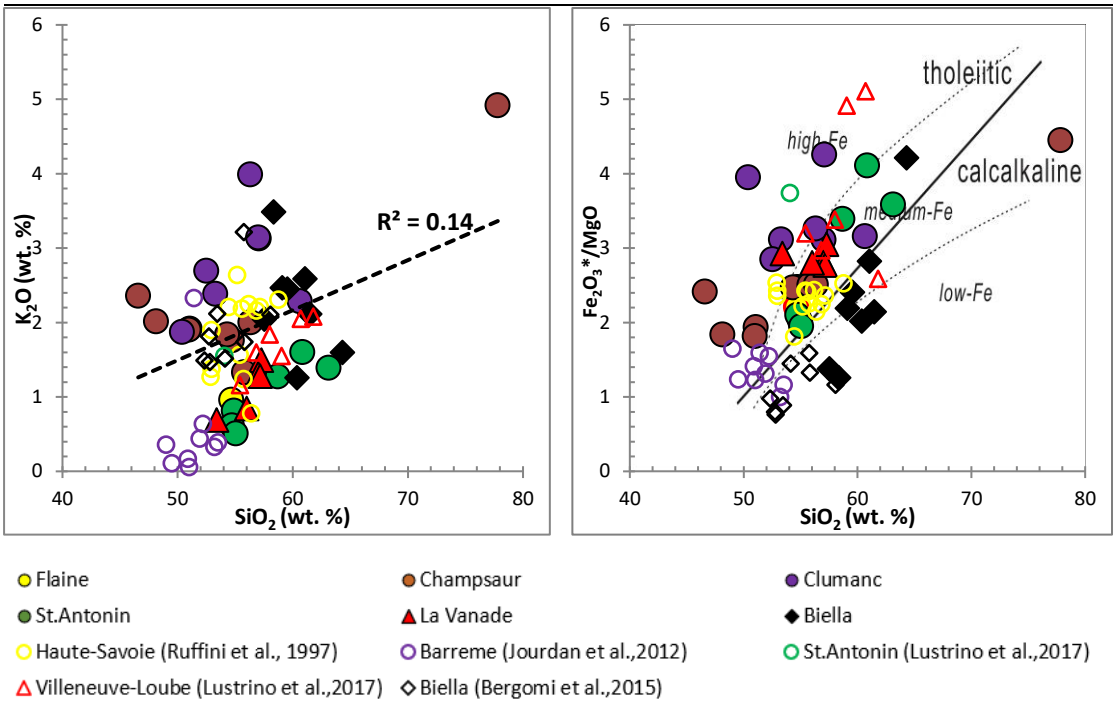

Figure 5.5 Binary diagrams of selected major elements vs SiO_2 and Fe_2O_3*/MgO vs SiO_2 diagram with discriminant boundaries from Arculus (2003) for the igneous samples from all regions.

5.5 Trace elements

In this section, the variation diagrams (Figure 5.6) are presented individually for samples from each region to show the geochemical relationships of sample between or within each region, plotted with datasets from previously published studies (data after Ruffini et al., 1997; Jourdan et al., 2012; Bergomi et al., 2015; Lustrino et al., 2017). The chondrite-normalised (McDonough and Sun, 1995) REE diagrams (Figure 5.7), primitive mantle (PM)-normalised (Sun and McDonough, 1989) multielement diagrams (Figure 5.8) and incompatible trace element ratio diagrams (Figure 5.9) are also presented to characterise and differentiate samples from each region. On the multielement diagrams, REE diagrams, and incompatible trace element ratio diagrams, geochemical data from this study will be plotted with datasets from previously published studies (Boyet et al., 2001; Callegari et al., 2004; Peccerillo and Martinotti, 2006; Conticelli et al., 2009; Jourdan et al., 2012; Bergomi et al., 2015; Lustrino et al., 2017).

5.5.1 Variation diagrams

On the variation diagrams (Figure 5.6), appreciable differences can be observed among samples from different regions, in particular for the most

incompatible elements. Most of the samples show a scattered distribution of minor and trace elements, especially those from Biella region, which generally possesses higher concentrations of trace elements, in particular HFSE.

The samples show an obvious variation on La-Th vs SiO_2 diagrams (Figure 5.6), with La concentration varying from 9.1 to 49.5 ppm, Th ranging between 1.2 - 30.1 ppm. Those from Clumanc and Biella regions distinguish themselves from the other samples in higher La and Th values, clearly separating themselves from the remaining samples of St. Antonin and La Vanade regions at the boundary of La = ~25 ppm and Th = ~7 ppm, respectively. Samples of Champsaur are kind of in between high La-Th value group and low La-Th value group.

As for Yb and Y (Figure 5.6), samples from all regions are comparatively in a cluster with little variation, Yb content ranging from 1.1 to 3.1 ppm, and Y varying between 11.7 and 25.9 ppm, both excluding one rhyolite sample, with few samples from Clumanc displaying slightly lower Yb-Y content. Those from Biella region are overlapping with other regions.

Similar patterns to La-Th are displayed on the Ta-Nb vs SiO_2 diagrams (Figure 5.6). Samples from Biella region are clearly separated from others with higher concentrations, those from Clumanc and Champsaur regions overlapping with moderate Ta-Nb concentrations. Those from St. Antonin and La Vanade are variously overlapping with each other.

The concentrations of all samples have relative low Ni and Cr values, ranging between 0.6 - 49.2 ppm and 6.6 - 46.6 ppm, respectively. The samples are generally more scattered in the Cr diagram than in the Ni diagram, overlapping with each region.

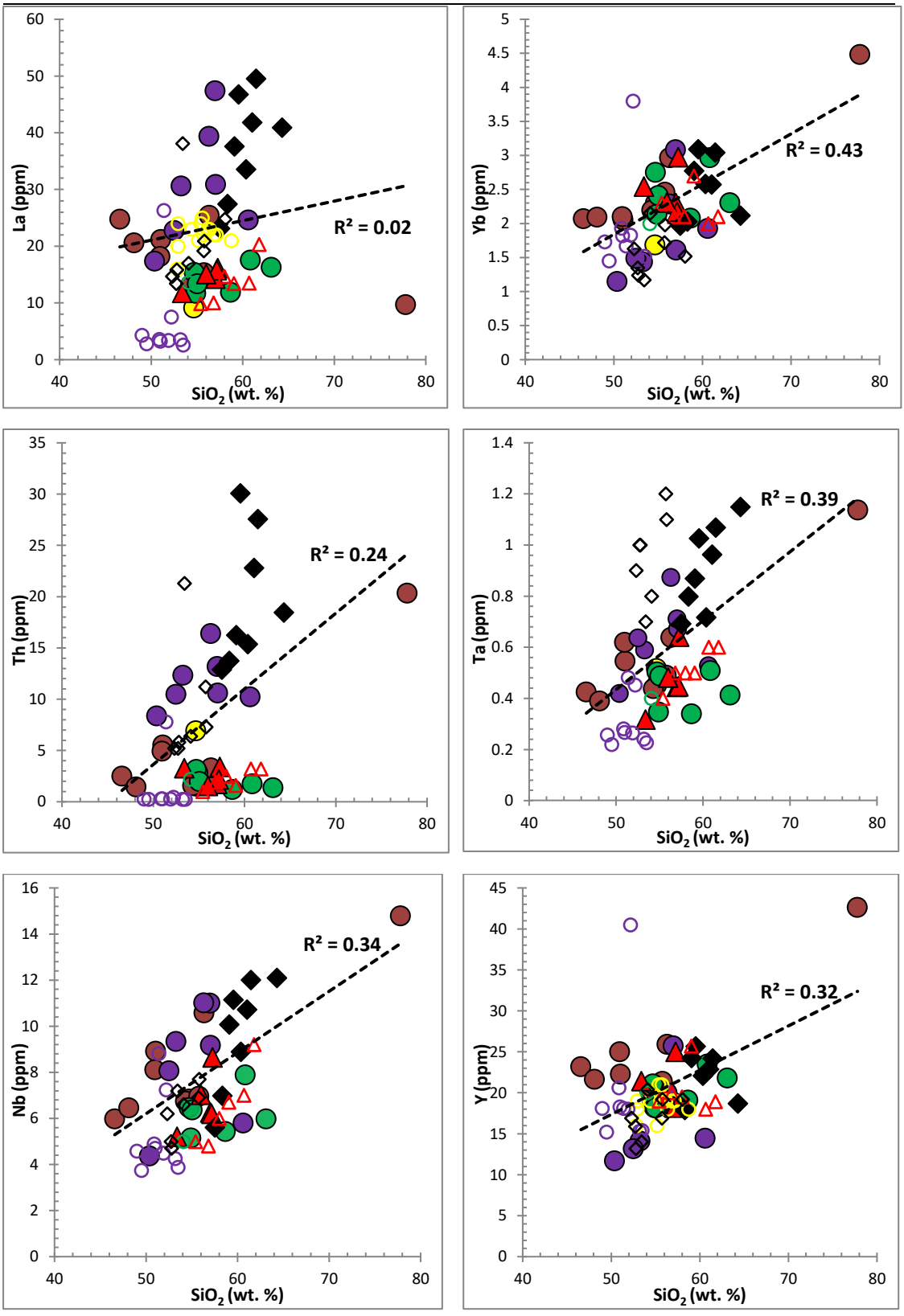
La (ppm)
SiO2 (wt. %)
R² = 0.02
Yb (ppm)
R² = 0.43
Th (ppm)
R² = 0.24
Ta (ppm)
R² = 0.39
Nb (ppm)
R² = 0.34
Y (ppm)
R² = 0.32

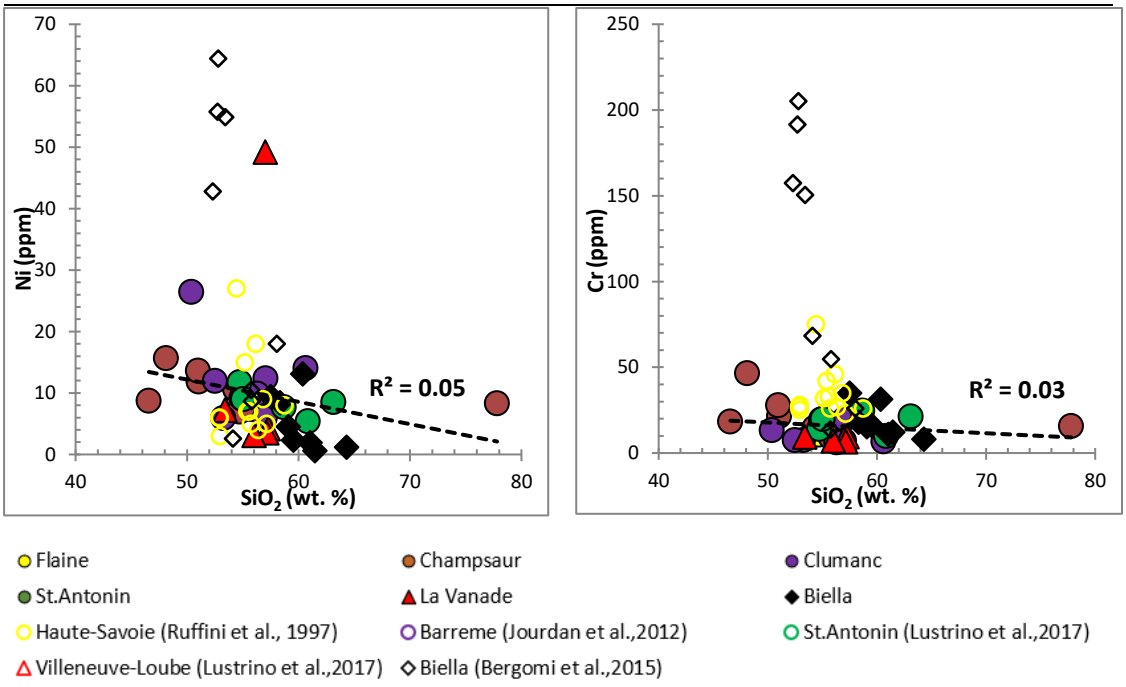

Figure 5.6 Binary diagrams of selected trace elements vs SiO_2 for the igneous samples from all regions.

5.5.2 REE patterns

On the chondrite-normalised REE diagrams, the REE patterns of samples from all regions alongside with compiled REE data of previous studies are grouped into three types (data after Boyet et al., 2001; Callegari et al., 2004; Peccerillo and Martinotti, 2006; Conticelli et al., 2009; Jourdan et al., 2012; Bergomi et al., 2015; Lustrino et al., 2017).

Type 1 corresponds to samples from Clumanc and Biella/Sesia-Lanzo regions (Figure 5.7 A, B), characterised by LREE enrichment (ΣLREE ranging from 77.3 to 202.4 ppm) over HREE (ΣHREE ranging from 5.7 to 13.6 ppm), with $(La/Yb)_N$ varying between 8.4 - 15.3, presenting the most fractionated pattern, and $(La/Gd)_N$ between 6.0 - 10.6, $(Gd/Yb)_N$ between 1.3 - 2.1, typical of enriched-LREE and flat-HREE patterns. Minor Eu anomaly presents, with Eu/Eu* varying between 0.77 - 1.27.

Type 2 is represented by samples from Flaine, St. Antonin and La Vanade/Villeneuve-Loubet regions (Figure 5.7 C, D), characterised by slight LREE enrichment (ΣLREE ranging from 56.3 to 87.8 ppm) over HREE (ΣHREE ranging from 8.9 to 13.0 ppm), with $(La/Yb)_N$ varying between 3.3 - 5.2, indicating a less fractionated pattern. $(La/Gd)_N$ and $(Gd/Yb)_N$ range between 3.0 - 4.2 and 1.0 - 1.2, respectively, reflecting a slightly enriched LREE and

extremely flat HREE pattern. No or negligible Eu anomaly presents, with Eu/Eu* varying between 0.93 - 1.06.

Type 3 includes samples from Champsaur region (Figure 5.7 E), characterised by moderate LREE enrichment (ΣLREE ranging from 67.1 to 115.0 ppm) over HREE (ΣHREE ranging from 9.7 to 12.6 ppm), with $(La/Yb)_N$ varying between 4.1 - 8.6, indicating a moderate fractionated pattern between the two previous categories. $(La/Gd)_N$ and $(Gd/Yb)_N$ range between 3.4 - 5.1 and 1.2 - 1.7, respectively, reflecting a moderate enriched LREE and flat HREE pattern. A common negative Eu anomaly presents, with Eu/Eu* varying between 0.70 - 0.91.

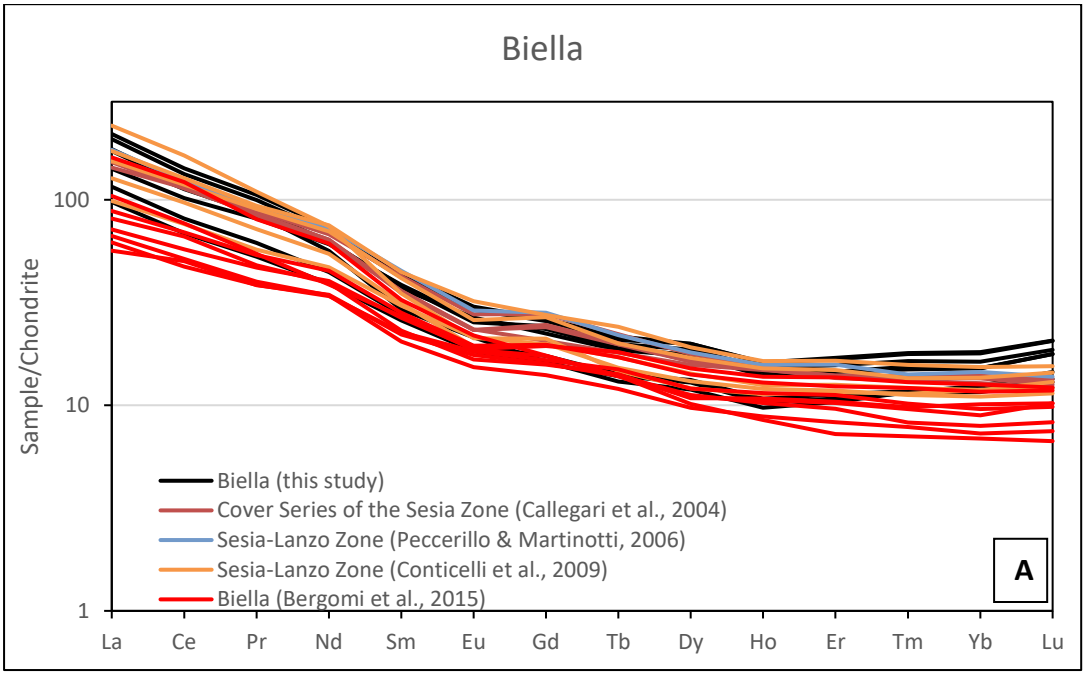

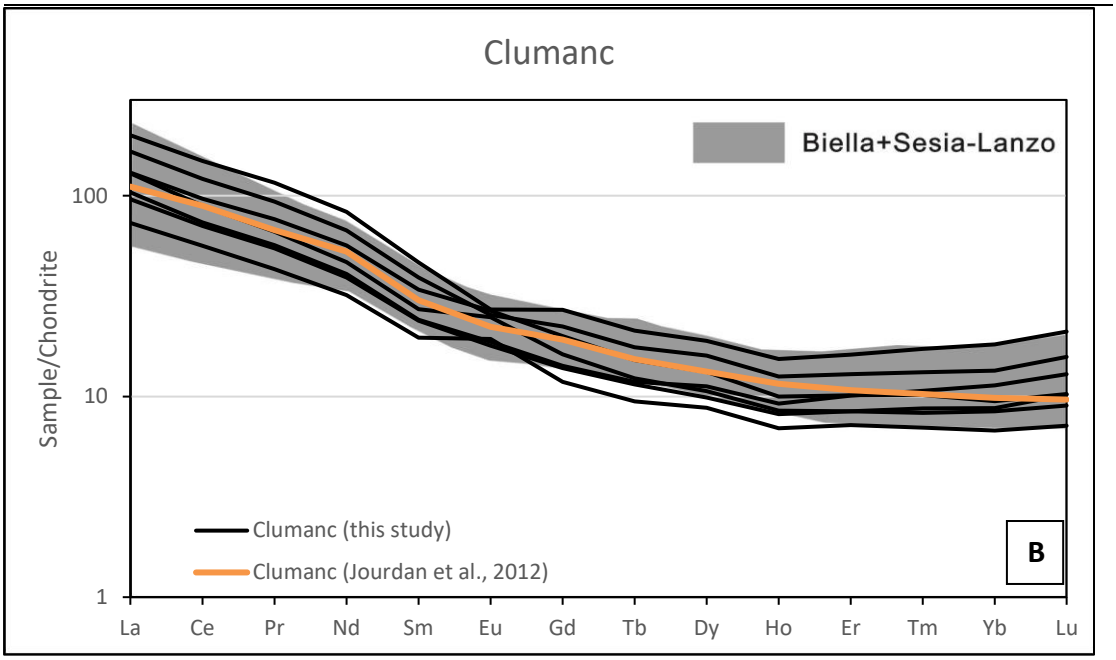
Clumanc
Biella+Sesia-Lanzo
Sample/Chondrite
100
10
1
Clumanc (this study)
Clumanc (Jourdan et al., 2012)
B
La
Ce
Pr
Nd
Sm
Eu
Gd
Tb
Dy
Ho
Er
Tm
Yb
Lu

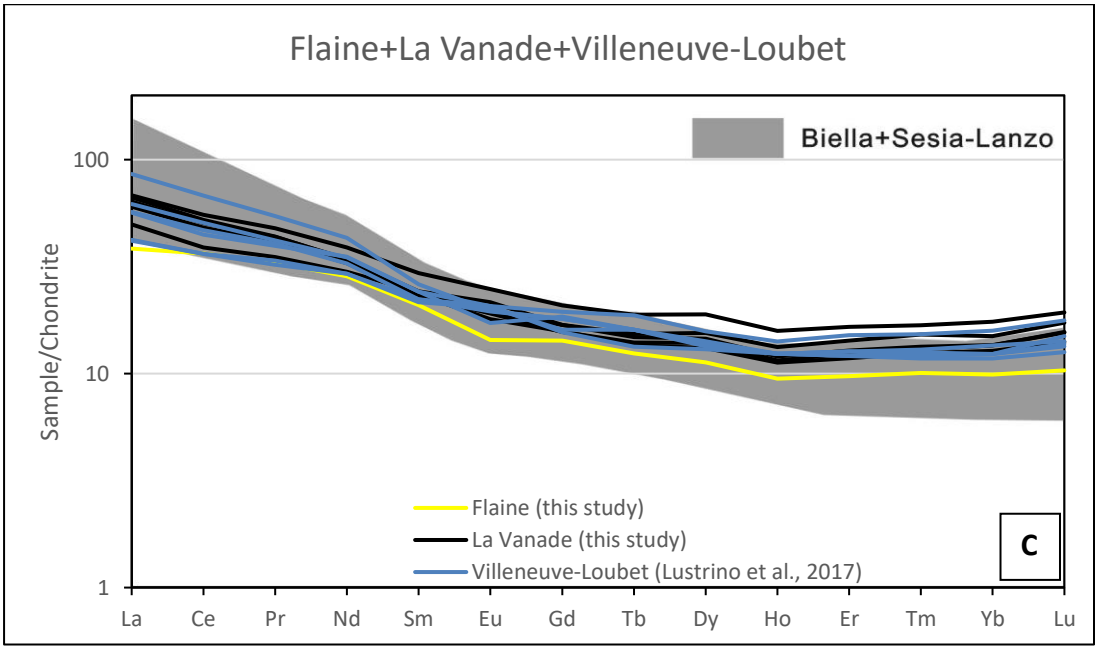
Flaine+La Vanade+Villeneuve-Loubet
Biella+Sesia-Lanzo
Sample/Chondrite
100
10
1
Flaine (this study)
La Vanade (this study)
Villeneuve-Loubet (Lustrino et al., 2017)
C
La
Ce
Pr
Nd
Sm
Eu
Gd
Tb
Dy
Ho
Er
Tm
Yb
Lu

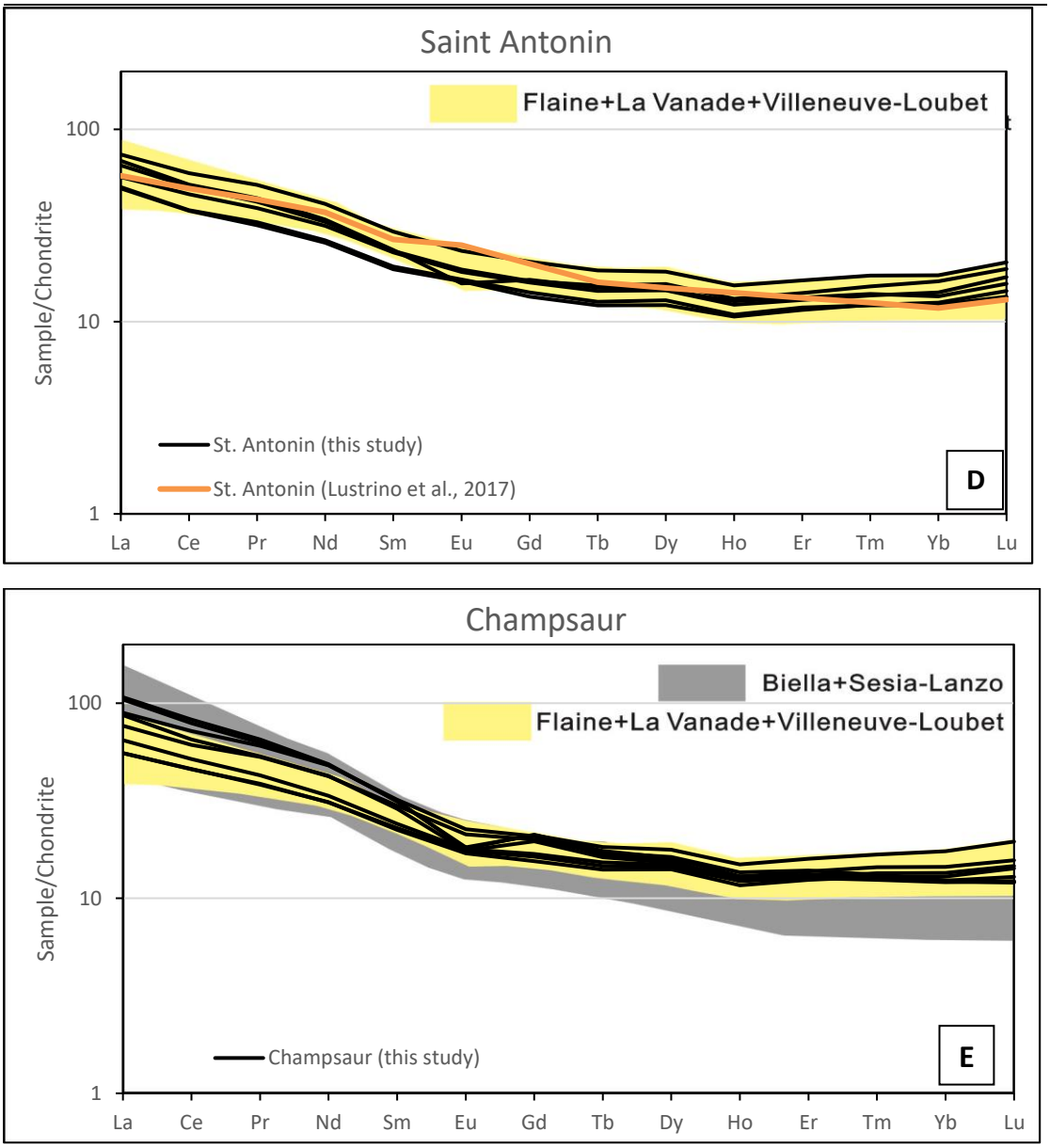

Figure 5.7 Chondrite-normalised REE diagrams for the igneous samples of all regions with compiled previous data for comparison (A-E). Compiled data of Biella/Sesia-Lanzo regions (A) are all calc-alkaline dykes (Peccerillo and Martinotti, 2006; Conticelli et al., 2009; Bergomi et al., 2015) except for the one from lavas of the Cover Series (Callegari et al., 2004). Clumanc data is compiled from glassy tuff (Jourdan et al., 2012), Villeneuve-Loubet and St. Antonin data both compiled from andesitic rocks (Lustrino et al., 2017).

5.5.3 Multielement diagrams

On the primitive mantle (PM)-normalised multielement diagrams (Figure 5.8), all samples show typical arc (supra-subduction)-related features with the enrichment of the most incompatible elements (Th-Sm) over the least incompatible elements (Eu-Lu), and negative Nb-Ta and Ti anomalies. Similar to the REE diagrams, the multielement patterns of samples from all regions

combined with compiled incompatible trace element data of previous studies are grouped into three types (Boyet et al., 2001; Peccerillo and Martinotti, 2006; Conticelli et al., 2009; Jourdan et al., 2012; Bergomi et al., 2015; Lustrino et al., 2017).

Type 1 corresponds to samples from Clumanc and Biella/Sesia-Lanzo regions (Figure 5.8 A, B), characterised by highly enriched Th (Th_N = 61 - 353, $(Th/Nb)_N$ = 7.0 - 22.6) and LREE, with $(La/Sm)_N$ varying between 2.6 - 6.6. Strong negative Nb-Ta anomaly is represented by Nb/Nb* and Ta/Ta* (Nb/Nb* = $Nb/(Th * La)^{1/2}$, Ta/Ta* = $Ta/(Th * La)^{1/2}$) values ranging between 0.09 - 0.24 and 0.14 - 0.25, respectively. Strong Ti anomaly is another noticeable feature, with all samples showing negative anomaly (Ti/Ti* = $Ti/(Eu*Gd)^{1/2}$) ranging between 0.27 - 0.84. Common Zr negative anomaly is also presented by Zr/Zr* = $Zr/(Nd*Sm)^{1/2}$ (0.61 - 0.90), with few samples from Clumanc displaying slightly positive anomaly.

Type 2 is represented by samples from Flaine, St. Antonin and La Vanade/Villeneuve-Loubet regions (Figure 5.8 C, D), characterised by slightly enriched Th (Th_N = 14-40, $(Th/Nb)_N$ = 1.7 - 5.3) and LREE concentrations, with $(La/Sm)_N$ varying between 1.9 - 3.3. Negative Nb-Ta anomaly is represented by Nb/Nb* and Ta/Ta* values ranging between 0.28 - 0.54 and 0.30 - 0.75, respectively. Ti negative anomaly in Type 2 is represented by Ti/Ti* values ranging between 0.40 - 0.75. Zr anomaly is not consistent, some showing negative anomaly while some showing positive anomaly, with Zr/Zr* ranging from 0.78 to 1.68.

Type 3 is composed of samples from Champsaur region (Figure 5.8 E), characterised by moderately enriched Th (Th_N = 17 - 65, $(Th/Nb)_N$ = 1.9 - 5.2) and LREE concentrations, with $(La/Sm)_N$ varying between 2.4 - 3.4. Moderate negative Nb-Ta anomaly is represented by Nb/Nb* and Ta/Ta* values ranging between 0.26 - 0.52 and 0.30 - 0.60, respectively. Moderate negative Ti anomaly is presented with Ti/Ti* values between 0.44 - 0.60. Zr anomaly is not uniform, some showing negative anomaly while some showing positive anomaly, with Zr/Zr* ranging from 0.68 to 1.56.

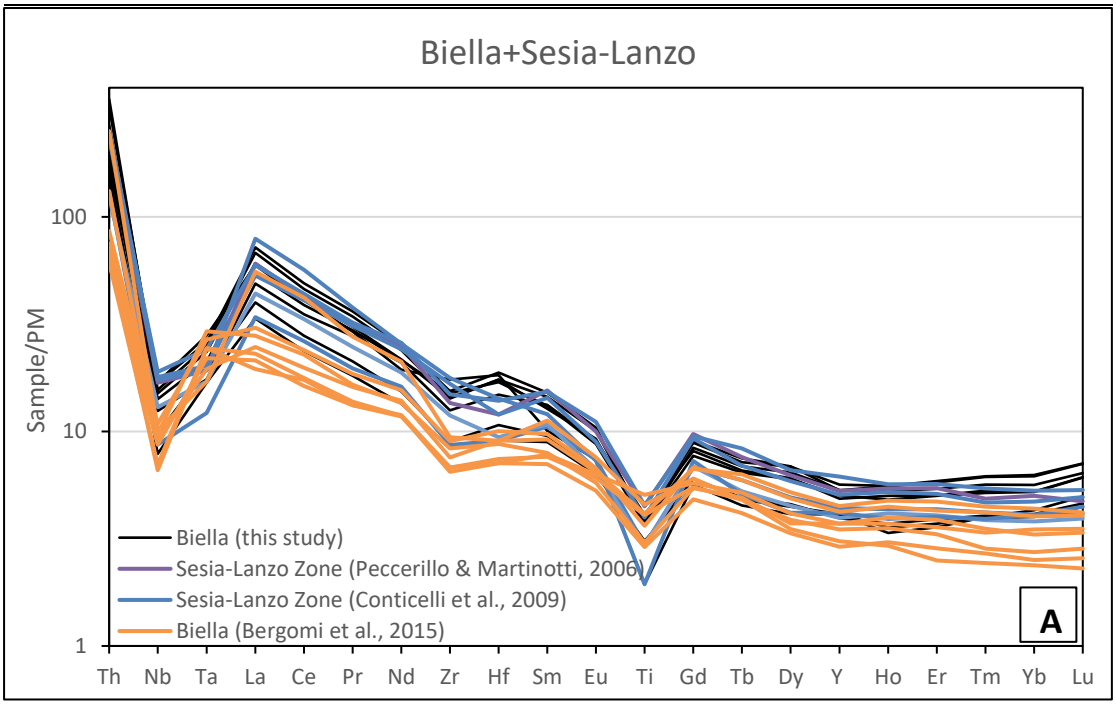
Biella+Sesia-Lanzo
Sample/PM
100
10
1
Th Nb Ta La Ce Pr Nd Zr Hf Sm Eu Ti Gd Tb Dy Y Ho Er Tm Yb Lu
Biella (this study)
Sesia-Lanzo Zone (Peccerillo & Martinotti, 2006)
Sesia-Lanzo Zone (Conticelli et al., 2009)
Biella (Bergomi et al., 2015)
A

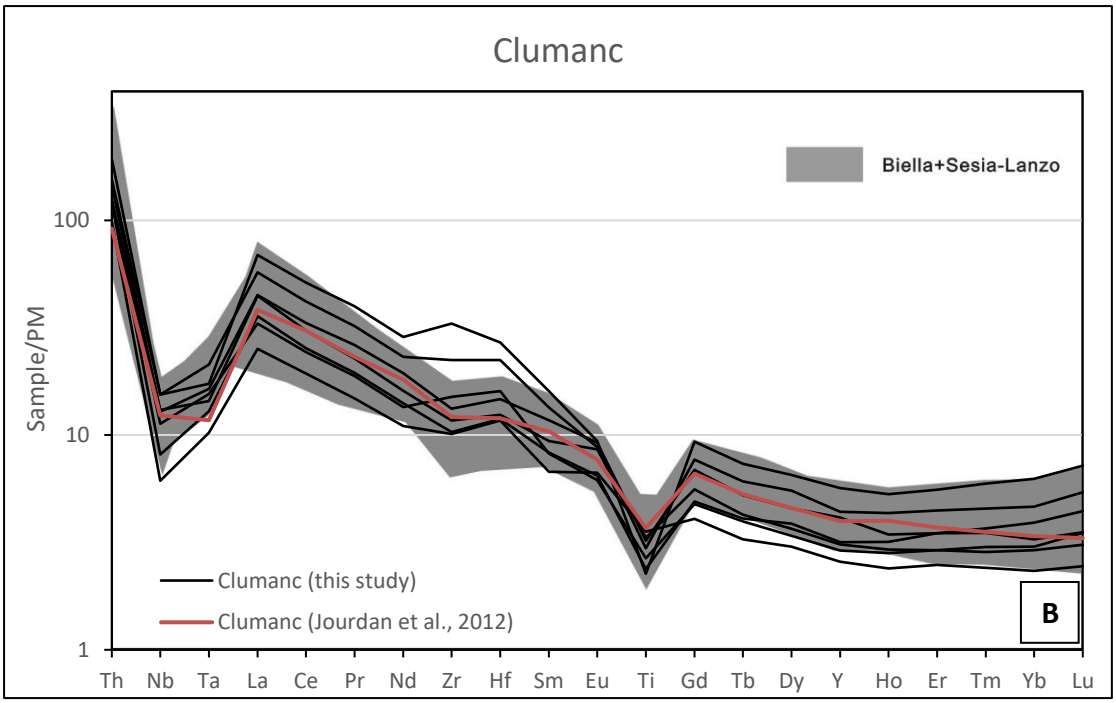
Clumanc
Biella+Sesia-Lanzo
Sample/PM
100
10
1
Th Nb Ta La Ce Pr Nd Zr Hf Sm Eu Ti Gd Tb Dy Y Ho Er Tm Yb Lu
Clumanc (this study)
Clumanc (Jourdan et al., 2012)
B

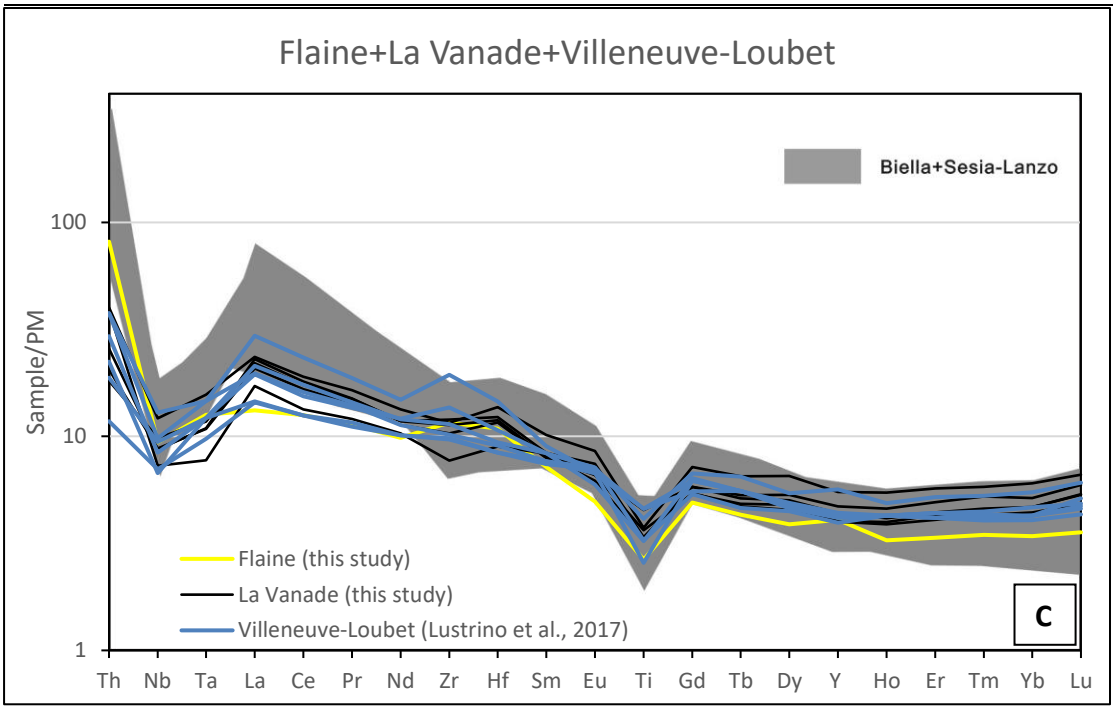
Flaine+La Vanade+Villeneuve-Loubet
Biella+Sesia-Lanzo
Sample/PM
100
10
1
Flaine (this study)
La Vanade (this study)
Villeneuve-Loubet (Lustrino et al., 2017)
C
Th Nb Ta La Ce Pr Nd Zr Hf Sm Eu Ti Gd Tb Dy Y Ho Er Tm Yb Lu

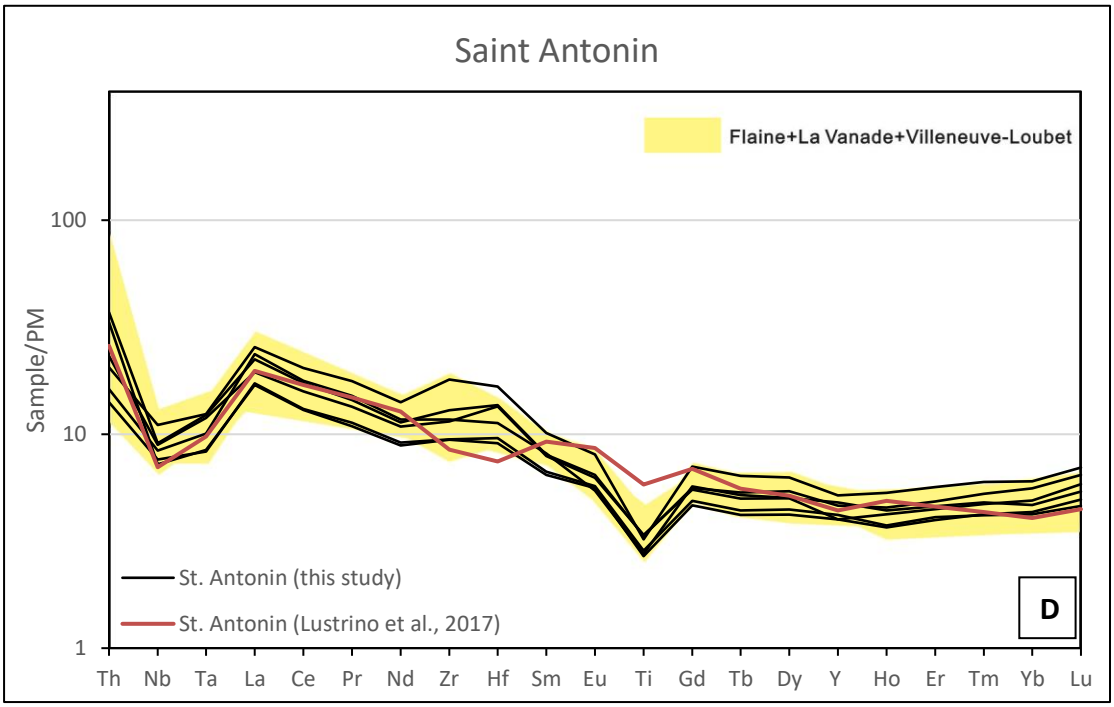
Saint Antonin
Flaine+La Vanade+Villeneuve-Loubet
Sample/PM
100
10
1
St. Antonin (this study)
St. Antonin (Lustrino et al., 2017)
D
Th Nb Ta La Ce Pr Nd Zr Hf Sm Eu Ti Gd Tb Dy Y Ho Er Tm Yb Lu

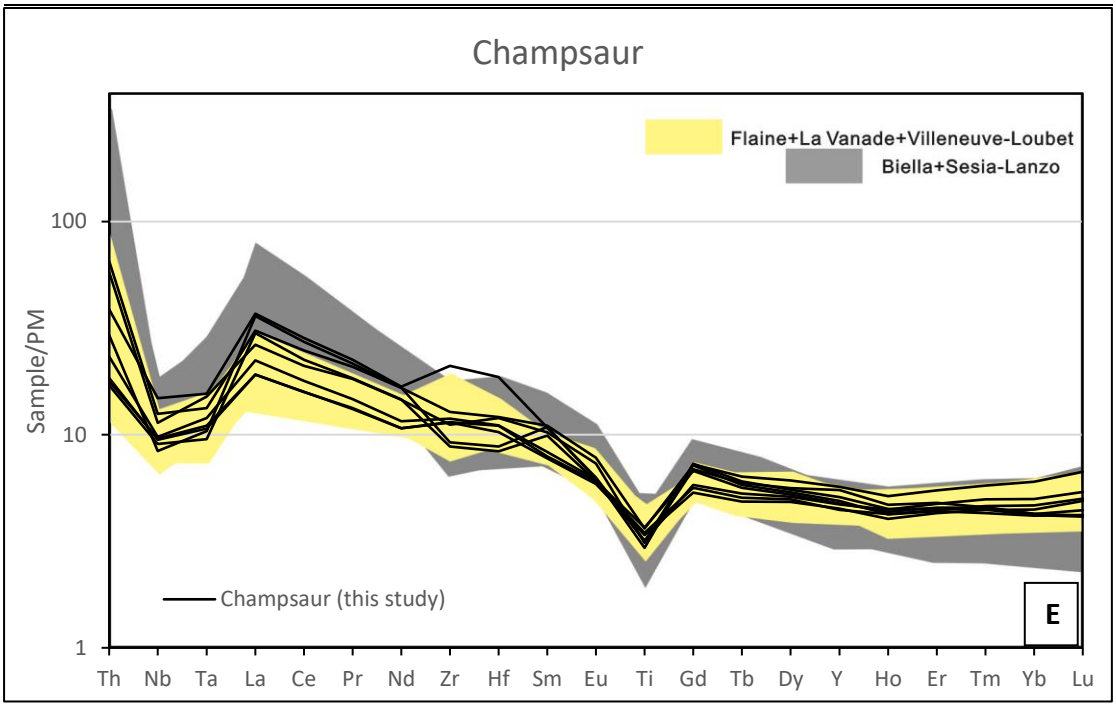

Figure 5.8 Primitive mantle-normalised multielement diagrams for the igneous samples of all regions with compiled previous geochemical data for comparison (A-E). Compiled data of Biella/Sesia-Lanzo regions (A) are all calc-alkaline dykes (Peccerillo and Martinotti, 2006; Conticelli et al., 2009; Bergomi et al., 2015). Clumanc data is compiled from glassy tuff (Jourdan et al., 2012), Villeneuve-Loubet and St. Antonin data both compiled from andesitic rocks (Lustrino et al., 2017).

5.5.4 Discrimination diagrams

In addition to the REE and multielement diagrams, a selection of geochemical discrimination diagrams (Figure 5.9) is also used to characterise the geochemical signatures and differentiate the igneous samples from all studied regions.

On the Nb/Yb vs Th/Yb diagram (Figure 5.9 A, after Pearce, 2008), all samples plot in the Volcanic Arc array with high Th/Yb ratios, above the MORB-OIB array. Generally, two subgroups are clearly separated: Subgroup 1 mainly includes samples from Clumanc and Biella/Sesia-Lanzo regions, in addition to one sample from Flaine and two from Champsaur, characterised by higher Th/Yb ratio and slightly higher Nb/Yb ratio; Subgroup 2 is represented by those from St. Antonin, La Vanade, Villeneuve-Loubet and Nice-Monaco regions, in addition to some from Champsaur region, characterised by lower Th/Yb ratio and slightly lower Nb/Yb ratio compared to Subgroup 1. Samples within either subgroup are plotted in a tight cluster.

On the $(La/Sm)_{PMn}$ vs $(Th/Nb)_{PMn}$ diagram (Figure 5.9 B), similar pattern to the Nb/Yb vs Th/Yb diagram has been displayed. Two subgroups are discriminated and divided by the boundary where $(Th/Nb)_{PMn} = 6$. Subgroup 1 mainly includes samples from Clumanc and Biella/Sesia-Lanzo regions, in addition to one sample from Flaine, characterised by higher $(Th/Nb)_{PMn}$ ratio and slightly higher $(La/Sm)_{PMn}$ ratio; Subgroup 2 is represented by those from Champsaur, St. Antonin, La Vanade, Villeneuve-Loubet and Nice-Monaco regions, in addition to one sample of Sesia-Lanzo region, characterised by lower $(Th/Nb)_{PMn}$ ratio and slightly lower $(La/Sm)_{PMn}$ ratio compared to Subgroup 1.

On the Dy/Yb vs Dy/Dy* diagram (Figure 5.9 C, after Davidson et al., 2013), majority of the samples plot below the MORB field, surrounding the continental crust estimates (red star), with few samples from Champsaur and Biella/Sesia-Lanzo regions plotting in the lowest part of the MORB field. Two subgroups could be discriminated as well by the dotted line, perpendicular to the LREE concentration array. Below the line are Subgroup 1, represented by samples from Clumanc and Biella/Sesia-Lanzo regions, in addition to some from the Champsaur region, characterised by more enriched LREE with lower Dy/Dy* and slightly higher Dy/Yb. Above the line is Subgroup 2, which is mainly composed of samples from Flaine, St. Antonin, La Vanade, Villeneuve-Loubet and Nice-Monaco regions, in addition to few samples from the Champsaur region, characterised by less enriched LREE with higher Dy/Dy* and slightly lower Dy/Yb. Within each subgroup, the distribution of plots is somewhat parallel to the amphibole/clinopyroxene fractionation trend, indicating the influence of amphibole/clinopyroxene fractionation on Dy/Dy* and Dy/Yb values during magma differentiation.

On the Ta/Yb vs Th/Yb diagram (Figure 5.9 D, after Pearce, 1982 and Bergomi et al., 2015), all samples plot in the island/continental arc field with calcalkaline affinity. Two subgroups are clearly discriminated and divided by the boundary where Th/Yb = 2. Subgroup 1 mainly includes samples from Clumanc and Biella/Sesia-Lanzo regions, in addition to one sample from Flaine and two from Champsaur, with most samples of Subgroup 1 falling in the pure continental arc field and part of them in the island-continental arc overlapping field; Subgroup 2 is represented by those from St. Antonin, La Vanade, Villeneuve-Loubet and Nice-Monaco regions, in addition to some from

Champsaur region, with all of Subgroup 2 samples plotting in the island-continental arc overlapping field.

On the Nb/Th vs Zr/Nb diagram (Figure 5.9 E, after Condie, 2005), all samples plot in cluster in the Arc field, with some plotted outside of the left side boundary of Arc field, displaying extremely low Nb/Th value. Generally, two subgroups are distinguished by the boundary where Nb/Th = 2. Subgroup 1 is represented by samples from Clumanc and Biella/Sesia-Lanzo regions, in addition to one sample from Flaine, characterised by extremely low Nb/Th ratio (< 2) with several samples from Clumanc region distinguishing themselves from the rest of Subgroup 1 samples with higher Zr/Nb. Subgroup 2 includes samples from Champsaur, St. Antonin, La Vanade, Villeneuve-Loubet and Nice-Monaco regions, characterised by higher Nb/Th (> 2) compared with Subgroup 1, falling in the overlapping part between Arc and OPB.

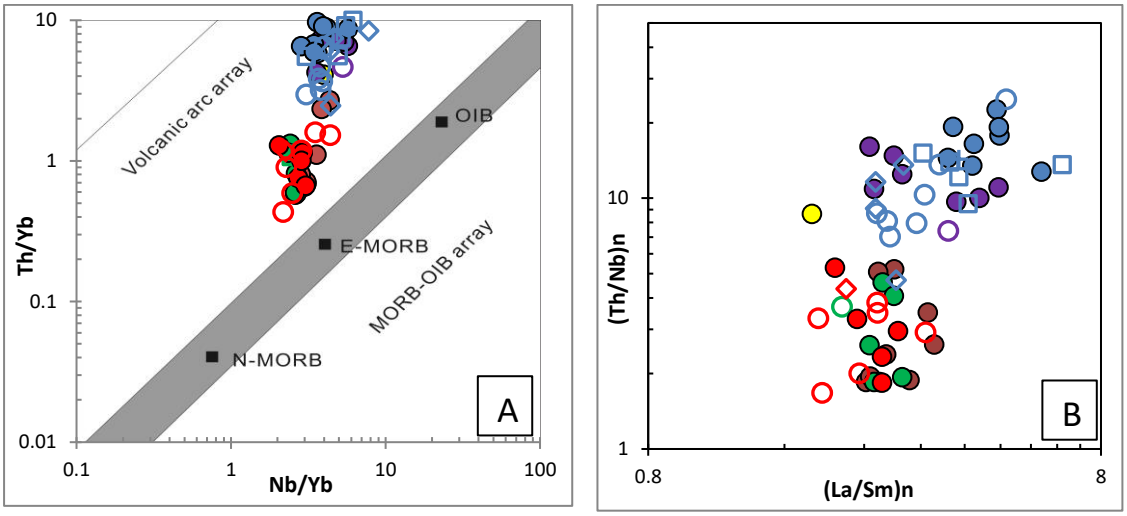

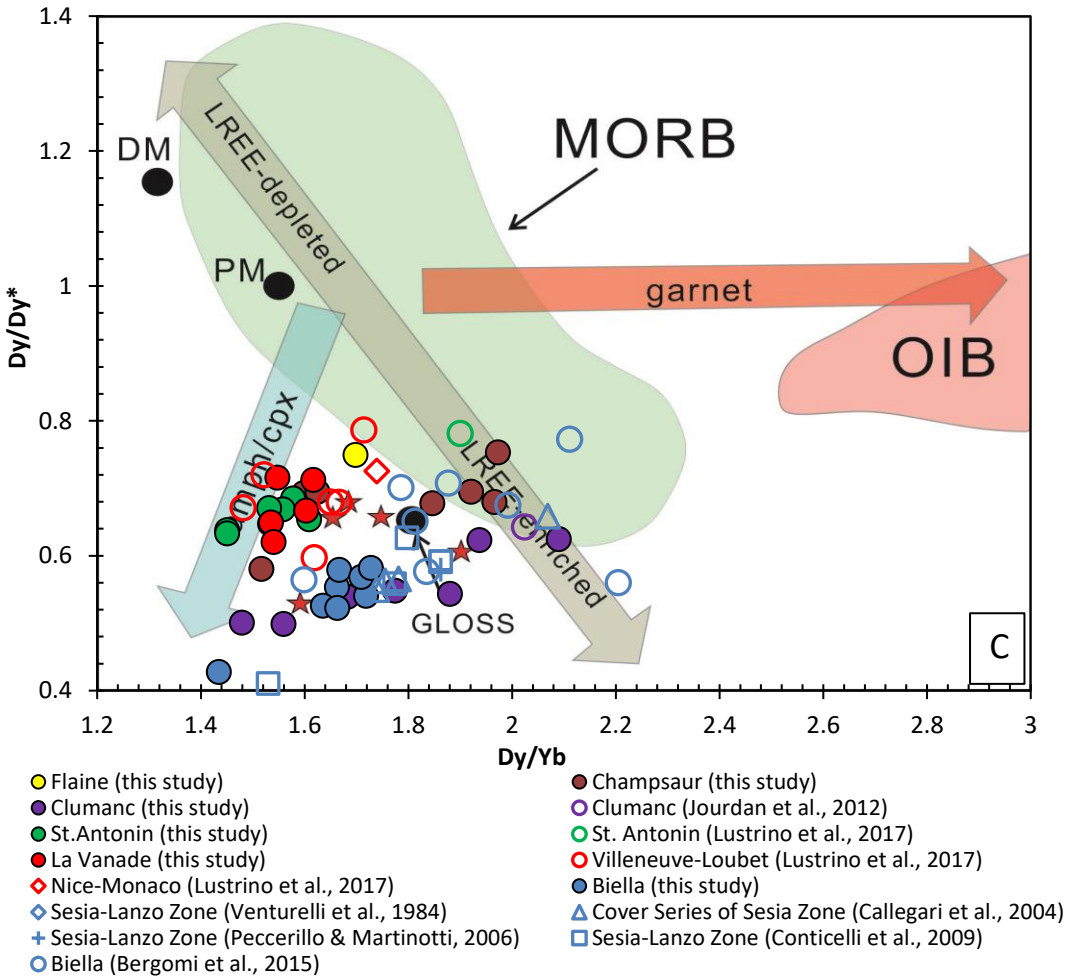
MORB
DM
PM
LREE-depleted
garnet
OIB
xpl/cpx
LREE-enriched
GLOSS
C
Dy/Dy*
Dy/Yb
1.4
1.2
1
0.8
0.6
0.4
1.2
1.4
1.6
1.8
2
2.2
2.4
2.6
2.8
3
Flaine (this study)
Clumanc (this study)
St.Antonin (this study)
La Vanade (this study)
Nice-Monaco (Lustrino et al., 2017)
Sesia-Lanzo Zone (Venturelli et al., 1984)
Sesia-Lanzo Zone (Peccerillo & Martinotti, 2006)
Biella (Bergomi et al., 2015)
Champsaur (this study)
Clumanc (Jourdan et al., 2012)
St. Antonin (Lustrino et al., 2017)
Villeneuve-Loubet (Lustrino et al., 2017)
Biella (this study)
Cover Series of Sesia Zone (Callegari et al., 2004)
Sesia-Lanzo Zone (Conticelli et al., 2009)

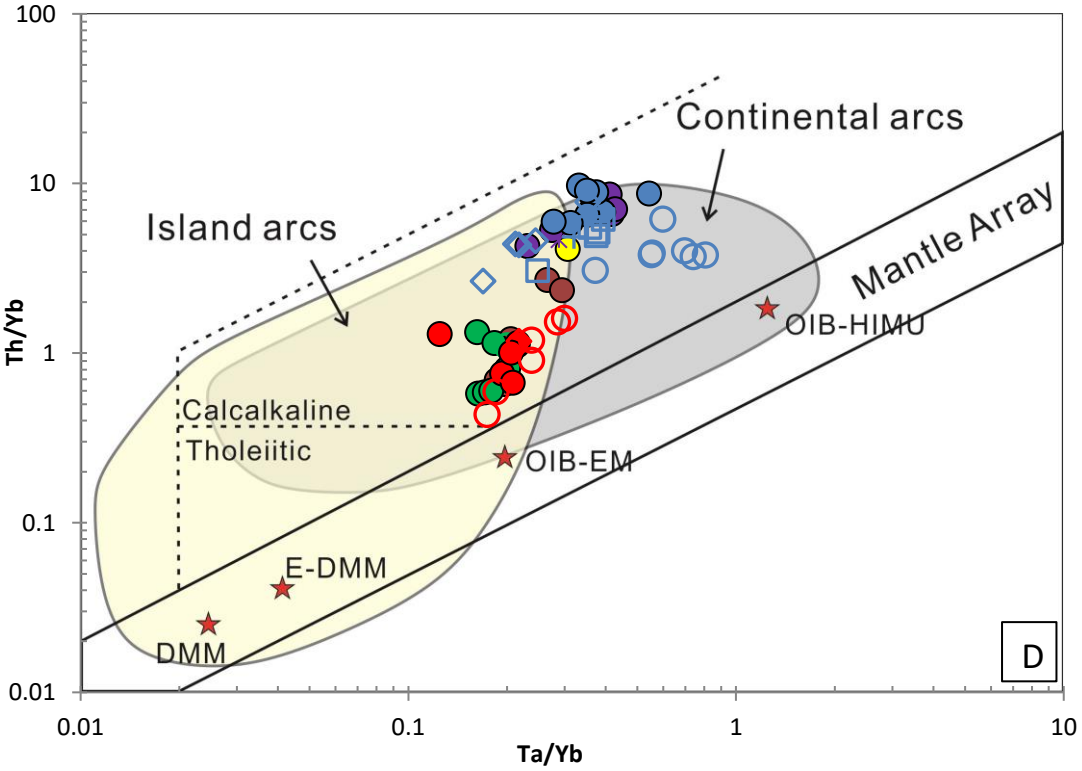
Continental arcs
Island arcs
Mantle Array
OIB-HIMU
Calcalkaline
Tholeiitic
OIB-EM
E-DMM
DMM
D
Th/Yb
Ta/Yb
100
10
1
0.1
0.01
0.01
0.1
1
10

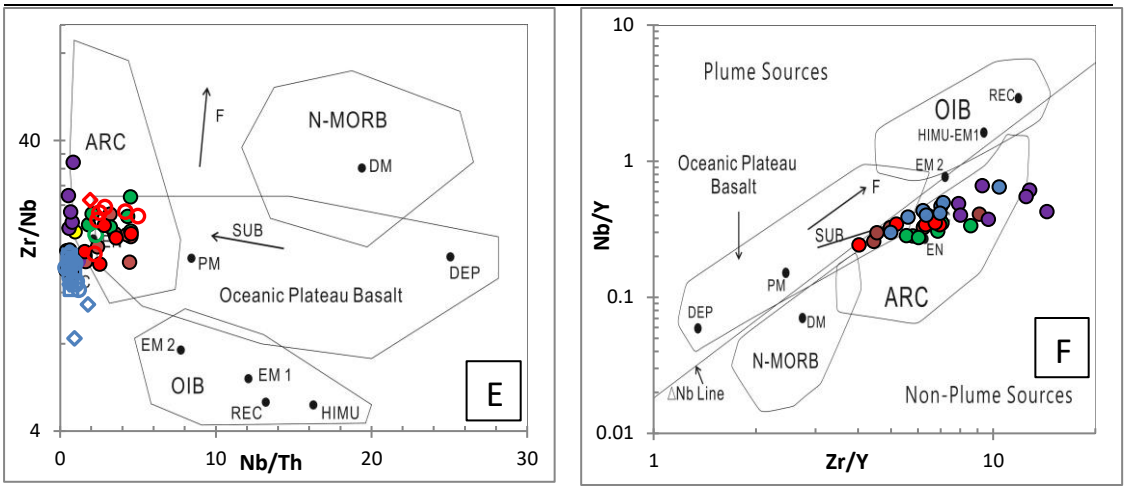

Flaine (this study)
Clumanc (this study)
St.Antonin (this study)
La Vanade (this study)
Nice-Monaco (Lustrino et al., 2017)
Sesia-Lanzo Zone (Venturelli et al., 1984)
Sesia-Lanzo Zone (Peccerillo & Martinotti, 2006)
Biella (Bergomi et al., 2015)
Champsaur (this study)
Clumanc (Jourdan et al., 2012)
St. Antonin (Lustrino et al., 2017)
Villeneuve-Loubet (Lustrino et al., 2017)
Biella (this study)
Cover Series of Sesia Zone (Callegari et al., 2004)
Sesia-Lanzo Zone (Conticelli et al., 2009)

Figure 5.9 Selected discrimination diagrams to determine the geochemical relationship of samples from studied regions and compiled previous geochemical data A) Nb/Yb vs Th/Yb crustal input proxy diagram (Pearce, 2008), B) Primitive mantle-normalised La/Sm vs Th/Nb, C) Dy/Yb vs Dy/Dy* diagram (Davidson et al., 2013), D) Ta/Yb vs Th/Yb diagram (Pearce, 1982 and Bergomi et al., 2015), E) Nb/Th vs Zr/Nb diagram (Condie, 2005), F) Zr/Y vs Nb/Y diagram (Condie, 2005). Abbreviations: OIB = oceanic island basalt, N-MORB = normal mid-ocean ridge basalt, E-MORB = enriched mid-ocean ridge basalt, PM = primitive mantle, DM = shallow depleted mantle, GLOSS = average global subducting sediment, OIB-HIMU = ocean island basalt-high μ, OIB-EM = ocean island basalt-enriched mantle, DMM = depleted MORB mantle, E-DMM = enriched depleted MORB mantle, UC = upper continental crust, HIMU = high mu (U/Pb) source, EM1 and EM2 = enriched mantle sources, REC = recycled component, ARC = arc related basalts, OPB = oceanic plateau basalt, DEP = deep depleted mantle, EN = enriched component, F = effects of batch melting and SUB = subduction effect.

On the Zr/Y vs Nb/Y diagram (Figure 5.9 F, after Condie, 2005), most samples plot in cluster in the Arc field below the △Nb line of non-plume source, with some samples from Biella/Sesia-Lanzo regions plotted along the boundary between Arc and OPB. Plots are not well discriminated in this diagram due to most spots clustering in a narrow band parallel to the SUB (subduction effect) arrow. However, previous Subgroups 1 and 2 are still somewhat applicable to this diagram, although the separation line is not as clear as those in other diagrams.

5.6 Summary

The samples of all studied regions have LOI values ranging between 0.3 and 10.9 wt. %, and all samples commonly show variable degrees of alteration under microscopic observation. On diagrams of major and trace elements against Zr, many elements (e.g., Ba, Rb, Pb) have poor correlations with Zr, clearly indicating that they may have been remobilised during secondary alteration. Meanwhile, some major elements (e.g., TiO_2) and trace elements including REE, Th, Nb, Hf, Ta, Y show moderate to good correlations with Zr, therefore suggesting that these elements remained immobile during alteration. These elements are suitable to be used to constrain the characteristics and origins of selected foreland samples to campare with previously studied nearby volcanic sources.

The majority of the samples plot in the basaltic andesite/andesite field with sub-alkaline affinity while a small number of samples are more evolved plotted in the dacite field, and few samples plot on the boundary between alkaline and sub-alkaline.

As for major elements, a general negative correlation is presented on TiO_2, Al_2O_3, CaO, MgO and Fe_2O_3 vs SiO_2 diagrams, in particular Al_2O_3, CaO. On the K_2O/Na_2O vs SiO_2 diagrams, samples are more scattered without showing clear trends due to the remobilisation of these elements during alteration processes.

On the chondrite-normalised REE diagram, all samples show typical arc signatures, with three types of REE patterns having been distinguished. Type 1 corresponds to samples from Clumanc and Biella/Sesia-Lanzo regions, characterised by highly enriched LREE and flat HREE with $(La/Yb)_N$ varying between 8.4 - 15.3; Type 2 corresponds to samples from Flaine, St. Antonin and La Vanade/Villeneuve-Loubet regions, characterised by slightly enriched LREE and extremely flat HREE with $(La/Yb)_N$ varying between 3.3 - 5.2; Type 3 includes samples from Champsaur region, characterised by moderate enriched LREE and flat HREE pattern with between $(La/Yb)_N$ varying 4.1 - 8.6, representing a middle pattern between Type 1 and Type 2.

On the primitive mantle-normalised diagram, all samples show typical arc-related features, represented by the strong enrichment of the most

incompatible elements (Th-Sm) over the least incompatible elements (Eu-Lu), and typical negative Nb-Ta-Ti anomalies. Similar to the REE diagrams, the multielement patterns have also been into three types. Type 1 corresponds to samples from Clumanc and Biella/Sesia-Lanzo regions, characterised by highly enriched Th (Th_N = 61 - 353, $(Th/Nb)_N$ = 7.0 - 22.6) and LREE concentrations, with $(La/Sm)_N$ varying between 2.6 - 6.6; Type 2 is represented by samples from Flaine, St. Antonin and La Vanade/Villeneuve-Loubet regions, characterised by slightly enriched Th (Th_N = 14 - 40, $(Th/Nb)_N$ = 1.7 - 5.3) and LREE concentrations, with $(La/Sm)_N$ varying between 1.9 - 3.3; Type 3 corresponds to samples from Champsaur region, characterised by moderately enriched Th (Th_N = 17 - 65, $(Th/Nb)_N$ = 1.9 - 5.2) and LREE concentrations, with $(La/Sm)_N$ varying between 2.4 - 3.4, representing a middle pattern between Type 1 and Type 2.

On the discrimination diagrams, generally majority of the samples plot in the arc field and two subgroups have been distinguished. Subgroup 1 mainly includes samples from Clumanc and Biella/Sesia-Lanzo regions, while Subgroup 2 corresponds to samples from St. Antonin, La Vanade, Villeneuve-Loubet and Nice-Monaco regions. Samples from Champsaur regions are plotted in both subgroups, part clustering with Subgroup 1 and part plotting together with Subgroup 2 in most of the diagrams.

In summary, whole-rock geochemical analysis provides new solid constraints on the geochemical signatures of all studied samples and on the origins of the igneous (andesitic) clasts from foreland regions and primary volcanics from paleo-volcanic centers. The igneous (andesitic) clasts from Clumanc foreland region share similar geochemical patterns to the dykes in Western Alps (Biella/Sesia-Lanzo), whereas some igneous (andesitic) clasts from Champsaur and primary volcanics from St. Antonin region are in good agreement with those volcanic suites from Provence volcanic system (La Vanade, Villeneuve-Loubet and Nice-Monaco). This is the first time systematic matchings were built between (1) Clumanc and Biella, (2) Champsaur/St. Antonin and Provence, shedding new light on the origins of the volcanic clasts.

Chapter 6: Clinopyroxene geochemistry

6.1 Introduction

This chapter presents the geochemistry of clinopyroxenes preserved in primary and secondary volcaniclastic rocks in Alpine foreland basins and a subset of clinopyroxene phenocrysts preserved in igneous rocks of the Internal Alps in N Italy. The purpose of conducting clinopyroxene geochemistry is to characterise and identify the compositional heterogeneity of clinopyroxenes from different regions in the whole NAFB, analysing the results from regional scale in order to see any spatial variability, to locality and sample scale in order to see any temporal variability within a limited area through time.

This chapter will first classify the mineral types of all clinopyroxenes from all studied regions using the Cpx quadrilateral diagram. Key major and trace elements will then be selected to establish Mg# vs elements variation diagrams, as well as some binary diagrams of Mg# vs element ratios (e.g., Mg# vs La/Sm, Mg# vs V/Ti). Existing tectonic discrimination diagrams of Leterrier et al. (1982) are also used to characterise the magmatic affinity of clinopyroxenes. There are other tectonic discrimination diagrams (e.g., Les Bas, 1962; Nisbet and Pearce, 1977). The use of the discrimination criteria of these diagrams has already been included in the Leterrier et al. (1982) diagrams. These diagrams are considered all need for more detailed evaluation of the distinct tectonic discrimination diagrams in Chapter 8.

A total of 6882 SEM-EDS analyses of 2138 clinopyroxene grains encountered in 28 samples of volcaniclastic sandstone, 6 samples of igneous pebbles/cobbles, 13 samples of primary volcaniclastic deposits and 1 sample of igneous rock, have been conducted. In addition, a total of 722 LA-ICP-MS analyses of 580 clinopyroxene grains in 15 samples of volcaniclastic sandstone, 6 samples of primary volcaniclastic deposits and 1 sample of igneous pebble have been conducted.

The method of calculating the mineral formula of clinopyroxene is according to Morimoto et al. (1988) and Stone and Niu (2009). In this method, the wt.% of the oxides is used to represent their molecular proportion, then their

atomic proportion which is subsequently used to calculate the ionic proportion of the elements. These ionic proportions were then used in the equations that calculate the Mg# of the pyroxenes (Equation 6.1) and end member proportions of the analysed pyroxenes (Equation 6.2, 6.3 and 6.4).

Equation 6.1 $Mg\# = Mg^{2+} / (Mg^{2+} + Fe^{2+}) \times 100$

Equation 6.2 $En = Mg^{2+} / (Mg^{2+} + Fe^{2+} + Ca^{2+}) \times 100$

Equation 6.3 $Fs = Fe^{2+} / (Mg^{2+} + Fe^{2+} + Ca^{2+}) \times 100$

Equation 6.4 $Wo = Ca^{2+} / (Mg^{2+} + Fe^{2+} + Ca^{2+}) \times 100$

Chemical microanalyses of major and trace elements of clinopyroxenes were carried out at Cardiff University with an Analytical Scanning Electron Microscope equipped with EDS detectors (ASEM-EDS) and an inductively coupled plasma-mass spectrometry equipped with laser ablation technique (LA-ICP-MS), respectively. The detailed method descriptions and SEM, LA-ICP-MS results are given in Appendix A for the analytical methods and uncertainties and in Appendix E3, E4 for the data.

6.2 Inter-region discrimination

Discrimination of clinopyroxenes from all six studied regions (i.e., E Switzerland, W Switzerland, Aravis, Champsaur, S France and N Italy) was conducted using diagrams introduced in Section 6.1. The detailed regional localities included in each broad region are provided in Chapter 3.

6.2.1 Classification of clinopyroxene

Major elements were used to classify the clinopyroxene in terms of their mineral types after the nomenclature of Morimoto et al. (1988). The majority of clinopyroxenes from all studied regions plots in large overlapping clusters. Most clinopyroxenes fall in the Mg-augite field, with subordinate diopside (Figure 6.1). The clinopyroxenes from N Italy are all augite, but this could be a bias due to the limited number of analyses in this area.

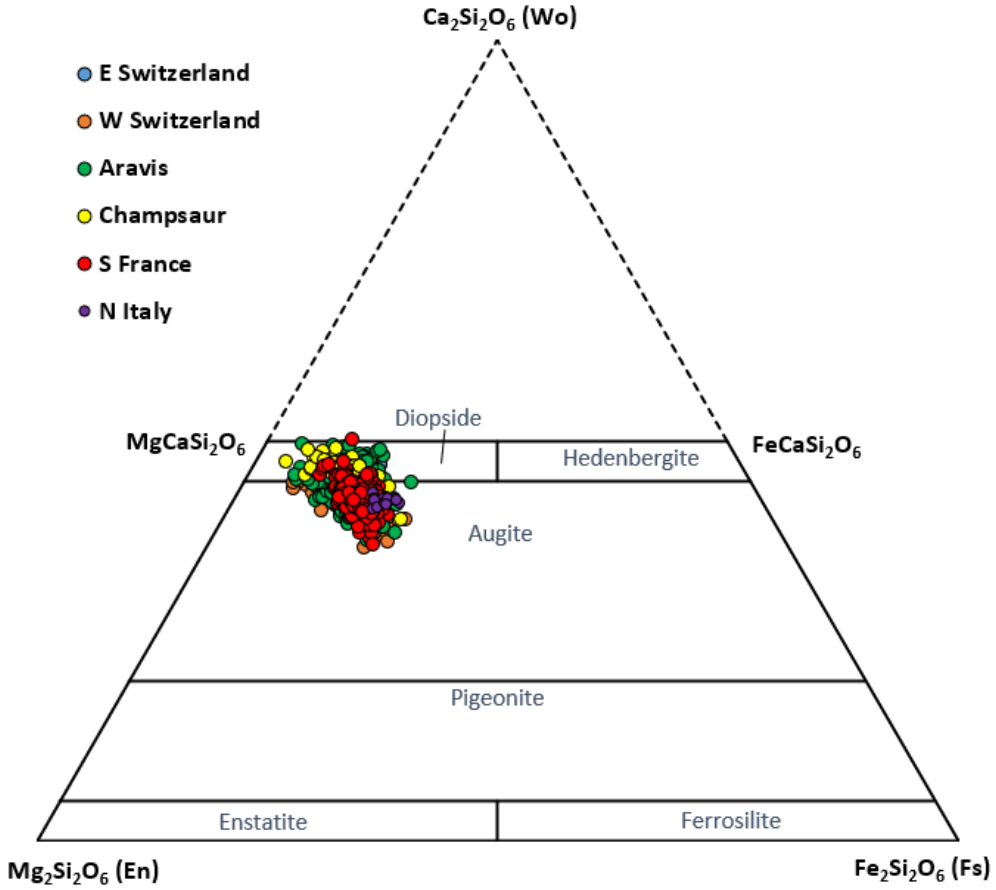

Figure 6.1 Classification diagram of clinopyroxenes from all studied region (After nomenclature of Morimoto et al., 1988).

6.2.2 Binary diagrams (Mg# vs Major elements)

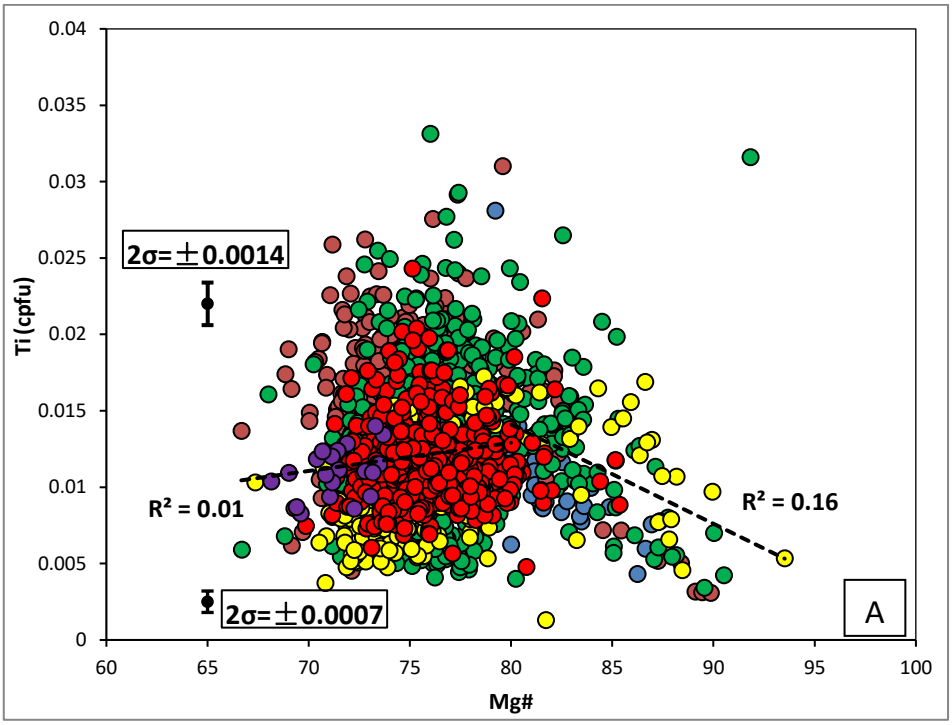

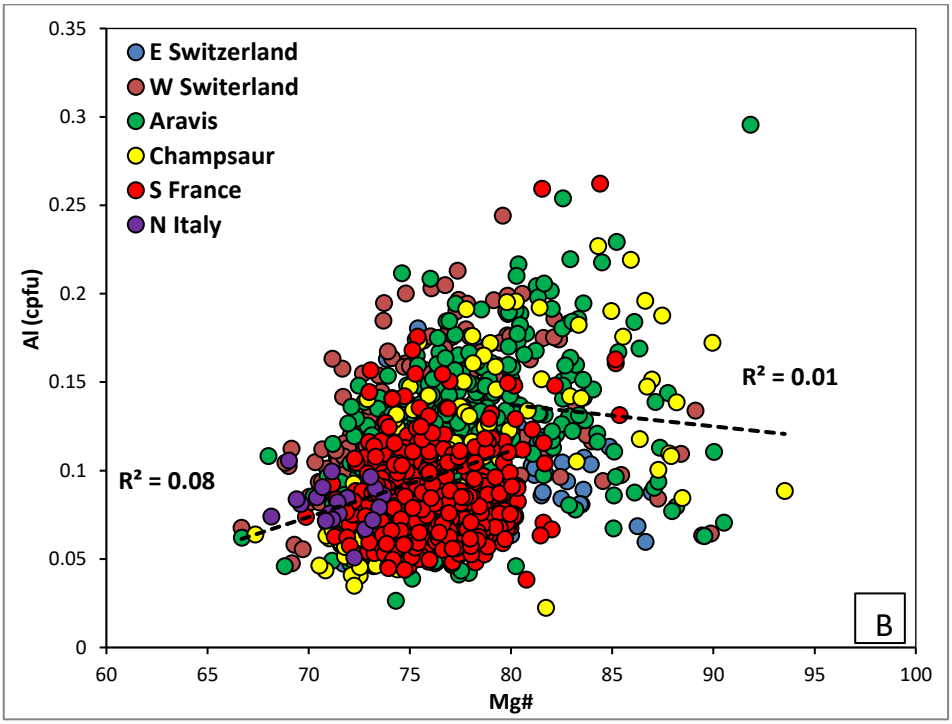

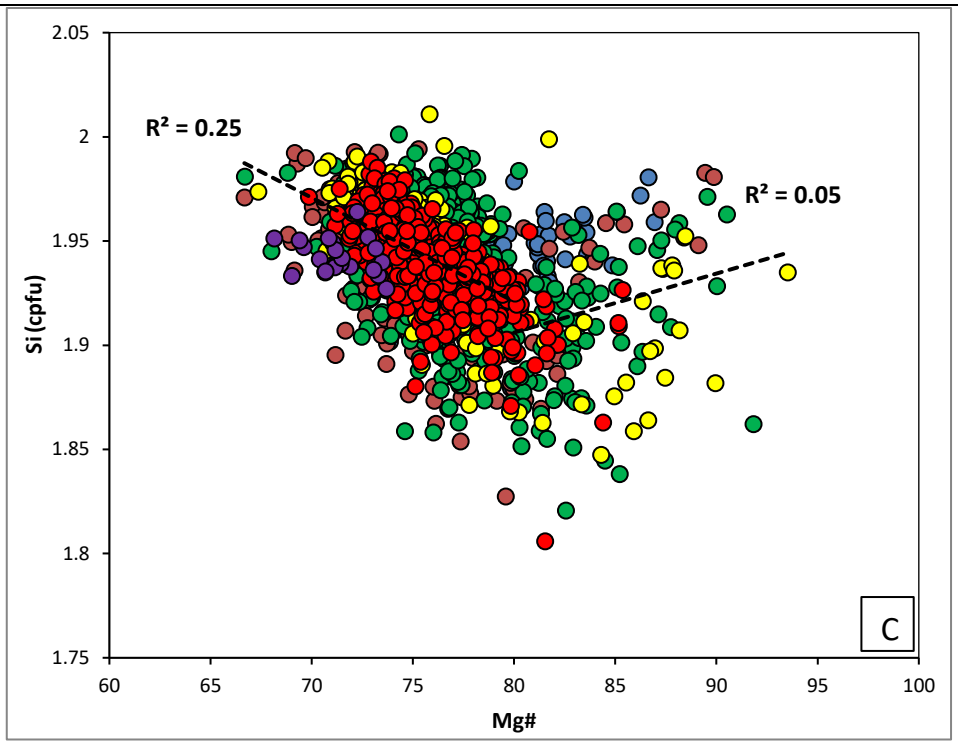
R² = 0.25
R² = 0.05
Si (cpfu)
Mg#
C

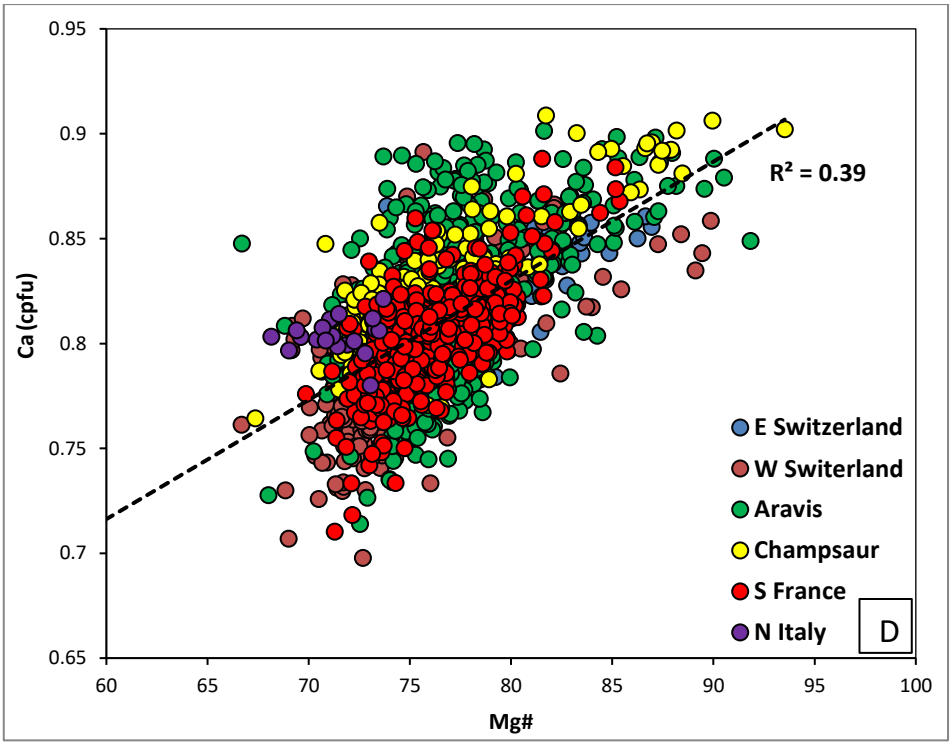
R² = 0.39
Ca (cpfu)
Mg#
E Switzerland
W Switerland
Aravis
Champsaur
S France
N Italy
D

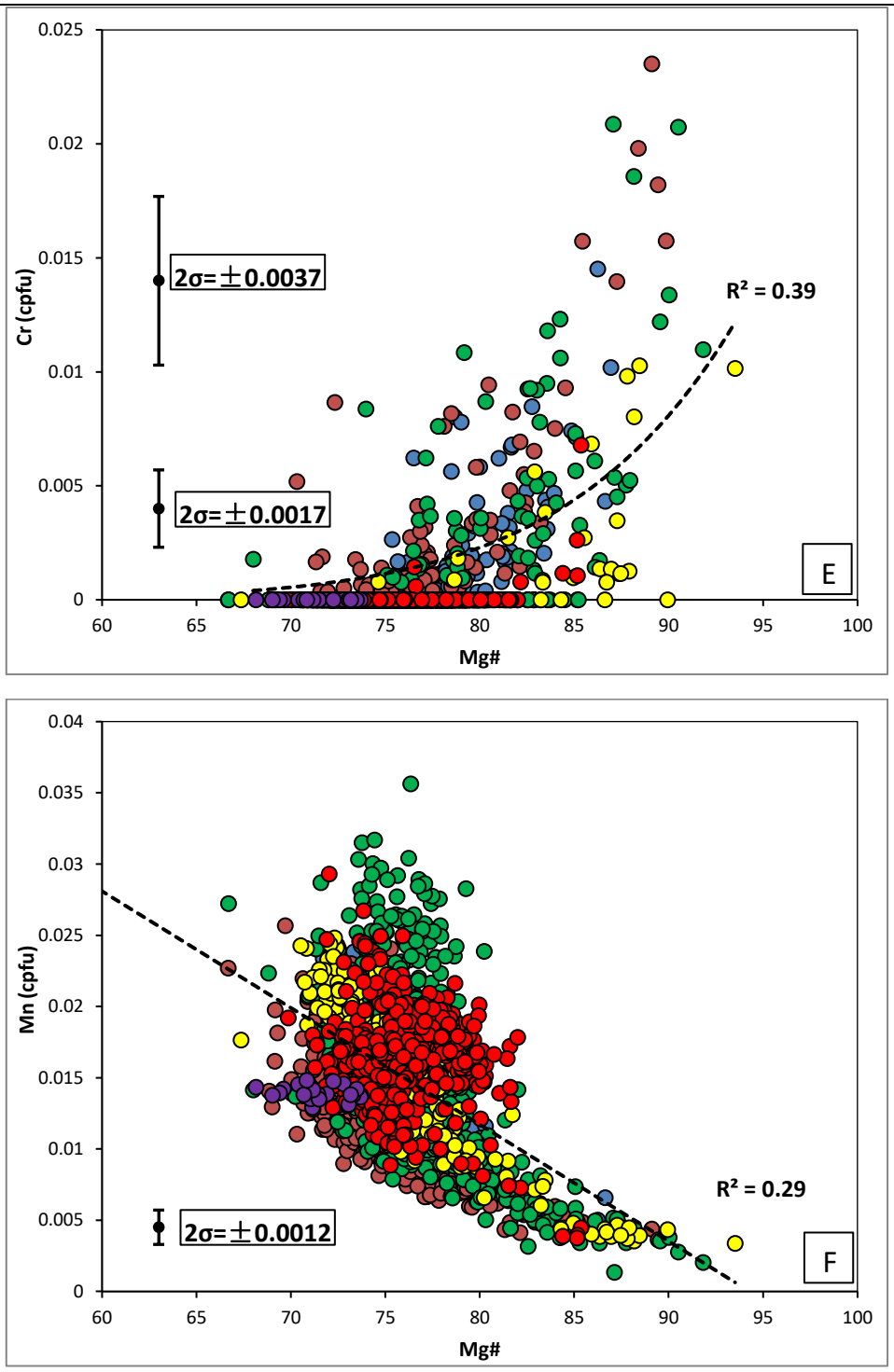

Figure 6.2 A-F) Binary diagrams of selected major elements vs Mg# of clinopyroxenes from all studied regions; error bars were calculated using results of standards (Smithsonian Augite NMNH 122142 and Astimex Cr-Diopside, see Appendix E3). Regression line in Cr vs Mg# diagram is power regression, whereas the remaining lines are linear regression.

On the binary diagrams (Figure 6.2 A-F), the majority of clinopyroxenes from all studied regions have Mg# varying between 70 - 90. In every diagram, clinopyroxenes from different regions are largely overlapping with each other,

indicating limited inter-regional major element diversity of Alpine clinopyroxenes. With the exception of N Italy clinopyroxenes that have lower Mg#, compositional trends of each region outline a remarkable change of behaviour in terms of pattern and/or compositional range ca. Mg# = 80. Therefore, in order to better study the variation trend of Ti, Al and Si, plots are divided into two subgroups (i.e., Mg# > 80 and Mg# < 80). Ti increases with decreasing Mg# (R^2 = 0.15) due to the incompatibility of Ti in mafic to intermediate magmatic melts. A change in the trend at Mg# = 80 likely reflect changes in crystallising minerals during differentiation. At lower Mg#, Ti appears to not have a clear trend, with a less pronounced correlation (R^2 = 0.01) with Mg#. This phenomenon could be explained by the apparition of ilmenite or Ti-magnetite. The Mg# vs Al diagram shows variation patterns similar to those of Mg# vs Ti. With decreasing Mg#, Al increases at high Mg# range, then decreases at lower Mg# range (R^2 = 0.09), probably due to the apparition of feldspar in the melt. As for the Mg# vs Si diagram, with decreasing Mg# at high Mg# range, Si shows a positive correlation (R^2 = 0.18) with Mg#, then increases with poor correlation (R^2 = 0.03) at lower Mg#.

With decreasing Mg#, Ca and Cr both decrease with a good positive correlation (R^2 = 0.48 and 0.34, respectively). The fractionation of clinopyroxene and Ca-plagioclase give rise to the consistent decrease of Ca in magma. This differentiation-related decrease is noteworthy for the interpretation of REE contents (see below), because REE commonly substitute with Ca in M2 crystallographic site of clinopyroxenes (McKay et al., 1986; Gallahan and Nielsen, 1992). As for Cr, early crystallisation of Cr-spinel and olivine in mantle-derived melts could explain the decreasing trend. It should be noted that analyses with Cr = 0 are caused by SEM detection limit ca. 0.1 wt. % (Appendix E3). As opposed to Ca and Cr, Mn shows a negative correlation (R^2 = 0.28) with Mg#, likely representing siderophile behaviour of Mn and a strong correlation with Fe^{2+} (and Mg#).

6.2.3 Tectonic discrimination diagram

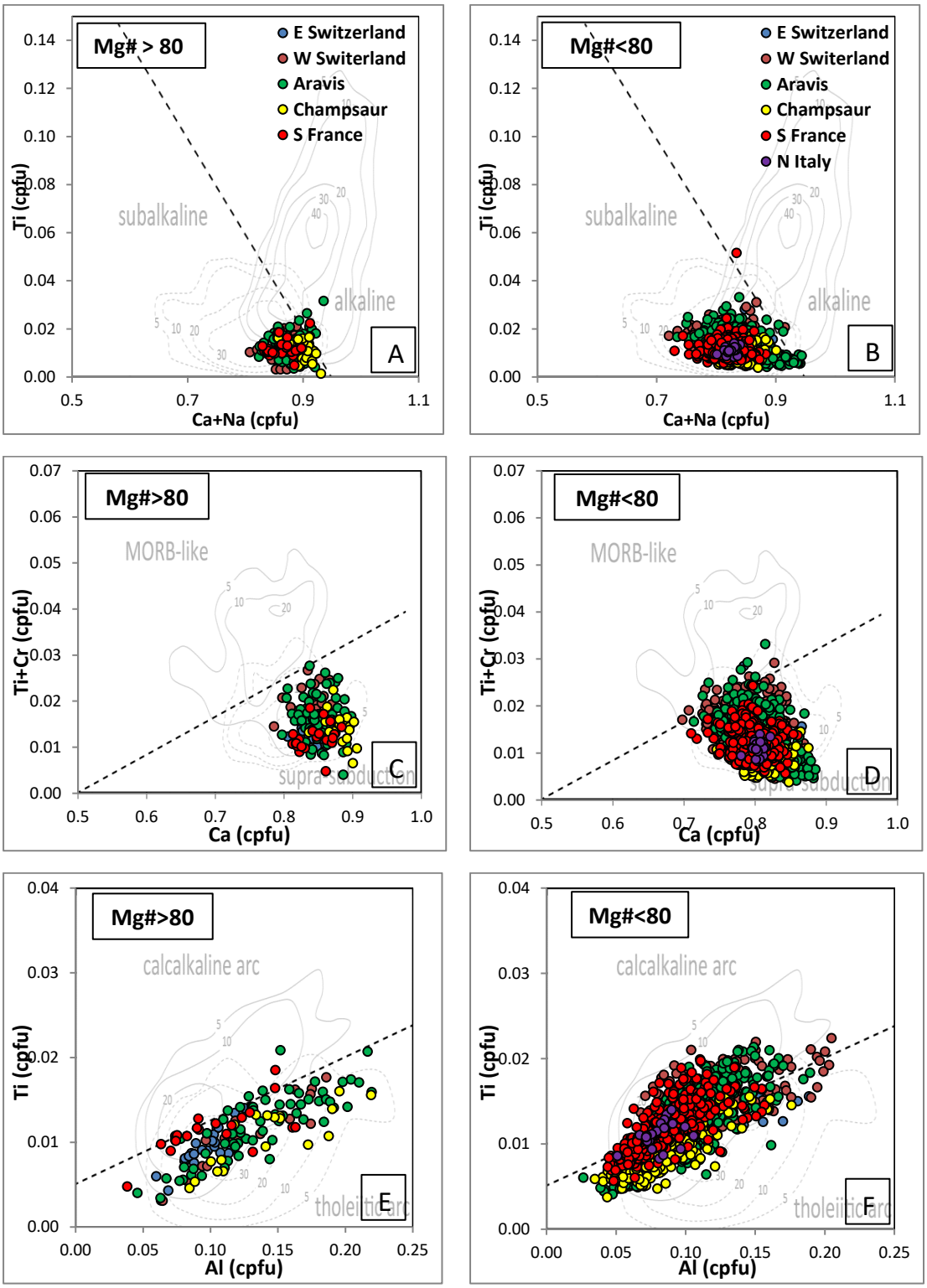

Figure 6.3 Tectonic discrimination diagrams of clinopyroxenes after Leterrier et al. (1982) applied to clinopyroxenes from all studied regions, including original density contours from Leterrier et al. (1982). Data expressed as cationic values from the structural formula of clinopyroxenes. No clinopyroxenes with Mg# > 80 in N Italy.

In order to better observe the variation trend among various localities and figure out how Mg# (magmatic differentiation) affects compositional ranges in distinct regions, clinopyroxenes of Mg# > 80 and Mg# < 80 are plotted separately on the tectonic discrimination diagrams after Leterrier et al. (1982) (Figure 6.3 A-F). Clinopyroxene compositions are largely overlapping in lower and higher Mg# ranges, with a few notable exceptions. First, there is a distinct range of Ca spread between clinopyroxenes of Mg# > 80 and Mg# < 80. In the higher Mg#, Ca varies mainly between 0.8 – 0.9 cpfu, whereas Ca ranges more broadly (0.7 – 0.9 cpfu) in lower Mg# values. Second, in the third pair of Al vs Ti diagram, clinopyroxenes from apparently more differentiated melts plot more often above the discrimination line. This phenomenon indicates that the Al vs Ti trend is not only controlled by tectonic affinity, but also could be influenced by magmatic differentiation.

In the first pair of discrimination diagrams (Figure 6.3 A-B), the vast majority of the clinopyroxenes from all studied regions have Sub-Alkaline affinity, with a small number of analyses falling above the dotted dividing line between Sub-Alkaline and Alkaline. On the second pair of discrimination diagrams (Figure 6.3 C-D), all clinopyroxenes of Mg# > 80 group plot in the Supra-Subduction field, whereas majority of the clinopyroxenes of Mg# < 80 group plot in the Supra-Subduction field with some grains mainly from W Switzerland and Aravis falling above the dotted dividing line between MORB-like and Supra-subduction field. Finally, on the third pair of discrimination diagrams (Figure 6.3 E-F), clinopyroxenes with Mg# >80 mainly plot in the Tholeiitic Arc field, whereas those with lower Mg# are more or less evenly plotted on both sides of the Calcalkaline-Tholeiitic Arc boundary line, indicating an Arc source of both calc-alkaline and tholeiitic affinity.

6.2.4 Binary diagrams (Mg# vs Trace elements)

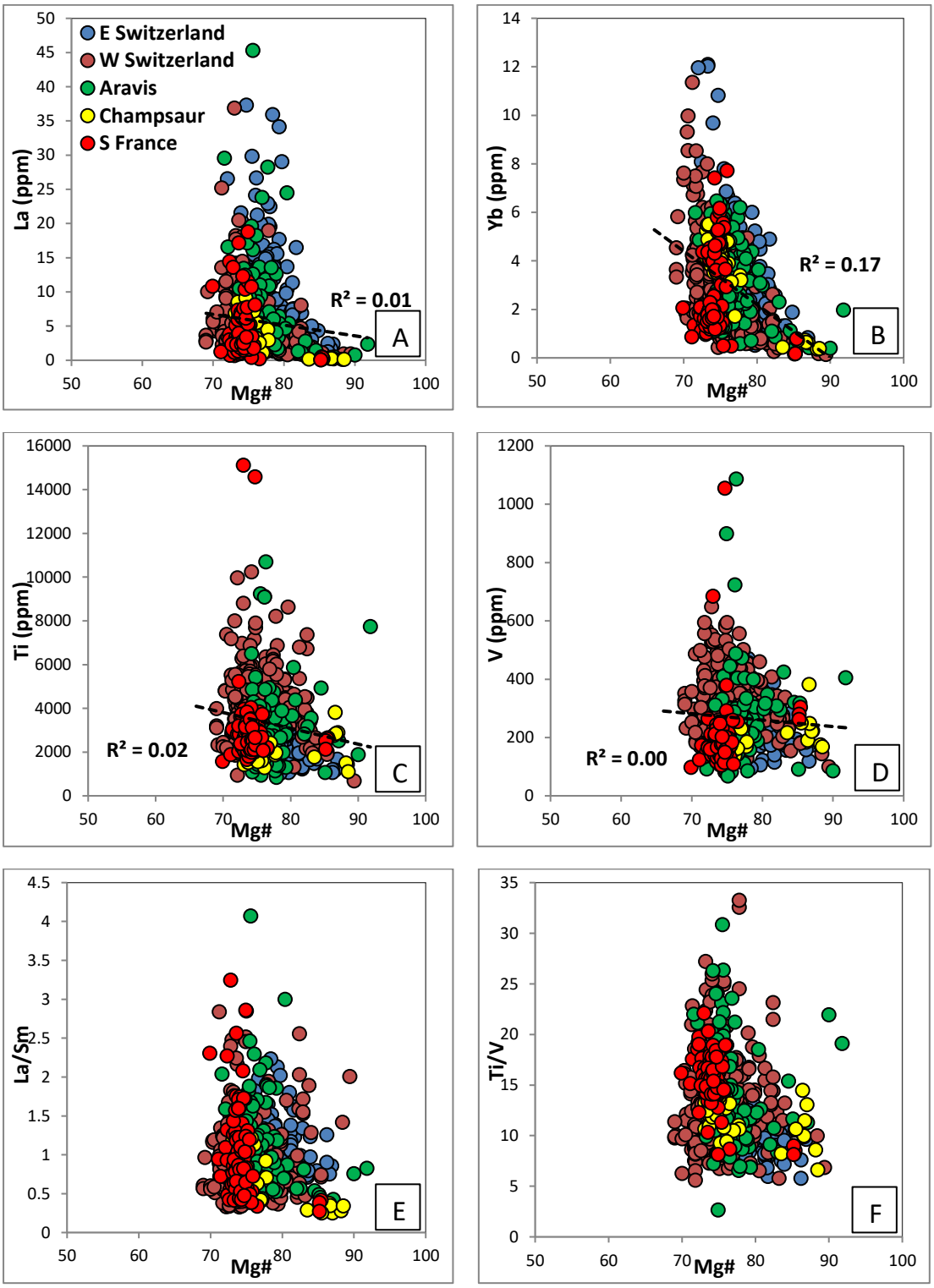

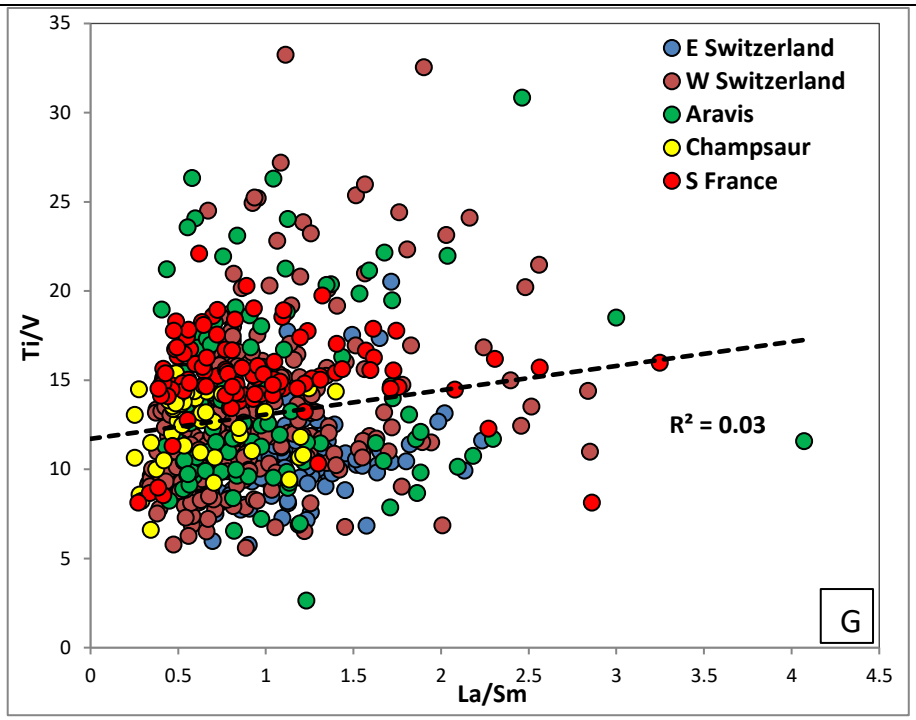

Figure 6.4 Binary diagrams of clinopyroxenes from all studied regions: A-D) selected trace element vs Mg#; E-F) selected trace element ratios vs Mg#; G) La/Sm vs Ti/V Note: no trace element data were collected for clinopyroxenes in N Italy.

On the Mg# vs selected trace element diagrams (Figure 6.4 A-D), no clear correlation (R^2 = 0.00 - 0.02) has been shown except for Yb, which has a moderate correlation (R^2 = 0.17) with Mg#. Those from S France have a narrow range of Mg# varying mainly between 70 – 77 compared with those from other regions whose Mg# mainly range between 70 - 90.

On the Mg# vs La/Sm diagram (Figure 6.4 E), most of the clinopyroxenes from W Switzerland and Aravis are plotted in a cluster. Those from E Switzerland have a distinctive, higher La/Sm and Mg# values. It should be noted that the clinopyroxenes from Champsaur with lower Mg# are overlapping with the main population. On the Mg# vs Ti/V diagram (Figure 6.4 F), most of the clinopyroxenes from W Switzerland and Aravis are plotted in a single cluster, and those from E Switzerland of lower Ti/V values are clearly plotted separately with those from S France of higher Ti/V values. It should be noted that part of clinopyroxenes from Champsaur of lower Mg# are overlapping with the main population.

On the La/Sm vs Ti/V diagram (Figure 6.4 G), it's clearly shown that most of the clinopyroxenes from W Switzerland and Aravis are plotted in cluster

without showing distinct variation, and those from E Switzerland of higher La/Sm values and lower Ti/V values are clearly plotted separately with those from S France of lower La/Sm values and higher Ti/V values. It should be noted that part of clinopyroxenes from Champsaur of lower Mg# are overlapping with the main population.

6.2.5 Summary

In summary, clinopyroxenes from all regions are generally classified as augite and with subordinate diopside. Compositional variability among the different regions is not recognised on the quadrilateral diagram.

On the binary diagrams (Mg# vs major elements), differentiation trends between Mg# and selected major elements are well documented. Compositional changes of the studied clinopyroxenes between different regions seem mostly controlled by magmatic differentiation effects, without a noticeable effect related to the compositionally contrasted parental melts. A same observation can be made for the Leterrier et al. (1982)'s discrimination diagrams, which do not support significant changes in the composition of the magmatic source(s) of the studied clinopyroxenes.

In contrast, trace element ratios at a given differentiation index (Mg#) reveal geochemical differences between the clinopyroxenes of different regions better. This is particularly clear using the La/Sm vs Ti/V diagram, where most of the clinopyroxenes from W Switzerland and Aravis plot over a large compositional spectrum. This probably indicates potentially broader volcanic sources providing sediments to the basin. Those from E Switzerland of higher La/Sm values and lower Ti/V values are clearly plotted separately with those from S France of lower La/Sm values and higher Ti/V values. This represents the different sources of clinopyroxenes between E Switzerland and S France. As for those from Champsaur, part of the clinopyroxenes is overlapping with S France population, indicating that some clinopyroxenes from Champsaur either derived from S France or share common volcanic system with those from S France.

6.3 Inter-locality discrimination

Discrimination of clinopyroxenes within regions including several localities (i.e., W Switzerland, Aravis, and S France) was conducted using the same selection

of diagrams presented above. Eastern Switzerland (Glarus) and Champsaur both only include one locality, which was discussed in Section 6.2.

6.3.1 Western Switzerland

This region includes a total of 1328 SEM analyses (352 detrital clinopyroxenes) and 334 LA-ICP-MS analyses (222 detrital clinopyroxenes) from 10 samples of volcaniclastic sandstone.

6.3.1.1 Classification of clinopyroxene

Overall, all clinopyroxenes from the five localities (Taveyannaz, Chaux Ronde, Creux de Champ, La Laya, La Tièche) in Western Switzerland foreland basins have similar compositions. The majority of detrital clinopyroxenes are Mg-augite with subordinate diopside (Figure 6.5).

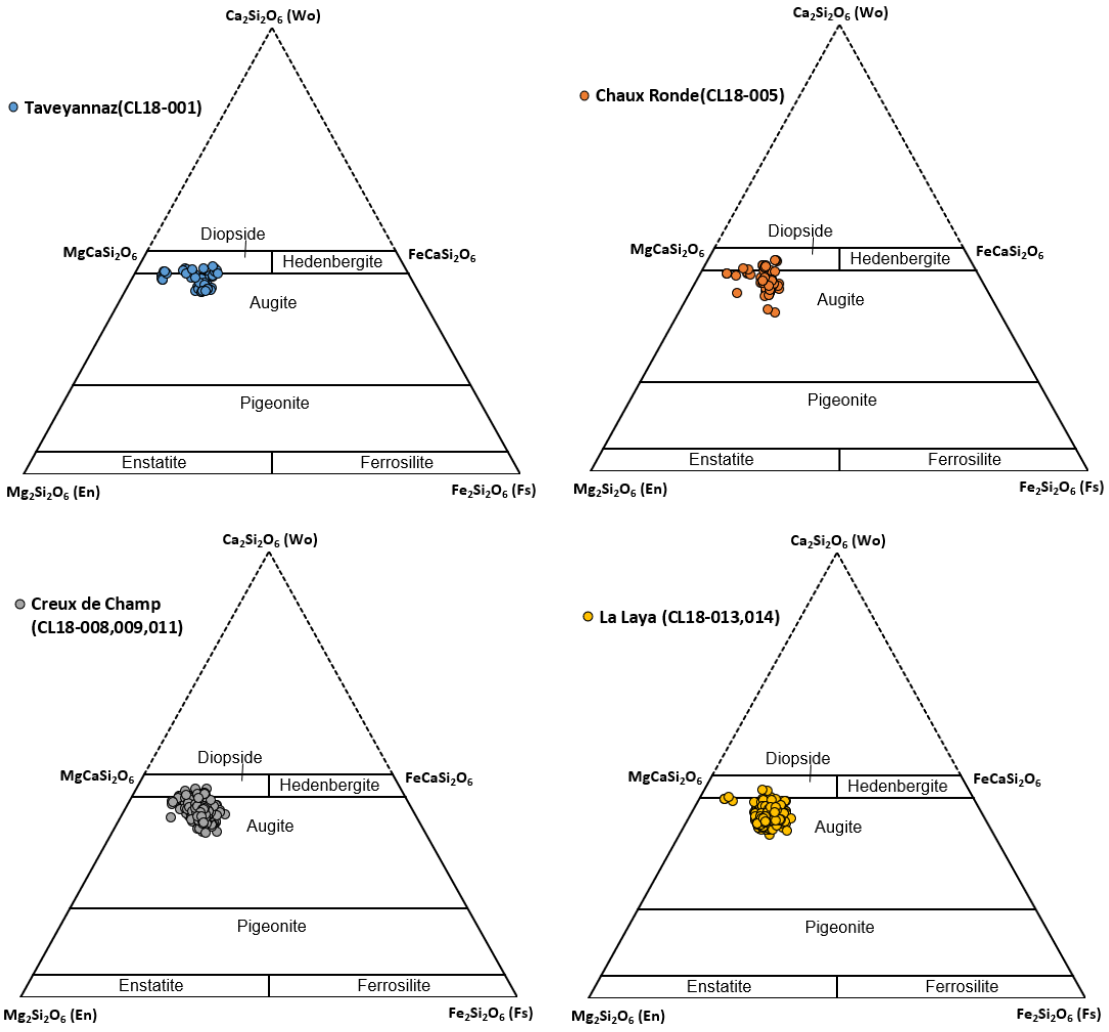

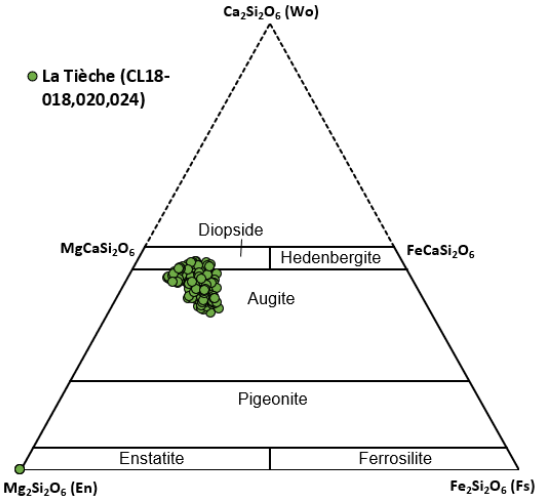

Figure 6.5 Clinopyroxene classification diagram of detrital clinopyroxenes from five localities of Western Switzerland region (After nomenclature of Morimoto et al., 1988).

6.3.1.2 Tectonic discrimination diagram

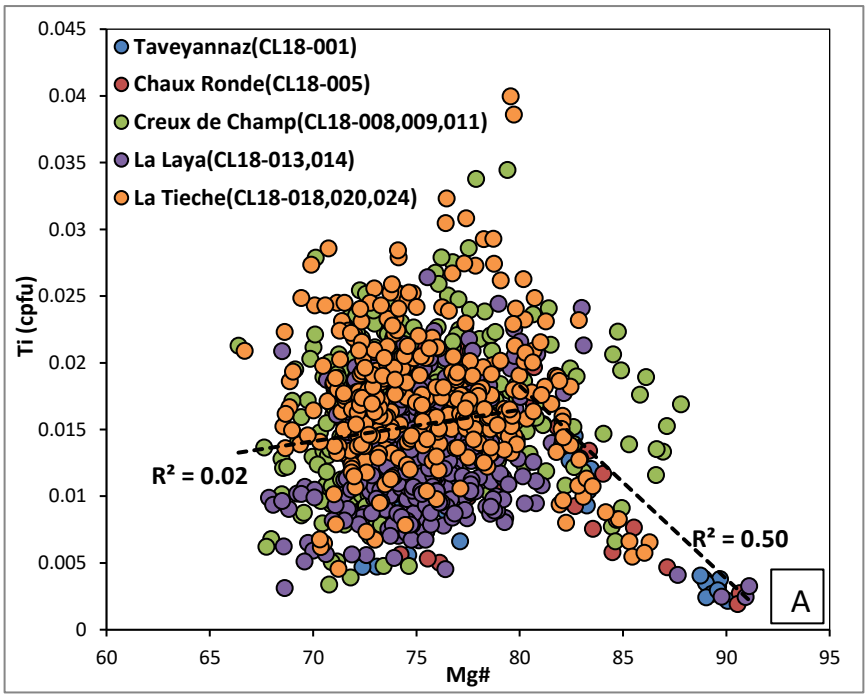

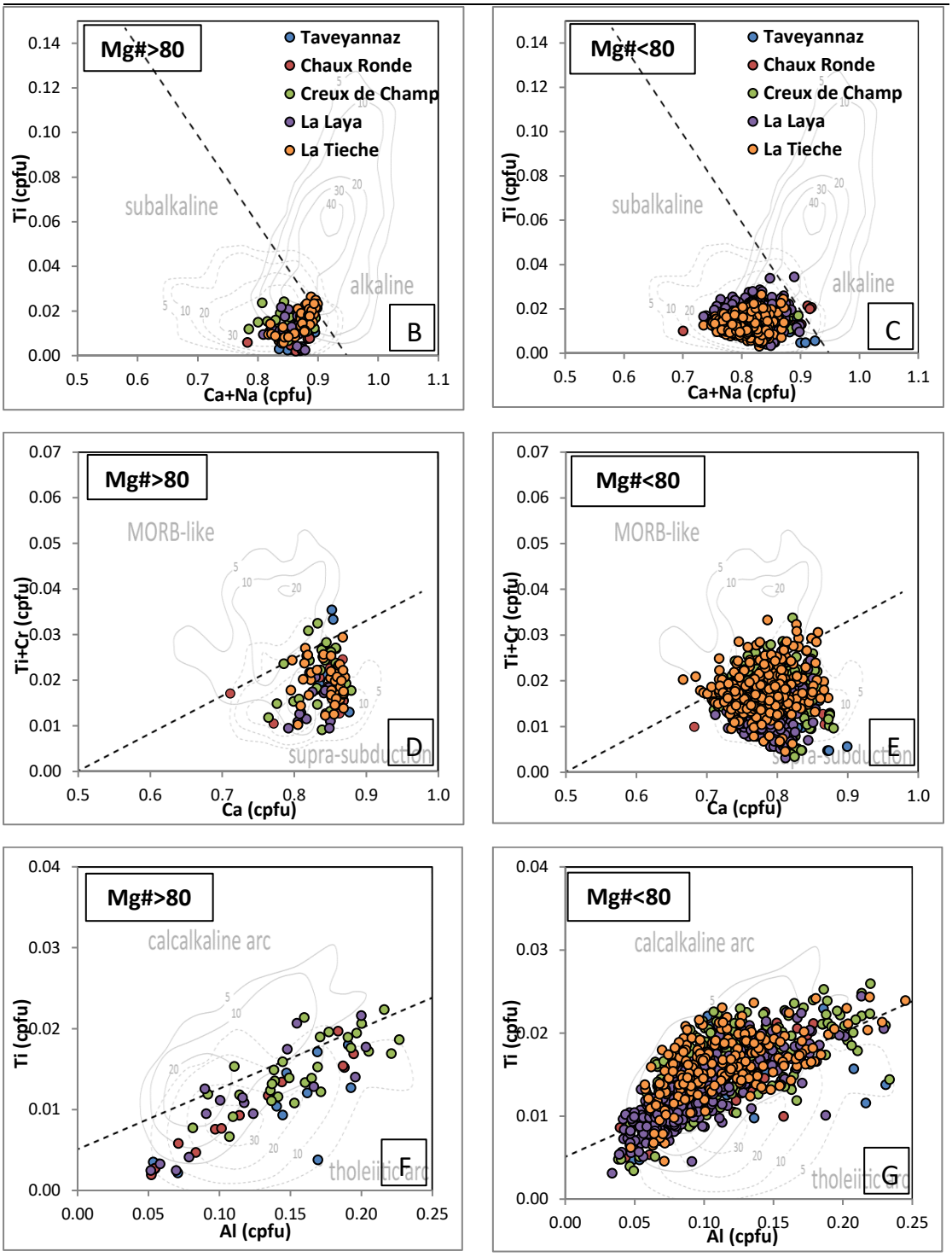

Figure 6.6 Tectonic discrimination diagrams of clinopyroxenes after Leterrier et al. (1982) applied to detrital clinopyroxenes from Western Switzerland foreland basins, including original density contours from Leterrier et al. (1982). Data expressed as cationic values from the structural formula of clinopyroxenes.

On the binary diagrams (Figure 6.6 A), the majority of clinopyroxenes have Mg# varying between 70 - 85, especially for clinopyroxenes from La Laya locality (Mg# < 80). With decreasing Mg#, Ti increases at high Mg# range (Mg# > 80), showing good correlation (R^2 = 0.80). At lower Mg# range (Mg# <

80), Ti content appears to not have a clear trend, with a poor correlation (R^2 = 0.01) with Mg#. For both groups, all clinopyroxenes in this region have Sub-Alkaline affinity in the first discrimination diagram (Figure 6.6 B-C), with only one exception from Chaux Ronde falling above the boundary line between Sub-Alkaline and Alkaline field. On the second discrimination diagram (Figure 6.6 D-E), all clinopyroxenes of both groups plot in the Supra-Subduction field, with only few grains from Mg# < 80 group falling above the boundary line. Finally, on the third discrimination diagram (Figure 6.6 F-G), clinopyroxenes with high Mg# are plotted mainly below the Calcalkaline-Tholeiitic Arc boundary line, indicating a Tholeiitic Arc affinity, whereas those with lower Mg# are mostly plotted in the Calcalkaline Arc field above the boundary line. This phenomenon is consistent with the Al vs Ti trend shown in Section 6.2, indicating that Ti vs Al trend is not only controlled by tectonic affinity, but also could be influenced by magmatic differentiation.

6.3.1.3 Representative binary diagrams

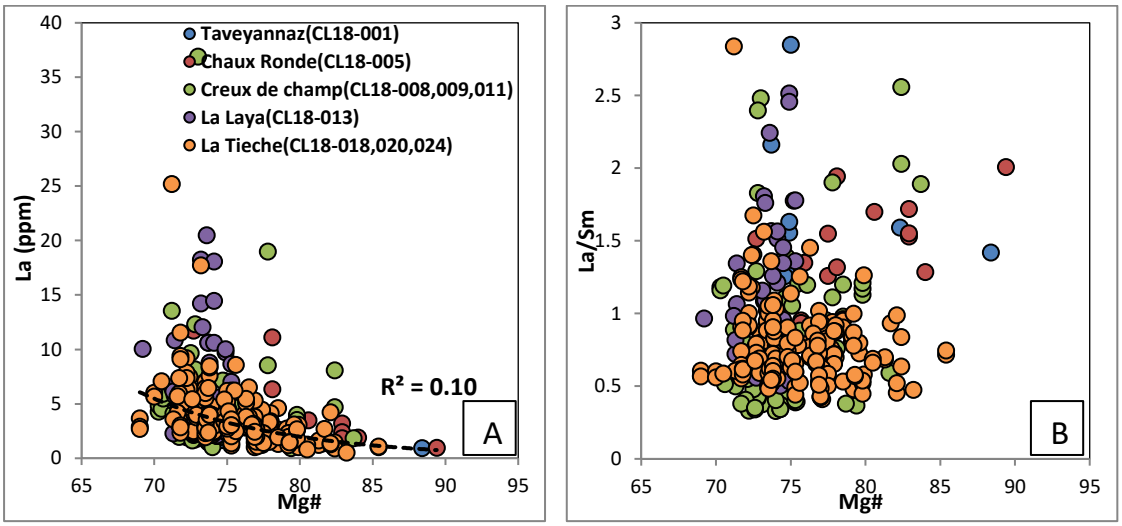

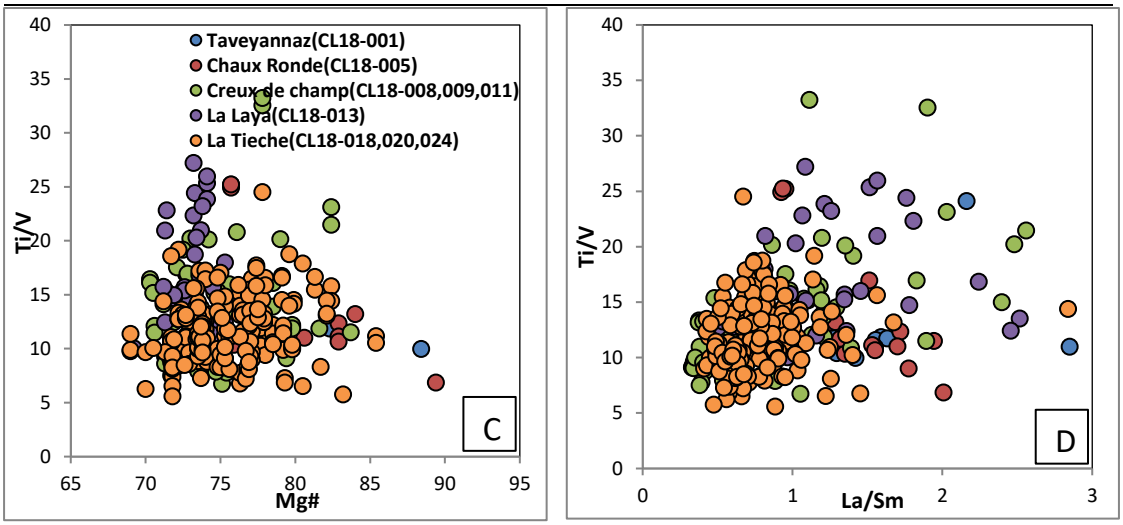

Figure 6.7 Binary diagrams of clinopyroxenes from all localities of Western Switzerland: A-C) selected trace element (ratios) vs Mg#; D) La/Sm vs Ti/V

Most of the clinopyroxenes from all regional localities in W Switzerland are plotted in cluster without showing distinct variation in the binary diagrams (Figure 6.7). On the best discriminative La/Sm vs Ti/V diagram (Figure 6.7 D), majority of clinopyroxenes are overlapping in cluster, except that a small amount of those from Creux de Champ and La Laya localities distinguish themselves with higher La/Sm and Ti/V ratios from the main overlapping population.

6.3.2 Aravis (Haute-Savoie)

This region includes a total of 2192 SEM analyses (732 clinopyroxenes) from 13 samples of volcaniclastic sandstone and 1 sample of andesitic clast and 100 LA-ICP-MS analyses (100 clinopyroxenes) from 5 samples of volcaniclastic sandstone.

6.3.2.1 Classification of clinopyroxene

All clinopyroxenes from the four localities (Flaine, Col de l'Oulettaz, La Clusaz and Thones) in Aravis foreland basins have similar composition with a small range of variation. The majority of clinopyroxenes in this region are Mg-augite and diopside, having slightly higher Ca^{2+} concentration than those clinopyroxenes from Western Switzerland (Figure 6.8).

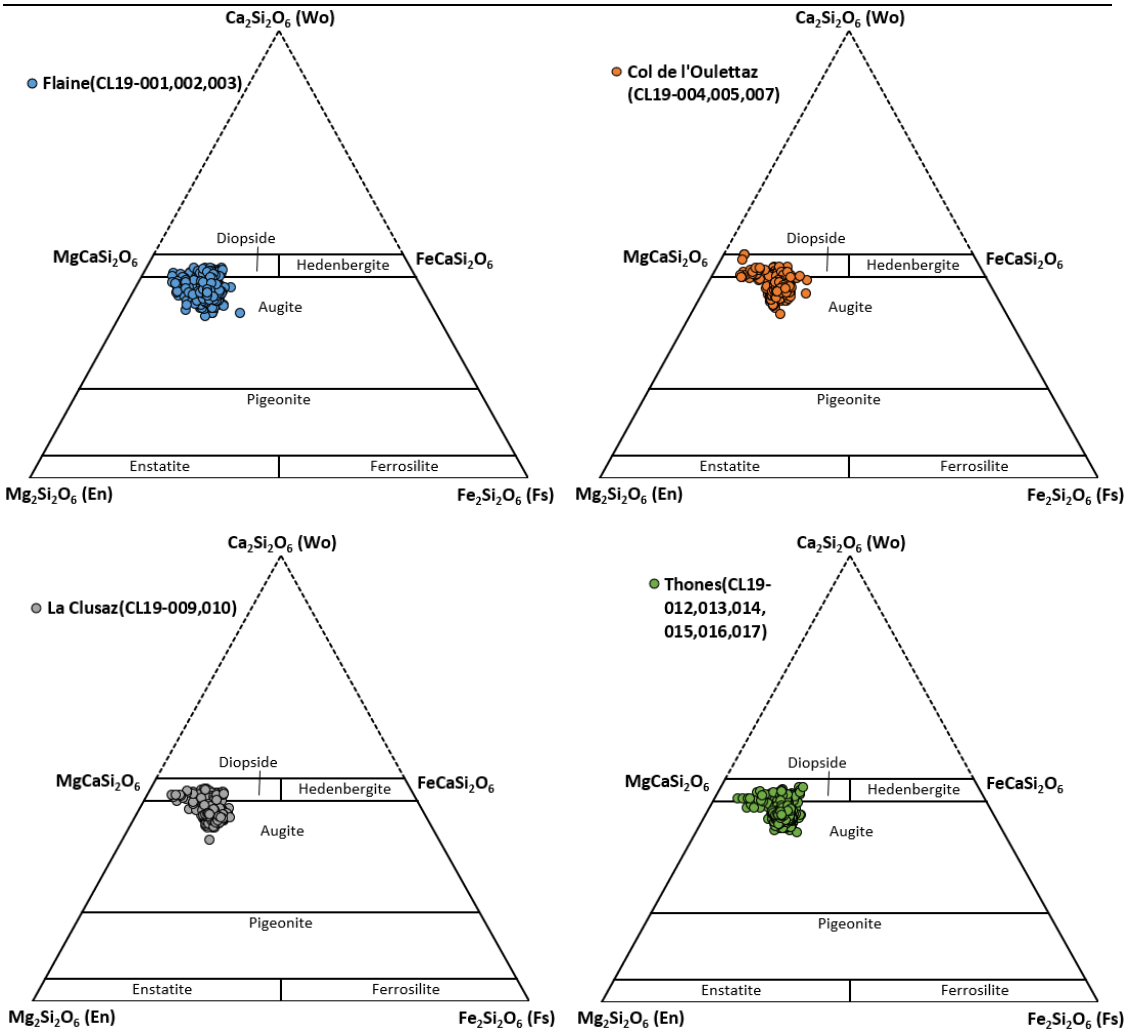

Figure 6.8 Clinopyroxene classification diagram of clinopyroxenes from four localities of Aravis (After nomenclature of Morimoto et al., 1988).

6.3.2.2 Tectonic discrimination diagrams

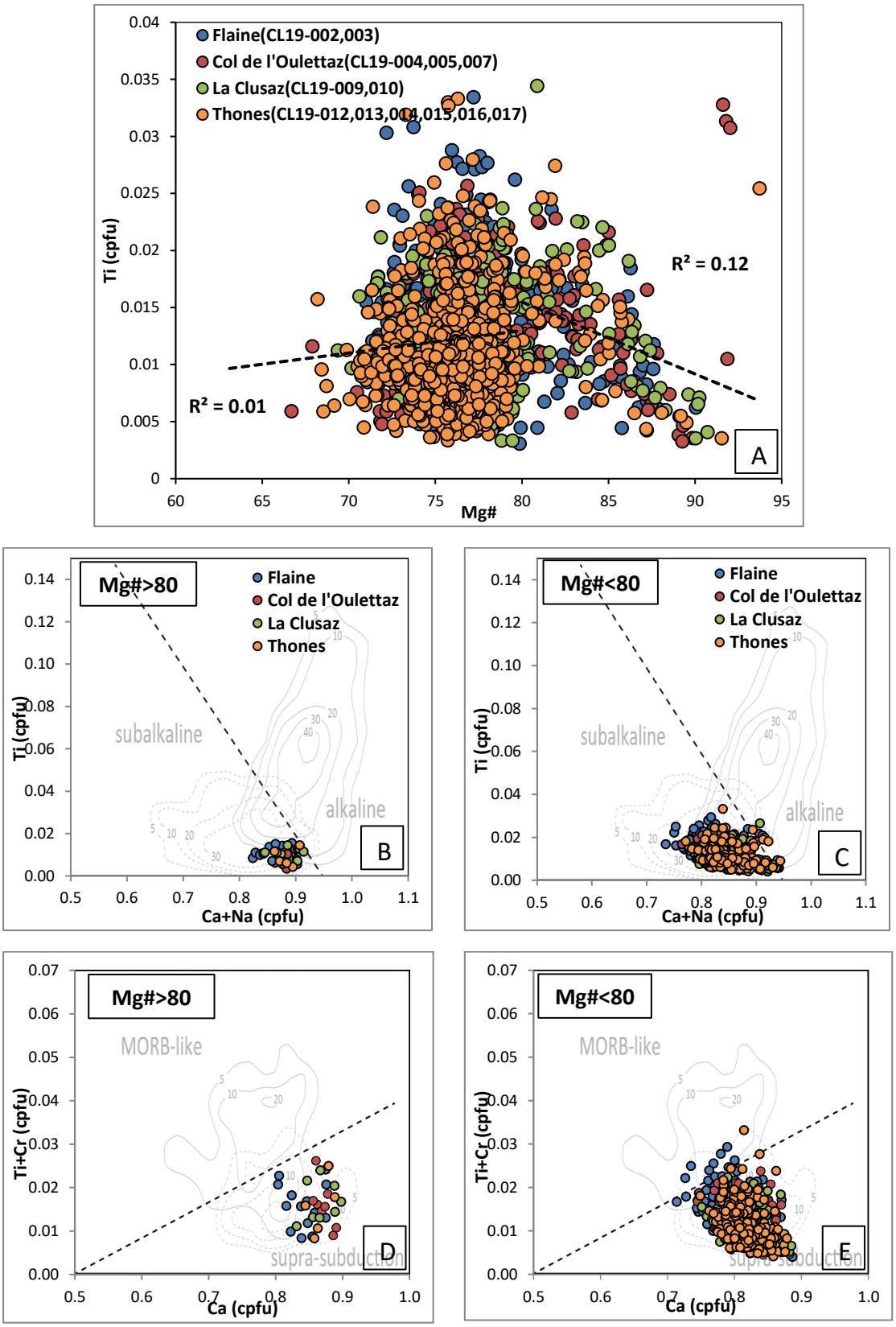

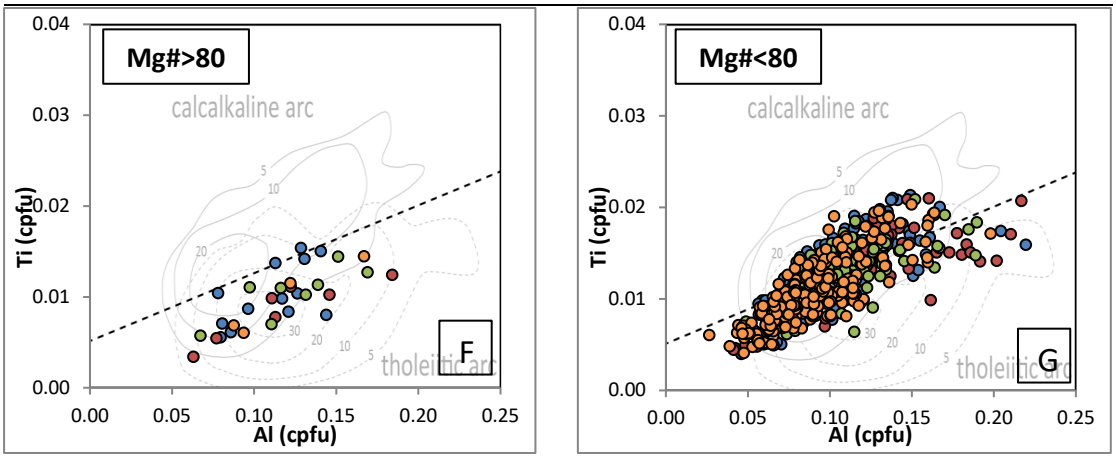

Figure 6.9 Tectonic discrimination diagrams of clinopyroxenes after Leterrier et al. (1982) applied to clinopyroxenes from Aravis foreland basins, including original density contours from Leterrier et al. (1982). Data expressed as cationic values from the structural formula of clinopyroxenes.

On the Mg# vs Ti variation diagrams (Figure 6.9 A), the majority of clinopyroxenes have Mg# varying between 70 – 90. With decreasing Mg#, Ti increases at high Mg# range (80 - 90) (R^2 = 0.12). At lower Mg# range (70 - 80), Ti content appears to not have a clear trend (R^2 = 0.01).

Clinopyroxenes of Mg# > 80 and Mg# < 80 are separately plotted on a series of tectonic discrimination diagrams (Figure 6.9 B-G) after Leterrier et al. (1982). For both groups, the vast majority of clinopyroxenes in this region have Sub-Alkaline affinity in the first discrimination diagram (Figure 6.9 B-C), with only few exceptions from La Clusaz falling above the boundary line between Sub-Alkaline and Alkaline field. On the second discrimination diagram (Figure 6.9 D-E), all clinopyroxenes of high Mg# (> 80) plot in the Supra-Subduction field, whereas some clinopyroxenes of Mg# < 80 group from Flaine falling above the boundary line between MORB-like and Supra-Subduction field. Finally, on the third discrimination diagram (Figure 6.9 F-G), clinopyroxenes of Mg# > 80 are all plotted below the boundary line, whereas those of Mg# < 80 fall on the both sides of the boundary line, indicating an Arc source of both calc-alkaline and tholeiitic affinity.

6.3.2.3 Representative binary diagrams

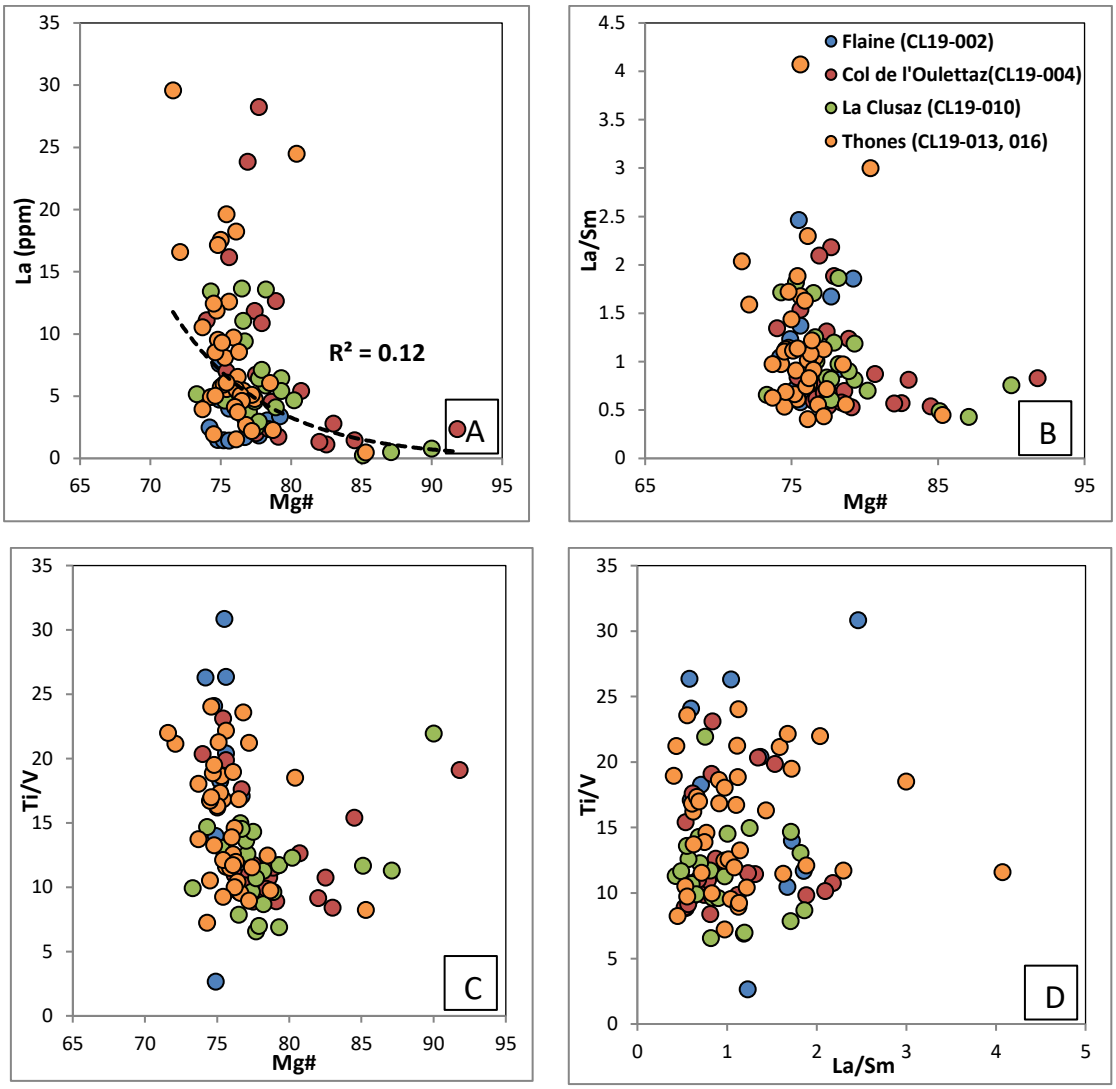

Figure 6.10 Binary diagrams of clinopyroxenes from all localities of Aravis: A-C) selected trace element (ratios) vs Mg#; D) La/Sm vs Ti/V

Most of the clinopyroxenes from all localities in northern SE France are plotted in cluster without showing distinct variation in the binary diagrams (Figure 6.10). On the best discriminative La/Sm vs Ti/V diagram (Figure 6.10 D), the majority of clinopyroxenes are overlapping in cluster, with similar range of spreading for clinopyroxenes of all localities.

6.3.3 Southern France

This region includes a total of 1474 SEM analyses (493 clinopyroxenes) from 12 samples of primary/proximal volcaniclastic deposits and 108 LA-ICP-MS analyses (108 clinopyroxenes) from 6 samples of andesitic clasts in volcanic breccias.

6.3.3.1 Classification of clinopyroxene

All clinopyroxenes from the three regional localities (Fontagne, Les Beylons, La Vanade) in S France have similar composition with a small range of variation. The majority of the clinopyroxenes in this region are Mg-augite with subordinate diopside, except for those from Les Beylons which are all augite (Figure 6.11).

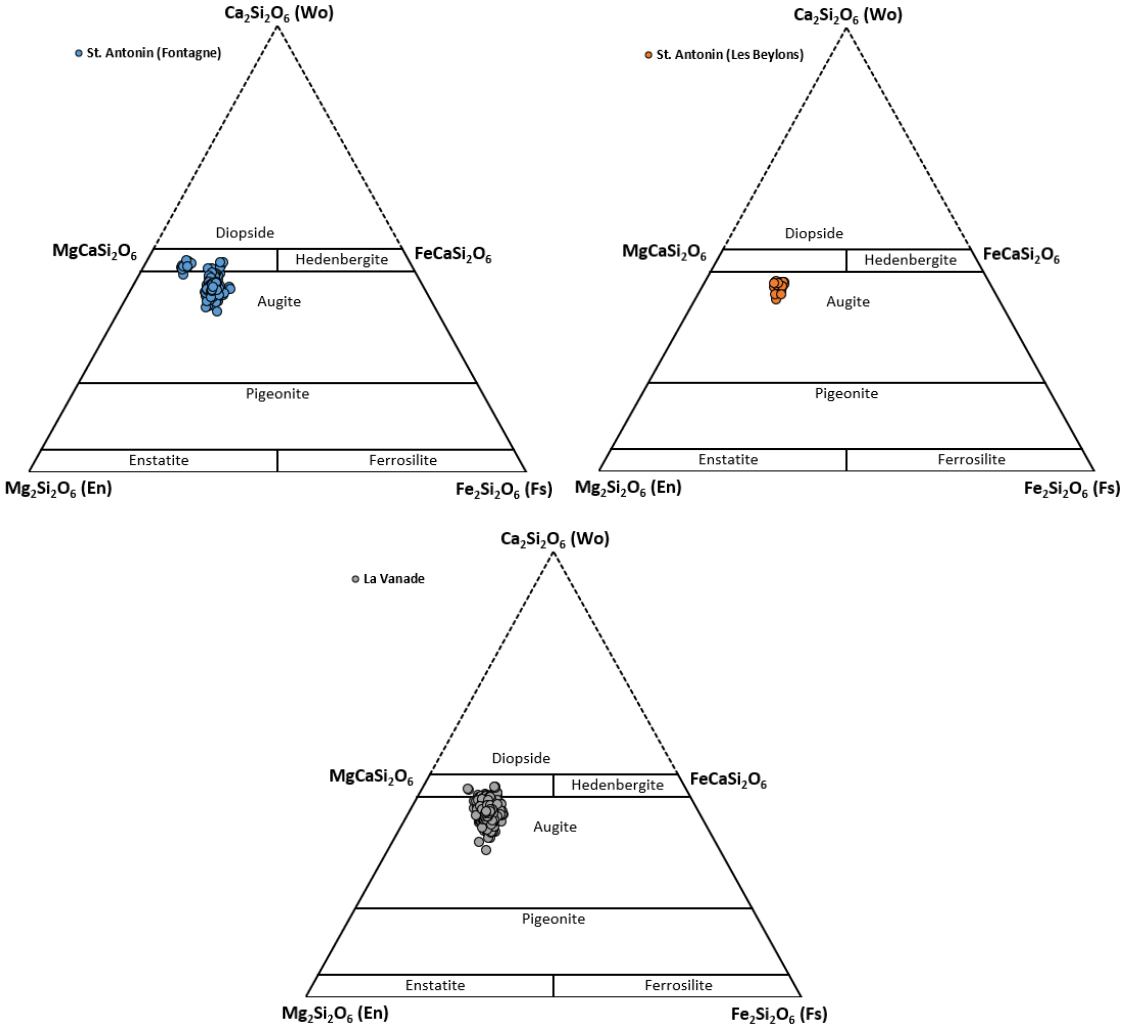

Figure 6.11 Clinopyroxene classification diagram of clinopyroxenes from three localities of S France (After nomenclature of Morimoto et al., 1988).

6.3.3.2 Tectonic discrimination diagrams

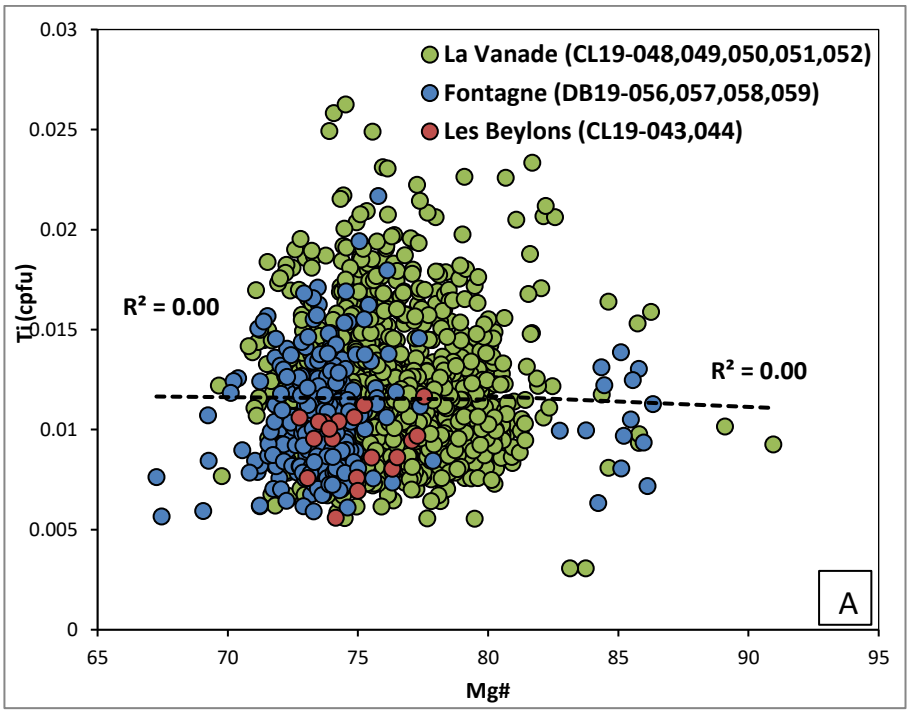

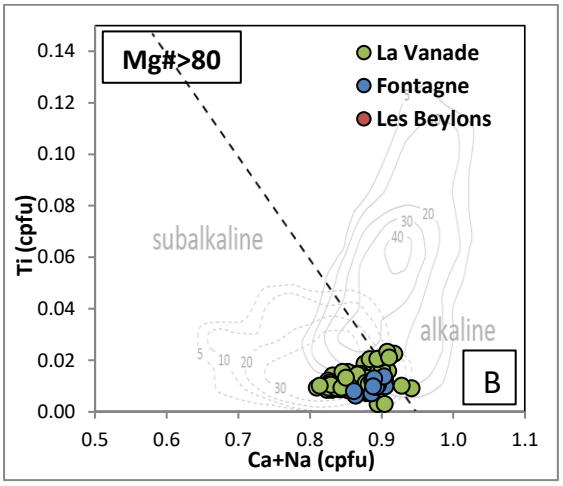

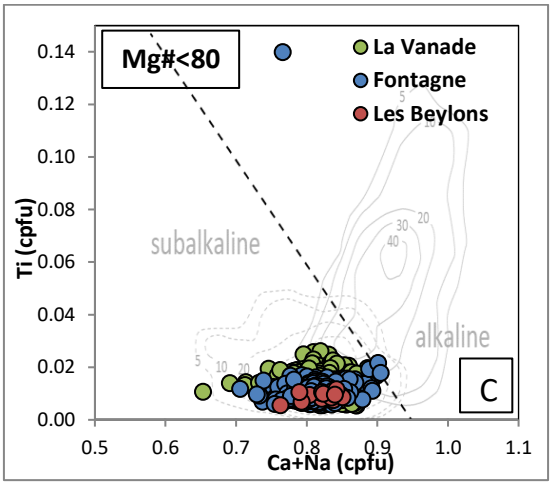

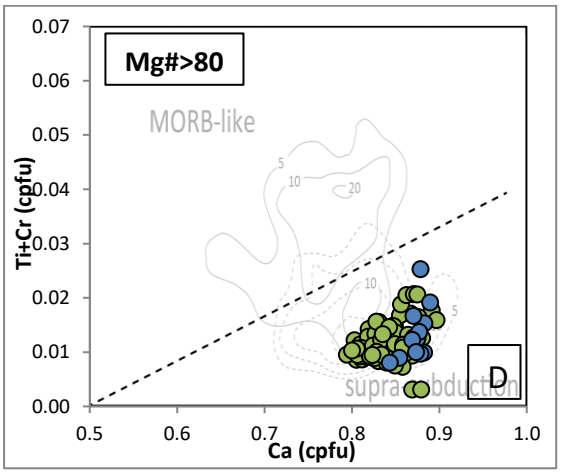

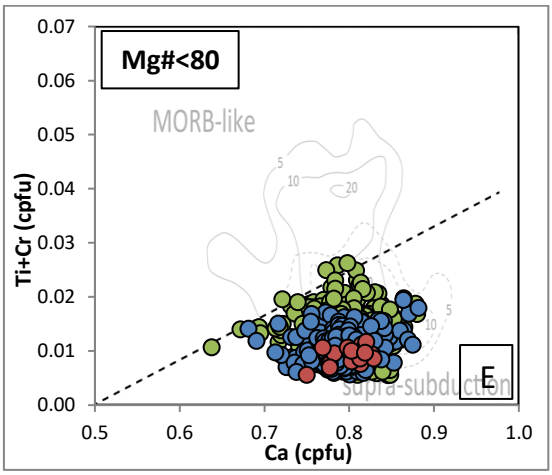

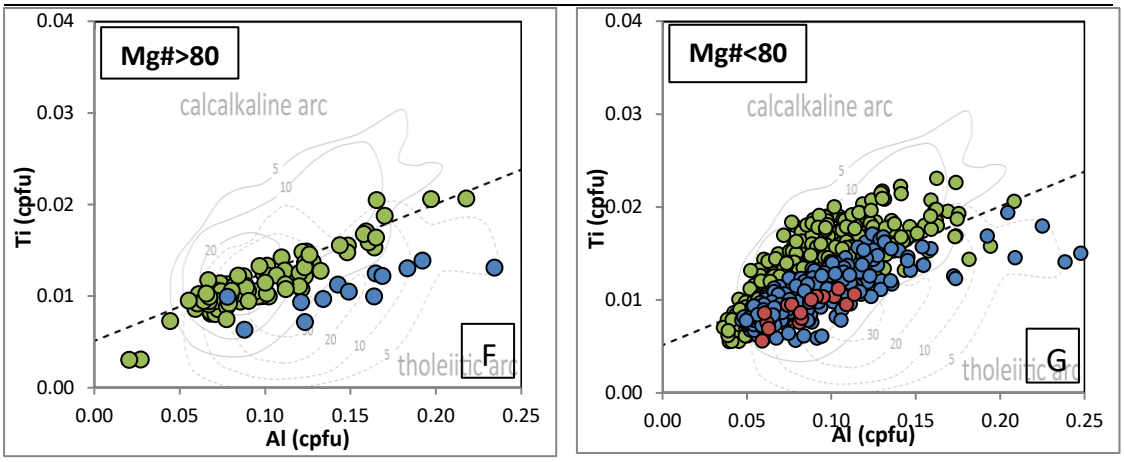

Figure 6.12 Tectonic discrimination diagrams of clinopyroxenes after Leterrier et al. (1982) applied to clinopyroxenes from S France, including original density contours from Leterrier et al. (1982). Data expressed as cationic values from the structural formula of clinopyroxenes.

On the binary diagrams (Figure 6.12 A), the majority of clinopyroxenes have Mg# varying between 70 - 80. With decreasing Mg#, Ti shows no correlation ($R^2 = 0$) for both high and low Mg# range. In the first pair of discrimination diagrams (Figure 6.12 B-C), vast majority of the clinopyroxenes have Sub-Alkaline affinity, with a small number of spots falling above the boundary line between Sub-Alkaline and Alkaline. In the second pair of discrimination diagrams (Figure 6.12 D-E), all clinopyroxenes of Mg# > 80 plot in the Supra-Subduction field, whereas the majority of the clinopyroxenes of Mg# < 80 plot in the Supra-Subduction field with some clinopyroxenes mainly from La Vanade falling above the boundary line between MORB-like and Spura-subduction. Finally, in the third pair of discrimination diagrams (Figure 6.12 F-G), clinopyroxenes of Mg# > 80 mainly plot in the Tholeiitic Arc field, whereas those with Mg# < 80 more or less evenly plot on both sides of the Calcalkaline-Tholeiitic Arc boundary line, indicating an Arc source of both calc-alkaline and tholeiitic affinity. It is noteworthy that clinopyroxenes from La Vanade are generally more calc-alkaline, plotted above those from St. Antonin with lower Ti/Al ratio.

6.3.3.3 Representative binary diagrams

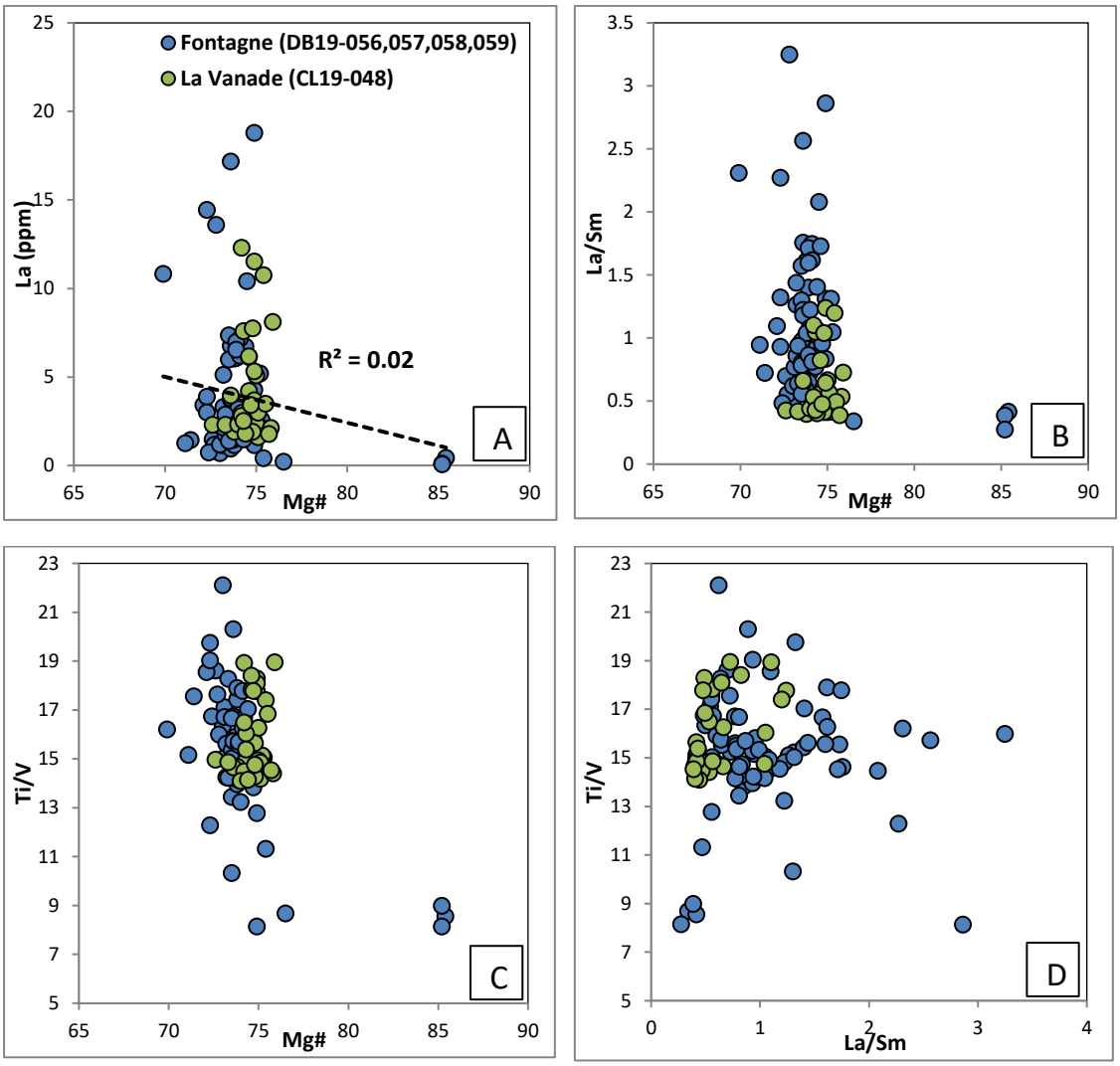

Figure 6.13 Binary diagrams of clinopyroxenes from three localities of southern SE France: A-B) selected trace element ratios vs Mg#; C) La/Sm vs Ti/V; D) Ca vs La; E) Ca vs Yb.

In the most discriminative La/Sm vs Ti/V diagram (Figure 6.13 D), clinopyroxenes from Fontagne are separated with those from La Vanade by higher La/Sm ratio and wider range of spreading.

6.3.4 Summary

In summary, most of the clinopyroxenes from localities in W Switzerland and Aravis generally plot in cluster without showing distinct variation in the classification diagrams, tectonic discrimination diagrams and binary diagrams. However, clinopyroxenes from S France localities are better discriminated by the tectonic discrimination diagrams where those from St. Antonin basin (Fontagne and Les Beylons) are characterised by lower Ti, and plot in the

Tholeiitic Arc field in contrast to those from La Vanade, characterised by higher Ti, plotted in the Calcalkaline Arc field. In the trace element binary diagrams, especially the best discriminative La/Sm vs Ti/V diagram, clinopyroxenes from Fontagne and La Vanade are also clearly discriminated.

6.4 Inter-sample discrimination

Discrimination of clinopyroxenes from various samples (more than one sample) within one single locality was conducted using the same selection of diagrams presented above, in order to outline possible differences of supply between stratigraphically similar samples. The localities including only one sample which have been discussed in Section 6.3 are not discussed in this section.

6.4.1 Creux de Champ (W Switzerland)

This locality includes a total of 398 SEM analyses (112 detrital clinopyroxenes) and 73 LA-ICP-MS analyses (55 detrital clinopyroxenes) from 3 samples of volcaniclastic sandstone.

6.4.1.1 Classification of clinopyroxene

All clinopyroxenes from the Creux de Champ locality in Western Switzerland have similar composition with a small range of variation. The majority of detrital clinopyroxenes are Mg-augite with subordinate diopside (Figure 6.14).

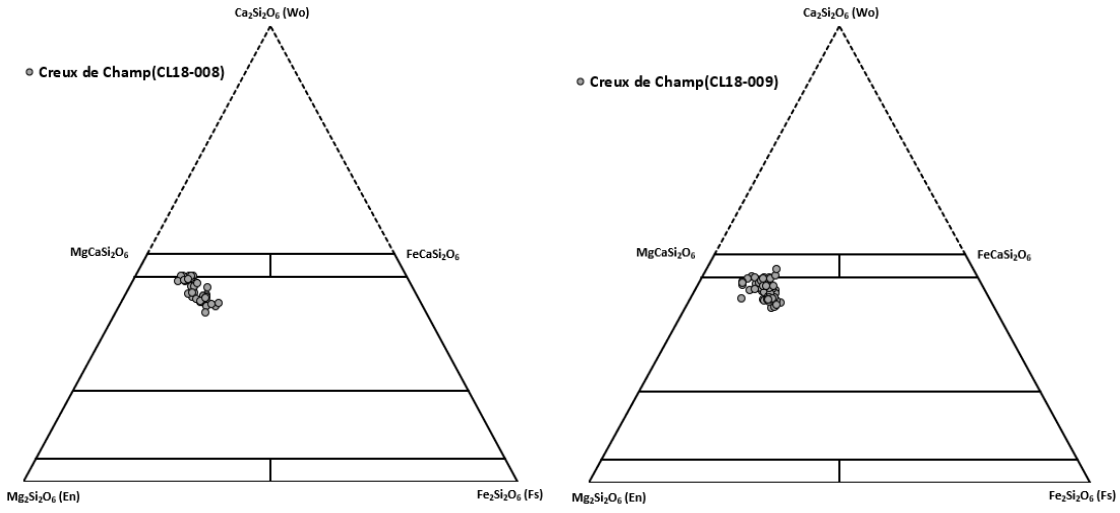

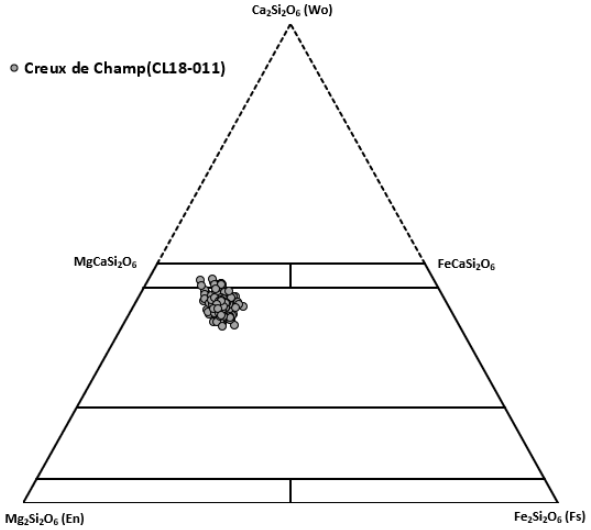

Figure 6.14 Clinopyroxene classification diagram of detrital clinopyroxenes from Creux de Champ locality of Western Switzerland (After nomenclature of Morimoto et al., 1988).

6.4.1.2 Tectonic discrimination diagrams

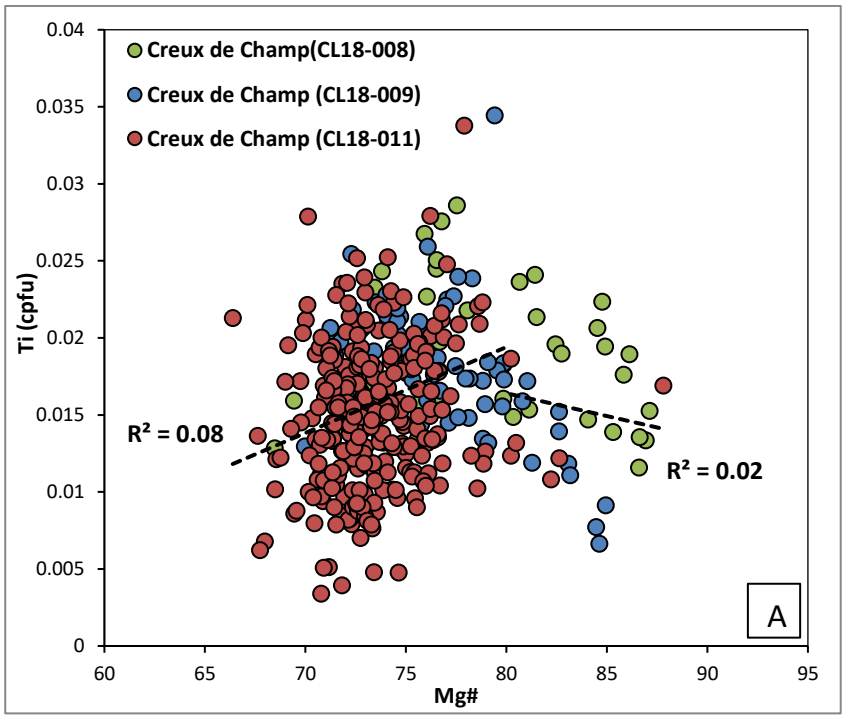

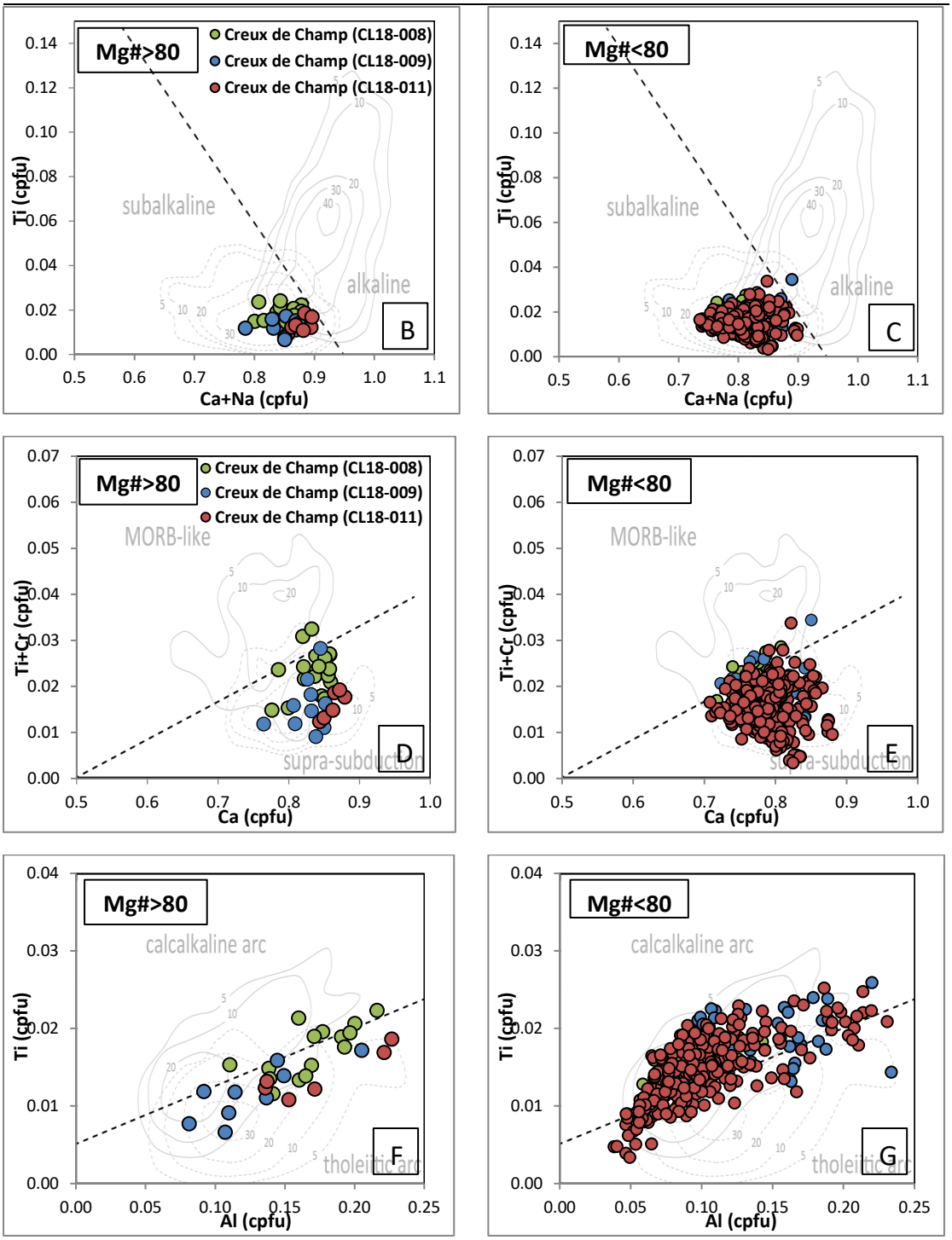

Figure 6.15 Tectonic discrimination diagrams of clinopyroxenes after Leterrier et al. (1982) applied to clinopyroxenes from Creux de Champ locality, including original density contours from Leterrier et al. (1982). Data expressed as cationic values from the structural formula of clinopyroxenes.

On the binary diagrams (Figure 6.15 A), the majority of clinopyroxenes have Mg# varying between 70 - 85. With decreasing Mg#, Ti shows poor correlation (R^2 = 0.02 and 0.08 respectively) for both high and low Mg# range. Overall compositional similarity is clearly shown on the Leterrier et al. (1982)

discrimination diagrams (Figure 6.15 B-G). In the first pair of discrimination diagrams (Figure 6.15 B-C), the vast majority of the clinopyroxenes of both groups have Sub-Alkaline affinity. In the second pair of discrimination diagrams (Figure 6.15 D-E), most of the clinopyroxenes of both groups plot in the Supra-Subduction field with few clinopyroxenes falling above the boundary line between MORB-like and Spura-subduction. Finally, in the third pair of discrimination diagrams (Figure 6.15 F-G), clinopyroxenes of Mg# > 80 mainly plot in the Tholeiitic Arc field, whereas those with Mg# < 80 more or less evenly plot on both sides of the Calcalkaline-Tholeiitic Arc boundary line, indicating an Arc source of both calc-alkaline and tholeiitic affinity.

6.4.1.3 Representative binary diagrams

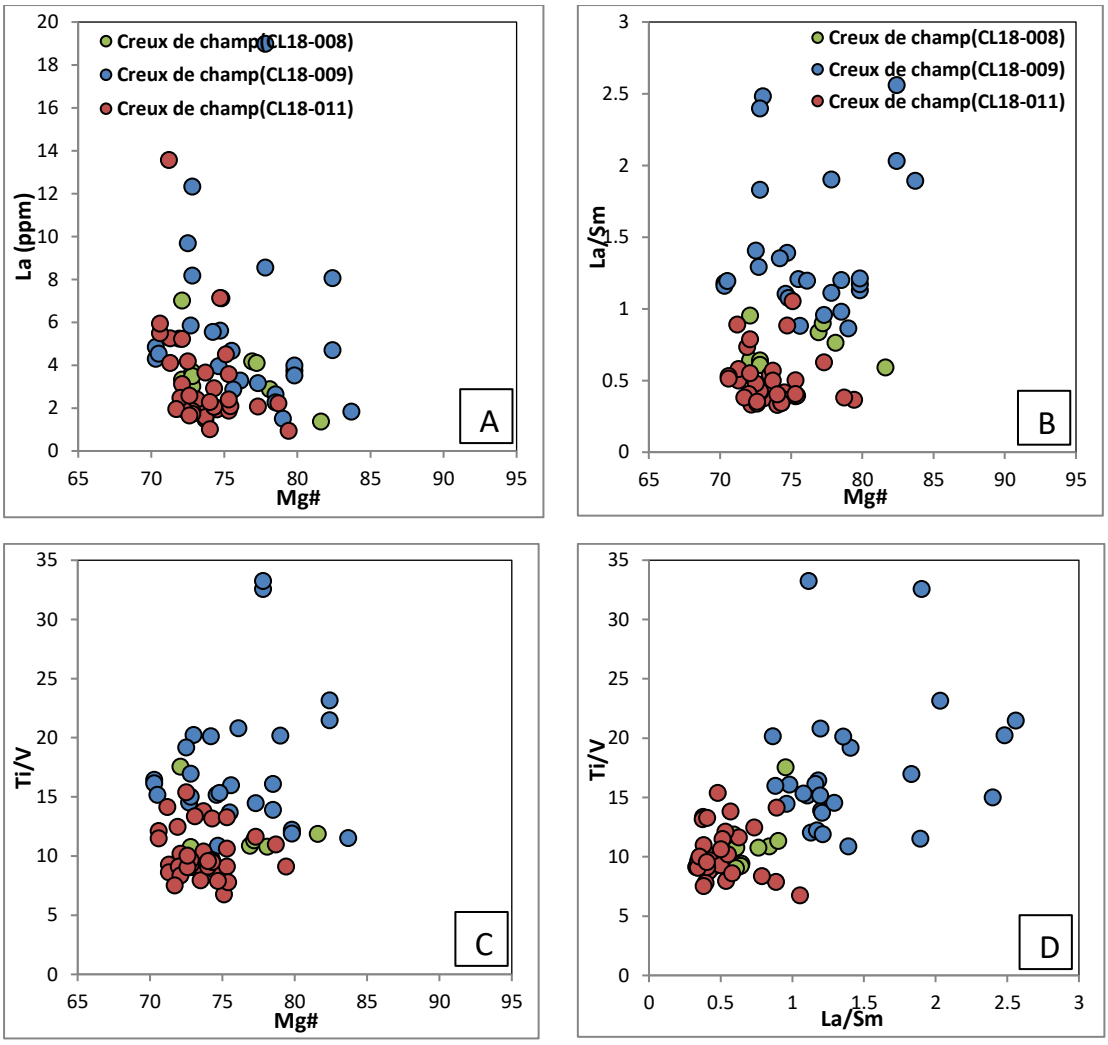

Figure 6.16 Binary diagrams of clinopyroxenes from three sandstones in Creux de Champ locality: A-C) selected trace element (ratios) vs Mg#; D) La/Sm vs Ti/V

On the binary diagrams of trace elements (Figure 6.16), the clinopyroxenes are well discriminated. The clinopyroxenes of sample CL18-009 are

characterised by higher La/Sm (> 1) and Ti/V (> 10), whereas those of sample CL18-011 have lower La/Sm (< 1) and Ti/V (< 15). Sample CL18-008 clinopyroxenes plot generally in between.

6.4.2 La Tièche (W Switzerland)

This locality includes a total of 298 SEM analyses (97 detrital clinopyroxenes) and 198 LA-ICP-MS analyses (94 detrital clinopyroxenes) from 3 samples of volcaniclastic sandstone.

6.4.2.1 Classification of clinopyroxene

All clinopyroxenes from the La Tièche locality in Western Switzerland have similar composition with a small range of variation. The majority of detrital clinopyroxenes are Mg-augite with subordinate diopside (Figure 6.17).

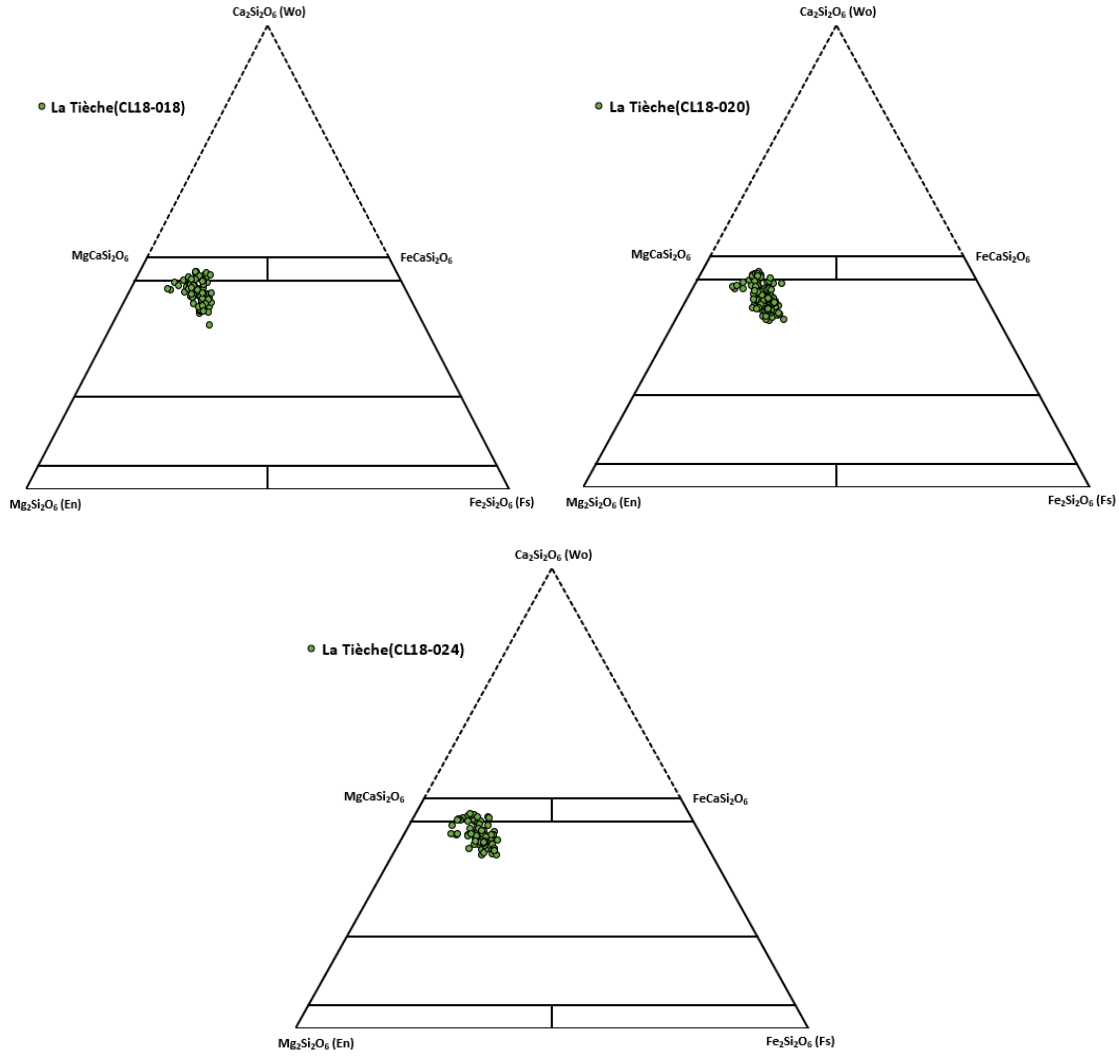

Figure 6.17 Clinopyroxene classification diagram of detrital clinopyroxenes from La Tièche locality of Western Switzerland (After nomenclature of Morimoto et al., 1988).

6.4.2.2 Tectonic discrimination diagrams

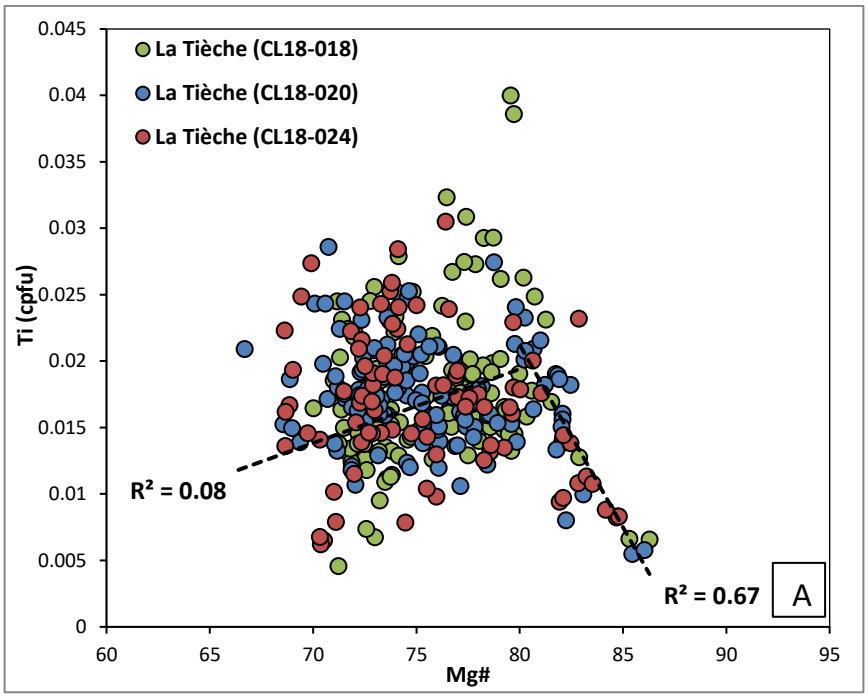

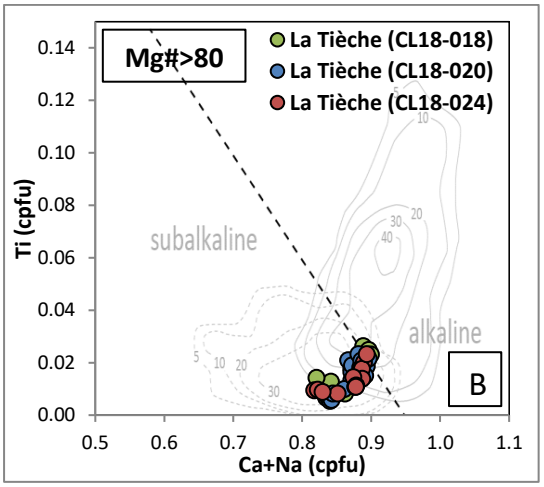

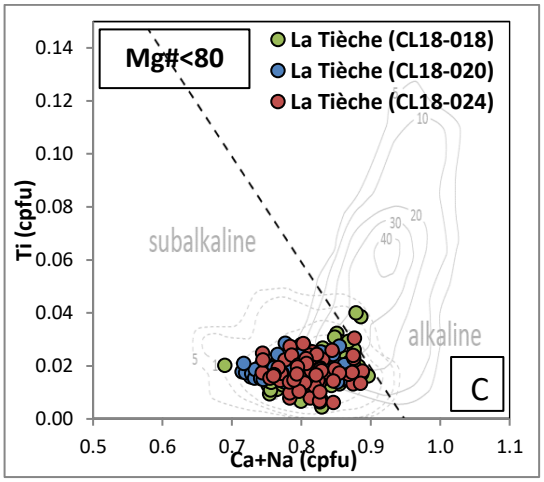

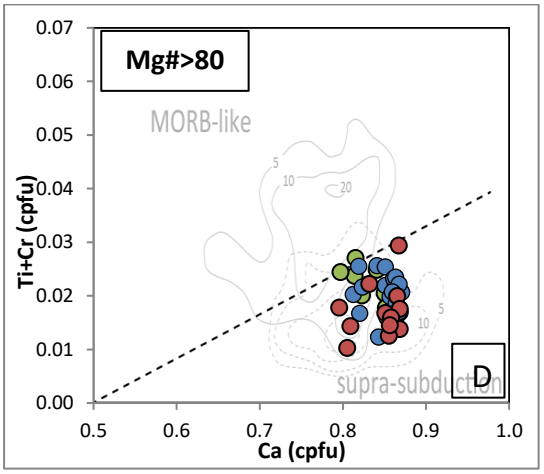

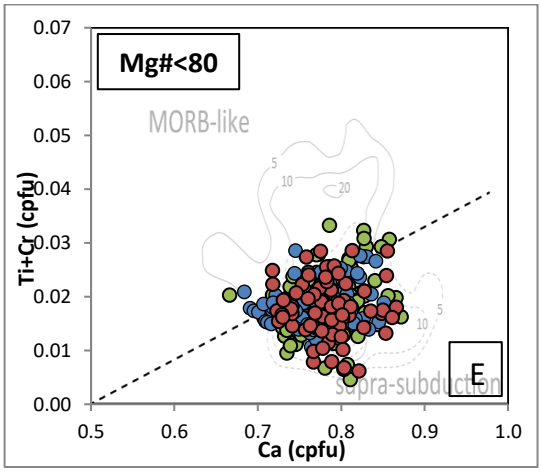

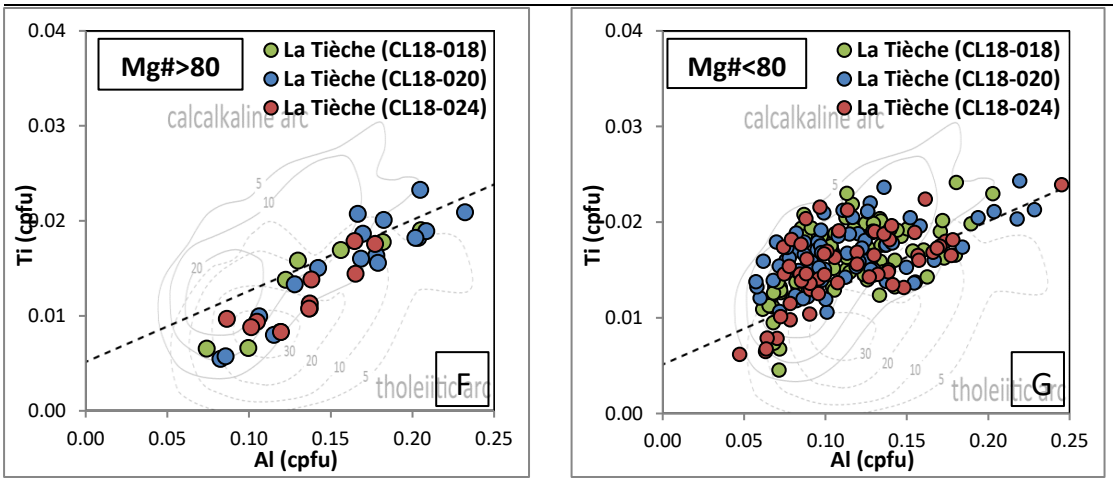

Figure 6.18 Tectonic discrimination diagrams of clinopyroxenes after Leterrier et al. (1982) applied to clinopyroxenes from La Tièche locality, including original density contours from Leterrier et al. (1982). Data expressed as cationic values from the structural formula of clinopyroxenes.

On the binary diagrams (Figure 6.18 A), the majority of clinopyroxenes have Mg# varying between 70 - 85. With decreasing Mg#, Ti shows good negative correlation (R^2 = 0.67) at high Mg# range (Mg# > 80), whereas at low Mg# (Mg# < 80), poor correlation (R^2 = 0.08) has been observed. Overall compositional similarity is clearly shown on the Leterrier et al. (1982) discrimination diagrams (Figure 6.18 B-G). In the first pair of discrimination diagrams (Figure 6.18 B-C), the vast majority of the clinopyroxenes of both groups have Sub-Alkaline affinity. In the second pair of discrimination diagrams (Figure 6.18 D-E), most of the clinopyroxenes of both groups plot in the Supra-Subduction field with few clinopyroxenes falling above the boundary line between MORB-like and Supra-subduction. Finally, in the third pair of discrimination diagrams (Figure 6.18 F-G), clinopyroxenes of Mg# > 80 mainly plot in the Tholeiitic Arc field, whereas those with Mg# < 80 mostly plot in the Calcalkaline Arc field. This is consistent with the primary conclusion that the Al vs Ti trend is not only controlled by tectonic affinity, but also could be influenced by magmatic differentiation.

6.4.2.3 Representative binary diagrams

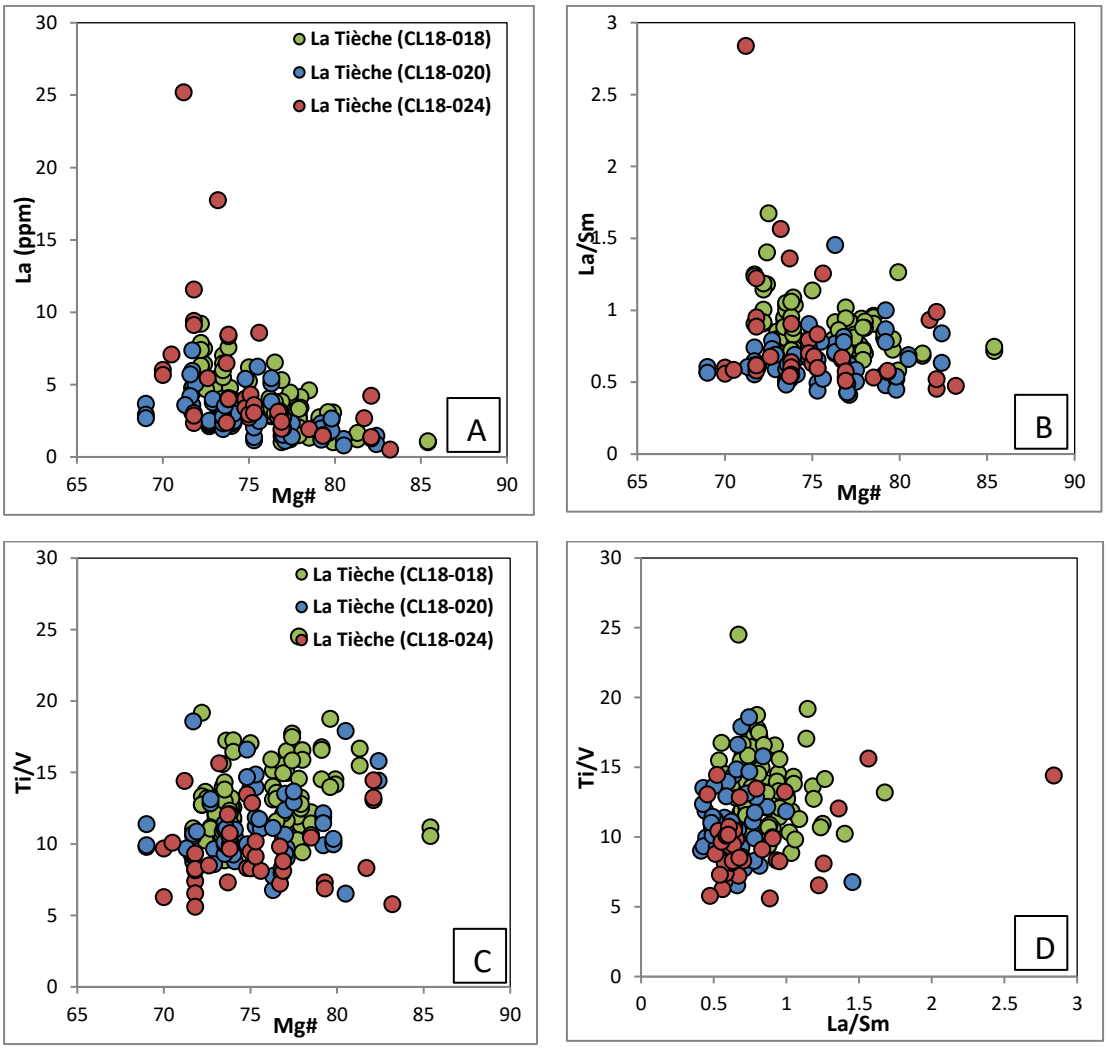

Figure 6.19 Binary diagrams of clinopyroxenes from three volcaniclastic sandstones in La Tièche locality: A-C) selected trace element (ratios) vs Mg#; D) La/Sm vs Ti/V

Most of the clinopyroxenes in the three samples in La Tièche plot in cluster without showing distinct variation in the binary diagrams (Figure 6.19). On the best discriminative La/Sm vs Ti/V diagram (Figure 6.19 D), most of clinopyroxenes are overlapping in cluster, though clinopyroxenes of CL18-018 characterised by higher La/Sm and Ti/V are distinguished from part of those of CL18-024 with lower La/Sm and Ti/V. However, clinopyroxenes of these two samples are both overlapping with sample CL18-020.

6.4.3 Champsaur

This locality includes a total of 1279 SEM analyses (435 clinopyroxenes) from 3 samples of volcaniclastic sandstone, 5 samples of igneous pebbles and 3 samples of andesitic clasts in volcanic breccias and 57 LA-ICP-MS analyses (57

clinopyroxenes) from 1 sample of igneous pebble and 1 sample of andesitic clast in volcanic breccia.

6.4.3.1 Classification of clinopyroxene

Overall, all clinopyroxenes of 11 samples from the Champsaur locality have similar composition with slight variability. Most of clinopyroxenes are Mg-augite with subordinate diopside (Figure 6.20).

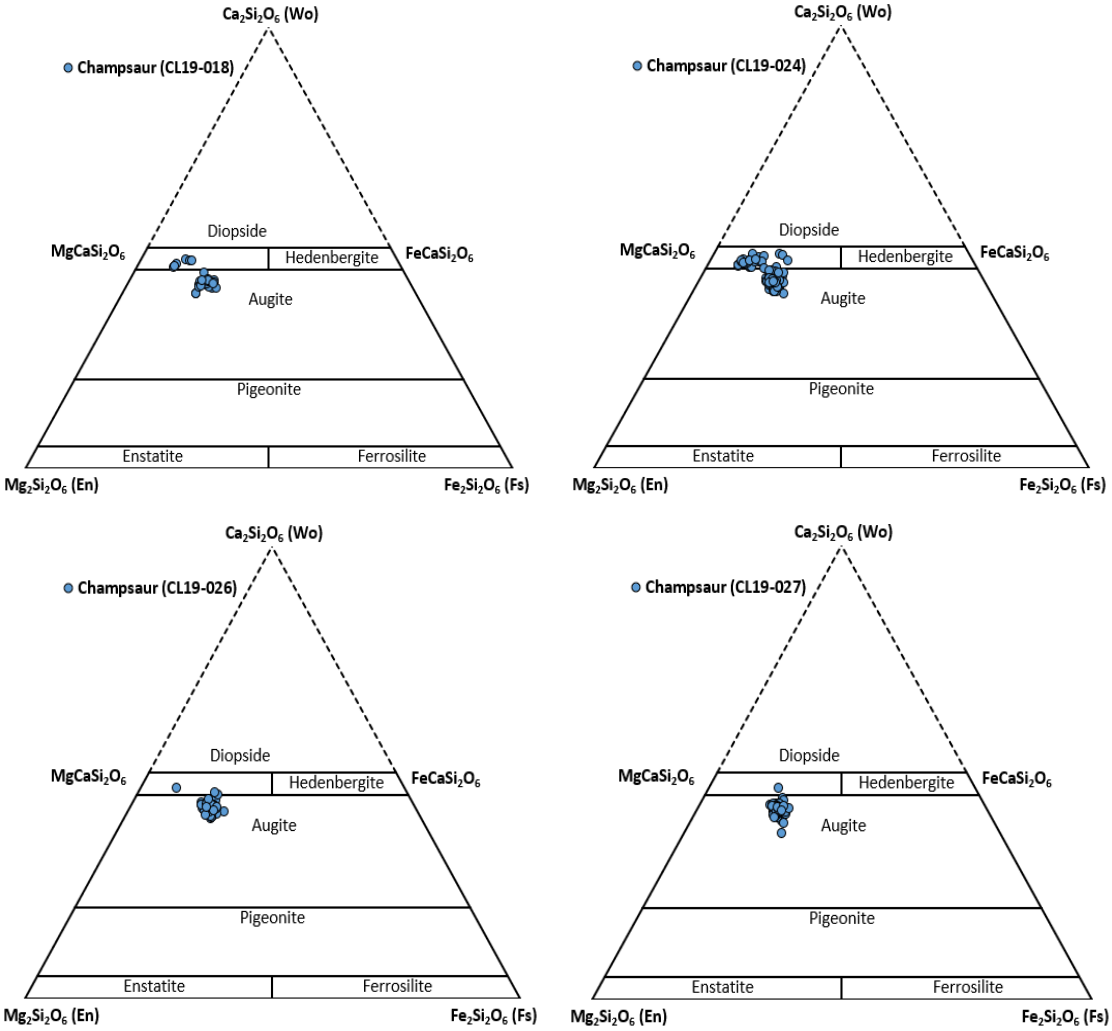

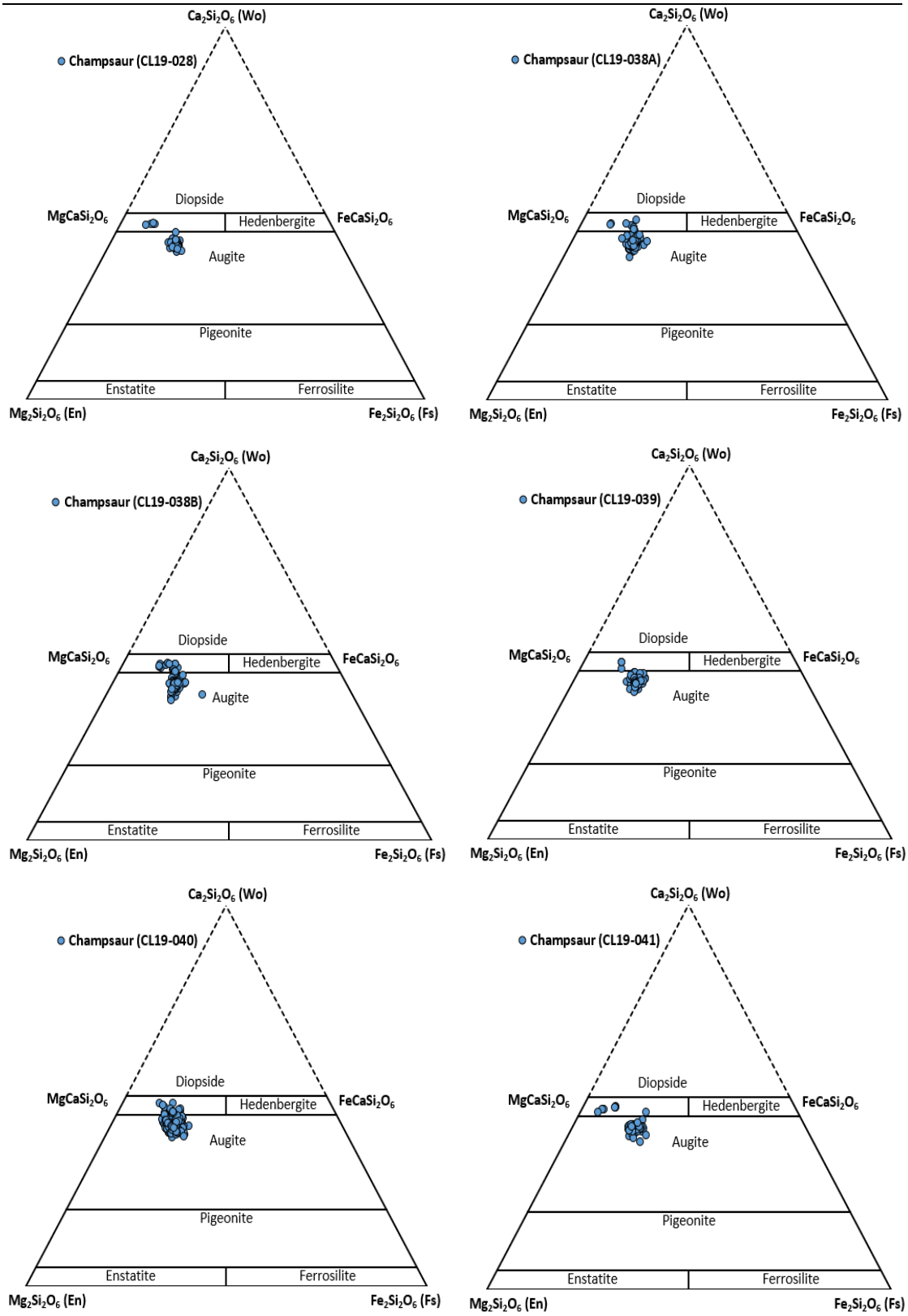

Figure 6.20 Clinopyroxene classification diagram of clinopyroxenes from Champsaur locality (After nomenclature of Morimoto et al., 1988).

6.4.3.2 Tectonic discrimination diagrams

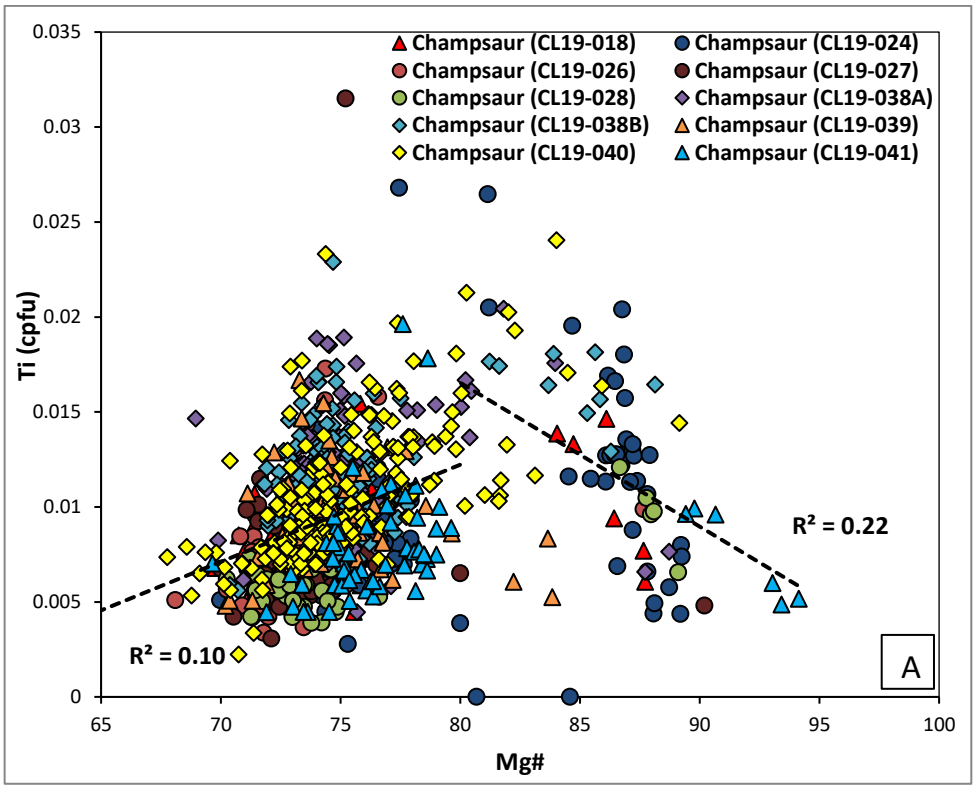

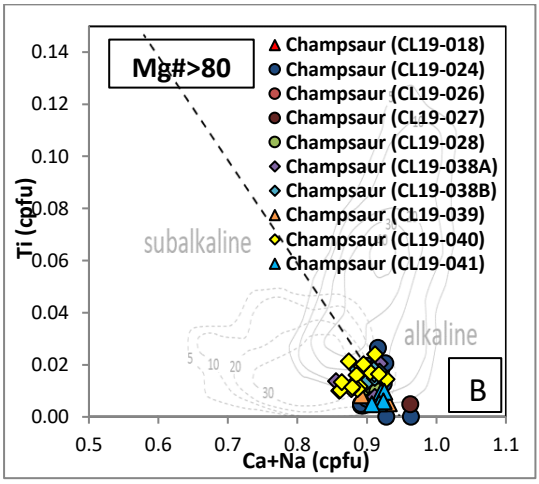

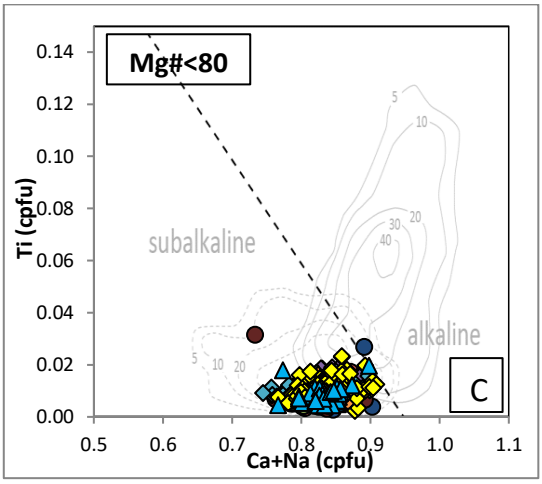

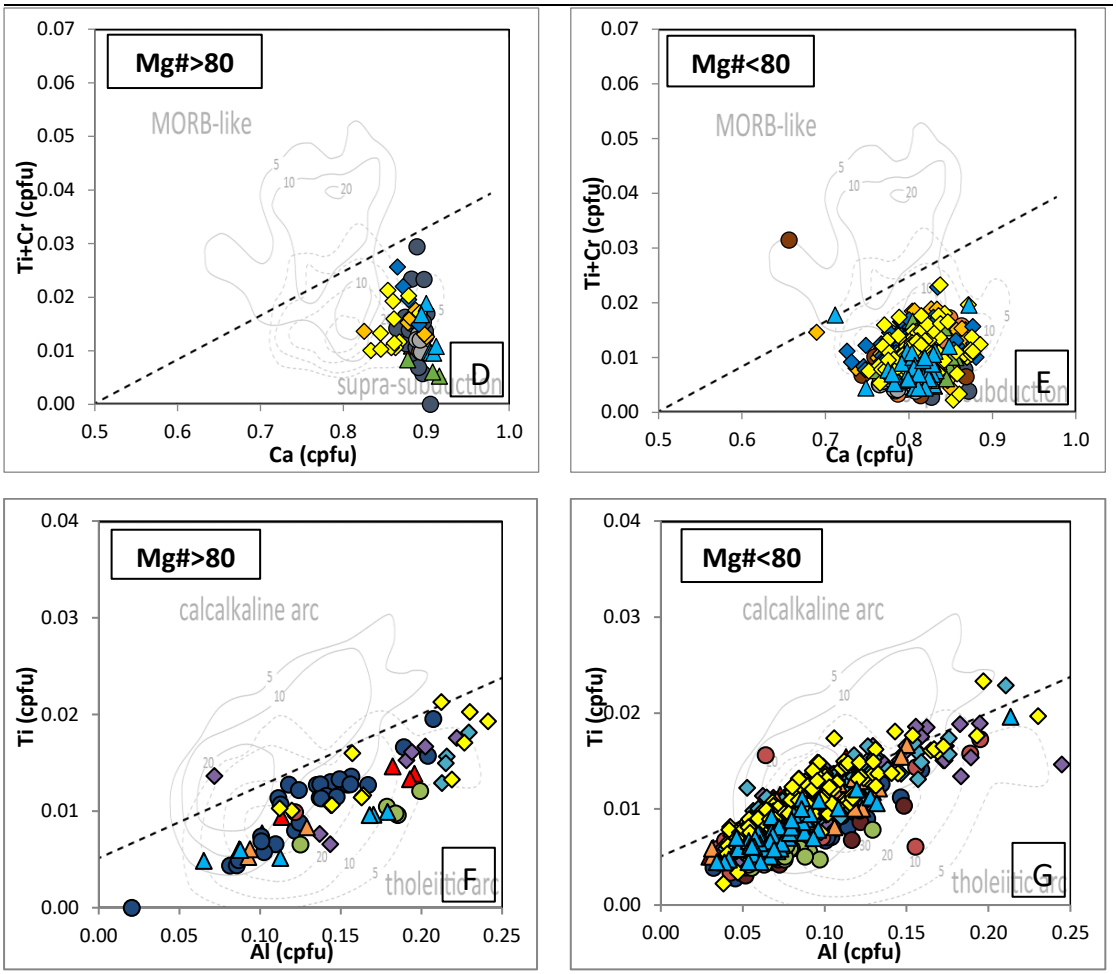

Figure 6.21 Tectonic discrimination diagrams of clinopyroxenes after Leterrier et al. (1982) applied to clinopyroxenes from Champsaur locality, including original density contours from Leterrier et al. (1982). Data expressed as cationic values from the structural formula of clinopyroxenes. Symbol: triangle denotes volcaniclastic sandstone; circle denotes igneous pebble; diamond denotes andesitic clasts in volcanic breccia.

On the binary diagrams (Figure 6.21 A), the majority of clinopyroxenes have Mg# varying between 70 - 80. With decreasing Mg#, Ti shows moderate negative correlation (R^2 = 0.22) at high Mg# range (Mg# > 80), whereas at low Mg# (Mg# < 80), poor correlation (R^2 = 0.10) has been observed. In the first pair of discrimination diagrams (Figure 6.21 B-C), the vast majority of clinopyroxenes of both groups have Sub-Alkaline affinity. In the second pair of discrimination diagrams (Figure 6.21 D-E), most of the clinopyroxenes of both groups plot in the Supra-Subduction field. Finally, in the third pair of discrimination diagrams (Figure 6.21 F-G), clinopyroxenes of Mg# > 80 all plot in the Tholeiitic Arc field, and those with Mg# < 80 are mostly plot in the Tholeiitic Arc field with some falling above the boundary line.

6.4.3.3 Representative binary diagrams

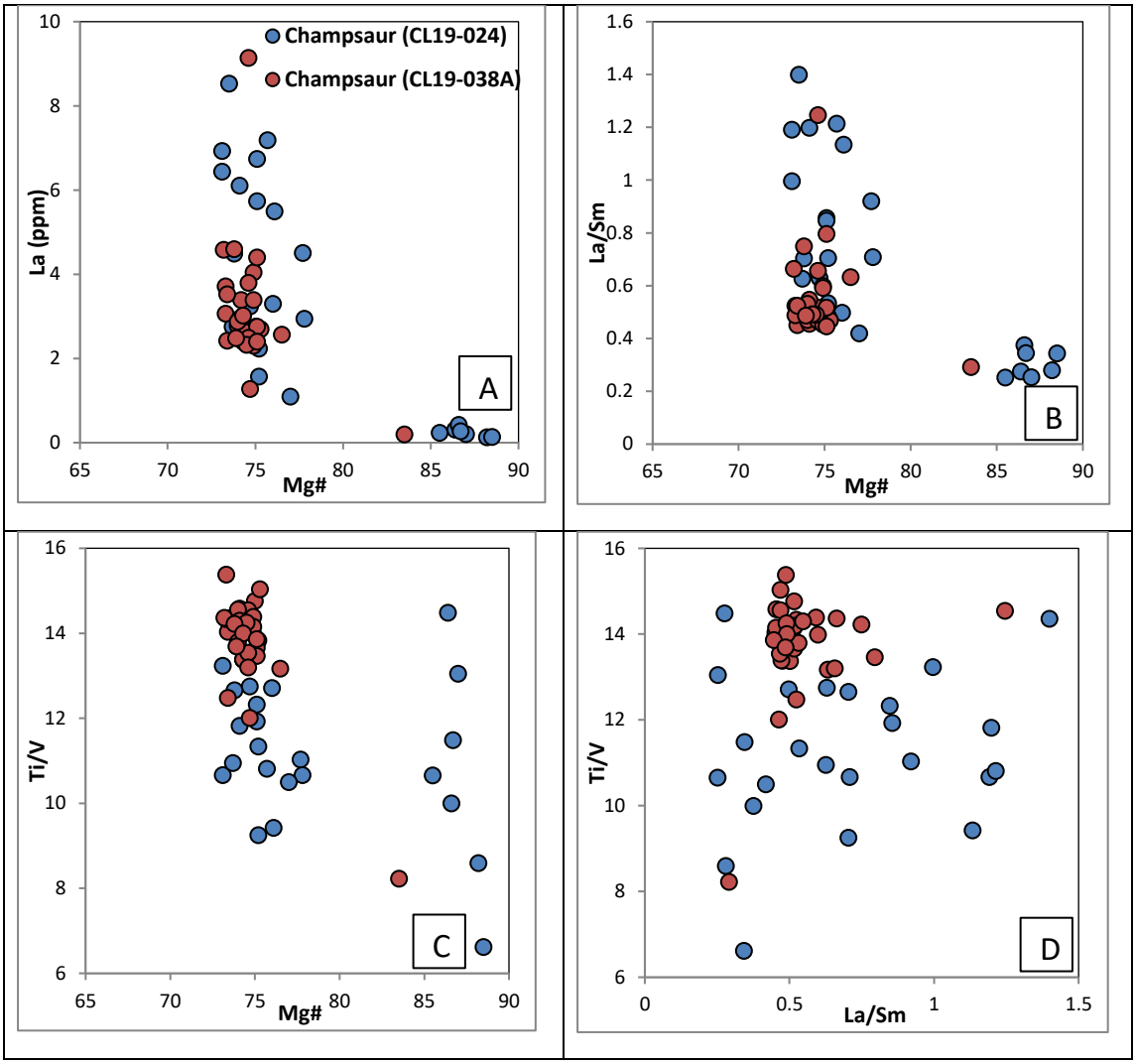

Figure 6.22 Binary diagrams of clinopyroxenes from one igneous pebble (CL19-024) and one andesitic clast (CL19-038A) in Champsaur locality: A-C) selected trace element (ratios) vs Mg#; D) La/Sm vs Ti/V

The clinopyroxenes of the two samples are discriminated well in the best discriminative La/Sm vs Ti/V diagram (Figure 6.22 D). The clinopyroxenes of sample CL19-024 are characterised by wider range of La/Sm (0.2 - 1.2) and Ti/V (6 - 15), whereas those of sample CL19-038A have narrower range of La/Sm (0.4 - 0.8) and Ti/V (12 - 15).

6.4.4 Fontagne (S France)

This locality includes a total of 294 SEM analyses (97 clinopyroxenes) and 75 LA-ICP-MS analyses (75 clinopyroxenes) from 3 samples of andesitic clasts within volcanic breccia and 1 sample of tuffaceous matrix.

6.4.2.1 Classification

All clinopyroxenes from the Fontagne locality have similar composition with a small range of variation. The majority of the clinopyroxenes are Mg-augite with subordinate diopside (Figure 6.23).

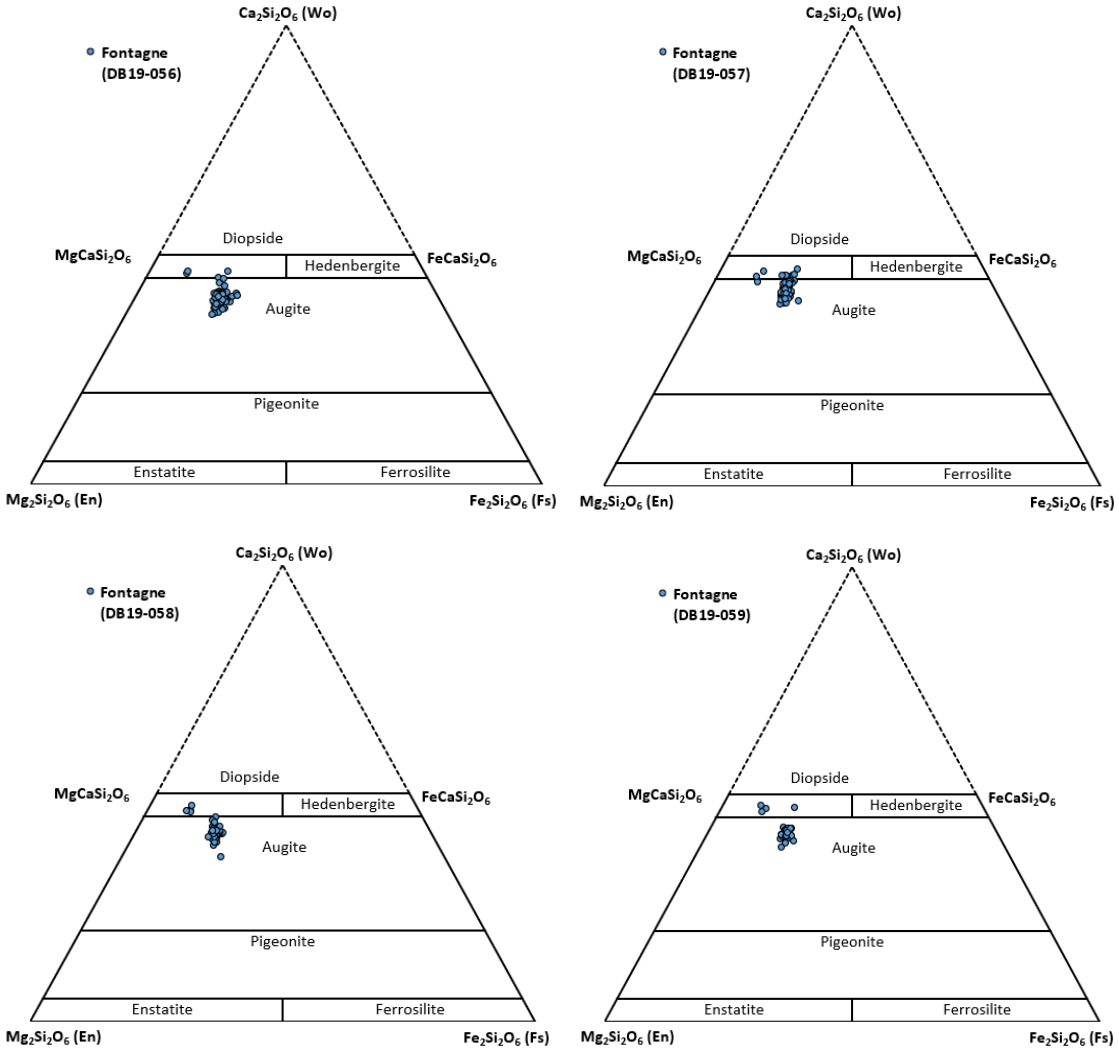

Figure 6.23 Clinopyroxene classification diagram of clinopyroxenes from Fontagne locality of St. Antonin basin (After nomenclature of Morimoto et al., 1988).

6.4.4.2 Tectonic discrimination diagrams

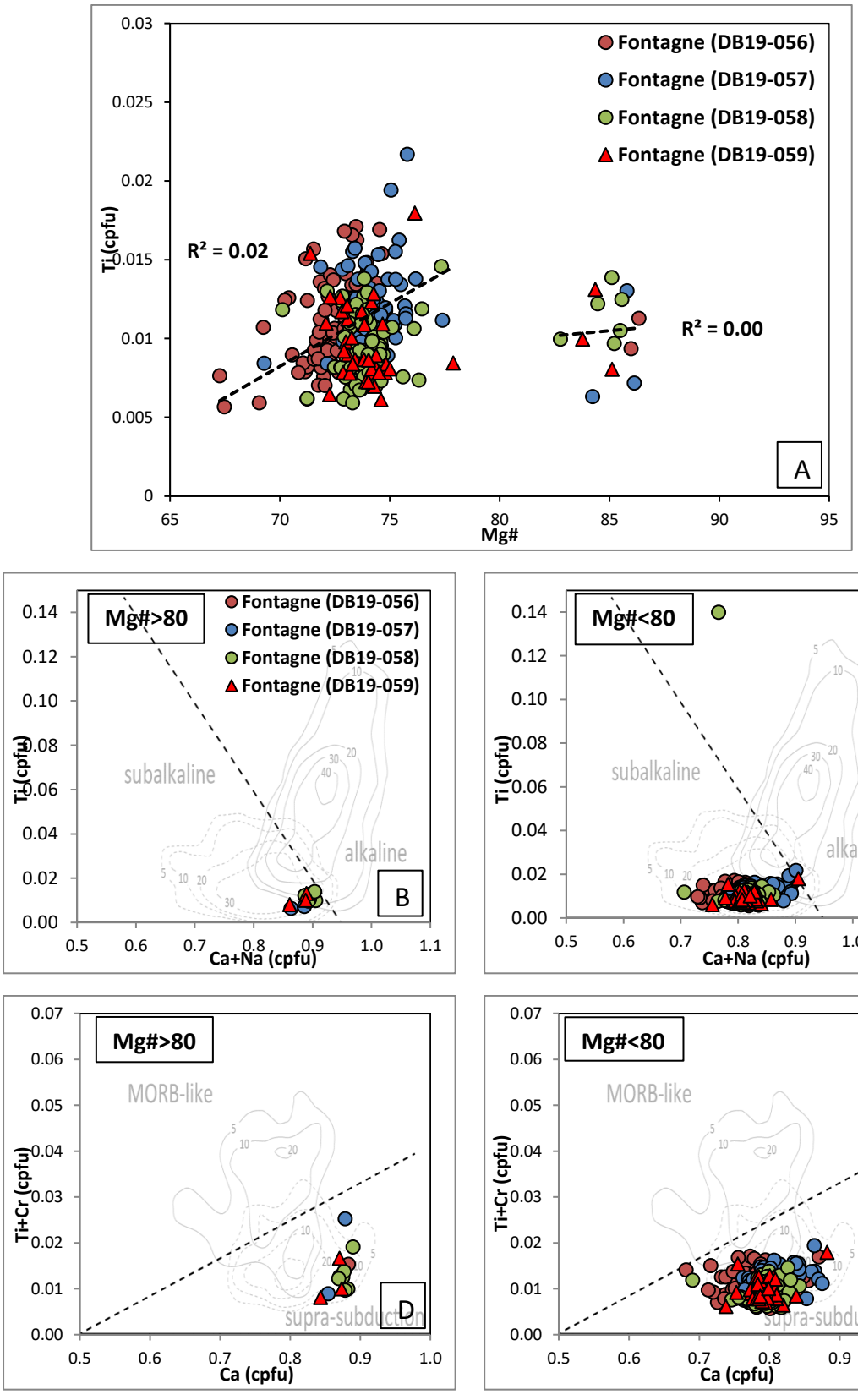

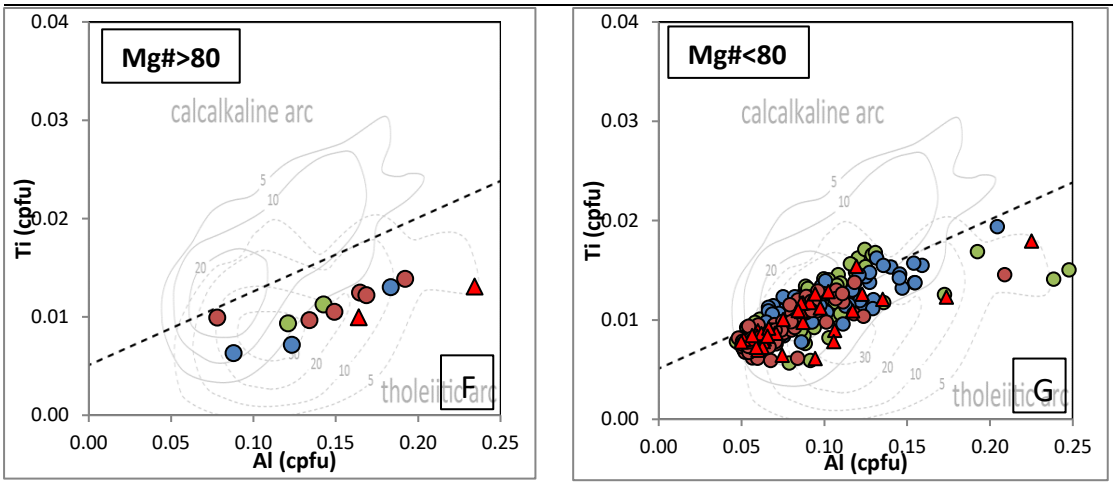

Figure 6.24 Tectonic discrimination diagrams of clinopyroxenes after Leterrier et al. (1982) applied to clinopyroxenes from Fontagne locality, including original density contours from Leterrier et al. (1982). Data expressed as cationic values from the structural formula of clinopyroxenes. Symbol: circle denotes andesitic clasts in volcanic breccia; triangle denotes tuffaceous matrix of volcanic breccia.

On the binary diagrams (Figure 6.24 A), the majority of clinopyroxenes have Mg# varying between 70 – 80, with few clinopyroxenes having high Mg# at ca. 85. With decreasing Mg#, Ti shows no correlation (R^2 = 0.00) at high Mg# range (Mg# > 80), whereas at low Mg# (Mg# < 80), poor correlation (R^2 = 0.02) has been observed. In the first pair of discrimination diagrams (Figure 6.24 B-C), vast majority of the clinopyroxenes of both groups have Sub-Alkaline affinity. In the second pair of discrimination diagrams (Figure 6.24 D-E), all clinopyroxenes of both groups plot in the Supra-Subduction field. Finally, in the third pair of discrimination diagrams (Figure 6.24 F-G), clinopyroxenes of Mg# > 80 all plot in the Tholeiitic Arc field, and those with Mg# < 80 also mostly plot in the Tholeiitic Arc field with some falling above the boundary line.

6.4.4.3 Representative binary diagrams

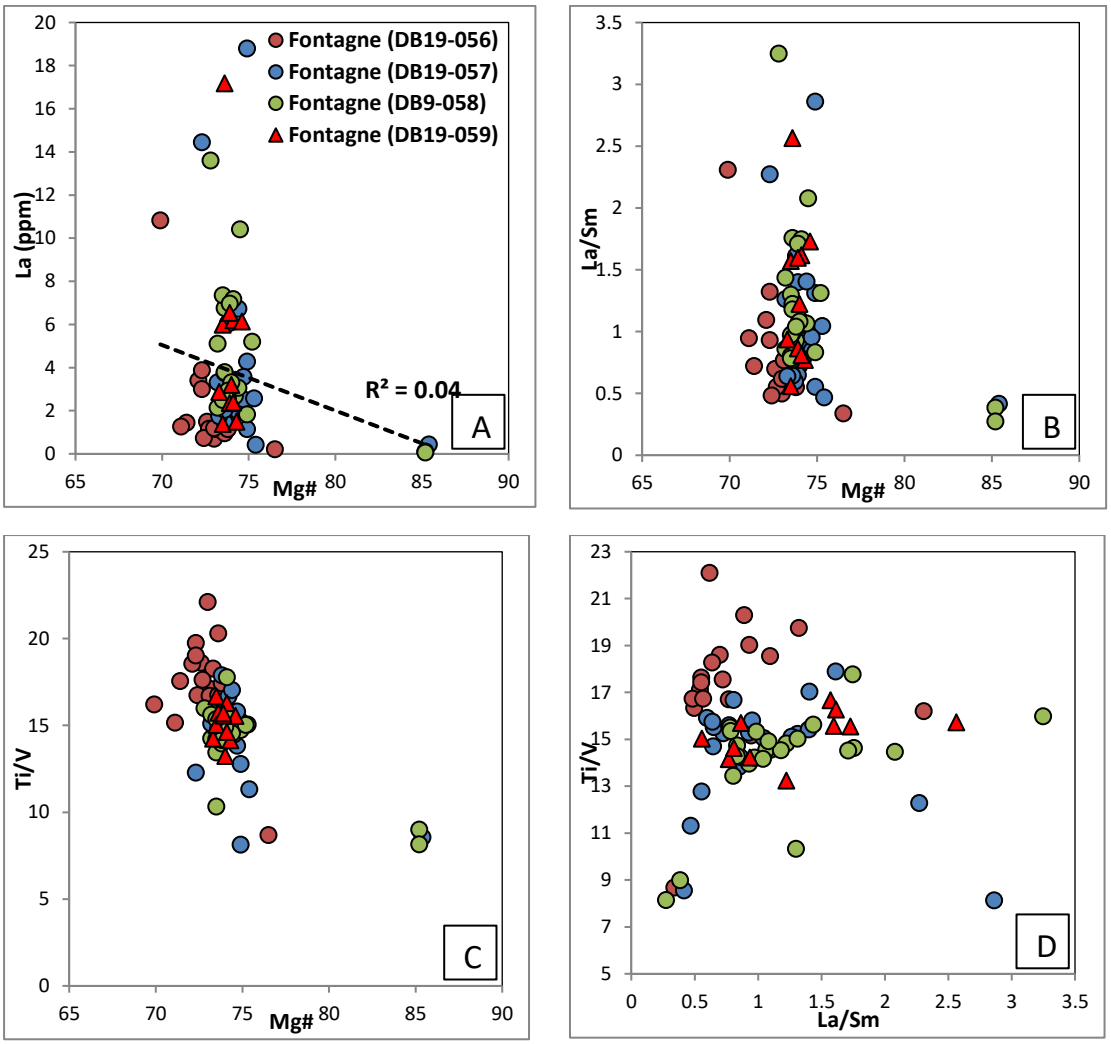

Figure 6.25 Binary diagrams of clinopyroxenes from three samples of andesitic clasts and one sample of tuffaceous matrix within volcanic breccia in Fontagne locality: A-C) selected trace element (ratios) vs Mg#; D) La/Sm vs Ti/V

Most of the clinopyroxenes from all four samples are overlapping without showing distinct separation on the diagrams (Figure 6.25). In the best discriminative La/Sm vs Ti/V diagram (Figure 6.25 D), clinopyroxenes from sample DB19-056 are characterised by higher Ti/V (> 17) which distinguish themselves from other samples.

6.4.5 Summary

In summary, most of the clinopyroxenes from multiple samples in each single locality (i.e., Creux de Champ, La Tièche, Champsaur and Fontagne) generally plot in cluster without showing distinct variation in the classification diagrams and the Leterrier et al. (1982) tectonic discrimination diagrams. On the trace element binary diagrams, especially the best discriminative La/Sm vs Ti/V

diagram, clinopyroxenes could be discriminated among different samples by La/Sm and /or Ti/V variability.

6.5 Summary

In this chapter, the discrimination of clinopyroxenes was conducted on three levels of geographical scale in the order of region, locality and sample by different types of diagrams. Several conclusions could be summarised as follows (Figure 6.26):

(1) The La/Sm vs Ti/V binary diagram offers the best compositional discrimination to identify clinopyroxenes from possibly distinct sources at the regional to local scales.

(2) Inter-regional discrimination shows that clinopyroxenes from W Switzerland and Aravis are largely similar over a large compositional spectrum. E Switzerland (one sample) includes clinopyroxenes with higher La/Sm values and lower Ti/V values that are clearly distinct from those from S France. As for those from Champsaur, part of the clinopyroxenes is overlapping with those from S France (Figure 6.4).

(3) Inter-locality discrimination shows that clinopyroxenes from the St. Antonin basin (Fontagne and Les Beylons localities) are characterised by lower Ti, and plot in the Tholeiitic Arc field. This contrasts with clinopyroxenes from La Vanade that are characterised by high Ti, and plot in the Calc-alkaline Arc field (Figure 6.12 F-G). However, the clinopyroxenes from Fontagne locality (Figure 6.24) are largely overlapping with Champsaur clinopyroxenes (Figure 6.21), both mostly plotting in the Tholeiitic Arc field.

(4) Small compositional variability generally exists among samples from a single locality (Section 6.4), but its extent does not exceed the overall compositional variability observed at larger (e.g., regional) scale.

(5) The composition of the studied clinopyroxenes is very similar, probably from the same tectonic settings, in contrast with previous works on clinopyroxenes (e.g., Le Bas, 1962; Leterrier et al., 1982) in which clinopyroxenes are derived from distinct tectonic settings in order to establish the tectonic discrimination diagrams using clinopyroxenes. Magmatic differentiation effects control a large part of the elemental variability in the Alpine samples (including in single igneous samples). This hinders the

determination of the relative contribution of potentially distinct volcanic sources for the turbidites. La/Sm vs Ti/V provides a much better insight into compositional variability than existing provenance discrimination approaches that are largely not effective to reveal distinct volcanic sources in the Alpine setting. In order to address this limitation, a new PCA method compared with O'Neill (2016) method is developed and applied to clinopyroxenes in Chapter 8.

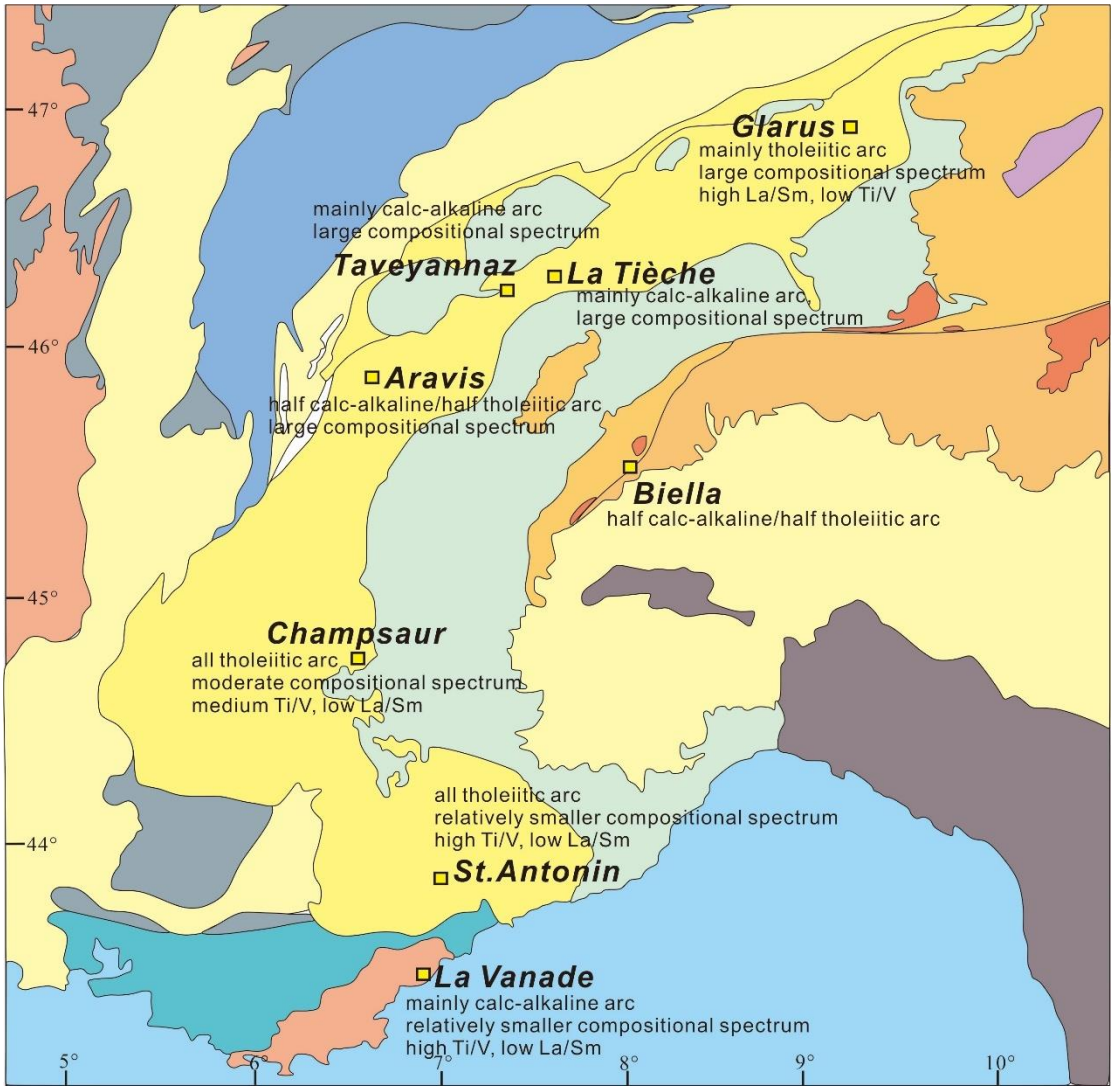

Figure 6.26 Geographical map summarising the main findings of clinopyroxenes in each region

Chapter 7: Amphibole geochemistry

7.1 Introduction

This chapter presents the geochemistry of amphiboles preserved in primary and secondary volcaniclastic rocks in Alpine foreland basins and a subset of amphibole phenocrysts preserved in igneous rocks of the Internal Alps in Northern Italy. The purpose of conducting amphibole geochemistry is to characterise and identify the compositional heterogeneity of amphiboles from different regions in the whole NAFB, analysing the results from regional scale in order to see any spatial variability, to locality and sample scale in order to see any temporal variability within a limited area through time.

This chapter will first classify the mineral types of all amphiboles from all studied regions using the classification diagram of calcium amphibole. Key major and trace elements will then be selected to establish MgO vs element variation diagrams, as well as some binary diagrams of MgO vs element ratios (e.g., MgO vs La/Sm, MgO vs V/Ti).

A total of 2660 SEM-EDS analyses of 906 amphibole grains encountered in 23 samples of volcaniclastic sandstone, 5 samples of igneous pebbles/cobbles, 15 samples of primary volcaniclastic deposits and 4 sample of igneous rocks have been conducted. In addition, a total of 105 LA-ICP-MS analyses of 103 amphibole grains in 6 samples of volcaniclastic sandstone, 1 sample of igneous pebble, and 6 samples of primary volcaniclastic deposits have been conducted.

7.2 Inter-region discrimination

Discrimination of amphiboles from all six studied regions (i.e., E Switzerland, W Switzerland, Aravis, Champsaur, S France and N Italy) was conducted using diagrams introduced in Section 7.1. The detailed localities included in each broad region are provided in Chapter 3.

7.2.1 Classification of amphibole

The classification of amphiboles follows the nomenclature scheme of the 2012 International Mineralogical Association (IMA 2012) (Hawthorne et al., 2012). Under such scheme, all amphiboles in studied regions are Calcium Amphibole (Figure 7.1). The vast majority of the amphiboles are defined as Pargasite

subgroup (82 %), mainly including (Ti-rich) pargasite (28 %) and (Ti-rich) magnesio-hastingsite (54 %) which contain more Mg^{2+} than Fe^{2+} at C position in the general formula $AB_2C_5T_8O_{22}W_2$ of amphibole. Subordinate amphiboles are in the Hornblende subgroup (14 %), mainly including magnesio-hornblende (5 %) and magnesio-ferri-hornblende (9 %) which also contain more Mg^{2+} than Fe^{2+} at C position. Only 3 % of amphiboles distinguish themselves from others with higher or lower $^{C}(Al+Fe^{3+}+2Ti)$ value (> 1.5 or < 0.5) defined as actinolite (1.5 %), sadanagaite, ferri-sadanagaite, and ferri-tschermakite (Table 7.1).

Table 7.1 The number and percentage of various types of end-member calcium amphiboles from various regions. Percentage in bracket denotes the proportion of the number to the total (n) of each region.

Number (percentage)	E Switz. (n=18)	W Switz. (n=44)	Aravis (n=326)	Champsaur (n=292)	S France (n=132)	N Italy (n=127)	Sub-total (n=939)
(Ti-rich) Pargasite	5 (28%)	30 (68%)	134 (41%)	23 (8%)	17 (13%)	50 (39%)	259 (28%)
(Ti-rich) Magnesio-hastingsite	7 (39%)	3 (7%)	128 (39%)	202 (69%)	113 (86%)	57 (45%)	510 (54%)
Magnesio-ferri-hornblende	5 (28%)	2 (5%)	48 (15%)	21 (7%)	0 (0%)	10 (8%)	86 (9%)
Magnesio-hornblende	0 (0%)	7 (16%)	10 (3%)	25 (8%)	0 (0%)	9 (7%)	51 (5%)
Other	1 (5%)	2 (4%)	6 (2%)	21(7%)	2 (1%)	1 (1%)	33 (3%)

Amphiboles in Eastern Switzerland are characterised by the even occurrence of (Ti-rich) Pargasite (28 %), (Ti-rich) magnesio-hastingsite (39 %) and magnesio-ferri-hornblende (28 %). Amphiboles in Western Switzerland are dominated by (Ti-rich) Pargasite (68 %), which is the highest proportion compared to other regions.

Amphiboles from Aravis and N Italy have similar percentage of end-member compositions. (Ti-rich) Pargasite are composed of 41 % and 39 % of total analyses of Aravis and N Italy, as well as (Ti-rich) magnesio-hastingsite of 39 % and 45 % respectively. Subordinate magnesio-ferri-hornblende and magnesio-hornblende make up 15 % and 3 % respectively in Aravis, and 8 % and 7 % respectively in N Italy.

Amphiboles from Champsaur and S France have similar percentage of end-member compositions. (Ti-rich) Pargasite are composed of 8 % and 13 % of total analyses of Champsaur and S France, as well as (Ti-rich) magnesio-hastingsite of 69 % and 86 % respectively.

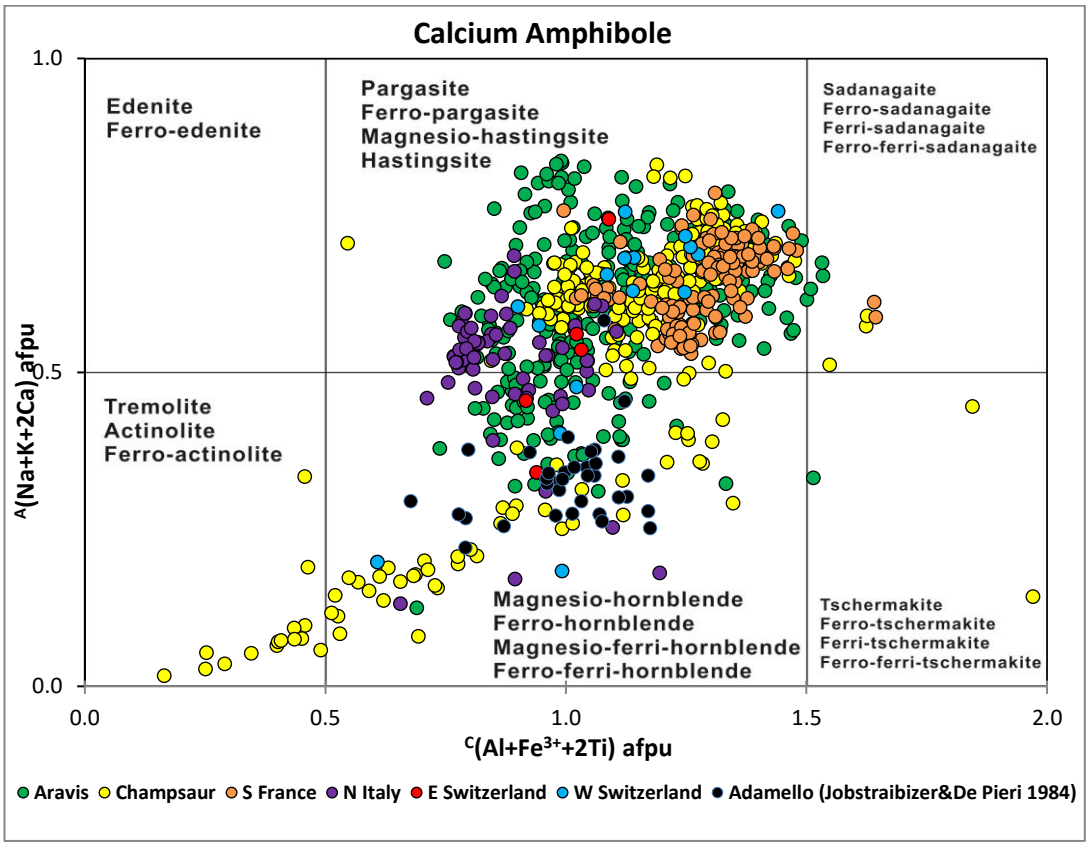

Figure 7.1 Calcium amphibole classification diagram of amphiboles from all studied regions after Hawthorne et al. (2012). Data of amphiboles in Adamello were compiled from Jobstraibizer and De Pieri (1984).

On the classification diagram (Figure 7.1), analyses of amphiboles from E Switzerland and W Switzerland are limited, mostly plotted in the wide spectrum of those from Aravis. Amphiboles from S France are overlapping with part of those from Champsaur. Within the Champsaur population, a series of analyses from sample CL19-030 are in continuous trend through hornblende to actinolite, showing a totally different mineral type. Amphiboles from N Italy are partially overlapping with Aravis amphiboles.

7.2.2 Binary diagrams (major elements)

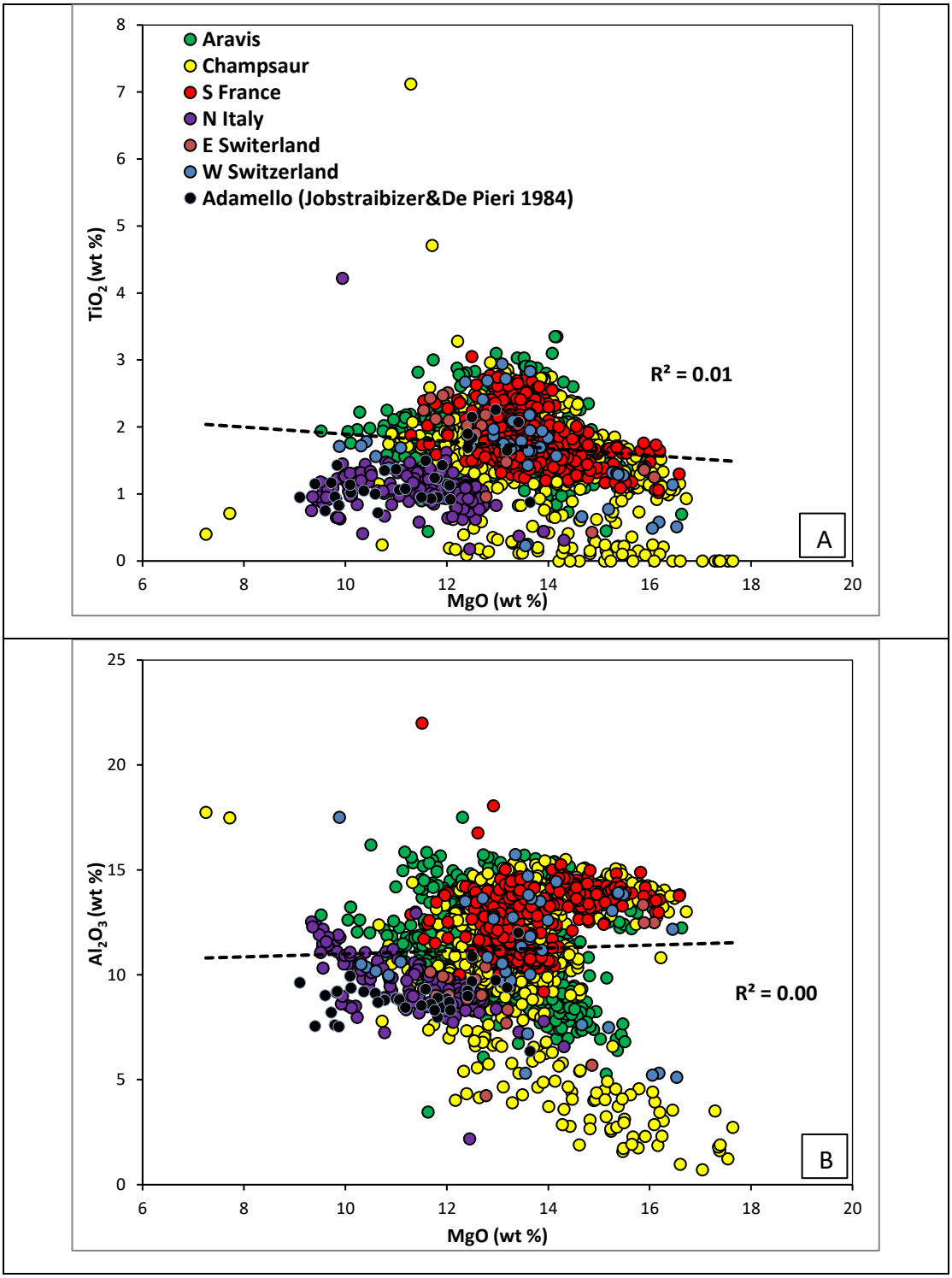

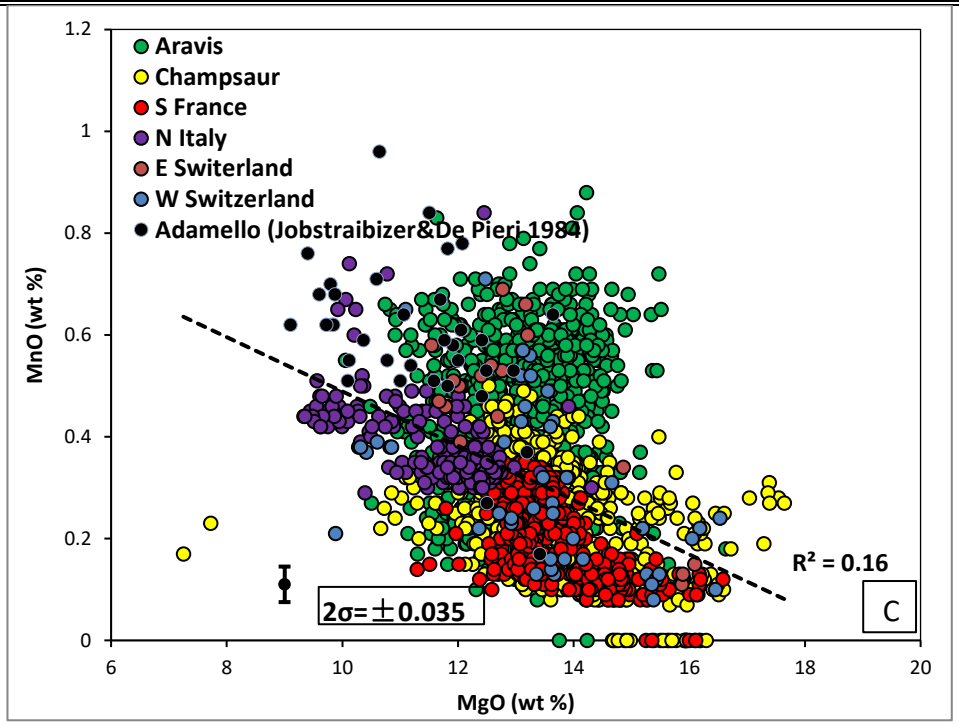
Aravis
Champsaur
S France
N Italy
E Switerland
W Switzerland
Adamello (Jobstraibizer&De Pieri 1984)
MnO (wt %)
MgO (wt %)
R² = 0.16
2σ=±0.035
C

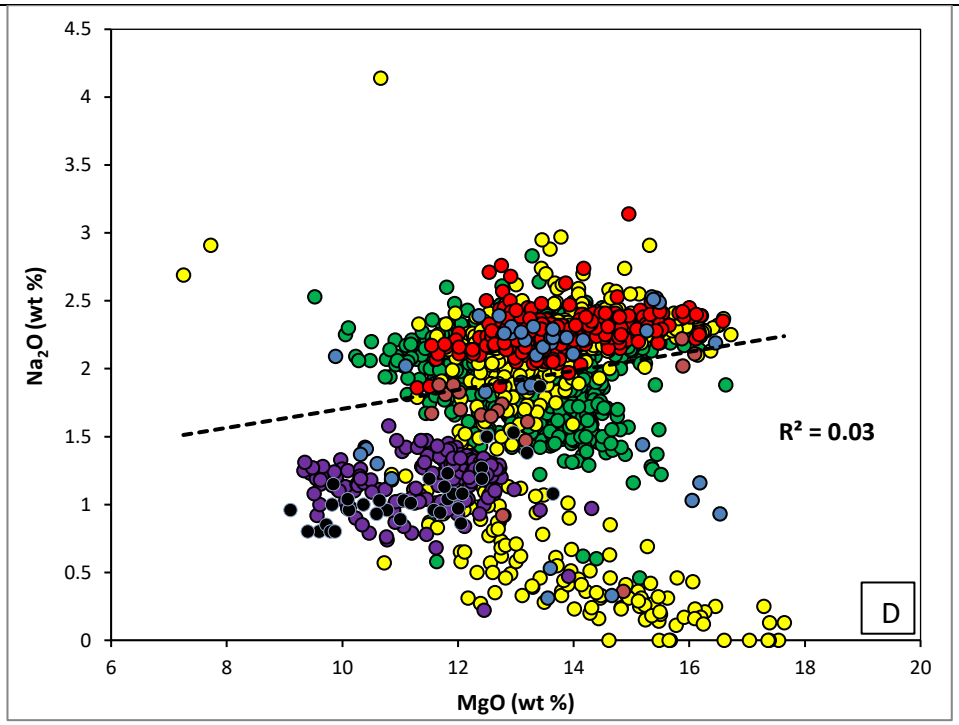
Na2O (wt %)
MgO (wt %)
R² = 0.03
D

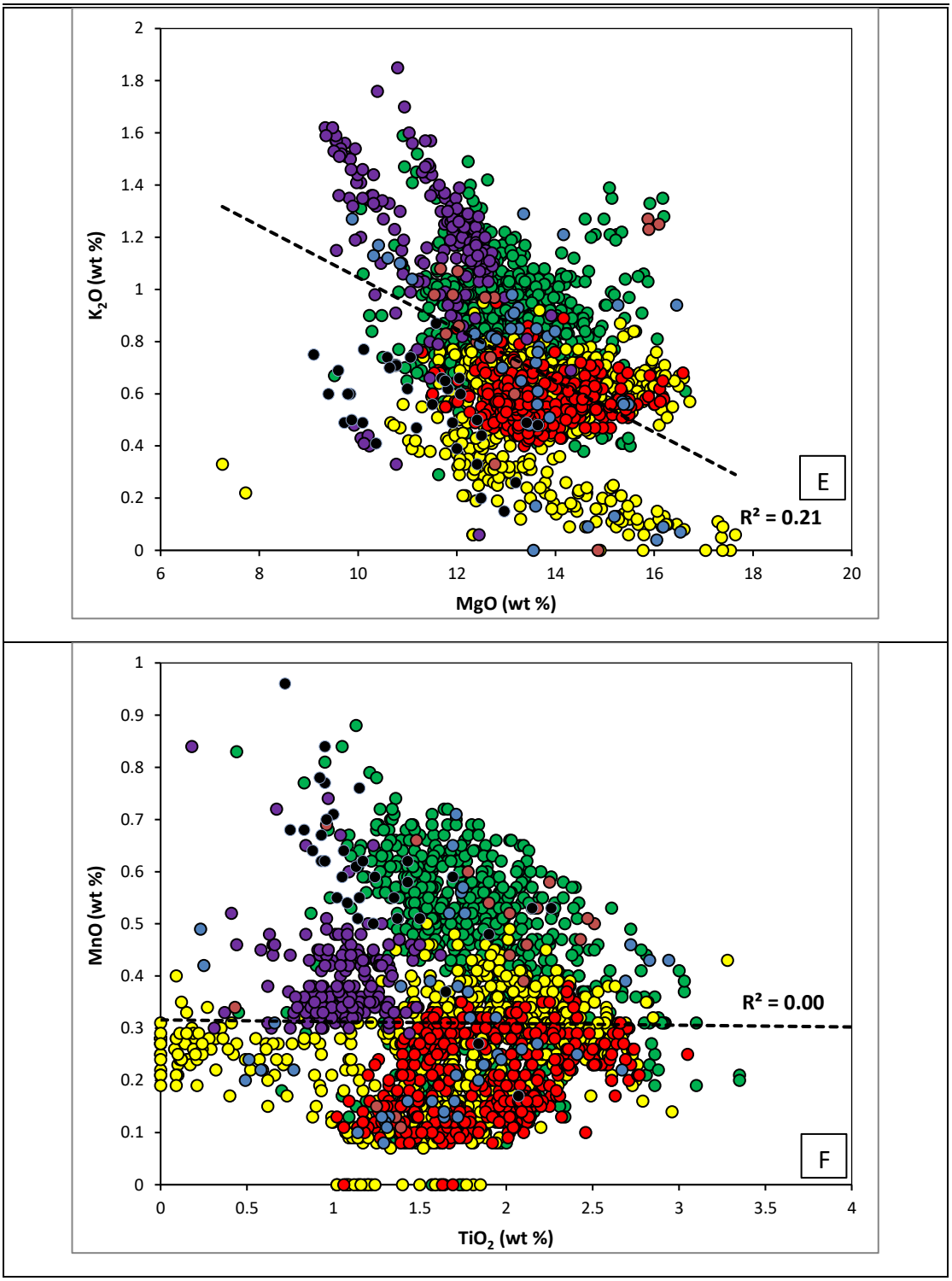

Figure 7.2 A-E) Binary diagrams of selected major elements vs MgO of amphiboles from all studied regions. F) TiO_2 vs MnO diagram. Error bars were calculated using results of standards (Smithsonian Kakanui Hornblende NMNH 143965, see Appendix E3). Data of amphiboles in Adamello were compiled from Jobstraibizer and De Pieri (1984).

On the binary diagrams (Figure 7.2 A-E), MgO was used as the differentiation index and most amphiboles from all studied regions have MgO content varying between 10 – 16 wt. %. The overall feature is that amphiboles from

sample CL19-030 in Champsaur and N Italy are well discriminated in most binary diagrams, whereas those from E Switzerland, W Switzerland, Champsaur (except CL19-030) and S France are largely overlapping with the large compositional spectrum of Aravis amphiboles.

On the TiO_2 vs MgO diagram (Figure 7.2 A), there is no correlation ($R^2 = 0.00$) between the two elements. Amphiboles in N Italy are separated from others by lower content of TiO_2 (< 2 wt. %) and MgO (< 13 wt. %), as well as those from CL19-030 in Champsaur characterised by extremely low TiO_2 (< 1 wt. %). Amphiboles from the remaining regions are largely overlapping, which represents the main population.

On the Al_2O_3 vs MgO diagram (Figure 7.2 B), there is no correlation ($R^2 = 0.01$) between the two elements. Amphiboles from N Italy are clearly separated from others by lower Al_2O_3/MgO ratio, as well as those from CL19-030 characterised by low Al_2O_3 (< 8 wt. %). Amphiboles from the remaining regions are largely overlapping, which represents the main population.

On the MnO vs MgO diagram (Figure 7.2 C), there is moderate negative correlation ($R^2 = 0.16$) between the two elements. It is the best discriminative diagrams which clearly separated amphiboles from Aravis by higher MnO, S France by lower MnO, N Italy by lower MgO and Champsaur (in between).

On the Na_2O vs MgO diagram (Figure 7.2 D), there is poor correlation ($R^2 = 0.03$) between the two elements. Amphiboles from N Italy are clearly separated from others by lower Na_2O (< 1.5 wt. %) and lower MgO (< 13 wt. %), as well as CL19-030 in Champsaur characterised by lower Na_2O (< 1 wt. %). Amphiboles from the remaining regions are largely overlapping, which represents the main population.

On the K_2O vs MgO diagram (Figure 7.2 E), there is good negative correlation ($R^2 = 0.21$) between the two elements. Amphiboles from CL19-030 in Champsaur are clearly separated by lower K_2O (< 0.5 wt. %) from the main population. Those from N Italy distinguish themselves from others by higher Na_2O (> 1 wt. %) and lower MgO (< 13 wt. %). Amphiboles from the remaining regions are largely overlapping, which represents the main population.

7.2.3 Binary diagrams (trace elements)

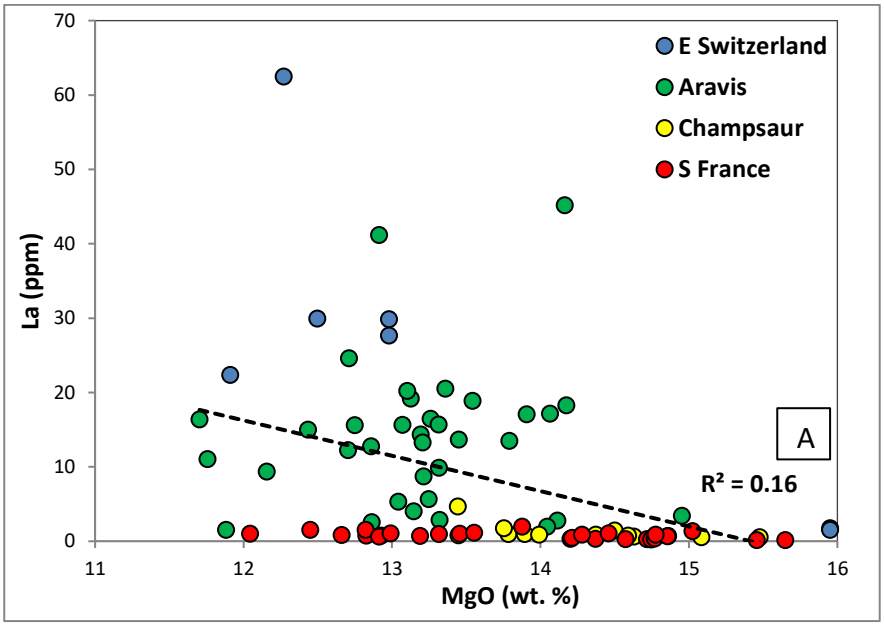

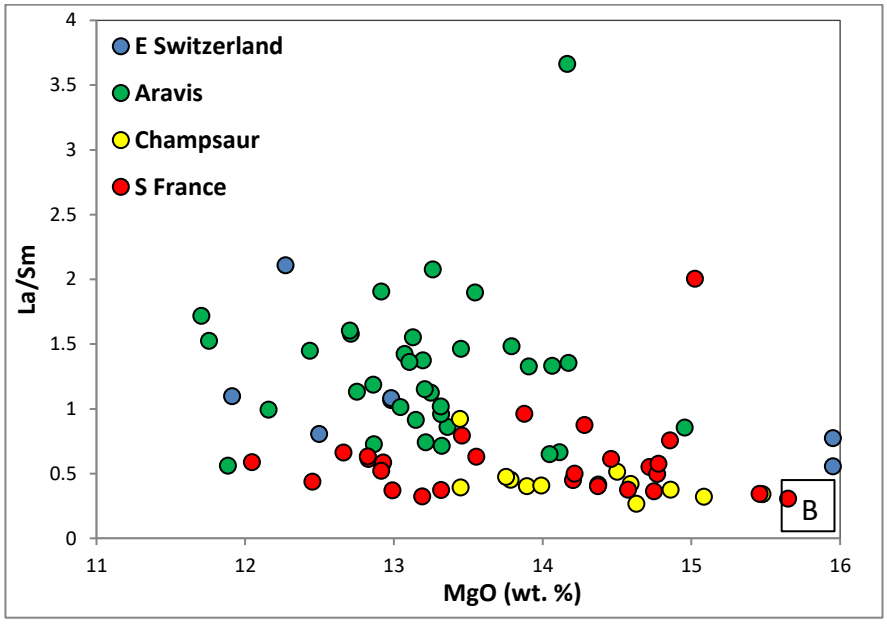

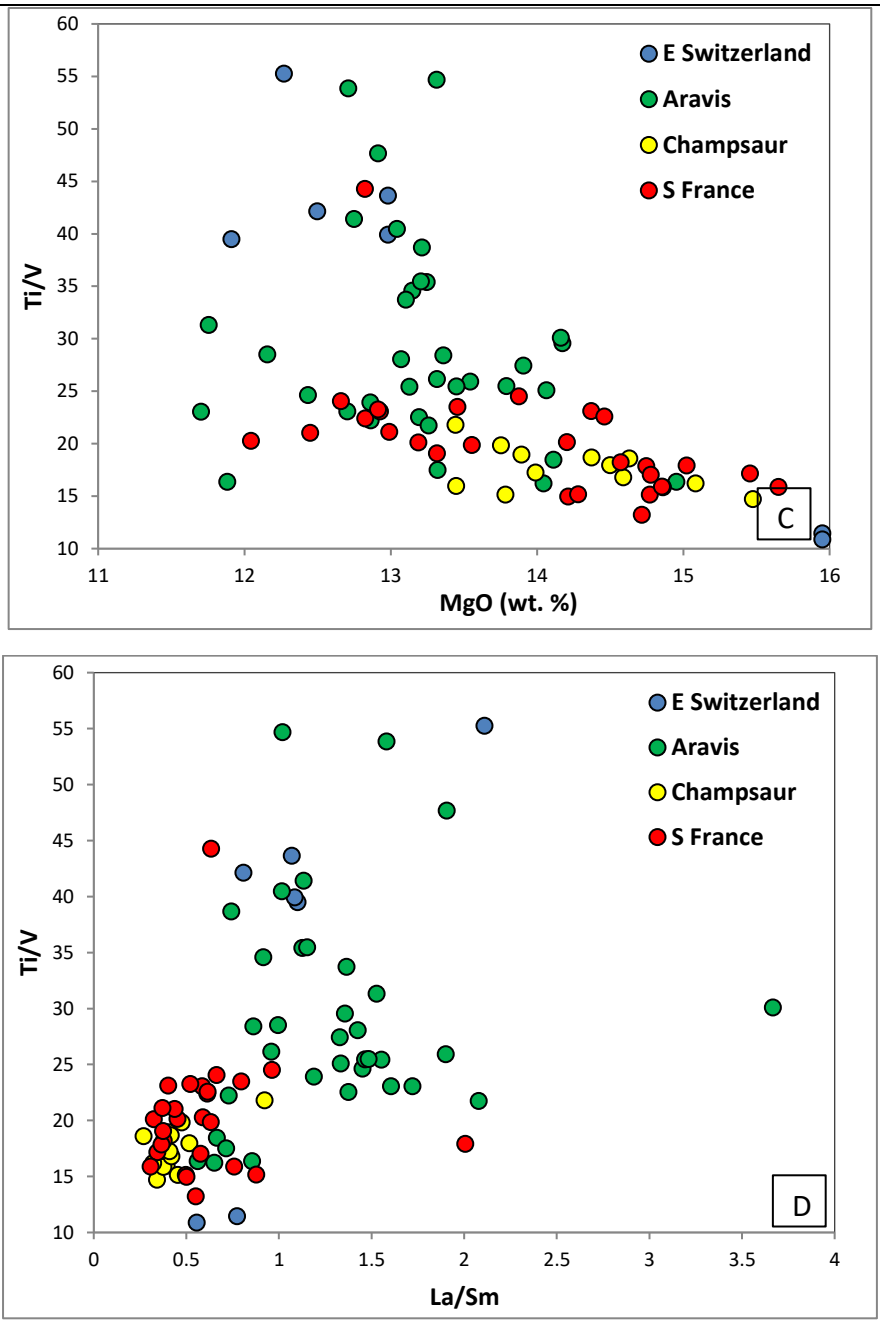

Figure 7.3 Binary diagrams of amphiboles from E Switzerland, Aravis, Champsaur and S France: A-C) selected trace element (ratio) vs MgO; D) La/Sm vs Ti/V. Note: no trace element data were collected for amphiboles in W Switzerland and N Italy.

On the MgO vs La diagrams (Figure 7.3 A), a moderate negative correlation (R^2 = 0.16) was shown between the two elements. Amphiboles from E Switzerland and Aravis of higher La concentration (> 2 ppm) plot separately from those in Champsaur and S France of extremely low La concentration (< 2 ppm). On the MgO vs La/Sm (Ti/V) diagram (Figure 7.3 B), similar trend has been shown on the discrimination between amphiboles from E Switzerland and Aravis of

higher La/Sm ratio (> 1), and amphiboles from Champsaur and S France of lower La/Sm ratio (< 1). On the MgO vs Ti/V diagram (Figure 7.3 C), similar trend has also been shown on the discrimination between amphiboles from E Switzerland and Aravis of higher Ti/V ratio (> 25), and amphiboles from Champsaur and S France of lower La/Sm ratio (< 25).

On the La/Sm vs Ti/V diagram (Figure 7.4 D), it's clearly shown that most of the amphiboles from E Switzerland and Aravis plot in cluster with higher La/Sm and Ti/V values, which are separated from those of Champsaur and S France with lower La/Sm and lower Ti/V values.

7.2.4 Summary

In summary, the overall mineral type of amphiboles from all regions are classified as (Ti-rich) magnesio-hastingsite (54 %), (Ti-rich) pargasite (28 %), magnesio-ferri-hornblende (9 %), magnesio-hornblende (5 %) and others. Compositional variability among different regions has been well recognised on the classification diagram. Amphiboles from Aravis spread a large compositional spectrum, overlapping with those from N Italy at left, with those from S France at right, with those from Champsaur at middle right. Only amphiboles from CL19-030 are well separated from the main population at bottom.

On the binary diagrams (MgO vs major elements), the overall feature is that amphiboles from sample CL19-030 in Champsaur and N Italy are clearly plotted separately in most binary diagrams, whereas those from E Switzerland, W Switzerland, Champsaur (except CL19-030) and S France are largely overlapping with those wide-spreading Aravis amphiboles.

On the binary diagrams (MgO vs trace elements), geochemical differences of amphiboles of different regions are better recognised, especially on the La/Sm vs Ti/V diagram where amphiboles from E Switzerland and Aravis covering a large spectrum plot separately from those of Champsaur and S France which spread in a relatively small range.

7.3 Inter-locality discrimination

Discrimination of amphiboles within regions including several localities (i.e., W Switzerland, Aravis, and S France) was conducted using the same selection of diagrams presented above. Eastern Switzerland (Glarus), Champsaur and N

Italy (Bergell) both only include one regional locality, which have been discussed in Section 7.2.

7.3.1 Western Switzerland

This region includes a total of 44 SEM analyses (16 detrital amphiboles) from 6 samples of volcaniclastic sandstone.

7.3.1.1 Classification of amphibole

The classification of amphiboles follows the nomenclature scheme of the 2012 International Mineralogical Association (IMA 2012) (Hawthorne et al., 2012). Under such scheme, all amphiboles in Western Switzerland are Calcium Amphibole. Most of the amphiboles are in the Pargasite subgroup (Figure 7.4), mainly including (Ti-rich) pargasite (68 %) and (Ti-rich) magnesio-hastingsite (7 %). Some amphiboles, in particular those from La Laya and Chaux Ronde locality, are in the Hornblende subgroup, mainly including magnesio-hornblende (16 %) and magnesio-ferri-hornblende (5 %). One amphibole grain from Taveyannaz locality distinguishes itself from others with higher $^{C}(Al+Fe^{3+}+2Ti)$ value named as sadanagalite.

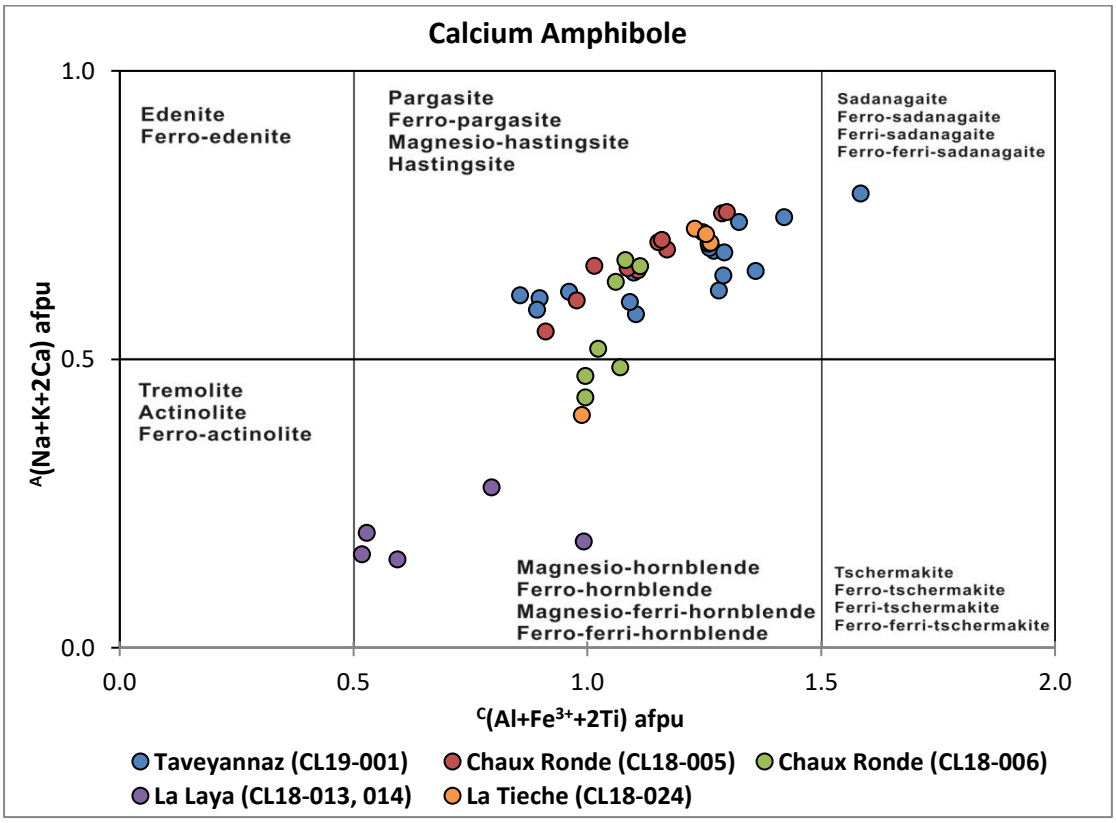

Figure 7.4 Calcium amphibole classification diagram of amphiboles from Western Switzerland after Hawthorne et al. (2012).

7.3.1.2 Binary diagrams (major elements)

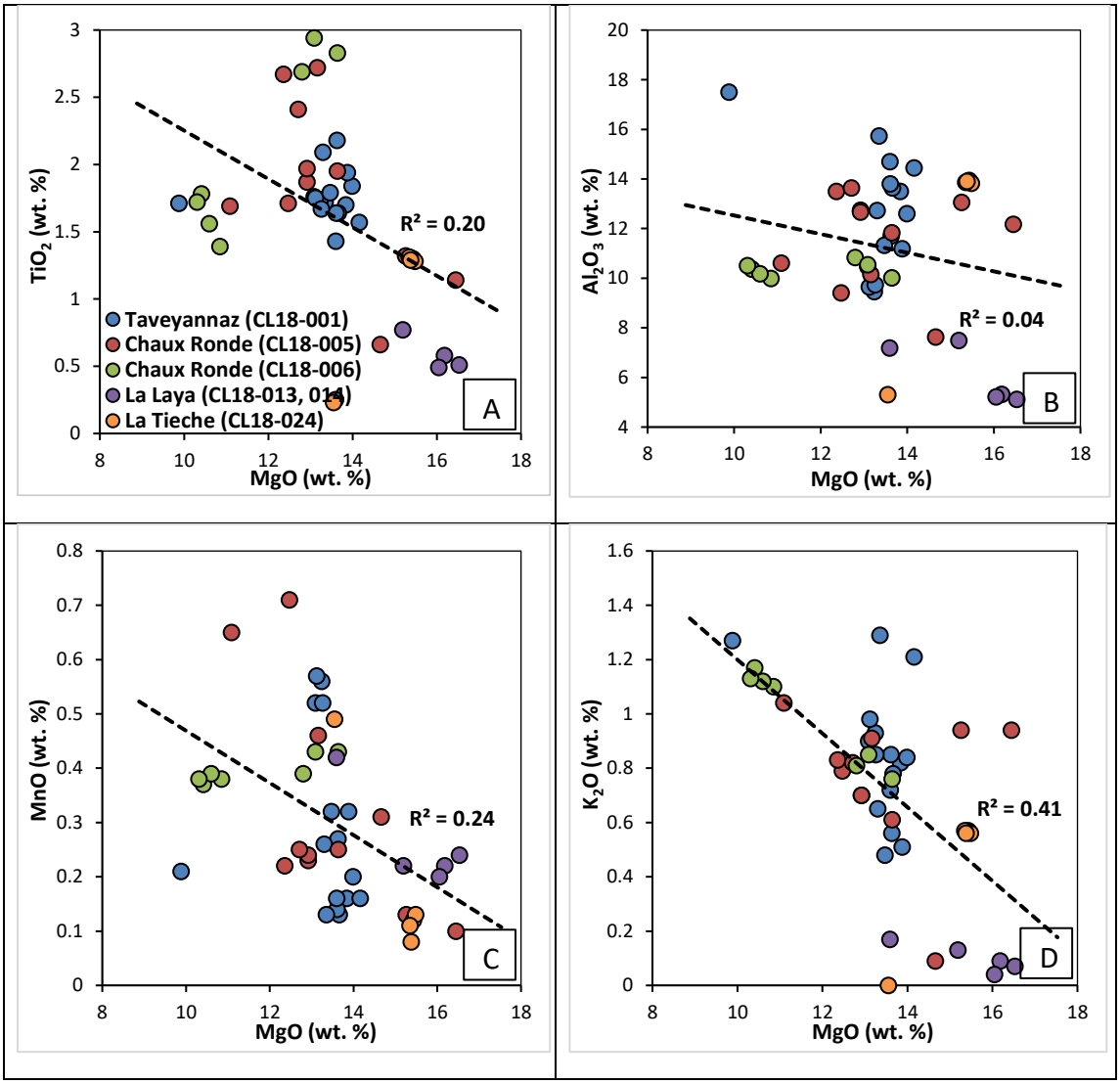

Figure 7.5 A-D) Binary diagrams of selected major elements vs MgO of amphiboles from Western Switzerland.

On the MgO vs major elements binary diagram (Figure 7.5 A-D), there is moderate negative or positive correlation between MgO and selected major elements (R^2 = 0.04 - 0.41). Amphiboles from W Switzerland show wide range of spreading given the limited number of amphibole analyses in the region. Amphiboles from the five localities show a certain degree of compositional variability though the results could be biased due to the limited number of analyses.

7.3.2 Aravis (Haute-Savoie)

This region includes a total of 895 SEM analyses (326 amphiboles) from 13 samples of volcaniclastic sandstone and 1 sample of andesitic clast and 35 LA-ICP-MS analyses (35 amphiboles) from 5 samples of volcaniclastic sandstone.

7.3.2.1 Classification of amphibole

All amphiboles in Aravis are Calcium Amphibole, most of which are in the Pargasite subgroup (Figure 7.6), mainly including (Ti-rich) pargasite (41 %), and (Ti-rich) magnesio-hastingsite (39 %), whereas some amphiboles, in particular those from Flaine locality, are plotted separately in the Hornblende subgroup, mainly including magnesio-hornblende (3 %) and magnesio-ferri-hornblende (15 %). Few amphibole grains from Col de l'Oulettaz locality distinguish themselves from others with higher $^{C}(Al+Fe^{3+}+2Ti)$ value (> 1.5) defined as sadanagalite and ferri-sadanagalite, one from La Clusaz named as ferri-tschermakite.

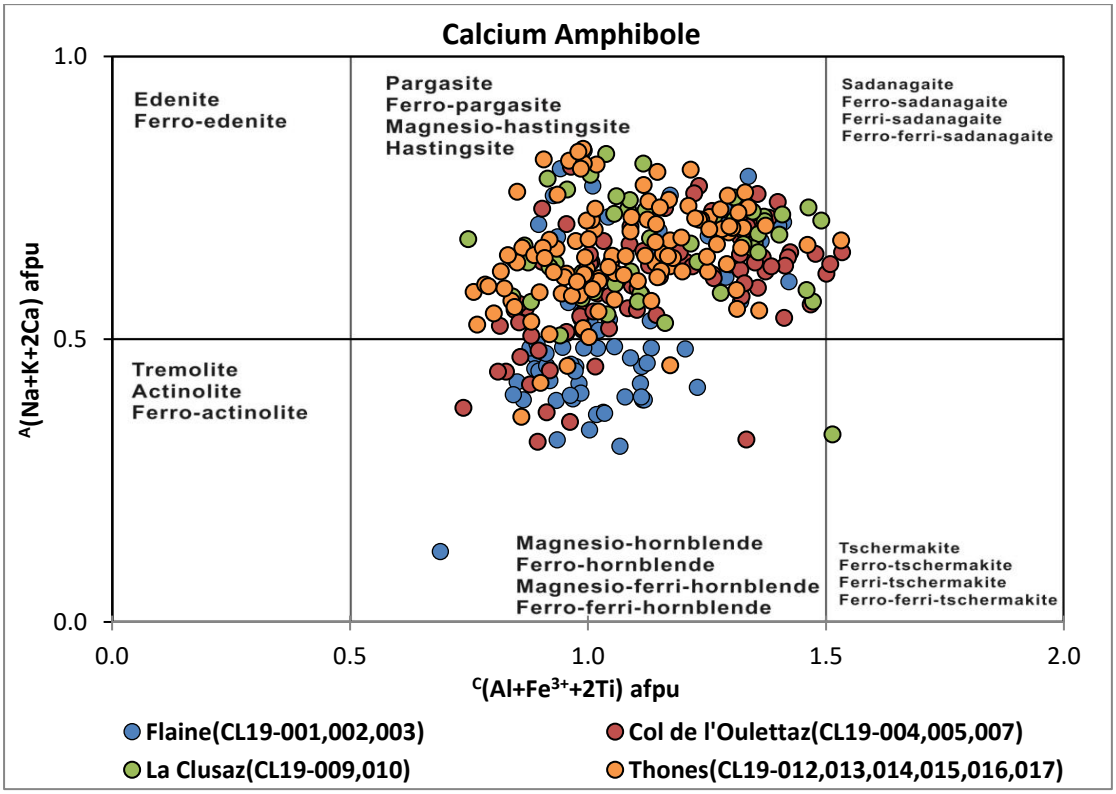

Figure 7.6 Calcium amphibole classification diagram of amphiboles from Aravis after Hawthorne et al. (2012).

7.3.2.2 Binary diagrams (major elements)

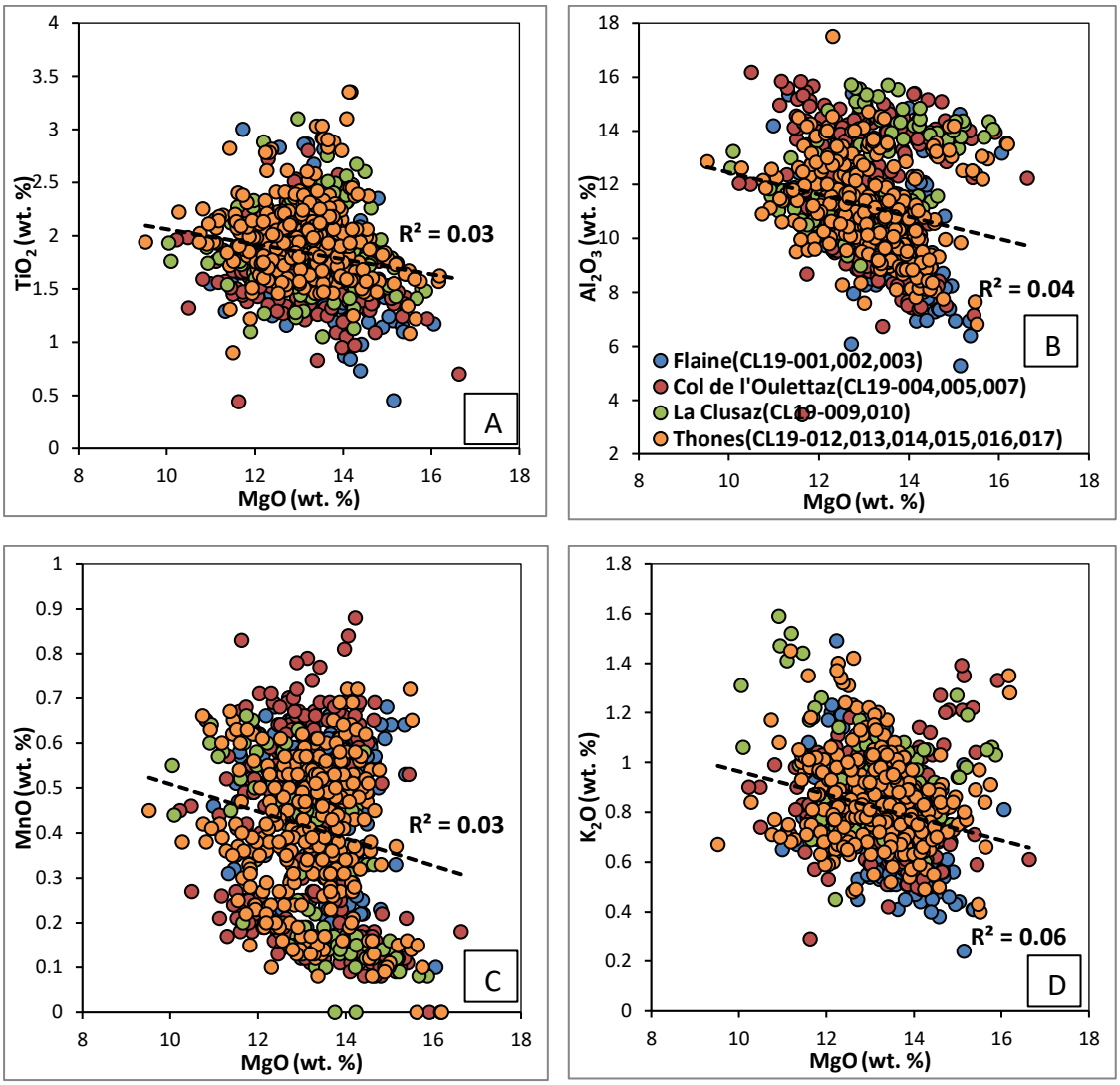

Figure 7.7 A-D) Binary diagrams of selected major elements vs MgO of amphiboles from Aravis.

On the MgO vs major elements binary diagram (Figure 7.7 A-D), there is poor to moderate negative or positive correlation between MgO and selected major elements (R^2 = 0.03 - 0.15). In general, amphiboles from four localities in Aravis are largely overlapping without showing distinct variation. Amphiboles from each locality are spreading in similar area on each binary diagram, indicating the strong compositional similarity of amphiboles in the region.

7.3.2.3 Binary diagrams (trace elements)

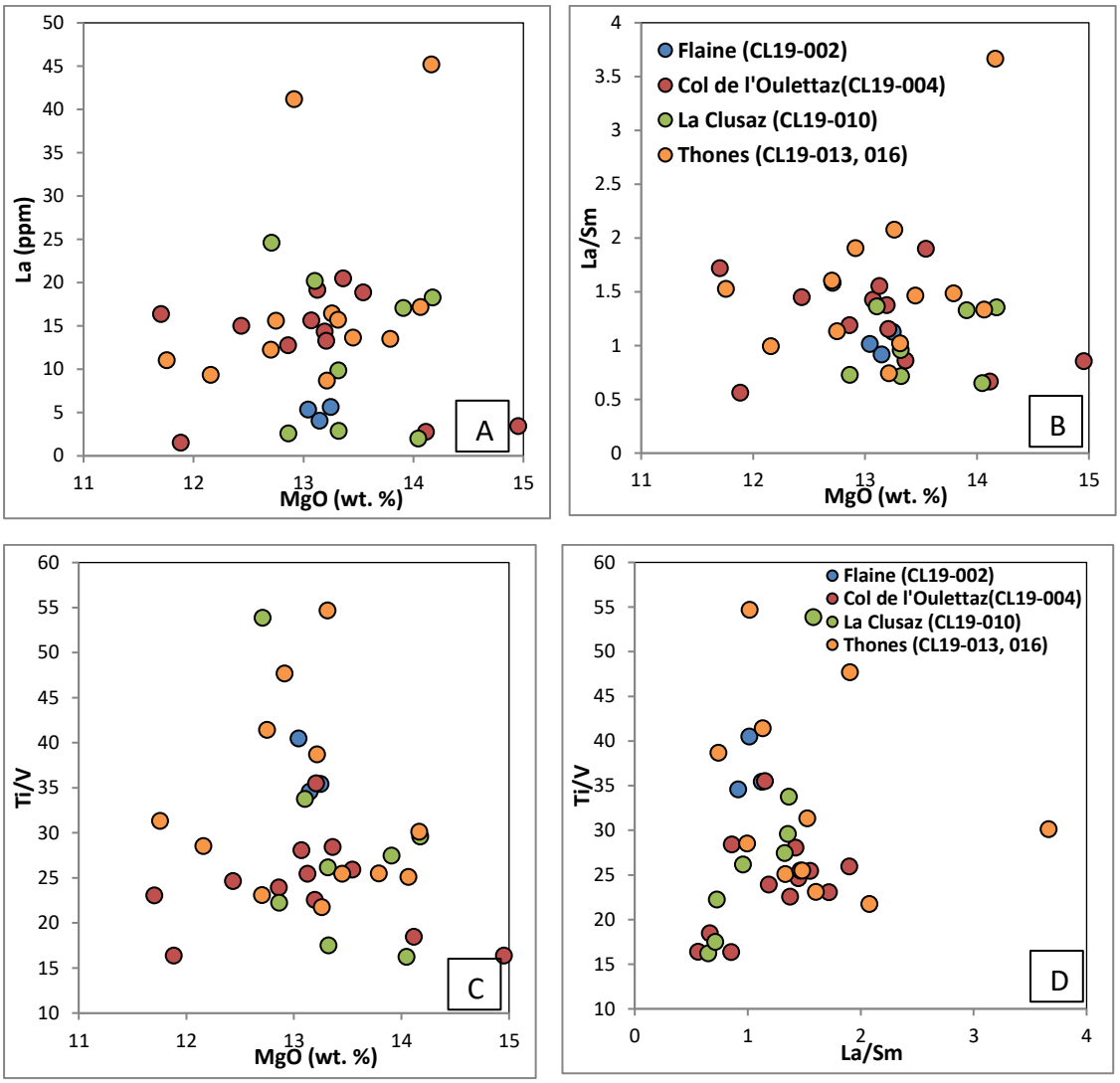

Figure 7.8 Binary diagrams of amphiboles from four localities of Aravis: A-C) selected trace element (ratios) vs MgO; D) La/Sm vs Ti/V

Amphiboles from four localities in Aravis are plotted without showing distinct variation in the binary diagrams (Figure 7.8). On the best discriminative La/Sm vs Ti/V diagram (Figure 7.8 D), most of the amphiboles plot in a similar spectrum except for those from Flaine where only three analyses were conducted.

7.3.3 Southern France

This region includes a total of 451 SEM analyses (164 amphiboles) from 12 samples of primary/proximal volcaniclastic deposits and 50 LA-ICP-MS analyses (50 amphiboles) from 5 samples of andesitic clasts in volcanic breccias.

7.3.3.1 Classification of amphibole

All amphiboles in S France are Calcium Amphibole. Amphiboles from St. Antonin and La Vanade are in the Pargasite subgroup (Figure 7.9), mainly including (Ti-rich) magnesio-hastingsite (85 %) and (Ti-rich) pargasite (13 %), except for two amphiboles from Fontagne locality distinguish themselves from others with higher $^{C}(Al+Fe^{3+}+2Ti)$ value (> 1.5) defined as sadanagalite and ferri-sadanagalite respectively.

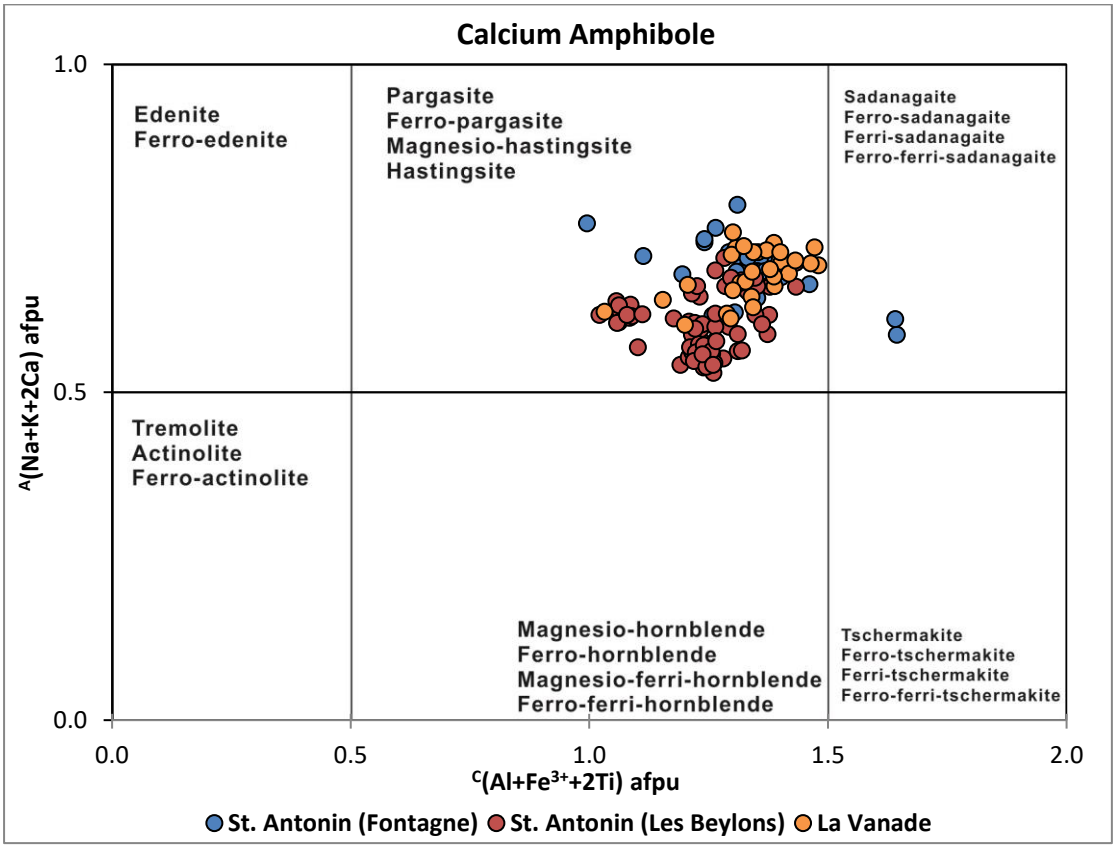

Figure 7.9 Calcium amphibole classification diagram of amphiboles from southern SE France after Hawthorne et al. (2012).

7.3.3.2 Binary diagrams (major elements)

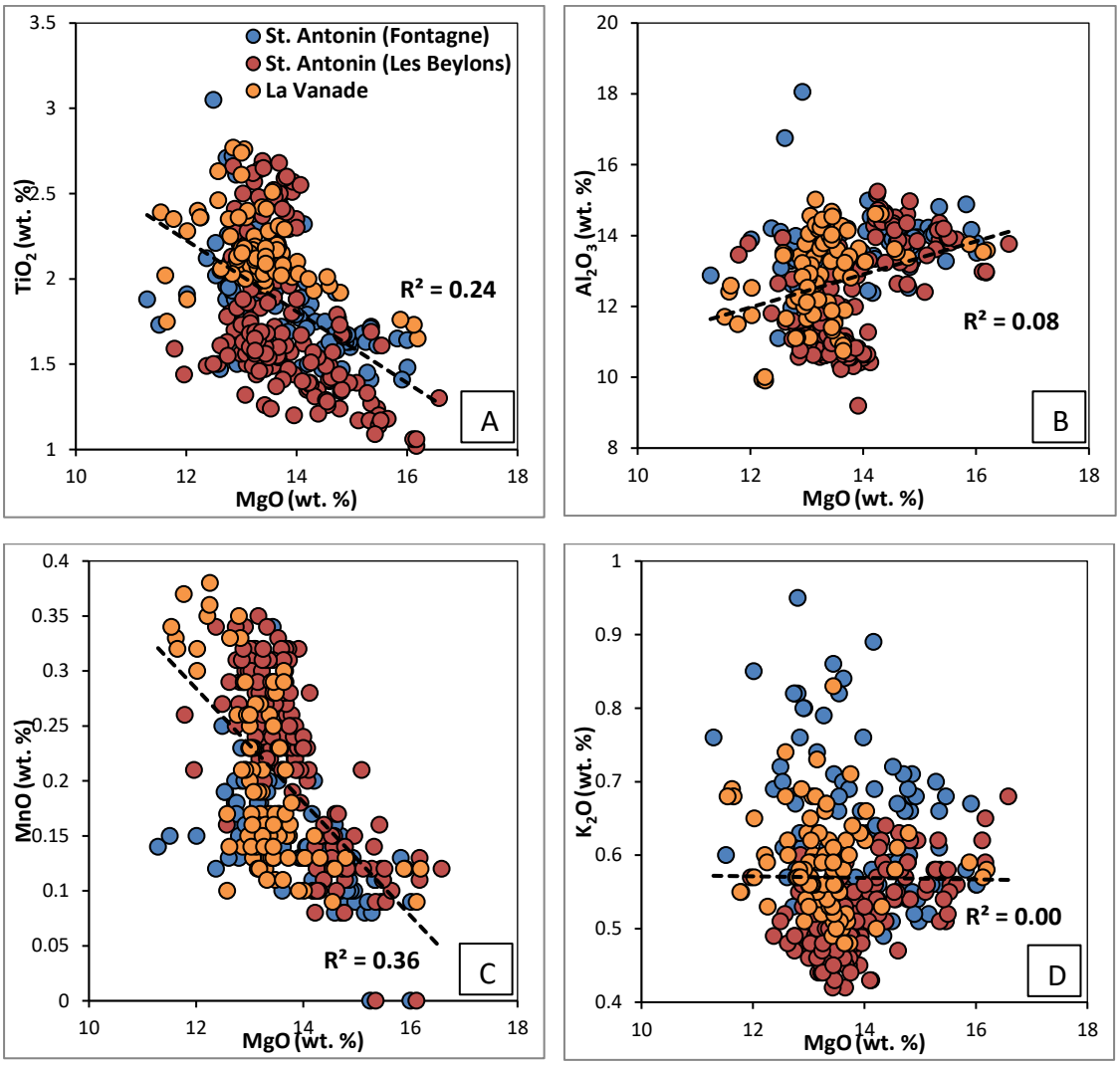

Figure 7.10 A-D) Binary diagrams of selected major elements vs MgO of amphiboles from S France

On the MgO vs major elements binary diagram (Figure 7.10 A-D), there is poor to moderate negative or positive correlation between MgO and selected major elements (R^2 = 0.01 - 0.36). In general, amphiboles from the three localities in S France are largely overlapping without showing distinct variation. Amphiboles from each locality are spreading in similar area on each binary diagrams, indicating the strong compositional similarity of amphiboles in the region.

7.3.3.3 Binary diagrams (trace elements)

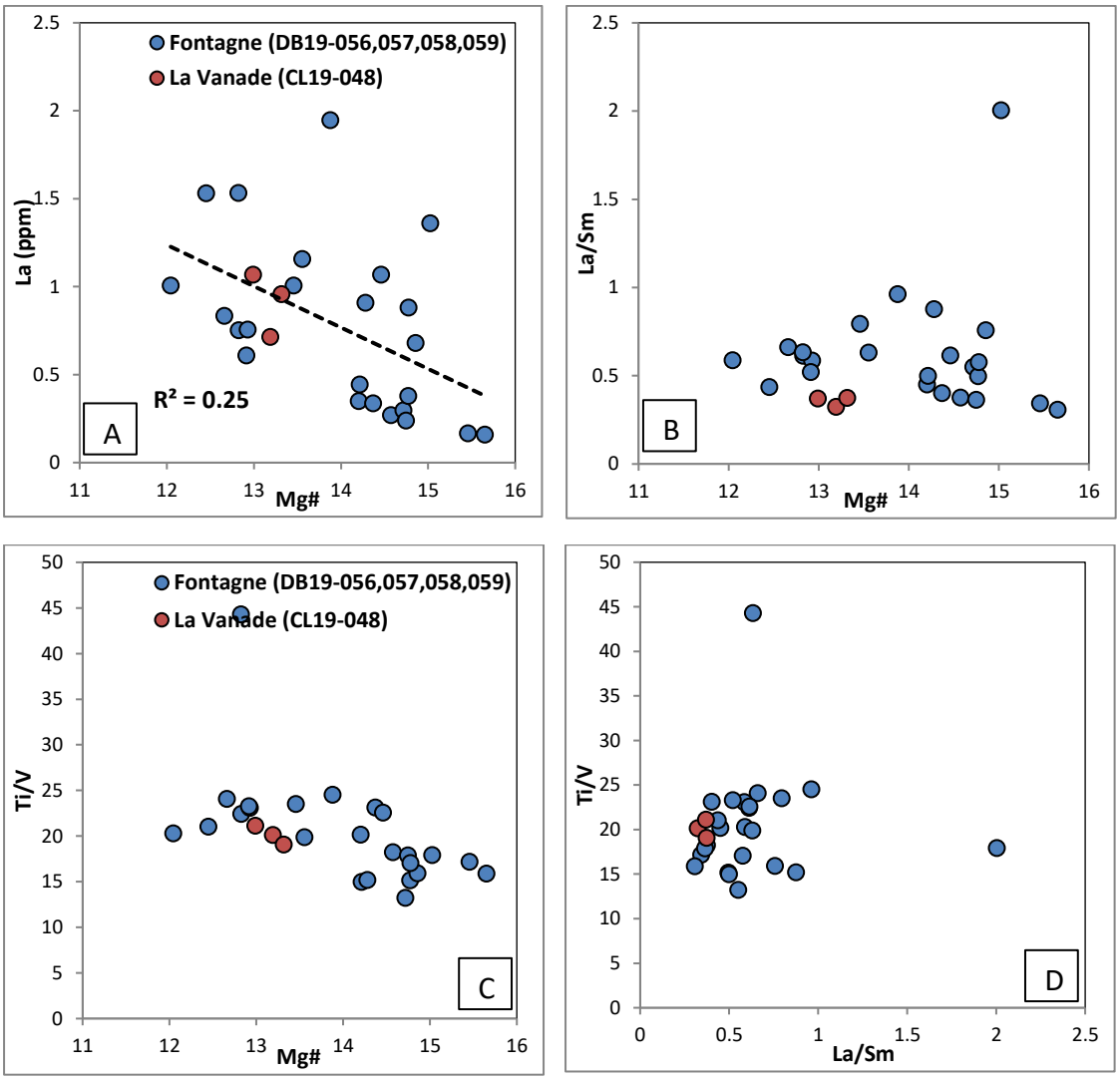

Figure 7.11 Binary diagrams of amphiboles from two localities of southern SE France: A-C) selected trace element (ratios) vs MgO; D) La/Sm vs Ti/V

Three amphiboles from La Vanade are plotted together with those from Fontagne without showing distinct difference in the binary diagrams (Figure 7.11). On the best discriminative La/Sm vs Ti/V diagram (Figure 7.11 D), three amphiboles from La Vanade plot in the spectrum of Fontagne amphiboles though the small amount of analyses impacts the accuracy of the results.

7.3.4 Summary

In summary, most of the amphiboles from localities in Aravis, W Switzerland and S France generally plot in cluster in the classification diagram and binary diagrams. However, amphiboles from localities in W Switzerland show a certain degree of compositional variability among different localities.

7.4 Inter-sample discrimination

Discrimination of amphiboles from various samples (more than one sample) within one single locality was conducted using the same selection of diagrams presented above, in order to outline possible differences of supply between stratigraphically similar samples. The localities including only one sample which have been discussed in Section 7.3 are not discussed in this section.

7.4.1 Thônes (Aravis)

This locality includes a total of 313 SEM analyses (115 amphiboles) from 5 samples of volcaniclastic sandstone and 12 LA-ICP-MS analyses (12 amphiboles) from 2 samples of volcaniclastic sandstone.

7.4.1.1 Classification of amphibole

All amphiboles in Thônes locality are Calcium Amphibole, most of which are in the Pargasite subgroup (Figure 7.12), mainly including (Ti-rich) pargasite (44 %), and (Ti-rich) magnesio-hastingsite (48 %). Few amphibole grains distinguish themselves from others with lower ^{A}(Na+K+2Ca) value (< 0.5) defined as magnesio-hornblende, and one from sample CL19-014 named as sadanagaite.

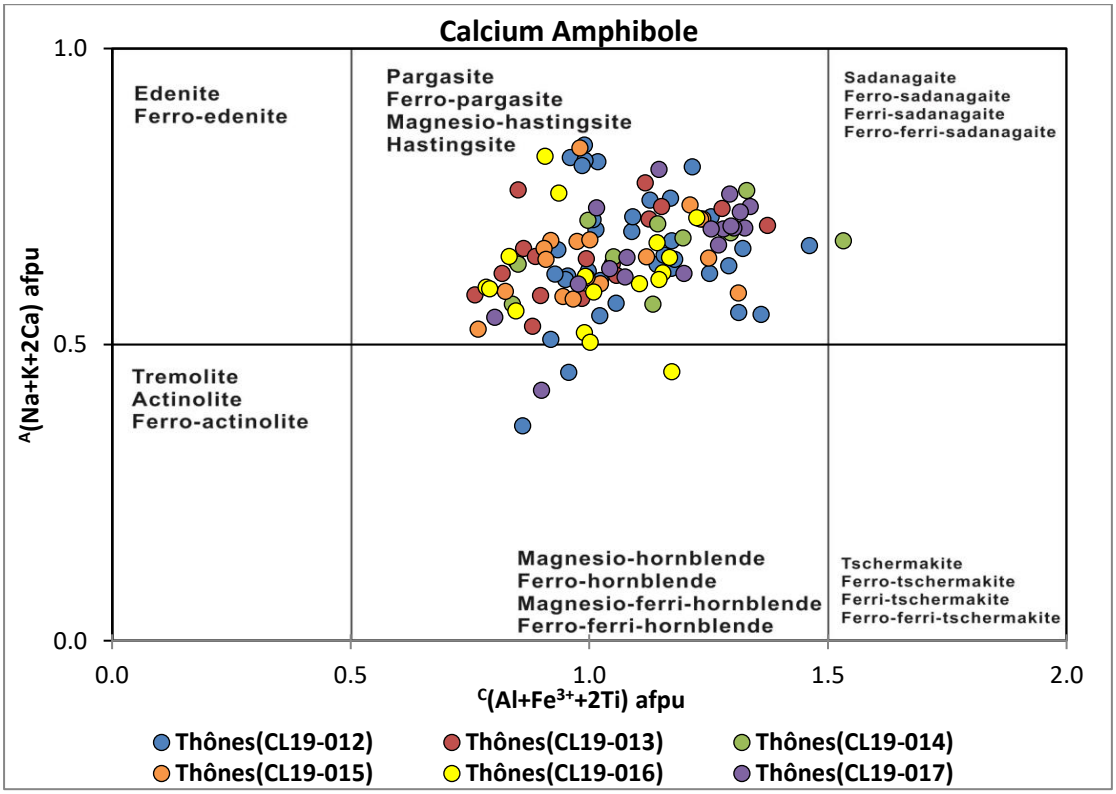

Figure 7.12 Calcium amphibole classification diagram of amphiboles from Thônes locality in Aravis after Hawthorne et al. (2012).

7.4.1.2 Binary diagrams (major elements)

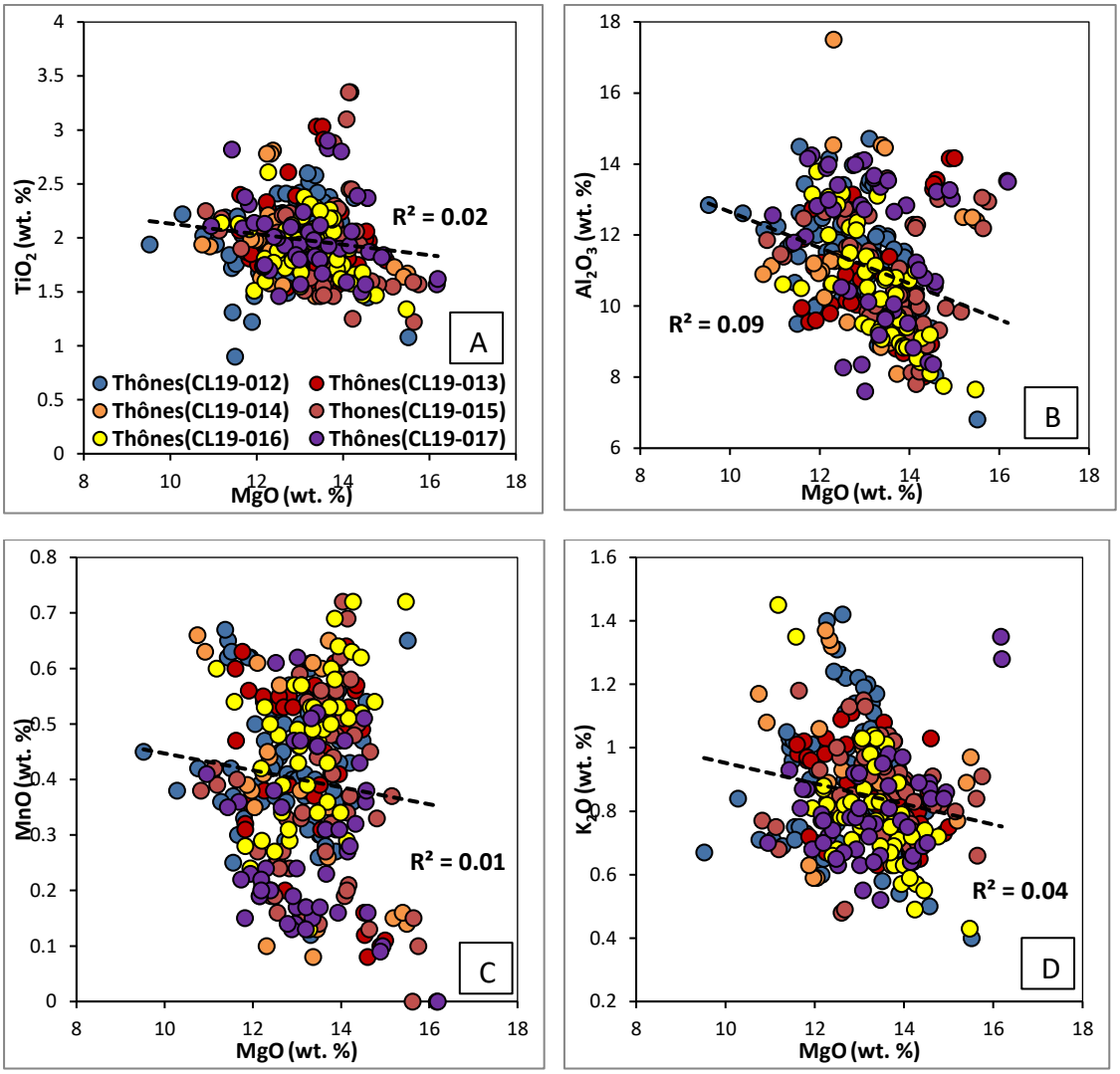

Figure 7.13 A-D) Binary diagrams of selected major elements vs MgO of amphiboles from Thônes locality in Aravis

On the MgO vs major elements binary diagram (Figure 7.13 A-D), there is poor to moderate negative or positive correlation between MgO and selected major elements (R^2 = 0.01 - 0.20). In general, amphiboles from the six samples in Thônes locality are largely overlapping without showing distinct variation. Amphiboles from each locality are spreading in similar spectrum on each binary diagrams, indicating the strong compositional similarity of amphiboles in the Thônes locality.

7.4.1.3 Binary diagrams (trace elements)

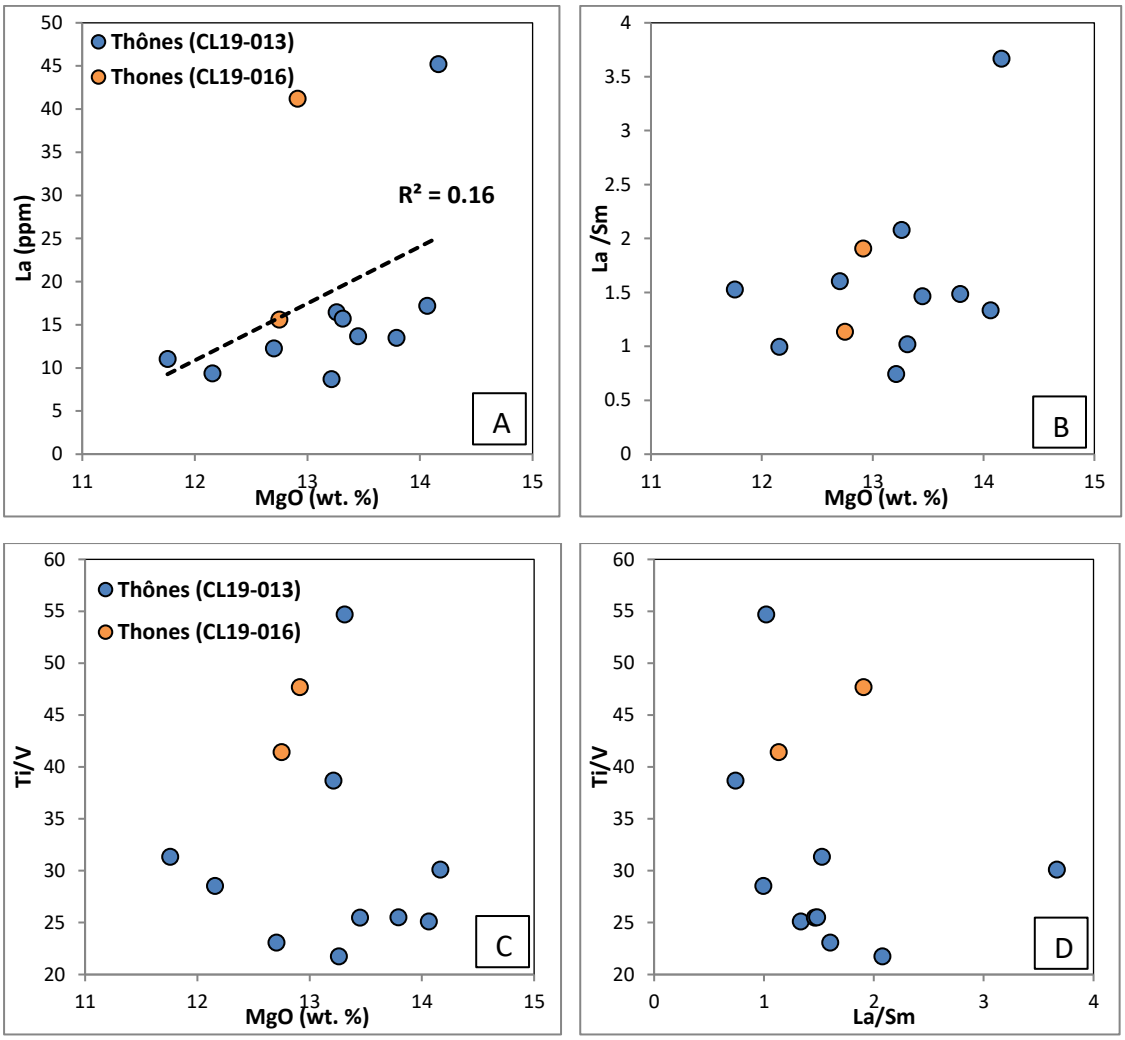

Figure 7.14 Binary diagrams of amphiboles from two samples in Thônes locality of northern SE France: A-C) selected trace element (ratios) vs MgO; D) La/Sm vs Ti/V

On the La/Sm vs Ti/V diagram (Figure 7.14 D), two amphibole grains of sample CL19-016 plot in the range of those from sample CL19-013 though the small amount of analyses impacts the accuracy of the results.

7.4.2 Champsaur

This locality includes a total of 856 SEM analyses (292 amphiboles) from 2 samples of volcaniclastic sandstone, 5 samples of igneous pebbles and 2 samples of andesitic clasts in volcanic breccias and 13 LA-ICP-MS analyses (13 amphiboles) from 1 sample of igneous pebble and 1 sample of andesitic clast in volcanic breccia.

7.4.2.1 Classification of amphibole

All amphiboles in Champsaur are Calcium Amphibole, except one grain of sample CL19-028, which is Sodium-Calcium Amphibole. The vast majority of the amphiboles (except for sample CL19-030) are in the Pargasite subgroup (Figure 7.15), mainly including (Ti-rich) pargasite (8 %) and (Ti-rich) magnesio-hastingsite (69 %) which all contain more Mg^{2+} than Fe^{2+}. Few amphibole grains distinguish themselves from others with higher $^{C}(Al+Fe^{3+}+2Ti)$ value (> 1.5) defined as ferri-sadanagalite and ferri-tschermakite. However, amphiboles of sample CL19-030 are classified very differently from other samples in Champsaur, where most of the amphiboles plot separately in the Hornblende and Actinolite subgroups, mainly including magnesio-hornblende (8 %), magnesio-ferri-hornblende (7 %) and actinolite (5 %).

Amphiboles from sample CL19-026, CL19-027 and CL19-041 are overlapping in a wide range of spectrum on the classification diagram, while amphiboles from sample CL19-038A, CL19-038B and CL19-039 plot in cluster with part of those from CL19-024. Some amphiboles from CL19-028 plot separately with the main population by higher $^{C}(Al+Fe^{3+}+2Ti)$ (> 1.5), while amphiboles from sample CL19-030 are distinctively discriminated by lower $^{A}(Na+K+2Ca)$ (< 0.5).

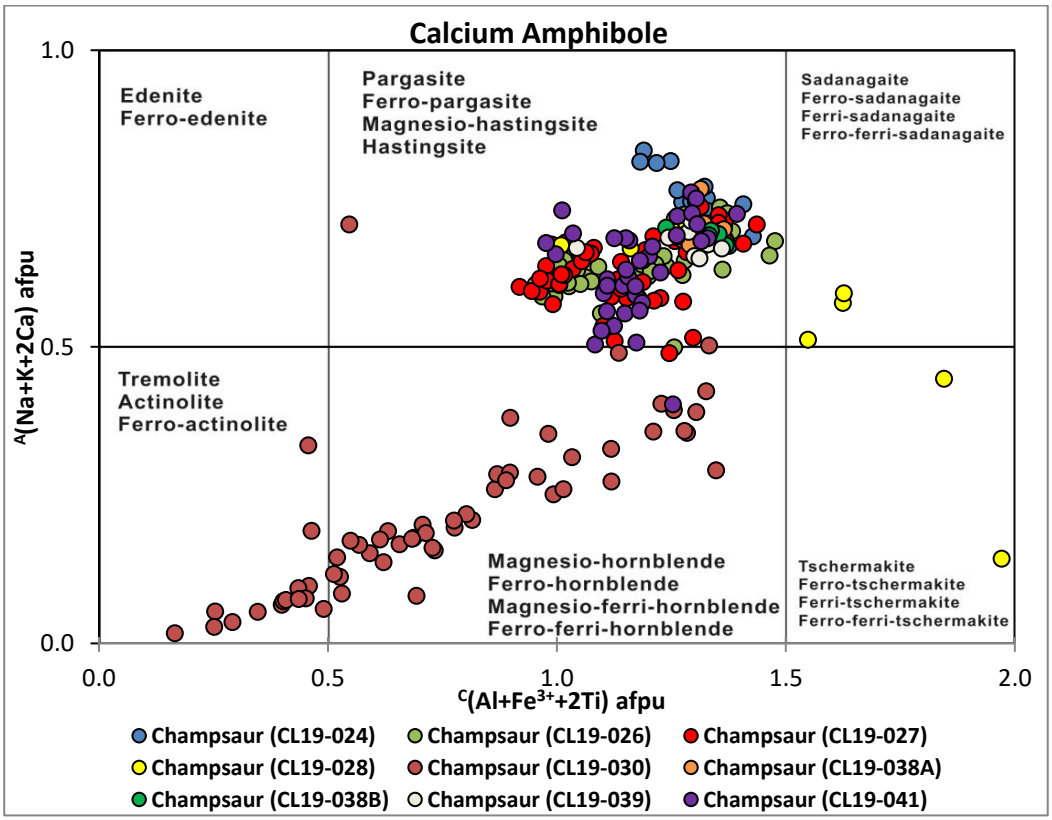

Figure 7.15 Calcium amphibole classification diagram of amphiboles in Champsaur locality after Hawthorne et al. (2012).

7.4.2.2 Binary diagrams (major elements)

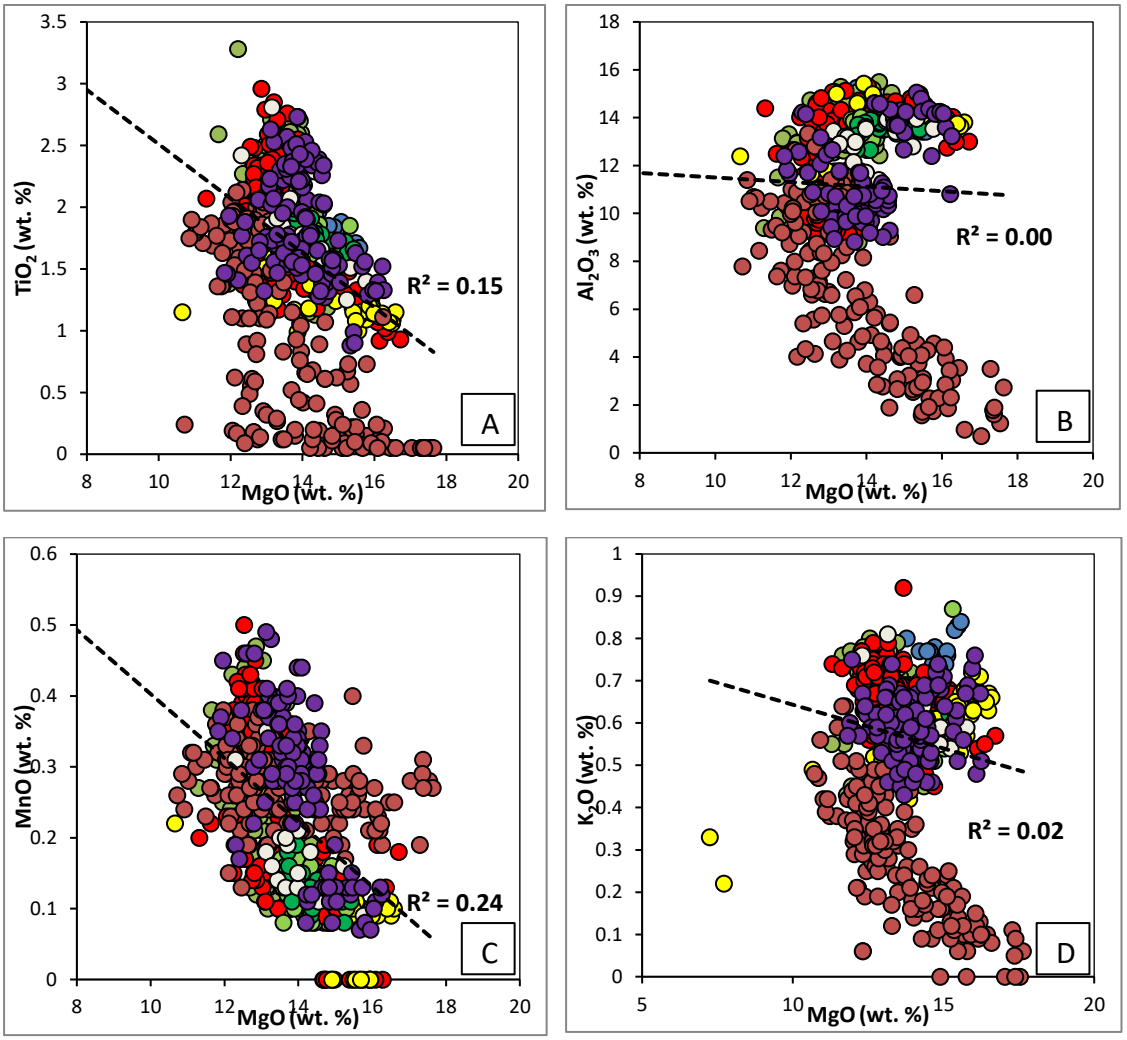

Figure 7.16 A-D) Binary diagrams of selected major elements vs MgO of amphiboles from Champsaur locality

On the MgO vs major elements binary diagram (Figure 7.16 A-D), there is poor to moderate negative or positive correlation between MgO and selected major elements (R^2 = 0.00 - 0.24). In general, amphiboles from the eight samples (except CL19-030) in Champsaur are largely overlapping. Sample CL19-030 presents totally different characteristics of amphibole geochemistry.

7.4.2.3 Binary diagrams (trace elements)

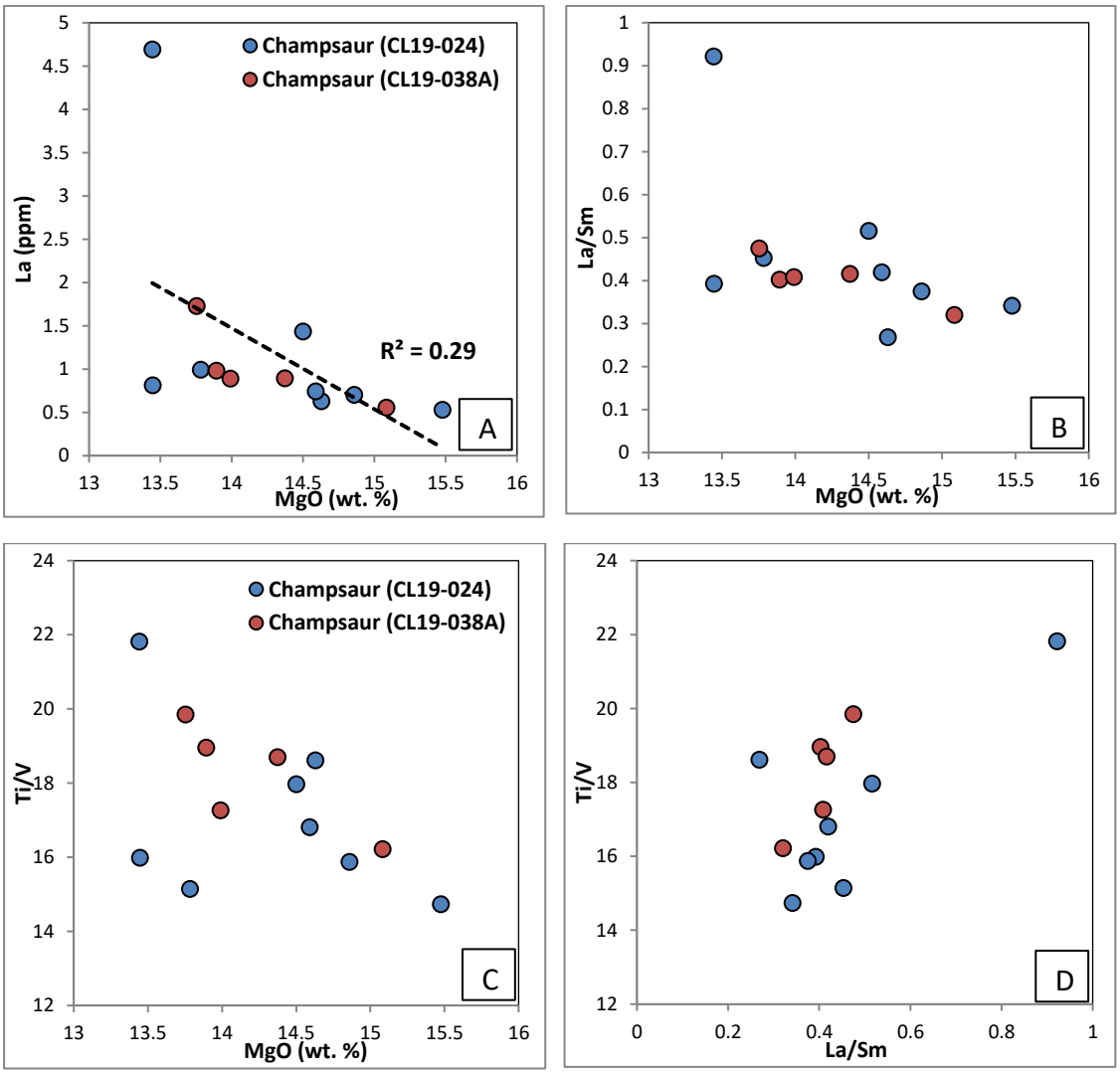

Figure 7.17 Binary diagrams of amphiboles from two samples in Champsaur of central SE France: A-C) selected trace element (ratios) vs MgO; D) La/Sm vs Ti/V

On the binary diagrams (Figure 7.17), amphiboles from sample CL19-024 generally plot together with those from sample CL19-038A without showing distinct difference. On the best discriminative La/Sm vs Ti/V diagram (Figure 7.17 D), amphiboles from CL19-024 plot in a wider spectrum than those from CL19-038A though the results could be biased due to limited number of analyses.

7.4.3 Fontagne (S France)

This locality includes a total of 87 SEM analyses (32 amphiboles) and 24 LA-ICP-MS analyses (24 amphiboles) from 3 samples of andesitic clasts within volcanic breccia and 1 sample of tuffaceous matrix.

7.4.3.1 Classification of amphibole

The vast majority of the amphiboles are in the Pargasite subgroup (Figure 7.18), mainly including pargasite (34 %) and (Ti-rich) magnesio-hastingsite (60 %) which all contain more Mg^{2+} than Fe^{2+}. Two amphibole grains distinguish themselves from others with higher $^{C}(Al+Fe^{3+}+2Ti)$ value (> 1.5) defined as ferri-sadanagalite and sadanagalite respectively. Amphiboles from the four samples are generally overlapping on the classification diagram without showing distinct discrimination.

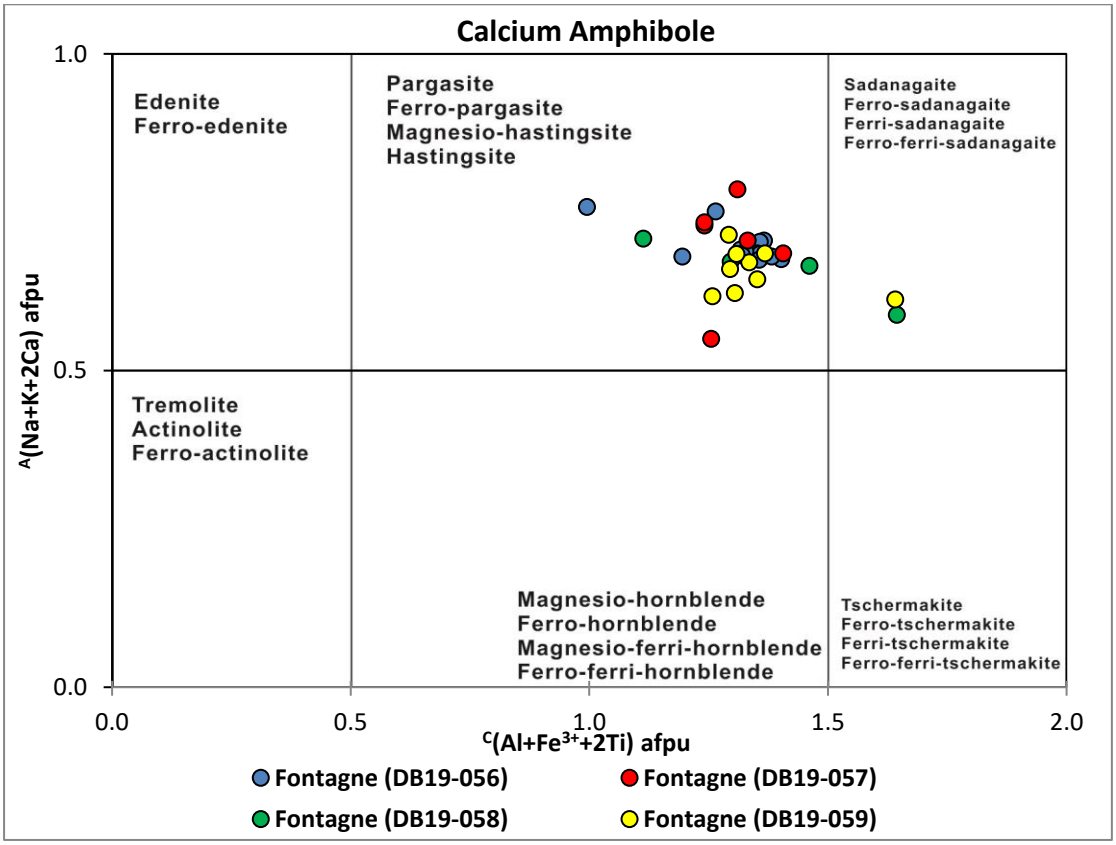

Figure 7.18 Calcium amphibole classification diagram of amphiboles in Fontagne locality after Hawthorne et al. (2012).

7.4.3.2 Binary diagrams (major elements)

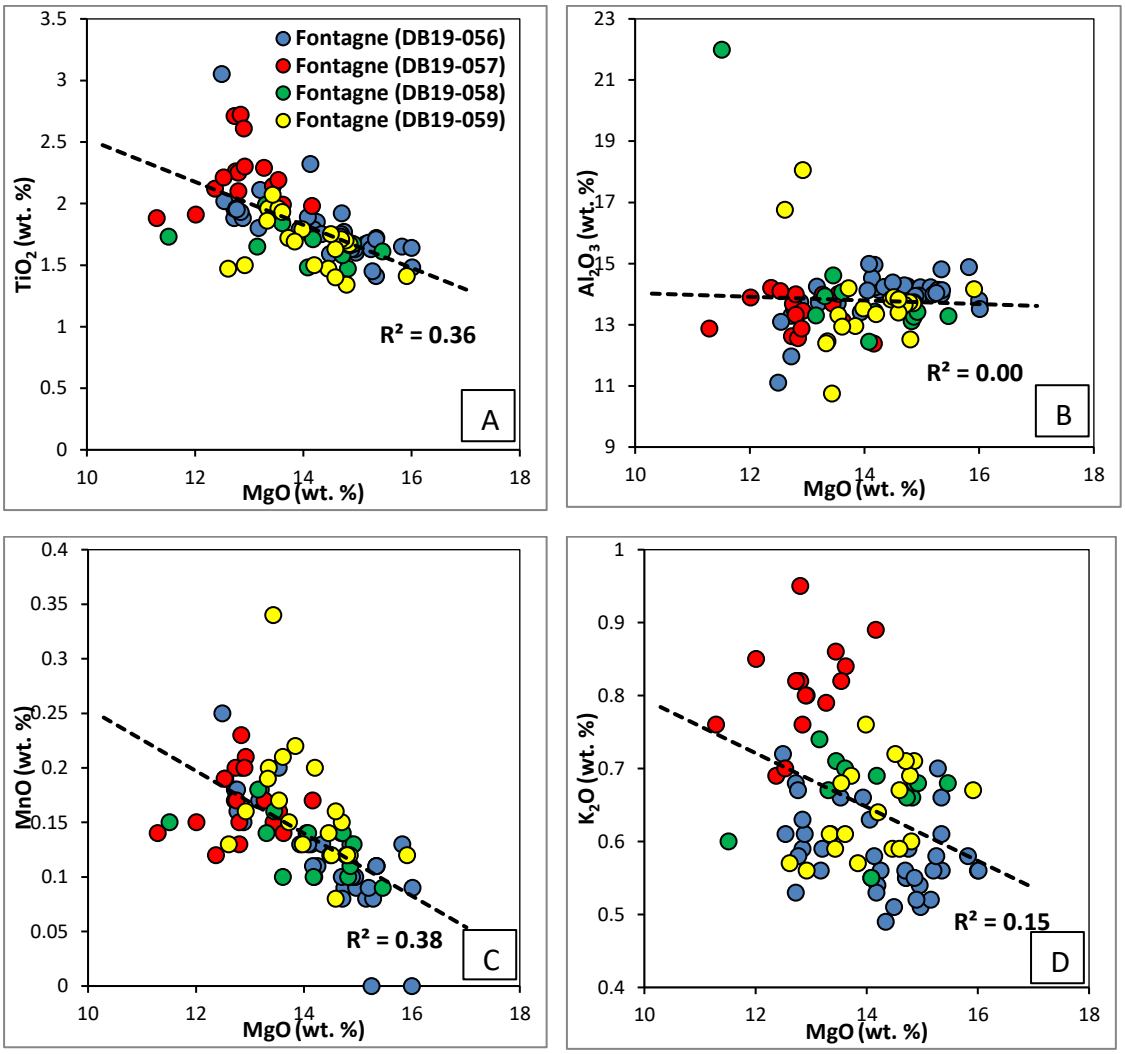

Figure 7.19 A-D) Binary diagrams of selected major elements vs MgO of amphiboles from Fontagne locality in S France

On the MgO vs major elements binary diagram (Figure 7.19 A-D), there is poor to moderate negative or positive correlation between MgO and selected major elements (R^2 = 0.00 - 0.38). Amphiboles from sample DB19-057 plot separately from the remaining three samples which are largely overlapping.

7.4.3.3 Binary diagrams (trace elements)

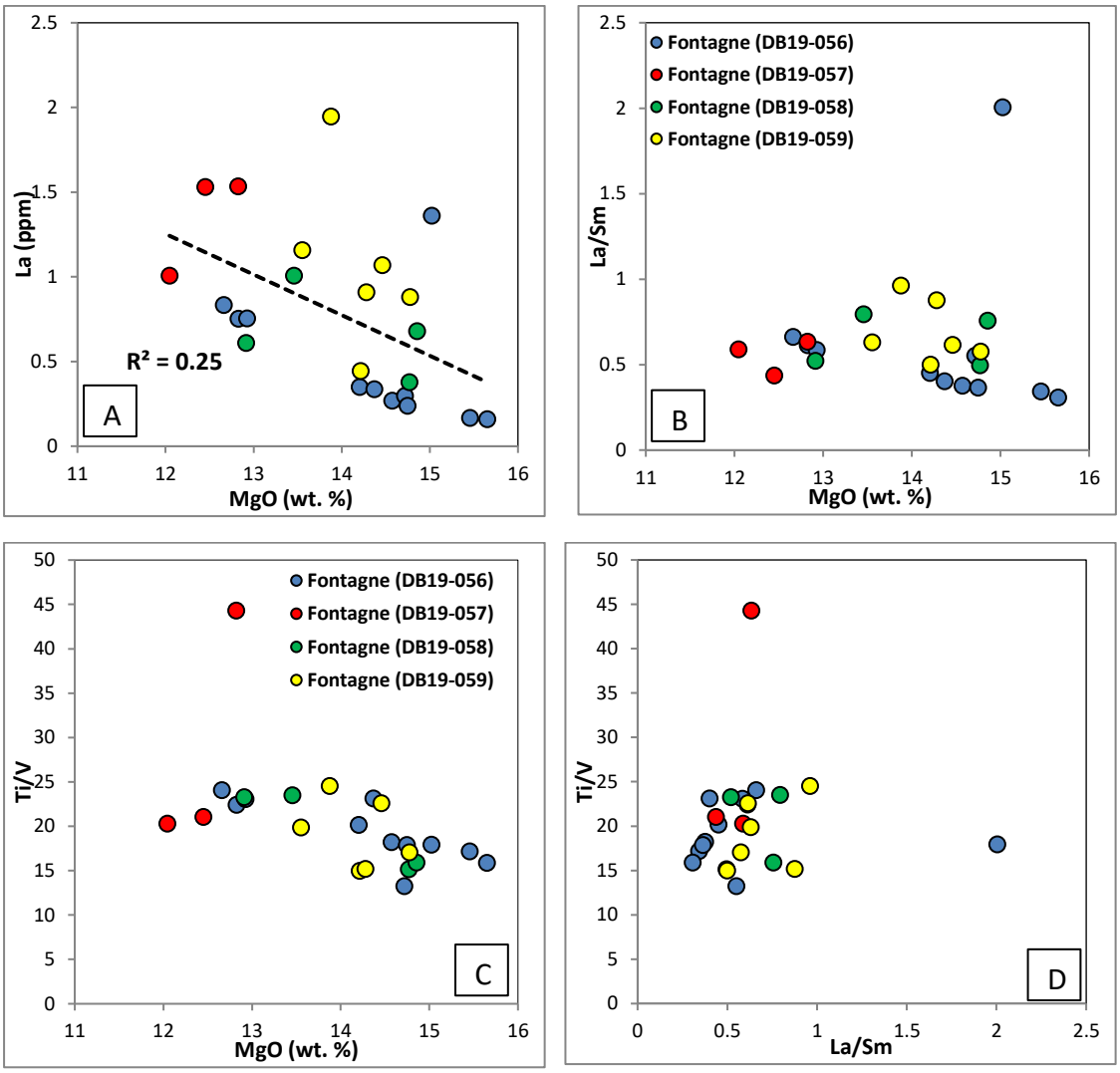

Figure 7.20 Binary diagrams of amphiboles from four samples in Fontagne locality of S France: A-C) selected trace element (ratios) vs MgO; D) La/Sm vs Ti/V

On the binary diagrams (Figure 7.20), amphiboles from the four samples generally plot together. On the best discriminative La/Sm vs Ti/V diagram (Figure 7.20 D), amphiboles from the four samples plot in cluster except the two amphiboles (one from DB19-056, another from DB19-057) which plot far from the main population.

7.4.4 Summary

In summary, most of the amphiboles from multiple samples in each single locality (i.e., Thônes, Champsaur and Fontagne) generally plot in cluster without showing distinct variation in the classification diagrams and binary

diagrams, except for sample CL19-030 in Champsaur locality which shows a totally different amphibole geochemistry with metamorphic characteristics. On the trace element binary diagrams, the results of amphibole geochemistry could be biased due to the limited number of LA-ICP-MS analyses.

7.5 Summary

In this chapter, the discrimination of amphiboles has been conducted on three levels of geographical scale in the order of region to locality to sample by different types of diagrams. Several conclusions could be summarised as follows (Figure 7.21):

(1) The amphibole classification diagram offers good compositional discrimination to identify amphiboles from possibly distinct sources at the regional to local scales.

(2) Inter-regional discrimination shows that amphiboles from Aravis are spreading over a large compositional spectrum, as well as those from E Switzerland and W Switzerland, though the results may be biased due to limited number of analyses in E Switzerland and W Switzerland. Amphiboles from Champsaur and S France are largely overlapping partially with the wide-spreading population of Aravis. Amphiboles from N Italy plot separately from the main population.

(3) Inter-locality discrimination shows that most of the amphiboles from different localities in Aravis, W Switzerland and S France generally plot in cluster without showing distinct variation. However, amphiboles from localities in W Switzerland show a certain degree of compositional variability among different localities.

(4) Inter-sample discrimination shows that most of the amphiboles from multiple samples in each locality (i.e., Thônes, Champsaur and Fontagne) generally plot in cluster without showing distinct variation, except for sample CL19-030 in Champsaur locality which shows a totally different amphibole geochemistry with metamorphic characteristics.

(5) Amphibole classification diagram provides a much better insight into compositional variability than other used discrimination approaches that are largely not effective to reveal distinct volcanic sources in the Alpine setting. In

order to address this limitation, a new PCA method compared with O'Neill (2016) method is developed and applied to amphiboles in Chapter 8.

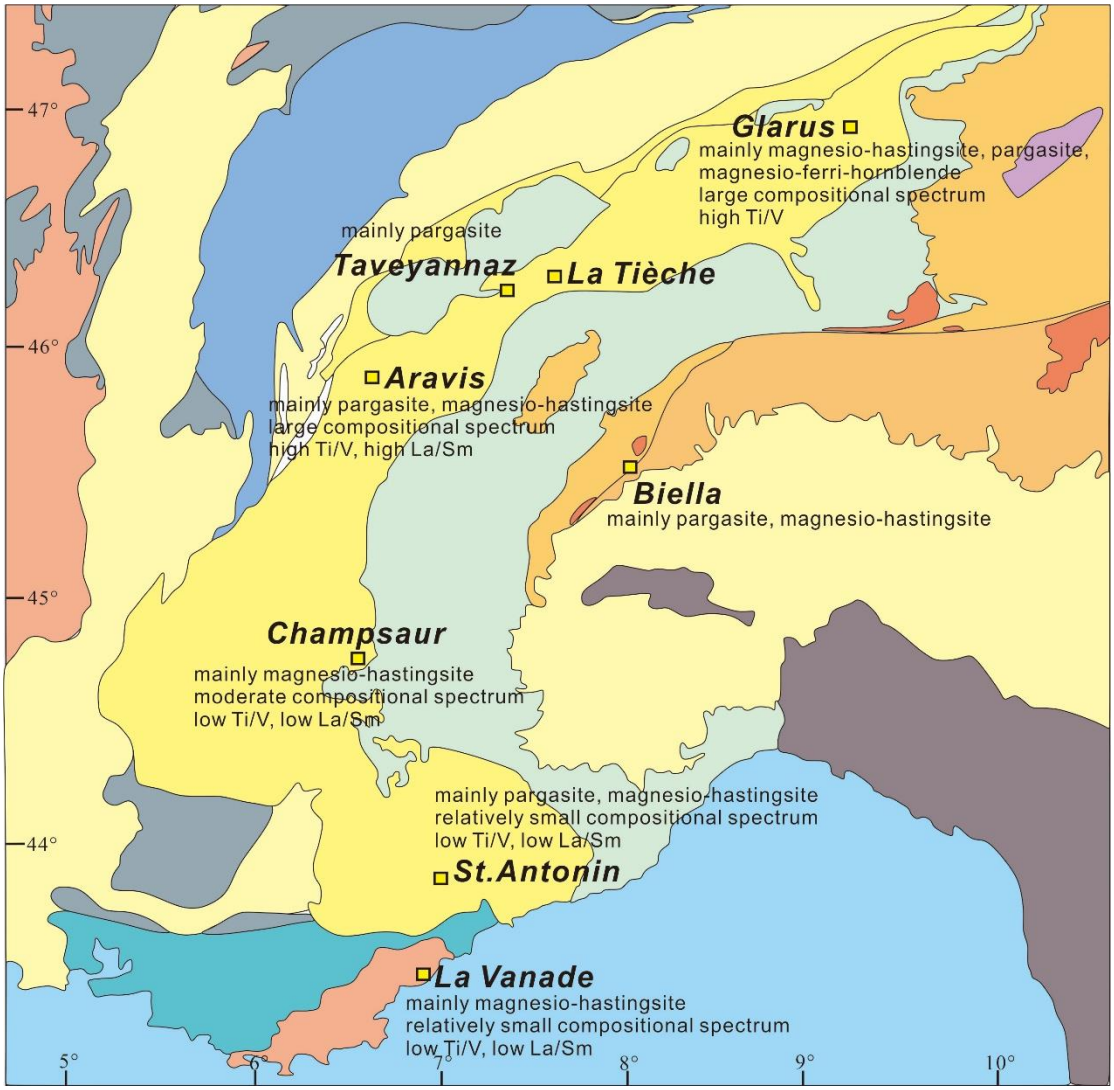

Figure 7.21 Geographical map summarising the main findings of amphiboles in each region

Chapter 8: New discrimination approaches of clinopyroxene and amphibole geochemistry for sediment provenance analysis

8.1 Introduction

As shown in chapters 6 and 7, there are two main limitations that need to be addressed to characterise the provenance of clinopyroxenes and amphiboles in Alpine volcaniclastic turbidites. First, there is limited compositional diversity of Alpine clinopyroxenes and amphiboles, which cannot be efficiently characterised using current techniques of discrimination. Second, these discrimination techniques are poorly effective at addressing magmatic differentiation that can obscure source effects. Therefore, a new discrimination approach based on Principle Component Analysis (PCA) was developed and applied in this study.

This chapter first summarises the development of previous methods for sediment provenance analysis and the new method rationale. Previous approaches on provenance analysis using clinopyroxene chemistry were reviewed. Then a case study using a population of compositionally relatively heterogenous clinopyroxenes in Japan was applied to PCA method and compared with the orthogonal polynomial approach of O'Neill (2016). Lastly, a case study using a population of compositionally relatively homogenous clinopyroxenes and amphiboles of our data in the Alps was applied to PCA method, also compared with the orthogonal polynomial approach.

8.2 Sediment provenance methods

Sediment provenance analysis fundamentally aims at reconstructing source-to-sink processes in subaerial to submarine sedimentary systems by using key proxies considered to reflect the composition (mineralogy and geochemistry) of the source(s) of clastic sediments and the compositional and textural transformations of these sediments during their transport-deposition, weathering and diagenesis.

Methods commonly used to determine the source(s) of a sediment or sedimentary rock include (i) petrographic analysis of framework grains (e.g.,

quartz, feldspars and lithics, Dickinson and Suczek, 1979; Dickinson, 1985; Garzanti et al., 2007), (ii) petrographic analysis of heavy minerals (Stattegger, 1987; Nechaev and Isphording, 1993; Garzanti and Andò, 2007a; Garzanti and Andò, 2007b), (iii) whole-rock geochemistry (Bhatia, 1985; McLennan et al., 1989; Feng and Kerrich, 1990; McLennan et al., 1993; Cullers, 2000), (iv) single-grain geochronology and thermochronology (Belousova et al., 2002; Bütler et al., 2011; Jourdan et al., 2013; Beltràn-Trivino et al., 2013; Jourdan et al., 2018; Lu et al., 2018; Lu et al., 2019), and (v) single-grain geochemistry (Nisbet and Pearce, 1977; Leterrier et al., 1982; Beccaluva et al., 1989; Tolosana-Delgado et al., 2018).

Each of these above-mentioned approaches is associated with its own advantages and limitations. For instance, petrographic and compositional changes of the bulk sediment, which are relatively easy to determine by microscope grain counting or quantitative analytical techniques, do not directly reflect the composition of the source(s), and are also controlled by sorting effects during the transport and deposition of minerals and lithics of variable size and density (e.g., Ingersoll, 1984). In addition, weathering and diagenesis can preferentially remove some of the sediment components depending on their relative chemical stability and physico-chemical conditions in the sedimentary environment/basin, independently from the size and density of these components, ultimately creating important changes in the composition of framework and heavy minerals independently from source effects (Morton, 1984; McBride, 1985; Rahn et al., 1995). Therefore, preferential alteration and segregation of some sediment components during transport, deposition and diagenesis, make the study of bulk sediment composition of limited value to characterise the source(s) of clastic sediments.

A more constrained approach to determine the nature of unknown sediment sources and characterise their contribution to a sedimentary system is to study the composition of single species of detrital minerals with similar sizes. This single grain quantitative approach is, arguably, best exemplified by the study of the composition of detrital zircons, that notably allows determination of crystallisation ages in a magmatic or metamorphic protolith (U-Pb geochronology), or cooling ages during exhumation of this protolith (U/Th-He thermochronology) (Belousova et al., 2002; Bütler et al., 2011; Jourdan et al.,

2013; Beltrán-Triviño et al., 2013; Jourdan et al., 2018; Lu et al., 2018; Lu et al., 2019). Zircons are extremely resilient to weathering and alteration, making them excellent source tracers and the longest-lived archive of Earth's history (Wilde et al., 2001; Grimes et al., 2007; Harrison, 2009).

However, detrital zircons are predominantly formed in slowly crystallised felsic magmas, which limits their value in sedimentary systems dominated by the erosion of mafic igneous rocks (e.g., andesitic volcanoes). Yet, sedimentary environments can be associated with volumetrically significant mafic volcaniclastics in the geological record, most particularly in convergent tectonic settings that are associated with arc and/or orogenic volcanism. In addition, the sources of detrital zircons are commonly determined by age constraints alone, which impedes discrimination of protoliths of similar age, and does not inform on compositional changes generally observed in distinct magmatic sources/volcanic systems. In contrast, the geochemistry of single-grain mafic minerals such as clinopyroxenes and amphiboles are better suited to characterise the detailed composition of mafic to intermediate volcanic sources (e.g., Leterrier et al., 1982; Beccaluva et al., 1989). However, these mafic minerals are more readily altered and dissolved by weathering and diagenesis than zircons. Yet, these minerals can be commonly preserved in ancient and modern volcano-sedimentary environments. Notable examples of preservation include occurrences in (i) Pleistocene-Pliocene volcaniclastic turbidites down to ~1 km depth in the Kumano forearc basin in Japan (Buchs et al., 2015), (ii) dismembered accreted trench deposits in the Eocene Osa subduction mélange in Costa Rica (Buchs and Oemering, 2020), and (iii) Oligocene volcaniclastic turbidites in foreland basins in the Swiss and French Alps (Vuagnat, 1952; Sinclair et al., 1992; Rahn et al., 1995; Ruffini et al., 1997; Boyet et al., 2001; Lu et al., 2018).

8.3 Previous studies on clinopyroxene provenance analysis

Clinopyroxene is a common mafic mineral in volcaniclastic rocks with mafic-intermediate affinity, which makes it a better indicator of magmatic variability compared to framework mineral (i.e., plagioclase), which is a comparatively late-stage mineral affected more by fractional crystallisation, and compared to detrital zircon, which is mostly formed by the erosion of felsic rocks and recycling of older sedimentary deposits. Leaving aside the effect of cooling

rate and fractional crystallisation as major factors influencing clinopyroxene chemistry, their composition appears to be essentially related to the source of host magma (Beccaluva et al., 1989).

Many attempts have been made in discriminating clinopyroxenes in basalts from various tectonic settings. Kushiro (1960) has found that the proportions of Si and Al in the tetrahedral position of pyroxene structure could indicate the magma type (i.e., the more alkaline the magma type, the more aluminous the clinopyroxene). Le Bas (1962) also demonstrated that the Al content of a clinopyroxene increases from tholeiitic rocks to alkaline rocks. These conclusions are both mainly achieved by using binary diagrams (e.g., SiO_2 vs. Al_2O_3). Leterrier et al. (1982) proposed a set of tectonic discrimination diagrams involving Ti, Cr, Ca, Al and Na contents of clinopyroxene of volcanic rocks from various magma types as parameters to identify the magmatic affinity of volcanic series. Beccaluva et al. (1989) proposed mainly binary (e.g., TiO_2 vs. Zr/Y) and ternary (e.g., TiO_2-Na_2O-SiO_2/100) discrimination diagrams for differentiating clinopyroxenes in basalts from high-Ti to low-Ti ophiolite complexes. A recent study of the provenance of volcaniclastic turbidites in a forearc in Japan suggests that the geochemistry of detrital clinopyroxene offers a very sensitive and innovative way to determine magmatic changes and/or the nature of volcanic sources along a convergent margin (Buchs et al., 2015). This study shows that a large range of mafic-intermediate volcanic sources can be identified based on selected trace element contents (e.g., REE) of detrital clinopyroxene, which cannot be recognised based on detrital zircon geochronology and geochemistry that are mostly controlled by the erosion of felsic intrusions and recycling of older sedimentary deposits.

However, existing discrimination approaches suffer from using only few geochemical variables (i.e., elements), but modern analytical techniques allow for the acquisition of an increased number of variables/elements that remain to be considered to improve discrimination. Existing discrimination approaches also suffer from a certain level of subjectivity because they are based on empirical determination of discrimination criteria, typically shown in the form of strict boundaries separating “defined” compositional fields in binary geochemical diagrams, but in practice minerals from single sources commonly extend across discrimination criteria/compositional fields.

Moreover, the existing methods are mainly created for discriminating volcanic rocks of distinct magmatic affinities/tectonic settings, but these methods are not advanced enough to make them applicable for regional provenance analysis where it is necessary to identify/discriminate compositionally similar sources (e.g., distinct volcanic sources within a short-lived magmatic system).

8.4 Developing a new provenance discrimination using single-grain mineral REE data

This section presents a new discrimination approach applicable to single-grain clinopyroxenes and amphiboles, which addresses many of the limitations discussed above. This is the first time it has been applied to clinopyroxene and amphibole compositional data. This method takes advantage of modern analytical techniques to determine trace element contents of these minerals with the application of a robust multivariate analysis. This method will combine our knowledge of geochemical controls on the change of clinopyroxene/ amphibole compositions in various (modern) magmatic systems (i.e., tholeiitic, calcalkaline and alkaline) and our innovative application of Principal Component Analysis (PCA) to provide a more robust characterisation of clinopyroxene and amphibole diversity, applicable to mineral populations having both large and small compositional ranges. In addition, this approach will allow to refine Buchs et al. (2015) method and will result in further development of a new technique of sediment provenance analysis applicable to volcano-sedimentary environments globally.

8.4.1 Principal Component Analysis (PCA)

Sediment provenance analysis has entered the so-called “Big Data” era. As large datasets are relatively easy to acquire through geochemical analysis, robust multivariate analysis is becoming increasingly needed to synthesise and interpret complex information (Vermeesch and Garzanti, 2015). Principal Component Analysis (PCA) is a classical multivariate statistical technique aimed at simplifying the handling and interpretation of large datasets. PCA was first introduced to compositional data analysis by Aitchison (1982), and has been applied to many aspects in geoscience field, including the discrimination study of tectonic settings by Butler and Woronow (1986), the investigation on detrital zircon age structure by Thern and Nelson (2012), the

sediment provenance study on clay mineral compositions by Lee et al. (2013), the provenance study on clastic sediments of polycyclic sources by Zhang et al. (2014) and the classification of host-rock groups based on garnet composition by Tolosana-Delgado et al. (2018).

PCA could transform numerous variables into several independent principal components. The new components are not correlated to each other and typically account for more than 90 % of the total variation (Aitchison, 1983; Aitchison and Greenacre, 2002). In other words, PCA successfully reduces the dimensionality of data and keep the information loss as little as possible. Therefore, the characteristics of the PCA approach seem particularly suitable to analyse large geochemical datasets (e.g., REE and trace elements). In the case of REE, which are widely known to be highly discriminative petrological indicators, it is neither practical to analyse independently all 14 REE (some of which are closely related to each other), nor to only select a few of the most informative elements to be analysed, because information contained in other elements could be lost. Therefore, PCA could help synthesise REE variability and create a set of new variables (i.e., principal components) to facilitate the characterisation of the composition of clinopyroxenes and amphiboles with both large and small compositional variability, e.g., within similar, or across distinct, tectonic settings.

Despite the clear advantages of the PCA approach, there are several limitations to be noted. Principal components that, by definition, combine the variability of a larger number of primary parameters can be difficult to interpret in complex systems. Principal components from major and trace element analyses are linear combinations of the variables (elements) from the original dataset, but they can be challenging to interpret in terms of geochemical or petrological processes (Vermeesch, 2006).

8.4.2 PCA operation procedure

The PCA calculation was performed on statistical software IBM SPSS Statistics 27.0.1, accessible from Cardiff Software (https://software.cardiff.ac.uk/SPSS). This software will automatically pre-process the data and conduct the transformation. In theory, centered log–ratio transformation should be applied to remove the non-negativity and constant-sum constraints on compositional variables (Aitchison, 1982). However, in this study, our trace

element data do not have a constant-sum issue because the total concentration of all used trace elements for PCA only makes up a small amount of the whole composition of the sample. This transformation was therefore not applied here.

REE are incompatible trace elements and thus their concentration increases in the melt during magmatic differentiation. This is commonly reflected by overall changes in the trace element contents of co-magmatic mafic minerals, e.g., a general increase in position of a pattern in a multi-element diagram. Although magmatic differentiation could be considered a useful discrimination for the characterisation of the provenance of mafic minerals, this could also be regarded as a bias of the information more directly related to compositional changes indicative of the intrinsic characteristics (as opposed to perhaps unspecific differentiation trends) of distinct volcanic centres/sources. A simple way to reduce differentiation effects is to divide all data by the value of a selected trace element (e.g., Yb), thus producing elemental ratios (e.g., La/Yb, Ce/Yb, etc.) that define a new set of chemical parameters to be used in the PCA. This approach works particularly well for REE which commonly show a gradual change of behaviour in magmatic systems, but it can in principle work for all elements as long as their compatibility is broadly similar to that of the normalising element (e.g., Yb).

When operating PCA, it is found that the following two methods of pre-processing data generate different results:

Method 1: When variables are the original data (or chondrite normalised or primitive mantle normalised or normalised by average value of each corresponding element), the PCA results are the same.

Method 2: When variables are original data divided by Yb, or CI/PM normalised data divided by Yb, the PCA results of Method 2 are the same, but different from the Method 1 results.

Following a standard PCA approach, the following procedure was used:

1. Normalise trace elements to be analysed by dividing their corresponding Yb to eliminate differentiation effects; this step can be skipped if the characterisation of magmatic differentiation is deemed advantageous for the discrimination.

	V/Yb	La/Yb	Ce/Yb	Pr/Yb	Nd/Yb	Zr/Yb	Hf/Yb	Sm/Yb	Eu/Yb	Ti/Yb	Gd/Yb	Tb/Yb	Dy/Yb	Y/Yb	Ho/Yb	Er/Yb	Tm/Yb
1	66.55	2.89	11.06	1.99	9.93	12.96	0.72	2.66	0.53	720.51	2.47	0.35	2.12	9.05	0.39	1.11	0.15
2	23.46	2.44	8.94	1.59	7.98	7.11	0.42	2.31	0.41	269.20	2.24	0.34	2.12	8.77	0.41	1.12	0.15
3	73.78	3.00	11.16	1.98	10.13	14.21	0.81	2.75	0.60	818.18	2.55	0.37	2.15	9.17	0.40	1.16	0.16
4	44.18	2.95	10.87	1.92	9.69	12.72	0.72	2.69	0.46	460.49	2.45	0.36	2.12	9.11	0.39	1.11	0.15
5	60.06	7.28	21.60	3.17	14.58	11.21	0.66	3.41	0.72	596.37	3.06	0.43	2.42	10.13	0.44	1.20	0.16

2. Calculate the correlation matrix of the standardised variables. Use three variables calculation as an example, if there are 17 variables as in this research, it will be a 17x17 correlation matrix.

$$\begin{bmatrix} V[X_1] & Cov[X_1, X_2] & Cov[X_1, X_3] \\ Cov[X_2, X_1] & V[X_2] & Cov[X_2, X_3] \\ Cov[X_3, X_1] & Cov[X_3, X_2] & V[X_3] \end{bmatrix}$$

Correlation Matrix																	
	V/Yb	La/Yb	Ce/Yb	Pr/Yb	Nd/Yb	Zr/Yb	Hf/Yb	Sm/Yb	Eu/Yb	Ti/Yb	Gd/Yb	Tb/Yb	Dy/Yb	Y/Yb	Ho/Yb	Er/Yb	Tm/Yb
V/Yb	1.00	.043	.056	.052	.088	.457	.398	.229	.469	.900	.314	.451	.512	.453	.536	.477	.390
La/Yb	.043	1.00	.963	.927	.878	.310	.250	.765	.509	.075	.620	.495	.363	.237	.270	.199	.207
Ce/Yb	.056	.963	1.00	.980	.940	.328	.339	.850	.584	.085	.688	.553	.415	.208	.296	.222	.219
Pr/Yb	.052	.927	.980	1.00	.985	.305	.383	.912	.650	.074	.772	.602	.442	.183	.296	.227	.207
Nd/Yb	.088	.878	.940	.985	1.00	.304	.426	.954	.720	.105	.847	.669	.502	.189	.343	.273	.233
Zr/Yb	.457	.310	.328	.305	.304	1.00	.703	.399	.388	.582	.349	.534	.545	.653	.542	.533	.491
Hf/Yb	.398	.250	.339	.383	.426	.703	1.00	.524	.614	.432	.508	.522	.499	.163	.396	.397	.273
Sm/Yb	.229	.765	.850	.912	.954	.399	.524	1.00	.816	.247	.933	.828	.690	.303	.532	.469	.390
Eu/Yb	.469	.509	.584	.650	.720	.388	.614	.816	1.00	.440	.860	.762	.666	.193	.545	.442	.309
Ti/Yb	.900	.075	.085	.074	.105	.582	.432	.247	.440	1.00	.317	.489	.541	.533	.565	.507	.423
Gd/Yb	.314	.620	.688	.772	.847	.349	.508	.933	.860	.317	1.00	.871	.739	.328	.591	.524	.415
Tb/Yb	.451	.495	.553	.602	.669	.534	.522	.828	.762	.489	.871	1.00	.937	.590	.853	.812	.697
Dy/Yb	.512	.363	.415	.442	.502	.545	.499	.690	.666	.541	.739	.937	1.00	.617	.948	.919	.802
Y/Yb	.453	.237	.208	.183	.189	.653	.163	.303	.193	.533	.328	.590	.617	1.00	.662	.651	.654
Ho/Yb	.536	.270	.296	.296	.343	.542	.396	.532	.545	.565	.591	.853	.948	.662	1.00	.932	.846
Er/Yb	.477	.199	.222	.227	.273	.533	.397	.469	.442	.507	.524	.812	.919	.651	.932	1.00	.889
Tm/Yb	.390	.207	.219	.207	.233	.491	.273	.390	.309	.423	.415	.697	.802	.654	.846	.889	1.00

3. Calculate the eigenvalues and eigenvectors of the correlation matrix.

4. Sort eigenvalues from the highest to the lowest. The eigenvector with the highest eigenvalue is the first principal component. Higher eigenvalues correspond to greater amounts of shared variance explained.

Total Variance Explained						
	Initial Eigenvalues			Extraction Sums of Squared Loadings		
Component	Total	% of Variance	Cumulative %	Total	% of Variance	Cumulative %
1	9.392	55.249	55.249	9.392	55.249	55.249
2	3.530	20.766	76.014	3.530	20.766	76.014
3	1.368	8.049	84.064	1.368	8.049	84.064
4	.964	5.672	89.735			
5	.778	4.579	94.314			
6	.351	2.062	96.376			
7	.147	.867	97.243			
8	.129	.757	98.000			
9	.098	.577	98.577			
10	.060	.356	98.932			
11	.055	.321	99.253			
12	.048	.283	99.535			
13	.033	.197	99.732			
14	.021	.123	99.855			
15	.015	.087	99.942			
16	.007	.043	99.985			
17	.003	.015	100.000			
Extraction Method: Principal Component Analysis.						

5. Only retain the largest two eigenvectors that together account for most of the variance.

6. Use correlation matrix times the selected two sets of eigenvectors to get a new component matrix.

Component Matrix		
	Component	
	1	2
V/Yb	.509	.534
La/Yb	.662	-.603
Ce/Yb	.714	-.625
Pr/Yb	.741	-.648
Nd/Yb	.781	-.611
Zr/Yb	.644	.314
Hf/Yb	.615	.058
Sm/Yb	.890	-.407
Eu/Yb	.810	-.175
Ti/Yb	.546	.555

Gd/Yb	.877	-.262
Tb/Yb	.945	.106
Dy/Yb	.896	.309
Y/Yb	.586	.473
Ho/Yb	.810	.454
Er/Yb	.755	.504
Tm/Yb	.670	.480
Extraction Method: Principal Component Analysis.		

7. Acquire component score coefficient matrix which contain the loadings of each variable of the new principal components (i.e., PC1 and PC2), which are linear combinations of the original variables.

Component Score Coefficient Matrix		
	Component	
	1	2
V/Yb	.054	.151
La/Yb	.070	-.171
Ce/Yb	.076	-.177
Pr/Yb	.079	-.184
Nd/Yb	.083	-.173
Zr/Yb	.069	.089
Hf/Yb	.066	.016
Sm/Yb	.095	-.115
Eu/Yb	.086	-.050
Ti/Yb	.058	.157
Gd/Yb	.093	-.074
Tb/Yb	.101	.030
Dy/Yb	.095	.087
Y/Yb	.062	.134
Ho/Yb	.086	.129
Er/Yb	.080	.143
Tm/Yb	.071	.136
Extraction Method: Principal Component Analysis.		

8. Put original variables into the new functions (determined under point 7) to get PC1, PC2 scores, then plot PC1 scores against PC2 scores on a biplot together with the loadings of each variable for PC1 and PC2.

PC1 = 0.054 * (V/Yb) + 0.070 * (La/Yb) + …… + 0.080 * (Er/Yb) + 0.071 * (Tm/Yb)

PC2 = 0.151 * (V/Yb) + (-0.171) * (La/Yb) + ……. + 0.143 * (Er/Yb) + 0.136 * (Tm/Yb)

8.5 Case study using a population of compositionally heterogenous clinopyroxenes in Japan

An integrated sediment provenance study conducted by Buchs et al. (2015) on detrital pyroxenes collected at eight major rivers in Japan and three IODP drill sites in the Kumano Basin and nearby slope environment shows that the use of REE contents in clinopyroxenes together with existing discrimination diagrams (e.g., Leterrier et al., 1982) is a powerful approach to characterise sediment flow routing in volcanic environments based on compositional variability of detrital clinopyroxenes.

Major and trace element contents of detrital pyroxenes found in modern river sediments outline compositionally distinct sources along the Japanese forearc, with significant differences between the Inner, Outer and Collision Zones. A broad Outer Zone source was defined based on the distinctive occurrence of clinopyroxenes likely originated from accreted oceanic crust with either alkaline or MORB-like affinities in the Kino, Kumano, Tenryu and Abe rivers; an Inner Zone source defined based on clinopyroxenes likely from older arc volcanoes with calc-alkaline affinity in the Kiso and Nagara rivers; and a Collision Zone source defined based on clinopyroxenes derived from volcanoes of the Izu-Bonin arc with calc-alkaline and tholeiitic affinities in the Fuji and Kano rivers. In addition, an Abe river source was defined using a La/Sm vs Dy/Yb diagram and three compositionally distinct detrital sources are outlined by orthopyroxenes in the Kumano, Tenryu and Kano rivers (Buchs et al., 2015).

Comprehensive discrimination using Leterrier et al. (1982) diagrams and La/Sm vs Dy/Yb diagram of detrital clinopyroxenes and % ferrosilite vs Al, Na and Ca diagrams of detrital orthopyroxenes supports a clear Kumano source and partial Inner source at site C0009, a predominant Inner Zone source and

minor Kumano source at site C0002, and a mixed source of Inner, Outer and Collision Zones but excluding Kumano and Tenryu sources at site C0001 (Buchs et al., 2015).

However, the existing discrimination approaches used in the study (e.g., Leterrier et al., 1982, La/Sm vs Dy/Yb diagram) suffer from using only few geochemical elements and losing potential important information contained in the unused elements. Therefore, the application of PCA approach will allow to refine Buchs et al. (2015) method. The dataset of Buchs et al. (2015) [Table T2. of Buchs et al. (2015)] comprises 388 analyses of detrital clinopyroxenes in Japan, which were analysed by LA-ICP-MS.

This dataset has several advantages, particularly for the statistical aspects, because it is large (388 analyses), all 14 REE were measured, the tectonic affinities range from alkaline to tholeiitic arc, and it comes with external estimates of the precision from replicate analyses of four standards, namely BCR-2G, BIR-1G, GOR128-G and MPI-DING-glasses StHs-6/80-G. The averages of the relative standard deviations (RSDs) of the 14 REE in these four standards are 2.9±0.8 % for BCR-2G, 3.0±0.7 % for BIR-1G, 2.7±0.6 % for GOR128-G and 3.3±0.9 % for MPI-DING-glasses StHs-6/80-G [Table T4. of Buchs et al. (2015)].

8.5.1 Application of PCA to trace element data of detrital clinopyroxenes in Japan

A total of 388 sets of selected trace element data of clinopyroxenes acquired by LA-ICP-MS in Japan have been used as variables for PCA through the procedure introduced in Section 8.4.2. The selected trace elements are incompatible elements, including V, Zr, Hf, Ti, Y and all REEs, which are least affected by secondary alteration and show no correlation with magmatic differentiation.

A biplot is used as a combined visual representation of elements and clinopyroxenes projected on the plane of the first two principal components, including loadings (the weights for each original variable shown as arrows in the reduced compositional space) for variables and scores for clinopyroxenes using the two different pre-processing methods (Figure 8.1 and 8.2).

Method 1: original data

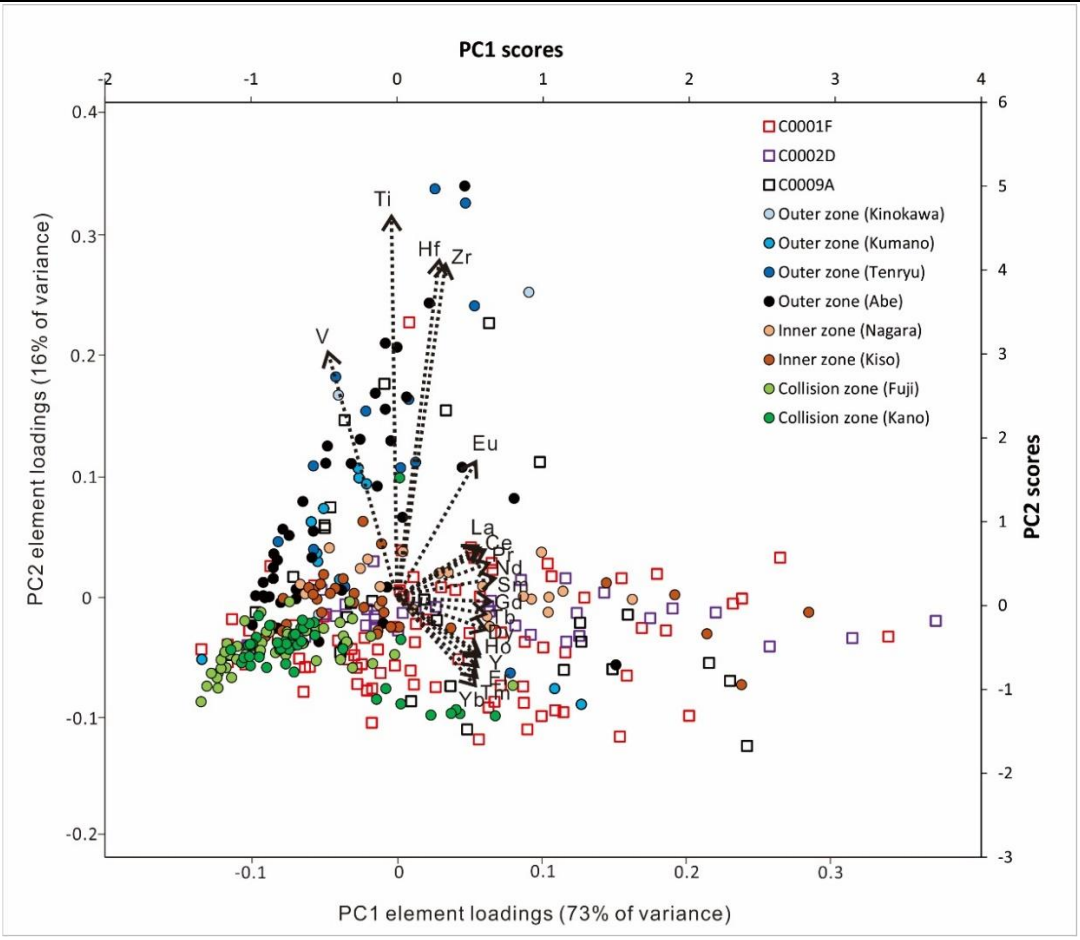

Figure 8.1 Biplot of PC1, PC2 element loadings and scores for selected trace element data on detrital clinopyroxenes in Japan applied to Principal Component Analysis (PCA) using Method 1 (i.e., original data) [dataset of Buchs et al. (2015), n = 388]

Method 2: normalised by Yb

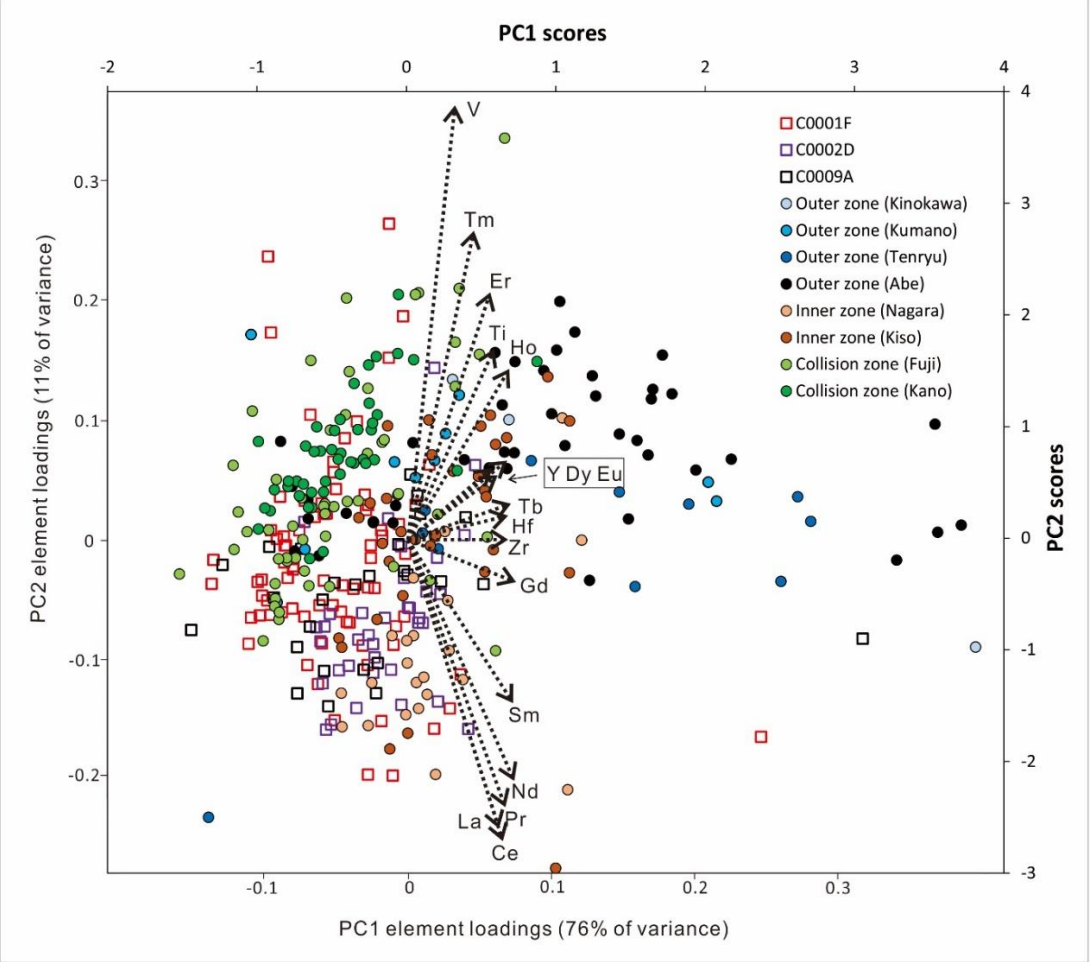

Figure 8.2 Biplot of PC1, PC2 element loadings and scores for selected trace element data on detrital clinopyroxenes in Japan applied to Principal Component Analysis (PCA) using Method 2 (i.e., normalised by Yb) [dataset of Buchs et al. (2015), n = 388]

On the biplot (Figure 8.1), the first principal component PC1 accounts for 73 % of the total variance and shows moderate positive loadings for REEs and Y. The second principal component PC2 accounts for 16 % of total variance and has high positive loadings for Ti, Hf, Zr and V. Eu is distinct from other trace elements, showing low positive loadings in PC1 and moderate positive loadings in PC2. It is clear that the spread of element loadings for REEs and Y are showing a continuous trend, which is correlated to their degree of compatibility.

On the biplot (Figure 8.2), the first principal component PC1 accounts for 76 % of the total variance and shows moderate positive loadings for all analysed elements. The second principal component PC2 accounts for 11 % of total variance. It has high positive loadings for V and HREEs, and high negative loadings for LREEs. Element loadings for REEs are showing a continuous trend

highlighted by PC1 from negative values in LREEs to positive values in HREEs. But element loadings for PC2 shows no distinct difference for all analysed elements.

Discrimination applied to PCA using Method 1 on detrital clinopyroxenes in Japan is explained as follows:

Clinopyroxenes at site C0009 are characterised by two groups of analyses: one is represented by high PC2 scores (> 1), similar to the range of clinopyroxenes from the Outer Zone; another is represented by low PC2 scores (-2 - 0) and wider range of PC1 scores (-1 – 2), overlapping with clinopyroxenes from Inner Zone. This result indicates the mixed sources (i.e., Outer Zone and Inner Zone) of clinopyroxenes at site C0009, consistent with the results based on REE content (i.e., La/Sm vs Dy/Yb diagram) of clinopyroxenes in Buchs et al. (2015) paper.

Clinopyroxenes at site C0002 are characterised by wide range of PC1 scores (-1 - 4) and narrow range of PC2 scores (-0.5 – 0.5), largely overlapping with those from Inner Zone, indicating a predominant Inner Zone source. This result corresponds to the Leterrier et al. (1982) diagrams in Buchs et al. (2015), showing predominant calcalkaline arc affinity at site C0002 already excluding a potential dominant Outer source which have an assemblage of alkaline, MORB-like and calcalkaline arc affinities.

Clinopyroxenes at site C0001 are characterised by wide range of PC1 scores (-1 - 4) similar to that of site C0002, and medium range of PC2 (-2 - 1). It's clear that clinopyroxenes at stie C0001 with low PC1 scores (< 0) and low PC2 scores (< 0) are most likely derived from Collision Zone which has the lowest PC2 scores among the three zones. As for those clinopyroxenes with positive PC1 scores at site C0001, they share similar compositional range with those of Inner Zone. Overall, the PCA results indicate a mixed source of Collision Zone and Inner Zone for clinopyroxenes at site C0001.

8.5.2 Application of orthogonal polynomial method to REE data of detrital clinopyroxenes in Japan

Another method of quantifying REE pattern shapes in a way that allows large numbers of REE analyses to be easily compared is to use orthogonal polynomial fitting proposed by O'Neill (2016). The precondition is that in

clinopyroxenes, it is assumed the resulting CI-normalized REE patterns usually appear smooth (excepting Eu), such that they may be fitted to polynomials in r_{REE} with three to five terms, depending on analytical precision. The polynomials can be rearranged into an orthogonal form:

$$\ln([REE]/[REE]_{CI}) = \lambda_0 + \lambda_1 f_1^{orth} + \lambda_2 f_2^{orth} + \lambda_3 f_3^{orth} + \ldots$$

where f_1^{orth}, f_2^{orth}, etc. are themselves polynomials of r_{REE} [e.g., $f_0^{orth} = 1$, $f_1^{orth} = r_{REE} - 1.05477$, $f_2^{orth} = (r_{REE} - 1.00533) \times (r_{REE} - 1.12824)$, etc.], and where the coefficients λ_0, λ_1, λ_2, etc. are not correlated with each other. The terms have a simple, intuitive meaning: λ_0 is the average of the logarithms of the CI-normalized REE abundances; λ_1 describes the linear slope of the pattern; λ_2 describes the quadratic curvature, etc. The λ_n, called the 'shape coefficients', can be used to compare the shapes of CI-normalized REE patterns quantitatively, allowing large numbers of data to be assessed, especially instructive λ_1 vs λ_2 diagram. The detailed introduction and illustrations of this REE polynomial fitting method are referred to O'Neill (2016).

An Excel spreadsheet containing a VBA macro was given in the Supplementary Data of O'Neill (2016), which does the polynomial fitting (up to λ_4) and also returns the statistics (e.g., λ_0, λ_1, λ_2, etc, calculated s(ln[REE]), ratios of $[REE]_{obs}/[REE]_{calc}$) . This spreadsheet allows to calculate shape coefficients for the dataset of detrital clinopyroxenes in Japan in order to compare with the PCA method.

The REE shape coefficient λ_0 from this dataset plots against MgO (wt. %) in Figure 8.3 A which shows a moderate negative correlation ($R^2 = 0.26$). The trend is due to the progressive enrichment of REE in the melts during magma evolution, therefore giving rise to the enrichment of REE partitioning into clinopyroxenes. The mean and standard deviation of λ_0 is 2.74 and 0.73 respectively, calculated from the returned λ_0 results. This variation is far large than the analytical uncertainty calculated from the function $s(\lambda_0) = \zeta_0 \times$ s(ln[REE]): if s(ln[REE]) were 5.0 %, then this expected analytical uncertainty would be 0.28 × 5 % = 0.014. Therefore, the analytical uncertainty of REE data is far less than the variability of λ_0.

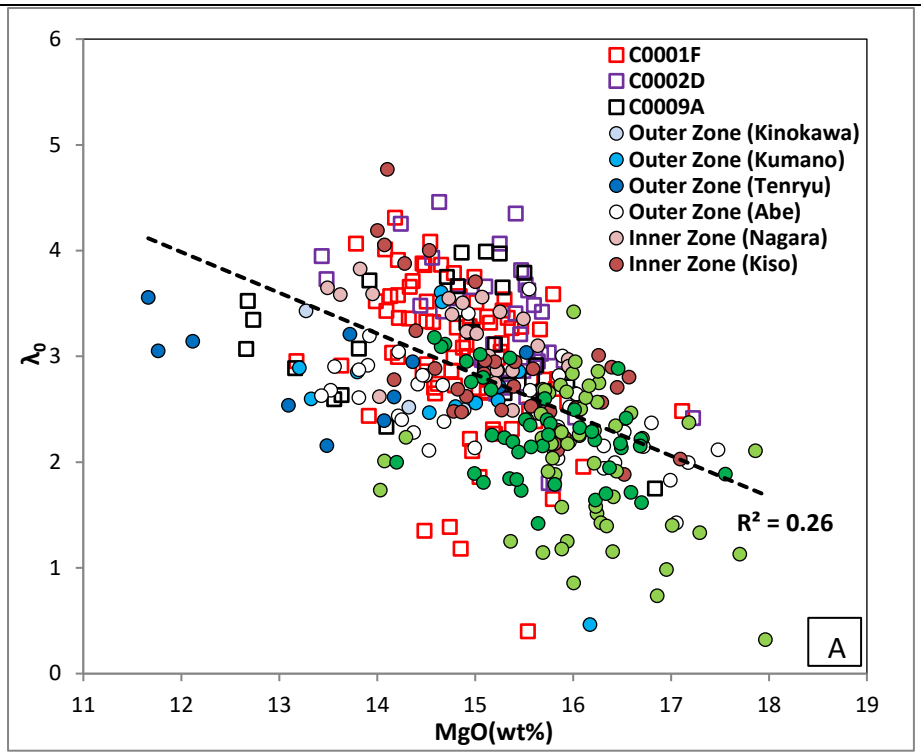
C0001F
C0002D
C0009A
Outer Zone (Kinokawa)
Outer Zone (Kumano)
Outer Zone (Tenryu)
Outer Zone (Abe)
Inner Zone (Nagara)
Inner Zone (Kiso)
R² = 0.26
A
λ0
MgO(wt%)

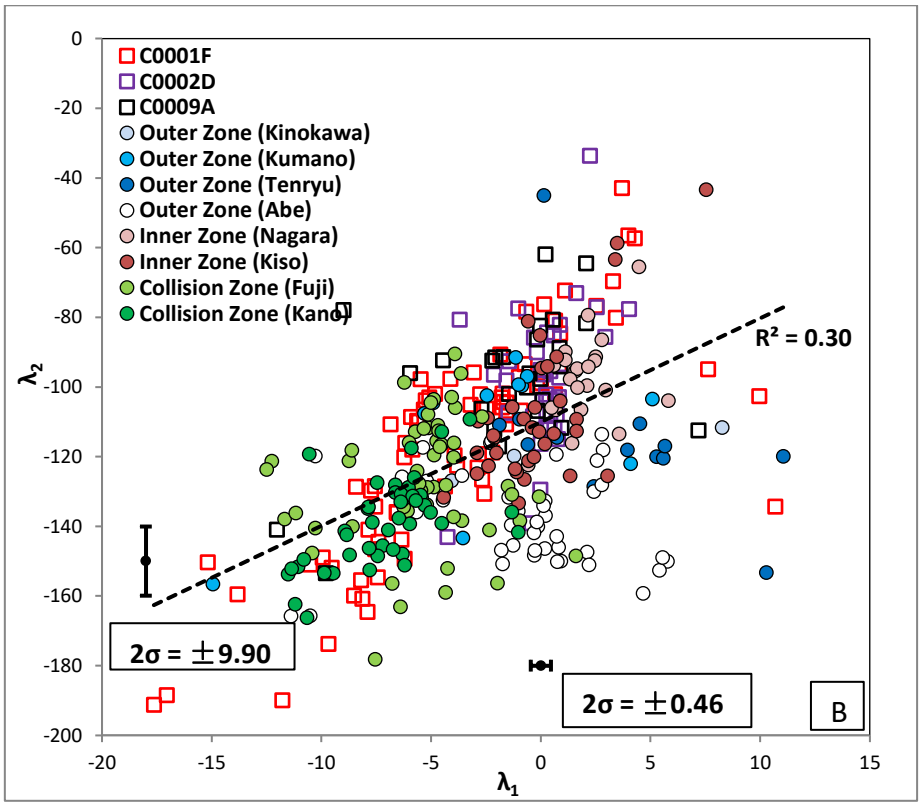
C0001F
C0002D
C0009A
Outer Zone (Kinokawa)
Outer Zone (Kumano)
Outer Zone (Tenryu)
Outer Zone (Abe)
Inner Zone (Nagara)
Inner Zone (Kiso)
Collision Zone (Fuji)
Collision Zone (Kano)
R² = 0.30
2σ = ±9.90
2σ = ±0.46
B
λ2
λ1

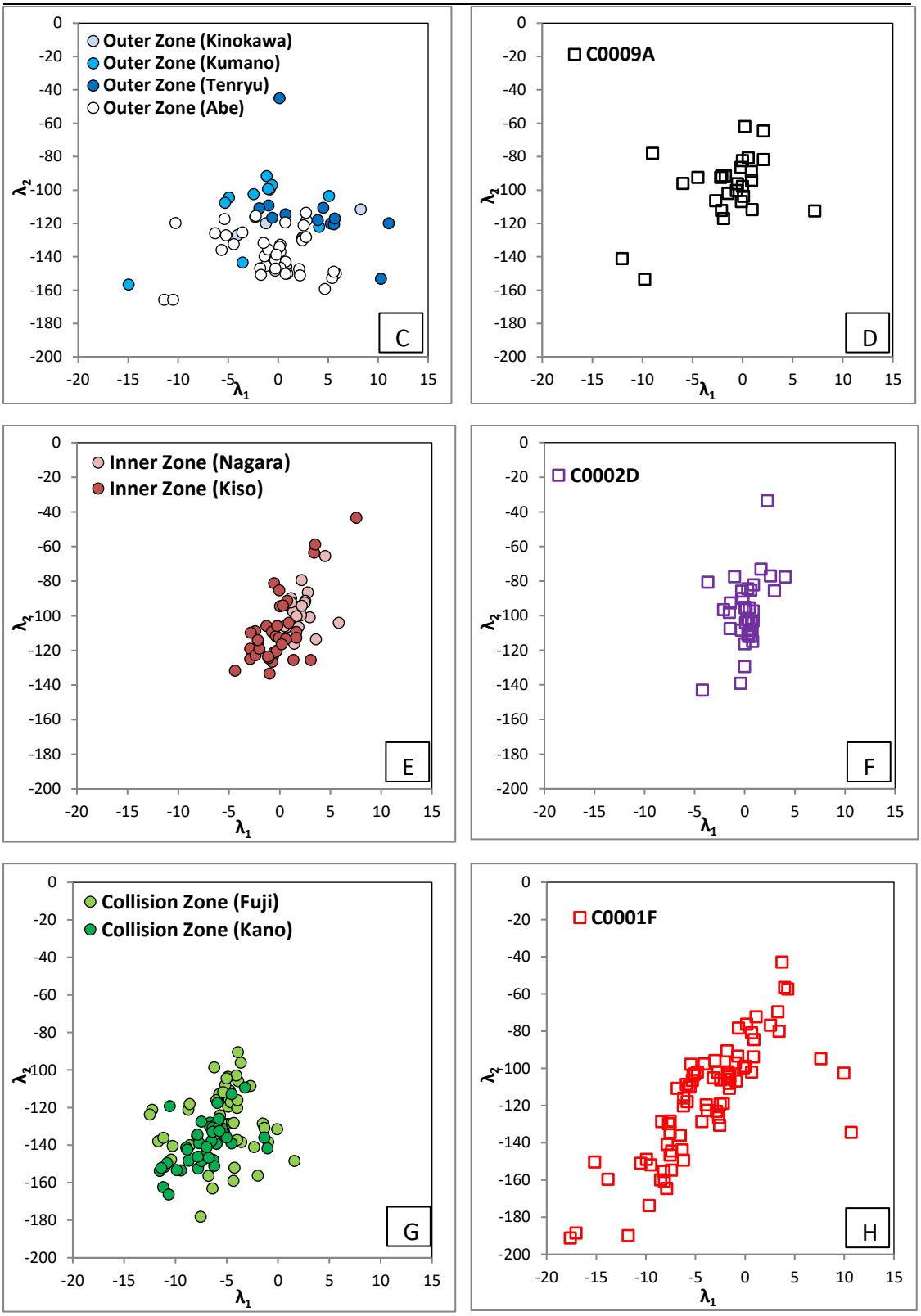

Figure 8.3 REE pattern shape coefficients on detrital clinopyroxenes in Japan applied to orthogonal polynomial fitting method (dataset of Buchs et al. (2015), n = 388). A) λ_0 vs MgO (wt. %); B) λ_1 vs λ_2; C-H) λ_1 vs λ_2 plotted separately in various broad zones and drill sites. Error bars for λ_1 and λ_2 are ± 2σ calculated by 5.0 % in s(ln[REE]); the error bar for λ_0 is not shown due to less than the size of the symbol.

On the λ_1 vs λ_2 diagram (Figure 8.3 B), there is a moderate positive correlation between λ_1 and λ_2 (R^2 = 0.30), which means that the curvatures of the REE patterns in clinopyroxenes are moderately related to their slopes. The standard deviation of λ_1 and λ_2 is 4.62 and 25.3 respectively, calculated from the returned λ_1 and λ_2 results, which is far large than the analytical uncertainty calculated from the function $s(\lambda_n) = \zeta_n \times s(\ln[REE])$: if s(ln[REE]) were 5.0 %, then the expected analytical uncertainty would be 4.6 × 5 % = 0.23 for λ_1 and 99 × 5 % = 4.95 for λ_2. Therefore, the $s(\lambda_n)$ caused by analytical uncertainty of REE data is far less than the variability of λ_n.

Clinopyroxenes at site C0009 are characterised by medium λ_1 values (-5 - 5) and medium λ_2 values (-120 – -60), similar to the range of some clinopyroxenes from the Outer Zone with higher λ_2 values (> -120), among which most are from the Kumano River. In addition, clinopyroxenes from Inner Zone also have similar compositional range to those of C0009, consistent with the results acquired by PCA in Section 8.5.1.

Clinopyroxenes at site C0002 are also characterised by medium λ_1 values (-5 - 5) and medium λ_2 values (-120 – -60), largely overlapping with those from Inner Zone, and with part of those from Outer Zone of higher λ_2 values (> -120). However, the Leterrier et al. (1982) diagrams in Buchs et al. (2015) showing predominant calcalkaline arc affinity at site C0002 already excluded a potential dominant Outer source which have an assemblage of alkaline, MORB-like and calcalkaline arc affinities.

Clinopyroxenes at site C0001 are characterised by broad range of both λ_1 values (-20 – 5) and λ_2 values (-200 – -40). It's clear that clinopyroxenes at stie C0001 with low λ_1 values (< -5) are most likely derived from Collision Zone which has the lowest λ_1 values among the three zones. As for those clinopyroxenes with medium λ_1 values (-5 - 5) at site C0001, they share similar compositional range with those of Inner and Outer Zones, characterised by medium λ_1 and λ_2 values.

8.5.3 Summary

In summary, the application of statistical PCA and orthogonal polynomial fitting methods on detrital clinopyroxenes in Japan has successfully converted the complex and interrelated information contained in the trace element

contents and REE patterns into simple principal components (i.e., PC1, PC2) and shape coefficients (e.g., λ_1, λ_2), which allow a large number of data (n = 388) in the case study to be assessed quantitatively.

The discrimination results of using the two new approaches both support a clear Kumano source and partial Inner source at site C0009, a predominant Inner Zone source and minor Outer source at site C0002, and a mixed source of Inner, Outer and Collision Zones at site C0001, consistent with the conclusion proposed in Buchs et al. (2015).

8.6 Case study using a population of compositionally similar clinopyroxenes and amphiboles in the Alps

8.6.1 Application of PCA to trace element data of clinopyroxenes in the Alps

Method 1: original data

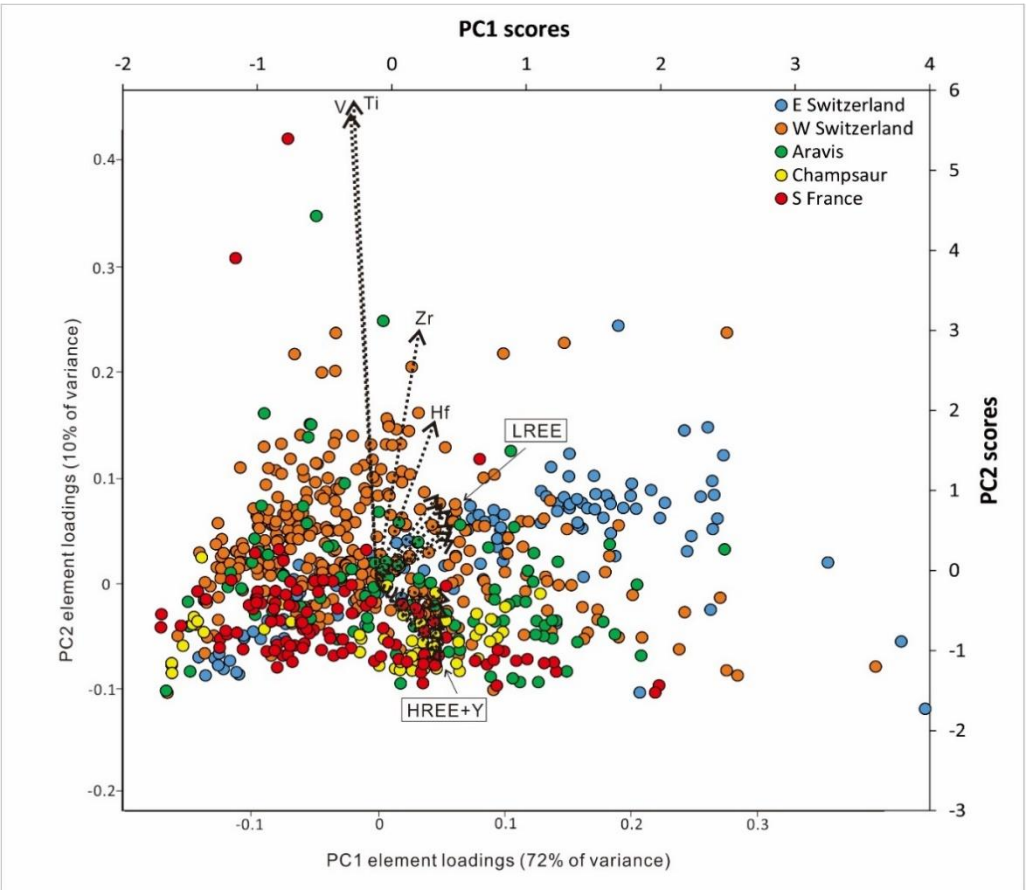

Figure 8.4 Biplot of PC1, PC2 element loadings and scores for selected trace element data on clinopyroxenes (n=722) in this study applied to Principal Component Analysis (PCA) using Method 1 (i.e., original data). Note: no trace element data were collected for clinopyroxenes in N Italy.

A total of 722 sets of selected trace element data of clinopyroxenes acquired by LA-ICP-MS in this study have been used as variables for PCA through the procedure introduced in Section 8.4.2. The selected trace elements are incompatible elements, including V, Zr, Hf, Ti, Y and all REEs, which are least affected by secondary alteration. A biplot is used as a combined visual representation of elements and clinopyroxenes projected on the plane of the first two principal components, including loadings for variables and scores for clinopyroxenes using two pre-processing methods (Figure 8.4 and 8.5).

Method 2: normalised by Yb

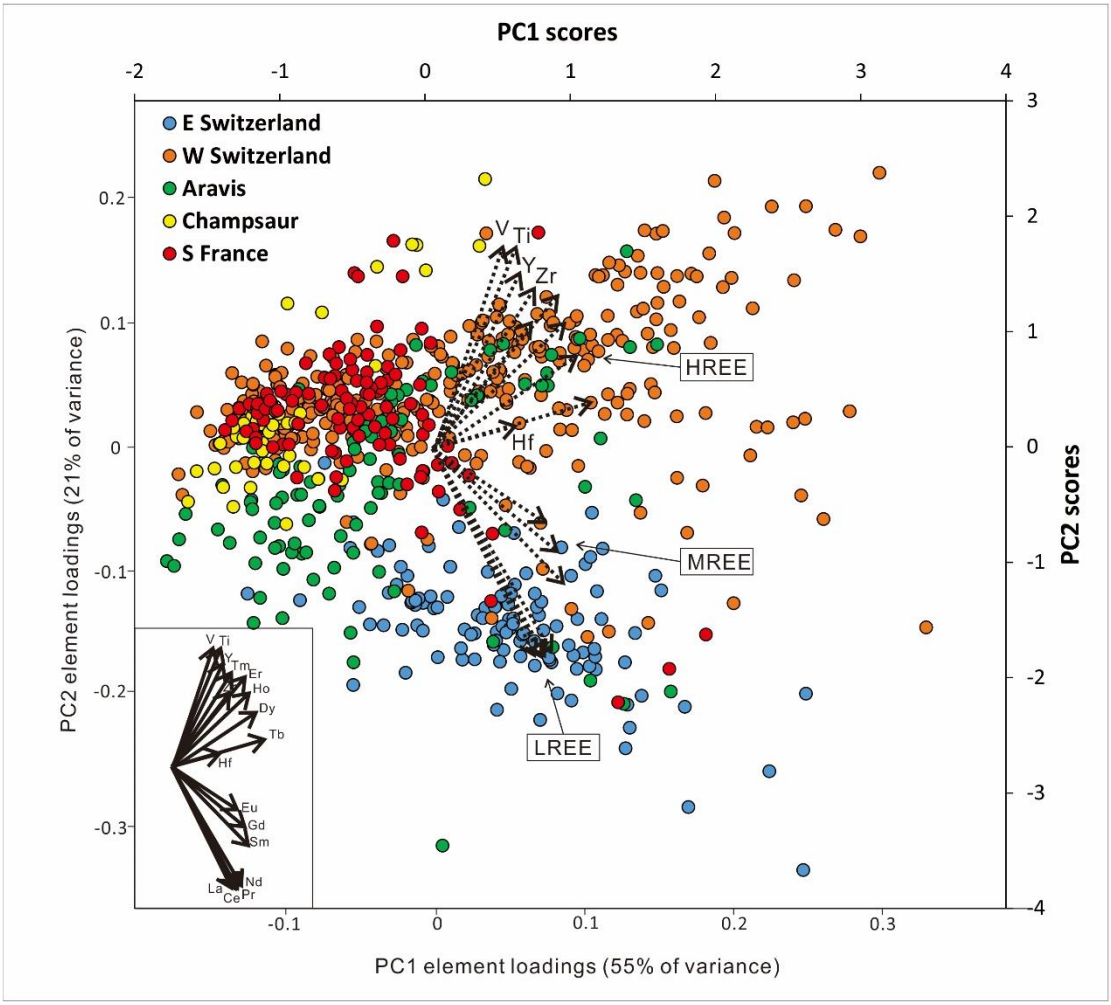

Figure 8.5 Biplot of PC1, PC2 element loadings and scores for selected trace element data on clinopyroxenes (n=722) in this study applied to Principal Component Analysis (PCA) using Method 2 (i.e., normalised by Yb). Insert denotes element loadings for PC1 and PC2. Note: no trace element data were collected for clinopyroxenes in N Italy.

On the biplot (Figure 8.4), the first principal component PC1 accounts for 77 % of total variance and shows similar positive loadings for REEs. The second

principal component PC2 accounts for 10 % of total variance and highlights high positive loadings for V, Ti, Zr, Hf and negative loadings for HREE. It is clear that element loadings for REEs and Y are showing a continuously similar trend mostly highlighted by PC1, which is different from the trend of element loadings of V, Ti, Hf and Zr highlighted by PC2.

On the biplot (Figure 8.5), the first principal component PC1 accounts for 55 % of total variance and shows positive loadings for all analysed trace elements. The second principal component PC2 accounts for 21 % of total variance and highlights positive loadings for V, Ti, Y, Zr and HREE, and negative loadings for MREE and LREE. It is clear that element loadings for LREE, and HREE are showing a continuously anticlockwise trend from negative to positive PC2 loadings.

Therefore, Method 2 works better for the differentiation of detrital clinopyroxenes in which clinopyroxenes from the same region are more plotted in cluster (Figure 8.5) compared to Method 1 in which clinopyroxenes from different regions are not well separated (Figure 8.4).

Discrimination applied to PCA using Method 2 on clinopyroxenes in Alps is explained as follows: clinopyroxenes from E Switzerland, W Switzerland and Aravis spread in a larger spectrum than those from Champsaur and S France. Clinopyroxenes from E Switzerland plot separately from others with lower PC2 scores (< -1), whereas clinopyroxenes from W Switzerland plot more in scatter with higher PC2 scores (> 0) and wide range of PC1 scores (-2 - 3). Clinopyroxenes from Aravis are partially overlapping with those from W Switzerland with higher PC2 scores, and partially separating from others with lower PC1 scores (< 0) and lower PC2 scores (< 0). Clinopyroxenes from Champsaur and S France mostly plot in cluster with lower PC1 scores (< 0) and higher PC2 scores (> 0), overlapping with those from W Switzerland and Aravis.

8.6.2 Application of PCA to trace element data of amphiboles in the Alps

A total of 82 sets of selected trace element data of amphiboles acquired by LA-ICP-MS in this study have been used as variables for PCA through the procedure introduced in Section 8.4.2. A biplot is used as a combined visual representation of elements and amphiboles projected on the plane of the first

two principal components, including loadings for variables and scores for amphiboles using two pre-processing methods (Figure 8.6 and 8.7).

Method 1: original data

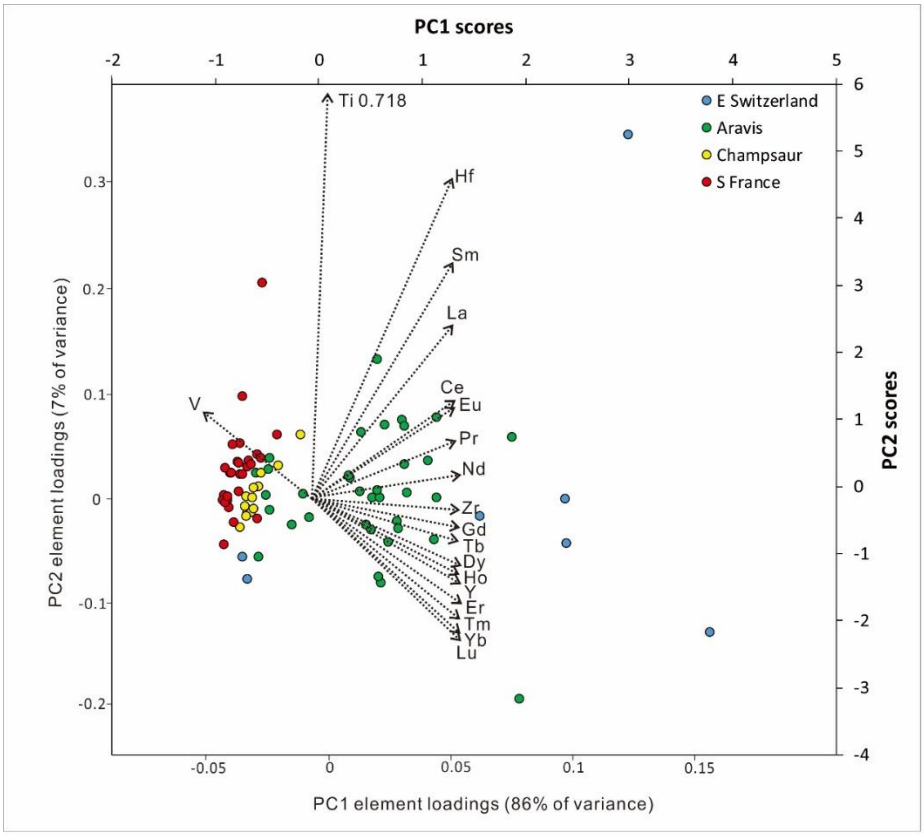

Figure 8.6 Biplot of PC1, PC2 element loadings and scores for selected trace element data on amphiboles (n=82) in this study applied to Principal Component Analysis (PCA) using Method 1 (i.e., original data). Note: no trace element data were collected for amphiboles in W Switzerland and N Italy.

On the biplot (Figure 8.6), the first principal component PC1 accounts for 86 % of total variance and shows positive loadings for all analysed element except for V. The second principal component PC2 accounts for 7 % of total variance and highlights extreme high positive loadings for Ti and high Hf. It is clear that element loadings for LREEs and HREEs are showing a continuously clockwise trend from positive to negative PC2 values.

On the biplot (Figure 8.7), the first principal component PC1 accounts for 53 % of total variance and shows positive loadings for Ti, V, Y, Hf, MREE and HREE, and negative loadings for LREE. The second principal component PC2 accounts for 27 % of total variance and highlights positive loadings for Zr and REE, and negative loadings for Ti, V and Y. It is clear that element loadings for LREE,

MREE and HREE are showing a continuously clockwise trend from negative to positive PC1 loadings.

Method 2: normalised by Yb

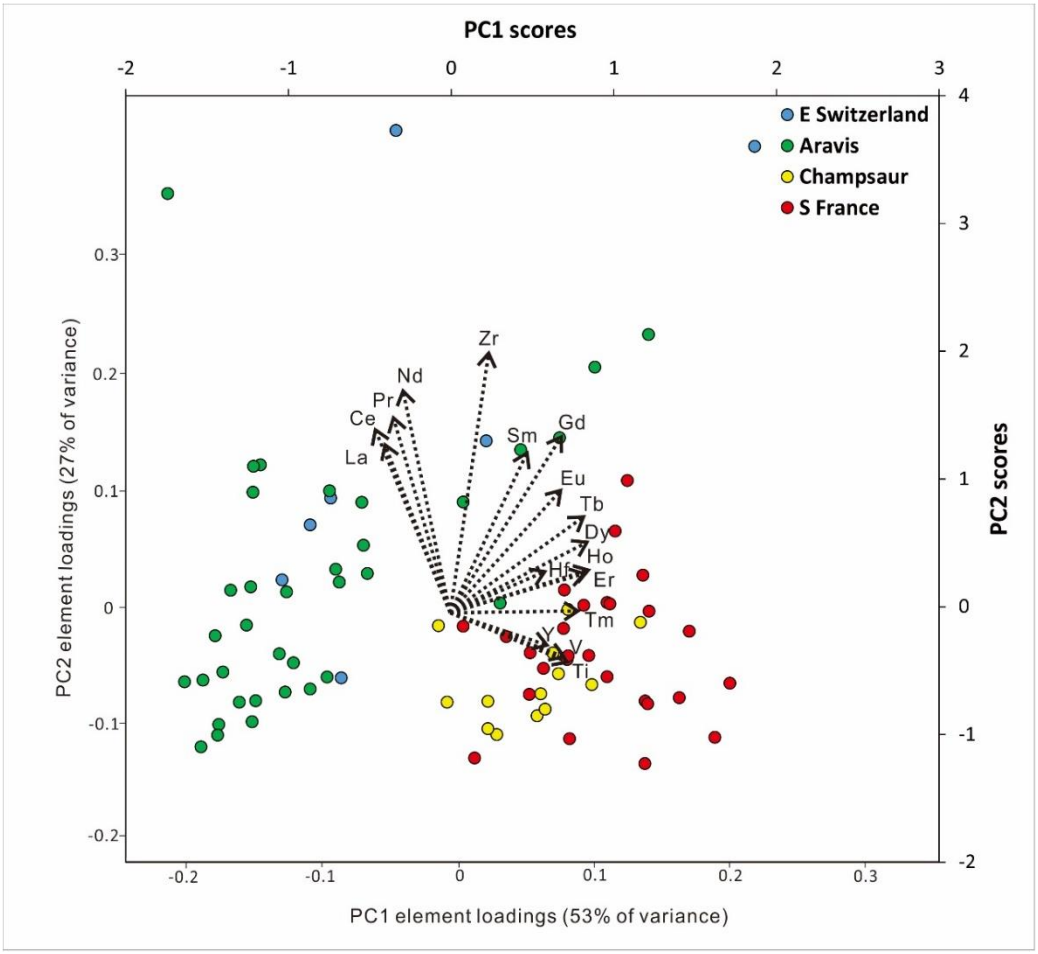

Figure 8.7 Biplot of PC1, PC2 element loadings and scores for selected trace element data on amphiboles (n=82) in this study applied to Principal Component Analysis (PCA) using Method 2 (i.e., normalised by Yb). Note: no trace element data were collected for amphiboles in W Switzerland and N Italy.

Therefore, Method 2 works better for the differentiation of amphiboles in which amphiboles from different regions are well separated (Figure 8.7) compared to Method 1 (Figure 8.6).

Discrimination applied to PCA using Method 2 on amphiboles in Alps is explained as follows: amphiboles from E Switzerland and Aravis are well separated from those Champsaur and S France. Amphiboles from E Switzerland and Aravis are overlapping in a relatively larger spectrum, characterised by lower PC1 scores (< 0), whereas amphiboles from Champsaur

and S France are characterised by higher PC1 scores (> 0). The discrimination result is consistent with the trace element results in Chapter 7.

8.6.3 Application of the orthogonal polynomial method to REE data of clinopyroxenes in the Alps

A total of 722 REE data of clinopyroxenes of this study was calculated in the Excel spreadsheet given in the Supplementary Data of O'Neill (2016). This spreadsheet allows to calculate shape coefficients for the dataset of detrital clinopyroxenes in the Alps in order to compare with the PCA method.

The REE shape coefficient λ_0 from this dataset plots against MgO (wt. %) in Figure 8.8 A which shows a moderate negative correlation ($R^2 = 0.12$). The trend is due to the progressive enrichment of REE in the melts during magma evolution, therefore giving rise to the enrichment of REE partitioning into clinopyroxenes. The mean and standard deviation of λ_0 is 3.02 and 0.67 respectively, calculated from the returned λ_0 results. This variation is far large than the analytical uncertainty calculated from the function $s(\lambda_0) = \zeta_0 \times s(\ln[REE])$: if $s(\ln[REE])$ were 5.0 %, then this expected analytical uncertainty would be 0.28 × 5 % = 0.014. Therefore, the analytical uncertainty of REE data is far less than the variability of λ_0.

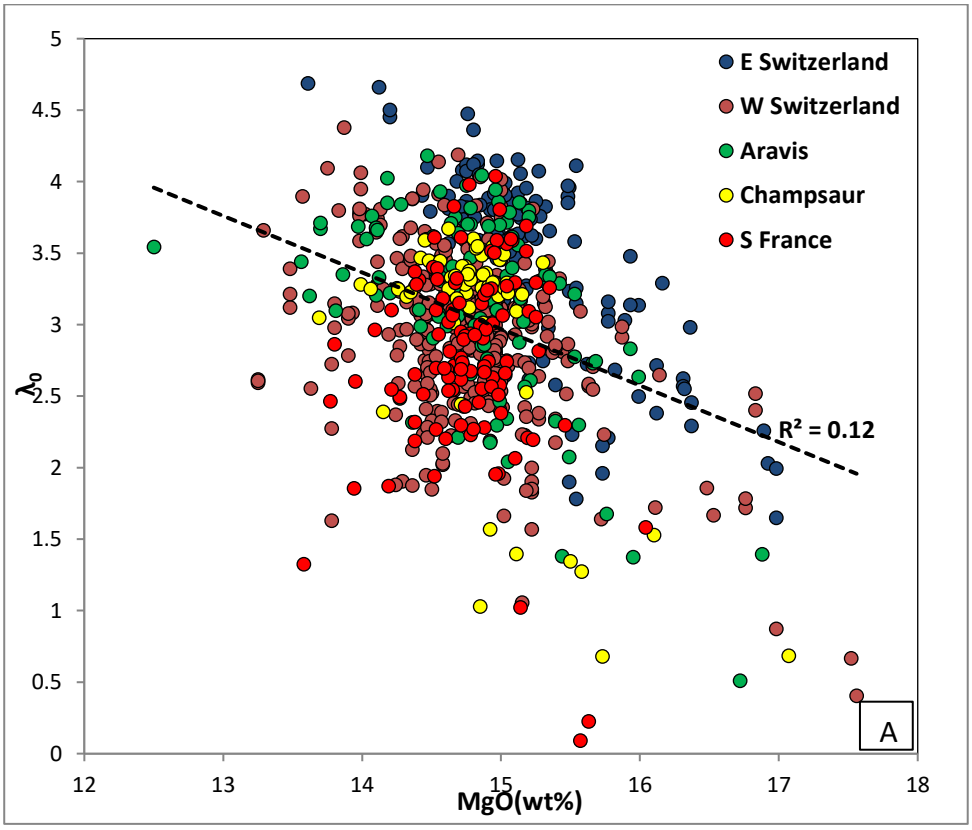

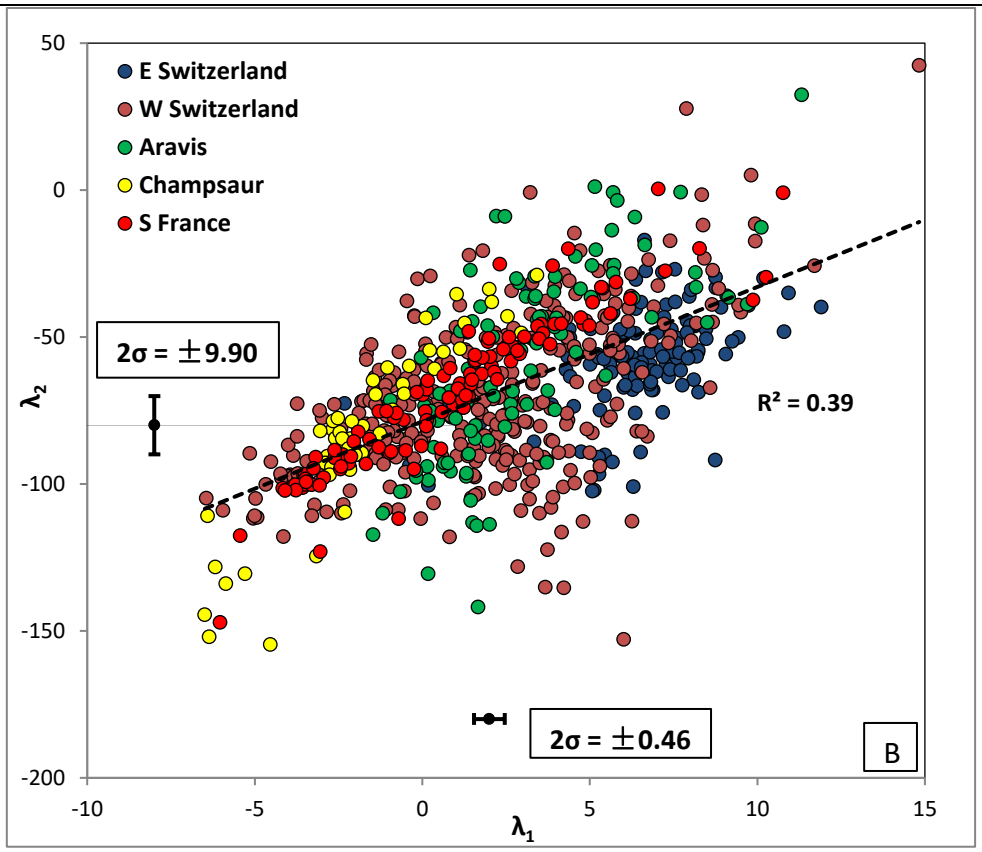

Figure 8.8 REE pattern shape coefficients on clinopyroxenes in this study applied to orthogonal polynomial fitting method. A) λ_0 vs MgO (wt. %); B) λ_1 vs λ_2. Error bars for λ_1 and λ_2 are ± 2σ calculated by 5.0 % in s(ln[REE]); the error bar for λ_0 is not shown due to less than the size of the symbol.

On the λ_1 vs λ_2 diagram (Figure 8.8 B), there is a moderate positive correlation between λ_1 and λ_2 (R^2 = 0.39), which means that the curvatures of the REE patterns in clinopyroxenes are related to their slopes. The standard deviation of λ_1 and λ_2 is 3.76 and 27.4 respectively, calculated from the returned λ_1 and λ_2 results, which is far large than the analytical uncertainty calculated from the function $s(\lambda_n) = \zeta_n \times s(\ln[REE])$: if s(ln[REE]) were 5.0 %, then the expected analytical uncertainty would be 4.6 × 5 % = 0.23 for λ_1 and 99 × 5 % = 4.95 for λ_2. Therefore, the $s(\lambda_n)$ caused by analytical uncertainty of REE data is far less than the variability of λ_n.

The discrimination of clinopyroxenes on the λ_1 vs λ_2 diagram (Figure 8.8 B) is not as good as PCA method due to the correlation between the two coefficients. But it's still clear that clinopyroxenes from E Switzerland with higher λ_1 values (> 5) plot separately from those of Champsaur and S France with lower λ_1 values (< 5). Clinopyroxenes from Aravis and W Switzerland are

spreading a large spectrum, overlapping with the other three regions (i.e., E Switzerland, Champsaur and S France).

8.6.4 Application of the orthogonal polynomial method to REE data of amphiboles in the Alps

A total of 82 REE data of amphiboles of this study was calculated in the Excel spreadsheet given in the Supplementary Data of O'Neill (2016). This spreadsheet allows to calculate shape coefficients for the dataset of detrital clinopyroxenes in the Alps in order to compare with the PCA method.

The REE shape coefficient λ_0 from this dataset plots against MgO (wt. %) in Figure 8.9 A which shows a moderate negative correlation ($R^2 = 0.32$). The trend is due to the progressive enrichment of REE in the melts during magma evolution, therefore giving rise to the enrichment of REE partitioning into clinopyroxenes. The mean and standard deviation of λ_0 is 2.86 and 1.16 respectively, calculated from the returned λ_0 results. This variation is far large than the analytical uncertainty calculated from the function $s(\lambda_0) = \zeta_0 \times s(\ln[REE])$: if $s(\ln[REE])$ were 5.0 %, then this expected analytical uncertainty would be 0.28 × 5 % = 0.014. Therefore, the analytical uncertainty of REE data is far less than the variability of λ_0.

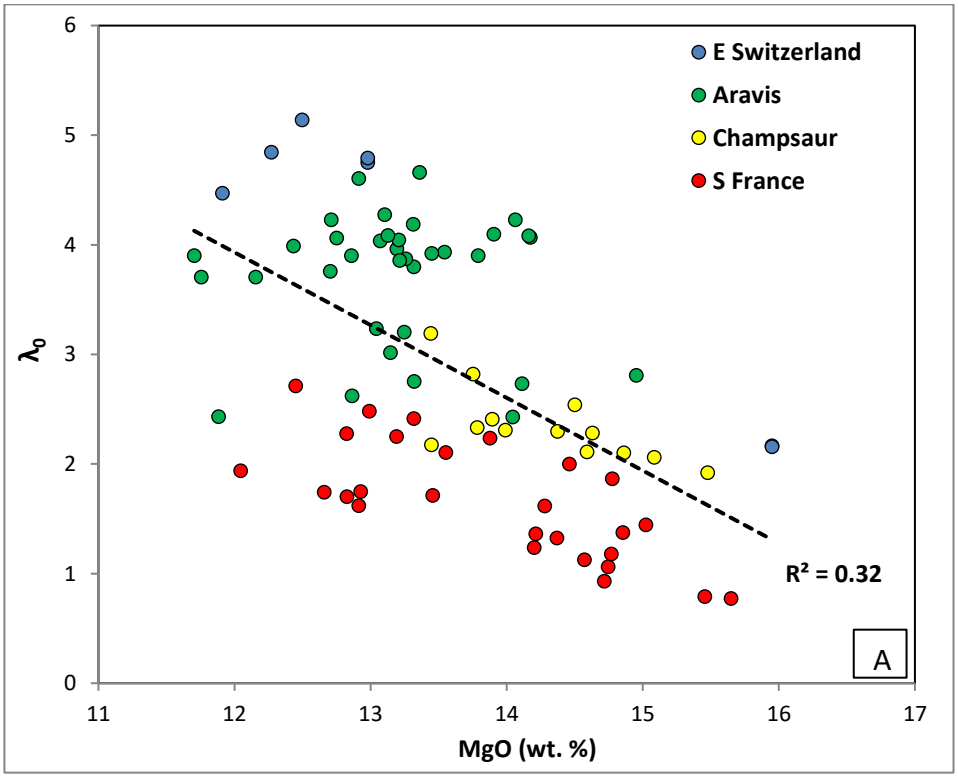

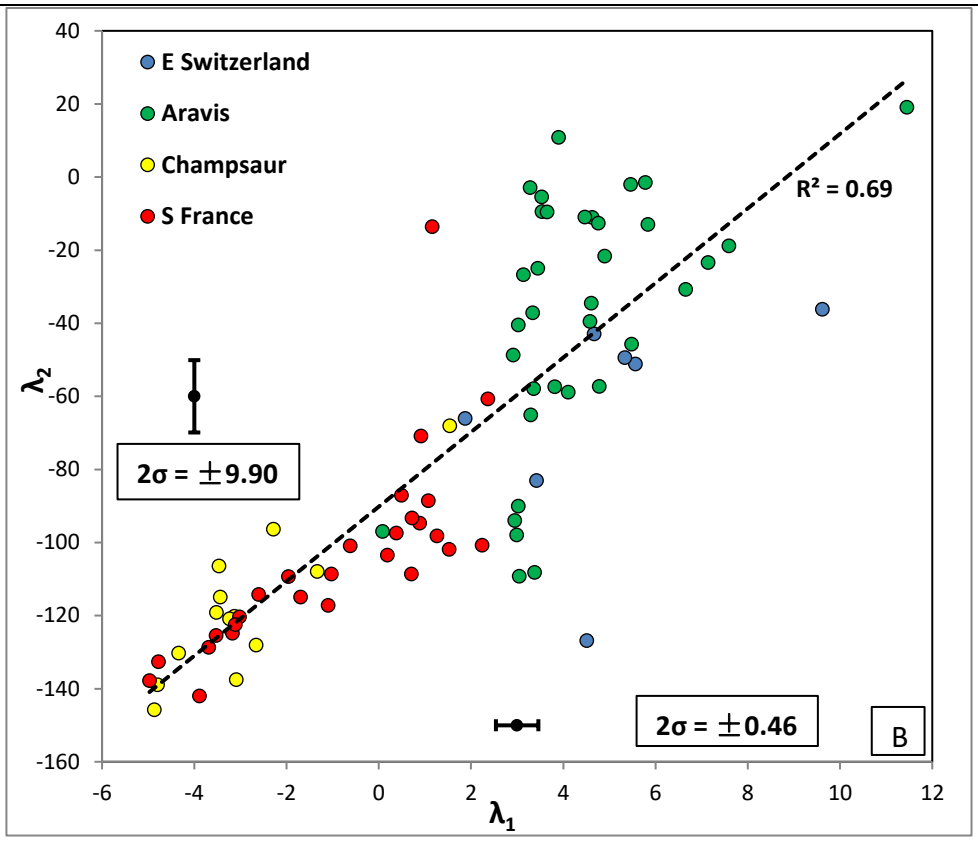

Figure 8.9 REE pattern shape coefficients on amphiboles in this study applied to orthogonal polynomial fitting method. A) λ_0 vs MgO (wt. %); B) λ_1 vs λ_2. Error bars for λ_1 and λ_2 are ± 2σ calculated by 5.0 % in s(ln[REE]); the error bar for λ_0 is not shown due to less than the size of the symbol.

On the λ_1 vs λ_2 diagram (Figure 8.9 B), there is a good positive correlation between λ_1 and λ_2 (R^2 = 0.69), which means that the curvatures of the REE patterns in clinopyroxenes are closely related to their slopes. The standard deviation of λ_1 and λ_2 is 3.70 and 45.3 respectively, calculated from the returned λ_1 and λ_2 results, which is far large than the analytical uncertainty calculated from the function $s(\lambda_n) = \zeta_n \times s(\ln[REE])$: if s(ln[REE]) were 5.0 %, then the expected analytical uncertainty would be 4.6 × 5 % = 0.23 for λ_1 and 99 × 5 % = 4.95 for λ_2. Therefore, the $s(\lambda_n)$ caused by analytical uncertainty of REE data is far less than the variability of λ_n.

Amphiboles from E Switzerland and Aravis, characterised by higher λ_1 values (> 2) and λ_2 values (> -100) plot clearly separately from those of Champsaur and S France with lower λ_1 values (< 2) and λ_2 values (< -100), consistent with the PCA results and results in Chapter 7.

8.6.5 Summary

In summary, PCA results on clinopyroxenes provide a more robust and clear discrimination showing that clinopyroxenes from W Switzerland and Aravis are largely similar over a large spectrum. E Switzerland (one sample) includes clinopyroxenes with higher PC1 values and lower PC2 values that are clearly distinct from those from Champsaur and S France, which are characterised by lower PC1 values and intermediate to low PC2 values. The orthogonal polynomial method on clinopyroxenes also gives a similar result for comparison though the distribution on λ_1 vs λ_2 diagram is not as scattered as the PCA diagram due to the good correlation between λ_1 and λ_2.

In terms of amphibole, PCA and orthogonal polynomial results both provide a clear discrimination, showing that amphiboles from E Switzerland and Aravis are largely similar, in contrast to those from Champsaur and S France.

8.7 Application of PCA to trace element dataset of clinopyroxenes in the Alps and Japan combined together

Method 1: original data

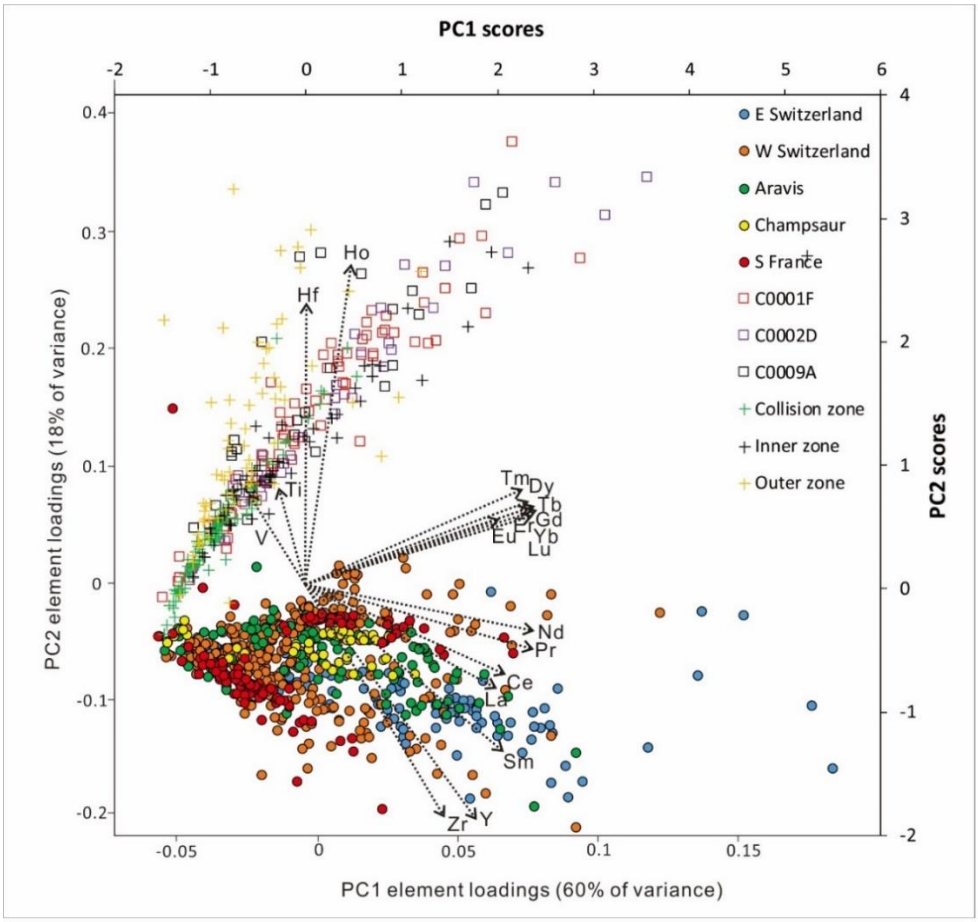

Figure 8.10 Biplot of PC1, PC2 element loadings and scores for selected trace element data on clinopyroxenes (n=1110) in this study and in Japan combined together applied to Principal Component Analysis (PCA) using Method 1 (i.e., original data).

A total of 1110 (722+388) sets of selected trace element data of clinopyroxenes in this study and in Japan combined together have been used as variables for PCA through the procedure introduced in Section 8.4.2 to assess possible effects of the discrimination approach related to the overall size and compositional range of a selected population of pyroxenes. The selected trace elements are incompatible elements, including V, Zr, Hf, Ti, Y and all REEs. A biplot is used as a combined visual representation of elements and clinopyroxenes projected on the plane of the first two principal components, including loadings for variables and scores for clinopyroxenes using the two pre-processing methods described above (Figure 8.10 and 8.11).

Method 2: normalised by Yb

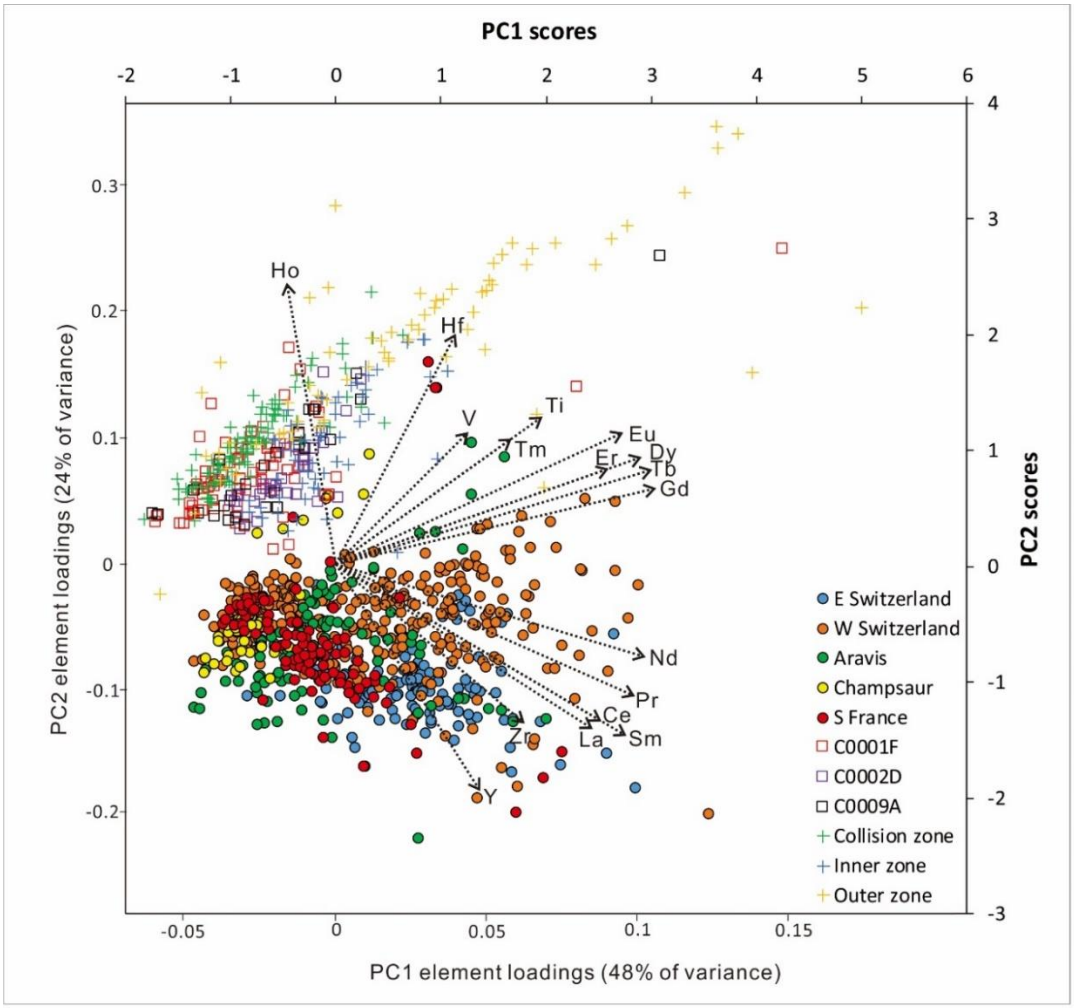

Figure 8.11 Biplot of PC1, PC2 element loadings and scores for selected trace

element data on clinopyroxenes (n=1110) in this study and in Japan combined together applied to Principal Component Analysis (PCA) using Method 2 (i.e., normalised by Yb).

On the biplot (Figure 8.10), the first principal component PC1 accounts for 60 % of total variance and shows similar positive loadings for analysed elements except for V, Ti, Hf and Ho. The second principal component PC2 accounts for 18 % of total variance and highlights high positive loadings for V, Ti, Hf, Ho and negative loadings for Zr and Y. It is clear that element loadings for REEs are showing an anticlockwise trend with increasing compatibility mostly highlighted by PC1, which is different from the trend of element loadings of V, Ti, Hf and Ho highlighted by PC2.

On the biplot (Figure 8.11), the first principal component PC1 accounts for 48 % of total variance and shows positive loadings for all analysed trace elements except for Ho. The second principal component PC2 accounts for 24 % of total variance and highlights positive loadings for V, Ti, Ho, Hf. It is clear that element loadings are generally showing a continuously anticlockwise trend from negative to positive PC2 loadings.

PCA results show that clinopyroxenes from Japan are more highlighted by higher PC2 scores (> 0) than those from the Alps (< 0), caused by the high positive PC2 loadings of V, Ti, Hf and Ho. Therefore, there is something fundamentally different between Japan and the Alps and none of the data actually overlap. V, Ti, Hf and Ho play a big role and make a big difference between the two datasets.

Chapter 9 Interpretation and Discussion

9.1 Introduction

Most previous researchers (Vuagnat, 1952; Martini, 1968; Lateltin, 1988; Waibel, 1990; Ruffini, 1997; Boyet, 2001; Lu et al., 2018) support the idea that Taveyannaz sandstones are traditionally reworked secondary sediments containing variable proportions of diverse volcanic components, transported by fluvial systems preceding the deposition in foreland basin; whereas a small group of researchers (Giraud and Didier, 1981; Giraud, 1983; Lapierre et al, 1995) consider the Taveyannaz sediments as primary volcanic deposits produced by “in situ” explosive volcanism.

Especially, a recent model proposed by Di Capua and Groppelli (2016) interprets that the enriched volcaniclastic detritus in Facies 3 of Taveyannaz sandstone are actually disaggregated pyroclastic density current deposits, discharged directly from eruptive volcanic activities in the internal Alps. The volcaniclastic deposits are not typical pyroclastic deposits with diagnostic features because shoreline and submarine explosions due to water/flow interaction disaggregate the PDCs while pyroclasts enter the basin. This process made the pyroclastic flow move downslope as cold, water-supported turbidite currents rather than hot, volatile-supported PDCs (Trofimovs et al., 2008; Carey and Schneider, 2011).

The key supporting elements of disaggregated PDC deposits comparable to modern PDC deposits in Di Capua and Groppelli (2016) include sand-wave structures, immaturity of sandstone components, large amounts of volcanic detritus, sediment compositions and differences in clear sand bodies and convolute cap layers, pervasive plastic deformation of microtextures, crystal alignments of few particles and fine grained banded pseudomatrix. However, these elements mainly focused on sedimentary structures and processes rather than volcanic detritus, and are perhaps not enough to indicate pyroclastic deposits.

Our new results show the petrographic variability of igneous lithics within the sandstone and the abundance of rounded igneous lithics. These two observations contradict with the interpretation of pyroclastic deposits,

because pyroclastic sediments should have similar igneous textures and compositions of volcanic lithics as they are from the same volcanic event. The abundant rounded volcanic lithics indicate relatively long distance fluvial transport through weathering and erosion of volcanic rocks with the surrounding land. Moreover, the new clinopyroxene composition result of this study showing high degree of compositional heterogeneity in Switzerland and Aravis strongly suggests a secondary volcaniclastic deposit compared with the low heterogeneity of primary deposits in St. Antonin and La Vanade as a reference. Therefore, the interpretation of Taveyannaz sandstone as PDC deposits could hardly explain the diversity and roundness of igneous lithics and the high degree of composition heterogeneity of detrital clinopyroxenes within the sandstone.

9.2 Are volcaniclastic sediments in foreland basins primary or secondary deposits?

9.2.1 Pyroclastic deposits

Our results show that the andesite breccia in Champsaur and pyroclastic deposits in Saint Antonin and La Vanade are clearly primary volcaniclastic deposits. This opinion has not been mentioned in recent publications (e.g., Di Capua and Groppelli, 2016; Lu et al., 2018) in terms of volcaniclastic deposits in Alpine foreland basin. They mainly focused on the turbidites in the northern part of NAFB, without much investigation in the southern part. There are actually some studies available describing pyroclastic deposits in the Provence volcanic province (e.g., Lapierre et al. 1995; Thomas, 2016; Lustrino et al., 2017; Jourdan et al., 2018), however Di Capua and other authors neglected the basins in the south where there are indeed primary volcaniclastic deposits and interpreted the secondary deposits in the north as primary deposits (i.e., disaggregated PDC deposits).

The reasons of pyroclastic deposits are as follows:

(1) Field observation results show the abundance of poorly reworked angular andesite clasts; occurrence of primary volcaniclastic deposits, such as andesitic breccia interpreted as block-and-ash flow deposits induced by dome collapse with tuffaceous cement, sometimes showing hot welding; coarser grain-size, even blocks over 3 m with higher abundance of conglomerate and

breccia; the occurrence of carbonised wood and dykes cutting the same volcaniclastic deposits; the occurrence of andesite veins;

(2) Petrography results show volcanic clasts more homogeneous with similar texture and composition; tuffaceous cement of the same material as the andesite clasts; occurrence of juvenile pyroclasts;

(3) Clinopyroxene composition results show low compositional variability in samples from Champsaur, St. Antonin and La Vanade, compared with samples from the north.

Overall, all evidence shows that sediments in the south are not deposits resulting from erosion and the transport of material from already "cooled" volcanic edifices, but, at least locally, pyroclastic flows. Therefore, the volcaniclastic deposits in Champsaur (andesite breccia), St. Antonin and La Vanade are primary/pyroclastic deposits without question.

9.2.2 Turbiditic deposits

Our results show that volcaniclastic deposits in Glarus (E Switzerland), W Switzerland, Aravis and Clumanc are very likely secondary volcaniclastic deposits.

The reasons are as follows:

(1) Field observation results show that detrital components are mostly extensively reworked with a high degree of mixing of possibly different sources and compositions in single volcanic systems; the absence of tuffs or tuffaceous layers mentioned by previous geologists (Vuagnat, 1952; Martini, 1968), and by our field observations in the regions; limited evidence for typical field indicators of primary volcaniclastic deposits;

(2) Petrography results show variability of andesitic clasts within single samples; rounded andesite clasts of various types of textures and compositions (Figure 9.1); If these deposits are primary, the fragmented magma will have similar petrography, thus creating clasts of homogeneous texture and composition; this viewpoint was also perfectly demonstrated in Vuagnat (1952), showing the diversity of andesitic textures. If these materials are primary deposits as Di Capua and Groppelli (2016) proposed, how to explain the petrographic variability of these volcanic clasts and the abundance

of rounded clasts? Pyroclastic deposits usually have low petrographic variability with same or similar composition and texture. Rounded clasts are not rounded due to single transportation directly from volcanic source to basin, but through weathering and erosion of volcanic rocks with the surrounding land;

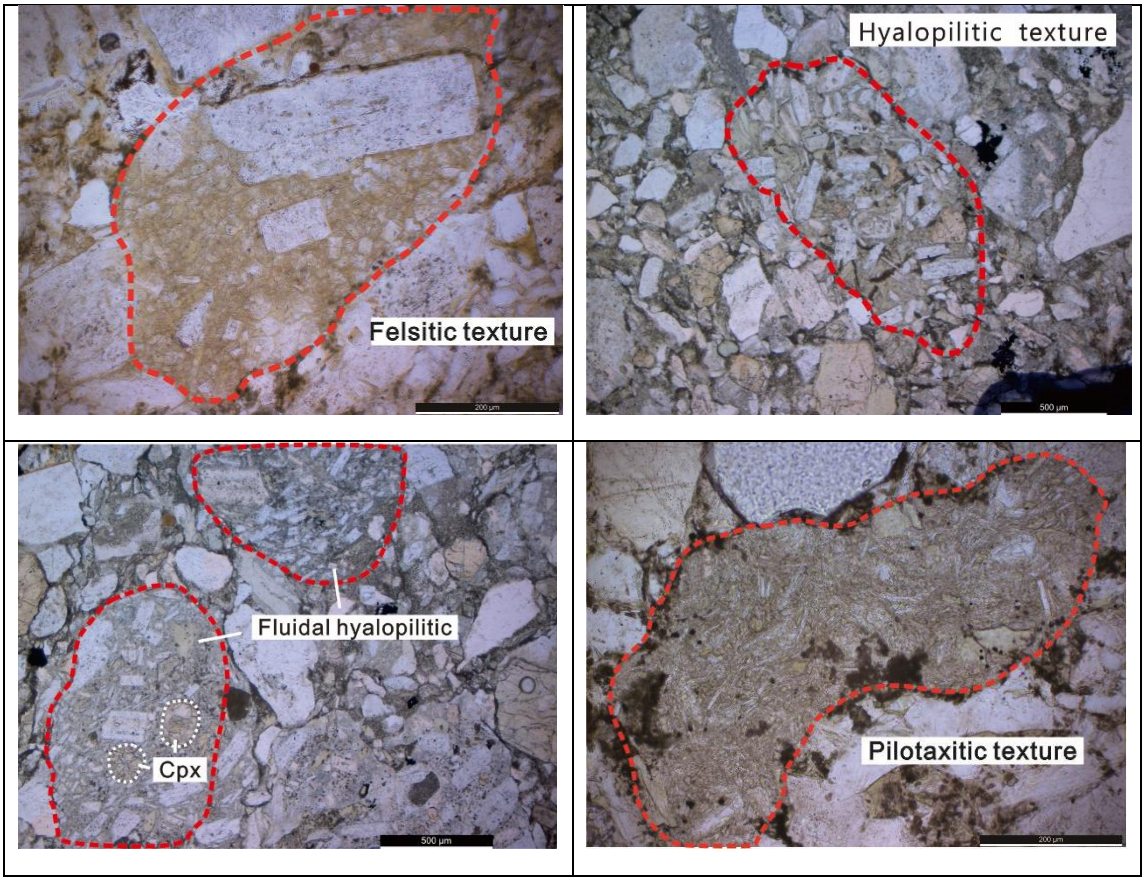

Figure 9.1 Example of petrographic heterogeneity within a single thin section (CL18-018) in La Tièche locality (W Switzerland), showing a variety of textures.

It should be noted that the amount of siliciclastic material might not be a direct indicator of whether deposit is primary or secondary. When the pyroclastic materials are avalanching on the slope, these materials are mixed with whatever is available in the environment and could end up having turbidites formed mainly by volcanic processes. Therefore, the materials in the sediments could be very heterogeneous, because the density currents could mix everything on the way down to the site of deposition. That's why volcanic components should be focused on to see if there is heterogeneity in terms of texture and composition in volcanic clasts in single thin sections.

(3) Clinopyroxene composition results show high degree of compositional variability in samples from Glarus (E Switzerland), W Switzerland (Taveyannaz + La Tièche) and Aravis, compared with samples from St. Antonin and La Vanade. In the biplot (Figure 9.2) produced in Chapter 8 by using PCA method, it's clear that the heterogeneity among clinopyroxenes from Glarus, W Switzerland and Aravis is much larger than those from Champsaur and S France (St. Antonin + La Vanade).

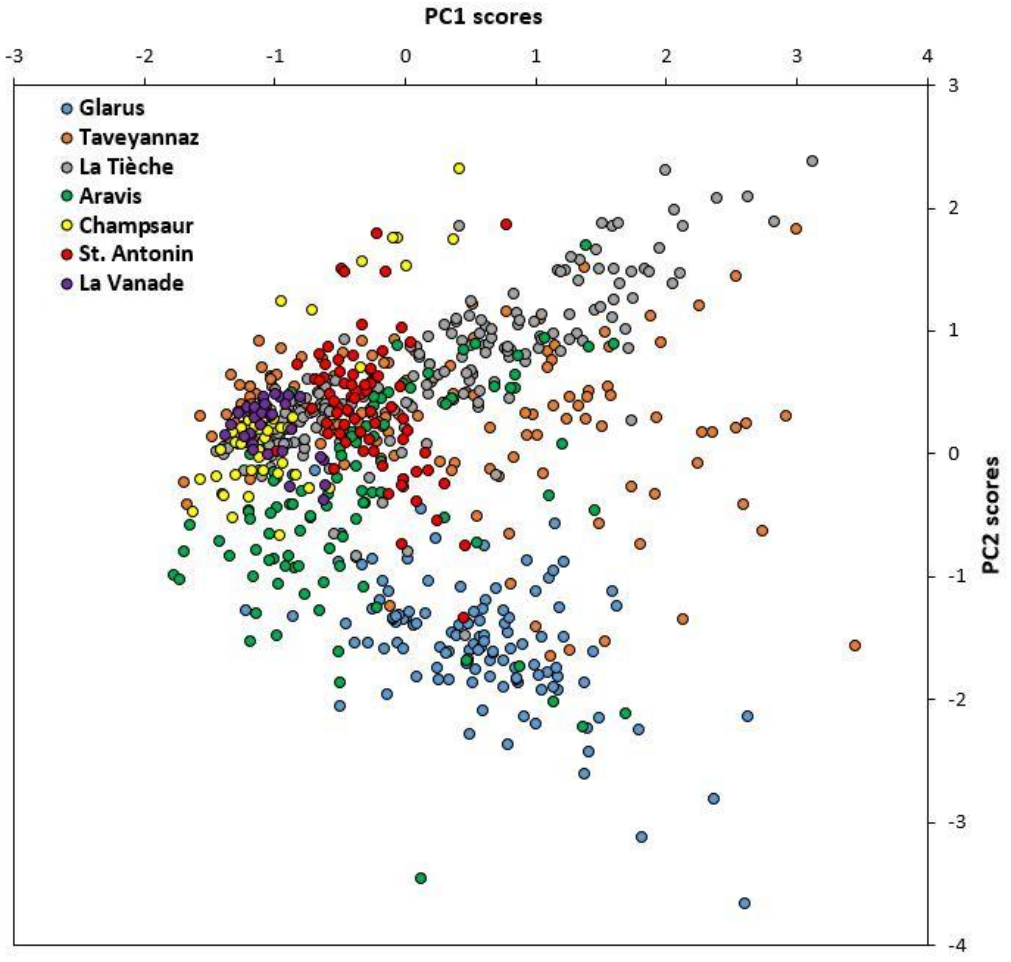

Figure 9.2 Diagrams of PC1, PC2 scores for selected trace element data on clinopyroxenes (n=722) applied to Principal Component Analysis (PCA) using Method 2 (i.e., normalised by Yb).

Overall, based on field observations, petrographic observations and composition of clinopyroxenes, it is believed that most of the materials in Glarus, W Switzerland and Aravis are reworked, although there is doubt for the out-sized amoeboid pebbles. There has no strong evidence, apart from the amoeboid pebbles in Glarus and Flaine, that there are some potentially

primary volcaniclastic deposits in Glarus, W Switzerland, Aravis and Clumanc area.

9.3 Compositional heterogeneity of clinopyroxenes in volcaniclastic deposits

Compositional heterogeneity exists at different scales, from sample scale up to Alpine scale. Therefore, before going into any regional interpretation, calibrations of the extent of compositional variability at a small-scale, well-constrained setting should be done in the Alpine context. This evaluation could not only provide comparable criteria of distinguishing primary deposits from secondary deposits, but also give comparable information about the source heterogeneity between primary and secondary deposits.

St. Antonin and La Vanade are both suitable localities to evaluate what would be the overall compositional variability in pyroclastic/primary samples of a restricted small basin. Based on results of previous chapters, it is for sure the non-diluted pyroclastic deposits in these two areas are very close to, and very likely at, the volcanic center. Therefore, the compositional heterogeneity of samples in St. Antonin and La Vanade can give a threshold of what kind of variability it will be in primary deposits of a single volcanic source. Anything exceeding this degree of variability would probably be an indication of reworking from several volcanic sources.

On the other hand, La Tièche and Taveyannaz are suitable localities with good stratigraphic control to evaluate the compositional variability in reworked/ secondary samples of an extended deep basin. There are probably several volcanic sources in W Switzerland because of the petrographic heterogeneity of andesite clasts.

Thus, there are two sort of endmembers in terms of compositional variability in the Alpine context, which include (1) pyroclastic endmember, represented by St. Antonin, La Vanade and one single pebble in Champsaur (Figure 9.3 A) and (2) sedimentary endmember, represented by La Tièche and Taveyannaz (Figure 9.3 B). They offer a chance to compare the compositional variability of clinopyroxenes within the samples and among the samples of these two representative endmembers.

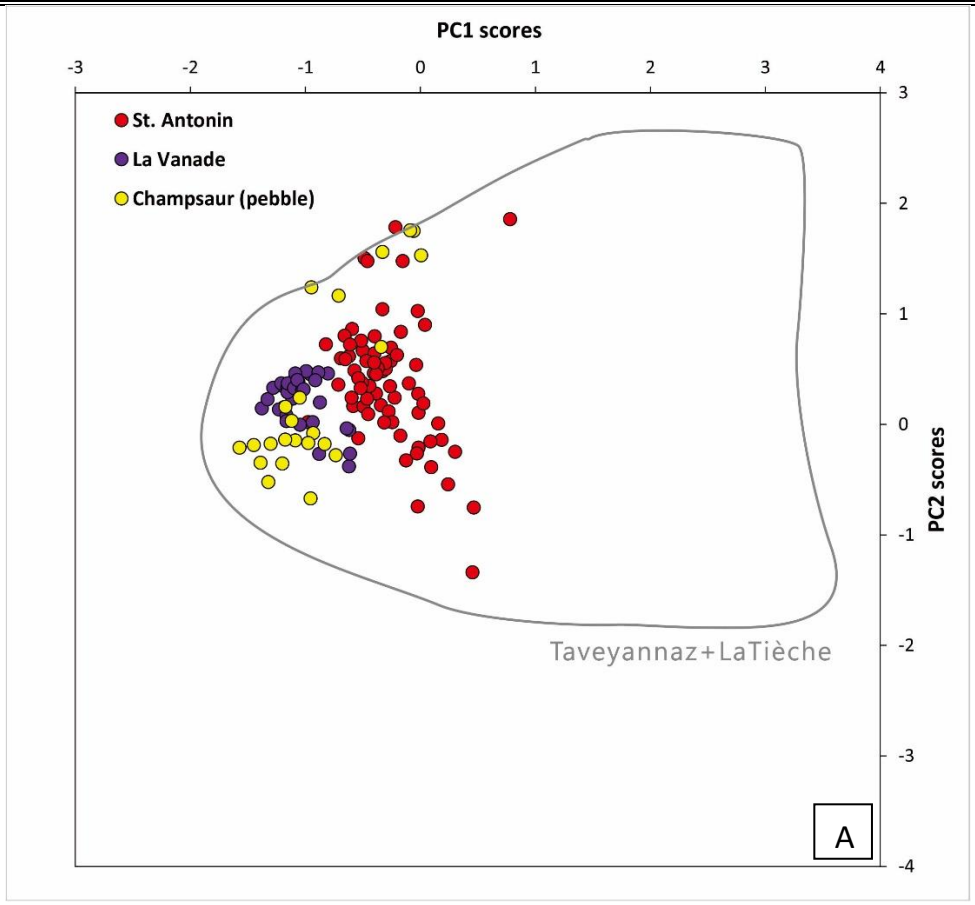
PC1 scores
-3
-2
-1
0
1
2
3
4
St. Antonin
La Vanade
Champsaur (pebble)
Taveyannaz+LaTièche
PC2 scores
3
2
1
0
-1
-2
-3
-4
A

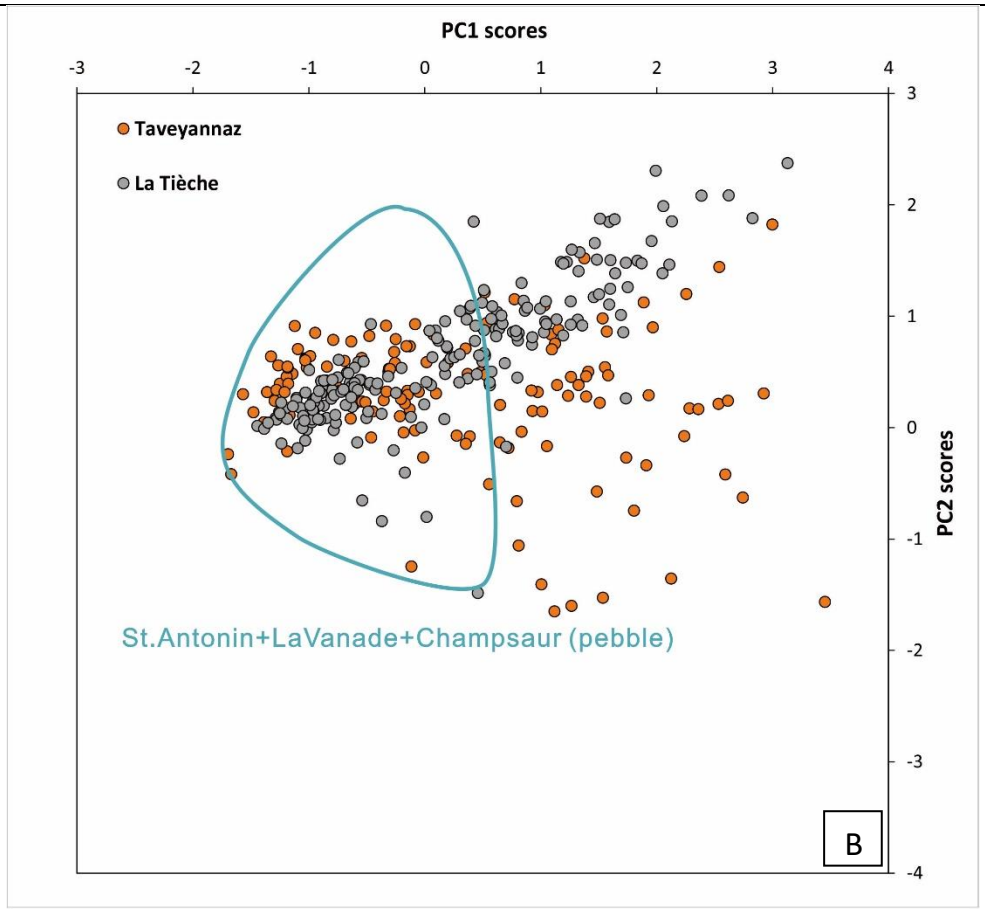
PC1 scores
-3
-2
-1
0
1
2
3
4
Taveyannaz
La Tièche
St.Antonin+LaVanade+Champsaur (pebble)
PC2 scores
3
2
1
0
-1
-2
-3
-4
B

Figure 9.3 Comparison between two endmembers in terms of compositional variability in diagrams of PC1, PC2 scores for selected trace element data on clinopyroxenes (n=722) applied to Principal Component Analysis (PCA) using Method 2 (i.e., normalised by Yb). Note: the datasets of the two endmembers were run through the same PCA process for the whole data of all regions as shown in Figure 9.2 and displayed independently in separate diagrams for clarity.

From the PCA diagrams (Figure 9.3 A, B), it's clear that the composition of clinopyroxenes from areas where there are more obvious reworking deposits (i.e., Taveyannaz and La Tièche) shows a greater variability than those from areas of very limited, even no reworking (i.e., St. Antonin and La Vanade) processes. It is worth noting that there is a certain degree of compositional variability in clinopyroxenes of primary volcaniclastic deposits, even within one single pebble as shown in Champsaur pebble of Figure 9.3 A, which is fairly rare.

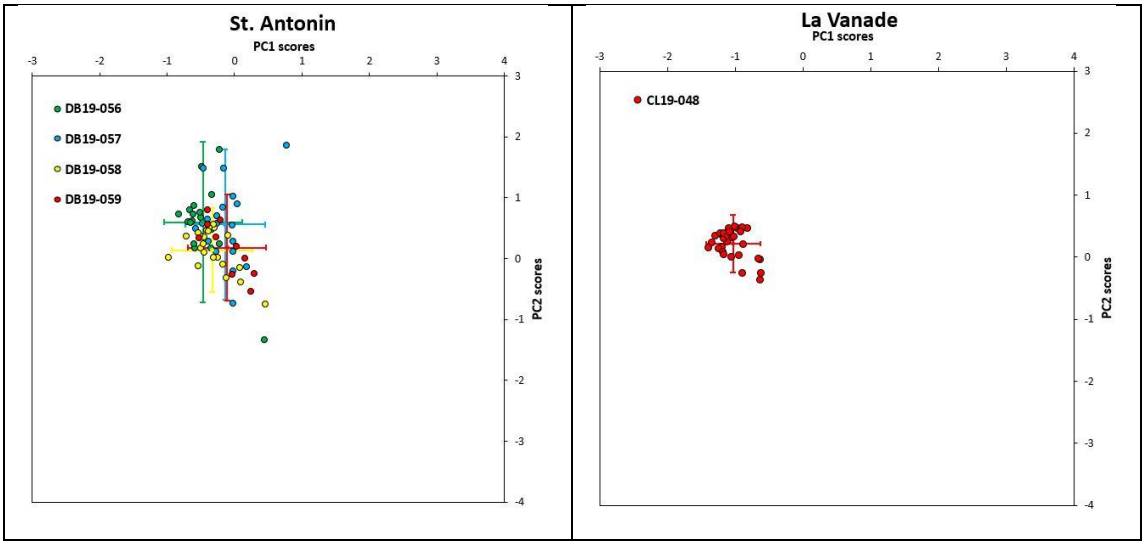

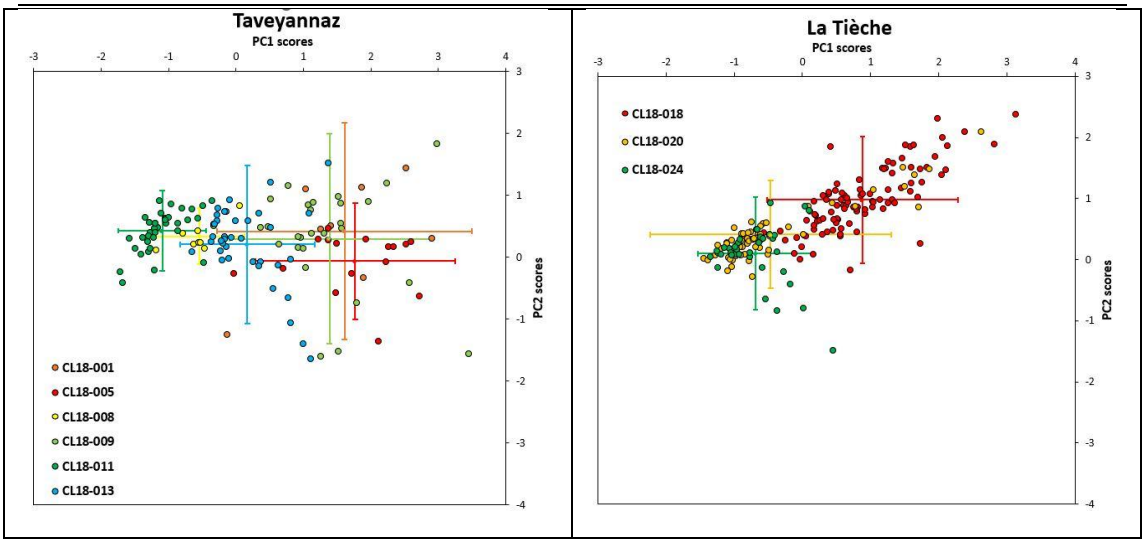

Figure 9.4 Comparison of within-sample compositional variability of four localities in diagrams of PC1, PC2 scores for selected trace element data on clinopyroxenes (n=722) applied to Principal Component Analysis (PCA) using Method 2 (i.e., normalised by Yb). Crosses are averages ± 2 standard deviation of each sample.

From the PCA diagrams (Figure 9.4), it's clear that the compositional variability of each single sample of sedimentary endmember localities is greater than the samples of pyroclastic endmember localities. For example, the spread of sample CL19-048 of La Vanade is smaller than any single sample from Taveyannaz and La Tièche. This could be easily recognised by comparing the size of crosses. In addition, inter-sample heterogeneity is more noticeable between sedimentary samples than pyroclastic samples. For example, sample CL19-005 and CL19-011 both from Taveyannaz locality are stratigraphically and geographically close. However, their compositional difference is very large, indicating that these two samples might have two distinct volcanic sources even though they are located at the same depositional site.

In summary, the compositional heterogeneity shown by samples from St. Antonin and La Vanade defines the degree of variability it will be expected in clinopyroxenes of primary volcaniclastic deposits in the Alpine context, whereas the heterogeneity shown in samples from Taveyannaz and La Tièche provides a comparable reference on how much compositional variability it will have in secondary volcaniclastic deposits which have potentially multiple volcanic sources.

9.4 Interpreting provenance of volcaniclastic deposits in foreland basins

The provenance of volcanic components within the Taveyannaz sandstone (s.l.) is one of the most attractive and complex problems of the Alpine geological history. Many studies have been dedicated to this problem for decades, but the hypotheses on the magmatic sources, the original position of the volcanic edifices and especially the mysterious geodynamic mechanism controlling the generation and distribution of andesitic volcanism remained highly uncertain. After reviewing and synthesising tens of associated published literatures in terms of the volcanic origin, the most popular and received perspectives include: (1) the volcanic components are secondary volcaniclastic deposits of local volcanic source, derived from the erosion of volcanoes located near or at the foreland basin (Sawatzki, 1975; Evans and Mange-Rajetzky, 1991; Jourdan et al., 2013; Pfiffner, 2014; Glarus B in Lu et al., 2018); (2) the volcanic components are secondary volcaniclastic deposits, derived from the erosion of intrusions along the Periadriatic Line and transported from internal Alps to the external foreland basin by long-distance fluvial processes (Vuagnat, 1952; Lateltin, 1988; Rahn et al., 1995; Sinclair, 1997; Glarus A in Lu et al., 2018); (3) the position of the original andesitic volcanoes was in the immediate vicinity of subduction zone, perhaps above the intrusive bodies situated along the Periadriatic Line. Then the volcanic edifices were detached from their foundation during continental collision, incorporated into one or several nappes, and transported by long-distance overthrusting and/or gravity sliding (Waibel, 1990; Waibel, 1993; Ruffini et al., 1997). In addition, Di Capua and Groppelli (2016) argue that volcaniclastic deposits are actually disaggregated pyroclastic density current (PDCs) discharged from internal Alps crossing tens to hundreds of kilometers directly to the basin.

Based on the integration of the results on field observations, petrographic analyses, whole-rock geochemistry, clinopyroxene and amphibole geochemistry in this study and a recent palaeogeographical model proposed by Lu et al., (2018) using detrital zircon results (Figure 9.5), it is proposed that the following palaeogeographical model (Figure 9.6) that the possible position of the volcanic center(s) (i.e., whether internal or external Alps) vary along the Alpine foreland basin. In addition, it is found innovatively that

secondary/epiclastic deposits of remote source and primary/pyroclastic deposits of proximal source are both recognised in several localities (e.g., Glarus, Aravis, Champsaur) (Figure 9.6). This indicates that there are very likely two types of volcanic systems supplying volcanic material to the basin.

The palaeogeographical model of Lu et al., (2018) (Figure 9.5) provides a thorough re-evaluation of the volcanic sources of the volcaniclastic deposits in the northern part of NAFB, in particular, in Glarus, Taveyannaz and Aravis (or Haute-Savoie) regions. They proposed that from 41 to 34 Ma, the Glarus A basin was supplied with volcanic debris from the northern Adamello intrusion; from 34 to 29 Ma, the Glarus B was supplied by the Bergell pluton, and the Taveyannaz and Aravis (Haute-Savoie) were supplied by the Biella volcanic system. However, they only focused on the northern part of NAFB without much investigation on the southern part. Therefore, it is the first time in this study that the volcaniclastic deposits in the whole NAFB was thoroughly investigated and the hypothesis of two types of volcanic systems controlling the source-to-sink systems respectively in the northern and southern part of NAFB was innovatively proposed.

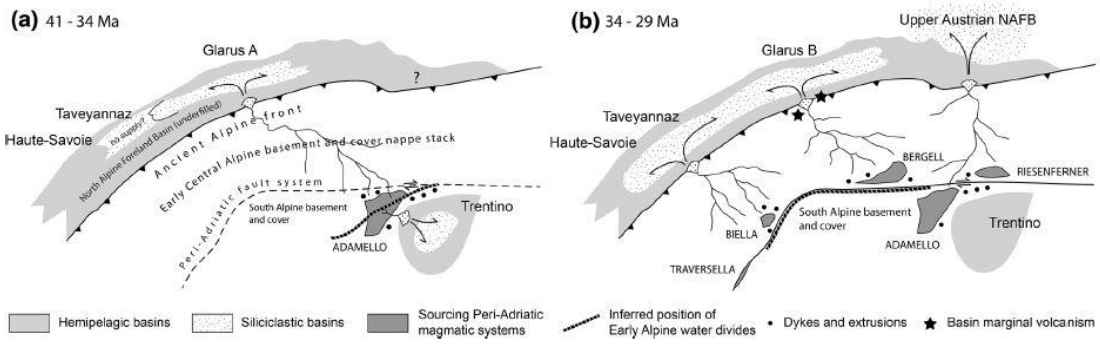

Figure 9.5 Palaeogeographic reconstruction of the late Liddle Eocene-Early Oligocene Alpine source-to-sink systems (from Lu et al., 2018)

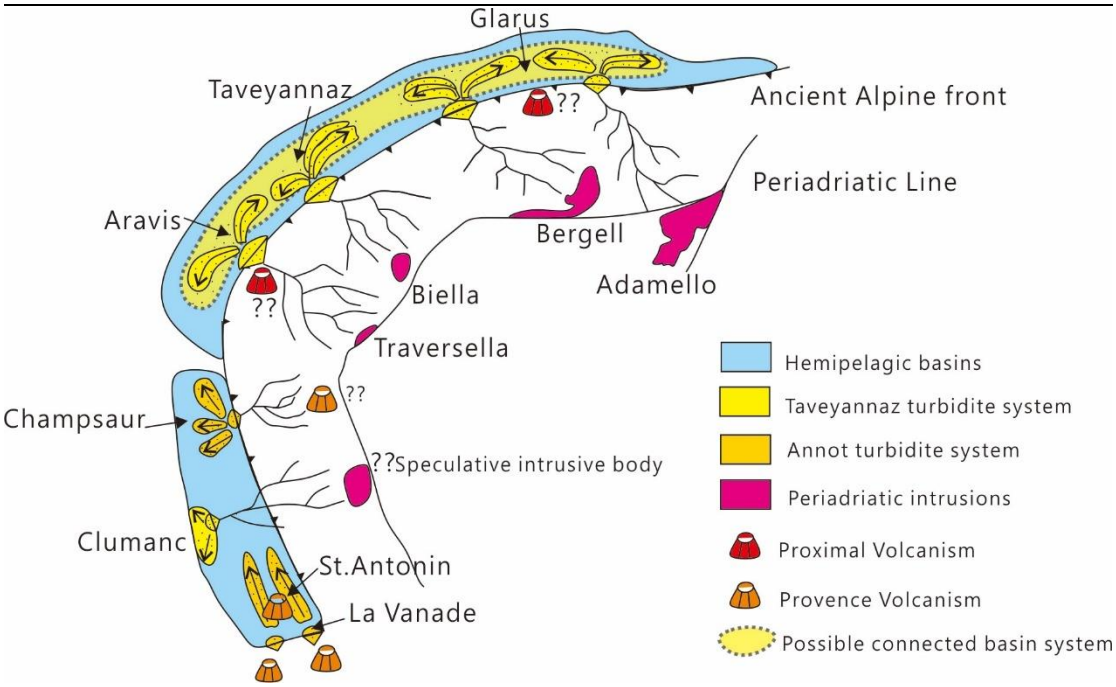

Figure 9.6 Paleogeographic reconstruction of the volcanic source-to-sink systems in Western Alps ca. 40-30 Ma.

9.4.1 Provenance of secondary volcaniclastic deposits

In Glarus, most volcanic components are probably derived from internal Alps as demonstrated in Lu et al. (2018), which proposed Adamello intrusion as a main source with detrital zircon U-Pb age (~41-32 Ma). However, the occurrence of the quenched amoeboid out-sized pebbles (Figure 9.7) which was suggested in Lu et al., (2018) gives strong and significant evidence for possible submarine effusive volcanism coming from relatively close area to the basin. However, this key finding was not emphasised by Lu and other authors in their paper. The source of these pebbles is not fully understood, but it is doubted that they could be transported more than 100 km with this large size from the internal Alps. Similar pebbles were also found in Flaine (northern Aravis) (Figure 9.8).

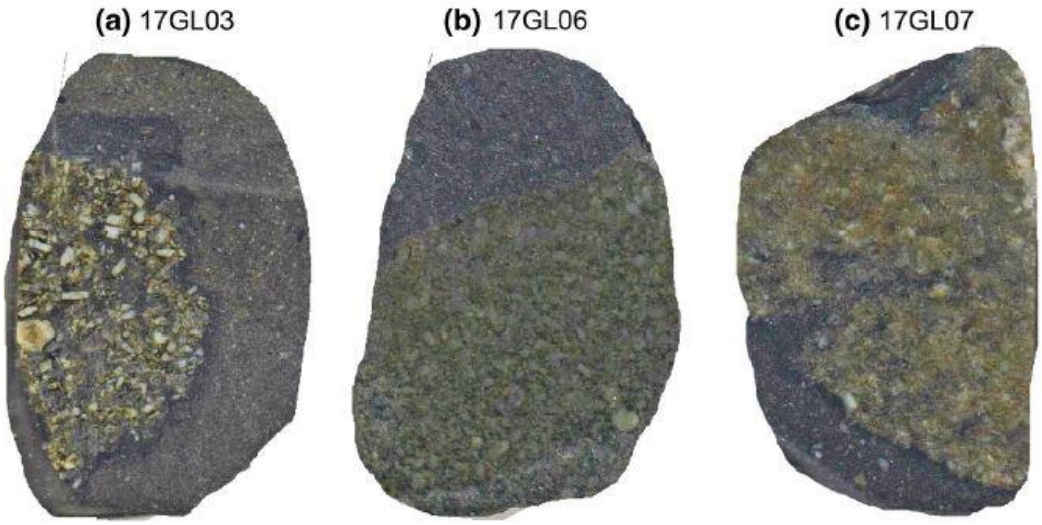

Figure 9.7 Rock chips of quenched amoeboid volcanic pebbles in the Glarus B Taveyannaz Fm. (from Lu et al., 2018).

Figure 9.8 Large angular quenched andesite clast inside spotted coarse sandstone in Flaine (northern Aravis)

The irregular-shaped amoeboid andesite pebbles with quenched/glassy margin clearly indicates the very limited transport produced by nearby submarine volcanism. This phenomenon is highly important with significant implications. The juvenile texture shows that it is very likely reworked purely in submarine conditions in order to retain its primary fabrics. This is not seen in subaerial environment, but by explosive magmatic fragmentation in water. Although these clasts are rare, they are very important. This phenomenon has not been mentioned and understood by pervious researchers in the Aravis area, though these fragile angular pebbles are not commonly observed in the turbidites in which most detrital components have been reworked.

Therefore, in Glarus and Aravis, there are not just materials being reworked from internal Alps, but also the quenched amoeboid andesite clasts generated by local submarine effusive volcanism.

From the PCA result, the provenance of volcanic components seems far more complex than the hypothesis proposed in Lu et al., (2018) in Glarus, La Tièche, Taveyannaz and Aravis areas, because they all have distinct sources despite various degree of overlapping with each other. In Lu et al., (2018), Aravis and Taveyannaz areas are discussed together and regarded as the same set of turbidites (~34-30 Ma), both receiving volcanic supply from Biella. However, our PCA result shows that there were probably several basins or several different volcanic sources supplying the same basin. Either case shows the along-strike variability in the supply of material. It's definitely not that everything in the foreland basin is homogenised, and not that the turbidites of similar composition extend for hundreds of kilometres along the Alps.

Clumanc is the northern part of Barrême basin located in between Champsaur and Provence region geographically and is supposed to have Provence-like magmatism because it is obviously closer to the Provence area than the internal Alps, but our results show that andesite pebbles are geochemically similar to Biella intrusions based on whole-rock geochemistry (Figures in Chapter 5). This could be explained by the growth of St. Lions anticline that progressively separated the Barrême basin from the Annot basin system to the east (Evans and Elliott, 1999). Thus, the structurally isolated small basin is disconnected from the erosion of the Provence volcanic front, leading to the volcanic material similar to those at the other (eastern) side of the Alps.

Clumanc andesitic pebbles are relatively large of cm-level size and could break down very quickly, both indicating the efficient, quick transport and close source. Therefore, the andesite pebbles are very unlikely derived from Biella region which is more 200 km away in the internal Alps. However, there is still no record of volcanic center with Biella-like signature close to a potential source for the Clumanc conglomerate. It is proposed that there is likely another proximal volcanic center of Alpine volcanic front located somewhere in the south of western Alps that has not been recorded, probably a small volcanic center without large intrusions. It is showing something that has not been recognised by people working on Alpine magmatism extending so far to

the south. Similar interpretation was also mentioned by few previous researchers (Evans and Mange-Rajetzky, 1991; Jourdan et al., 2013), but they have not focused on the geochemical signature of these volcanic rocks and not built the linkage between Clumanc andesitic pebbles and Alpine magmatism. The complexity of Clumanc volcanism is likely related to the fact that Barrême basin is at the junction of the two magmatic system (i.e., Alpine magmatism and Provence magmatism).

In summary, there is a complex supply of materials reworked from different volcanic sources in the north, and the volcanic compositions are different to some extent among Glarus, La Tièche, Taveyannaz and Aravis. The compositional heterogeneity is larger than expected for these secondary deposits. In Glarus and Aravis, a proximal submarine volcanic center located very close to the basin possibly also provided volcanic supplies to the basin. In Clumanc, a speculative volcanic center located to the east of Barrême basin probably provided volcanic supplies with Biella-like signature to the basin.

9.4.2 Provenance of primary volcanic clastic deposits

In Champsaur, the occurrence of the block-and-ash flow deposits (i.e., blocks of andesite breccia) shows solid evidence for proximal volcanic centres which were not recognised before in the region. This is an important outcome of our fieldwork in Champsaur area. At the same time, both whole-rock (Figures in Chapter 5) and mineral geochemistry (Figures in Chapter 6 and 7) show that Champsaur is compositionally similar to S France, though it's not exactly the same in whole-rock geochemistry and clinopyroxene geochemistry. This is not a problem because there is a certain degree of compositional variability in the Provence magmatism. Take sample CL19-024 which is an andesitic pebble as an example (Figure 9.9). The clinopyroxene result shows that the compositional variability of one single pebble produced by the erosion of lava flow can be relatively high and it seems having a bimodal composition because either there were crystallised at two stages or analysed at different parts of the crystals (e.g., core vs margin).

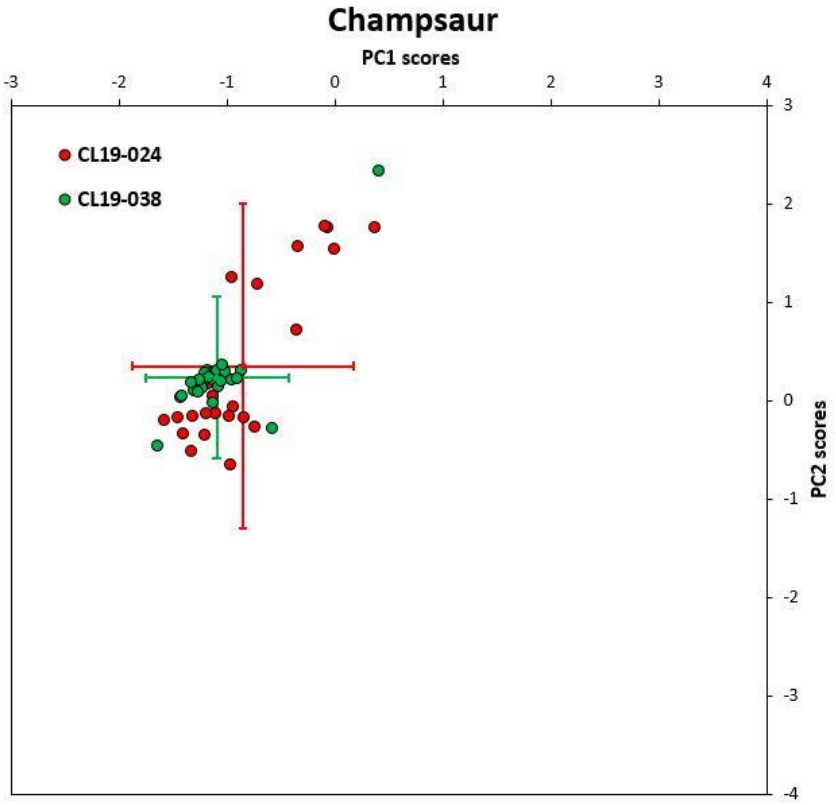

Figure 9.9 Compositional variability of Champsaur in diagrams of PC1, PC2 scores for selected trace element data on clinopyroxenes (n=722) applied to Principal Component Analysis (PCA) using Method 2 (i.e., normalised by Yb). Crosses are averages ± 2 standard deviation of each sample.

Amphibole geochemistry (see Figure 8.7) shows the similarity very well between Champsaur and S France. Therefore, the magmatic activity in Champsaur is likely the northern extension of the Provence volcanism (Figure 9.5). This interpretation is consistent with a recent model proposed by Butler et al., (2020) in terms of the extent of the Annot turbidite system, which connects the proximal areas in Provence to the more distal regions in the north until the Aiguilles d'Arves basin, via the Eastern Champsaur Basin. However, the interpretation of Provence magmatism as the source of Champsaur volcanic materials could not explain the large blocks of the primary andesitic breccia of very close origin. It is impossible to move these large blocks for such a long distance from Provence area. It's clear evidence for in-situ magmatic activity. Therefore, it is believed that there was another proximal volcanic center with Provence-like affinity supplying materials to the basin or the northern extension of Provence volcanic front all the way up to the Champsaur region.

In St. Antonin and La Vanade, both field and petrography observations indicate a more proximal volcano-sedimentary environment where volcanic components experienced very limited or no transport of reworking, and that the volcanoes are very close to the basin margin. The low compositional variability in clinopyroxenes is also in agreement with our interpretation of the immediate volcanic source. The whole-rock geochemistry shows that these primary volcaniclastic deposits are all related to Provence magmatism, which is mainly characterised by the emplacement of calc-alkaline pyroclastic to effusive rocks with a subduction-related geochemical signature in Provence region (Lustrino et al., 2017). Apart from St. Antonin and La Vanade, a series of contemporaneous igneous rocks crop out along the south-eastern French coast of similar volcano-sedimentary environments, including the Le Dramont estérellites (~32.7 ± 0.9 Ma) (Féraud et al., 1995), the Villeneuve-Loubet lavas and pyroclasts dated at 26.2 ± 1.0 Ma (Bellon and Brousse, 1971), and two pyroclastic layers between Monaco and Cap-d'Ail with younger age. Dating on samples taken from the volcanic formations of St. Antonin, with a calc-alkaline character, gave ages of 32.4 ± 1.6 Ma and 30.5 ± 3 Ma (Thomas, 2016).

In summary, our results refine the extension of the Provence magmatism all the way up to the Champsaur region where local products are clearly documented by the pyroclastic deposits and poorly reworked clasts. There was probably another proximal volcanic center with Provence-like affinity supplying materials to the basin. Further south, entering the Provence volcanic province, the terrestrial proximal pyroclastic deposits in St. Antonin and La Vanade have clear geochemical similarity with Provence magmatism.

9.4.3 Two distinct tectonic settings: Alpine volcanism and Provence volcanism

Alpine magmatism resulted from the subduction of European plate beneath Adriatic plate (A in Figure 9.9) (Dickinson, 1974; Allen and Homewood, 2009); whereas Provence magmatism probably resulted from the subduction of the Ligurian oceanic crust below the southeast margin of the newly assembled Europe-Iberia plate during late Cretaceous to Eocene (B in Figure 9.10) (Rosenbaum et al., 2002; Apps et al., 2004). The Provence Orogeny is genetically separated from the Alpine Orogeny with two slabs subducting at opposite direction, although they are coeval (Apps et a., 2004).

Our results reveal the distinct volcano-sedimentary environments and geochemical signatures in the volcaniclastic deposits between Alpine volcanic province in the north and Provence volcanic province in the south. This is probably because the two distinct tectonic settings (one related to Alpine magmatism, another related to Provence magmatism) were controlling the volcanic source-to-sink system separately.

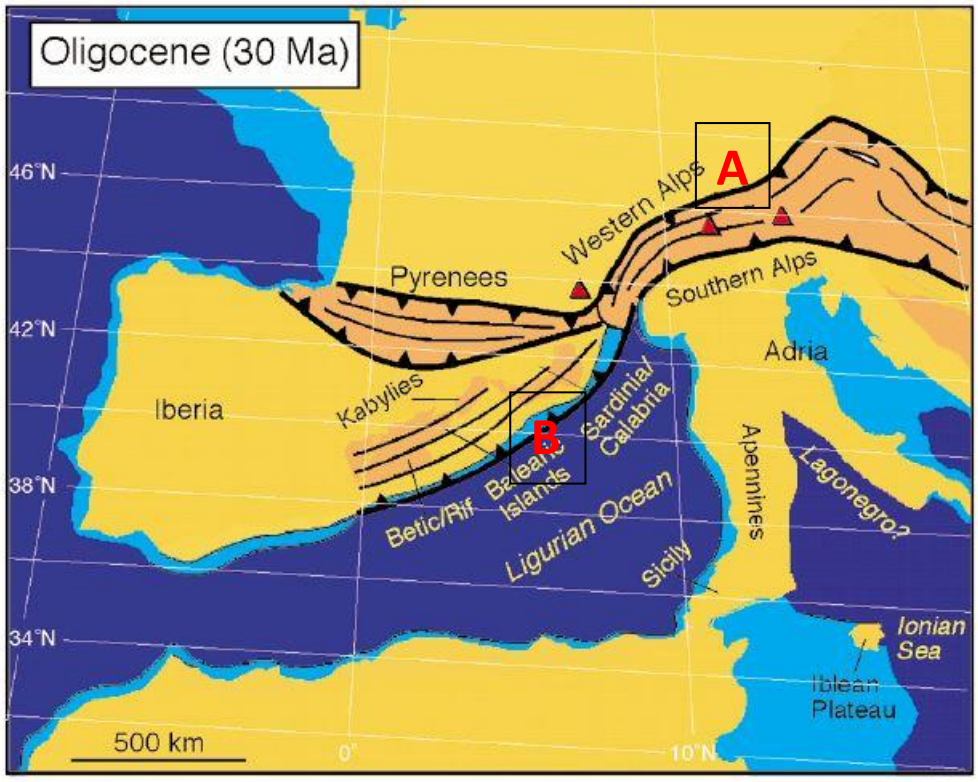

Figure 9.10 Reconstruction of the tectonic map of the western Mediterranean in Early Oligocene ca. 30 Ma (from Rosenbaum et al., 2002)

Although the new results of this study could not give further information on testing which tectonic model (mentioned in Section 1.1) is right and which is wrong, and on whether there was a slab breakoff or not, new constraint could be made that a simple model of breakoff of the Alpine slab could not fully explain the existence of possibly two volcanic fronts (i.e., one related to the subduction of Alpine slab, one related to Provence slab in the south). For some reason studies that have included one of these two in the past have not really considered the whole tectono-magmatic framework of the Alps. Therefore, the comprehensive and holistic results of this study, in particular clinopyroxene and amphibole geochemistry from two distinct tectonic settings,

offers a unique and valuable opportunity to constrain on the geographical locations of two volcanic fronts and geochemical differences.

9.5 Compositional heterogeneity in distinct tectonic settings: the Alpine foreland and Japan forearc systems

The application of the new PCA method using a previously published pyroxene dataset from Pliocene volcaniclastic turbidites in the Kumano forearc basin in Japan, offers a valuable point of comparison with the Alpine foreland system. Moreover, the PCA approach is additionally evaluated through a comparison of its output using both the Alpine and Japanese datasets together.

The PCA results (Figure 9.11) show that none of the clinopyroxene data actually overlap. There is something fundamentally different between Japan and the Alps volcanic systems.

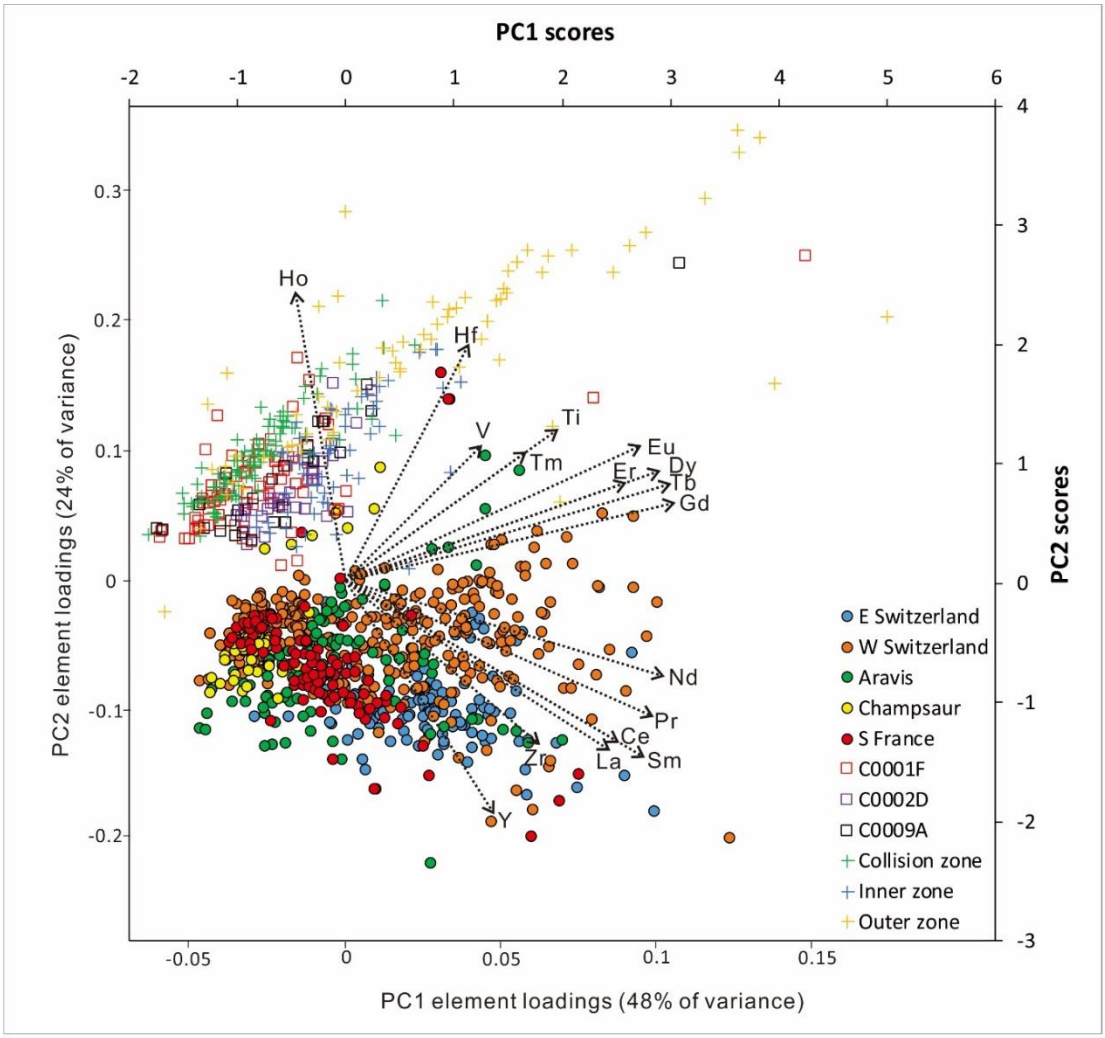

Figure 9.11 Biplot of PC1, PC2 element loadings and scores for selected trace element data on clinopyroxenes (n=1110) in this study and in Japan combined together applied to Principal Component Analysis (PCA) using Method 2 (i.e., normalised by Yb).

These results have further-reaching implications in volumetrically significant mafic volcaniclastics in the geological record, most particularly in convergent tectonic settings that are associated with arc and/or orogenic volcanism when detrital zircons, predominantly formed in slowly crystallised felsic magmas, are limited in their value in sedimentary systems dominated by the erosion of mafic igneous rocks (e.g., andesitic volcanoes). And the geochemistry of single-grain mafic minerals such as clinopyroxenes and amphiboles characterised the detailed composition of mafic to intermediate volcanic sources (e.g., Leterrier et al., 1982; Beccaluva et al., 1989), especially for the use of the trace elements in clinopyroxenes for sediment provenance studies. The PCA method overcomes the limitations of traditional discrimination approaches in that it not only efficiently recognised the limited compositional heterogeneity of Alpine clinopyroxenes and amphiboles, but also eliminated the magmatic differentiation caused by source effects. This study developed a new method to offer a new insight into the provenance of mafic-intermediate volcaniclastics globally.

9.6 Future work

1. Collect additional data on single-grain (i.e., clinopyroxene and amphibole) and whole-rock geochemical composition of igneous rocks from Alpine Periadriatic intrusions that could correspond to the roots of eroded volcanoes. The purpose is to characterise and identify the compositional variations of igneous rock from Periadriatic Line intrusions, then use these results to compare with the volcaniclastic deposits in foreland basin. Some samples in Biella were collected in this study, but unfortunately, they don't contain proper pyroxenes for analytical experiments.

2. Conduct single-grain amphibole Ar-Ar dating on amphiboles in volcaniclastic deposits and igneous rocks. The purpose is to have better geochronological constraints on the ages of both volcaniclastic deposits and their potential sources. The absolute age is always a reliable indicator in provenance analysis in terms of matching the source with the sink.

3. Collect additional data of whole-rock geochemistry of possible andesite clasts, which are big enough to extract, preserved within sandstones in Switzerland (e.g., Taveyannaz, La Tièche, Glarus) and Aravis region in order to compare with our current dataset of the andesitic clasts incorporated in the conglomerate/breccia beds and tuffs in Champsaur, Clumanc, Saint Antonin and La Vanade, and with new data of Periadriatic intrusions. The whole-rock geochemistry of pure igneous clasts can provide solid constraints on the magmatic affinities of volcaniclastic deposits and help better differentiate the volcanic sources.

4. Collect additional samples of irregular-shaped amoeboid andesite pebbles, if possible, which are rarely cropped out in Glarus and Flaine area. The geochemistry of this type of deposits is significant to better understand and constrain the possible proximal submarine volcanism in Alpine foreland basin.

5. Collect additional sandstone samples in Glarus and Clumanc, and some andesitic pebbles in Barrême basin, which contain a certain amount of fresh mafic minerals (i.e., clinopyroxene and amphibole). The mafic minerals in some samples of this study are completed altered, making them unsuitable to conduct any analytical experiments. Therefore, additional fresh samples containing unaltered mafic minerals are needed to complete the clinopyroxene/amphibole datasets and have a better understanding of the geochemical compositions and variations in Glarus, Clumanc and Barrême regions, although it is always not easy to identify the degree of alteration and judge whether the mafic minerals are suitable or not in the field.

Chapter 10: Conclusions

This study provides new field, petrographic and geochemical constraints on Alpine syn-orogenic magmatism, allowing to recognise regional differences of volcanic sources along the north alpine foreland basin (NAFB) from E Switzerland (NE) to Provence (SW), and to reconstruct the spatial and temporal evolution of syn-orogenic volcanism along the Alpine orogeny.

Field observations and sedimentological investigation reveal that there are probably two drainage systems taking control of the erosion, transport, and deposition of volcaniclastic deposits in NAFB. In the northern part of NAFB, the source-to-sink system is dominantly controlled by long distance sub-aerial transport with limited spatial and temporary distribution of poorly-reworked sedimentary and primary volcanic components; whereas in the southern part of NAFB, the long distance riverine system is perhaps still working, but more volcanic components are transported into the basin with much less amount of distance, indicating that another proximal source-to-sink system starts providing volcanic inputs to the basin. Primary andesitic breccia and primary volcaniclastic deposits even indicate a source-within-sink relationship between the volcanoes and the basin, in which juvenile pyroclasts produced by explosive volcanism of neighbouring volcanoes are directly injected into the basin. More importantly, the occurrence of quenched amoeboid andesitic pebbles in Glarus and Flaine is highly significant. It clearly indicates the very limited transport of local submarine effusive volcanism and provides new evidence of proximal volcanic activity in the foreland basin. Therefore, the volcanic sources of the volcaniclastic deposits in the two regions are not only from the internal Alps represented by subaerial reworked materials, but also from proximal submarine volcanic centers represented by quenched amoeboid andesitic clasts.

Petrographic study shows that the Taveyannaz sandstone (s.l.) originated mainly from dissected to transitional volcanic arcs and crystalline basement with minor contributions from sedimentary sources. The volcanic clasts have a dominant microlitic texture, corresponding to the intermediate nature of Taveyannaz volcanism. Most sandstones are enriched in clinopyroxene andesite clasts with a high proportion of heavily altered andesite clasts, in

particular in Glarus, Clumanc and Champsaur regions. Most of the igneous clasts are clinopyroxene andesite with vitrophyric texture. The percentage of ferro-magnesian phenocrysts varies between 10 - 30 %.

The whole-rock geochemistry shows that majority of the igneous samples are basaltic andesite and andesite with sub-alkaline affinity while a small number of samples are more evolved dacite. On the chondrite-normalised REE and multielement diagrams, all igneous samples show typical arc signatures, with three types of patterns having been distinguished. Type 1 corresponds to samples from Clumanc and Biella/Sesia-Lanzo regions, characterised by highly enriched LREE (Th) and flat HREE; Type 2 corresponds to samples from St. Antonin and La Vanade/Villeneuve-Loubet regions, characterised by slightly enriched LREE (Th) and extremely flat HREE; Type 3 includes samples from Champsaur region, characterised by moderate enriched LREE (Th) and flat HREE, representing a middle pattern between Type 1 and Type 2. On the discrimination diagrams, generally majority of the samples plot in the arc field and two subgroups have been distinguished. Subgroup 1 mainly includes samples from Clumanc and Biella/Sesia-Lanzo regions, while Subgroup 2 corresponds to samples from St. Antonin, La Vanade, Villeneuve-Loubet and Nice-Monaco regions. Samples from Champsaur regions are plotted in both subgroups, part clustering with Subgroup 1 and part plotting together with Subgroup 2 in most of the diagrams. The igneous clasts from Clumanc foreland region share similar geochemical patterns to the dykes in western Alps (Biella/Sesia-Lanzo), whereas some igneous clasts from Champsaur and primary volcaniclastic deposits from St. Antonin region are in good agreement with those volcanic suites from Provence volcanic province (La Vanade, Villeneuve-Loubet and Nice-Monaco).

Clinopyroxene geochemistry shows that majority of the clinopyroxenes are Mg-augite with subordinate diopside, characterised by supra-subduction affinity in Leterrier et al. (1982) diagrams. High SiO_2 together with low TiO_2 and Al_2O_3 contents in the clinopyroxene are typical of pyroxenes crystallising from orogenic, subalkaline magmas. The La/Sm vs Ti/V binary diagram offers the best compositional discrimination to identify clinopyroxenes from possibly distinct sources at the regional to local scales. It shows that clinopyroxenes from W Switzerland and Aravis are largely similar over a large compositional

spectrum. E Switzerland (one sample) includes clinopyroxenes with higher La/Sm values and lower Ti/V values that are clearly distinct from those from S France. As for those from Champsaur, part of the clinopyroxenes is overlapping with those from S France. Small compositional variability generally exists among samples from a single locality (Section 6.4), but its extent does not exceed the overall compositional variability observed at larger (e.g., regional) scale.

Amphibole geochemistry shows that all amphiboles are Calcium Amphibole and vast majority of the amphiboles are defined as Pargasite subgroup (82 %), mainly including (Ti-rich) pargasite (28 %) and (Ti-rich) magnesio-hastingsite (54 %). The amphibole classification diagram offers good compositional discrimination to identify amphiboles from possibly distinct sources at the regional to local scales. It shows that amphiboles from Aravis are spreading over a large compositional spectrum, as well as those from E Switzerland and W Switzerland, though the results may be biased due to limited number of analyses in E Switzerland and W Switzerland. Amphiboles from Champsaur and S France are largely overlapping partially with the wide-spreading population of Aravis. Amphiboles from N Italy plot separately from the main population.

The new technique of using Principal Component Analysis (PCA) method on a large dataset of clinopyroxenes from different areas in foreland basin with different geological characteristics shows the compositional variability which was not recognised previously in both primary and secondary deposits. PCA results on clinopyroxenes provide more robust constraints, showing high compositional variability in samples from Glarus, La Tièche, Taveyannaz and Aravis, compared with samples from Champsaur, St. Antonin and La Vanade. In the north (i.e., Glarus, La Tièche, Taveyannaz and Aravis), they all have distinct compositions and sources based on clinopyroxene PCA results. Therefore, the provenance of the volcanic components seems far more complex than that proposed in new sediment provenance models based on U-Pb and isotope composition of detrital zircons, which have linked the volcaniclastic deposits only to Adamello and Biella sources.

The compositional heterogeneity shown by samples from St. Antonin and La Vanade defines the degree of variability it will be expected in clinopyroxenes

of primary volcaniclastic deposits in the Alpine context, whereas the heterogeneity shown in samples from Taveyannaz and La Tièche provides a comparable reference on how much compositional variability it will be in secondary volcaniclastic deposits which have potentially multiple volcanic sources.

The application of the new PCA method using a previously published pyroxene dataset from Pliocene volcaniclastic turbidites in the Kumano forearc basin in Japan combined with our Alpine foreland data offers a valuable point of comparison. The PCA results show that none of the clinopyroxene data actually overlap. There is something fundamentally different between Japan and the Alps volcanic systems. These results have further-reaching implications in volumetrically significant mafic volcaniclastics in the geological record, most particularly in convergent tectonic settings that are associated with arc and/or orogenic volcanism when detrital zircons, predominantly formed in slowly crystallised felsic magmas, are limited in their value in sedimentary systems dominated by the erosion of mafic igneous rocks (e.g., andesitic volcanoes). Thus, this study developed a new method to offer an innovative insight into the provenance of mafic-intermediate volcaniclastics globally.

The provenance study refines the extension of the Provence magmatism all the way up to the Champsaur region where local products are clearly documented by the pyroclastic deposits and poorly reworked clasts, one of which (i.e., andesite breccia) has compositional variability similar to pyroclastic deposits in terms of clinopyroxene. In Clumanc, the volcaniclastic materials with Biella-like affinity are perhaps derived from another proximal volcanic center of the Alpine volcanic front located somewhere at the other side of the Alps which has not been recorded, refining the southern extension of the influence of Alpine magmatism until Barrême basin. Further south, entering the Provence volcanic system, the terrestrial proximal pyroclastic deposits in St. Antonin and La Vanade have clear geochemical similarity with Provence magmatism. There are probably two distinct tectonic settings controlling volcanic source-to-sink systems and causing the two types of volcano-sedimentary environments and geochemical signatures in the volcaniclastic deposits between Alpine volcanic province in the north and

Provence volcanic province in the south. This new finding provides new constraints on the tectonic models proposed by previous researchers mentioned in Introduction chapter. It indicates that a simple slab breakoff model could not fully explain the existence of two volcanic fronts. A whole tectono-magmatic framework of the Alps should be considered in terms of forming a hypothesis on tectonic model.

The possible position of the volcanic center(s) varies along the Alpine foreland basin, with the transition from Provence volcanic province in the south of small, disconnected basins containing proximal deposits of local source to the north of deeper, extended basins containing secondary deposits possibly derived from internal Alps. In addition, it's very likely there were magmatic activities within the foreland basin of submarine/subaerial environments supported by the occurrence of quenched amoeboid clasts and blocks of andesitic breccia. This is a totally different overview of Alpine volcanism from anything which has been proposed so far with strong and robust set of integrated results based on field observations, petrographic observations, whole-rock geochemistry, clinopyroxene and amphibole geochemistry.

References

Agard, P. and Handy, M.R., 2021. Ocean subduction dynamics in the Alps. *Elements: An International Magazine of Mineralogy, Geochemistry, and Petrology*, *17*(1), pp.9-16.

Aitchison, J. and Greenacre, M., 2002. Biplots of compositional data. *Journal of the Royal Statistical Society: Series C (Applied Statistics)*, *51*(4), pp.375-392.

Aitchison, J., 1982. The statistical analysis of compositional data. *Journal of the Royal Statistical Society: Series B (Methodological)*, *44*(2), pp.139-160.

Aitchison, J., 1983. Principal component analysis of compositional data. *Biometrika*, *70*(1), pp.57-65.

Alagna, K.E., Peccerillo, A., Martin, S. and Donati, C., 2010. Tertiary to present evolution of orogenic magmatism in Italy. *Journal of the Virtual Explorer*, *36*(18).

Allen, P.A. and Homewood, P. eds., 2009. *Foreland basins*. John Wiley & Sons.

Allen, P.A., Crampton, S.L. and Sinclair, H.D., 1991. The inception and early evolution of the North Alpine Foreland Basin, Switzerland. *Basin Research*, *3*(3), pp.143-163.

Ampferer, O. and Hammer, W., 1911. Geologischer Querschnitt durch die Ostalpen vom Allgäu zum Gardasee. *Jahrbuch der Kaiserlich-Königlichen Geologischen Reichsanstalt*, *61*(3/4), pp.532-710.

Apps, G., Peel, F. and Elliott, T., 2004. The structural setting and palaeogeographical evolution of the Grès d'Annot basin. *Geological Society, London, Special Publications*, *221*(1), pp.65-96.

Apps, G.M., 1987. *The evolution of the Gres d'Annot Basin, SW Alps* (Doctoral dissertation, University of Liverpool).

Arculus, R.J., 1987. The significance of source versus process in the tectonic controls of magma genesis. *Journal of Volcanology and Geothermal Research*, *32*(1-3), pp.1-12.

Arculus, R.J., 2003. Use and abuse of the terms calcalkaline and calcalkalic. *Journal of petrology*, *44*(5), pp.929-935.

Beach, A., 1981. Thrust tectonics and crustal shortening in the external French Alps based on a seismic cross-section. *Tectonophysics*, *79*(1-2), pp.T1-T6.

Beccaluva, L., Bianchini, G., Bonadiman, C., Coltorti, M., Milani, L., Salvini, L., Siena, F. and Tassinari, R., 2007. Intraplate lithospheric and sublithospheric components in the Adriatic domain: Nephelinite to tholeiite magma generation in the Paleogene Veneto volcanic province, southern Alps. *Special Papers-Geological Society of America*, *418*, p.131.

Beccaluva, L., Bigioggero, B., Chiesa, S., Colombo, A., Fanti, G. and Gatto, G.O., 1983. Post collisional orogenic dyke magmatism in the Alps. *Memorie della Societa Geologica Italiana*, *26*(1), pp.341-359.

Beccaluva, L., Coltorti, M., Galassi, B., Macciotta, G. and Siena, F., 1994. The Cainozoic calcalkaline magmatism of the western Mediterranean and its geodynamic significance. *Bollettino di geofisica teorica ed applicata*, *36*(141-144), pp.293-308.

Beccaluva, L., Macciotta, G., Piccardo, G.B. and Zeda, O., 1989. Clinopyroxene composition of ophiolite basalts as petrogenetic indicator. *Chemical Geology*, *77*(3-4), pp.165-182.

Beller, S., Monteiller, V., Operto, S., Nolet, G., Paul, A. and Zhao, L., 2018. Lithospheric architecture of the South-Western Alps revealed by multiparameter teleseismic full-waveform inversion. *Geophysical Journal International*, *212*(2), pp.1369-1388.

Bellieni, G., Fioretti, A.M., Marzoli, A. and Visonà, D., 2010. Permo–Paleogene magmatism in the eastern Alps. *Rendiconti Lincei*, *21*(1), pp.51-71.

Belousova, E.A., Griffin, W.L., O'Reilly, S.Y. and Fisher, N.L., 2002. Igneous zircon: trace element composition as an indicator of source rock type. *Contributions to mineralogy and petrology*, *143*(5), pp.602-622.

Beltrán-Triviño, A., Winkler, W. and Von Quadt, A., 2013. Tracing Alpine sediment sources through laser ablation U–Pb dating and Hf-isotopes of detrital zircons. *Sedimentology*, *60*(1), pp.197-224.

Berger, A. and Bousquet, R., 2008. Subduction-related metamorphism in the Alps: review of isotopic ages based on petrology and their geodynamic consequences. *Geological Society, London, Special Publications*, *298*(1),

pp.117-144.

Berger, A., Thomsen, T.B., Ovtcharova, M., Kapferer, N. and Mercolli, I., 2012. Dating emplacement and evolution of the orogenic magmatism in the internal Western Alps: 1. The Miagliano Pluton. *Swiss journal of geosciences*, *105*(1), pp.49-65.

Bergomi, M.A., Zanchetta, S. and Tunesi, A., 2015. The Tertiary dike magmatism in the Southern Alps: geochronological data and geodynamic significance. *International Journal of Earth Sciences*, *104*(2), pp.449-473.

Beuf, S., Biju-Duval, B. and Gubler, Y., 1961. Les formations volcano-détritiques du tertiaire de Thones (Savoie), du Champsaur (Hautes-Alpes) et de Clumanc (Basses-Alpes). *Travaux Labo. Géol. Fac. Sc. Grenoble*, pp.143-152.

Bhatia, M.R., 1985. Rare earth element geochemistry of Australian Paleozoic graywackes and mudrocks: provenance and tectonic control. *Sedimentary geology*, *45*(1-2), pp.97-113.

Bianchini, G., Beccaluva, L. and Siena, F., 2008. Post-collisional and intraplate Cenozoic volcanism in the rifted Apennines/Adriatic domain. *Lithos*, *101*(1-2), pp.125-140.

Bigioggero, B., Colombo, A., Del Moro, A., Gregnanin, A., Macera, P. and Tunesi, A., 1994. The Oligocene Valle del Cervo pluton: an example of shoshonitic magmatism in the Western Italian Alps.

Bini, A., Sciunnach, D., Bersezio, R., Scardia, G. and Tomasi, F., Note illustrative della Carta Geologica d'Italia alla scala 1: 50000. Foglio Seregno. ISPRA 2015.

Bird, P., 1979. Continental delamination and the Colorado Plateau. *Journal of Geophysical Research: Solid Earth*, *84*(B13), pp.7561-7571.

Bistacchi, A., Dal Piaz, G., Massironi, M., Zattin, M. and Balestrieri, M., 2001. The Aosta–Ranzola extensional fault system and Oligocene–Present evolution of the Austroalpine–Penninic wedge in the northwestern Alps. *International Journal of Earth Sciences*, *90*(3), pp.654-667.

Bodelle, J., 1971. *Les formations nummulitiques de l'arc de Castellane* (Vol. 2). BRGM.

Bouma, A.H., 1962. Sedimentology of some flysch deposits. *Agraphic*

approach to facies interpretation, *168*.

Boyet, M., Lapierre, H., Tardy, M., Bosch, D. and Maury, R., 2001. Sources of the andesitic components in the Taveyannaz Sandstones and Chapsaur Sandstones: implications for the Paleogene geodynamic evolution of the Alps. *Bulletin-Societe Geologique de France*, *172*(4), pp.487-502.

Broderick, C., Wotzlaw, J.F., Frick, D.A., Gerdes, A., Ulianov, A., Günther, D. and Schaltegger, U., 2015. Linking the thermal evolution and emplacement history of an upper-crustal pluton to its lower-crustal roots using zircon geochronology and geochemistry (southern Adamello batholith, N. Italy). *Contributions to Mineralogy and Petrology*, *170*(3), pp.1-17.

Buchs, D.M. and Oemering, S.A., 2020. Long-term non-erosive nature of the south Costa Rican margin supported by arc-derived sediments accreted in the Osa Mélange. *Earth and Planetary Science Letters*, *531*, p.115968.

Buchs, D.M., Cukur, D., Masago, H. and Garbe-Schönberg, D., 2015. Sediment flow routing during formation of forearc basins: Constraints from integrated analysis of detrital pyroxenes and stratigraphy in the Kumano Basin, Japan. *Earth and Planetary Science Letters*, *414*, pp.164-175.

Bussy, F. and Epard, J.L., 1984. Essai de zonéographie métamorphique entre les Diablerets et le massif de l'Aar (Suisse occidentale), basée sur l'étude des Grès de Taveyanne. *Schweizerische Mineralogische und Petrographische Mitteilungen*, *64*(1-2), pp.131-150.

Bütler, E., Winkler, W. and Guillong, M., 2011. Laser ablation U/Pb age patterns of detrital zircons in the Schlieren Flysch (Central Switzerland): new evidence on the detrital sources. *Swiss Journal of Geosciences*, *104*(2), pp.225-236.

Butler, J.C. and Woronow, A., 1986. Discrimination among tectonic settings using trace element abundances of basalts. *Journal of Geophysical Research: Solid Earth*, *91*(B10), pp.10289-10300.

Butler, R.W., 1992. Thrust zone kinematics in a basement-cover imbricate stack: Eastern Pelvoux massif, French Alps. *Journal of Structural Geology*, *14*(1), pp.29-40.

Butler, R.W., Lickorish, H.W., Vinnels, J. and McCaffrey, W.D., 2020.

Untangling the Annot sand fairway: structure and stratigraphy of the Eastern Champsaur Basin (Eocene–Oligocene), French Alps. *Journal of the Geological Society*, *177*(6), pp.1197-1209.

Callec, Y., 2001. *La déformation synsédimentaire des bassins paléogènes de l'Arc de Castellane (Annot, Barrême, Saint-Antonin)* (Doctoral dissertation, Paris, ENMP).

Callegari, E. and Brack, P., 2002. Geological map of the tertiary Adamello batholith (northern Italy). *Explanatory notes and legend. Mem Sci Geol*, *54*, pp.19-49.

Callegari, E., Cigolini, C., Medeot, O. and D'Antonio, M., 2004. Petrogenesis of calc-alkaline and shoshonitic post-collisional Oligocene volcanics of the Cover Series of the Sesia Zone, Western Italian Alps. *Geodinamica Acta*, *17*(1), pp.1-29.

Cann, J.R., 1970. Rb, Sr, Y, Zr and Nb in some ocean floor basaltic rocks. *Earth and Planetary Science Letters*, *10*(1), pp.7-11.

Carey, S.N. and Schneider, J.L., 2011. Volcaniclastic processes and deposits in the deep-sea. In *Developments in Sedimentology* (Vol. 63, pp. 457-515). Elsevier.

Carminati, E., Lustrino, M., Cuffaro, M. and Doglioni, C., 2010. Tectonics, magmatism and geodynamics of Italy: what we know and what we imagine. *Journal of the Virtual Explorer*, *36*(8), pp.10-3809.

Coletti, G., Vezzoli, G., Di Capua, A. and Basso, D., 2016. Reconstruction of a lost carbonate factory based on its biogenic detritus (Ternate-Travedona Formation and Gonfolite Lombarda Group-northern Italy). *Riv. Ital. Paleontol. Stratigr*, *122*, pp.1-22.

Condie, K.C., 1989. Geochemical changes in basalts and andesites across the Archean-Proterozoic boundary: Identification and significance. *Lithos*, *23*(1-2), pp.1-18.

Condie, K.C., 2005. High field strength element ratios in Archean basalts: a window to evolving sources of mantle plumes?. *Lithos*, *79*(3-4), pp.491-504.

Conticelli, S., Guarnieri, L., Farinelli, A., Mattei, M., Avanzinelli, R., Bianchini, G., Boari, E., Tommasini, S., Tiepolo, M., Prelević, D. and Venturelli, G., 2009.

Trace elements and Sr–Nd–Pb isotopes of K-rich, shoshonitic, and calc-alkaline magmatism of the Western Mediterranean Region: genesis of ultrapotassic to calc-alkaline magmatic associations in a post-collisional geodynamic setting. *Lithos*, *107*(1-2), pp.68-92.

Coombs, D.S., Nakamura, Y. and Vuagnat, M., 1976. Pumpellyite-actinolite facies schists of the Taveyanne Formation near Loèche, Valais, Switzerland. *Journal of Petrology*, *17*(4), pp.440-471.

Cullers, R.L., 2000. The geochemistry of shales, siltstones and sandstones of Pennsylvanian–Permian age, Colorado, USA: implications for provenance and metamorphic studies. *Lithos*, *51*(3), pp.181-203.

D'Adda, P., Zanchi, A., Bergomi, M., Berra, F., Malusà, M.G., Tunesi, A. and Zanchetta, S., 2011. Polyphase thrusting and dyke emplacement in the central Southern Alps (Northern Italy). *International Journal of Earth Sciences*, *100*(5), pp.1095-1113.

Dal Piaz, G.V., Bistacchi, A. and Massironi, M., 2003. Geological outline of the Alps. *Episodes Journal of International Geoscience*, *26*(3), pp.175-180.

Dal Zilio, L., Ruh, J. and Avouac, J.P., 2020. Structural evolution of orogenic wedges: interplay between erosion and weak décollements. *Tectonics*, *39*(10), p.e2020TC006210.

Davidson, J., Turner, S. and Plank, T., 2013. Dy/Dy*: variations arising from mantle sources and petrogenetic processes. *Journal of Petrology*, *54*(3), pp.525-537.

Davies, J.H. and von Blanckenburg, F., 1995. Slab breakoff: a model of lithosphere detachment and its test in the magmatism and deformation of collisional orogens. *Earth and Planetary Science Letters*, *129*(1-4), pp.85-102.

De Graciansky, P.C., Roberts, D.G. and Tricart, P., 2010. *The Western Alps, from rift to passive margin to orogenic belt: an integrated geoscience overview*. Elsevier.

De Quervain, F., 1928. The Swiss Statistics concerning Toxic Goitre. *Schweizerische Medizinische Wochenschrift*, *58*.

DeCelles, P.G. and Giles, K.A., 1996. Foreland basin systems. *Basin*

research, *8*(2), pp.105-123.

Deer, W.A., Howie, R.A. and Zussman, J. eds., 1997. Rock-forming minerals: single-chain silicates, Volume 2A. Geological Society of London.

Dewey, J.F., Helman, M.L., Knott, S.D., Turco, E. and Hutton, D.H.W., 1989. Kinematics of the western Mediterranean. *Geological Society, London, Special Publications*, *45*(1), pp.265-283.

Di Capua, A. and Groppelli, G., 2016. Application of actualistic models to unravel primary volcanic control on sedimentation (Taveyanne Sandstones, Oligocene Northalpine Foreland Basin). *Sedimentary Geology*, *336*, pp.147-160.

Di Giulio, A., Carrapa, B., Fantoni, R., Gorla, L. and Valdisturlo, A., 2001. Middle Eocene to Early Miocene sedimentary evolution of the western Lombardian segment of the South Alpine foredeep (Italy). *International Journal of Earth Sciences*, *90*(3), pp.534-548.

Di Giulio, A., Dunkl, I., Falletti, P. and Sciunnach, D., 2005. Plagioclas-arenites from the Northern Apennines and Southern Alps: Record of a Paleogene island arc related to Alpine subduction. In *Proceedings of the 7th Alpine Workshop, Opatija, Croatia* (Vol. 29).

Dickinson, W.R. and Suczek, C.A., 1979. Plate tectonics and sandstone compositions. *Aapg Bulletin*, *63*(12), pp.2164-2182.

Dickinson, W.R., 1970. Interpreting detrital modes of graywacke and arkose. *Journal of Sedimentary Research*, *40*(2), pp.695-707.

Dickinson, W.R., 1974. Plate tectonics and sedimentation.

Dickinson, W.R., 1985. Interpreting provenance relations from detrital modes of sandstones. In *Provenance of arenites* (pp. 333-361). Springer, Dordrecht.

Dickinson, W.R., Beard, L.S., Brakenridge, G.R., Erjavec, J.L., Ferguson, R.C., Inman, K.F., Knepp, R.A., Lindberg, F.A. and Ryberg, P.T., 1983. Provenance of North American Phanerozoic sandstones in relation to tectonic setting. *Geological Society of America Bulletin*, *94*(2), pp.222-235.

Doglioni, C., 1994. Foredeeps versus subduction zones. *Geology*, *22*(3), pp.271-274.

Doglioni, C., Mongelli, F. and Pialli, G., 1998. Boudinage of the Alpine belt in the Apenninic back-arc. *Mem. Soc. Geol. It*, *52*, pp.457-468.

Doudoux, B., Chaplet, M. and Tardy, M., 1987. Les séries marines paléogènes post-lutétiennes du Massif subalpin des Bornes (Alpes occidentales). *Gèologie Alpine*, *13*, pp.299-312.

Dumont, T., Schwartz, S., Guillot, S., Simon-Labric, T., Tricart, P. and Jourdan, S., 2012. Structural and sedimentary records of the Oligocene revolution in the Western Alpine arc. *Journal of Geodynamics*, *56*, pp.18-38.

Elliot, T., Apps, G., Davies, H., Evans, M., Ghibudo, G. and Graham, R.H., 1985. Field excursion B: a structural and sedimentological traverse through the Tertiary foreland basin of the external Alps of south-east France. In *International Symposium on Foreland Basins Guidebook, Excursion* (Vol. 3, pp. 39-73).

Elter, P., Catanzariti, R., Ghiselli, F., Marroni, M., Molli, G., Ottria, G. and Pandolfi, L., 1999. The Aveto Unit (Northern Apennines); lithostratigraphy, biostratigraphy, sandstone petrography. *Boll. Soc. Geol. It*, *118*, pp.41-63.

Escher, A., Masson, H. and Steck, A., 1993. Nappe geometry in the western Swiss Alps. *Journal of structural Geology*, *15*(3-5), pp.501-509.

Evans, M.J. and Elliott, T., 1999. Evolution of a thrust-sheet-top basin: The Tertiary Barreme basin, Alpes-de-Haute-Provence, France. *Geological Society of America Bulletin*, *111*(11), pp.1617-1643.

Evans, M.J. and Mange-Rajetzky, M.A., 1991. The provenance of sediments in the Barrême thrust-top basin, Haute-Provence, France. *Geological Society, London, Special Publications*, *57*(1), pp.323-342.

Ewart, A. and Le Maitre, R.W., 1980. Some regional compositional differences within Tertiary—Recent orogenic magmas. *Chemical Geology*, *30*(3), pp.257-283.

Fantoni, R., Bersezio, R., Forcella, F., Gorla, L., Mosconi, A. and Picotti, V., 1999. New dating of the Tertiary magmatic products of the central Southern Alps, bearings on the interpretation of the Alpine tectonic history. *Memorie di Scienze Geologiche*, *51*(1), pp.47-61.

Feng, R. and Kerrich, R., 1990. Geochemistry of fine-grained clastic sediments

in the Archean Abitibi greenstone belt, Canada: implications for provenance and tectonic setting. *Geochimica et Cosmochimica Acta*, *54*(4), pp.1061-1081.

Féraud, G., Ruffet, G., Stéphan, J.F., Lapierre, H., Delgado, E. and Popoff, M., 1995. Nouvelles données géochronologiques sur le volcanisme paléogène des Alpes occidentales: existence d'un événement magmatique bref généralisé. *Séance Spéciale de la Société géologique de France et de l" Association des Géologues du SE" Magmatismes dans le sud-est de la France", Nice*, pp.25-26.

Ford, M. and Lickorish, W.H., 2004. Foreland basin evolution around the western Alpine Arc. *Geological Society, London, Special Publications*, *221*(1), pp.39-63.

Ford, M., Lickorish, W.H. and Kusznir, N.J., 1999. Tertiary foreland sedimentation in the Southern Subalpine Chains, SE France: a geodynamic appraisal. *Basin research*, *11*(4), pp.315-336.

Gallahan, W.E. and Nielsen, R.L., 1992. The partitioning of Sc, Y, and the rare earth elements between high-Ca pyroxene and natural mafic to intermediate lavas at 1 atmosphere. *Geochimica et cosmochimica acta*, *56*(6), pp.2387-2404.

Garzanti, E. and Andò, S., 2007. Heavy mineral concentration in modern sands: implications for provenance interpretation. *Developments in Sedimentology*, *58*, pp.517-545.

Garzanti, E. and Andò, S., 2007. Plate tectonics and heavy mineral suites of modern sands. *Developments in Sedimentology*, *58*, pp.741-763.

Garzanti, E., Doglioni, C., Vezzoli, G. and Ando, S., 2007. Orogenic belts and orogenic sediment provenance. *The Journal of Geology*, *115*(3), pp.315-334.

Gavazzi, A., Miletta, S., Sciunnach, D. and Tremolada, F., 2003. Eocene plagioclase-arenites from the Southern Alps: Record of a “meso-Alpine” volcanic arc. *Ann. Uniservitatis Sci. Bp. Sect. Geol*, *35*, pp.102-103.

Gazzi, P., 1966. Le arenarie del flysch sopracretaceo dell'Appennino modenese; Correlazioni coni flysch di Monghidoro. *Miner Petrogr Acta*, *12*, pp.69-97.

Gerrard, J., 1990. *Mountain environments: an examination of the physical*

geography of mountains. MIT press.

Giacomuzzi, G., Chiarabba, C. and De Gori, P., 2011. Linking the Alps and Apennines subduction systems: new constraints revealed by high-resolution teleseismic tomography. *Earth and Planetary Science Letters*, *301*(3-4), pp.531-543.

Gianola, O., Schmidt, M.W., von Quadt, A., Peytcheva, I., Luraschi, P. and Reusser, E., 2014. Continuity in geochemistry and time of the Tertiary Bergell intrusion (Central Alps). *Swiss Journal of Geosciences*, *107*(2), pp.197-222.

Gidon, M. and Pairis, J.L., 1976. Le rôle des mouvements tectoniques éocènes dans la genèse des structures de l'extrémité NE du Dévoluy et dans celle du chevauchement de Digne. *Géologie alpine*, *52*, pp.73-83.

Gidon, M., 1979. Le rôle des étapes successives de déformation dans la tectonique alpine du massif du Pelvoux (Alpes occidentales).

Gill, J.B., 1981. Bulk chemical composition of orogenic andesites. In *Orogenic Andesites and Plate Tectonics* (pp. 97-167). Springer, Berlin, Heidelberg.

Giraud, J. and Didier, J., 1981. Occurrence of volcanic autochthonous manifestations in the lower part of the gres de Taveyanne, Flaine-Larbaron (Haute-Savoie, France). *Comptes rendus de l academie des sciences series II*, *292*(3), pp.369-372.

Giraud, J.D., 1983. *L'arc andésitique paléogène des Alpes occidentales: pétrologie, volcanologie, signification géodynamique* (Doctoral dissertation, Université Nice Sophia Antipolis).

Girault, J.B., Bellahsen, N., Boutoux, A., Rosenberg, C.L., Nanni, U., Verlaguet, A. and Beyssac, O., 2020. The 3-D thermal structure of the Helvetic nappes of the European Alps: Implications for collisional processes. *Tectonics*, *39*(3), p.e2018TC005334.

Goffé, B. and Bousquet, R., 2004. Metamorphic structure of the Alps: Western and Ligurian Alps. *Nature*, *387*, pp.586-589.

Grimes, C.B., John, B.E., Kelemen, P.B., Mazdab, F.K., Wooden, J.L., Cheadle, M.J., Hanghøj, K. and Schwartz, J.J., 2007. Trace element chemistry of zircons from oceanic crust: A method for distinguishing detrital zircon

provenance. *Geology*, *35*(7), pp.643-646.

Gupta, S., 1997. Tectonic control on paleovalley incision at the distal margin of the early Tertiary Alpine foreland basin, southeastern France. *Journal of Sedimentary Research*, *67*(6), pp.1030-1043.

Handy, M.R., Schmid, S.M., Bousquet, R., Kissling, E. and Bernoulli, D., 2010. Reconciling plate-tectonic reconstructions of Alpine Tethys with the geological–geophysical record of spreading and subduction in the Alps. *Earth-Science Reviews*, *102*(3-4), pp.121-158.

Harrison, T.M., 2009. The Hadean crust: evidence from> 4 Ga zircons. *Annual Review of Earth and Planetary Sciences*, *37*, pp.479-505.

Hastie, A.R., Kerr, A.C., Pearce, J.A. and Mitchell, S.F., 2007. Classification of altered volcanic island arc rocks using immobile trace elements: development of the Th–Co discrimination diagram. *Journal of petrology*, *48*(12), pp.2341-2357.

Hawthorne, F.C., Oberti, R., Harlow, G.E., Maresch, W.V., Martin, R.F., Schumacher, J.C. and Welch, M.D., 2012. Nomenclature of the amphibole supergroup. *American Mineralogist*, *97*(11-12), pp.2031-2048.

Herb, R., 1988. Eocaene Paläogeographie und Paläotektonik des Helvetikums. *Eclogae Geologicae Helvetiae*, *81*(3), pp.611-657.

Hofmann, A.W. and White, W.M., 1983. Ba, Rb and Cs in the Earth's mantle. *Zeitschrift für Naturforschung A*, *38*(2), pp.256-266.

Homewood, P., Allen, P.A. and Williams, G.D., 1986. Dynamics of the Molasse Basin of western Switzerland. In *Foreland basins* (Vol. 8, pp. 199-217). Oxford, UK: Blackwell Scientific Publications.

Houseman, G.A., McKenzie, D.P. and Molnar, P., 1981. Convective instability of a thickened boundary layer and its relevance for the thermal evolution of continental convergent belts. *Journal of Geophysical Research: Solid Earth*, *86*(B7), pp.6115-6132.

Howie, R.A., Zussman, J. and Deer, W., 1992. *An introduction to the rock-forming minerals* (p. 696). London, UK: Longman.

Hua, Y., Zhao, D. and Xu, Y., 2017. P wave anisotropic tomography of the

Alps. *Journal of Geophysical Research: Solid Earth*, *122*(6), pp.4509-4528.

Hürlimann, N., Müntener, O., Ulmer, P., Nandedkar, R., Chiaradia, M. and Ovtcharova, M., 2016. Primary magmas in continental arcs and their differentiated products: petrology of a post-plutonic dyke suite in the Tertiary Adamello batholith (Alps). *Journal of Petrology*, *57*(3), pp.495-534.

Ingersoll, R.V., Bullard, T.F., Ford, R.L., Grimm, J.P., Pickle, J.D. and Sares, S.W., 1984. The effect of grain size on detrital modes: a test of the Gazzi-Dickinson point-counting method. *Journal of Sedimentary Research*, *54*(1), pp.103-116.

Ji, W.Q., Malusà, M.G., Tiepolo, M., Langone, A., Zhao, L. and Wu, F.Y., 2019. Synchronous Periadriatic magmatism in the Western and Central Alps in the absence of slab breakoff. *Terra Nova*, *31*(2), pp.120-128.

Jolivet, L. and Faccenna, C., 2000. Mediterranean extension and the Africa-Eurasia collision. *Tectonics*, *19*(6), pp.1095-1106.

Jolivet, L., Faccenna, C. and Piromallo, C., 2009. From mantle to crust: Stretching the Mediterranean. *Earth and Planetary Science Letters*, *285*(1-2), pp.198-209.

Joseph, P. and Lomas, S.A., 2004. Deep-water sedimentation in the Alpine foreland basin of SE France: New perspectives on the Grès d'Annot and related systems—An introduction. *Geological Society, London, Special Publications*, *221*(1), pp.1-16.

Jourdan, S., Bernet, M., Hardwick, E., Paquette, J.L., Tricart, P., Senebier, F. and Coeur, F., 2018. Geo-thermochronology of the Saint Antonin basin, south-eastern France. *Bulletin de la Société Géologique de France*, *189*(3).

Jourdan, S., Bernet, M., Schwartz, S., Guillot, S., Tricart, P., Chauvel, C., Dumont, T., Montagnac, G. and Bureau, S., 2012. Tracing the Oligocene-Miocene evolution of the Western Alps drainage divide with pebble petrology, geochemistry, and Raman spectroscopy of foreland basin deposits. *The Journal of Geology*, *120*(6), pp.603-624.

Jourdan, S., Bernet, M., Tricart, P., Hardwick, E., Paquette, J.L., Guillot, S., Dumont, T. and Schwartz, S., 2013. Short-lived, fast erosional exhumation of the internal western Alps during the late early Oligocene: Constraints from geothermochronology of pro-and retro-side foreland basin

sediments. *Lithosphere*, *5*(2), pp.211-225.

Kapferer, N., Mercolli, I., Berger, A., Ovtcharova, M. and Fügenschuh, B., 2012. Dating emplacement and evolution of the orogenic magmatism in the internal Western Alps: 2. The Biella Volcanic Suite. *Swiss Journal of Geosciences*, *105*(1), pp.67-84.

Kästle, E.D., Rosenberg, C., Boschi, L., Bellahsen, N., Meier, T. and El-Sharkawy, A., 2020. Slab break-offs in the Alpine subduction zone. *International Journal of Earth Sciences*, *109*(2), pp.587-603.

Kisch, H.J., 1979. Mineralogy and petrology of burial diagenesis (burial metamorphism) and incipient metamorphism in clastic rocks. In *Developments in Sedimentology* (Vol. 25, pp. 289-493). Elsevier.

Kissling, E. and Schlunegger, F., 2018. Rollback orogeny model for the evolution of the Swiss Alps. *Tectonics*, *37*(4), pp.1097-1115.

Kleboth, P., 1982. Stratigraphie und Sedimentologie der höheren Oberkreide und des Alttertiärs der Brianza (Provinz Como, Italien). *Memorie degli Istituti di Geologia e Mineralogia dell'Universita di Padova*, *35*, pp.213-292.

Koulakov, I., Kaban, M.K., Tesauro, M. and Cloetingh, S.A.P.L., 2009. P-and S-velocity anomalies in the upper mantle beneath Europe from tomographic inversion of ISC data. *Geophysical Journal International*, *179*(1), pp.345-366.

Kushiro, I., 1960. Si-Al relation in clinopyroxenes from igneous rocks. *American journal of science*, *258*(8), pp.548-554.

Lacombe, O. and Jolivet, L., 2005. Structural and kinematic relationships between Corsica and the Pyrenees-Provence domain at the time of the Pyrenean orogeny. *Tectonics*, *24*(1).

Lapierre, H., Tardy, M., Tricart, P., Feraud, G., Mascle, G.H., Stephan, J.F. and Senebier, F., 1995. Contexte géodynamique des magmatismes calco-alcalins des grès de Taveyannaz, du Champsaur et de Saint Antonin. *Magmatisme dans le Sud-Est de la France, Nice*, pp.25-26.

Lateltin, O. and Muller, D., 1987. Evolution paleogeographique du bassin des gres de Taveyannaz dans les Aravis (Haute-Savoie) a la fin du paleogene. *Eclogae Geologicae Helvetiae*, *80*(1), pp.127-140.

Lateltin, O., 1988. Les dépots turbiditiques Oligocenes d'avant pays entre Annecy (Haute Savoie) et la Sanetsch (Suisse) [Ph.D.thesis]: Fribourg. *Switzerland, University of Fribourg*.

Le Bas, M.J., 1962. The role of aluminum in igneous clinopyroxenes with relation to their parentage. *American Journal of Science*, *260*(4), pp.267-288.

Le Maitre, R.W., Streckeisen, A., Zanettin, B., Le Bas, M.J., Bonin, B. and Bateman, P. eds., 2005. *Igneous rocks: a classification and glossary of terms: recommendations of the International Union of Geological Sciences Subcommission on the Systematics of Igneous Rocks*. Cambridge University Press.

Leterrier, J., Maury, R.C., Thonon, P., Girard, D. and Marchal, M., 1982. Clinopyroxene composition as a method of identification of the magmatic affinities of paleo-volcanic series. *Earth and planetary science letters*, *59*(1), pp.139-154.

Lippitsch, R., Kissling, E. and Ansorge, J., 2003. Upper mantle structure beneath the Alpine orogen from high-resolution teleseismic tomography. *Journal of Geophysical Research: Solid Earth*, *108*(B8).

Lowe, D.R., 1982. Sediment gravity flows; II, Depositional models with special reference to the deposits of high-density turbidity currents. *Journal of sedimentary research*, *52*(1), pp.279-297.

Lu, G., Di Capua, A., Winkler, W., Rahn, M., Guillong, M., von Quadt, A. and Willett, S.D., 2019. Restoring the source-to-sink relationships in the Paleogene foreland basins in the Central and Southern Alps (Switzerland, Italy, France): A detrital zircon study approach. *International Journal of Earth Sciences*, *108*(6), pp.1817-1834.

Lu, G., Winkler, W., Rahn, M., von Quadt, A. and Willett, S.D., 2018. Evaluating igneous sources of the Taveyannaz formation in the Central Alps by detrital zircon U–Pb age dating and geochemistry. *Swiss Journal of Geosciences*, *111*(3), pp.399-416.

Lundberg, N., 1991. Detrital record of the early Central American magmatic arc: Petrography of intraoceanic forearc sandstones, Nicoya Peninsula, Costa Rica. *Geological Society of America Bulletin*, *103*(7), pp.905-915.

Lustrino, M., Fedele, L., Agostini, S., Di Vincenzo, G. and Morra, V., 2017. Eocene-Miocene igneous activity in Provence (SE France): 40Ar/39Ar data, geochemical-petrological constraints and geodynamic implication. *Lithos*, *288*, pp.72-90.

Lyu, C., Pedersen, H.A., Paul, A., Zhao, L. and Solarino, S., 2017. Shear wave velocities in the upper mantle of the Western Alps: new constraints using array analysis of seismic surface waves. *Geophysical Journal International*, *210*(1), pp.321-331.

Malusà, M.G., Danišík, M. and Kuhlemann, J., 2016. Tracking the Adriatic-slab travel beneath the Tethyan margin of Corsica–Sardinia by low-temperature thermochronometry. *Gondwana Research*, *31*, pp.135-149.

Malusà, M.G., Faccenna, C., Baldwin, S.L., Fitzgerald, P.G., Rossetti, F., Balestrieri, M.L., Danišík, M., Ellero, A., Ottria, G. and Piromallo, C., 2015. Contrasting styles of (U) HP rock exhumation along the Cenozoic Adria-Europe plate boundary (Western Alps, Calabria, Corsica). *Geochemistry, Geophysics, Geosystems*, *16*(6), pp.1786-1824.

Malusà, M.G., Guillot, S., Zhao, L., Paul, A., Solarino, S., Dumont, T., Schwartz, S., Aubert, C., Baccheschi, P., Eva, E. and Lu, Y., 2021. The deep structure of the Alps based on the CIFALPS seismic experiment: A synthesis. *Geochemistry, Geophysics, Geosystems*, *22*(3), p.e2020GC009466.

Malusà, M.G., Villa, I.M., Vezzoli, G. and Garzanti, E., 2011. Detrital geochronology of unroofing magmatic complexes and the slow erosion of Oligocene volcanoes in the Alps. *Earth and Planetary Science Letters*, *301*(1-2), pp.324-336.

Malusà, M.G., Zhao, L., Eva, E., Solarino, S., Paul, A., Guillot, S., Schwartz, S., Dumont, T., Aubert, C., Salimbeni, S. and Pondrelli, S., 2017. Earthquakes in the western Alpine mantle wedge. *Gondwana Research*, *44*, pp.89-95.

Manatschal, G. and Müntener, O., 2009. A type sequence across an ancient magma-poor ocean–continent transition: the example of the western Alpine Tethys ophiolites. *Tectonophysics*, *473*(1-2), pp.4-19.

Marsaglia, K.M., 1991. Provenance of Sands and Sandstones from a Rifted Continental Arc, Gulf of California Mexico.

Marsaglia, K.M., Johnsson, M.J. and Basu, A., 1993. Basaltic island sand provenance. *Special Papers-Geological Society of America*, pp.41-41.

Marsaglia, K.M., Taylor, B. and Fujioka, K., 1992. Petrography and provenance of volcaniclastic sands recovered from the Izu-Bonin Arc, Leg 126. In *Proceedings of the Ocean Drilling Program, Scientific Results* (Vol. 126, pp. 139-154). Ocean Drilling Program College Station.

Martin, S. and Macera, P., 2014. Tertiary volcanism in the Italian Alps (Giudicarie fault zone, NE Italy): insight for double alpine magmatic arc. *Italian Journal of Geosciences*, *133*(1), pp.63-84.

Martini, J. and Vuagnat, M., 1965. Essai de distinction mineralogique entre les termes fins du flysch helvetique. *Archives des sciences*, *18*(1), pp.114-120.

Martini, J., 1968. Etude pétrographique des Grès de Taveyanne entre Arve et Giffre (Haute-Savoie, France). *Schweizerische mineralogische und petrographische Mitteilungen*, *48*(2), pp.539-654.

Mattioli, M., Lustrino, M., Ronca, S. and Bianchini, G., 2012. Alpine subduction imprint in Apennine volcaniclastic rocks. Geochemical–petrographic constraints and geodynamic implications from Early Oligocene Aveto-Petrignacola Formation (N Italy). *Lithos*, *134*, pp.201-220.

McBride, E.F., 1985. Diagenetic processes that affect provenance determinations in sandstone. *Provenance of arenites*, pp.95-113.

McCarthy, A., Chelle-Michou, C., Müntener, O., Arculus, R. and Blundy, J., 2018. Subduction initiation without magmatism: The case of the missing Alpine magmatic arc. *Geology*, *46*(12), pp.1059-1062.

McDonough, W.F. and Sun, S.S., 1995. The composition of the Earth. *Chemical geology*, *120*(3-4), pp.223-253.

McKay, G., Wagstaff, J. and Yang, S.R., 1986. Clinopyroxene REE distribution coefficients for shergottites: The REE content of the Shergotty melt. *Geochimica et Cosmochimica Acta*, *50*(6), pp.927-937.

Mckenzie, D.A.N. and Bickle, M.J., 1988. The volume and composition of melt generated by extension of the lithosphere. *Journal of petrology*, *29*(3), pp.625-679.

McLennan, S.M., Hemming, S., McDaniel, D.K. and Hanson, G.N., 1993. Geochemical approaches to sedimentation, provenance, and tectonics. *Special Papers-Geological Society of America*, pp.21-21.

McLennan, S.M., Taylor, S.R., McCulloch, M.T. and Maynard, J.B., 1990. Geochemical and Nd-Sr isotopic composition of deep-sea turbidites: crustal evolution and plate tectonic associations. *Geochimica et cosmochimica acta*, *54*(7), pp.2015-2050.

Morimoto, N., Fabries, J., Ferguson, A.K., Ginzburg, I.V., Ross, M., Seifert, F.A., Zussman, J., Aoki, K. and Gottardi, G., 1988. *Nomenclature of pyroxenes. Mineralogical magazine, 52(367)*, pp.535-550.

Morton, A.C., 1984. Stability of detrital heavy minerals in Tertiary sandstones from the North Sea Basin. *Clay minerals*, *19*(3), pp.287-308.

Müntener, O., Ulmer, P. and Blundy, J.D., 2021. Superhydrous arc magmas in the Alpine context. *Elements*, *17*(1), pp.35-40.

Nechaev, V.P. and Isphording, W.C., 1993. Heavy-mineral assemblages of continental margins as indicators of plate-tectonic environments. *Journal of Sedimentary Research*, *63*(6), pp.1110-1117.

Nisbet, E.G. and Pearce, J.A., 1977. Clinopyroxene composition in mafic lavas from different tectonic settings. *Contributions to mineralogy and petrology*, *63*(2), pp.149-160.

O'Neill, H.S.C., 2016. The smoothness and shapes of chondrite-normalized rare earth element patterns in basalts. *Journal of Petrology*, *57*(8), pp.1463-1508.

Ori, G.G. and Friend, P.F., 1984. Sedimentary basins formed and carried piggyback on active thrust sheets. *Geology*, *12*(8), pp.475-478.

Oudet, J., Münch*, P., Borgomano, J., Quillevere, F., Melinte-Dobrinescu, M.C., Demory, F., Viseur, S. and Cornee, J.J., 2010. Land and sea study of the northeastern golfe du Lion rifted margin: the Oligocene–Miocene of southern Provence (Nerthe area, SE France). *Bulletin de la Société géologique de France*, *181*(6), pp.591-607.

Paffrath, M. and Friederich, W., 2020. *Teleseismic P-wave travel time tomography of the Alpine upper mantle using AlpArray seismic network*

data (No. EGU2020-13779). Copernicus Meetings.

Pairis, J.L., 1988. *Paléogène marin et structuration des Alpes Occidentales françaises (domaine externe et confins sud-occidentaux du subbriançonnais)* (Doctoral dissertation, Université Joseph-Fourier-Grenoble I).

Pearce, J.A. and Cann, J.R., 1973. Tectonic setting of basic volcanic rocks determined using trace element analyses. *Earth and planetary science letters*, *19*(2), pp.290-300.

Pearce, J.A., 1976. Statistical analysis of major element patterns in basalts. *Journal of Petrology*, *17*(1), pp.15-43.

Pearce, J.A., 1996. A user's guide to basalt discrimination diagrams. *Trace element geochemistry of volcanic rocks: applications for massive sulphide exploration. Geological Association of Canada, Short Course Notes*, *12*(79), p.113.

Pearce, J.A., 2008. Geochemical fingerprinting of oceanic basalts with applications to ophiolite classification and the search for Archean oceanic crust. *Lithos*, *100*(1-4), pp.14-48.

Peccerillo, A. and Martinotti, G., 2006. The Western Mediterranean lamproitic magmatism: origin and geodynamic significance. *Terra Nova*, *18*(2), pp.109-117.

Peccerillo, A. and Taylor, S.R., 1976. Geochemistry of Eocene calc-alkaline volcanic rocks from the Kastamonu area, northern Turkey. *Contributions to mineralogy and petrology*, *58*(1), pp.63-81.

Pfiffner, O.A., 2014. *Geology of the Alps*. John Wiley & Sons.

Pfiffner, O.A., Frei, W., Valasek, P., Stäuble, M., Levato, L., DuBois, L., Schmid, S.M. and Smithson, S.B., 1990. Crustal shortening in the Alpine Orogen: Results from deep seismic reflection profiling in the eastern Swiss Alps, Line NFP 20-east. *Tectonics*, *9*(6), pp.1327-1355.

Picazo, S., Müntener, O., Manatschal, G., Bauville, A., Karner, G. and Johnson, C., 2016. Mapping the nature of mantle domains in Western and Central Europe based on clinopyroxene and spinel chemistry: Evidence for mantle

modification during an extensional cycle. *Lithos*, *266*, pp.233-263.

Piromallo, C. and Morelli, A., 2003. P wave tomography of the mantle under the Alpine-Mediterranean area. *Journal of Geophysical Research: Solid Earth*, *108*(B2).

Poletti, L., Silva, I.P., Masetti, D., Pipan, M. and Claps, M., 2004. Orbitally driven fertility cycles in the Palaeocene pelagic sequences of the Southern Alps (Northern Italy). *Sedimentary Geology*, *164*(1-2), pp.35-54.

Premoli Silva, I., Tremolada, F., Sciunnach, D. and Scardia, G., 2009. Aggiornamenti biocronologici e nuove interpretazioni ambientali sul Paleocene-Eocene della Brianza (Lombardia). *Rendiconti Istituto Lombardo*.

Rahn, M., Mullis, J., Erdelbrock, K. and Frey, M., 1994. Very low-grade metamorphism of the Taveyanne greywacke, Glarus Alps, Switzerland. *Journal of Metamorphic Geology*, *12*(5), pp.625-641.

Rahn, M., Stern, W.B. and Frey, M., 1995. The origin of the Taveyannaz sandstone – Arguments from whole-rock and clinopyroxene composition. *Schweizerische mineralogische und petrographische Mitteilungen*, *75*(2), pp.213-224.

Rahn, M., Mullis, J., Erdelbrock, K. and Frey, M., 1995. Alpine metamorphism in the North Helvetic flysch of the Glarus Alps, Switzerland. *Eclogae Geologicae Helvetiae*, *88*(1), pp.157-178.

Ramos, V.A. and Folguera, A., 2009. Andean flat-slab subduction through time. *Geological Society, London, Special Publications*, *327*(1), pp.31-54.

Réhault, J.P., Honthaas, C., Guennoc, P., Bellon, H., Ruffet, G., Cotten, J., Sosson, M. and Maury, R.C., 2012. Offshore Oligo-Miocene volcanic fields within the Corsica-Liguria Basin: Magmatic diversity and slab evolution in the western Mediterranean Sea. *Journal of Geodynamics*, *58*, pp.73-95.

Ricci Lucchi, F., 1986. The Oligocene to Recent foreland basins of the northern Apennines. *Foreland basins*, pp.103-139.

Rosenbaum, G. and Lister, G.S., 2005. The Western Alps from the Jurassic to Oligocene: spatio-temporal constraints and evolutionary reconstructions. *Earth-Science Reviews*, *69*(3-4), pp.281-306.

Rosenbaum, G., Lister, G.S. and Duboz, C., 2002. Relative motions of Africa, Iberia and Europe during Alpine orogeny. *Tectonophysics*, *359*(1-2), pp.117-129.

Rosenberg, C.L., 2004. Shear zones and magma ascent: a model based on a review of the Tertiary magmatism in the Alps. *Tectonics*, *23*(3).

Ruffini, R., Cadoppi, P., D'Atri, A.R. and Novaretti, A., 1995. Ash layers in the Monferrato (NW Italy): records of two types of magmatic source in Oligocene-Miocene time. *Eclogae Geologicae Helvetiae, 88*, pp.347-363.

Ruffini, R., Polino, R., Callegari, E., Hunziker, J.C. and Pfeifer, H.R., 1997. Volcanic clast-rich turbidites of the Taveyanne sandstones from the Thônes syncline (Savoie, France): Records for a Tertiary postcollisional volcanism. *Schweizerische mineralogische und petrographische Mitteilungen*, *77*, pp.161-174.

Ruffini, R., 1995. Evidences of Tertiary volcanic activity in the Western Alps: problem and hypotheses. *Plinius*, *13*, pp.214-220.

Salimbeni, S., Malusà, M.G., Zhao, L., Guillot, S., Pondrelli, S., Margheriti, L., Paul, A., Solarino, S., Aubert, C., Dumont, T. and Schwartz, S., 2018. Active and fossil mantle flows in the western Alpine region unravelled by seismic anisotropy analysis and high-resolution P wave tomography. *Tectonophysics*, *731*, pp.35-47.

Samperton, K.M., Schoene, B., Cottle, J.M., Keller, C.B., Crowley, J.L. and Schmitz, M.D., 2015. Magma emplacement, differentiation and cooling in the middle crust: Integrated zircon geochronological–geochemical constraints from the Bergell Intrusion, Central Alps. *Chemical Geology*, *417*, pp.322-340.

Sawatzki, G.G., 1975. *Etude géologoque et minéralogique des flyschs a grauwackes volcaniques du synclinal de Thones (Haute-Savoie, France): grès de Taveyanne et grès du val d'Illiez* (Doctoral dissertation).

Schaltegger, U., Brack, P., Ovtcharova, M., Peytcheva, I., Schoene, B., Stracke, A., Marocchi, M. and Bargossi, G.M., 2009. Zircon and titanite recording 1.5 million years of magma accretion, crystallization and initial cooling in a composite pluton (southern Adamello batholith, northern Italy). *Earth and Planetary Science Letters*, *286*(1-2), pp.208-218.

Schlunegger, F. and Castelltort, S., 2016. Immediate and delayed signal of slab breakoff in Oligo/Miocene Molasse deposits from the European Alps. *Scientific reports*, *6*(1), pp.1-11.

Schlunegger, F. and Kissling, E., 2015. Slab rollback orogeny in the Alps and evolution of the Swiss Molasse basin. *Nature communications*, *6*(1), pp.1-10.

Schmid, S.M., Fügenschuh, B., Kissling, E. and Schuster, R., 2004. Tectonic map and overall architecture of the Alpine orogen. *Eclogae Geologicae Helvetiae*, *97*(1), pp.93-117.

Schmid, S.M., Pfiffner, O.A., Froitzheim, N., Schönborn, G. and Kissling, E., 1996. Geophysical-geological transect and tectonic evolution of the Swiss-Italian Alps. *Tectonics*, *15*(5), pp.1036-1064.

Schmidt, D., Schmidt, S.T., Mullis, J., Ferreiro Mählmann, R. and Frey, M., 1997. Very low grade metamorphism of the Taveyanne formation of western Switzerland. *Contributions to Mineralogy and Petrology*, *129*(4), pp.385-403.

Schoene, B., Schaltegger, U., Brack, P., Latkoczy, C., Stracke, A. and Günther, D., 2012. Rates of magma differentiation and emplacement in a ballooning pluton recorded by U–Pb TIMS-TEA, Adamello batholith, Italy. *Earth and Planetary Science Letters*, *355*, pp.162-173.

Schwab, F.L., 1986. Sedimentary 'signatures' of foreland basin assemblages: real or counterfeit?. *Foreland basins*, *8*, pp.395-410.

Schwartz, S., Guillot, S., Tricart, P., Bernet, M., Jourdan, S., Dumont, T. and Montagnac, G., 2012. Source tracing of detrital serpentinite in the Oligocene molasse deposits from the western Alps (Barrême basin): implications for relief formation in the internal zone. *Geological Magazine*, *149*(5), pp.841-856.

Sciunnach, D. and Borsato, A., 1994. Plagioclase-arenites in the Molveno Lake area (Trento): record of an Eocene volcanic arc. Trento.

Séranne, M., 1999. The Gulf of Lion continental margin (NW Mediterranean) revisited by IBS: an overview. *Geological Society, London, Special Publications*, *156*(1), pp.15-36.

Siddans, A.W.B., 1979. Arcuate fold and thrust patterns in the Subalpine

chains of Southeast France. *Journal of Structural Geology*, *1*(2), pp.117-126.

Siegenthaler, C., 1974. *Die Nordhelvetische Flysch-Gruppe im Sernftal (Kt. Glarus)* (Doctoral dissertation, Geologisches Institut der Eidg. Technischen Hochschule und der Universität Zürich).

Sinclair, H.D., 1992. Turbidite sedimentation during Alpine thrusting: the Taveyannaz sandstones of eastern Switzerland. *Sedimentology*, *39*(5), pp.837-856.

Sinclair, H.D., 1997. Tectonostratigraphic model for underfilled peripheral foreland basins: An Alpine perspective. *Geological Society of America Bulletin*, *109*(3), pp.324-346.

Solarino, S., Malusà, M.G., Eva, E., Guillot, S., Paul, A., Schwartz, S., Zhao, L., Aubert, C., Dumont, T., Pondrelli, S. and Salimbeni, S., 2018. Mantle wedge exhumation beneath the Dora-Maira (U) HP dome unravelled by local earthquake tomography (Western Alps). *Lithos*, *296*, pp.623-636.

Spakman, W. and Wortel, R., 2004. A tomographic view on western Mediterranean geodynamics. In *The TRANSMED atlas. The Mediterranean region from crust to mantle* (pp. 31-52). Springer, Berlin, Heidelberg.

Stampfli, G.M. and Hochard, C., 2009. Plate tectonics of the Alpine realm. *Geological Society, London, Special Publications*, *327*(1), pp.89-111.

Stanley, D.J., 1980. The Saint-Antonin conglomerate in the Maritime Alps: A model for coarse sedimentation on a submarine slope.

Stattegger, K., 1987. Heavy minerals and provenance of sands; modeling of lithological end members from river sands of northern Austria and from sandstones of the Austroalpine Gosau Formation (Late Cretaceous). *Journal of Sedimentary Research*, *57*(2), pp.301-310.

Stone, S. and Niu, Y., 2009. Origin of compositional trends in clinopyroxene of oceanic gabbros and gabbroic rocks: A case study using data from ODP Hole 735B. *Journal of Volcanology and Geothermal Research*, *184*(3-4), pp.313-322.

Sun, S.S. and McDonough, W.F., 1989. Chemical and isotopic systematics of oceanic basalts: implications for mantle composition and processes. *Geological Society, London, Special Publications*, *42*(1), pp.313-345.

Sun, W., Zhao, L., Malusà, M.G., Guillot, S. and Fu, L.Y., 2019. 3-D Pn tomography reveals continental subduction at the boundaries of the Adriatic microplate in the absence of a precursor oceanic slab. *Earth and Planetary Science Letters*, *510*, pp.131-141.

Tajčmanová, L., Manzotti, P. and Alvaro, M., 2021. Under pressure: high-pressure metamorphism in the Alps. *Elements: An International Magazine of Mineralogy, Geochemistry, and Petrology*, *17*(1), pp.17-22.

Tiepolo, M., Tribuzio, R., Ji, W.Q., Wu, F.Y. and Lustrino, M., 2014. Alpine Tethys closure as revealed by amphibole-rich mafic and ultramafic rocks from the Adamello and the Bergell intrusions (Central Alps). *Journal of the Geological Society*, *171*(6), pp.793-799.

Tolosana-Delgado, R., von Eynatten, H., Krippner, A. and Meinhold, G., 2018. A multivariate discrimination scheme of detrital garnet chemistry for use in sedimentary provenance analysis. *Sedimentary Geology*, *375*, pp.14-26.

Trofimovs, J., SPARKS, R.S.J. and Talling, P.J., 2008. Anatomy of a submarine pyroclastic flow and associated turbidity current: July 2003 dome collapse, Soufrière Hills volcano, Montserrat, West Indies. *Sedimentology*, *55*(3), pp.617-634.

Trümpy, R., 1980. Geology of Switzerland. A: An outline of the geology of Switzerland.

Trümpy, R., 1991. The structure of the Alps: 1891 to 1991. *Časopis pro mineralogii a geologii*, *36*(4), pp.185-192.

Ulmer, P. and Trommsdorff, V., 1995. Serpentine stability to mantle depths and subduction-related magmatism. *Science*, *268*(5212), pp.858-861.

van Keken, P.E., Hacker, B.R., Syracuse, E.M. and Abers, G.A., 2011. Subduction factory: 4. Depth-dependent flux of H2O from subducting slabs worldwide. *Journal of Geophysical Research: Solid Earth*, *116*(B1).

Venturelli, G., Thorpe, R.S., Dal Piaz, G.V., Del Moro, A. and Potts, P.J., 1984. Petrogenesis of calc-alkaline, shoshonitic and associated ultrapotassic Oligocene volcanic rocks from the Northwestern Alps, Italy. *Contributions to Mineralogy and Petrology*, *86*(3), pp.209-220.

Vermeesch, P. and Garzanti, E., 2015. Making geological sense of 'Big Data'in

sedimentary provenance analysis. *Chemical Geology*, *409*, pp.20-27.

Vermeesch, P., 2006. Tectonic discrimination diagrams revisited. *Geochemistry, Geophysics, Geosystems*, *7*(6).

Vinnels, J.S., Butler, R.W., McCaffrey, W.D. and Lickorish, W.H., 2010. Sediment distribution and architecture around a bathymetrically complex basin: an example from the eastern Champsaur Basin, SE France. *Journal of Sedimentary Research*, *80*(3), pp.216-235.

von Blackenburg, F., 1992. Combined high-precision chronometry and geochemical tracing using accessory minerals: applied to the Central-Alpine Bergell intrusion (central Europe). *Chemical Geology*, *100*(1-2), pp.19-40.

von Blanckenburg, F. and Davies, J.H., 1995. Slab breakoff: a model for syncollisional magmatism and tectonics in the Alps. *Tectonics*, *14*(1), pp.120-131.

Vuagnat, M., 1952. Pétrographie, répartition et origine des microbrèches du Flysch nordhelvétique.

Waibel, A.F., 1990. *Sedimentology, petrographic variability, and the very-low metamorphism of the Champsaur Sandstone (Paleogene, Hautes-Alpes, France); evolution of volcaniclastic foreland turbidites in the external Western Alps* (Doctoral dissertation, Doctoral thesis, Universite de Geneve, Geneva).

Wilde, S.A., Valley, J.W., Peck, W.H. and Graham, C.M., 2001. Evidence from detrital zircons for the existence of continental crust and oceans on the Earth 4.4 Gyr ago. *Nature*, *409*(6817), pp.175-178.

Wilson, M. ed., 1989. *Igneous petrogenesis*. Dordrecht: Springer Netherlands.

Winchester, J.A. and Floyd, P.A., 1977. Geochemical discrimination of different magma series and their differentiation products using immobile elements. *Chemical geology*, *20*, pp.325-343.

Yogodzinski, G.M., Brown, S.T., Kelemen, P.B., Vervoort, J.D., Portnyagin, M., Sims, K.W., Hoernle, K., Jicha, B.R. and Werner, R., 2015. The role of subducted basalt in the source of island arc magmas: Evidence from seafloor lavas of the western Aleutians. *Journal of Petrology*, *56*(3), pp.441-492.

Zanchetta, S., Garzanti, E., Doglioni, C. and Zanchi, A., 2012. The Alps in the

Cretaceous: a doubly vergent pre-collisional orogen. *Terra Nova*, *24*(5), pp.351-356.

Zhang, Y., Pe-Piper, G. and Piper, D.J., 2014. Sediment geochemistry as a provenance indicator: Unravelling the cryptic signatures of polycyclic sources, climate change, tectonism and volcanism. *Sedimentology*, *61*(2), pp.383-410.

Zhao, L., Paul, A., Malusà, M.G., Xu, X., Zheng, T., Solarino, S., Guillot, S., Schwartz, S., Dumont, T., Salimbeni, S. and Aubert, C., 2016. Continuity of the Alpine slab unraveled by high‐resolution P wave tomography. *Journal of Geophysical Research: Solid Earth*, *121*(12), pp.8720-8737.

Zuffa, G.G., 1980. Hybrid arenites; their composition and classification. *Journal of Sedimentary Research*, *50*(1), pp.21-29.

Zuffa, G.G., 1985. Optical analyses of arenites: influence of methodology on compositional results. In *Provenance of arenites* (pp. 165-189). Springer, Dordrecht.

Appendix A – Laboratory Methods

A.1 Whole rock geochemistry analysis

Whole rock samples in this study were analysed at Cardiff University. All whole rock geochemistry results and analysed external standard results are provided in Appendix E2.

A.1.1 Preparation of sample powders

All rock samples were prepared to make them into powder using the rock preparation facilities at Cardiff University. Weathered rock surfaces, veins and alteration patches were cut off using a rock saw. Samples were then crushed to a coarse size by an Mn-steel jaw crusher. Small blocks of samples of each sample were then ground to a fine powder in an agate ball mill or an agate ring-and-puck mill. Then approximately 2 g of each powdered sample was sent to an oven for two hours at 110°C to drive off molecular water, then ignited for two hours in a furnace at 900°C to drive off volatile substances and determine loss on ignition (LOI) values.

The LOI of all samples were calculated using the following equation (Equation A.1):

$$\text{LOI (wt. \%)} = \frac{Mass\ of\ dry\ powder - mass\ of\ ignited\ powder}{Mass\ of\ dry\ powder} \times 100 \quad \text{Equation A.1}$$

A.1.2 Preparation of solutions for ICP-OES and ICP-MS

Samples were prepared for ICP analysis using the lithium metaborate fusion method. To prepare the samples, 0.1 ± 0.001 g of each ignited sample was mixed with 1.0 ± 0.010 g of lithium metaborate flux in a platinum crucible. Samples were then fused using the Claisse M4 Fluxy automated fusion system. The fused melt was then dissolved in a 50 ml solution containing 20 ml of 10% nitric acid plus 30 ml of deionised water. When the glass particles had fully dissolved, 1 ml of the 50 ppm Rh spike was added to the solution which was then made up to 100 ml with deionised water. Approximately 20 ml of each solution was run on ICP-OES to obtain major element and some trace element abundances. An aliquot of 1 ml of each solution was added to 1 ml of In and Tl plus 8 ml of 2% nitric acid. The mixed solution was run on the ICP-MS to obtain trace element abundances. The instruments used at Cardiff University

are a Thermo iCAP 7000 for ICP-OES and a Thermo iCAP RQ for ICP-MS. The samples were run on the mass spectrometers by Dr. Iain McDonald.

A.1.3 Evaluation of the accuracy of analytical data

Three external standards (i.e., JB1A, JB2 and JG3) were used to assess the accuracy of the whole rock elemental data. Results of the standards are given in Appendix E2 along with relative errors of the measured values compared to certified values. The relative errors for all elements in the standards are calculated using the following equation (Equation A.2):

Relative error %=

$$\frac{Difference\ between\ measured\ and\ certified\ concentrations\ of\ element}{Certified\ concentrations\ of\ element} \text{ x100} \quad \text{Equation A.2}$$

The absolute values of relative errors (%) for most of the trace elements in JB1A are < 2 % as shown in Figure A.1, which suggests that the accuracy of trace elements analysed by ICP-MS is good. As for another two standards JB2 and JG3, the relative errors of most of the trace elements are generally < 10 %, with few exceptions having % error > 10 % as shown in the Appendix E2.

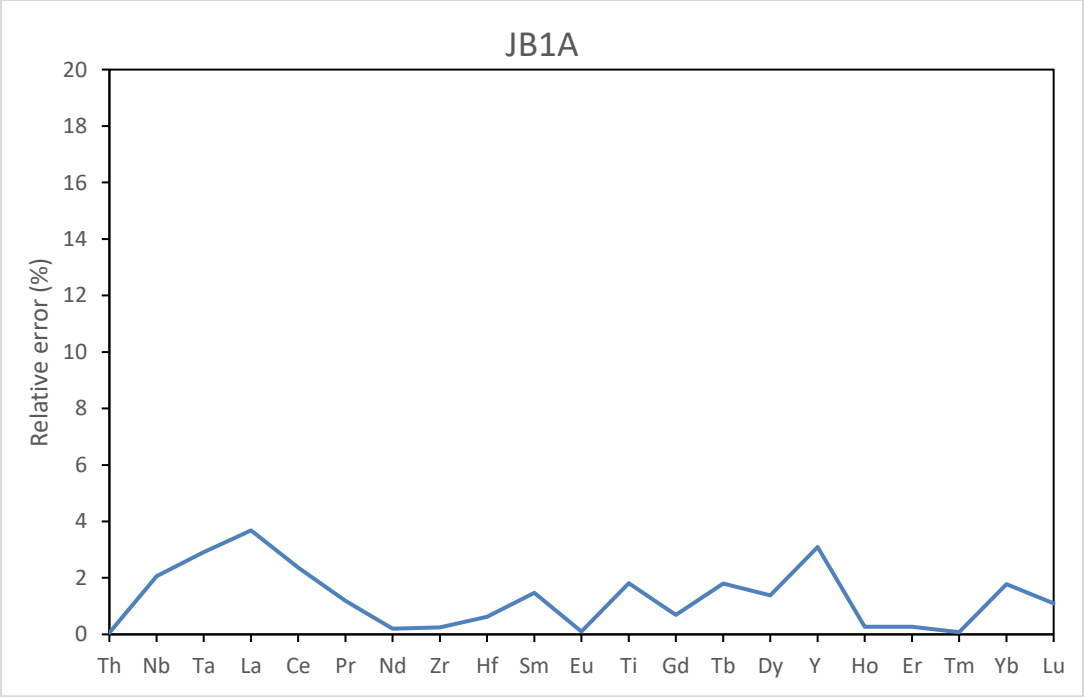

Figure A.1 Absolute values of relative errors of selected trace elements in JB1A

A.2 ASEM-EDS analysis

A.2.1 Analytical methods

Quantitative chemical analysis by Energy Dispersive Spectroscopy (EDS) on flat, polished thin sections of clinopyroxene and amphibole was carried out using a Zeiss Sigma HD Analytical Scanning Electron Microscope at Cardiff University equipped with Oxford X-Max dual 150 mm^2 silicon drift EDS detectors and Oxford Instruments Aztec software. A beam energy of 20 kV was used with a 60 µm aperture at a working distance of 8.9 mm. Each analysis takes counting time of 20 seconds. The analyses were fully standardised with elements calibrated using mineral standards from Astimex Standards Ltd and Smithsonian Microbeam Standards. Accuracy and precision were measured using repeated analysis of Augite (NMNH 122142), Chrome Diopside (Astimex) and Kakanui Hornblende (NMNH 143965). Spot analyses were used for clinopyroxenes and amphiboles. Beam drift was measured every 30 minutes using cobalt as a reference standard. SEM results and the results of analysed standards during the analysis are given in Appendix E3.

A.2.2 Evaluation of the accuracy and precision of analytical data

The results of replicate analysis of secondary standards show that elements in augite, chrome diopside and hornblende similar to those clinopyroxenes and amphiboles encountered in this study have a relative error (compared to certified values) generally < 2% for any major elements, and < 5 % for minor elements (below ~2 wt. %) (Appendix E3). Exceptions occur in elements close to their detection limit of ~0.10 wt. %, for example, 10.9 % for Mn (0.13 wt. %) in augite, 24.9 % for Al (0.30 wt. %) and 10.9 % for Cr (0.55 wt. %) in chrome diopside, and 17.7 % for Mn (0.09 wt. %) in hornblende. Overall, the relative error values show that our calibration is producing accurate data for our secondary standards.

The relative standard deviation (RSD) of the replicate analysed standards are also generally < 2 % for any major elements and < 10 % for minor elements (below ~1 wt. %) (Appendix E3). Exceptions occur in elements close to their detection limit of ~0.10 wt. %, for example, 22.8 % for Cr (0.13 wt. %) and 12.8 % for Mn (0.13 wt. %) in augite, 14.8 % for Ti (0.09 wt. %) and 13.2 % for Cr (0.30 wt. %) in chrome diopside, and 16.7 % for Mn (0.09 wt. %) in

hornblende. Thus, SEM analytical error is significantly lower than the natural variability of our samples.

A.3 LA-ICP-MS analysis

A.3.1 Analytical methods

Two batches of analysis were conducted by two different analytical instruments at Cardiff University. The first batch includes 458 clinopyroxene analyses and 7 amphibole analyses, which were conducted in 4 sessions covering 5 days. An ESI UP-213 laser ablation system coupled to a Thermo X Series 2 ICP-MS was used for the measurements. Ablation was carried out in He gas, then mixed with argon and nitrogen just before introduction into the ICP plasma. Laser ablation size of 100 µm was operated with 10 HZ pulse frequency at a fluence of ~ 3 J/cm^2. Any single measurement comprises data acquisition for 48 elements of 20 seconds of laser warmup time of total 70 seconds of duration time. To reduce potential error introduced from both sample surface contamination and instable aerosol particle distribution during the first laser shots, the first couple of seconds of each sample acquisition interval was discarded from data integration. Data being affected from inclusions of other minerals or melts were skipped from sample integration. Further data processing was done using the LAtools package which is a state-of-the-art LA-MS data processing tool, characterised by its objectivity and reproducibility. This method solved the problem that independent analysts will obtain significantly different results from the same raw data. Processed LA-ICP-MS data of clinopyroxene and amphibole are provided in Appendix E4.

The second batch includes 265 clinopyroxene analyses and 75 amphibole analyses, which were conducted in 2 sessions covering 3 days. A 193 nm Excimer laser ablation system coupled to an Agilent 8900 triple-quad ICP-MS was used for the measurements. Ablation was carried out in He gas at a flow rate of 384 ml/min, then mixed with argon and nitrogen at a flow rate of 3.4 ml/min just before introduction into the ICP plasma. Laser ablation size of 64 µm was operated with 5 HZ repetition rate at laser energy of 4.0 mJ. Any single measurement comprises data acquisition for 47 isotopes of 60 seconds of ablation time of total 120 seconds duration time. Data being affected from inclusions of other minerals or melts were skipped from sample integration. Further data processing was done using the LAtools package which is a state-

of-the-art LA-MS data processing tool, characterised by its objectivity and reproducibility. This method solved the problem that independent analysts will obtain significantly different results from the same raw data. Processed LA-ICP-MS data are provided in Appendix E4.

A.3.2 Evaluation of the accuracy and precision of analytical data

In the first batch, external calibration was done with the silicate glass standard reference material NIST SRM612 using ^{43}Ca for internal standardisation and preferred values from Jochum et al. (2011). Data obtained this way with non-matrix matched NIST-glass calibration typically has a systematic bias of the results because of different sample matrices. Thus, a second matrix-matched calibration step using a series of certified rock SRMs (BIR-1G, BHVO-2G, BCR-2G: preferred values from GeoRem online data repository) was applied. Data for replicate analyses of reference materials are compiled in Appendix E4.

The results of replicate analysis of certified rock SRMs show that all analysed elements in BIR-1G, BHVO-2G and BCR-2G have relative errors (compared to certified values) generally < 6 %. The average absolute values of relative error for all analysed elements are 4.2 % for BIR-1G (excluded abnormal U of 26.1 %), 4.8 % for BHVO-2G (excluded abnormal Pb of 51.8 %) and 1.9 % for BCR-2G. Overall, the relative error values show that our calibration is producing accurate data for the certified standards. The relative standard deviations (RSD) are generally < 10 % for all analysed elements. The average values of RSD for all analysed elements are 6.3 % for BIR-1G (excluded abnormal U of 33.6 %), 8.2 % for BHVO-2G (excluded abnormal Pb of 71.9 %) and 3.1 % for BCR-2G. Thus, the trace element analytical error is significantly lower than the natural variability of our samples.

In the second batch, external calibration was done with the silicate glass standard reference material NIST SRM612 using ^{43}Ca for internal standardisation and preferred values from Jochum et al. (2011). Replicate analysis of BHVO-2G certified standard was used as quality control. Data for replicate analyses of reference materials are compiled in Appendix E4.

The results of replicate analysis of BHVO-2G show that all analysed elements have relative errors (compared to certified values) generally < 5 %., even < 2 % for REEs. The average absolute value of relative error for all analysed element

is 3.9 % (excluded abnormal Mn for 33.5 % and Zn for 33.2 %). The relative standard deviations (RSD) are generally < 7 % for all analysed elements. The average value of RSD for all analysed elements is 4.4 % (excluded abnormal Zn of 12.5 %). Thus, the trace element analytical error is significantly lower than the natural variability of our samples.

List of Electronic Appendices

The electronic appendices containing all the data presented in this thesis are listed below:

Appendix E1 - Location and description of all collected samples

Appendix E2 - All whole-rock major and trace element data and analysed external standard results

Appendix E3 - Major element data of clinopyroxenes and amphiboles by using SEM-EDS and results of analysed external standards

Appendix E4 - Trace element data of clinopyroxenes and amphiboles by using LA-ICP-MS and replicate analyses of reference materials